KENS REPORT-XI

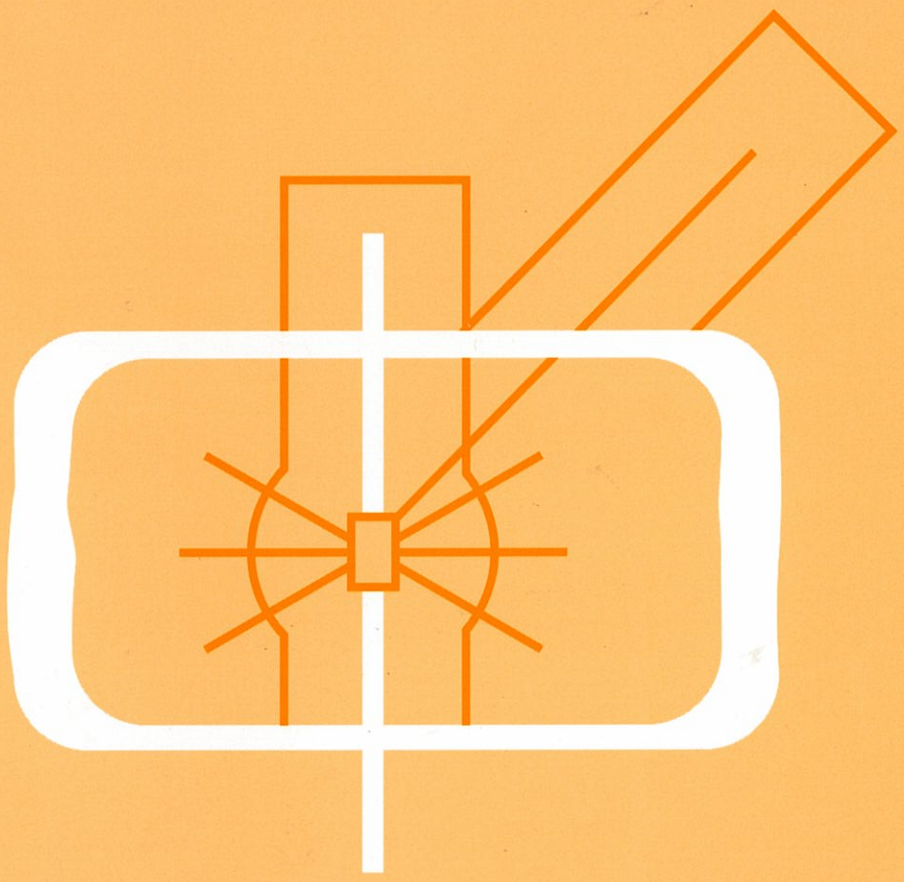

1995 / 96

NATIONAL LABORATORY FOR HIGH ENERGY PHYSICS, KEK

KENS REPORT - XI

1995/96

Edited by S. ITOH and M. ARAI

KEK Progress Report 96-4 M

KEK Reports are available from:

Technical Information & Library
National Laboratory for High Energy Physics
1-1 Oho, Tsukuba-shi
Ibaraki-ken, 305
JAPAN

Phone: 0298-64-5136
Telex: 3652-534 (Domestic)
(0)3652-534 (International)
Fax: 0298-64-4604
Cable: KEK OHO
E-mail: Library@kekvax.kek.jp
Internet: http://www.kek.jp

KENS NEUTRON SCATTERING FACILITY

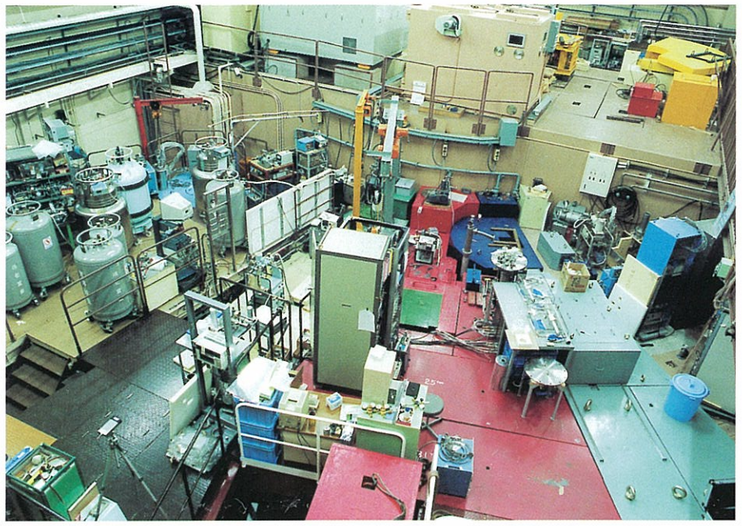

Neutron Scattering Experimental Hall B.

MAX	Coherent Inelastic Scattering Spectrometer
MRP	Medium Resolution Diffractometer under Extreme Conditions
HIT	Liquid and Amorphous Diffractometer
LAM-D	Molecular Spectrometer
FOX	Single Crystal Diffractometer
PEN	Polarized Epithermal Neutron Spectrometer
CAT	Sub-eV Spectrometer
RAT	eV Spectrometer
INC	Chopper Spectrometer
LAM-40	Quasi-elastic Spectrometer
WINK	Small and Medium Angle Scattering Instrument
VEGA	Versatile Neutron Diffractometer
HRP-II	High Resolution Powder Diffractometer-II
LAM-80ET	High Redolution Quasi-elastic Spectrometer
LAM-80cl	High Resolution Spectrometer under Extreme Conditions
TOP	Polarized Cold Neutron Spectrometer
SWAN	Small Angle Scattering Instrument

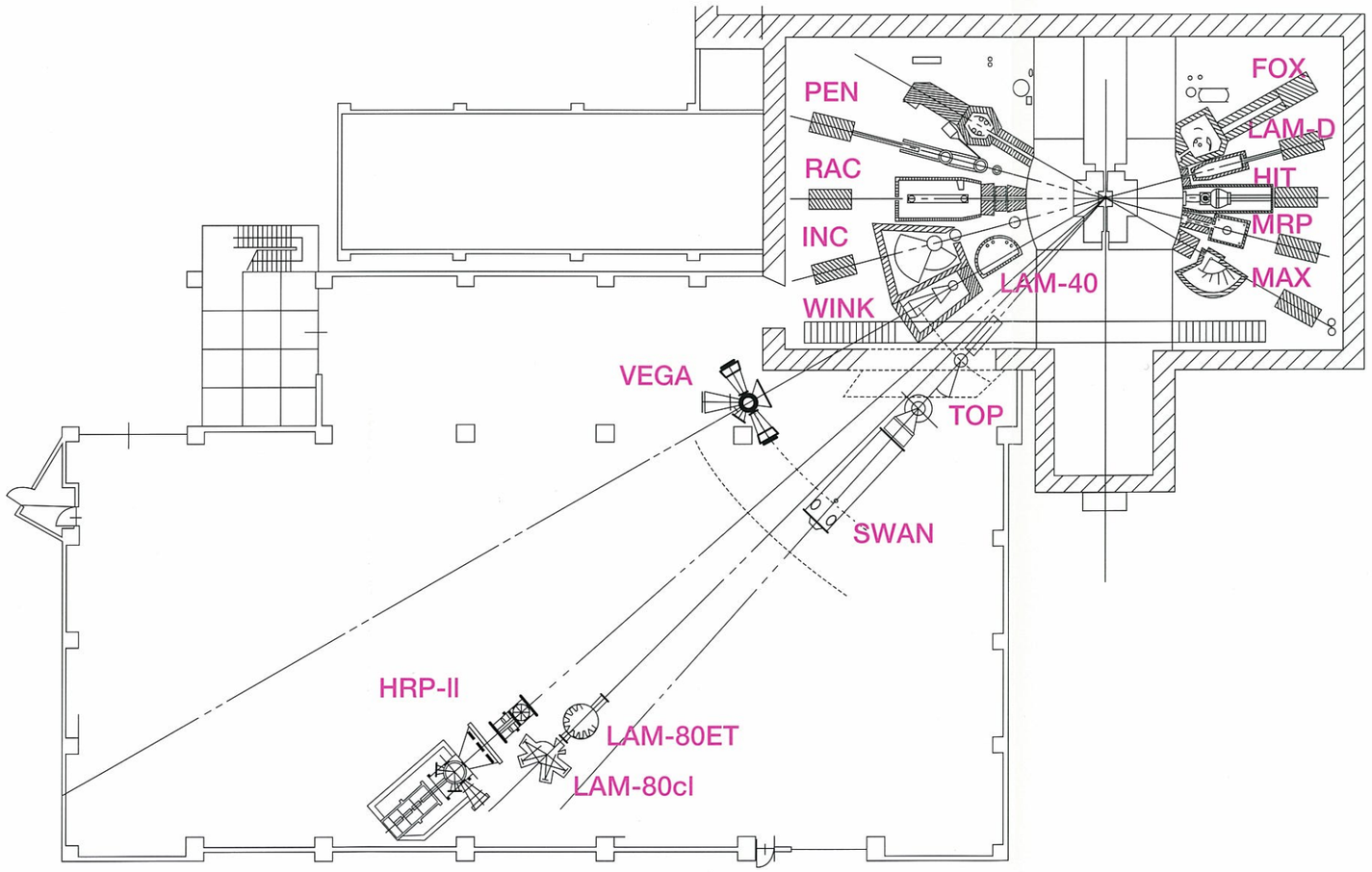

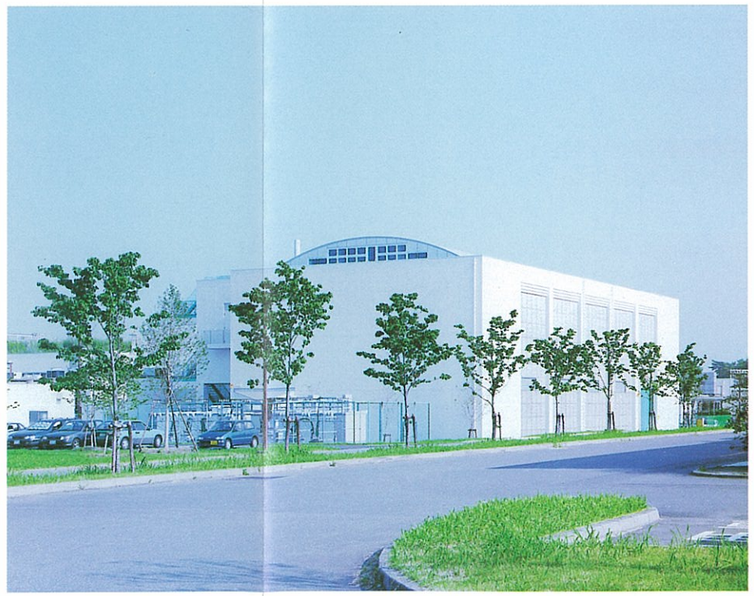

Cold Neutron Experimental Hall

PREFACE

The present issue follows a previous issue, KENS Report-X published in January 1995, and summarizes research progress at the KENS facility during the period between January 1995 and December 1996.

The new Director of the Booster Synchrotron Utilization Facility (BSF), Professor Hironobu Ikeda, took office on April 1, 1995 and this is the first issue in his service. The budget for a new cold-neutron guide hall (1400 m^2) was approved by Monbusho, and the construction was completed. In order to help advance of the scientific subjects at KENS, a new powder diffractometer (HRP-II) was installed in the new guide hall, and the spectrometers utilizing cold neutrons were reconfigured in the guide hall. Fruitful scientific results will be expected. The uranium target, which had been used over the past 10 years without any problem, revealed small leaks of ^{135}Xe, a fission product from uranium. After every installation of a new uranium target, ^{135}Xe was still detected, finally, a tantalum target was installed in the target station.

A new research organization will be established in April 1, 1997, in unification of National Laboratory for High Energy Physics and Institute for Nuclear Study, the University of Tokyo, in order to realize the Japan Hadron Project (JHP). Under the JHP, we have a project of N-arena, a neutron scattering facility with a high power pulsed spallation source of 0.6MW. The realization of the JHP has been the long time dream. In this opportunity, we introduce the new research organization and the development of the N-arena by devoting one chapter in this issue.

January 1997
Editors of KENS Report-XI
S. Itoh and M. Arai

Contents

Liquids and Glasses

Dynamics in Solids

Surface

Biology

Large Scale Structures

Magnetic Structures and Excitations

Nuclear Physics

Instrumentations

OUTLINE

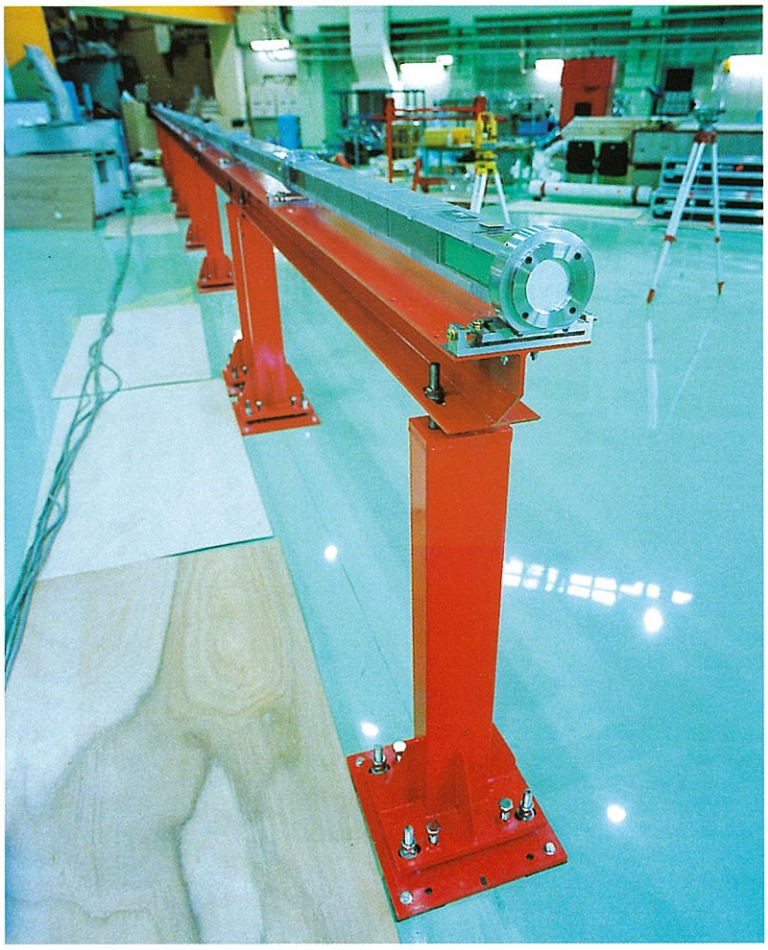

The supermirror neutron guide tube on the C3 beam line at the new cold neutron guide hall. Through the guide tube, neutrons are propagated to the new powder diffracrometer.

Overview of the Progress at KENS

H. Ikeda and S. Ikeda

National Laboratory for High Energy Physics, 1-1 Oho, Tsukuba-shi, Ibaraki 305

Outline

In the beginning of FY 1995, the beam-time of about 1500 hours was allocated to neutron scattering facility, and a total of 95 experiments were accepted. Figure 1 shows the annual variation in the number of proposals, the total and the number accepted. Here, (A) indicates the proposals for the construction or R&D of new instruments, (B1) the proposals by large user's groups responsible for the operation maintenance and improvement of the instrument, and (B2) the proposals by small user's groups. The total number is steadily increasing, while the number accepted has become saturated in recent yeas. The reasons for the saturation is due to the fact that the beam-time, total number of the instruments, and the amount of the budget for experiments and travel have not increased over several years. Figure 2 shows the share of scientific subject in the number of proposals for FY 1995. It is clear that the main part of the scientific subject is shared in crystal structure and excitations. In order to help forward these subject, the new powder diffractometer, HRP-II, was installed in the new experimental hall (see Fig.3). In the HRP-II, the higher resolution, $\Delta d/d=9\times10^{-4}$ is expected.

On July, 1995, the small amount of ^{137}Xe was found in the uranium-target cooling system which had been safely operated since 1985. It indicates that a tiny hole might be formed in a cladding of the target. On September, 1995, the target was replaced by the spare one. However, ^{137}Xe was again detected after the proton irradiation on October, 1995. On September, 1996, the new uranium target was produced and installed in the target station but ^{137}Xe was again found. Finally, the tantalum target was installed on December, 1996.

On November, 1995, the proton-irradiation on the neutron production target had been stopped because the construction of a new neutron scattering experimental hall was started on end of November. The structure of this hall is shown in Figure 4. The construction was completed on July, 1996. By this construction, the beam-time actually distributed to the neutron scattering facility was reduced up to about 1120 hours in FY 1995, and some accepted experiments could not be performed.

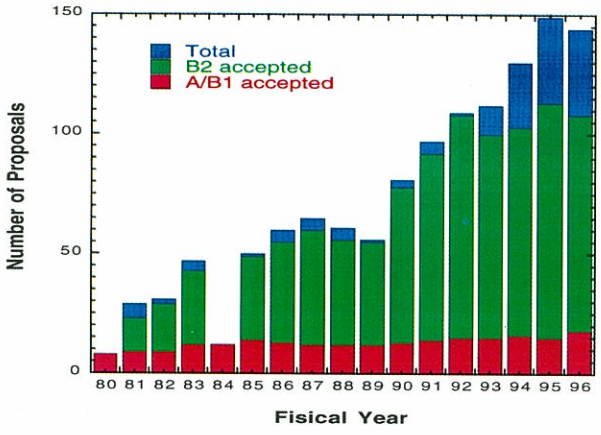

Fig.1 Annual variation in the number of proposals.

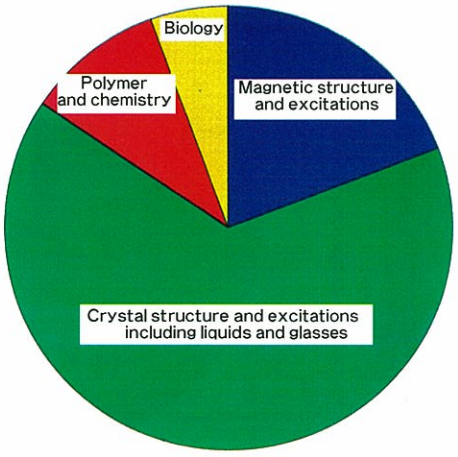

Fig.2 Share of each scientific subject regarding the number of proposals (FY1995).

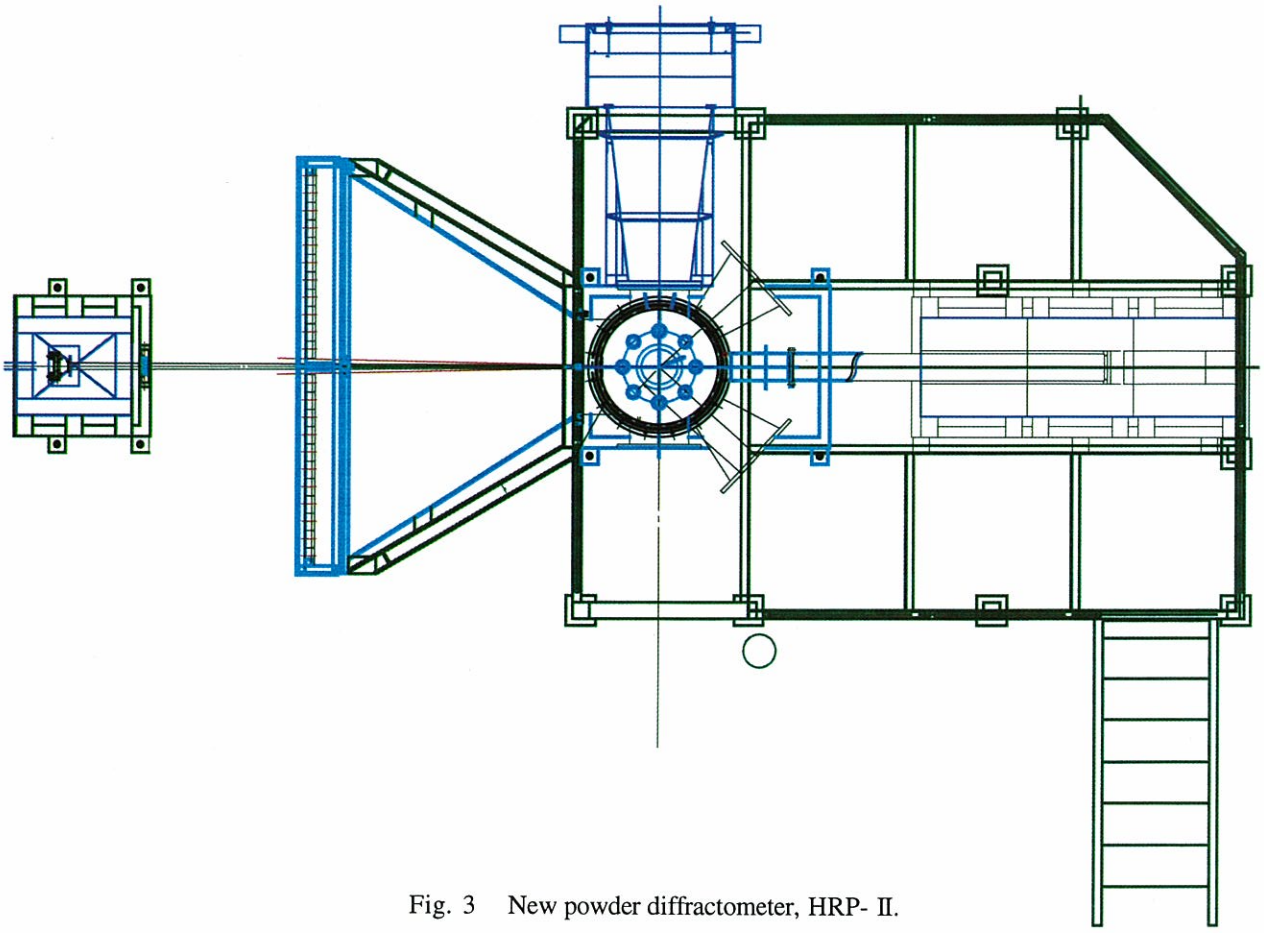

Fig. 3 New powder diffractometer, HRP- II.

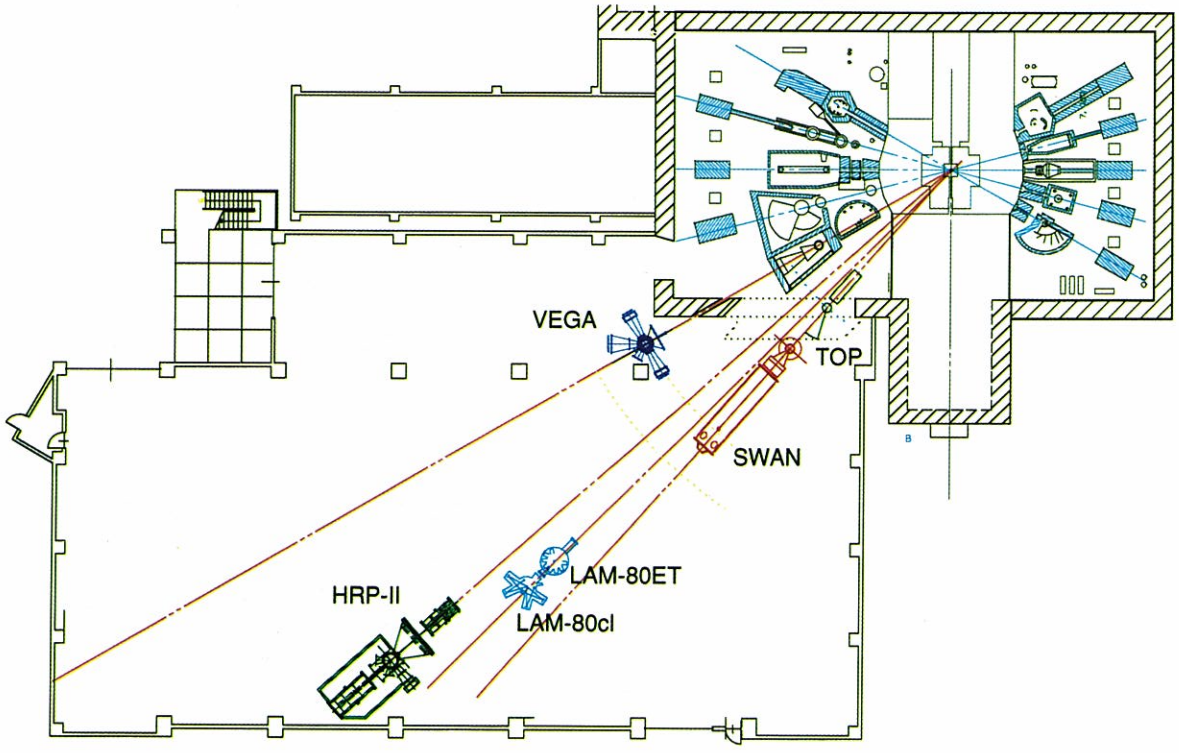

Fig.4 New cold-neutron guide hall.

Neutron Scattering Experiment

Human hair consists primarily of several fibrous proteins (*molecular weight of about* 50,000) containing α-helix, called keratin, and globular proteins (*molecular weight of about* 20,000), as shown in Fig. 5. These proteins are highly cross-linked by an intermolecular cystine bond (SS bond). This is the reason that hair shows physical properties, tough but flexible rheology, of the fibers formed with macromolecules, and shows configuration anamnesis. Therefore, the ordinal method used to permanently change the configuration anamnesis is a reduction of the SS bonds and a sequential reoxidation of the SH residues. However, reducing the SS bonds often causes an irreversible deterioration of hair, although the amount of SS bond was scarcely changed by the chemical treatment. This problem was recently clarified by scattering from chemical treated hair in deuterized water (D_2O).

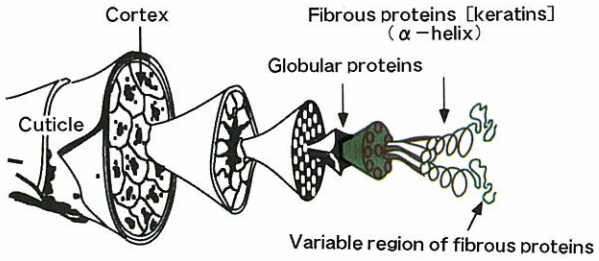

Fig. 5 Schematic diagram of human hair.

As shown in Fig.6, a chemical treatment was found to cause a penetration of D_2O into the disordered and more minute structures, thus causing a disintegration of the coagulated form. On the other hand, a new approach for permanent changes in configuration anamnesis has recently been proposed without any reduction of the SS bonds (Fig. 7). When hair was treated in deuterized propylene glycol at 120°C, it was interesting that its shape could be permanently changed, at the same time, when a chemical treatment was added to it and the scattered intensity was inversely proportional to the 4th-power of the momentum transfer (q) (Fig. 6). This relation is the typical Porod's law, and the ideal phase separation between the variable region of fibrous proteins and globular proteins was suggested to be generated by the alternation of hydrogen bonds with the treatment process.

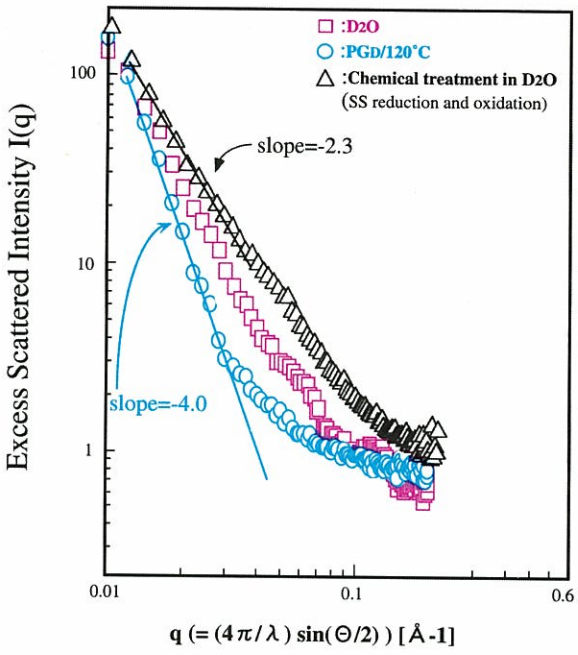

Fig.6 Neutron scattering of hair.

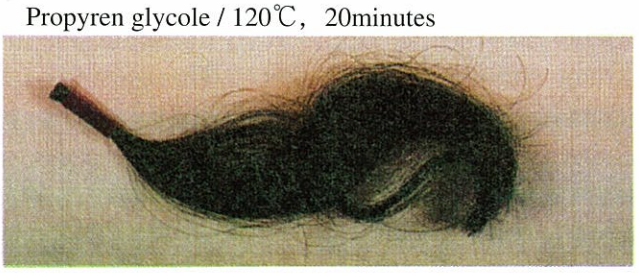

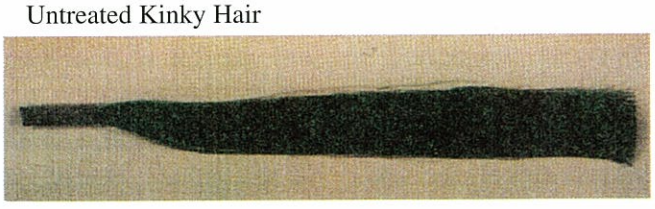

Fig.7 Permanent straight of kinky hair treated by propyren glycole at 120° C. Kinky hair was spontaneously straightened in the propyren glycole at 120° C.

UK-Japan Collaboration

In fiscal year 1995 the ISIS facility realized the goal concerning the proton current in their synchrotron accelerator. The averaged proton current during one day was more than 200 μA, which was the target value for the present machine. We all congratulate them for their great achievement.

After the uranium target failure in May, the target was replaced by a tantalum target, and has been operated throughout this year without any problem. A methane flow in the 95K-methane moderator was reversed in order to reduce a blockage due to a radio-chemical product in the moderator. This modification increased the reliability of the moderator, which has been safely operated in this year. Hence, the duty cycle of the ISIS target station was quite good, and is about 95% of the scheduled machine time of 200 days.

Fifteen Japanese experiments were performed in ISIS among 24 proposals submitted to the experimental selection panel. Most of the experiments were performed on MARI, IRIS and HRPD. The total experimental time allocated to the accepted proposal was 73 days.

One of the outstanding results were direct observation of the quantum-spin continuum in the excited states of an 1D-antiferromagnet, $CuGeO_3$, which possesses a spin-Peierls transition due to a strong spin-lattice interaction. The quantum-spin fluctuation is strong in low-dimensional S=1/2 antiferromagnet. For this system the spin-excited states are not well-known spin wave states, but are the so-called double-spinon states. The excitation spectrum becomes broad and continuous, and is surrounded by the de Cloizeaux Pearson mode at the lower boundary and by an upper boundary, which is twice in the periodicity and energy of the lower boundary. The total image of the excitation was clearly observed for the first time by taking advantage of the ability of the MARI instrument, which covers a wide range of the Q-E space in one measurement.

A second one was an observation of the anomalous diffusion in $Rb_2Co_{0.6}Mg_{0.4}F_4$. It is theoretically suggested that there is an anomalous diffusion process in the dynamics of the spin correlation in a magnet with fractal geometry. By observing the self-correlation function of the spins, (S(E)), it can assess the single-particle motion of spins. Therefore, the experiment was performed on the IRIS instrument. S(E) was obtained by integrating S(Q,E) over a wide region of Q-space. The results show that S(E) is proportional to $E^{-0.34}$, which has confirmed the fractal model described by the anomalous diffusion process.

A third one was a study on the coherent excitation of an amorphous system. It has been suggested by a Monte-Carlo computer simulation that even in an amorphous system there should be a phonon dispersion-like excitation. The observation was performed on $Ni_{67}Zr_{33}$ metallic amorphous on the MARI instrument. The preliminary results are depicted in Fig. 8. Because of the fairly low incident energy, Brillioun scattering was not in the observable range at a small momentum transfer, though a roton-like dispersion was definitely observed over a wide range of the momentum transfer. A detailed analysis of the data will contribute to a large advancement in this scientific field.

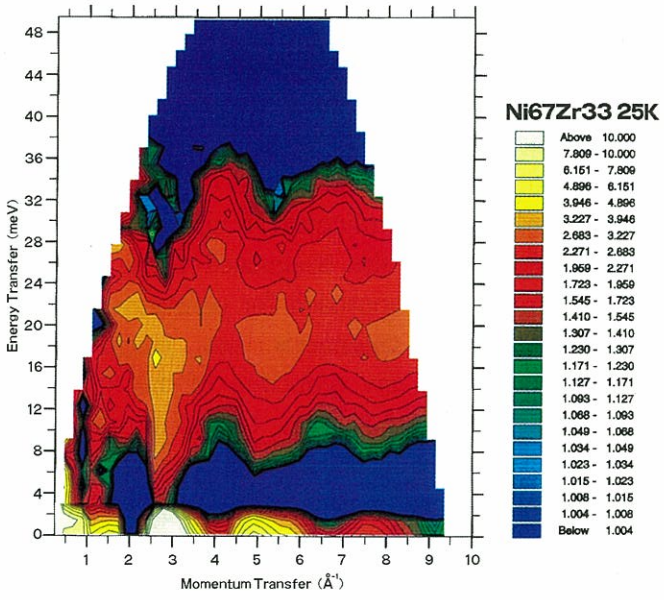

Fig.8 Phonon dispersion relation of $Ni_{67}Z_{33}$ metallic amorphous observed in $G(Q,E) = S(Q,E) \times E/Q^2$.

This year there was a review assessment on the Japan-UK collaboration by two committees in the Japan side and the UK side individually. Here, the Joint Comments are summarized:

1)The research performed under this collaboration is of very high quality and extends into many vital areas of condensed-matter research.

2)The MARI instrument built at the ISIS Pulsed Neutron Facility as a result of the Japan-UK Collaboration can be considered to be the most advanced chopper spectrometer in the world. It has enabled a number of key experiments to be performed, and has opened up entirely new areas in condensed-matter research.

3)The Japan-UK Collaboration has fostered many close scientific collaborations between the Japanese and UK neutron-scattering scientists, and has led to an intensive exchange of information and ideas on technological and technique specific issues.

On the basis of these conclusions it is recommended to:

1) Continue the operation and development of the MARI spectrometer,

2) Continue the very successful collaboration at such a level to exploit the full opportunities afforded at what is currently the world's most powerful pulsed neutron source,

3) Intensify the existing collaboration in order to respond to the increased neutron-scattering activities in Japan, and to keep Japan at the forefront of neutron scattering until a state-of-the-art spallation neutron source is realized in Japan which will fulfill the needs of the Asia-Pacific community.

Meetings

N-Arena Studies

This meeting is aimed to make a conceptual design of a pulsed neutron source for the future project. The name of the meeting is related to the neutron facility proposed in the Japan Hadron Project (JHP). Since the first meeting was held on June 11, 1993, it has been held almost every month. In the series of the meetings, the neutron source for the Japanese future project was preliminary designed and the following reports were issued:

(1) Preconceptual Design of a Target Station in Neutron-Arena of JHP (KEK Report 96-4),

(2) High-Performance Instruments in Neutron-Arena of JHP (Preliminary Version) (KEK Report 96-5).

Present and Future of Powder Diffractometry

This workshop was held on January 30 - 31, 1996, in KEK, in order to discuss on instrumentations, sample environments under extreme conditions, data analysis and recent scientific results. A new high resolution powder diffractometer to be installed in the new cold-neutron guide-hall at KENS was also introduced.

JHP-Workshop on Nuclear Physics and Fundamental Physics with Neutrons

This workshop was held on March 15 -16, 1996, in KEK, in order to discuss fundamental physics. It was noticed that the fundamental physics using low-energy neutrons can achieve important and unique progress in physics.

International Workshop on Science in Neutron-Arena of JHP

The new research organization of KEK will start from FY1997, and the organization is scheduled to start the construction of JHP, which contains the new pulsed spallation neutron facility (Neutron-Arena) with 0.6MW. This international workshop was held on March 26 - 27, 1996, in KEK, in order to discuss the scientific opportunity and merits triggered with the Neutron-Arena.

Time-Dependent Phenomena Investigated by Neutrons

This workshop was held on December 19 -20, 1996, in KEK, in order to discuss science in time-dependent phenomena. It was noticed that the intense pulsed neutron source of JHP is important to scientific interpretations of phenomena varying with real time (non-equilibrium phenomena).

Beam-line Operation and Development

Y.Yano, S.Muto, H.Fujimori, N.Kaneko, T.Tahara and Y.Kobayashi

BSF, National Laboratory for High Energy Physics, 1-1 Oho, Tsukuba-shi, Ibaraki 305

1.Summary of BSF Operation

Figure 1 is a summary of BSF operation from January, 1995 through December, 1996. Total operation time was 7,780 hours and the number of protons delivered to BSF experiments and cancer therapy was 6.6×10^{20}. Figure 2 shows the history of the average beam intensity and current delivered to the neutron and meson experiments.

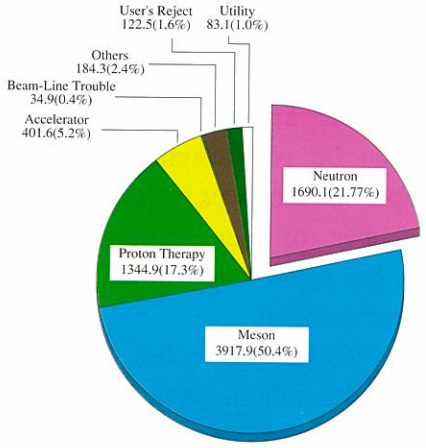

Fig. 1 Summary of BSF operation from January, 1995 through December, 1996 (units are hours).

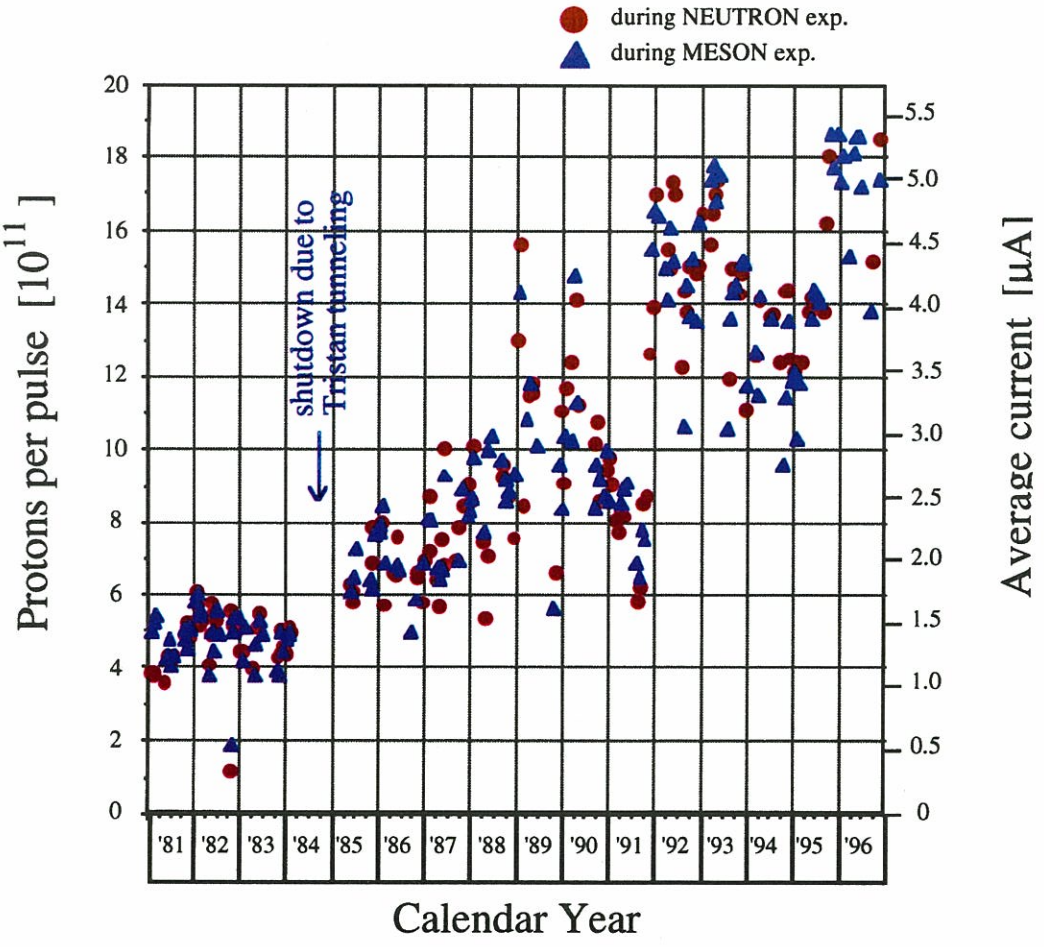

Fig. 2 Average beam intensity and current delivered to the neutron and meson experiments.

2.Instrumentation

The control system for BSF beam line has been replaced with the programmable controller (P.C.), which is produced by OMRON. The new control system consists of six P.C. , for safety control, pulsed power supply control, DC power supply control, vacumm control, steering magnet control, beam monitor control. These P.C. connected with SYSNET (produced by OMRON). Figure 3 shows P.C. and the factory computer for DDE I/O server.

Fig. 3 Programable controller for safety and the factory computer for DDE I/O server.

Human interface of this system is programed with InTouch which is an object-oriented, graphical man-machine interface (MMI) application generator. Figure 4 shows BSF status display.

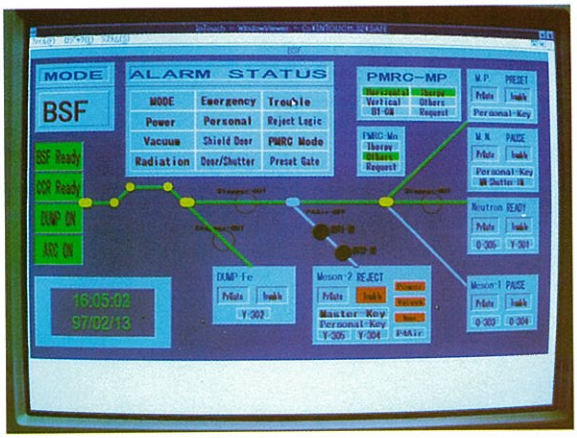

Fig. 4 Display of BSF sutatus in operation.

Figure 5 shows BSF beam line control system and data acquisition system. The data acquisition system consists of three blocks. One is taking law data and averaging the data of beam intensity, beam profile and beam loss monitor (by boad computer). Two is collecting these data (by DOS/V computer). Tree is the data server (by UNIX FreeBSD computer). The data server is connected to Ethernet for control and Ethernet in KEK. We can get an averaged beam data any time.

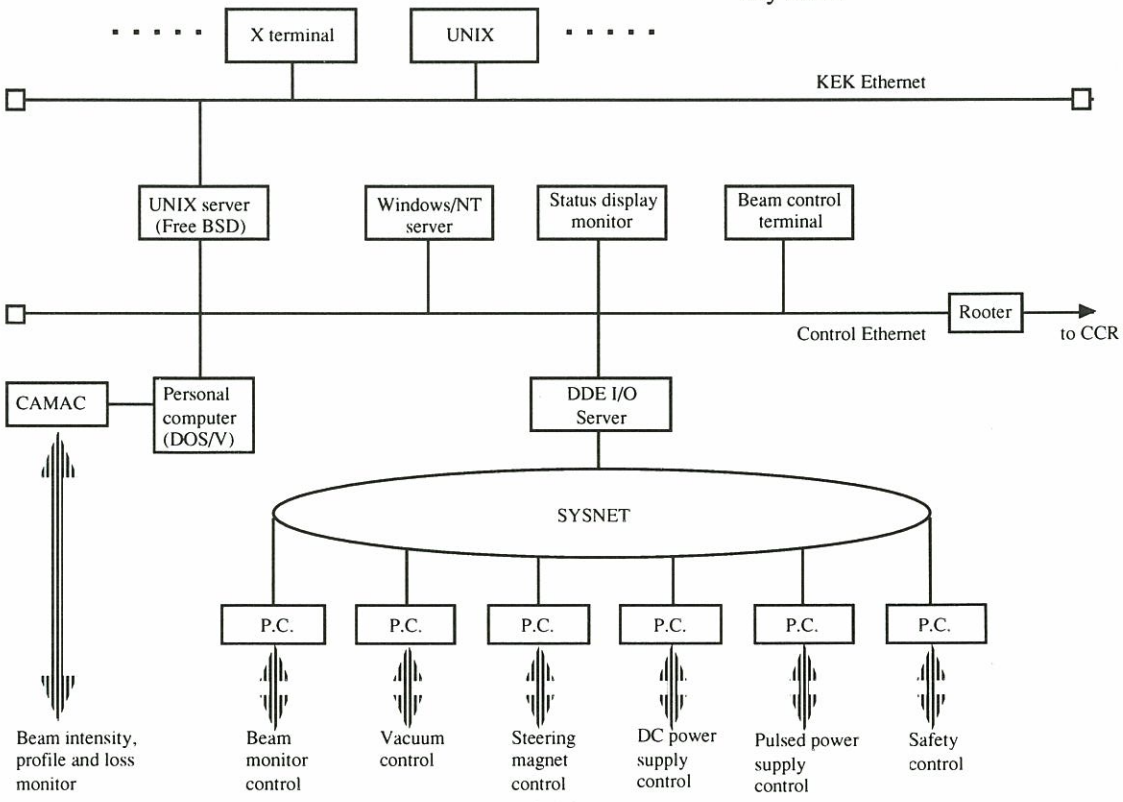

Fig. 5 Beam line control and beam data acquisition system.

FUTURE PROJECT

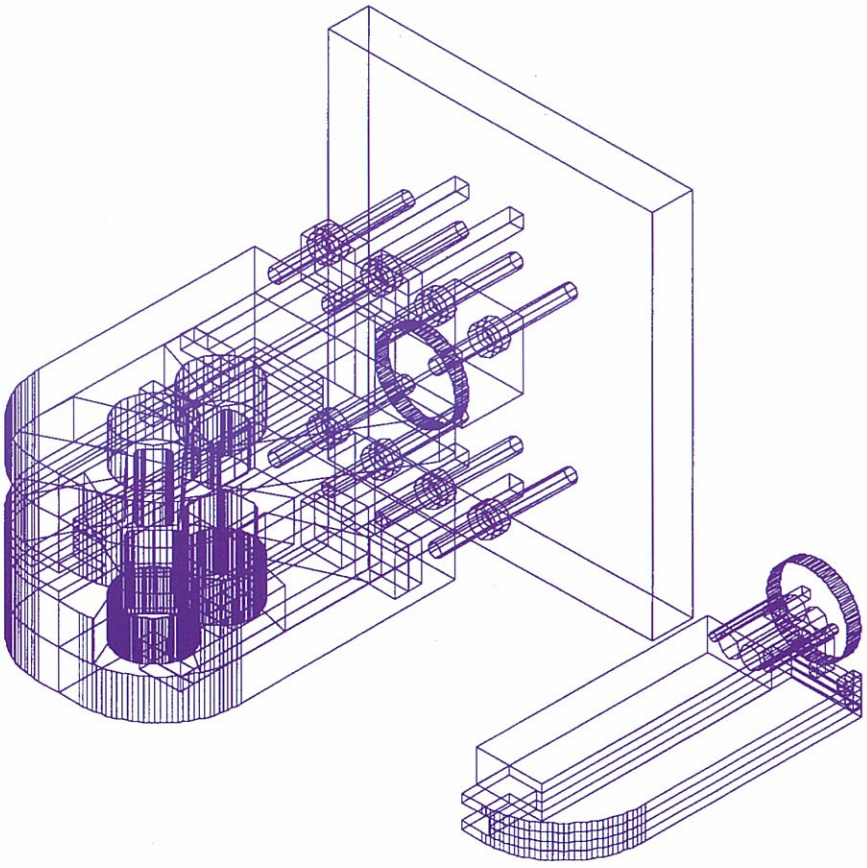

Conceptual design of the target-moderator-reflector assembly proposed in N-arena, the intense pulsed neutron facility of JHP.

JHP and the new Research Organization

Hironobu Ikeda

BSF, National Laboratory for High Energy Physics, Oho 1-1, Tsukuba 305

Japan Hadron Project (JHP) is an interdisciplinary project among particle physics, nuclear science and material science, which utilizes world-most-intensive proton beam produced by synchrotron accelerators. The Institute of Nuclear Study of University of Tokyo (INS), which has been devoting to realize JHP for a long time, will be merged to KEK in April 1997, and KEK will be re-organized to be a new Research Institute, i.e. the High Energy Accelerator Research Organization (new KEK). The neutron science facility, so called Neutron-arena (N-arena) for material research and other related science will produce intensive pulsed neutron beam by 3GeV, 200μA proton synchrotron.

The formal Committee for discussing about the future of accelerator science in Japan, which was organized in April 1995 in MONBUSHO (Ministry of Education, Science, Sports and Culture), reported the decision of establishment of new organization, mentioned above, in 30th of April 1996. It says, " Under considering the evolution of accelerator science and scientific importance in particle physics, nuclear science, meson science, synchrotron radiation science and neutron science, it is decided to have a comprehensive research institute by combining the three laboratories, i.e. KEK, INS and the Meson Science Laboratory of University of Tokyo (UT-MSL), and reform them to make continuous development of the accelerator science and lead international initiative in the related scientific field." Hence two new institutes, i.e. the Institute of Particle and Nuclear Studies and the Institute of Materials Structure Science, will be formed in the new KEK. These institutes will share the backbone accelerators in collaborative fashion with keeping independent research scheme.

The budget proposal for the new organization was sent off to the Ministry of Finance from MONBUSHO in August 1996 and approved by the government in December 1996. Under the new KEK, the Neutron Science Laboratory will be composed from four units for the neutron scattering research division and three units for the neutron target development division. (One unit contains three research staffs and one or two technical staffs.) The outline of the new organization is shown below. Total staffing at new KEK amounts to 769 full-time permanent positions.

High Energy Accelerator Research Organization (new KEK)

- Institute of Particle and Nuclear Studies
- Institute of Materials Structure Science
  - Synchrotron Radiation Laboratory
  - Neutron Science Laboratory
  - Meson Science Laboratory
- Accelerator Laboratory
- Applied Research Laboratory
  - Radiation Science Center
  - Computer Science Center
  - Low Temperature Technology Center
  - Manufacturing Center

The one of the aim of the new organization is to realize JHP, which has been a long time dream of researchers in the related scientific fields, especially neutron scientists. The accelerator complex is composed from the 200MeV proton linac, the 3GeV proton booster synchrotron and the 50GeV synchrotron. 3GeV protons of 200μA (0.6MW, 25Hz) will be supplied for N-arena (neutron arena), M-arena (meson arena) and E-arena (exotic-nuclei science arena). 50GeV protons of 10μA will be supplied for K-arena (K-on, pi-meson, anti-protons, neutrino science arena). After five-year construction, the JHP will be operational by 2003. In order to reduce the construction costs, the existing tunnel for the present 12GeV proton synchrotron and infrastructure, such as the electric power facility, the cooling water facility and so on, will be refurbished and used for JHP. Figure 1 shows the outline of the JHP.

In general it is much difficult to construct high current proton accelerators. On realizing 0.6MW proton accelerator with sharp pulse structure for JHP, it is indispensable to overcome the development of a high power ion-source and to

reduce proton beam loss as possible as can be by a well sophisticated beam control technology.

The N-arena is aimed at producing the world highest neutron flux by utilizing newly developed moderators. It is six times for thermal neutrons and 36 times for cold neutrons compared to those of the ISIS facility of the Rutherford Appleton Laboratory. Hence it is over 200 times of the present flux of the KENS facility, and a large number of fruitful scientific outputs are highly expected. In addition, for endowing further uniqueness to JHP, a possible research scheme of multi-beam experiment with using neutron, muon and synchrotron radiation, and development of high performance spectrometer are under consideration. In the N-arena more than twenty spectrometers will be installed. Those are small-angle scattering instrument, diffractometers, inelastic spectrometers, polarization analysis instruments, reflectometer and so on, which will be served for studying static and dynamic structure of materials including biological substances and basic nuclear science.

After realizing the performance of 0.6MW in the neutron source, there will be possible upgrading to 1.2MW by increasing the operational frequency of the accelerator to 50Hz. Further increase of the proton power can be achieved by improving the 200MeV lineac, which will reserve available site for this purpose. It is, however, indispensable to develop a component for high power accelerator and a new type of neutron target for high power neutron source, because even liquid metal target is not proved yet to be usable above a few MW. Those issues should be solved in the future by the related working force. Working for N-arena program is underway by the power users. The working group for scientific case is lead by Prof. Y.Endoh (Tohoku University). The working group for target station is lead by Prof. M.Furusaka (KEK) and for spectrometers by Prof. M.Arai (KEK). The cost estimation for the target station of N-arena is under way intensively for submitting the gloss budget proposal for the government by the end of FY1996.

The N-arena will be opened for the outside users after completion of the construction, and it will be also opened for international community. Hence it is important to consider the strategy of the management of the facility. KEK has been making collaboration with any foreign countries without collateral beam costs. In this sense collaborations among ICANS (international collaboration on advanced neutron sources) members, such as Rutherford Appleton Laboratory (UK), Paul Scherrer Institut (Switzerland), INR (Russia) are under way on the development of the target station etc.

The development of target station, spectrometers, sample environments and data analysis software, the decision of the strategy of the management of the facility for achieving high performance, establishing the relation between foreign countries in competing way and collaborative way and improving research environment for in-house staff, those all should be well discussed and considered among neutron community to realize JHP, which will be really an important project for continuous development of the neutron science in the next century.

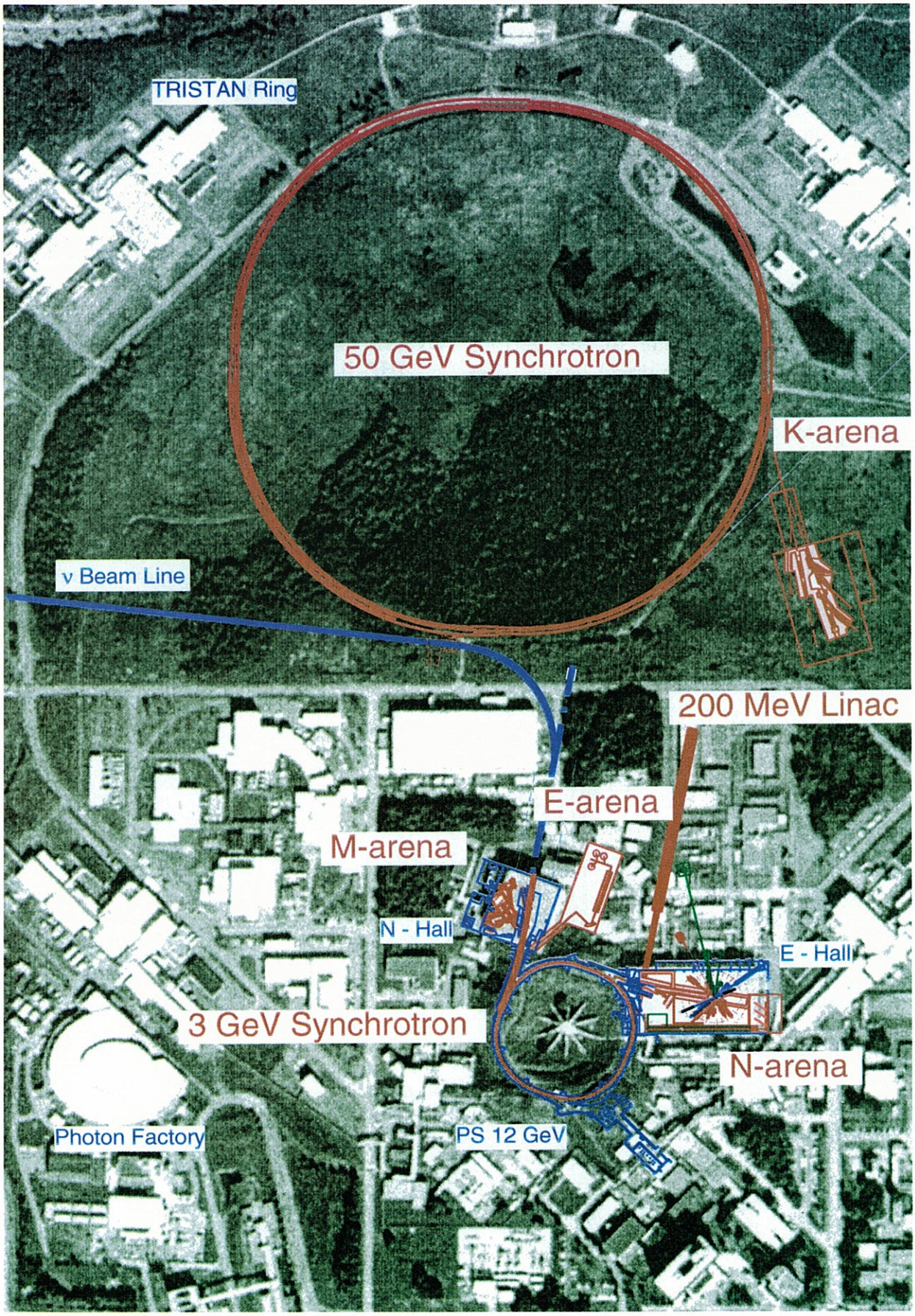

Fig.1 Layout of JHP in KEK area.

Outline of N-arena Target Station

M. Furusaka, H. Ikeda and N-arena design group

National Laboratory for High Energy Physics, 1-1 Oho, Tsukuba-shi, Ibaraki 305

Introduction

It is becoming ever more difficult to build new high-power research reactors for neutron-scattering experiments due to the various reasons, including technical issues and construction. Thus interest in the construction of pulsed spallation neutron sources (SNS) is arising around the world; EU and USA are now aiming at building megawatt-class SNSs, which have about one order of magnitude higher power than the existing SNS, ISIS in UK. Neutron Scattering Facility (N-arena) of Japan Hadron Project (JHP) is one of such projects, which is likely to take the lead to build a megawatt-class SNS.

Overview of JHP

JHP is a project based on high intensity proton accelerator complex, aiming at interdisciplinary scientific research using a variety of particles produced by the proton beam. JHP is consisting of four facilities, namely, N-arena, M-arena (meson science), E-arena (unstable nuclear beam) and K-arena (nuclear and particle physics). The layout around the N-arena is shown in Fig. 1. It is a five year project

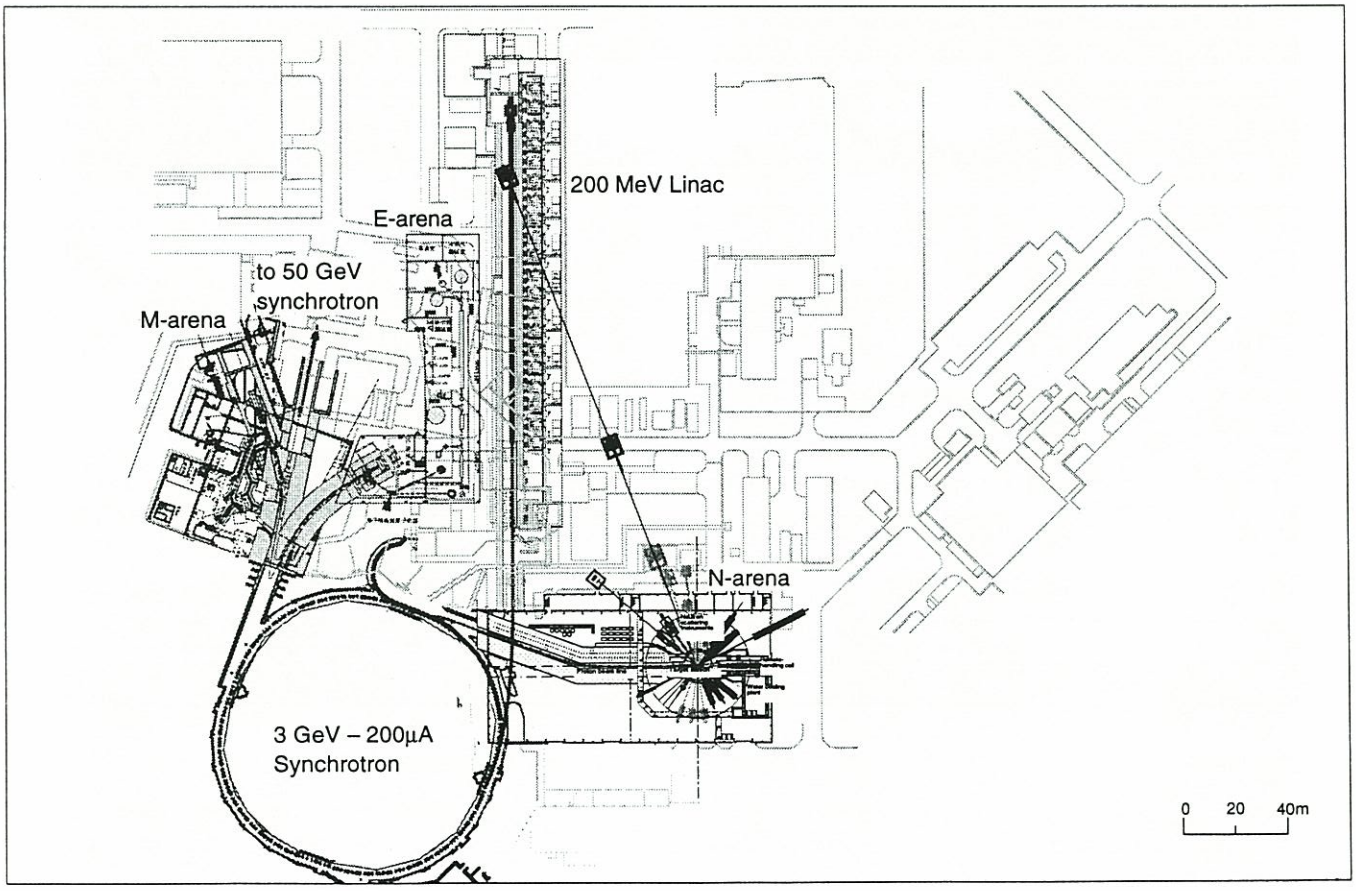

Fig. 1. Layout around N-arena.

aiming at operations of the facilities in 2003.

The accelerator complex is consisting of a 200 MeV – 400 μA linac, a 3 GeV – 200 μA (25 Hz, 0.6 MW) and a 50 GeV –10 μ A (5 MW) synchrotron accelerators. We have plans to upgrade the 3 GeV accelerator to 1.2 MW after the initial completion of JHP.

In order to reduce overall costs, 3 GeV synchrotron will be built in a tunnel currently used for a 12 GeV proton accelerator system, and a N-arena will be built in the existing East Counter Hall (50×100 m^2).

N-arena design group

A working group for designing the neutron source for the JHP (N-arena design group) was organized in 1993. The members of the group are all neutron scientists; core members are staffs of the neutron scattering facility (KENS) at National Laboratory for High Energy Physics (KEK) and others are from outside universities. In 1996, new collaborations with scientists from Research Reactor Institute of Kyoto University (KUR) and Kobe University have been started, aiming at research and development (R&D) of a high power neutron generation target and cryogenic moderators. Collaborations with some foreign laboratories have also started.

Science and instruments at N-arena

Scientific fields to be studied at N-arena had been discussed by a working group headed by Prof. Endoh and a report has been already published[1].

Neutron scattering instruments to be built are obviously important for actual scientific activity. An instrument working group has also been lead by Prof. Arai and a preliminary report has been published[2].

Conceptual design of N-arena

Roughly speaking, a high power SNS target station has following components as shown in Fig. 2 and 3 (a proton beam transport line; a

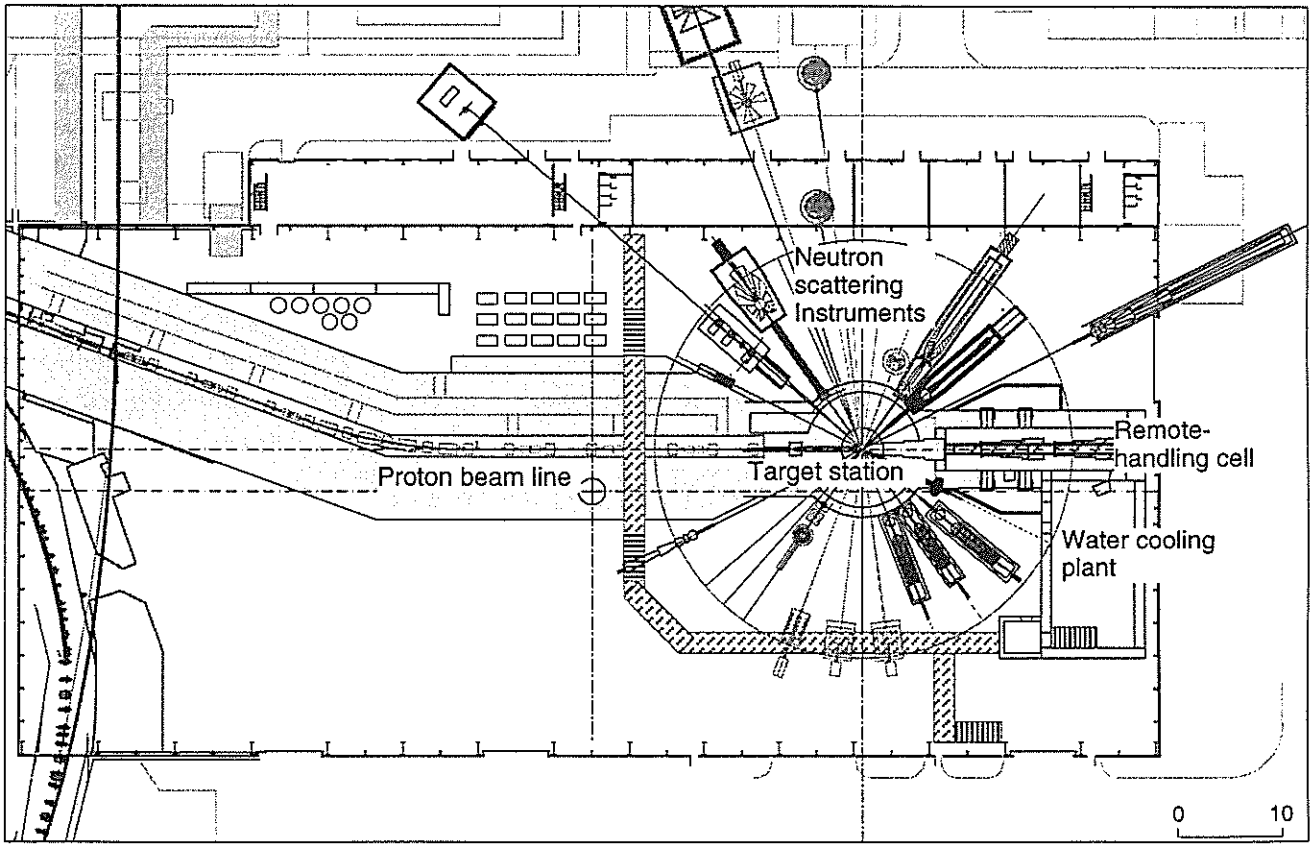

Fig. 2. Layout of N-arena experimental hall.

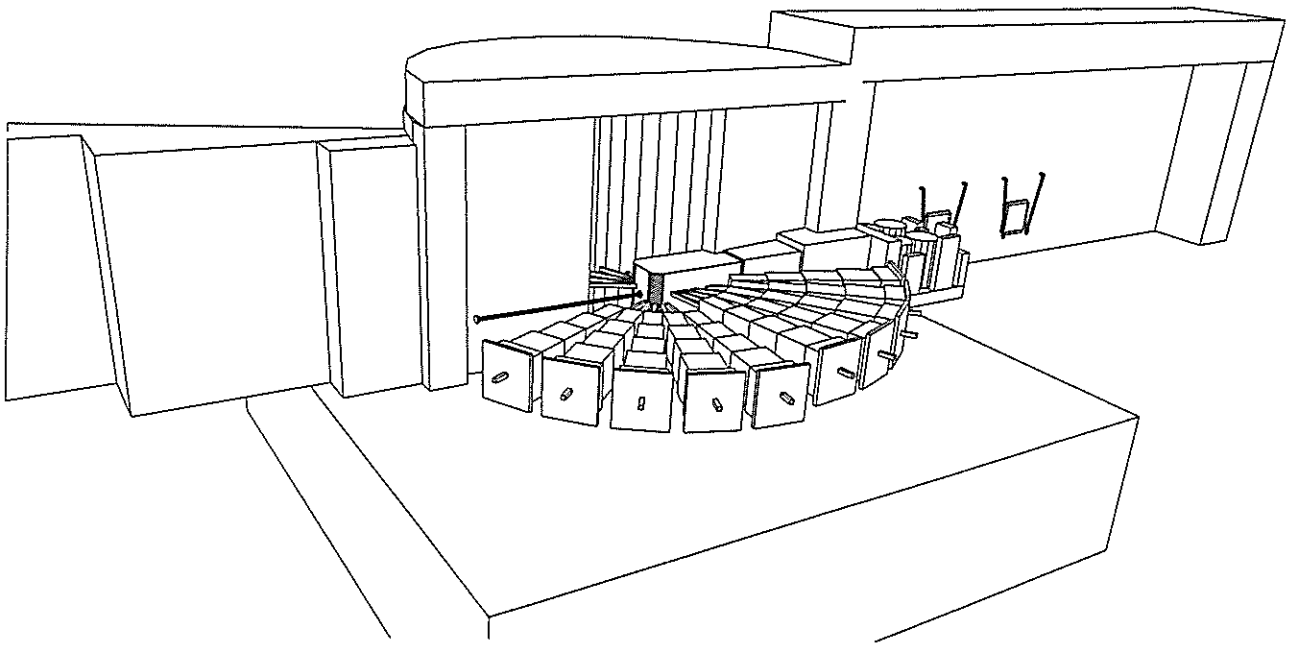

Fig. 3. A cutout view of N-arena target station.

target-moderator-reflector-assembly (TMRA) including liquid hydrogen and possibly a liquid methane moderator system; a container (He vessel) which confine the TMRA; a biological shielding made mainly of massive iron and concrete layer outside; neutron beam lines with neutron shutters which are also mainly made of iron; a remote-handling facility to maintain the TMRA; a ventilation system for the remote-handling equipment and water cooling systems for the TMRA and shielding).

A cut out view of the target station is shown in Fig. 3. The biological shield has about 6.5 m in radius, mostly made of iron blocks. The outmost layer is a shielding made of concrete with 1m thickness. Inside of the biological shield, a target-moderator-reflector-assembly (TMRA) is set on a heavily shielded target trolley. The TMRA is surrounded by a helium vessel which has width of about 1 m. When maintain the TMRA, such as replacing a target or a moderator, the trolley is extracted in the cell. Over the region of 2 m from the target, helium gas should be filled in order to avoid the induced activities. Liquid hydrogen and methane cold boxes for the moderators are also set on the trolley. The remote handling facility for maintenance of the target system is located at the downstream of the target station.

We employed rotary shutter mechanism for the neutron shutter. They are schematically shown as plugs in the Fig. 3 together with neutron flight tubes. Some of the plugs will accommodate a few bunched guide tubes. In total, nearly twenty plugs will be implemented and nearly 30 instruments will be installed eventually.

One of the key components of the target station is the target itself; as the incoming power of proton beams is nearly one megawatt, heat density generated in the target becomes enormous and almost come to the limit of water cooling technology. Moreover, from a neutronics-performance point of view, a target should be very compact to make coupling between the target and moderators tight enough. Therefore, it is very hard to design the target.

As the first step of the design of a target, we decided to construct a solid-metal target which we will be able to build by using current technologies. For the target beyond a megawatt, in the second stage of JHP, we will employ liquid-metal target. We have just started research and development (R&D) of solid-metal target, in collaborating with outside experts. We do not discard a possibility of using liquid metal target,

such as lead-bismuth or mercury, even for sub-megawatt power; we are now starting the R&D for a liquid-metal target system.

Parameters of the other components are almost determined by a radiation protection point of view; the thickness of the biological shielding is determined by radiation level outside of the shielding as well as the level at site boundaries, and activation of soil and underground water below the target station. We have to confine induced activities inside of the target station, such as activated argon-41 in the atmosphere and so on. Tritium and beryllium-7 production by spallation reaction of target cooling water is another important issue. A remote handling facilities are necessary for the maintenance of the TMRA.

The main difficulties of the conceptual design is to find the best and a consisting way of building a target station, which can safely confine the radio active materials and safely maintain the TMRA. Since many components are correlated in a very complex manner, it is not a trivial task. For example, the TMRA and its cooling plants should be extracted to the remote-handling cell to maintain them. Thus, there should be seals between many components such as the TMRA, the helium vessel, the biological shielding, neutron beam flight tubes and neutron shutters. Furthermore the pipings between the TMRA and the cooling circuits have to be remotely disassembled by the remote-handling facilities.

We have almost finish construction of a conceptual model which can be regarded as a basis of cost estimation. Of course this is just the starting point of the conceptual design; Basic neutronics calculations to backup the design are now underway. LAHET Code System (LCS) has been installed and neutronics calculations are being performed, such as an estimation of neutron flux, a heat generation in various components, a shielding calculation and so on.

Other subjects to be considered are how to evacuate and reuse the experimental hall currently used for nuclear physics experiments. A part of the floor of the hall has induced activities due to the targets, beam dumps of current facilities. To avoid unnecessary exposure to radiation during construction of N-arena target station, we have to locate the target station almost at the east end of the hall.

R&D of high-performance TMRA

Continuing efforts to develop a better TMRA system is undergoing, mainly at Hokkaido university using an electron linac.

Last year, further optimization studies for a coupled liquid hydrogen moderators and reflector studies for short pulse thermal neutrons have been performed, as well as very fundamental studies on low energy neutron spectra far below the Maxwellian peak. Neutronic studies on the target are also undergoing. A new type of cold moderator will be examined near future. The detailed descriptions of some of them will be found in the following report.[4)]

Beamline

The design work of the proton beam line components as well as beam transport calculation is underway. Since we have to reuse the existing counter hall, the radiation level produced by a beam loss of the proton beam transport should be within a certain limit; activation of soil and underground water should be negligible. Normally, beam loss of such beam transport system is an order of a percent of main proton beam current per 100 m. In order to meet such requirements, we have to reduce the level to 10^{-4}/100 m, which is not so easy to realize. We are now assuming that the apertures of a beam-transport line to be 150 mmϕ.

References

1) Ed. M. Furusaka and Y. Endoh, KEK Report 95-19 (1995) (In Japanese).
2) Ed. M. Furusaka, S. Itoh, T. Otomo and Y. Kiyanagi, KEK Report 96-4 (1996) (In Japanese).
3) Ed. M. Furusaka, S. Itoh, T. Otomo and M. Arai, KEK Report 96-4 (1996) (In Japanese).
4) Y. Kiyanagi, Y. Ogawa, H. Kuramoto, J. Kanbara, M. Furusaka and N. Watanabe, this report.

Current status of neutronic studies on the target-moderator-reflector assembly for N-arena

Y. KIYANAGI, Y. OGAWA, H. KURAMOTO, J. KANBARA, M. FURUSAKA* and N. WATANABE**

Division of Quantum Energy Engineering, Faculty of Engineering, Hokkaido Univ., Sapporo 060
*National Laboratory for High Energy Physics, 1-1 Oho, Tsukuba-shi, Ibaraki 305
**Japan Atomic Energy Research Institute, Tokai-mura, Ibaraki 319-11

1. Introduction

We have been extensively studying neutronics of target-moderator-reflector assemblies(TMRA) for JHP N-arena. We studied optimal hydrogen thickness for a coupled liquid-hydrogen moderator and found the optimal is about 5 cm [1]. We also examined a narrow beam extraction, a Be reflector-filter and grooved surface moderator to increase cold neutron intensity from a coupled liquid-hydrogen moderator system[1][2]. We studied some methods to improve pulse characteristics of a coupled liquid-hydrogen moderator for neutron scattering experiments which need short pulses and it was found that the premoderator decoupling is one of the most effective methods [3].

Here, we report succeeding works about low energy neutron spectra, further optimization studies for a coupled liquid hydrogen moderator and reflector studies for short pulse thermal neutrons.

2. Moderator neutronics -Low energy spectrum-

Precise determination of the incident neutron spectrum is important in time-of-flight (TOF) neutron scattering experiments utilizing white beams. The statistics of a measured spectrum at lower energies far below the Maxwellian peak is usually rather poor and the spectrum is not Maxwellian which is simply characterized by an effective neutron temperature. When we obtain the scattering function from a scattering data, a reliable and smoothed incident neutron spectrum is indispensable for data correction. Therefore, we usually fit a measured incident neutron energy spectrum by a modified Maxwellian of the form,

$$M(E)=P1*E^{**}P3 \exp(-E/P2),$$

where E is the neutron energy and P1, P2 and P3 are the fitting parameters. In the case of a Maxwellian spectrum, P3 is 1, but usually not 1. The deviation of the value of P3 from 1 is important, which gives a measure of the deviation of the spectrum from a Maxwellian at lower energies. For instance, recently we are interested in VCN (very cold neutron) as source neutrons for ultra cold neutrons. The intensity of VCN from a cold neutron moderator strongly depend on the value of P3. If P3 is considerably larger than 1, the decrease in intensity in the VCN region becomes tremendous compared to a Maxwellian like case.

As far as we know the mechanism of such spectral depression has not been well understood. In order to obtain a better understanding on this phenomenon, we started systematic measurements on cold neutron spectra from various moderators. In the present note we report preliminary results on these measurements.

2.1 Experimental

As a first step we measured three different cold moderators; decoupled liquid hydrogen and solid methane at 18 K, and coupled liquid-hydrogen with premoderator. In all cases the dimensions of the cryogenic moderators are 12 cm x 12 cm x 5 cm thick. Figure 1 shows measured spectra after necessary corrections. Dotted curves show fitted results using a modified Maxwellian mentioned above. The values of fitted parameters P1, P2 and P3 are shown in the boxes of the same figure. The

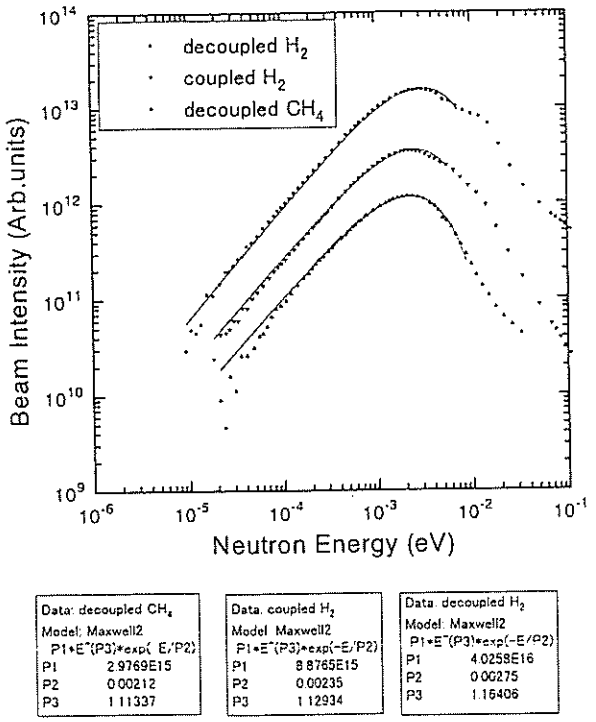

Fig. 1 Energy spectra from three different types of cold moderators.

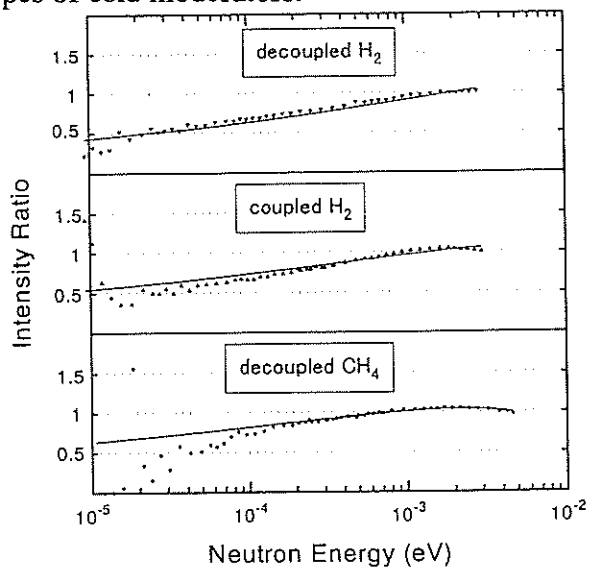

Fig. 2 Intensity ratios of observed data to Maxwellian fits for cold moderator spectra.

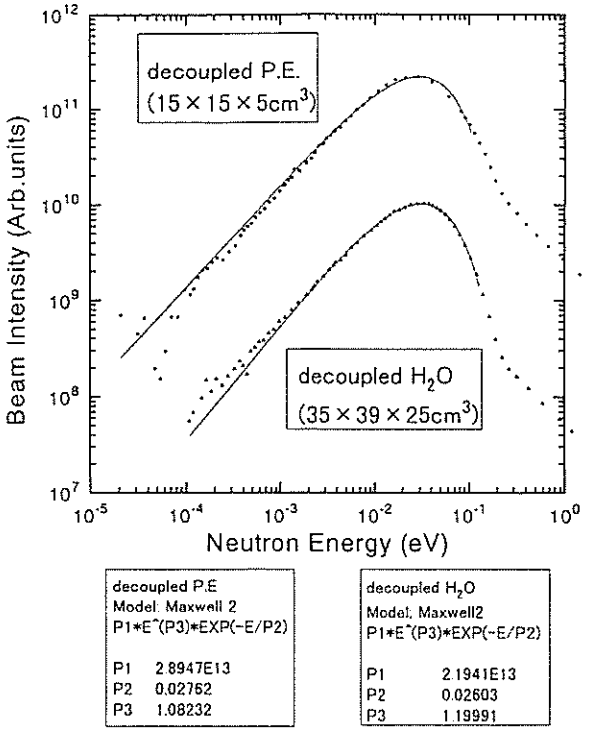

Fig. 3 Energy spectra from two different types of thermal moderators.

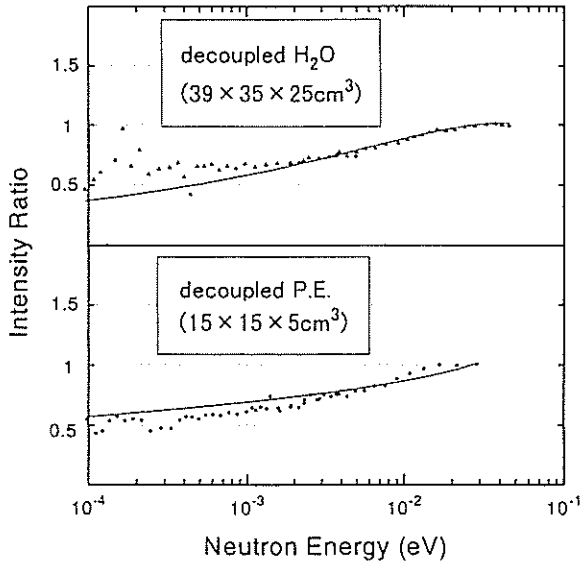

Fig. 4 Intensity ratios of observed data to Maxwellian fits for thermal moderator spectra.

fitting looks reasonably good except for a higher energy part above 14 meV, where it is well known that a hump appears due to a sudden change in hydrogen cross section. Figure 2 shows the deviation from a Maxwellian of the same characteristic temperature to the measurement as a ratio of measured spectrum to the Maxwellian normalized at the Maxwellian peak. The solid curves are the results of modified Maxwellian fits. The intensities at about 0.02 meV, about two orders of magnitude lower energy from the Maxwellian peak, are almost 50% of the ideal intensities assuming normal Maxwellians. In the case of the decoupled solid methane moderator, a remarkable deviation is seen below 0.1 meV although the statistics are not adequate. At the present stage the reason is not clear, but it may

be due to a different energy transfer mechanism in solid methane. In the case of liquid-hydrogen the major energy transfer mechanism at very low energies is hydrogen diffusion, while in the case of solid methane there is no such mechanism.

In order to investigate the origins of such a deviation from normal Maxwellian spectrum, we performed further experiments with room temperature moderators. Two decoupled light water moderators of different sizes, 15 cm x 15 cm x 5 cm and 39 cm x 35 cm x 25 cm, were examined. The results of the spectral measurements are shown in Fig.3. The fits by modified Maxwellians look good except for the epithermal region where 1/E spectrum takes over the Maxwellian. The fitted parameters are shown in the boxes under the spectra. Intensity ratios to normal Maxwellian spectra are shown in Fig.4. The intensities at about 0.2 meV, about two orders of magnitude lower energy from the Maxwellian peak, are again about 50% of the ideal intensities assuming normal Maxwellian.

2.2 Discussions

In all moderators we studied, we observed a considerable spectral deviation from a normal Maxwellian spectrum at low energies. We considered following possible origins for such spectral deviations at low energies;

(1) imperfect data corrections, especially for low energy neutron attenuation between moderator and detector and for the detector efficiency at low energies;

(2) effect of considerably larger absorption cross section at low energies;

(3) different energy exchange mechanism for different moderator material;

(4) moderator size effect;

(5) leakage neutron spectrum from moderator viewed surface, not stored neutron spectrum inside the moderator;

(6) time average spectrum before reaching the thermal equilibrium due to a finite energy exchange cross section;

Roughly speaking, we obtained almost the same values of P3 for the same moderator temperature, in spite of different moderator materials and different moderator sizes. This result will rule out the assumed origins (3) and (4). If the effect of (1) is dominant, we cannot explain the drastic difference between the spectra in Figs.1 and 3. At the moment we are thinking that the origins (5) and (6) are most likely. Further investigations are in progress.

3. Further efforts for increasing cold neutron intensity with coupled liquid-hydrogen moderators

For more than several years we have been studying a coupled composite moderator system consisting of liquid-hydrogen and premoderator at ambient temperature. Various efforts have been devoted for increasing both time integrated and peak intensities. Among the various tests we performed, following two cases were successful for increasing intensity [1][3];

(1) Narrow beam extraction; partial enhancement of the intensity by masking a remaining viewed surface with an additional premoderator [1];

(2) Grooving the viewed surface of liquid-hydrogen [2].

However, the intensity gains obtained by these methods were not large; only 15-40%. Our conclusion at the present time is that further intensity gain is very difficult to achieve. For example, for increasing cold neutron intensity, it is well known that a cooled Be reflector-filter located in front of the viewed surface is very effective [4]. However, our measured result with a 1.5 cm cooled Be did not show such a remarkable gain. We think this is due to the fact that the system is already close to an ideal. Since the thickness of the Be reflector-filter we examined in the previous experiment [1] was rather thin, this time we performed similar measurement with a thicker Be (4 cm). The measured spectral intensity is shown in Fig.5 with previous result. It is found that again there is no gain at all in cold neutron intensity. While in the thermal neutron region, there are considerable intensity gains for both thickness. We did not expected such gains above Be cut-off energy (about 5 meV): This result is very

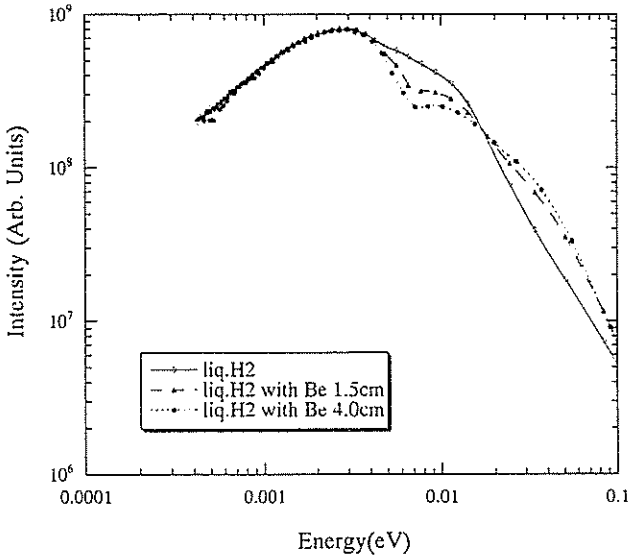

Fig. 5 Energy spectra from coupled liquid-hydrogen moderators with and without Be reflector-filter.

unusual. This is probably due to the reason that thermal neutrons escaping from the viewed surface will be reflected back into liquid hydrogen which may provide a small gain in cold neutron intensity, while thermal neutrons which originally enter into liquid hydrogen from the reflector through the viewed surface will be eliminated by the Be reflector-filter, resulting in the decrease in gain. The overall gain in cold neutron intensity is just unchanged by the cancellation of both effects. The intensity hump above Be cut-off would be thermal neutrons scattered by the Be reflector-filter. This is consistent with the explanation mentioned above. Although this method is null for increasing cold neutron intensity, the observed phenomenon is very interesting.

We are continuously studying a coupled composite moderator system consisting of a grooved cryogenic moderator and premoderator. We already obtained a reasonably large gain at longer wavelengths with a grooved hydrogen [2]. However, how to realize such a complicated shape at an intense spallation source would be an another important issue. A narrower angular coverage of this type of moderator due to the existence of the side-premoderator would be a demerit. However, the intensity decrease by shortening side-premoderator for ensuring a reasonable angular coverage would be small. Detailed consideration on this is another issue.

4. Reflector studies for a short thermal neutron pules moderator

The choice of the optimal size and material for the reflector depend on the size and material of the target, the moderator and the target-moderator coupling method.

As a bench mark experiment in the first step, we started experiments with room temperature H_2O moderators in two different reflectors, graphite and iron, for two cases of coupled and decoupled systems. The size of the moderator was 10 cm x 10 cm x 4.5 cm and those of the reflectors were about 80 cm x 80 cm x 80 cm. Decoupling energy of a B_4C decoupler was about 2-3 eV. We were interested in whether a coupled moderator at room temperature in an iron reflector can take over the performance of a decoupled moderator in a graphite reflector.

The results on time integrated thermal neutron intensities from the coupled and the decoupled moderators in the iron reflectors are compared with the result from the decoupled moderator in the graphite reflector in Fig. 6. The thermal neutron intensity from these three

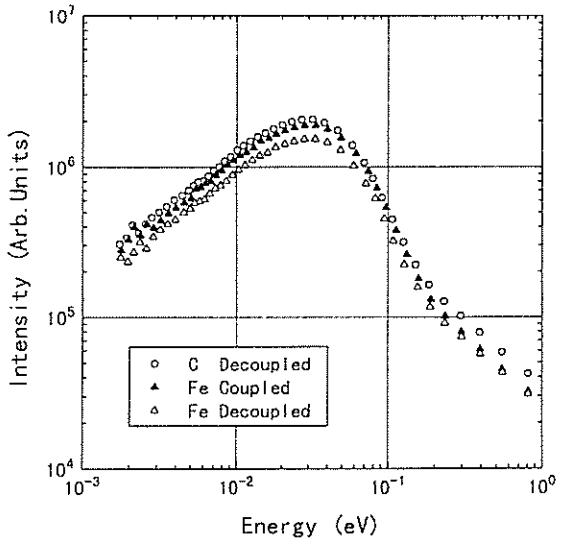

Fig. 6 Energy spectra from water moderators in a coupled and a decoupled Fe reflectors and a decoupled C reflector.

moderators are approximately the same. Then we measured the pulse shapes of thermal neutrons and the results are shown in Figs.7 and 8. The pulse shape from the coupled moderator in the iron reflector looks to be almost the same to that from the decoupled moderator in the graphite reflector in the linear plots. However, in the semi-logarithmic plots, there exists a finite difference in the die-away tails.

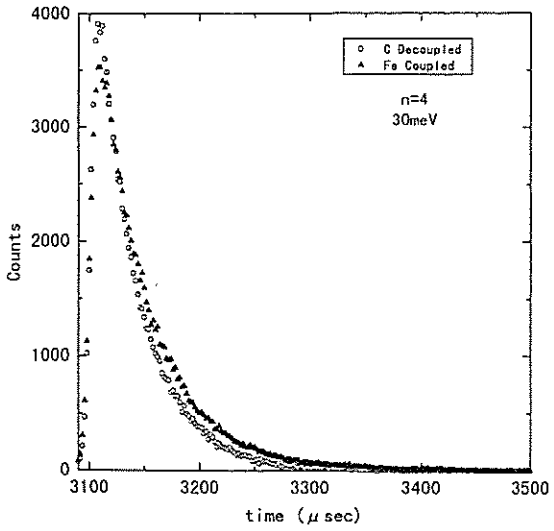

Fig. 7 Pulse shapes from moderators in coupled Fe reflector and decoupled C reflector (Linear plots).

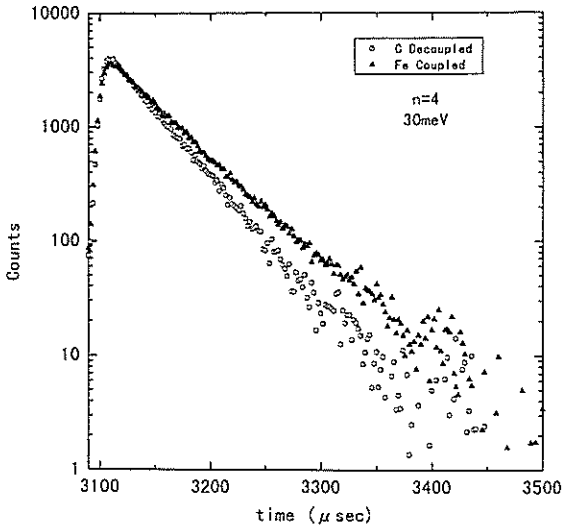

Fig. 8 Pulse shapes from moderators in coupled Fe reflector and decoupled C reflector (Semi-logarithmic plots).

From these experimental results we conclude that even in the case of a non-moderating reflector with relatively large absorption cross section we need a decoupler to produce the neutron pulses as narrow as those in decoupled case. We also have done Monte Carlo simulations for reflector studies for in the case of 3GeV spallation source. Preliminary results suggest that the neutron intensity do not depend so much on reflector materials. Much efforts will be necessary to find the optimal reflector especially for a TMRA including both of decoupled and coupled moderators.

5. Conclusion

We could not get much intensity enhancement in the case of the coupled liquid hydrogen moderator. It suggests that this system in itself has very high efficiency to produce cold neutrons. Another type of composite cold moderator have been proposed recently, which consists of liquid hydrogen and pelletized solid methane. We are now planing to measure neutronic performances of composite moderator of liquid hydrogen and pelletized polyethylene as a simulation of the hydrogen and pelletized methane composite moderator.

We are also continuing the study about reflector and post liquid methane moderator.

References

(1) Y. Kiyanagi et al., Proc. ICANS-XIII, Vol. II, p654-658(1995).
(2) Y. Ogawa et al., J. Neutron Research, to be published.
(3) Y. Kiyanagi et al., Proc. ICANS-XIII, Vol. II, p666-671(1995).
(4) S. N. Ishmaev et al., Report IAE-2019(1970).

EXPERIMENTAL STUDY ON NEUTRON YIELD FOR 12GeV PROTONS

H.SHIBAZAKI, M.ARAI[1], Y.INAMURA, N.WATANABE[2], M.FURUSAKA[1], S.ITOH[1], T.OTOMO[1], M.NUMAJIRI[1], S.SATOH[1], Y.KIYANAGI[3], Y.OGAWA[3], Y.SUDA[3]

Dept. of Phys., Kobe University, 1-1 Rokkodai, Nada-ku, Kobe 657
[1]National Lab. for High Energy Physics, 1-1 Oho, Tsukuba, Ibaraki 305
[2]Japan Atomic Energy Research Institure, Tokai, Ibaraki 319-11
[3]Department of Nuclear Engineering, Hokkaido University, Sapporo 060

ABSTRACT

We have carried out an experiment on neutron yields from typical cylindrical lead targets for 12 GeV protons by means of the Mn-bath moderation method. Our experimental results are consistent with the study by Russian groups done for lower proton energies by independent methods. The neutron yield from a 20 cm (diam.) x 60 cm (length) lead target is 185 neutrons/proton for the 12 GeV protons. That is to say, the neutron yield is almost proportional to the proton beam energy at least up to 12 GeV. Some neutronic calculations by HETC/KFA2 have also been achieved and the results have given an reasonable agreement with the experiment.

1. Introduction

The proton beam energy is one of the most important parameters for the design of an intense spallation neutron source. Our calculations have shown that a higher proton energy is effective at least up to 3 GeV [1]. Recently, higher proton energies (beyond 3 GeV) are under consideration for next-generation spallation neutron sources at various laboratories (for example, 3.6 GeV at Brookhaven and 10 GeV at Argonne), mainly from an accelerator point of view. Thus the reliable values of the neutron yield in such an energy range become important. However there exist only two measurements in this range. Vassil'kov et al. measured the neutron yields from lead targets for various ions including protons in the energy range from 1 GeV to 8.1 GeV using a moderation method [2]. Nikolaev et al. also measured the yield for protons from 1 GeV to 3.7 GeV using a threshold detector technique [3]. Their results showed that neutron yield is nearly proportional to the proton beam energy up to 8.1 GeV. There is almost no data above 8.1 GeV. Therefore, we were motivated to measure neutron yield by 12 GeV protons which are available at KEK. We have performed an experimental study on neutron yield by means of the Mn-bath moderation method, as well as a neutronic calculation using a well improved hadron transport code HETC/KFA2.

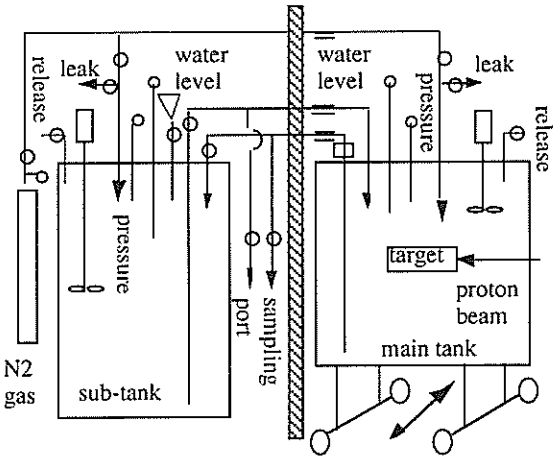

Fig. 1 Whole experimental system, which is composed from two tanks. One is the main tank in the proton beam line and another is the sub-tank outside the beam line.

2. Experimental

Experiments were performed at the P1 beam line in the East Counter Hall of the 12 GeV Proton Synchrotron at KEK. Figure 1 shows our experimental system. The system contains two tanks, a main tank and a sub-tank, and a control panel, from which all valves can be controlled and the water level and the gas pressure can be monitored. Each tanks have a pressure gauge, a water level gauge and an

agitator, which was used to uniform the spatial distribution of the irradiated Mn ions in the tank. The main tank including the lead target at the center was placed at the P1 beam line and the sub-tank was used to prepare the water solution of $MnSO_4$ and for its storage. The $MnSO_4$ solution can be transported between the two tanks by raising the pressure of N_2 gas, up to 1 kg/cm^2 (gauge pressure), in either of the tank. The lead targets used in the experiments are cylindrical ; 60 cm in length composed from six segments of 10 cm in length.

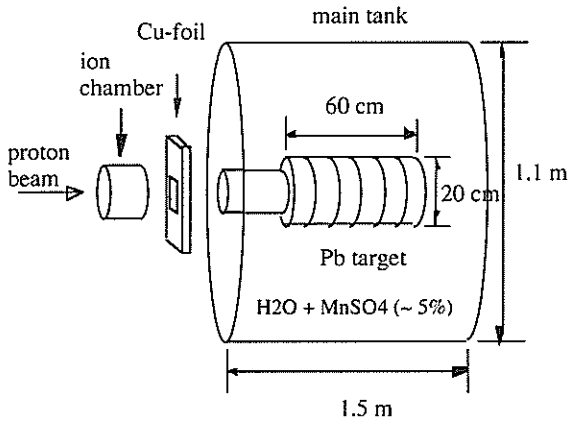

Fig.2 The layout of the main tank. The lead target, 60 cm in length and 20 cm in diam., is surrounded by 5 % $MnSO_4$ solution. The incident proton beam is monitored by an ion chamber, which efficiency was calibrated by a Cu-foil.

Two kinds of diameter, 20 and 10 cm, were arranged. The main tank, which has a cylindrical shape of 150 cm in length and 110 cm in diameter, was filled with the $MnSO_4$ solution with the Mn-ion content of 49.2 g/l, i.e, 5.0 %. In order to control the proton-beam intensity, the proton transport line has an iron collimator (narrower), an iron beam-shutter, a bending magnet, etc. just at the upstream of the target. Therefore it is necessary to check the possible contamination in proton beam mainly by high-energy neutrons. An Al-foil was used to detect such neutrons in the incident proton-beam using the Al(n,α)^{24}Na reaction and we confirmed that the proton beam is not contaminated with neutrons. The incoming proton beam intensity was monitored by an ion chamber, which absolute efficiency was calibrated by a Cu-foil using the Cu(p,X)^{24}Na reaction (3.59 $\pm$ 0.14 m barns) [4]. As we will see in the following results this cross section gave the largest ambiguity to the present results. The fast neutrons produced in the target by the spallation reaction emit out of the surface of the target, which are slowed down and thermalized in the $MnSO_4$ solution, and finally captured mainly by manganese, sulfur and hydrogen nuclei. In this process ^{55}Mn changes to radioactive ^{56}Mn with the half life of 2.58 hours.

$$^{55}Mn + n \rightarrow {}^{56}Mn \quad (T_{1/2} = 2.58\ h)$$

The target was exposed to the proton beam for about 500 seconds, which correspond to about 3.0 x 10^8 protons. In each experiment, the $MnSO_4$ solution of 2 litters was sampled just before and after the irradiation to determine the number of the ^{56}Mn nuclei in the solution. The sampled solution was transferred to a standard liquid sample container, a well-type cylinder, and the gamma rays at 846.8 keV emitted from ^{56}Mn were measured by a Ge detector. The efficiency of the detector was calibrated by a standard sample solution in the same container at the same geometry. In order to reduce the background from the short-lived nuclei, the gamma ray measurements were performed after a cooling time of 2 hours. We measured the gamma rays from the sample three or four times in every several hours to confirm the half life of ^{56}Mn. Thus, the total number of the thermalized neutrons in the Mn-bath was determined. The neutron yield from the target was obtained by taking into account the fraction of the neutron absorption cross-section for the nuclei contained in the Mn-bath with assuming as a uniform mixture. Experiments were performed for two target systems of the different diameters, 10 cm and 20 cm, changing the target length from 0 to 60 cm by a 10 cm step.

3. Calculation

We have performed some neutronic calculations on the total neutron yields and the spatial distributions for 12 GeV protons using HETC/KFA2, which is applicable up to 15 GeV protons. In these calculations we considered two systems, i.e. one is the Mn-bath system and another is the bare lead target system. The Mn-bath system contains the 20 cm (diam.) x 60 cm (length) lead target, the $MnSO_4$ solution and the stainless steel tank of 1.0 cm in thickness. For comparison, calculations with different proton energies of 1, 3, 8, 12 and 15 GeV were also performed for the bare target system.

4. Results and Discussions

4.1 Total yield

Figure 3 shows the preliminary results of our experiments and calculations for the total neutron yield together with other experimental results [2, 3]. In all measurements, the target geometry is the same, i.e. cylindrical shape of 60 cm in length and 20 cm in diameter. The present experimental results, are about 185 ± 11 neutrons/proton for target of 20 cm in diameter and 140 ± 8 neutrons/proton for the target of 10 cm in diameter (The latter is not shown in Fig.3).

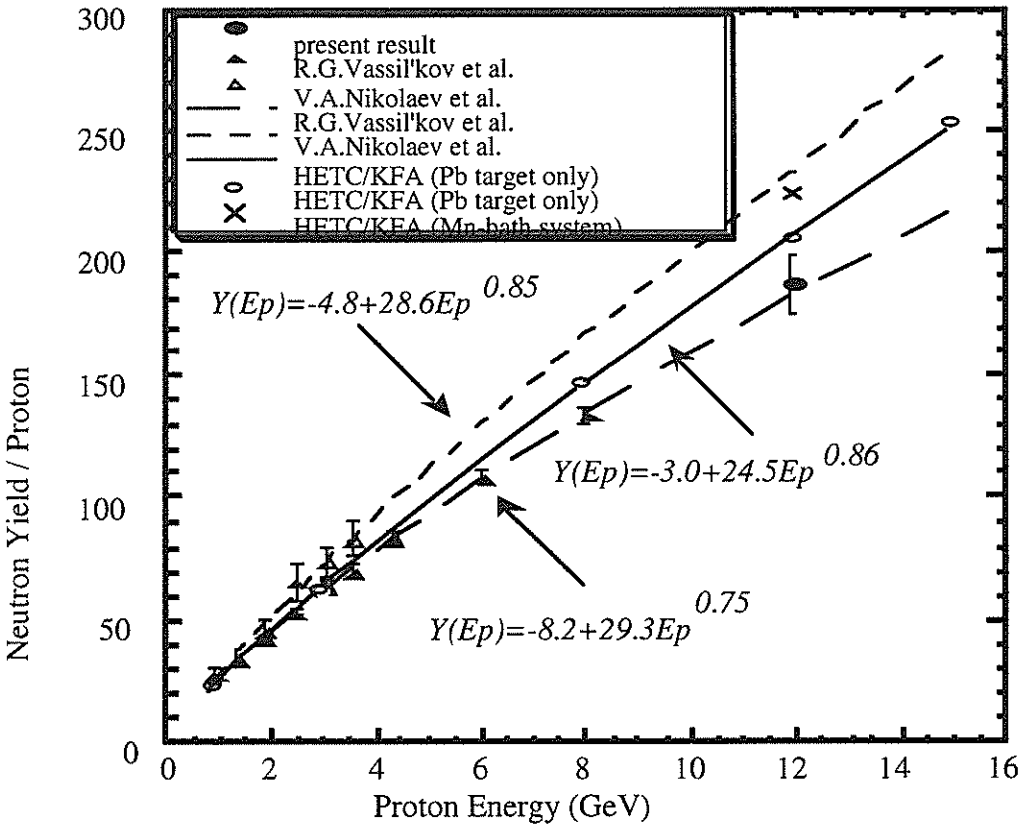

Fig.3 Total neutron yield as a function of incident proton energies. The detail is in the text.

The lower and the upper curves show the fitted results of Vassil'kov et al. and Nikolaev et al., which are expressed by

$$Y(Ep) = -8.2 + 29.3 \times Ep^{0.75}$$ for the lower curve and

$$Y(Ep) = -4.8 + 28.6 \times Ep^{0.85}$$ for the higher curve respectively.

The present result is well within those experimental boundaries and we have confirmed the consistency with the independent experimental results. We also fitted our calculated results done on the bare target system with a function of

$$Y(Ep) = -3.0 + 24.5 \times Ep^{0.86}.$$

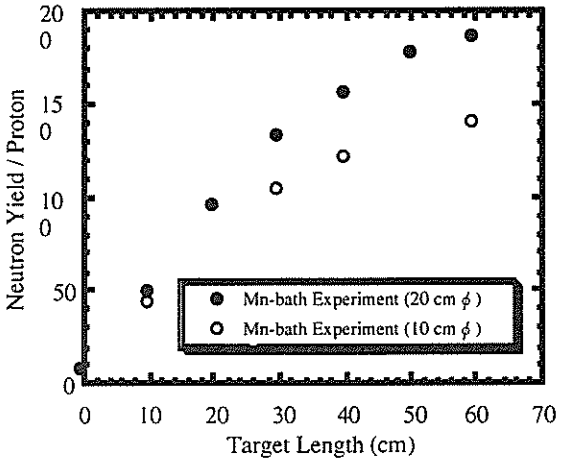

Fig.4 Total neutron yield as a function of the target length.

The error value of our experimental data is about 6.0 percent, which is mainly due to the ambiguity of the cross section for $Cu(p,X)^{24}Na$ reaction of Cu-foil. The statistical error in the present experiment is very small and it is less than one percent. Although the present experimental and calculated results are preliminary, we can confirm the consistency between them and we can conclude that the total neutron yield increases almost linearly with the incident proton energies at least up to 12 GeV. Here we note that our results is not corrected for the possible leakage of neutrons from the main tank. Thus, if we take this into account, the total neutron yield increases by about several percent. This estimation is under way by calculation. We also remark that the calculated results on the bare target system is closer to the experimental results than on the Mn-bath total system.

4.2 Spatial distribution

In order to estimate the spatial distribution (axial dependence) of the neutron yield, the target length was changed from 60 cm to 10 cm by removing the target segments one by one. This method does not give the true spatial distribution of the produced neutrons because of neglecting the effect of the back-scattered hadrons from the downstream target component. However, we can make calculation for the same target geometry and obtain a reasonable agreement between the experiments and calculations. The experimental results are shown in Fig.4. By taking the differences between the results for successive target segments, we obtained a sort of spatial distribution of neutron yield as a function of target length. The results are shown in Fig.5 with the calculated results for the same target geometry, i.e. cylindrical lead targets of 20 cm in diameter with various target lengths. In Fig.5 the calculated results are normalized so as to give the same total neutron yield with the experimental ones. There are small differences between experiments and calculations for the Mn-bath system. In Fig.5 the calculated results for the bare target system are also plotted. The peak position, the most intensive part, of the distribution is about 15 cm in depth from the incident target surface, which does not largely differ from the peak position for lower proton energies ; for instance 7 cm for 3 GeV protons. A considerable difference between the calculations for the Mn-bath system and the bare target system appears at the shallow region (1st target segment). This may be attributed to an additional spallation process in the $MnSO_4$ solution.

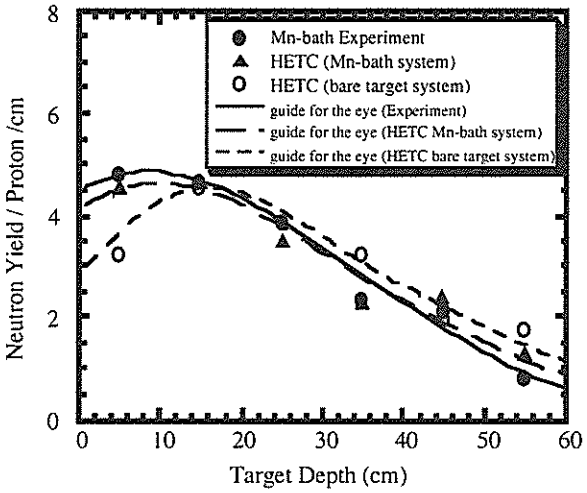

Fig.5 Spatial distribution of neutron yield, which was obtained by taking deviation of the neutron yield for successive target lengths.

5. Conclusion

From the present experimental results on the total neutron yield and those by Russian groups, we can conclude that the total neutron yield increases almost in proportional to the incident proton energies up to 12 GeV. We have also confirmed that the experimental results are reasonably consistent with the calculated results by HETC/KFA2 up to 12 GeV.

6. References

[1] Y.Kiyanagi, N.Watanabe and M. Arai, Jpn. J. Appl. Phys. 33, (1994) p2774
[2] R.G.Vassil'kov, et al., ICANS-XI, Tsukuba, (1990) p340
[3] V.A.Nikolaev, et al., ICANS-XI, Tsukuba, (1990) p612
[4] S.I.Baker, et al. , Phys. Rev. C43, (1991) p2862

SCIENTIFIC REPORTS

The new high resolution powder diffractometer, HRP-II, installed at the new cold neutron guide hall. A higher resolution of $\Delta d/d=1x10^{-3}$ is expected.

Ab initio structure determination of the low temperature phase of KNO_2 crystal by neutron powder diffraction

N. ONODA-YAMAMURO, H. HONDA, R. IKEDA, O. YAMAMURO*, T. MATSUO*, K. OIKAWA†, T. KAMIYAMA† AND F. IZUMI‡

Department of Chemistry, University of Tsukuba, Tsukuba, Ibaraki 305
*Department of Chemistry, Graduate School of Science, Osaka University, Toyonaka, Osaka 560
†Institute of Material Science, University of Tsukuba, Tsukuba, Ibaraki 305
‡National In stitute for Research in Inorganic Materials, Tsukuba, Ibaraki 305

Introduction

Potassium nitrite KNO_2, which is composed of spherical K^+ and V- shaped NO_2^- ions, is known to be a typical "ionic plastic crystal". KNO_2 has three crystalline phases including plastic ones.[1] The structure of the highest temperature phase I (T > 315 K) is NaCl type cubic and that of the phase II (264 K < T < 315 K) is rhombohedral (space group $R\bar{3}m$). In these phases, the orientation of the NO_2^- ion is highly disordered.[2] The crystal is mechanically deformable under stress in these crystals. The phase III (T < 264 K) has a monoclinic structure in which NO_2^- ions are supposed to be ordered.[2] No further structural study has been done for the phase III since a single crystal shatters at the II-III transition.

An unusual feature of KNO_2 is the existence of the large excess heat capacity over a wide temperature range (80 - 260 K) below the phase transition.[1] Such an anomaly has never been observed in molecular plastic crystals. The corresponding excess entropy is 15.1 J K^{-1} mol^{-1}, which is larger than the first-order component (discontinuous part) of the III-II transition entropy (10.8 J K^{-1} mol^{-1}). Our recent NMR[3] and dielectric[4] studies revealed that the excess heat capacity is caused by the gradual development of the orientational disorder of the NO_2^- ion.

The aim of the study is to determine the structure of the phase III and to clarify the structural aspect of the II-III transition including the mechanism of the gradual orientational disorder of NO_2^-. Neutron diffraction is useful for determination of the positions of the disordered N and O atoms whose discrimination is difficult by X-ray diffraction. The coherent neutron scattering lengths of N and O atoms are different enough (9.36 fm and 5.803 fm, respectively).

Experimental

As the commercial KNO_2 sample contained ca. 0.5 % of Na^+ and ca. 3 % of NO_3^- ions, the KNO_2 sample used in this study was prepared from $NaNO_2$ using the cation-exchange method.[1] The sample purity was checked by ICP emission spectroscopy and ion chromatography. The purified sample (~3.5 g) was contained within a vacuum-tight cylindrical can made of vanadium.

The neutron powder diffraction data of KNO_2 were collected on the time-of-flight (TOF) type diffractometer VEGA.[5] The TOF range of 4.5-42 ms, corresponding to the d-spacing range of 0.5-4.3 Å, was covered in this measurement. The resolution of the data ($\Delta d/d$) was about 0.2 %. The measurement was performed at 4, 120, 180, 220 and 250 K. In this report, however, we present only the result obtained at 4 K, whose analysis has been completed.

Results and Discussion

The unit cell was determined using the auto-indexing program DICVOL-91.[6] A monoclinic cell (a = 4.401(2) Å, b = 9.596(2) Å, c = 6.981(2) Å, β = 108.28(4)°, Z = 4) was determined with figures of merit $M(48)$ = 9.4 and $F(48)$=16.0. From the systematic absence of the diffraction peak (h0l: h+l≠2n, 0k0: k≠2n), the space group was determined to be $P2_1/c$.

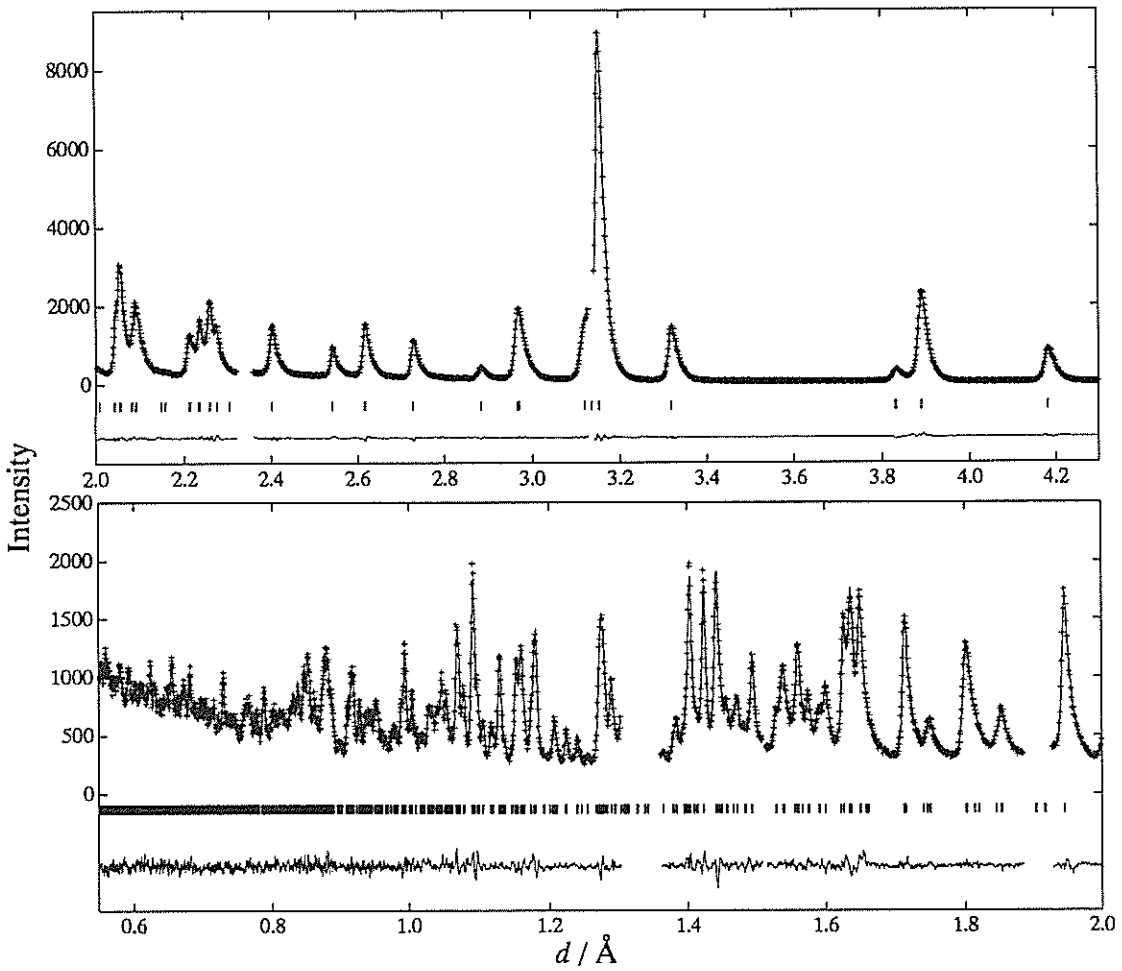

Fig. 1 Observed (plus marks) and calculated (line) neutron powder diffraction patterns of KNO_2 at 4 K. The calculated peak positions are given by the tick marks and difference between the observed and calculated intensities are shown below them.

This space group was confirmed by the cell and peak intensity refinement[7] using the program CAILS.[8] One molecule is contained in the asymmetric unit indicating that both K^+ ion and NO_2^- ions are located on general positions.

We searched a starting model for Rietveld refinement by a trial-and-error method. The program used was RIETAN-96T written by Ohta *et al.*[9] A number of trial models were constructed by changing the positions and orientations of K^+ and NO_2^- ions based on the known structures of several NO_2 and NO_3 compounds. For each model, a quick Rietveld refinement was performed using a limited number of parameters. The slack constraint technique was utilized in this stage; the N-O bond length and ONO angle were constrained to be within 1.24 ± 0.2 Å and $115.0 \pm 2.0°$, respectively. The central values of the bond length and angles were determined from the structure of $NaNO_2$.[10] A model derived from the structure of NH_2NO_2 gave a satisfactory small S value (R_{wp} / R_e) as a starting structure. The next stage of the refinement was performed without any constraint for structural parameters. A new technique named profile-relaxed Rietveld method[9] was used in the final stage of the refinement to give an excellent S value of 1.08. The final structural parameters are summarized in Table 1. Further analysis with anisotropic temperature factors was unsuccessful. The N-O bond length of 1.255(2) Å and the ONO bond angle of 116.4(2) ° are both reasonable compared with the values of $NaNO_2$ (see above). The

Table 1 Refined structural parameters of KNO_2 at 4 K.

Monoclinic: space group $P2_1/c$ (No. 14)
Lattice constants: a = 4.4024(2), b = 9.5979(3), c = 6.9847(3) Å, β = 108.295(3), Z = 4
R_I = 1.05 %, R_{wp} = 4.24 %, R_{exp} = 3.93 % and S = 1.08 for 3700 profile points and 113 basic variables.

	x	y	z	B_{iso}(Å^2)
K	0.4111(7)	0.1407(3)	0.2119(5)	0.08(6)
N	-0.0738(3)	0.4105(2)	0.1840(2)	0.36(3)
O1	0.2051(5)	0.4126(2)	0.4126(3)	0.43(4)
O2	-0.1600(6)	0.2995(2)	0.0871(3)	0.45(4)

final results of the profile fitting are illustrated in Fig. 1.

Figure 2 shows the monoclinic structure of KNO_2 at 4 K thus determined. Four molecules are contained in the unit cell. The orientation of the NO_2^- ion is completely ordered. In addition to the most stable orientation shown here, some metastable orientations may be excited thermally at higher temperatures. Such an excitation may reflect the gradual disorder of the NO_2^- ions. The Rietveld refinement including metastable orientations is in progress for the data obtained at higher temperatures.

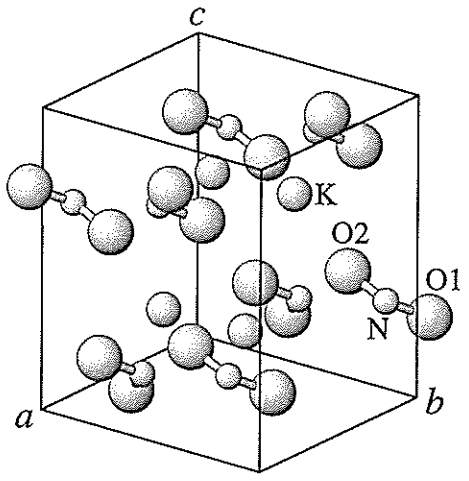

Fig. 2 Illustration of the crystal structure of KNO_2 at 4 K.

References

1) S. C. Mraw, R. J. Boak and L. A. K. Staveley, J. Chem. Thermodynamics 10, 359 (1978).
2) J. K. Solbakk and K. O. Stromme, Acta Chem. Scand. 23, 300 (1969).
3) M. Kenmotsu, H. Honda, H. Ohki, R. Ikeda, T. Erata, A. Tasaki, Y. Furukawa, Z. Naturforsch. 49a, 247 (1993).
4) H. Honda, N. Onoda-Yamamuro, R. Ikeda, O. Yamamuro and T. Matsuo, to be published.
5) T. Kamiyama, K. Oikawa, N. Tsuchiya, H. Asano, N. Watanabe, M. Furusaka, S. Satoh, I. Fujikawa, T. Ishigaki and F. Izumi, Physica B, 213&214, 875 (1995).
6) A. Boultif and D. Louer, J. Appl. Cryst. 24, 987 (1991).
7) G. S. Pawley, J. Appl. Cryst. 14, 357 (1981).
8) W. I. F. David, R. M. Ibberson and J. C. Matthewman, Report RAL-92-032 (1992).
9) T. Ohta, F. Izumi, K. Oikawa and T. Kamiyama, Physica B, in press.
10) M. I. Kay, B. C. Frazer and R. Ueda, Acta Cryst. 15, 506 (1962).

Structure of $Tl_2Ru_2O_{7-\delta}$ Pyrochlores Synthesized under High-Pressure

R. Kanno, T. Takeda, M. Nagata, T. Kamiyama*, F. Izumi**

Department of Chemistry, Faculty of Science, Kobe Univ. Kobe 657
**Institute of Material Science, Tukuba Univ. Tukuba 305*
***National Institute for Research in Inorganic Materials, Tukuba 305*

The pyrochlore ruthenates are technologically important materials as catalysts, electrocatalysts, and conducting components in thick-film resistors. Their electronic properties are of intrinsic interest, since Ru:4d electrons are on the borderline between localized and itinerant behavior. The thallium pyrochlore $Tl_2Ru_2O_{7-\delta}$ was first synthesized by Sleight et al. in 1970 under 3kbar of supporting pressure, and showed metallic property with nearly temperature independent resistivity[1]. Later, Jarret et al. have reported that $Tl_2Ru_2O_{7-\delta}$ synthesized under high pressure showed a metal-semiconductor(MS) transition around 120K[2]. However no information has been reported. Recently, we synthesized the thallium pyrochlores using high-pressure(1GPa) conditions. Our synthesis experiments clarified that the amount of oxygen vacancy was controlled by the synthesis condition; the samples synthesized under high-oxygen-pressure showed the MS transition at 120K with a decrease in the magnetization, and those synthesized at high-pressure without oxidizing reagent showed a transition at 50K with a spin-glass-like behavior.

In the present study, neutron diffraction was measured for the samples prepared under high-pressure conditions; (a) the sample synthesized at 1GPa, 1173K, with high-oxygen-pressure using $KClO_4$(T_{MS}= 120K, first order transition with a drastic resistivity change at T_{MS}), and (b) the sample synthesized at 1GPa, 1173K without $KClO_4$(T_{MS}=50K, higher order transition with a spin-glass-like behavior). The diffraction measurements were carried out at room temperature. The structural parameters were refined with the space group $Fd\bar{3}m$ using the program RIETAN.

Table 1(a) and (b) show the refinement results. Fig 1 illustrates the profile fit and difference patterns for both samples. The site occupancy of the O(2) site was determined to be 1.00 ($Tl_2Ru_2O_{7.00}$) for the sample (a) and 0.96(3) ($Tl_2Ru_2O_{6.96}$) for the sample (b). The Ru-O(1)-Ru angles are 133.7(2)° and 134.2(2)° for the samples (a) and (b), respectively. In the pyrochlore structure, the Ru-O(1)-Ru angle plays an important role for their electrical properties[3]. Larger angles lead to metallic properties, and smaller angles lead to semiconducting properties. The boundary between metallic and semiconducting behavior is situated around 134°. The Ru-O(1)-Ru values observed for $Tl_2Ru_2O_{7-\delta}$ correspond to the borderline between the metallic and semiconducting behavior.

References

1) A. W. Sleight and J. L. Gillson, Mat. Res. Bull., 6, 781 (1971)
2) H. S. Jarrett et al., Valence instabilities and related narrow-band phenomena, Edited by R. D. Parks, Plenum, P. 545 (1977)
3) R. Kanno, J. Huang and A. W. Sleight, JAERI-M 93-238, vol. 2, 347 (1993)

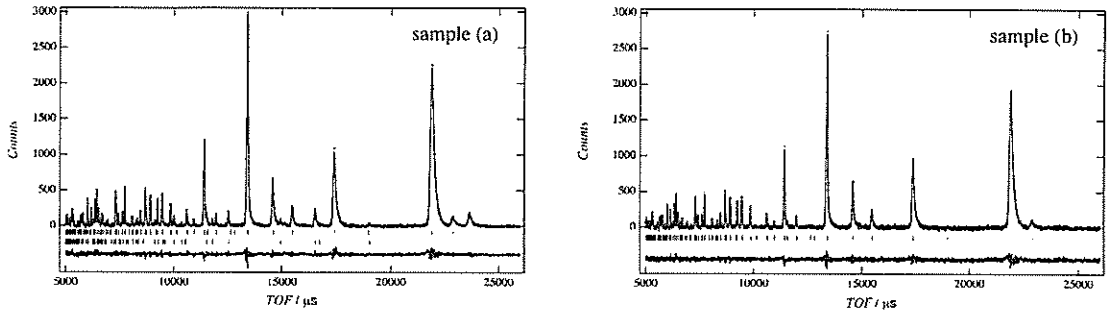

Fig.1 Observed, calculated, and difference plots of the samples (a) and (b).

Table 1(a)

Structural parameters for the sample (a) in $Fd\bar{3}m$.

(synthesized under high oxygen pressure, Metallic-semiconducting transition at 120K)

(a=10.1865(2) Å, R_{wp}=9.55%, R_p=6.96%, R_R=13.50%, R_e=7.75%, R_I=3.66%, R_F=3.08%, S=R_{wp}/R_e=1.23)

Atom	Site	g	x	y	z	B_{eq} / Å^2
Tl	16d	1.0	1/2	1/2	1/2	1.46
Ru	16c	1.0	0.0	0.0	0.0	1.28
O(1)	48f	1.0	0.3256(4)	1/8	1/8	1.68
O(2)	8b	1.0	3/8	3/8	3/8	1.63
Atom	U_{11} / Å^2	U_{22} / Å^2	U_{33} / Å^2	U_{12} / Å^2	U_{13} / Å^2	U_{23} / Å^2
Tl	0.0184(16)	= U_{11}	= U_{11}	-0.0012(17)	= U_{12}	= U_{12}
Ru	0.0162(15)	= U_{11}	= U_{11}	0.000(2)	= U_{12}	= U_{12}
O(1)	0.024(2)	0.0199(16)	= U_{22}	0	0	0.04(2)
O(2)	0.021(3)	= U_{11}	= U_{11}	0	0	0

Table 1(b)

Structural parameters for the sample (b) in $Fd\bar{3}m$.

(synthesized under high pressure, Metallic-semiconducting transition at 50K)

(a=10.1831(2) Å, R_{wp}=6.86%, R_p=5.36%, R_R=20.66%, R_e=6.13%, R_I=3.74%, R_F=3.04%, S=R_{wp}/R_e=1.12)

Atom	Site	g	x	y	z	B_{eq} / Å^2
Tl	16d	1.0	1/2	1/2	1/2	1.46
Ru	16c	1.0	0.0	0.0	0.0	1.34
O(1)	48f	1.0	0.3247(4)	1/8	1/8	1.61
O(2)	8b	0.96(3)	3/8	3/8	3/8	1.45
Atom	U_{11} / Å^2	U_{22} / Å^2	U_{33} / Å^2	U_{12} / Å^2	U_{13} / Å^2	U_{23} / Å^2
Tl	0.0185(14)	= U_{11}	= U_{11}	-0.0006(16)	= U_{12}	= U_{12}
Ru	0.0170(14)	= U_{11}	= U_{11}	0.000(2)	= U_{12}	= U_{12}
O(1)	0.023(2)	0.0189(16)	= U_{22}	0	0	0.04(2)
O(2)	0.018(4)	= U_{11}	= U_{11}	0	0	0

Orientational Disorder of ND_4^+ Ions in $(ND_4)_2SeCl_6$ and $(ND_4)_2PtBr_6$ Crystals: The Origin of the Large Isotope Effect on the Phase Transitions

O. YAMAMURO, K. OKISHIRO, T. MATSUO, N. ONODA-YAMAMURO[a], K. OIKAWA[b], T. KAMIYAMA[b], Y. KUME[c] AND F. IZUMI[d]

Department of Chemistry, Graduate School of Science, Osaka University, Toyonaka, Osaka 560
[a] Department of Chemistry, University of Tsukuba, Tsukuba, Ibaraki 305
[b] Institute of Materials Science, University of Tsukuba, Tsukuba, Ibaraki 305
[c] Department of Environmental Science, Azabu University, Sagamihara, Kanagawa 229
[d] National Institute for Research in Inorganic Materials, Tsukuba, Ibaraki 305

Introduction

$(ND_4)_2SeCl_6$ and $(ND_4)_2PtBr_6$ belong to a large family of ammonium hexahalometallates $(NH_4)_2MX_6$ (M = Se, Pt, Te, Pb, Pd, X = Cl, Br) which share the same crystal structure. The basic structure of these salts is of the antifluorite type with NH_4^+ tetrahedra occupying the cation sites at (1/4,1/4,1/4) of an fcc unit cell and MX_6^{2-} octahedra situated at (0,0,0).

Recent heat capacity studies[1-6] have revealed that these compounds undergo novel phase transitions with a large deuterium substitution effect (isotope effect) on the transition temperature (T_{trs}) and entropy ($\Delta_{trs}S$); the extent of the isotope effect depended on the metal and halogen atoms. The transition appears only in the deuterated sample for $(ND_4)_2PtCl_6$, $(ND_4)_2PdCl_6$ and $(ND_4)_2TeCl_6$ and the deuterated compounds exhibited higher T_{trs} and larger $\Delta_{trs}S$ than protonated ones for others. The magnitude of $\Delta_{trs}S$ of the deuterium compounds ($\Delta_{trs}S > R \ln 2$) suggest that the transitions are of order-disorder type. The symmetry of the cation sites ($43m$) coincides with that of an NH_4^+ ion. Therefore, there are no obvious reasons for the cation to be disordered. These phase transitions are of interest in relation to the basic problem of the collective behavior of quantum mechanical rotators with a small moment of inertia restricted in a shallow rotational potential. This situation is different from that of the deuteration effects in the hydrogen-bonded systems in KH_2PO_4 and $K_3H(SO_4)_2$ families.

In the present study, a neutron diffraction experiment was carried out on the high-temperature phases of $(ND_4)_2SeCl_6$ and $(ND_4)_2PtBr_6$; the former exhibits large isotope effect and the latter small effect as shown in the next table (the units of T_{trs} and $\Delta_{trs}S$ are K and $JK^{-1}mol^{-1}$, respectively):

compound	T_{trs}(H)	T_{trs}(D)	$\Delta_{trs}S$(H)	$\Delta_{trs}S$(D)
$(ND_4)_2SeCl_6$	24.5	48.2	1.3	12.1
$(ND_4)_2PtBr_6$	56.1	68.4	22.3	33.9

The purpose of this experiment is to determine the orientational disorder of ND_4^+ ions and clarify the structural aspect of their ordering transition. The X-ray diffraction of $(ND_4)_2SeCl_6$[7] and the neutron diffraction of $(ND_4)_2PtBr_6$,[8] $(ND_4)_2TeCl_6$[9,10] and $(NH_4)_2TeCl_6$[11] have been performed so far, but determination of the orientation of ammonium ions was not the chief concern of the previous works.

Experimental

Neutron diffraction data were collected on the time-of-flight (TOF) powder diffractometer (VEGA).[12] The sample crystal was contained in a vacuum-tight cylindrical can made of vanadium (10 mm in diameter and 50 mm in height) under a helium atmosphere. The data were recorded with the back scattering bank of detectors in the TOF range 4.5 - 42 ms, corresponding to the d-spacing range 0.5 - 4.3 Å. The resolution ($\Delta d/d$) of the data was about 0.2 %. The diffraction data were collected at 63 K for $(ND_4)_2SeCl_6$ and 90 K for $(ND_4)_2PtBr_6$. These temperatures are low enough for the thermal motion to be sufficiently subdued so that preferred molecular orientations are well defined and, at the same time, reasonably remote from the transition temperature. It took about 6 h to collect a set of data with sufficient counting statistics for the Rietveld refinement.

Results and Discussion

Figure 1 shows the neutron powder diffraction pattern of the high-temperature phase of $(ND_4)_2SeCl_6$ and $(ND_4)_2PtBr_6$ crystal. The plus marks denote the observed intensities and the dotted line those calculated as described below. The densely-distributed experimental points are barely discernible from the calculated curve. The Rietveld refinement was performed on the experimental data to determine the crystal structure including the positions of the D atoms using the data of the d-spacing 0.5-2.3 Å. The computer program used for the profile fitting was RIETAN-96T written by Ohta *et al.*[13]

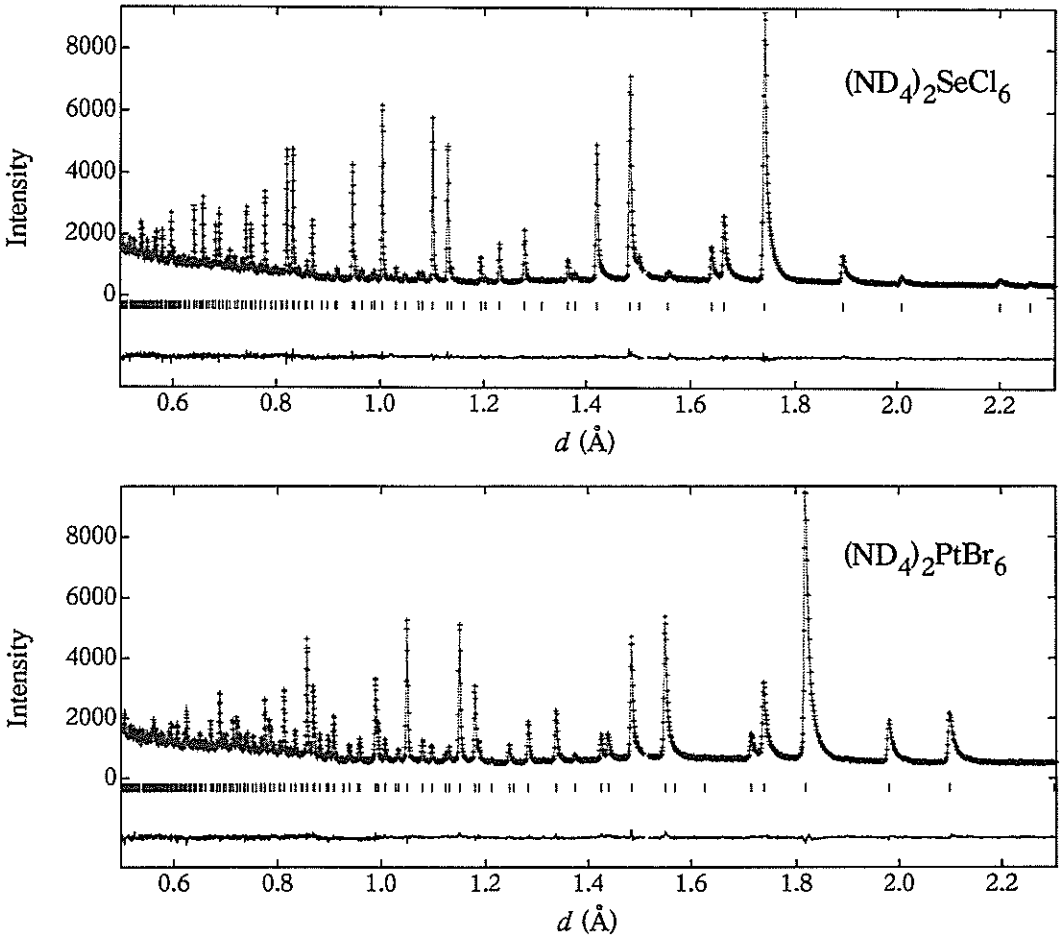

Fig. 1. Neutron powder diffraction patterns of the high-temperature phases of $(ND_4)_2SeCl_6$ and $(ND_4)_2PtBr_6$ crystals recorded at 63 K and 90 K, respectively. The plus marks denote the observed intensities and the dotted line those calculated from the best-fit model of the Rietveld refinement.

The observed peak positions in the diffraction patterns of both samples were completely reproduced by the space group *Fm3m*. Hence, the unit cell structures of the room-temperature $(ND_4)_2SeCl_6$ (a = 9.9616 Å, x(Cl) = 0.24111) determined by X-ray diffraction[7] was employed for the starting models of the refinement for both samples.

For the following analysis, we will describe only for $(ND_4)_2SeCl_6$ while giving only the corresponding numbers for $(ND_4)_2PtBr_6$ in brackets since the procedure of the analysis was almost the same for both samples. The four D atoms of an ND_4^+ ion were placed on the crystallographic 3-fold axes (32*f* positions, site symmetry: 3*m*) pointing from the central N atom to the four Se atoms located tetrahedrally at the 4 corners of the (1/2×1/2×1/2) cube of the unit cell. The N-D bond length was set to the literature value of ND_4Cl (1.03 Å).[14] The ND_4^+ ion is orientationally ordered in this model. This "ordered model" was refined using the 40 variable parameters (12 background parameters, 1 scale factor, 18 profile parameters, 1 lattice constant, 2 atomic coordinates, 6 anisotropic temperature factors) against 2672 intensity data in the TOF range between 5 and 23 ms. The position of the D atom was inverted and rapidly converged to the opposite side to the Se atom. The R_{wp} value of the fitting was 4.42 % (6.03 %) against R_e of 3.28 % (3.13 %) at this stage. The temperature factor of the D atom (B_{eq} = 7.0 Å^2 (11.3 Å^2)) was much larger than those of other atoms (*e.g.* B_{eq}(N) = 0.92 Å^2 (0.96 Å^2)). In the next stage, therefore, the D atoms were placed off the crystallographic 3-fold axes and in the mirror planes (96*k* positions, site symmetry: *m*). This model, previously proposed for the cubic form of $(NH_4)_2SiF_6$,[15] has 12 equivalent D atom positions for each ND_4^+ ion, thus representing 3-fold orientational disorder. The least-squares fitting of the "3-fold model" was performed using three additional

parameters (3) for the D atom. Rapid convergence was obtained again to give a better R_{wp} value of 4.02 % (4.07 %). The distance between the D atom and the 3-fold axis was 0.35 Å (0.46 Å), corresponding to an ND_4^+ rotation angle of 20.4° (27.4°). The diffraction intensities calculated from the "3-fold model" are shown by the solid line in Fig. 1. Further refinement was performed using a "6-fold model" in which the D atoms were placed at the 192*l* sites (general positions). However, the refinement was quite unstable and no significant improvement of R_{wp} was obtained.

Figure 2 reproduces the Fourier contour map (F_{obs}) of the (111) section at the level containing the D atom (calculated from the final structure of the refinements) using the phase data of F_{calc}. This map clearly shows that the D atoms of $(ND_4)_2SeCl_6$ is distributed at fairly wide region around the 3-fold axis probably with 3 maximum positions in the mirror planes whereas those of $(ND_4)_2PtBr_6$ are located at 3 definite positions in the mirror planes away from the 3-fold axis.

$(ND_4)_2SeCl_6$

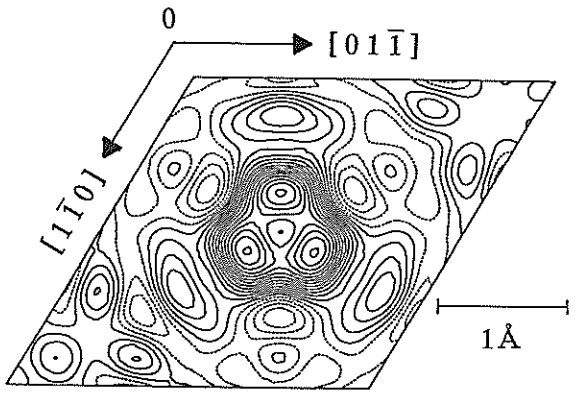

$(ND_4)_2PtBr_6$

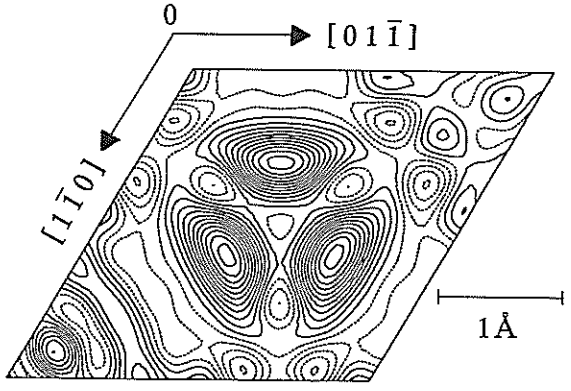

Fig. 2. Fourier counter map (F_{obs}) of the (111) section at the level containing the D atoms of the ND_4^+ ion. The crystallographic 3-fold axis is located at the center of the map.

The present result indicates that the phase transitions of $(ND_4)_2SeCl_6$ and $(ND_4)_2PtBr_6$ are both due to the ordering to an unknown structure from the dynamically disordered state of the ND_4^+ orientation. The orientational disorder of ND_4^+ in $(ND_4)_2PtBr_6$ is a quite usual (classical) one in which each orientation is definitely distinguished from others by relatively large potential barrier. On the other hand, in $(ND_4)_2SeCl_6$, ND_4^+ does not have absolutely stable orientations and the considerable part of ND_4^+ orientation is distributed apart from the most stable orientations (probably on the mirror planes). We call this type of disorder "quantum disorder". The transition entropy reported previously[2,6] is consistent with the present result; $\Delta_{trs}S$ of $(ND_4)_2PtBr_6$ is larger than that of $(ND_4)_2SeCl_6$. It is also reasonable that the large isotope effect was observed in the quantum disorder system $(ND_4)_2SeCl_6$. Theoretical transition models with accompanying for such large quantum effects are desirable for the $(NH_4)_2MX_6$ family.

References

1) Y. Kume, Y. Miyazaki, T. Matsuo and H. Suga, J. Phys. Chem. Solids **53**, 1297 (1992).
2) Y. Kume, H. Muraoka, T. Matsuo and H. Suga, J. Chem. Thermodyn. **26**, 211 (1994).
3) R. D. Weir and E. F. Westrum Jr., J. Chem. Thermodyn. **23**, 653 (1991).
4) J. E. Callanan, R. D. Weir and E. F. Westrum Jr., J. Chem. Thermodyn. **24**, 1001 (1992).
5) H. Muraoka, T. Matsuo and Y. Kume, Solid State Commun. **93**, 529 (1995).
6) H. Muraoka, T. Matsuo and Y. Kume, to be published.
7) W. Abriel, Acta Cryst. **C42**, 1113 (1986).
8) A. N. Fitch and J. K. Cockcroft, Phase Transitions **39**, 161 (1992).
9) Y. Kume, Y. Miyazaki, T. Matsuo, H. Suga, W. I. F. David and R. M. Ibberson, Europhys. Lett. **16**, 265 (1991).
10) Y. Kume, Y. Miyazaki, T. Matsuo, H. Suga, W. I. F. David and R. M. Ibberson, Physica B **180-181**, 594 (1992).
11) R. L. Armstrong, P. Dufort and B. M. Powell, Can. J. Phys. **69**, 137 (1991).
12) T. Kamiyama, K. Oikawa, N. Tsuchiya, M. Osawa, H. Asano, N. Watanabe, M. Furusaka, S. Satoh, I. Fujikawa, T. Ishigaki and F. Izumi, Physica B **213&214**, 875 (1995).
13) T. Ohta, F. Izumi, K. Oikawa and T. Kamiyama, Physica B, in press.
14) H. A. Levy and S. W. Peterson, Phys. Rev. **86** (1952) 766.
15) E. O. Schlemper, W. C. Hamilton and J. J. Rush, J. Chem. Phys. **44** (1966) 2499.

Determination of the Superstructure of $YSr_2Cu_2AlO_7$ by Neutron Powder Diffraction

N. R. KHASANOVA, F. IZUMI, T. OHTA, M. ISOBE, E. TAKAYAMA-MUROMACHI and T. KAMIYAMA[a]

National Institute for Research in Inorganic Materials, 1-1 Namiki, Tsukuba, Ibaraki 305
[a] Institute of Materials Science, University of Tsukuba, Tennodai, Tsukuba, Ibaraki 305

$YSr_2Cu_3O_{7-\delta}$ is a superconductor structurally related to $YBa_2Cu_3O_{7-\delta}$ with a unit cell of $a_p \times a_p \times 3a_p$, where a_p (= 0.38–0.39 nm) is the typical lattice parameter of the perovskite-type oxide. Two different Cu sites are included in $YSr_2Cu_3O_{7-\delta}$: Cu1 on the z = 0 plane and Cu2 on the CuO_2 sheet. Cu1 atoms are substituted by a variety of metals, M (M = Al, Fe, Co, Ga, Pb, *etc.*), to yield solid solutions $YSr_2Cu_2(Cu_{1-x}M_x)O_{7-\delta}$. An electron microscopic study of $YSr_2Cu_2AlO_7$, where Al is fully substituted for Cu1, revealed a superstructure with dimensions of $2a_p \times 4a_p \times 6a_p$.[1] In this work, we determined the structure of $YSr_2Cu_2AlO_7$ by neutron powder diffraction, taking into account this unique superstructure.[2]

Time-of-flight neutron powder diffraction data of $YSr_2Cu_2AlO_7$ were measured on VEGA and analyzed with RIETAN-96T. A refinement based on a tetragonal subcell with space group P4/mmm gave systematic disagreement due to a slight difference between a and b for the $a_p \times a_p \times 3a_p$ subcell and a large R_{wp} of 7.35% (R_e = 3.61%). Then, we constructed several structural models with two different orthorhombic space groups: Pmmm with the subcell and Pm2m with the $2a_p \times 4a_p \times 6a_p$ supercell. The best model adopting Pm2m afforded an R_{wp} of 6.29%, which is somewhat lower than 6.69% obtained with the Pmmm model. Therefore, results obtained with the best Pm2m model will be described in what follows.

The lattice parameters of $YSr_2Cu_2AlO_7$ were refined to be a = 0.77173(2), b = 1.54729(3), and c = 2.21933(4) nm. In its structure, AlO_4 tetrahedra are linked to each other by sharing corners to form meandering $(AlO_3^{3-})_\infty$ chains running parallel with the [100] direction, which leads to the lattice parameter of $a \approx 2a_p$ (Fig. 1). Sr_2AlO_3 blocks composed of the infinite chains and Sr^{2+} ions alternate with $Y(CuO_2)_2$ blocks that contain two CuO_2 sheets sandwiching Y^{3+} ions in eightfold coordination. Each AlO_4 tetrahedron shares the so-called apical oxygen, O(ap), with a CuO_5 square pyramid. The Cu–O(ap) distance is *ca.* 0.234 nm. The supercell of $b \approx 4a_p$ is related to the alternation of $(AlO_3^{3-})_\infty$ chains with different orientations along the [010] direction. On the other hand, the lattice parameter of $c \approx 6a_p$ results from relative shifts of infinite chains in two Sr_2AlO_3 blocks (z = 0 and 1/2) interleaved with an $Y(CuO_2)_2$ block along the b axis.

References

1) J. Ramirez-Castellanos *et al.*, submitted to J. Solid State Chem.
2) N. R. Khasanova, F. Izumi, T. Ohta, M. Isobe, E. Takayama-Muromachi and T. Kamiyama, in preparation.

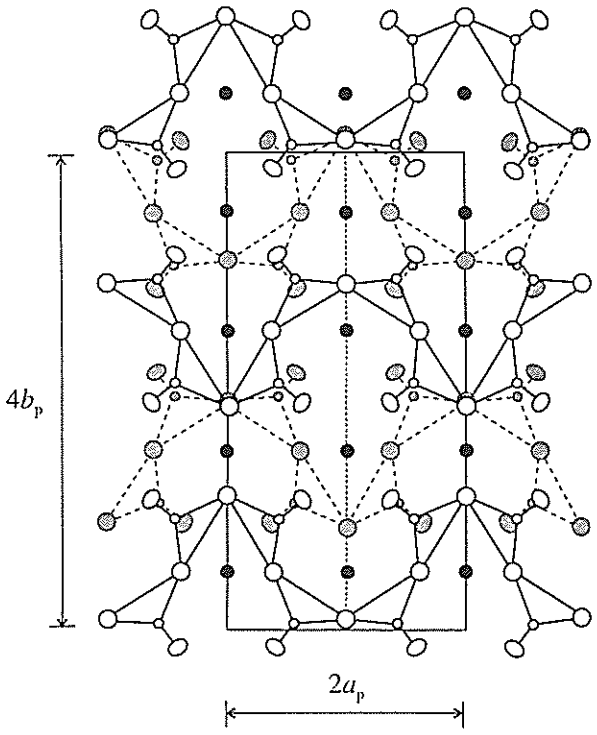

Fig. 1 Projection of Sr^{2+} ions and $(AlO_3^{3-})_\infty$ chains along the c axis. Open and shaded circles are atoms constituting AlO_4 tetrahedra where Al atoms have z coordinates of 0 and 1/2, respectively.

Rietveld analysis of intensity data taken on the TOF neutron powder diffractometer VEGA

T. OHTA, F. IZUMI, K. OIKAWA* and T. KAMIYAMA*

National Institute for Research in Inorganic Materials, 1-1 Namiki, Tsukuba, Ibaraki 305
*Institute of Materials Science, University of Tsukuba, Tennodai, Tsukuba, Ibaraki 305

Since 1993, a time-of-flight (TOF) neutron powder diffractometer, VEGA,[1] has been operated at the KENS pulsed spallation neutron source in place of the previous one, HRP. VEGA has backward, 90°, and forward banks, each of which is equipped with an array of one-dimensional ^{3}He position-sensitive detectors to cover a wide solid angle two-dimensionally. This novel geometry makes it possible to enhance the efficiency of data collection without sacrificing resolution ($\Delta d/d \approx 2\times10^{-3}$ for the backward bank).

In our previous Rietveld-refinement program, RIETAN, for TOF neutron diffraction,[2] we adopted a profile function optimized for HRP, *i.e.*, the linear combination of two Cole-Windsor functions[3] in a $(1-R):R$ ratio. Preliminary Rietveld refinements of intensity data measured with the backward bank of VEGA using RIETAN revealed that this profile function no longer fits observed patterns very well. In particular, observed intensities tend to exceed calculated ones in leading edges.

The above profile function was modified in such a way that the leading part is represented by a pseudo-Voigt function containing three primary profile parameters (PPP's), σ_0, σ_1, and η:

$$F(\Delta t_{ik}) = \eta\left(1+\Delta t_{ik}^2/2\sigma_0^2\right)^{-1} + (1-\eta)\exp\left(-\Delta t_{ik}^2/2\sigma_1^2\right), \qquad (1)$$

where $\Delta t_{ik} = t_i - t_k < 0$, t_i = TOF at step i, and t_k = TOF at the peak position.[4] Figure 1 shows the results of individual profile fitting for the 311 reflection in intensity data of Si (NIST SRM 640b) measured on VEGA. The calculated profile fits the observed profile much better with the new profile function (R_{wp} = 2.50%) than with the previous one[2] (R_{wp} = 7.37%). The marked improvement in the fit in the leading edge (magnified in Fig. 1) is evidently due to contribution of the Lorentzian component (first term) in Eq. (1). Both the previous and present profile functions achieve excellent fit at the expense of physical foundations.

We determined the dependence of 7 PPP's (σ_0, σ_1, η, σ_2, γ_1, γ_2, and R) in the present profile function on the lattice-plane spacing, d, with TableCurve 2D. The PPP's other than σ_0 and η are identical with those in the previous profile function.[2] The new profile function was then combined with the resulting 7 equations including 18 secondary profile parameters and incorporated into the latest version of our Rietveld-refinement program, RIETAN-96T. This native PowerPC code can be run fast on the Power Macintosh. It has convenient features of a user-friendly input system called F^{3}IS and creating Igor text files storing results of Rietveld analysis as well as simulation.

Figure 2 shows observed, calculated, and difference diffraction patterns of Si. The fit between the observed and calculated intensities was very satisfactory; R factors were R_{wp} = 4.72% ($S = R_{wp}/R_e$ = 1.02), R_p = 3.35%, R_B = 0.81%, and

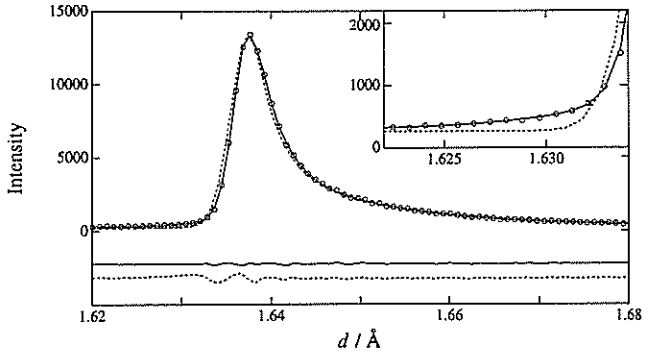

Fig. 1 Observed (open circles), calculated (upper lines), and difference (lower lines) patterns for the 311 reflection of Si. Solid lines were calculated with Eq. (1), and broken ones with the profile function for HRP.[2]

R_F = 0.60%. The isotropic atomic displacement parameter, B, of Si was 0.0049(4) nm^2, which is very near to the value reported in the literature: 0.00461 nm^2.

RIETAN-96T has another original feature of partial profile relaxation,[4] where the PPP's of (nearly) isolated reflections specified by the user are locally refined independently of secondary profile parameters for the relevant phase. The PPP's of these reflections are all or partially freed from equality constraints relating PPP's to d and diffraction indices, hkl. On the other hand, t_k's and integrated intensities for the user-selected reflections are, respectively, calculated from lattice and structure parameters in the same manner as those for the other reflections. Though the profiles of only low-Q reflections can be substantially relaxed, better fits in this region lead to improvement of fits in a high-Q region, where the profile shape mainly depends on the equipment and characteristics of neutron beams rather than the crystallinity of samples.

Partial profile relaxation is especially suitable for samples showing anisotropic profile broadening. We have been successfully applying this innovative method to a variety of compounds. Figure 3 exemplifies the results of conventional and profile-relaxed Rietveld refinements for an oxygen-deficient pyrochlore-type oxide, $Tl_2Nb_2O_{7-\delta}$.[5] When the PPP's of 10 reflections were relaxed to be varied directly, R_{wp} decreased from 4.98% to 4.30% (S = 1.05), and R_B from 0.86% to 0.70%. Onoda-Yamamuro *et al.*[6] has recently determined the crystal structure of KNO_2 at 4 K with RIETAN-96T. R factors were dramatically reduced when our technique of profile relaxation was applied to its structure refinement.

We are now extending the profile-relaxed Rietveld method to angle-dispersive neutron and X-ray diffraction; this work will be published elsewhere.

References

1) T. Kamiyama, K. Oikawa, N. Tsuchiya, M. Osawa, H. Asano, N. Watanabe, M. Furusaka, S. Satoh, I. Fujikawa, T. Ishigaki and F. Izumi, *Physica B* 213&214 (1995) 875.
2) F. Izumi, H. Asano, H. Murata and N. Watanabe, *J. Appl. Crystallogr.* 20 (1987) 411.
3) I. Cole and C. G. Windsor, *Nucl. Instrum. Methods* 171 (1980) 107.
4) T. Ohta, F. Izumi, K. Oikawa and T. Kamiyama, *Physica B*, in press.
5) H. Mizoguchi *et al.*, to be submitted.
6) N. Onoda-Yamamuro *et al.*, in this report.

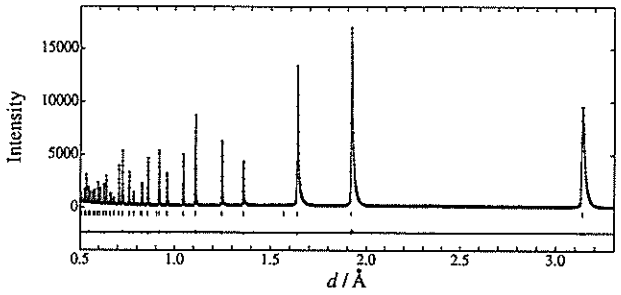

Fig.2 Rietveld-refinement pattern of the neutron powder diffraction data for Si.

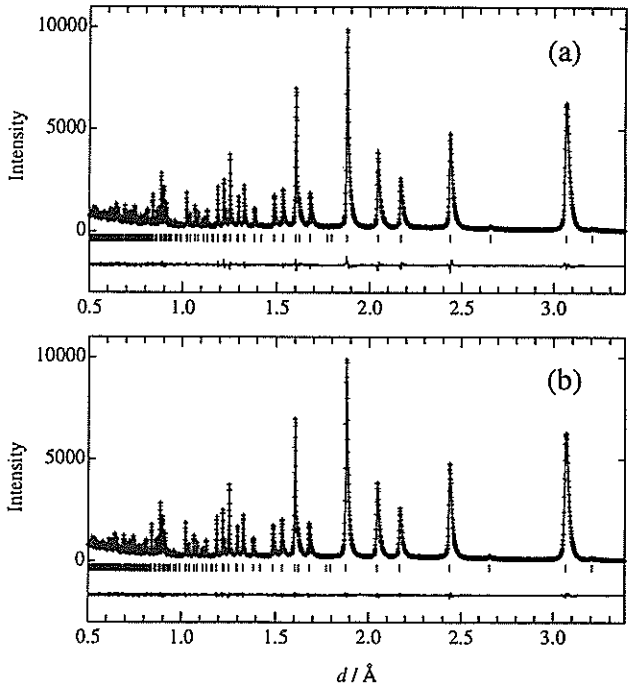

Fig.3 Observed (crosses), calculated (upper solid line), and difference (lower solid line) patterns obtained in the (a) conventional and (b) profile-relaxed Rietveld refinements of $Tl_2Nb_2O_{7-\delta}$.

Correlation between the structure of $LiMn_{2-y}Cr_yO_4$ and the cycle performance of Li–ion batteries

K. OIKAWA, F. IZUMI*, T. KAMIYAMA, D. NAKAZATO**, H. IKUTA** and M. WAKIHARA**

Institute of Materials Science, University of Tsukuba, Tennodai, Tsukuba, Ibaraki 305
*National Institute for Research in Inorganic Materials, 1–1 Namiki, Tsukuba, Ibaraki 305
**Department of Chemical Engineering, Tokyo Institute of Technology, Ookayama, Meguro–ku, Tokyo 152

The spinel–type oxide, $LiMn_2O_4$, has been studied extensively in recent years as a potential cathode for rechargeable Li–ion batteries. Solid solutions with a general formula $LiMn_{2-y}M_yO_4$ (M = Cr, Co, and Ni) have been prepared to improve the cycle performance of $LiMn_2O_4$ as a cathode of 4 V class batteries.[1)]

X–Ray Rietveld refinements of $LiMn_{2-y}M_yO_4$ with space group $Fd\bar{3}m$ showed that doped metals such as Cr substitute not for Li at the tetrahedral 8a site but for Mn at the octahedral 16d site.[1)] The atomic scattering factors of Li and O are, however, too small to obtain their reliable structure parameters in these solid solutions. In the present work, we determined the crystal structures of $LiMn_{2-y}Cr_yO_4$ by time–of–flight (TOF) neutron powder diffraction.

Samples with Cr contents, y, of 0, 1/9, 1/6, and 1/3 were synthesized in the same way as reported previously.[1)] Their TOF neutron powder diffraction data were measured on VEGA at room temperature and analyzed by the Rietveld method with RIETAN–96T.

In preliminary refinements, the occupation factor, g, of Li at the interstitial 16c site proved to be nearly negligible. It was, therefore, fixed at zero in subsequent refinements. The occupancy of O at a 32e site was very near to 1, *e.g.*, 0.98(2) in $LiMn_2O_4$. The slight apparent deficiency at this site may result from strong correlations between g(O) and other parameters, in particular, a scale factor and atomic displacement parameters. Thermogravimetry revealed that oxygen was hardly released on raising temperature up to 1200 °C. Then, the 32e site was thereafter regarded as fully occupied.

Tables 1 and 2 respectively list final structure parameters and metal–oxygen bond lengths in the $(Mn,Cr)O_6$ octahedron. The oxidation states, z, of Mn calculated from the chemical formulae were also included in Table 2.

X–Ray powder diffraction indicated that $LiMn_{2-y}Cr_yO_4$ showed anisotropic profile broadening with a broadening axis of [100]. This profile broadening seemed to decrease with increasing Cr content. Figure 2 gives $(\Delta d_s - \Delta d_i)/d$ *vs.* d curves for $LiMn_2O_4$ and $LiMn_{5/3}Cr_{1/3}O_4$, where Δd_s and Δd_i denote the full–widths at half–maximum (FWHM) due to the sample and X–ray instrument, respectively. A curve for Cr_2O_3, which exhibits isotropic broadening because of a crystallite–size effect, is also included in this figure. The dispersion of data points is caused by anisotropic profile broadening, and the gradient of each curve increases with decreasing crystallite size. Figure 2 clearly demonstrates that increasing y suppresses the anisotropy of profile broadening and, simultaneously, reduces the crystallite size.

Tarascon *et al.*[2)] reported that the reversible capacity of a cell containing $LiMn_2O_4$ increased with lowering synthesis temperature while the grain size of its powder decreased . In other word, decreasing the crystallite size improved the cycle performance of the cell, which is consistent with our analysis of the diffraction profiles for $LiMn_{2-y}Cr_yO_4$.

It is well known that highly broadened X–ray diffraction profiles are observed in the Li spinels used as cathodes after repeating insertion/extraction of Li ions. Such profile broadening has been ascribed to the stress caused by changes in lattice parameters during the discharge/charge processes. In stoichiometric $LiMn_2O_4$, 50% of Jahn–Teller Mn^{3+} ions occupy the octahedral 16d site. The changes in the lattice parameters can be suppressed by substituting cations with no Jahn–Teller electronic configuration, *e.g.*, Cr, for Mn^{3+} ions.

Table 1. Structural parameters of $LiMn_{2-y}Cr_yO_4$. Li atoms, (Mn,Cr) atoms and O atoms are located at the 8a site (1/8,1/8,1/8), the 16d site (1/2,1/2,1/2) and the 32e site (x,x,x). The anisotropic atomic displacement parameters for (Mn,Cr) and O atoms are $U_{11}=U_{22}=U_{33}$ and $U_{12}=U_{13}=U_{23}$ in Å^2.

$y = 0$	R_{wp} = 4.61%, R_p = 3.45%, S = 0.9494			
atom	x	10^2U_{11}	10^2U_{12}	Beq(Å^2)
Li		1.32(26)	0	1.040
Mn		0.89(7)	–0.22(9)	0.700
O	0.26300(13)	1.76(7)	–0.36(5)	1.388

$y = 1/9$	R_{wp} = 4.54%, R_p = 3.44%, S = 0.9339			
atom	x	10^2U_{11}	10^2U_{12}	Beq(Å^2)
Li		1.17(22)	0	0.924
Mn,Cr		0.63(6)	–0.23(7)	0.498
O	0.26299(10)	1.32(7)	–0.33(4)	1.039

$y = 1/6$	R_{wp} = 3.81%, R_p = 2.88%, S = 0.9705			
atom	x	10^2U_{11}	10^2U_{12}	Beq(Å^2)
Li		1.33(20)	0	1.050
Mn,Cr		0.82(6)	–0.22(7)	0.651
O	0.26295(9)	1.46(5)	–0.29(4)	1.152

$y = 1/3$	R_{wp} = 3.76%, R_p = 2.89%, S = 0.9171			
atom	x	10^2U_{11}	10^2U_{12}	Beq(Å^2)
Li		1.15(18)	0	0.905
Mn,Cr		0.54(6)	–0.14(8)	0.430
O	0.26296(8)	1.07(4)	–0.24(3)	0.843

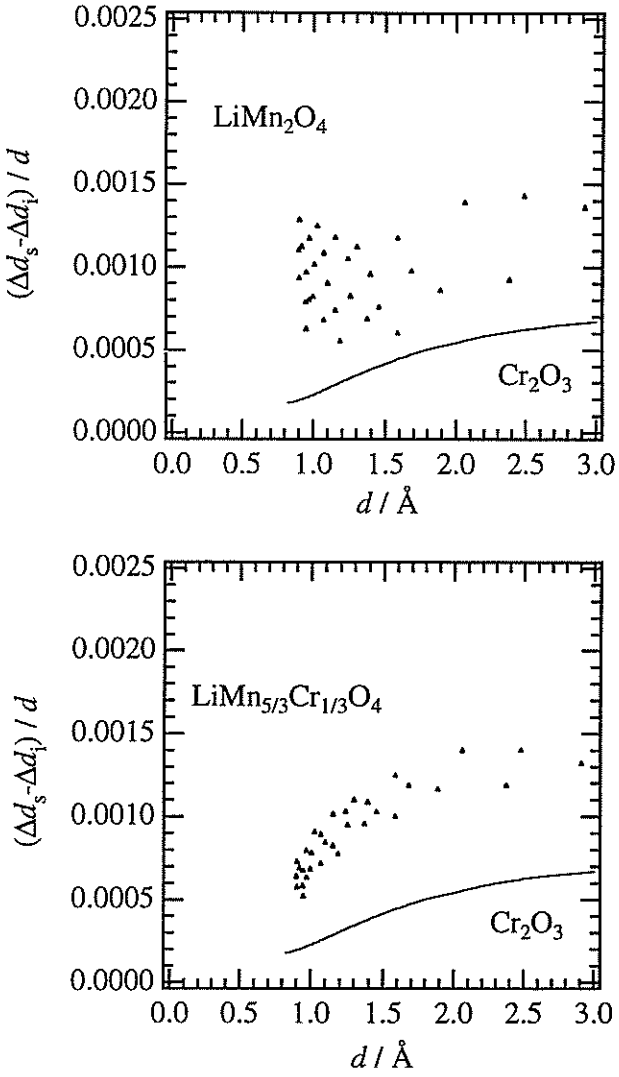

Fig. 2. $(\Delta d_s - \Delta d_i)/d$ *vs.* d in $LiMn_2O_4$ and $LiMn_{5/3}Cr_{1/3}O_4$.

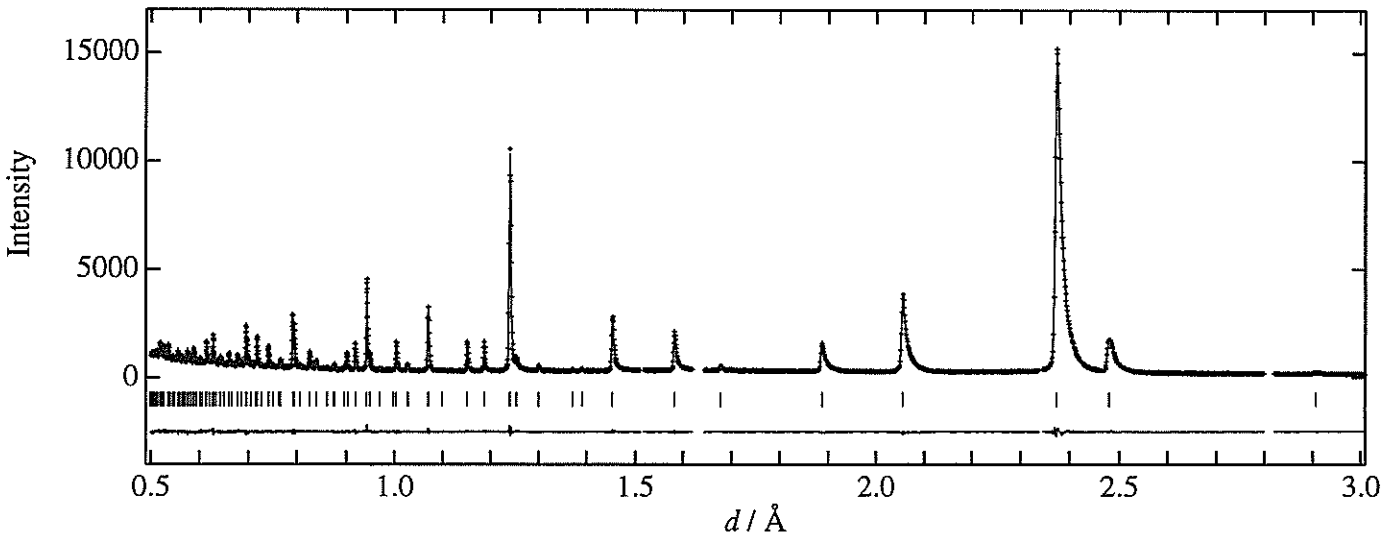

Fig. 1 Rietveld refinement pattern of $LiMn_{5/3}Cr_{1/3}O_4$

Ohzuku *et al.*[3] suggested that strain free insertion into or extraction from the solid matrix is the most important factor for the improvement in the cycle performance, which is consistent with our conclusion obtained from the diffraction profile analysis.

Anisotropic profile broadening was also observed in our TOF neutron powder diffraction data. We applied a new feature of partial profile relaxation in RIETAN–96T to the present materials. This method significantly improved *R* factors for $LiMn_2O_4$ which shows the most pronounced anisotropic profile broadening of the four members of the solid solution $LiMn_{2-y}Cr_yO_4$. Quantitative profile analysis of TOF data similar to that of X–ray data is now in progress; this will be reported elsewhere.

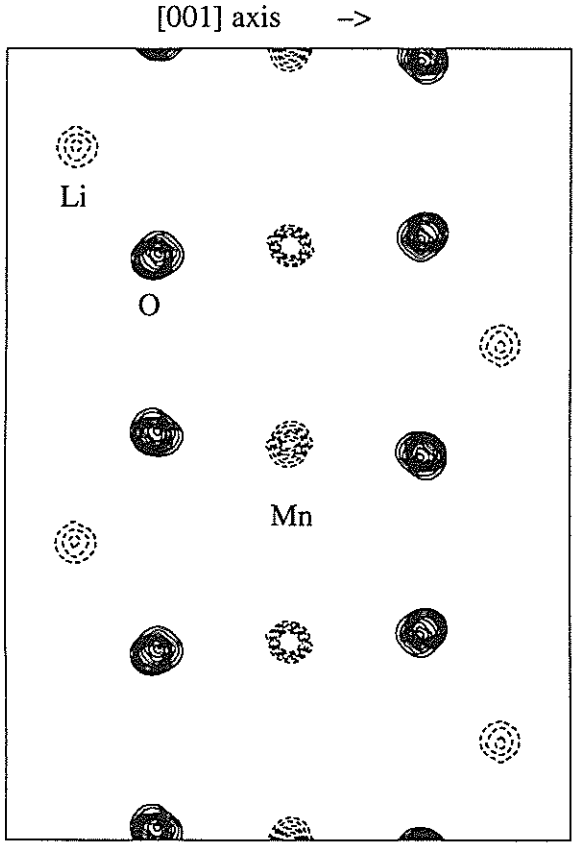

Fig. 3. Fourier map of $LiMn_{11/6}Cr_{1/6}O_4$ (110) plane which contains 8a, 16d, 32e and 'empty' 16c site.

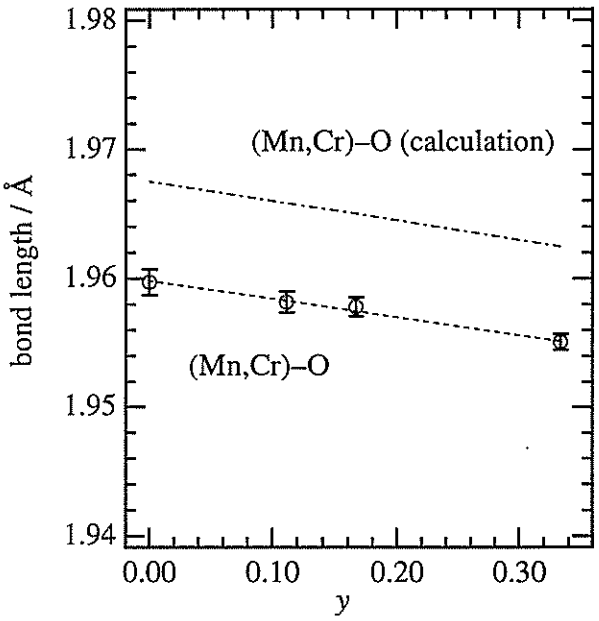

Fig. 4. (Mn,Cr)–O bond lengths.

Table 2. Lattice parameter, *a*, and (Mn,Cr)–O distances, *l*, in $LiMn_{2-y}Cr_yO_4$. l_c is the expected (Mn,Cr)–O distance calculated from effective ionic radii.

y	*a* (Å)	*l* (Å)	l_c (Å)	*z*
0	8.24376(13)	1.9597(10)	1.9675	3.50
1/9	8.23741(10)	1.9582(8)	1.9658	3.53
1/6	8.23451(7)	1.9578(7)	1.9650	3.55
1/3	8.22337(4)	1.9551(6)	1.9625	3.60

References

1) L. Guohua, H. Ikuta, T. Uchida and M. Wakihara, J. Electrochem. Soc. **143** (1996) 178.
2) J. M. Tarascon, E. Wong, K. Shokoohi, W. R. McKinnon and S. Coloson, J. Electrochem. Soc. **138** (1991) 2859.
3) T. Ohzuku, A. Ueda and N. Yamamoto, J. Electrochem. Soc. **142** (1995) 1431.

Structure Analysis of Mixed Alkali glasses

F. UTSUNO, H. MATSUMOTO, I.YASUI and T. FUKUNAGA*

Institute of Industrial Science, University of Tokyo, Roppongi 7-22-1, Minato-ku, Tokyo 106
*Department of Crystalline Materials Science, Nagoya University, Nagoya 464

The mixed alkali effect has long been posed as a controversial problem and many extensive investigations have been carried out. This anomalous phenomenon was summarized in reviews[1] and several kinds of explanations have been proposed and discussed[2,3]. In the present work structures of mixed alkali glasses and especially R-O (R=Li, Na, K, Rb, Cs) bond length in glasses were investigated by Neutron diffraction to understand the difference between single and mixed alkali glasses and vice versa .

The composition of lithium di-silicate Li_2O-$2SiO_2$ was chosen as single alkali glass and $0.5Li_2O$-$0.5R_2O$-$2SiO_2$ as mixed alkali glass. These glasses were prepared by melting method with enriched lithium (^7Li). Neutron diffraction measurements were carried out by time of flight with pulsed neutron using HIT-II. After correction of diffraction data, radial distribution functions (RDF) were calculated.

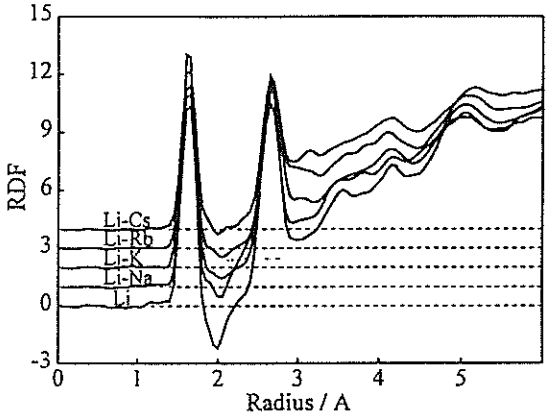

Figure 1 Neutron radial distribution functions of Li_2O-SiO_2 and $0.5Li_2O$-$0.5R_2O$-$2SiO_2$ glasses.

The observed RDF curves of R_2O-$2SiO_2$ glasses are shown in figure 1. Figure 2 shows the five peaks assigned to Li-O bond in their glasses. It was found that mixed alkali glasses had the different Li-O bond length distribution in relation to glass composition; the bond length of Li-O changed as the larger second alkali component was introduced into the glass and visa versa. The increase and decrease in Li-O bond length is ascribed to the presence of the second cations in local arrangement around oxygen atoms. As mixed alkali glasses showed negative deviation from compositional linearity in their total internal energies[4], this seems to be based on the difference of R-O bond distribution in single and mixed alkali glasses and the structural difference should be one of the origins of nonlinear behavior in mixed alkali glass systems.

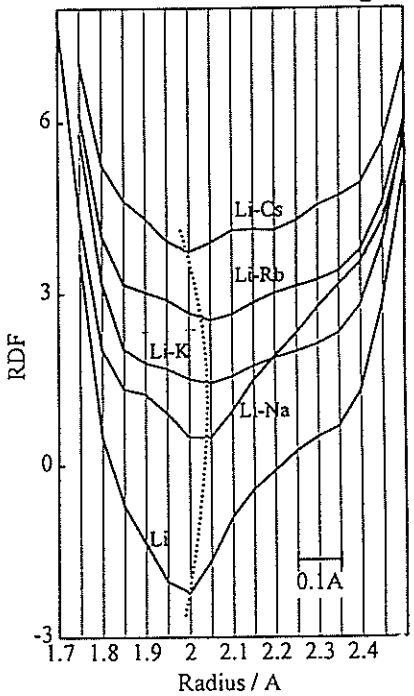

Figure 2 A part of RDF curves for Li-O bond.

References

1) M. D. Ingram, Phys. Chem. Glasses, **28(6)**, 215-34(1987).
2) M. D. Ingram, Phys. Chem. Glasses, **63**, 248(1980).
3) H. A. Dietzel, Phys. Chem. Glasses, **24**, 170-82(1983).
4) K. Takahashi et al., Zairyo, **26**, 72(1977).

Neutron Diffraction Study of Liquid Tl-As_2X_3 Systems (X: Se, Te)

Y. Kameda, T. Usuki, O. Uemura and T. Fukunaga†

Department of Material and Biological Chemistry, Faculty of Science, Yamagata University, Yamagata 990
†Department of Crystalline Materials Science, Nagoya University, Nagoya 464

Liquid Tl-As_2Te_3 and Tl-As_2Se_3 systems, which both undergo the metal-nonmetal transition, exhibit a different electronic behavior, although Te and Se belong to the same VIB group[1,2]. Recent EXAFS measurements for liquid As_2Te_3 have shown the presence of As-As bonds[3] which was not recognized by previous diffraction studies on liquid As_2X_3 (X: Se or Te)[4,5].

In this report, we describe results of TOF neutron diffraction measurements on both liquid Tl-As_2Te_3 and Tl-As_2Se_3 systems in order to investigate the difference between the two systems in light of their structures[6].

The alloy components with more than 4N purity were sealed in an evacuated quartz cell, melted together, and reacted for 48 h at about 200 °C above the liquidus temperature. The cell containing the melt was water-quenched to keep the homogeneity of the sample. TOF neutron diffraction measurements of samples sealed in an evacuated quartz cell (7.3 mm in inner diameter and 0.5 mm in thickness) were carried out using a HIT spectrometer[7] installed at the pulsed spallation neutron source (KENS) of the National Laboratory for High Energy Physics, Tsukuba, Japan. Details of data correction and normalization procedures were described elsewhere[5]. The compositions investigated were x = 0 (500 °C), 60 (700 °C), 83 (700 °C), 90 (800 °C) and 100 (500 °C) in the liquid $Tl_x(As_2Te_3)_{100-x}$ system, and y = 0 (500 °C), 60 (500 °C), 83 (800 °C) in the liquid $Tl_y(As_2Se_3)_{100-y}$ system, respectively.

Figures 1 and 2 show structure factors, $S(Q)$, and pair distribution functions, $g(r)$, in the liquid $Tl_x(As_2Te_3)_{100-x}$ system with x = 0, 60, 83, 90 and 100. The first sharp diffraction peak (FSDP) in $S(Q)$ at 1.2 $Å^{-1}$ is slightly visible at x = 0, but rapidly disappears with the addition of Tl. The asymmetric first peak in $g(r)$ in liquid As_2Te_3 (x = 0) denotes the involvment of multiple atomic pair correlations, such as As-Te and As-As bonds. The first two peaks in $g(r)$, at about 2.70 and 3.80 Å at x = 0, rapidly weaken with increasing Tl content, and above x = 60 the first peak position is increased to about 3.25 Å due to the enhancement of partially ionic Tl-Te bonds.

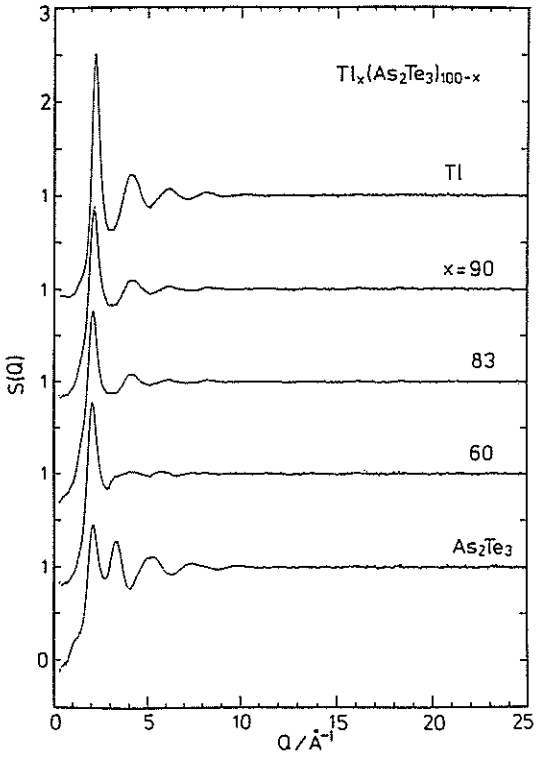

Fig. 1 Structure factors, $S(Q)$, in the liquid $Tl_X(As_2Te_3)_{100-X}$ system.

Figures 3 and 4 gives $S(Q)$ and $g(r)$ in the liquid $Tl_y(As_2Se_3)_{100-y}$ system with y = 0, 60, 83 and 100. The FSDP in $S(Q)$ at 1.2 $Å^{-1}$ in liquid As_2Se_3 (y = 0) is as sharp as that in amorphous state, implying that pyramidal $AsSe_{3/2}$ units connect each other, although partly, even in the liquid state. This FSDP rapidly fades away with the addition of Tl, as in the telluride system. The well-resolved first peak in $g(r)$ at y = 0 indicates that the first coordination shell is composed of strong As-Se bonds alone. The peak in $g(r)$ at 2.43 Å remains strong at y = 83, which is very close to the

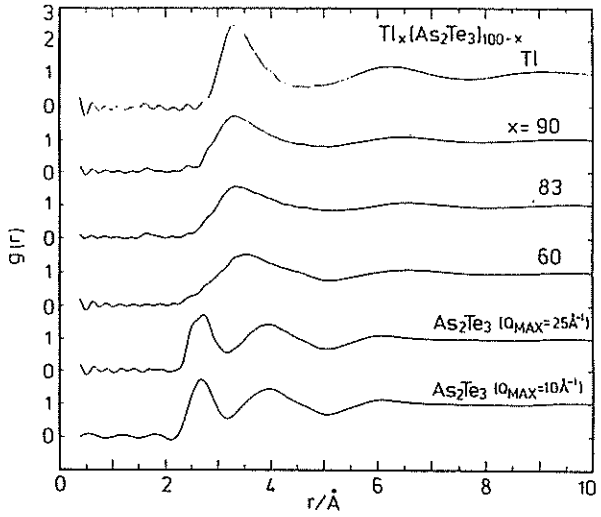

Fig. 2 Pair distribution functions, $g(r)$, in the liquid $Tl_x(As_2Te_3)_{100-x}$ system. Q_{MAX} denotes the upper limit of Q on the Fourier transform of $S(Q)$.

metal-nonmetal transition composition, indicating that covalent As-Se bonds in the selenide system remain even in Tl-rich region. The difference in electronic behaviors between the two systems may be reasonably explained by the present structural results.

The authors would like to acknowledge the members of HIT group during the course of diffraction measurements.

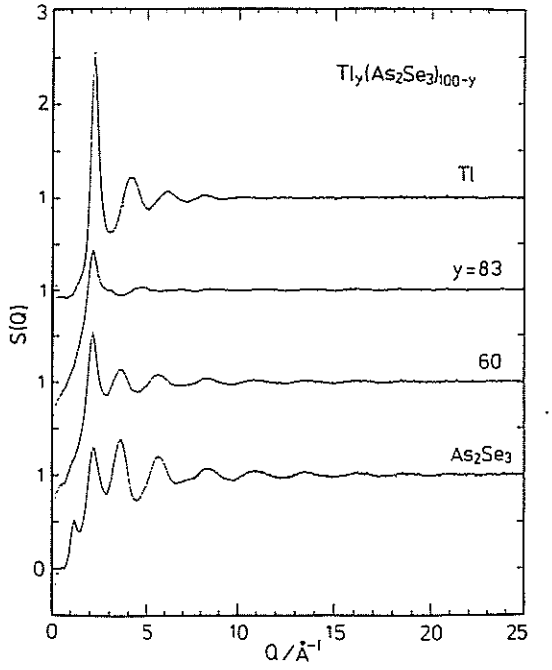

Fig. 3 Structure factors, $S(Q)$, in the liquid $Tl_y(As_2Se_3)_{100-y}$ system.

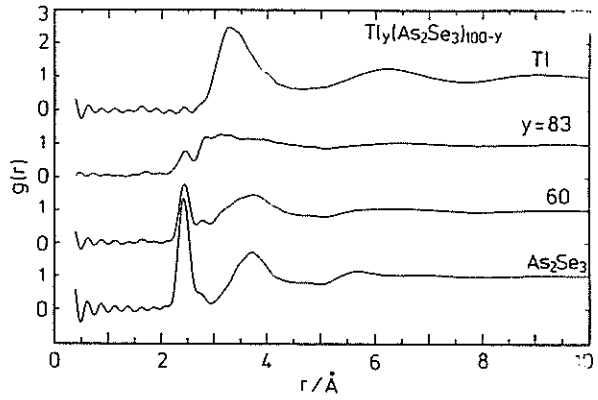

Fig. 4 Pair distribution functions, $g(r)$, in the liquid $Tl_y(As_2Se_3)_{100-y}$ system.

References

1) Y. Nakamura, M. Hirata and H. Hashimoto, *J. Non-Cryst. Solids*, **117-118**, 289 (1990).

2) T. Mineta, O. Uemura and T. Satow, *Mater. Trans. JIM*, **32**, 20 (1991).

3) S. Hosokawa, K. Tamura, M. Inui and H. Endo, *J. Non-Cryst. Solids*, **156-158**, 712 (1993).

4) O. Uemura, Y. Sagara, D. Muno and T. Satow, *J. Non-Cryst. Solids*, **30**, 155 (1978).

5) O. Uemura, Y. Sagara, M. Tsushima, T. Kamikawa and T. Satow, *J. Non-Cryst. Solids*, **33**, 71 (1979).

6) Y. Kameda, T. Usuki and O. Uemura, *J. Non-Cryst. Solids*, in press.

7) N. Watanabe, T. Fukunaga, T. Shinohe, K. Yamada and T. Mizoguchi, *Proc. 4th International Collaboration on Advanced Neutron Sources (ICANS-IV), KEK, Tsukuba*, (1981), ed. by Y. Ishikawa et al., p. 539.

Structure of Concentrated Aqueous DCOONa Solutions

Y. Kameda, T. Mori, T. Usuki, O. Uemura and T. Fukunaga†

Department of Material and Biological Chemistry, Faculty of Science, Yamagata University, Yamagata 990
†Department of Crystalline Materials Science, Nagoya University, Nagoya 464

Studies of the formate ion, $HCOO^-$, have occupied an important position in the field of coordination chemistry, because its versatile coordination behavior. A number of complexes involving $HCOO^-$ as the ligand have been synthesized, and the crystalline structures of these complexes have been extensively investigated[1]. However, despite extensive structural studies for solutions containing $HCOO^-$, only a little information concerning the molecular structure and the hydrogen bonded structure in the aqueous solution, are known.

In this report, we describe results of TOF neutron diffraction measurements for 15 mol% DCOONa solution in D_2O[2]. A fully deuterated aqueous 15 mol% DCOONa solution was prepared by dissolving the required amount of DCOONa (99.0 % D, MSD ISOTOPES) into D_2O (99.8 % D, Aldrich Chemical Co. Inc.). A TOF neutron diffraction measurement was carried out at 25 °C using a HIT-II spectrometer installed at the pulsed spallation neutron source (KENS) of the National Laboratory for High Energy Physics, Tsukuba, Japan. The observed scattering intensities from the sample were corrected for background, absorption, multiple and incoherent scatterings. The data from 66 sets of lower scattering angle detectors located at $10 \le 2\theta \le 51°$ were combined, and employed for the subsequent analysis. The least squares fitting analysis of the observed total interference term in the range of $6.0 \le Q \le 32.0$ Å^{-1} was made using the theoretical model function which involves contributions from the intramolecular interference within $DCOO^-$ and D_2O, the nearest neighbor hydrogen bonded O···D and D···D interactions, and the nearest neighbor Na^+···O and Na^+···D interactions.

The least squares fit for the observed total interference term ($i_N(Q)$) is shown in Fig.1. A satisfactory agreement was obtained between the observed and calculated $i_N(Q)$ in the $6.0 \le Q \le 32.0$ Å^{-1} range. The present value of the intramolecular C-O distance within $DCOO^-$ (r_{CO}=1.272(7) Å) is in reasonable agreement with that reported by X-ray diffraction studies for crystalline HCOONa (r_{CO}= 1.27 Å[3], 1.246 Å[4]). Bond angles within $DCOO^-$ (∠OCO = 118(3)°, ∠DCO=121(4)°) calculated from the present r_{CD}, r_{CO}, r_{OO} and r_{OD} values, apparently indicate a planer molecular structure of the formate ion in aqueous solution. The structural parameters for D_2O molecule in an aqueous 15 mol% DCOONa solution is in complete agreement with those reported in pure liquid D_2O within the experimental error, implying that the structure of the D_2O molecule remains unchanged in such a concentrated DCOONa solution. Further, the present intermolecular hydrogen bond distances (r(O···D)=1.92(2) Å, r(D···D) =2.42(2) Å) are almost identical to those reported in pure liquid water. The coordination number, n(O···D), determined in the present analysis, is close to 2, suggesting that a tetrahedral hydrogen bonded network among water molecules exists in the solution.

The authors would like to acknowledge the member of HIT group during the course of diffraction measurements.

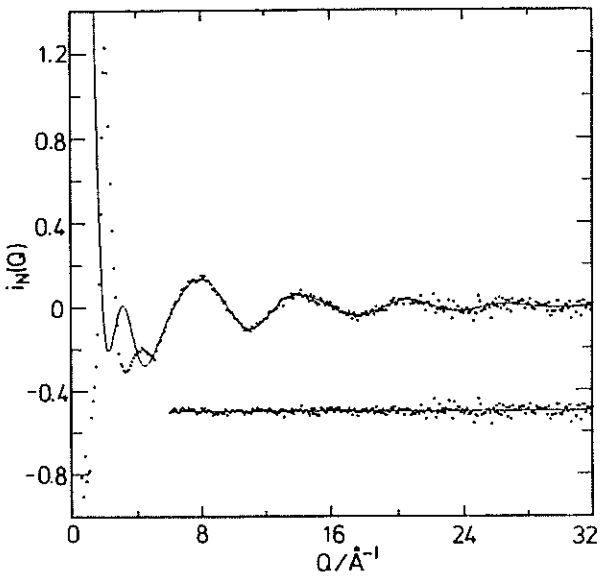

Fig. 1 The observed neutron total interference term (dots) and the best fit with the theoretical one (solid line). The residual function (dots) is shown below.

References

1) C. Oldham, "Comprehensive Coordination Chemistry", ed by G. Wilkinson, Pergamon Press (1987), Vol.2, p. 435.
2) Y. Kameda, T. Mori, T. Nishiyama, T. Usuki and O. Uemura, *Bull. Chem. Soc. Jpn.*, **69**, 1495 (1996).
3) W. H. Zachariasen, *J. Am. Chem. Soc.*, **62**, 1011 (1940).
4) P. L. Markila, S. J. Rettig and J. Trotter, *Acta. Cryst.*, **B31**, 2927 (1975).

Short-Range Order of Amorphous and Liquid Ge-Te Alloys

Y. Kameda, O. Uemura, T. Usuki and T. Fukunaga†

Department of Material and Biological Chemistry, Faculty of Science, Yamagata University, Yamagata 990
†Department of Crystalline Materials Science, Nagoya University, Nagoya 464

In recent years, considerable attention has been paid to amorphous germanium chalcogenides, which exhibit novel photostructural and thermostructural changes[1], as future potential materials for electronic devices. The local order of amorphous Ge-S and Ge-Se alloys has extensively been investigated and confirmed to be interpreted by the 4-fold Ge and 2-fold S (or Se) coordination model based on the atomic arrangement in the crystalline state[2,3]. On the other hand, various structure models have been proposed on the amorphous structure of Ge-Te alloys[4-6]. Liquid Ge-Te alloys are known to have a much more metallic character than liquid Ge-S and Ge-Se alloys[7]. However, the structural origin for the metallicity lies under discussion at present. Further structural information is necessary to solve these problems.

In this report, we describe results of TOF neutron diffraction measurements for Te-enriched Ge-Te alloys in amorphous and liquid states, and discuss their short-range structure and bonding feature.

TOF neutron diffraction measurements of samples sealed in an evacuated quartz cell (7.3 mm in inner diameter and 0.5 mm in thickness) were carried out using a HIT-II instrument[8] with the infrared image furnace installed at the pulsed spallation neutron source (KENS) of the National Laboratory for High Energy Physics, Tsukuba, Japan. Details of the sample preparation and data analysis were described elsewhere[9].

Figure 1 shows the observed interference function, $i(Q)$, of Ge_xTe_{1-x} alloys with $x = 0.16$ and 0.20 in the amorphous state, and $x = 0$, 0.16, 0.20 and 0.33 in the liquid state, respectively. The amorphous $i(Q)$ has the first sharp diffraction peak (FSDP) at $Q \approx 10$ nm^{-1}, while this peak is less clear in the liquid $i(Q)$. The corresponding pair distribution functions, $g(r)$, of the Ge-Te alloys in both states are given in Fig. 2. The first peak in the amorphous $g(r)$ is sufficiently resolved and its position is relatively short, suggesting that the strong covalency acts between Ge and Te atoms. However, it can be pointed out that Te-Te bonds are included in the first peak besides Ge-Te ones, because it is somewhat asymmetric and its position varies with x. By contrast, the first peak in the liquid $g(r)$ is broadened beyond the thermal effect and overlaps with the neighboring peaks. The first peak position in the liquid $g(r)$ is also longer than that in the amorphous one. Therefore, it can be asserted that the covalent nature drastically disappears in the liquid state. The present result corresponds well to a rapid enhancement of the metallicity in liquid Ge-Te alloys.

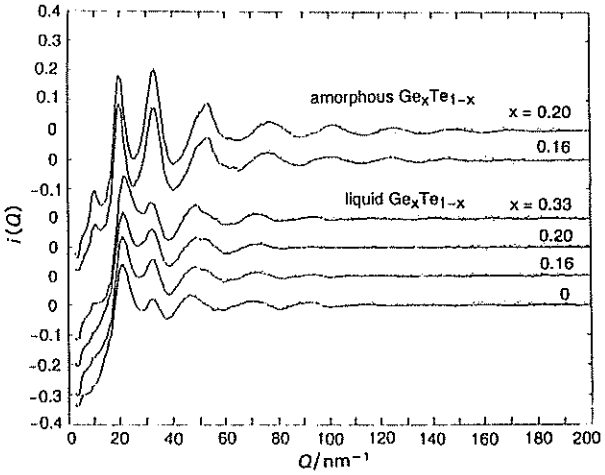

Fig. 1 Interference functions, $i(Q)$, of Ge_xTe_{1-x} alloys at $x = 0.16$ and 0.20 in the amorphous state and at $x = 0$ (550 °C), 0.16 (480 °C), 0.20 (530 °C) and 0.33 (700 °C) in the liquid state, respectively.

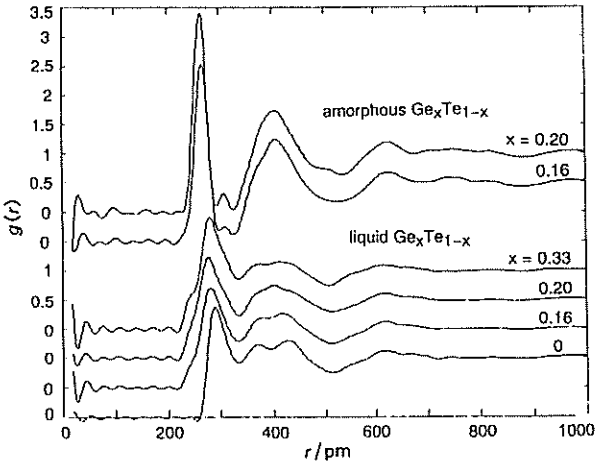

Fig. 2 Pair distribution functions, $g(r)$, of Ge_xTe_{1-x} alloys at $x = 0.16$ and 0.20 in the amorphous state and at $x = 0$ (550 °C), 0.16 (480 °C), 0.20 (530 °C) and 0.33 (700 °C) in the liquid state, respectively.

The present result has shown that the first peak in

$g(r)$ in both amorphous and liquid Ge_xTe_{1-x} alloys is composed of more than one atomic pair correlation, i. e., Ge-Te and Te-Te. However, it is impossible to obtain the bond length of each atomic pair from the first peak position in the observed $g(r)$. Under the assumption that partial distribution functions, $g_{GeGe}(r)$, $g_{GeTe}(r)$ and $g_{TeTe}(r)$, are unchanged between x = 0.16 and 0.20, we obtain two difference distribution functions, $\Delta g_1(r)$ and $\Delta g_2(r)$, in which a particular $g_{ij}(r)$ is omitted, using the observed $g(r)$ at both compositions,

$$\Delta g_1(r) = [-0.874 g_{16}(r) + g_{20}(r)] \times 10.549 = g_{GeTe}(r) + 0.322 g_{GeGe}(r), \quad (1)$$

$$\Delta g_2(r) = [g_{16}(r) - 0.872 g_{20}(r)] \times 6.945 = g_{TeTe}(r) - 0.108 g_{GeGe}(r), \quad (2)$$

where $g_{16}(r)$ and $g_{20}(r)$ correspond to the observed $g(r)$ at x = 0.16 and 0.20, respectively. Figure 3 illustrates $\Delta g_1(r)$ and $\Delta g_2(r)$ functions in the amorphous state. Since the Ge-Te term is predominant in $\Delta g_1(r)$, the position of the well resolved first peak in $\Delta g_1(r)$, 259 pm, can reasonably be assigned to the nearest neighbor Ge-Te bond length. Similarly, the nearest neighbor Te-Te bond length is obtained to be 276 pm from the first peak position in $\Delta g_2(r)$, in which the Te-Te term is rather predominant. These bond lengths are in good agreement with the results of our recent X-ray structural analysis on Ge-Te and Ge-Te-X (X: S, Se) alloys; r_{GeTe} = 261~262 pm and r_{TeTe} = 278 pm[4] and the result from the Ge K-edge EXAFS study of $Ge_{0.2}Te_{0.8}$[10].

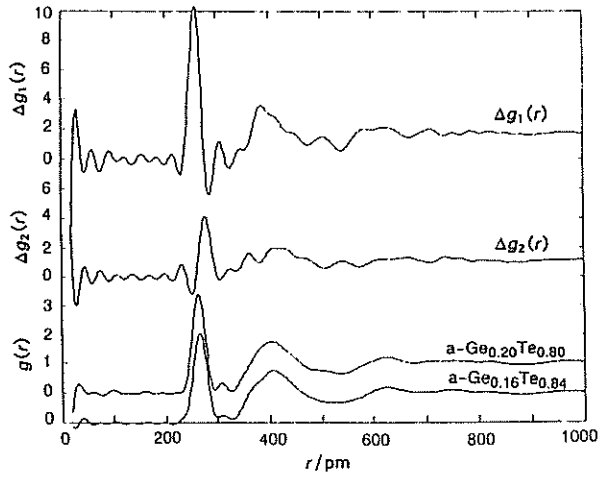

Fig. 3 Difference distribution functions, $\Delta g_1(r)$ and $\Delta g_2(r)$, in the amorphous state, together with the observed $g(r)$ at x = 0.16 and 0.20, respectively.

Figure 4 describes $\Delta g_1(r)$ and $\Delta g_2(r)$ obtained using both $g_{16}(r)$ and $g_{20}(r)$ in the liquid state. Assuming again that the Ge-Ge contribution to the first peak in both difference functions is negligible, we can find r_{GeTe} = 267 pm and r_{TeTe} = 292 pm in the liquid state from the first peak position in both the difference functions. The Ge-Te distance apparently increases by melting, implying that the liquid structure is considerably different from that in the amorphous state. The Te-Te bond length in the liquid state is also changed as compared with that in the amorphous state. The value, r_{TeTe}, remains almost equal to the first peak position, 291 pm, in $g(r)$ for pure liquid Te.

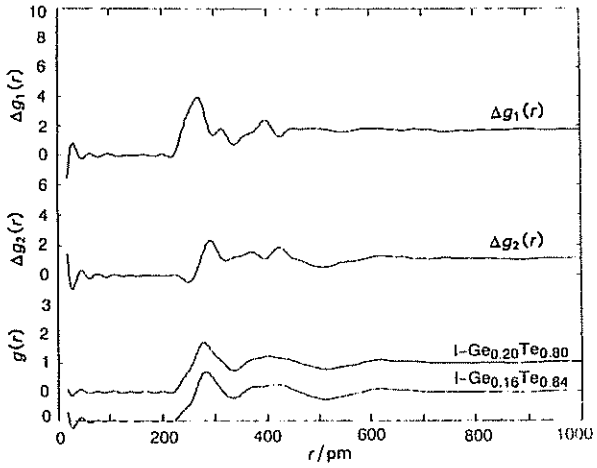

Fig. 4 Difference distribution functions, $\Delta g_1(r)$ and $\Delta g_2(r)$, in the liquid state, together with the observed $g(r)$ at x = 0.16 (480 °C) and 0.20 (530 °C), respectively.

References

1) K. Inoue, K. Kawamoto and K. Murase, *J. Non-Cryst. Solids*, **95&96**, 517 (1987).

2) S. C. Rawland, S. Narasimhan and A. Bienenstock, *J. Appl. Physics*, **43**, 2741 (1972).

3) R. W. Fawsett, C. N. J. Wagner and G. S. Cargill III, *J. Non-Cryst. Solids*, **8-10**, 369 (1972).

4) O. Uemura, N. Hayasaka, S. Toukairin and T. Usuki, *J. Non-Cryst. Solids*, (1996) in press.

5) S. J. Pickart, Y. P. Sharma and J. P. de Neufville, *J. Non-Cryst. Solids*, **34**, 183 (1979).

6) K. Ichikawa, Y. Kameda, Q. Xu and M. Misawa, *J. Non-Cryst. Solids*, **95&96**, 185 (1987).

7) M. Cutler, "*Liquid Semiconductors*", Academic Press, New York, (1977) p.13.

8) T. Fukunaga, M. Misawa, I. Fujikura and S. Satoh, *KENS-REPORT IX*, (1993), p. 16.

9) Y. Kameda, O. Uemura and T. Usuki, *Marerials Trans. JIM*, **37**, 1655 (1996).

10) O. Uemura, N. Hayasaka, Y. Kameda and T. Usuki, *phys. stat. sol (b)*, in press.

The Short-Range Structure around Li^+ in Concentrated Aqueous Lithium Formate Solutions

Y. Kameda, S. Suzuki, T. Usuki, O. Uemura and T. Fukunaga†

Department of Material and Biological Chemistry, Faculty of Science, Yamagata University, Yamagata 990
†Department of Crystalline Materials Science, Nagoya University, Nagoya 464

The neutron diffraction using the isotopically substituted sample, is one of the most suitable experimental method which provides direct information concerning the local structure of complex liquid. The hydration structure of solute ions as well as the inter-ionic structure in various aqueous solutions have been investigated by this method[1-3].

In this report, we describe results of the TOF neutron diffraction measurement for 12 mol% lithium formate solutions in D_2O to determine the solvation structure of both Li^+ and $HCOO^-$ in concentrated aqueous solutions.

Isotopically enriched 12 mol% $^*HCOO^*Li$ solutions (I, II, III and IV) were prepared by dissolving weighted amounts of anhydrous salts, $DCOO^6Li$, $DCOO^7Li$, $HCOO^6Li$ and $HCOO^7Li$, into D_2O. Sample parameters are listed in Table 1.

Neutron diffraction measurements were carried out at 25 °C using the HIT-II spectrometer[4] installed at KENS. The observed scattering intensities were corrected for the absorption, multiple and incoherent scatterings. The first-order difference functions[1-3], ${}^D\Delta_{Li}(Q)$ and ${}^H\Delta_{Li}(Q)$, were derived from the difference in the scattering cross sections between two solutions having common hydrogen isotopes for the formyl hydrogen, and different lithium isotopes (${}^D\Delta_{Li}(Q)$ = I-II, ${}^H\Delta_{Li}(Q)$ = III-IV). $\Delta_{Li}(Q)$ scaled by a stoichiometric unit, $(^*HCOO^*Li)_x(D_2O)_{1-x}$, can be written as a linear combination of the following six partial structure factors related to the lithium ion,

$$\Delta_{Li}(Q)=A[a_{LiLi}(Q)-1]+B[a_{LiH_f}(Q)-1]+C[a_{LiC}(Q)-1] +D[a_{LiO_f}(Q)-1]+E[a_{LiO}(Q)-1]+F[a_{LiD}(Q)-1], \quad (1)$$

where,

$A=x^2(b_{Li}^2-b_{Li'}^2)$, $B=2x^2(b_{Li}-b_{Li'})b_{H_f}$,
$C=2x^2(b_{Li}-b_{Li'})b_C$, $D=4x^2(b_{Li}-b_{Li'})b_O$,
$E=2x(1-x)(b_{Li}-b_{Li'})b_O$, $F=4x(1-x)(b_{Li}-b_{Li'})b_D$.

O and O_f denote the oxygen atom of the heavy water molecule and the carboxyl oxygen atom within the formate ion, respectively. The weighting factors in Eq. 1 are numerically listed in Table 2. The distribution function around the lithium ion can be represented as

Table 1. Isotopic compositions and mean scattering lengths of the lithium and the formyl hydrogen, b_{Li} and b_{H_f}, of the sample solutions used in this work.

Sample	^6Li/%	^7Li/%	H/%[a]	D/%[a]	b_{Li}/10^{-12}cm	b_{H_f}/10^{-12}cm
I	52.6	47.4	0.5	99.5	0	0.662
II	0.1	99.9	0.5	99.5	−0.222	0.662
III	52.6	47.4	100	0	0	−0.374
IV	0.1	99.9	100	0	−0.222	−0.374

a) For the formyl hydrogen atoms.

Table 2. Values of the coefficients of $[a_{ij}(Q)-1]$ in Eq. 1.

Difference function	A/barns	B/barns	C/barns	D/barns	E/barns	F/barns
${}^D\Delta_{Li}(Q)$	−0.0007	0.0042	0.0042	0.0074	0.0272	0.0624
${}^H\Delta_{Li}(Q)$	−0.0007	−0.0024	0.0042	0.0074	0.0272	0.0624

$$G_{Li}(r)=1+(A+B+C+D+E+F)^{-1}(2\pi^2\rho r)^{-1} \times\int_0^{Q_{max}} Q\Delta_{Li}(Q)\sin(Qr)\,dQ \quad (2)$$
$$= [Ag_{LiLi}(r)+Bg_{LiH_f}(r)+Cg_{LiC}(r)+Dg_{LiO_f}(r) +Eg_{LiO}(r)+Fg_{LiD}(r)](A+B+C+D+E+F)^{-1}$$

The upper limit of the Fourier integral (Q_{max}) was set to 20.0 Å^{-1}. The Li-H_f partial structure factor, $a_{LiH_f}(Q)$, is derived by the second-order difference between two $\Delta_{Li}(Q)$s, in which the isotopic state of the formyl hydrogen atom is changed,

$${}^D\Delta_{Li}(Q) - {}^H\Delta_{Li}(Q) =2x^2(b_{Li}-b_{Li'})(b_{H_f}-b_{H_f'})[a_{LiH_f}(Q)-1] \quad (3)$$

Figures 1 and 2 show the observed difference function $\Delta_{Li}(Q)$ and the distribution function $G_{Li}(r)$, respectively. The functional form of the present ${}^DG_{Li}(Q)$ characterized by well defined nearest neighbor Li-O (~1.9 Å) and Li-D (~2.5 Å) peaks, indicates the stable hydration geometry around the Li^+ in the solution. The number of oxygen atom around Li^+, n_{LiO}, was estimated to be ca. 3 from the area under the first peak of ${}^DG_{Li}(r)$. On the other hand, the coordination number, n_{LiD}, calculated from the area under the second peak was ca. 9, which seems much larger than the value, n_{LiD} = 6, expected for 3 D_2O

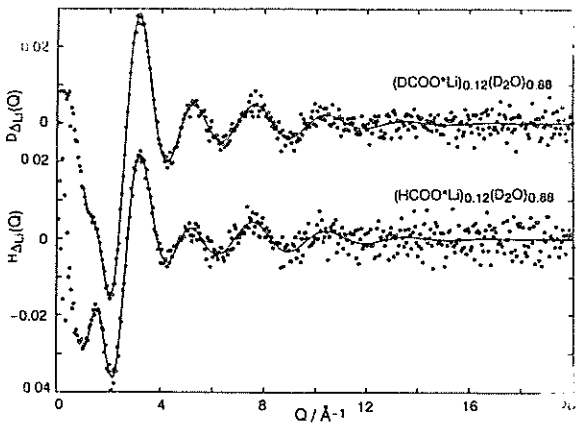

Fig 1. Observed difference functions, ${}^D\Delta_{Li}(Q)$ and ${}^H\Delta_{Li}(Q)$, for aqueous 12 mol% lithium formate solutions in D_2O.

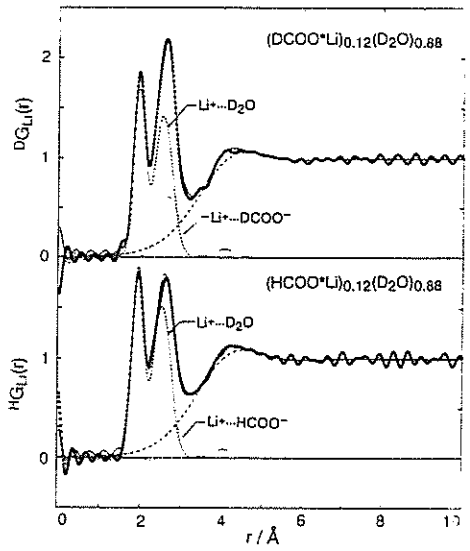

Fig 2. Distribution functions around Li^+, ${}^{D}G_{Li}(r)$ and ${}^{H}G_{Li}(r)$, for aqueous 12 mol% lithium formate solutions in D_2O.

molecules. The fact may indicates that the contribution from the nearest neighbor $Li^+\cdots DCOO^-$ pair is partially involved in the second peak of the present ${}^{D}G_{Li}(r)$. A marked difference in the relative intensity of the second peak between the present ${}^{D}G_{Li}(r)$ and ${}^{H}G_{Li}(r)$ functions seem to provide additional evidence in support of the above idea.

In order to obtain more detailed structural information on the local structure around the lithium ion, the least squares fitting analysis was applied for the observed $\Delta_{Li}(Q)$ functions. In the model function, the contributions from the nearest neighbor $Li^+\cdots D_2O$, $Li^+\cdots DCOO^-$, the second nearest neighbor $Li^+\cdots D_2O$ and the long-range continuous distribution of atoms around Li^+ were taken into account by the following equation.

$$\Delta_{Li}^{calc}(Q) = \Sigma 2xn_{Lij}b_j(b_{Li}-b_{Li})\exp(-l_{Lij}^2Q^2/2)\sin(Qr_{Lij})/(Qr_{Lij}) + 4\pi\rho(A+B+C+D+E+F)\exp(-l_{0Lij}^2Q^2/2) \times[Qr_{0Lij}\cos(Qr_{0Lij})-\sin(Qr_{0Lij})]. \quad (5)$$

For the $Li^+\cdots DCOO^-$ complex, the bond length, $r(Li^+\cdots O_f)$, the dihedral angle, α, between the plane involving atoms, Li^+, O_f, C and the molecular plane of $DCOO^-$, and the bond angle, β (=$\angle Li^+\cdots O_f$-C), are treated as independent parameters. The intramolecular bond lengths of $DCOO^-$ were referred to that obtained in our previous work for aqueous 15 mol% DCOONa solution[5]. The fitting was carried out in the range of $1.0 < Q < 20.0$ Å^{-1} for the observed ${}^{D}\Delta_{Li}(Q)$ and ${}^{H}\Delta_{Li}(Q)$ functions simultaneously. In this result, the final values of the independent parameters are summarized in Table 3.

Table 3. Results of the least squares refinements for the observed ${}^{D}\Delta_{Li}(Q)$ and ${}^{H}\Delta_{Li}(Q)$.

Interaction	i–j	r_{ij}/Å	l_{ij}/Å	n_{ij}
$Li^+\cdots D_2O$	Li–O	1.947(1)	0.137(1)	2.90(2)
	Li–D	2.545(2)	0.218(2)	(5.8)[a]
$Li^+\cdots DCOO^-$	Li–O_f	2.68(3)	0.208(8)	1.154(5)
		α=30(2)°	β=87(1)°	
$Li^+\cdots D_2O$(II)	Li–D_2O	4.212(5)	0.747(5)	5.34(5)
long range	Li–X[b]	4.161(8)	1.11(1)	–

a) Calculated from $2n_{LiO}$. b) X: O, H(D), C and Li.

Figures 3 shows the observed $Li^+\cdots H_f$ partial structure factor, $a_{LiH_f}(Q)$, and its Fourier transform, $g_{LiH_f}(r)$. The nearest neighbor $Li^+\cdots H_f$ distance was determined to be 2.568(2) Å from the least squares fit of the observed $a_{LiH_f}(Q)$ in the range of $1.0 < Q < 20.0$ Å^{-1}. In aqueous 12 mol% lithium formate solution, each Li^+ is surrounded by, on the average, three water molecules and one formate ion, which is similar to that found in highly concentrated aqueous lithium acetate solution[6]. The present result indicates that the first hydration shell of Li^+ is significantly modified by the presence of carboxylate anion in concentrated aqueous solutions.

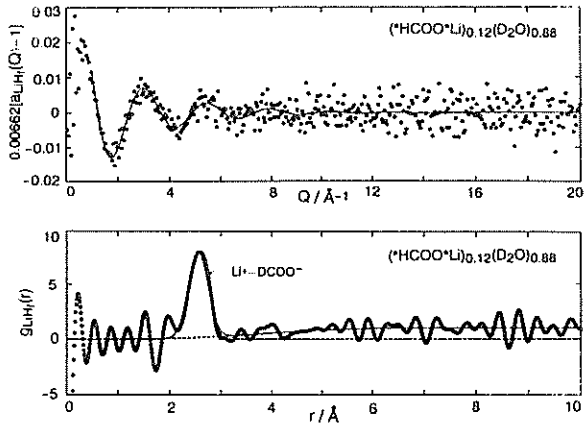

Fig 3. The observed partial structure factor, $a_{LiH_f}(Q)$, and the partial distribution function, $g_{LiH_f}(r)$, for aqueous 12 mol% lithium formate solutions in D_2O.

The authors would like to acknowledge the members of HIT group during the course of diffraction measurements.

References

1) A. K. Soper, G. W. Neilson, J. E. Enderby and R. A. Howe, *J. Phys., C: Solid State Phys.*, **10**, 1793 (1977).
2) G. W. Neilson and J. E. Enderby, *Adv. Inorg. Chem.*, **34**, 195 (1989).
3) G. W. Neilson, R. D. Broadbent, I. Howell and R. H. Tromp, *J. Chem. Soc., Faraday Trans.*, **89**, 2927 (1993).
4) T. Fukunaga, M. Misawa, I. Fujikura and S. Satoh, *"KENS REPORT-IX"*, (1993), p. 16.
5) Y. Kameda, T. Mori, T. Nishiyama, T. Usuki and O. Uemura, *Bull. Chem. Soc. Jpn.*, **69**, 1495 (1996).
6) K. Ichikawa, S. Kotani, M. Izumi and T. Yamanaka, *Mol. Phys.*, **77**, 677 (1992).

Network Structure of Fine Silica Particles Constituting Silica Aerogels

K. IGARASHI, K. TAJIRI, S. TANEMURA, R. NUNBU* and T. FUKUNAGA*

National Industrial Research Institute of Nagoya, Nagoya 462
*Department of Crystalline Materials Science, Nagoya University, Foro-cho, Chikusa-ku, Nagoya 464

Monolithic silica aerogel has properties such as high transparency for visible light, low density, and very low thermal conductivity. Such properties were thought to arise from a fractal structure with a porosity more than 90% composed of silica particles of several nanometrs in diameter. The structure of silica aerogels has been the subject of a number of recent investigations[1, 2]. Walrafen et al. reported that the skeletal density of silica in the aerogel was 1.83-1.87g/cm^3 [3] These values are clearly smaller than that 2.19g/cm^3, of fused silica. This difference indicates that the Si-O-Si network structure of silica in small particles may be different from that in fused silica. We have found from Raman spectroscopic study that the network structure in small silica particles constituting aerogel is connected loosely and changes at relatively low temperature up to 500°C [4].

In the present paper, we have performed TOF neutron diffraction measurements using a pulsed spallation neutron source in order to elucidate the network structure of the fine silica particles constituting the aerogels and the structure change with temperature.

The preparation method of silica aerogels was described in detail in previous paper[4]. Silica wet gels were prepared by the hydrolysis of tetramethyl orthosilicate(TMOS) diluted with methyl alcohol. The mole ratio of TMOS, water and alcohol is 1:6:20. An ammonium aqueous solution of 0.1N as a catalysis was used in this reaction. The gels obtained were transferred into anhydrous methyl alcohol and kept at a prescribed temperature for 24hrs. to give homogeneity. After those processes, the gels were placed in an autoclave and were then dried under the supercritical condition (250°C, 9MPa) of the alcohol to remove solvent. The bulk density of aerogels prepared was 0.08g/cm^3.

The skeletal density was measured by helium pycnometry to obtain the atomic number density using in the analysis of RDF.

Heating the aerogel in atmosphere methyl groups bonded chemically with Si-O networks are decomposed rapidly at 259°C and a contraction of volume occurs at the same time. The ratios of shrinkage of the volume depended on a heat treatment temperature and they were 6.2% for 300°C, 9.6% for 400°C, and 10.7% for 500°C for 2.5 hrs. The shrinkage of the volume leads to the increase of the density. The skeletal densities of the samples treated under the same conditions were obtained by helium pycnometry and were 1.68, 1.90, and 2.03g/cm^3, respectively. The skeletal density is also found to increase with increasing treatment temperature as well as bulk densities.

The structure factors S(Q) for silica aerogels treated under the same conditions as described above are shown in Fig.1, together with that of fused silica. The S(Q) curves of the aerogels Q>6.5 Å^{-1} are similar to that of fused silica, although an amplitude of S(Q) curves for the aerogels is small. But the amplitude of this region tends to increase with increasing temperature. There is a large difference between the S(Q) curves of the aerogels and fused silica in the range of Q<1 Å^{-1}. The S(Q) curves of the aerogels in this region show high intensities because they contain intense contributions from small angle scattering.

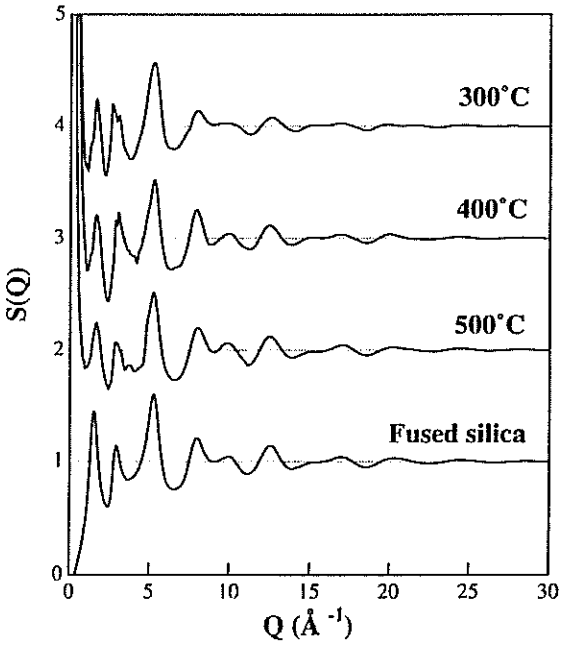

Fig. 1 Structure factors S(Q) of silica aerogels and fused silica.

The RDF curves obtained from Fourier transform of S(Q) are shown in Fig.2. The first peak was observed at 1.61 Å for all the samples, corresponding to the expected Si-O distance of the Si-O network.

The second peak appeared around 2.64 Å for the all samples, assignable to the O-O correlation. The dotted lines on the second peaks indicate the calculated data by assuming the Gaussian distribution of the pair. The coordination number of O atoms around a Si atom is calculated by integrating an area under the first peak. From the second peak, the coordination number of O-O pairs was also calculated. In Table 1, we summarized the obtained parameters of the peak positions and coordination numbers. The third shoulder-like small peak around 3.15-3.25 Å corresponds to Si-Si correlation. This distance decreased with the increase of temperature.

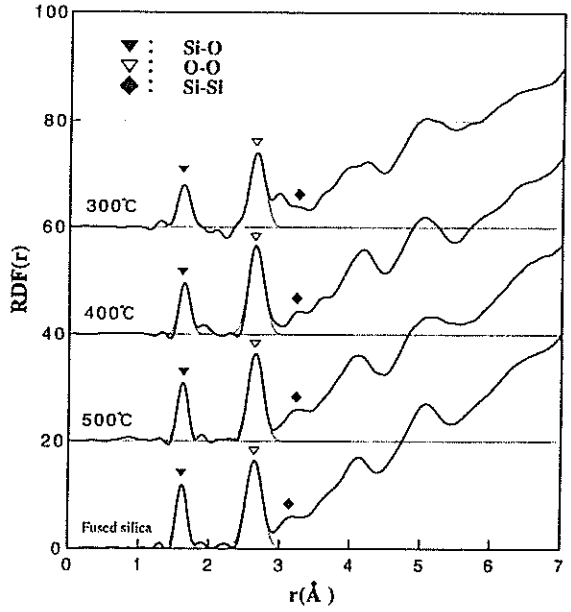

Fig. 2 Radial distribution functions RDF(r) of silica aerogls and fused silica.

Table 1. Peak positions, r_{ij} (in Å) and coordination numbers, n_{ij}, of Si-O, O-O, and Si-Si correlations.

temp.in °C	$r_{Si\text{-}O}/n_{Si\text{-}O}$	$r_{O\text{-}O}/n_{O\text{-}O}$	$r_{Si\text{-}Si}$
300	1.61/3.01	2.64/4.69	3.23
400	1.61/3.13	2.64/5.52	3.21
500	1.61/3.51	2.64/5.55	3.20
fused silica	1.61/3.89	2.64/5.91	3.15

A unit of structure constituting fused silica is SiO_4 tetrahedron and these units are connected three-dimensionally in fused silica. Thus the average coordination numbers of O atoms around a Si atom is 4, and the coordination number O-O interaction is 6. As seen in Table 1, the average distance of Si-O and O-O correlations of the three aerogels are the same values as those of fused silica. But the coordination numbers of them are smaller than those of fused silica. The coordination number of the aerogel treated at 300°C is particularly small with both interactions. These facts indicate that this structure contains many dangling bonds for the Si-O-Si bonds after the thermal decomposition of methyl groups and the network structure results in imperfect. The coordination number of Si-O pairs increased with increasing heat treatment temperature because of an oxidation. As result, the coordination number of the O-O pair increased. At the sample treated at 500°C, it is found that the coordination number is close to that of fused silica. The peak position of Si-Si correlation gives the average distance of the inter-tetrahedron. In the neutron diffraction analysis, it is difficult to read exactly Si-Si distance of the silica and silica aerogels from the RDF curves, since the contribution to the RDF curve of the Si-Si interactions is not so large because scattering length of Si atom for thermal neutrons is smaller than that of O atom and the number of interactions is also less than those of O-O pairs. The distances of the Si-Si pairs of the aerogels, however, are longer slightly than those of fused silica. The distance of the Si-Si correlations depends on the distance of Si-O pairs and the angle of Si-O-Si bond. Because in the aerogels, the distance of Si-O correlations is the same as those of fused silica, it is considered that the Si-O-Si bond angle affects the distance of the Si-Si pairs. From the Si-Si and Si-O distances, the bond angle in fused silica is calculated to be 156°, while the bond angles of the aerogels are obtained to be 167°-171°. These results imply that the silica network in the aerogels is loosely connected. In the case of the aerogel treated at 300°C, this tendency is remarkable. The results of the Raman spectra and the skeletal density measurements support also these ones[5].

References

1) Frike, J.: Aerogels. Edn. Berlin: Springer 1985.
2) Gesser, H.D., Goswami, P.C.: Chem. Rev. **89**, 765(1989).
3) Walrafen, G.E., Hokmabadi, M.S., Holmes, N.C., Nellis, W.J., Henning, S.: J. Chem. Phys. **82**, 2472 (1985).
4) Igarashi, K., Tajiri, K., Tai, Y., Tanemura, S.: Z. Phys. D **26**, S207(1993).
5) Igarashi, K., Tajiri, K., Tanemura, S., Nunbu, R., and Fukunaga, T.:Z. Phys. D (in press).

Structure of Amorphous Al-Cu-Y and Mg-Cu-Y Ternary Alloys

T. Fukunaga, H. Sugiura, N. Takeichi and U. Mizutani

Department of Crystalline Materials Science, Nagoya University, Furo-cho, Chikusa-ku, Nagoya 464

The atomic structure[1], electronic structure and electron transport properties [2-3] have been studied in a large number of amorphous Al-LT-ET and Mg-LT-ET (LT=Ni and Cu, ET=Ti, Y, Zr, La) alloys. An addition of Al into the amorphous Ni-Zr alloy, for example, results in an increase in resistivity, a sharp decrease in the electronic specific heat coefficient and a reversal in a sign of the Hall coefficient from a negative to a positive value. On the other hand, the resistivity decreases and the Hall coefficient remains negative when Mg is added to the amorphous $Ni_{40}La_{60}$ and $Cu_{40}Y_{60}$ alloys. Therefore, it has been realized that Al and Mg affect the electronic structure and electron transport in different mechanisms.

Among LT-ET amorphous alloys, the amorphous Cu-Y alloy can dissolve both Al and Mg to a large extent and, hence, may well be suited to extract the role of Al and Mg in a common amorphous matrix. The electron transport properties have been already studied for a series of the amorphous $Al_x(Cu_{0.4}Y_{0.6})_{100-x}$ and $Mg_x(Cu_{0.4}Y_{0.6})_{100-x}$ ($0<x<85$) alloys. In the present work, we have employed the same series of amorphous Al-Cu-Y and Mg-Cu-Y alloys and studied atomic structure by utilizing neutron diffraction technique.

$Al_x(Cu_{0.4}Y_{0.6})_{100-x}$ ($0\leq x\leq 85$) and $Mg_x(Cu_{0.4}Y_{0.6})_{100-x}$ ($0\leq x\leq 80$) alloy ingots were prepared by arc-melting appropriate amounts of pure elements 99.999%Al, 99.9%Mg, 99.99%Cu and 99.9%Y. The first two series of alloys are hereafter abbreviated as [Al]x and [Mg]x, respectively. Pure Y metal containing the least oxygen content (≤0.4 at.%O) was purchased from Shinetsu Chemicals, LTD, Japan. Amorphous ribbons were formed in the following alloys, using a single-roll spinning wheel apparatus operated in Ar-gas atmosphere; [Al]x (x=0, 5, 10, 15, 20, 30, 80 and 85), [Mg]x (x=10, 20, 30, 40, 60 and 80). The X-ray diffraction measurements with Cu-K_α radiation revealed that an amorphous single phase region splits into $0\leq x\leq 0.3$ and $0.8\leq x\leq 0.85$ in the [Al] alloy system, whereas it extends continuously over the range $0\leq x\leq 0.8$ in the [Mg] alloy system. The crystallization temperature is measured, using the differential scanning calorimeter (DSC) with a heating rate of 15 K/min.

1. Thermal property

The crystallization temperature Tx, as manifested by an exothermic peak of the DSC thermograms for a series of amorphous [Al]x and [Mg]x ($0\leq x\leq 85$) alloys, is plotted in Fig.1 as a function of Al or Mg concentration. It is clear that the value of Tx increases rapidly up to 30 at.%Al but drops substantially when Al content exceeds 80 at.%. In contrast, the value of Tx in the amorphous

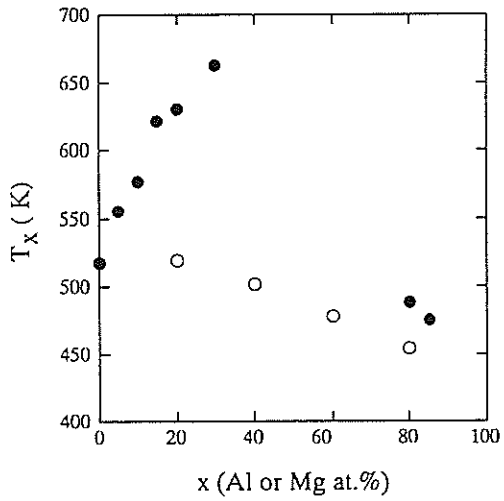

Fig. 1 Crystallization temperature T_X as a function of Al or Mg concentration for amorphous $Al_x(Cu_{0.4}Y_{0.6})_{100-x}$ ($0\leq x\leq 85$) and $Mg_x(Cu_{0.4}Y_{0.6})_{100-x}$ ($0\leq x\leq 80$) alloy.

[Mg] alloys monotonically decreases over a whole Mg concentration range. This already indicates that Al and Mg atoms play a different role, when dissolved into the amorphous Cu-Y matrix. It is also suggestive that the Al atom, when its concentration is in the range $0<x<30$, tends to form strong bonding with Cu and Y atoms and strengthens the bonding over the amorphous Cu-Y alloy, but that the Mg atom apparently weakens it on average.

The crystalline phases formed after being heated up to 770 K were investigated by using X-ray diffraction with Cu-K_α radiation. The binary $Cu_{40}Y_{60}$ and ternary alloys with x=10 and 20 are partitioned into CuY and remaining phases. However, the [Al]30 sample is identified as an almost single phase of the hexagonal AlCuY intermetallic compound isostructural to Fe_2P. Similarly, the major diffraction lines of the [Al]80 and [Al]85 samples can be indexed in terms of the τ_2 phase[4], which is isostructural to $BaAl_4$.

In the case of the crystallized [Mg] alloys, the CuY compound remains observed up to x=20 as a major phase. Pure Mg is definitely precipitated in the crystallized [Mg]80 sample. The diffraction lines for the alloys with intermediate Mg concentrations x=30 and 40 cannot be indexed in terms of any single phase, as opposed to the [Al]30 alloy. Indeed, the SEM (Scanning Electron Microscopy) micrograph revealed that the crystallized [Mg]30 is partitioned into a mixture of Mg-rich and Mg-poor phases. The lattice constant of the resulting CuY compound in both [Al] and

[Mg] alloys is plotted in Fig.2 as a function of Al or Mg concentration. It is seen that the lattice constant increases in the case of [Al] but remains unchanged in [Mg]. This implies that Al atoms are well substituted in the CuY lattice but that Mg atoms are apparently depleted from the CuY compound. All these evidences suggest that the atomic environment and the bonding nature among constituent atoms are substantially different, depending on whether Al or Mg is introduced in the Cu-Y amorphous matrix.

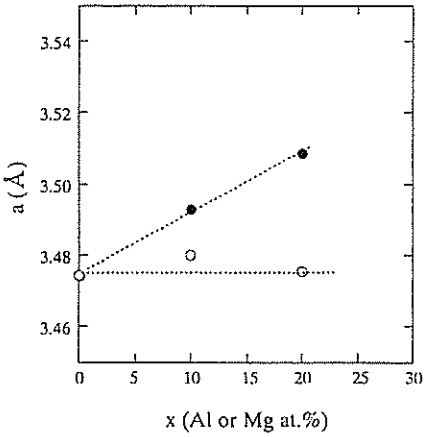

Fig. 2 Lattice constant of the CuY compound phase obtained after crystallization of amorphous $Al_x(Cu_{0.4}Y_{0.6})_{100-x}$ (●) and $Mg_x(Cu_{0.4}Y_{0.6})_{100-x}$ ($0 \leq x \leq 85$) (○) alloy.

2. Atomic structure

Figure 3 shows the structure factors S(Q) for $Al_{30}(Cu_{0.4}Y_{0.6})_{70}$, $Al_{80}(Cu_{0.4}Y_{0.6})_{20}$, $Mg_{30}(Cu_{0.4}Y_{0.6})_{70}$ and $Mg_{80}(Cu_{0.4}Y_{0.6})_{20}$ amorphous alloys. All S(Q)s have a characteristic feature of a metal-metal amorphous alloy. The 1st peak of S(Q) for the amorphous Al-Cu-Y alloys changes the position to the higher Q side with increasing Al content, whilst no change is visible as a function of the Mg content for the Mg-Cu-Y amorphous alloys. The radial distribution functions RDF(r) derived from the Fourier transformation of S(Q) are shown in Figs. 4 and 5 for the amorphous Mg-Cu-Y and Al-Cu-Y amorphous alloys, respectively, along with the RDF(r) of $Cu_{33}Y_{67}$ amorphous alloy observed by Maret et al.[5]. The short range arrangement below about 4 Å drastically changes when Al is introduced into the Cu-Y amorphous alloy matrix. In contrast, the characteristic split peak observed in the Cu-Y amorphous alloy is smeared with increasing Mg concentration for the Mg-Cu-Y amorphous alloys.

The total RDF of $Cu_{33}Y_{67}$ amorphous alloy, which is shown in Fig.4(a), consists of two peaks positioned at 2.9 Å and 3.6 Å. A comparison with the partial RDF led them to conclude that the former originates from the Cu-Y pair and the latter from the Y-Y pair. The Cu-Y distance of 2.9 Å is shorter than the value of 3.08 Å deduced from the hard sphere model given as a sum of the respective Goldschmidt radii. This indicates that strong bonding states are formed between the Cu and Y atoms. As an additional unique feature, they found that Cu atom has no direct contact with neighboring Cu atoms.

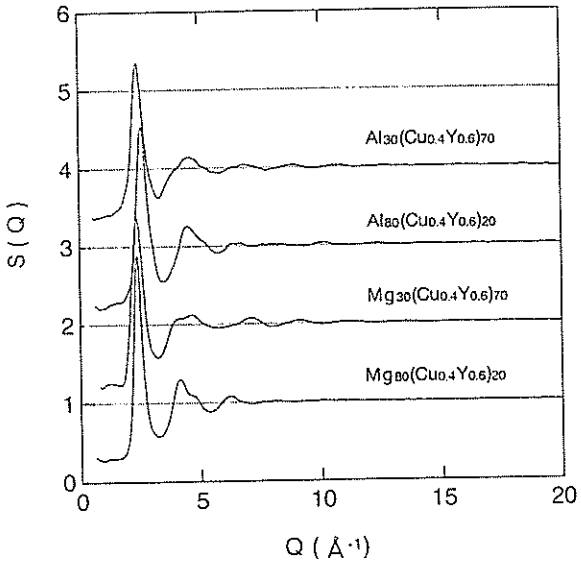

Fig. 3 Total structure factor S(Q) for amorphous $Al_x(Cu_{0.4}Y_{0.6})_{100-x}$, $Mg_x(Cu_{0.4}Y_{0.6})_{100-x}$ (x=30 and 80) alloys.

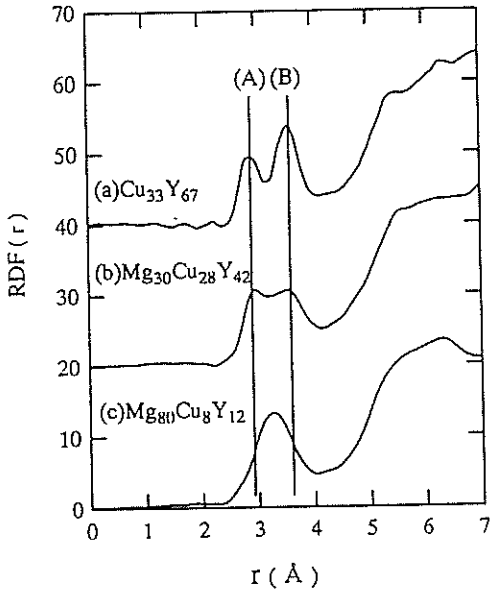

Fig. 4 Total radial distribution function RDF(r) for amorphous $Mg_x(Cu_{0.4}Y_{0.6})_{100-x}$ (x=30 and 80) alloys. The data for the amorphous $Cu_{33}Y_{67}$ alloy were reproduced from Maret et al.. Peaks (A) and (B) correspond to the Cu-Y and Y-Y correlations, respectively.

The total RDF spectra for the amorphous [Mg]30 and [Mg]80 alloys are shown in Fig.4(b) and (c). It is seen that the main peaks (A) and (B) corresponding to the Cu-Y and Y-Y atomic pairs in the binary Cu-Y alloy remain visible in the amorphous [Mg]30 alloy. This is consistent with the

data shown in Fig.2, where the lattice constant of the CuY compound phase formed upon crystallization of an amorphous phase, exhibits no Mg concentration dependence. Therefore, we believe that the interaction of Mg atoms with surrounding Cu and Y atoms must be weak.

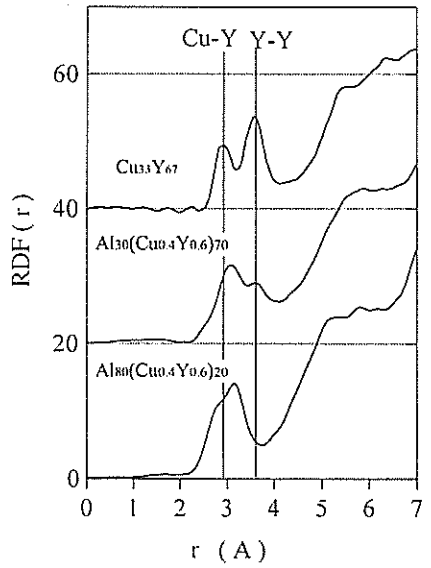

Fig. 5 Total radial distribution function RDF(r) for amorphous $Cu_{33}Y_{67}$ and $Al_x(Cu_{0.4}Y_{0.6})_{100-x}$ (x=30 and 80) alloys.

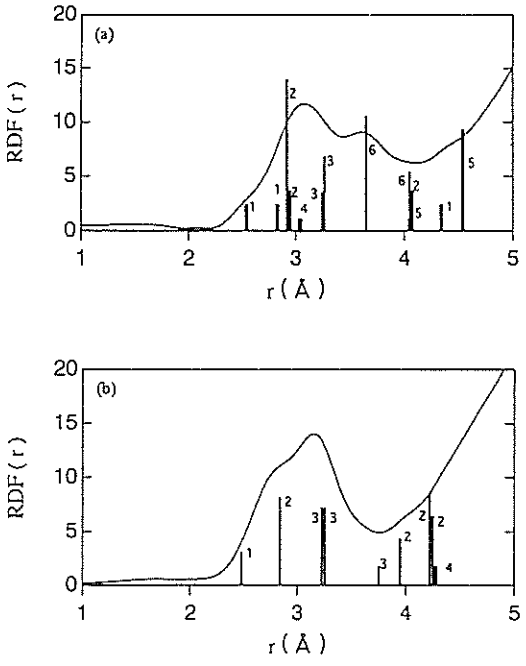

Fig. 6 RDF(r) for amorphous (a) $Al_{30}(Cu_{0.4}Y_{0.6})_{70}$ and (b) $Al_{80}(Cu_{0.4}Y_{0.6})_{20}$ alloys. Vertical lines refere to atomic positions of (a) hexagonal AlCuY compound and (b) τ_2 phase compound. It s height is drawn in proportion to the coordination number. The number attached to each vertical line refers to the following: (1)Al-Cu, (2)Cu-Y, (3)Al-Y, (4)Al-Al, (5)Cu-Cu and (6)Y-Y in the AlCuY compound and (1)Al-Cu, (2)Al-Al, (3)Al-Y, and (4)Y-Y in the τ_2 compound.

The RDF spectrum for the amorphous [Mg]80 alloy consists of a single peak centered at 3.3 Å. This peak reflects definitely the Mg-Mg pair, as expected from the hard sphere model. Note here that the Goldschmidt radius for Mg atom is between those of Cu and Y atoms: r_{Mg}=1.6 Å, r_{Cu}=1.28 Å and r_Y=1.80 Å. But the broadness of the peak strongly suggests that the Cu-Y and Y-Y correlations still remain at the same position as in the amorphous Cu-Y binary alloy. Therefore, the atomic structure of the amorphous [Mg]80 alloy may be viewed as the randomly distributed Mg atoms, in which the Cu-Y clusters may be embedded.

The enlarged RDF spectra for the amorphous [Al]x alloys with x=30 and 80 are shown in Fig.6. First of all, it should be noted that the RDF spectra for both [Al]30 and [Al]80 alloys are asymmetric, as opposed to more symmetric spectra for the [Mg] alloys. This suggests that the local atomic environment in the amorphous [Al] alloys possesses some unique local structure. We noted that the amorphous [Al]30 alloy is crystallized into the hexagonal AlCuY intermetallic compound. According to its crystallographic data, Al-Cu, Cu-Y, Al-Al, Al-Y, Y-Y and Cu-Cu pairs are found in the distance of 2.54, 2.92, 3.04, 3.25, 3.65 and 4.06 Å, respectively. The distances of the Al-Cu and Cu-Y pairs are shorter than those given by the hard sphere model, whereas those of Al-Al and Cu-Cu pairs are longer. Particularly, the distribution of Al atoms is somewhat unique. They are always united in three, each Al atom being separated from the other two by 3.04 Å, and exist as a cluster. The Al cluster thus formed is separated from each other by more than 4. Å. Hence, even the intracluster Al-Al distance is much longer than that of 2.86 Å expected from the Al-Al hard sphere model or the nearest neighbor distance in fcc Al or liquid Al.

The RDF spectrum for the amorphous [Al]30 alloy is now compared with the local atomic structure of the AlCuY intermetallic compound. The position and height of the vertical line represent the distance and relative coordination number of the atomic pairs in the AlCuY compound, respectively. A comparison with the AlCuY compound allows us to identify the local atomic structure in the amorphous [Al]30 phase: a small peak at 2.5 Å most likely corresponds to the Al-Cu pair, a shoulder around 2.9 Å to the Cu-Y and Al-Cu pairs, a central peak around 3.2 Å to the Al-Al and Al-Y pairs and a peak around 3.7 Å to the Y-Y pair. We believe from this comparison that the atomic structure of the amorphous [Al]30 alloy reflects well the local structure of the AlCuY compound and is characterized by the formation of the Al-Y and Al-Cu nearest neighbor atomic pairs while the lack of the Al-Al and Cu-Cu nearest neighbor pairs.

Similarly, a comparison is made with the τ_2-phase compound for the amorphous [Al]80 alloy. Here a small amount of Cu atoms is assumed to be randomly substituted for Al atoms in the $BaAl_4$ structure. Note that the largest Y atom in the τ_2

phase is completely surrounded by totally 16 Al and Cu atoms and, hence, no Y-Y nearest neighbor atomic pair exists. By comparing with the atomic structure of the τ_2 phase, we can attribute a finite RDF near 2.5 Å to the Al-Cu pair. The second largest peak observed at 2.8 Å must be attributed to the Al-Al pair, while the largest peak at 3.2 Å to the Al-Y pair. We believe, therefore, that the atomic structure in the amorphous [Al]80 alloy reflects well that of the τ_2-phase compound: each Al atom always possesses an Al atom as a nearest neighbor in the close-packed distance, while the Y-Y nearest neighbor pair no longer exists. The Cu-Cu nearest neighbor pair would also be scarcely formed because of its low concentration of only 8 at.%. This unique atomic structure must be responsible for the emergence of the free electron-like electronic structure and free electron-like transport properties.

These structual difference between amorphous [Mg]x and [Al]x alloys deeply is correlated to the thermal properties and electronic properties and structures[6]. We have been measured the electronic properties and structures (XPS, SXS) in the amorphous [Mg]x and [Al]x alloys. By combining RDF,, XPS and SXS data together, we reach the following conclusions: hybridization of Al-3p states with both Cu-3d and Y-4d states is so strong that the original hybridization between Cu-3d and Y-4d states is weakened in amorphous [Al] alloys. This is reflected in the RDF spectrum for the [Al]30 alloy as the formation of Al-Cu and Al-Y atomic pairs with the absence of the Al-Al nearest neighbor atomic pair and as a growth of the bonding states of the Al-3p states with Cu-3d and Y-4d states in the Al-K_β spectrum. Strong hybridization eventually results in the isolated Cu and Y atoms in the Al matrix, as the Al concentration exceeds 80 at.%. This is consistent with the observed RDF spectrum and also free-electron-like XPS and SXS spectra. Furthermore, we could point out that these unique local atomic structures resemble well those in the nearby intermetallic compounds AlCuY and τ_2-phase existing in the equilibrium phase diagram. In contrast, hybridization of the Mg-3p states, particularly with Cu-3d states is so weak that hybridization between Cu-3d and Y-4d remains up to the highest Mg concentration. Indeed, a series of the observed RDF spectra for the amorphous [Mg] alloys can be simply interpreted as the sum of the Cu-Y, Y-Y and Mg-Mg pairs. The XPS and SXS spectra were also successfully interpreted along this line. Our conclusion for the local atomic structure in amorphous [Al]x and [Mg]x alloys with x=30 and 80 may be schematically illustrated in Fig.7.

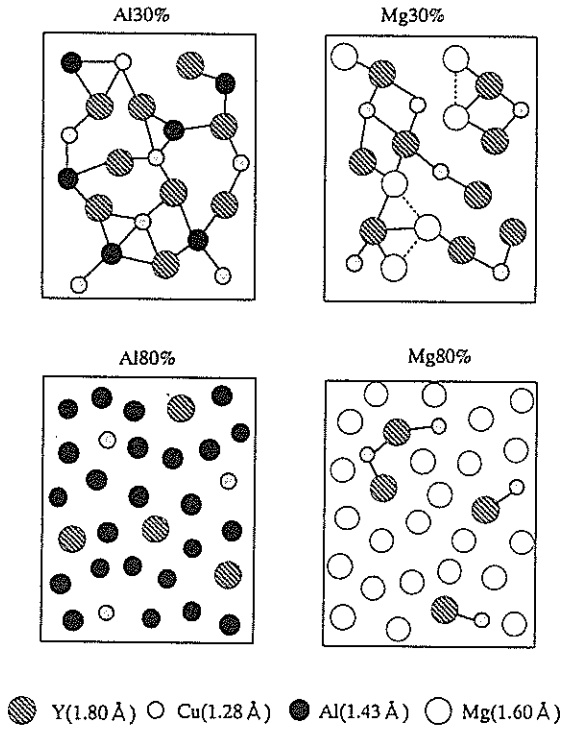

Fig. 7 Schematic illustration of local atomic structures for amorphous [Al]x (x=30 and 80) and [Mg]x (x=30 and 80) alloys.

References

1) U.Mizutani, phy.stat.sol. (b) 176 (1993) 9.
2) M.Matsuura, Y.Yamada and U.Mizutani, J.Non-Cryst.Solids 122 (1990) 45.
3) U.Mizutani, K.Tanaka, T.Matsuda, N.Suzuki, T.Fukunaga, Y.Ozaki, Y.Yamada and K.Nakayama, J.Non-Crystalline Solids 156-158 (1993) 297.
4) O.S.Zarechnyuk and I.F.Kolobnev, Izv. Acad. Nauk SSSR Metall. 5 (1968) 208.
5) M.Maret, P.Chieux, P.Hicter, M.Atzmon and W.L.Johnson, J.Phys.F: 17 (1987) 315.
6) T.Fukunaga, H.Sugiura, N.Takeichi and U.Mizutani, Phys. Rev. B 54 (1996) 3200.

Structural Change across the Metal-Insulator Transition in Amorphous V_xSi_{100-x} Alloys

T. Fukunaga, T. Ishizuka, T. Koyano and U. Mizutani

Department of Crystalline Materials Science, Nagoya University, Furo-cho, Chikusa-ku, Nagoya 464

Amophous M_xSi_{100-x} or M_xGe_{100-x} alloys[1-4] can be relatively easily formed either by the vapor deposition or by the sputtering technique when M is chosen from the transition metal elements. Amorphous Si or Ge alloys have been claimed to be advantageous over heavily doped crystalline semiconductoers, since an amorphous single phase can be formed over a wide composition range across a critical composition associated with the metal-insulator transition. Experimental studies so far reported have largely concentrated on a change in the electron transport properties upon the transition from metallic to activated hopping conduction. A change in the scattering mechanism has been generally discussed without calling much attention to the distribution of metal atoms in an amorphous matrix.

Recently, however, Regan et al. [5] pointed out the existence of the phase separated region in amorphous Mo-Ge and Fe-Si alloys through the observation of small angle x-ray scattering spectra. They showed that the size of metallic clusters extends to the order of 10 Å in the growth plane and 15-20 Å in the granular metals. They suggested that such nano-scale segregation of metallic cluster would explain a finite electronic specific heat coefficient observed in the insulating regime ($x<10$) of the amorphous Mo_xGe_{100-x} alloys [6]. Then, one cannot draw a conclusion as to whether the observed finite density of states at the Fermi level simply reflects the metallic character of a cluster or the localized state inherent to a "homogeneous" amorphous structure. Therefore, the detailed structural characterization of amorphous alloys employed for studies of the metal-insulator transition must be important.

Only limited works have been so far reported concerning the composition dependence of the atomic structure across the metal-insulator transition. We consider it to be crucially important to study the atomic structures. In the present study, we employed a series of the amorphous VxSi100-x thick films ($7<x<74$) prepared by DC sputtering and studied atomic structures to understand the metal-insulator transition. The local atomic structure was investigated by means of a combination of the neutron and X-ray diffraction techniques.

An alloy ingot was prepared in the button form with 30mm in diameter and 7 mm in thickness by arc-melting appropriate amounts of pure Si shot (99.9999%) and pure V flakes (99.95%). The button-shaped ingot was directly used as a target for the triode DC sputtering. The chamber was baked at 120°C for about 20 hr in vacuum and then the background pressure was reduced to 6×10^{-8} Torr before the introduction of pure Ar ga pressure was maintained at 8×10^{-3} Torr. The sputtering rate was about 700 Å/min. The deposition was continued for about 72 hr until the fil thickness reaches about 300 μm. A thick film was mechanically removed from the substrate without difficulty.

The X-ray diffraction spectra were taken with Cu-Ka radiation. The formation of an amorphous single phase was confirmed by examining the appearance of only halo pattern without any Bragg peaks. The composition of an amorphous sample was checked by the energy-dispersive X-ray analyzer. The formation of an amorphous phase was also checked by using the differential scanning calorimeter. The density was measured using toluene as working fluid in the Archimedes method.

The structure factor and the radial distribution functions (RDF) were determined by using a combination of X-ray and neutron diffraction techniques. The Mo-Ka radiation was employed in the step-scanning mode in the X-ray diffraction experiment. The neutron diffraction spectra were taken using High Intensity Total (HIT-II) scattering spectrometer at National Laboratory for High Energy Physics, Tsukuba, Japan. The sample was crushed into small pieces and packed in a cylindrical container made f vanadium with 40 mm in height , 8mm in inner diameter and 25 μm in wall thickness.

Figures 1 and 2 show the structure factors derived from neutron and X-ray diffraction experiments for a series of amorphous V_xSi_{100-x} alloys, respectively. It is clear that no Bragg peaks exist in both sets of data, indicating the lack of long-range order characteristic of an amorphous phase. One can further see in the neutron diffraction spectra that small oscillation remains visible to high scattering wavenumbers, suggesting the existence of a local short-range order in the amorphous structure. Moreover, a substantial difference is seen between the neutron and X-ray structure factors. This is certainly due to the difference in the scattering amplitude or scattering factor of constituent atoms V and Si for neutron and X-ray radiation.

A total structure factor for the binary V-Si alloy is expressed as

$$S(Q) = \frac{C_{Si}^2 b_{Si}^2}{\langle b\rangle^2} S_{SiSi}(Q) + \frac{2C_V C_{Si} b_V b_{Si}}{\langle b\rangle^2} S_{SiV}(Q) + \frac{C_V^2 b_V^2}{\langle b\rangle^2} S_{VV}(Q) \quad (1)$$

in the Faber-Ziman expression and $\langle b\rangle$ is given by

$$\langle b \rangle = C_{Si} b_{Si} + C_V b_V , \quad (2)$$

where c_i and b_i are concentration and scattering amplitude associated with i=Si or V atom, respectively. $S_{ij}(Q)$ represents the partial structure factor for the i-j atomic pair. The scattering amplitudes of V and Si atoms for a neutron beam are known to be -0.0382 and 0.4149×10^{-12} cm, respectively. On the other hand, the scattering factors of V and Si atoms for X-ray photon beam are proportional to their atomic numbers 23 and 14, respectively. For example, the neutron and X-ray total structure factors for the amorphous $V_{12}Si_{88}$ alloy can be expressed as

$$S^N(Q)=1.02562S_{SiSi}(Q)-0.02578S_{SiV}(Q) +0.00016S_{VV}(Q) \quad (3)$$

$$S^X(Q)=0.52104S_{SiSi}(Q)+0.34841S_{SiV}(Q) +0.05051S_{VV}(Q). \quad (4)$$

By eliminating from equations (3) and (4), we obtain

$$S_1(Q)=0.9362S^N(Q)+0.06927S^X(Q)$$

$$=0.9963S_{SiSi}(Q)+0.0036S_{VV}(Q) . \quad (5)$$

Equation (5) indicates that the contribution from the V-V atomic pair amounts to only 0.3% in $S_1(Q)$. This contribution certainly increases with increasing V concentration but reaches only 5% even for the x=37 sample. Thus, we say that $S_1(Q)$ represents well the Si-Si correlation. Likewise, we obtain

$$S_2(Q)= 0.90438S_{SiSi}(Q)+0.09562S_{VV}(Q) , \quad (6)$$

if $S_{SiSi}(Q)$ is eliminated from equations (3) and (4). The contribution of $S_{VV}(Q)$ in equation (6) is about 10 % of the total $S_2(Q)$ but reaches 31% for the V-richest sample with x=37.

The radial distribution function (RDF) spectra can be calculated by Fourier-transforming the $S_1(Q)$ and $S_2(Q)$, both of which were truncated at the wavenumber Qmax=15.5 Å^{-1}. Note here that both $S_1(Q)$ and $S_2(Q)$ are derived as a linear combination of the X-ray and neutron total structure factors and, hence, the Qmax value is limited by a smaller one; Qmax turned out to be about 15.5 and 23 Å^{-1} for the present X-ray and neutron diffraction measurements, respectively. Since $S_1(Q)$ and $S_2(Q)$ mainly represent the Si-Si and Si-V correlations, the corresponding RDF spectra shown in Figs.3 and 4 may be denoted as $RDF_{SiSi}(r)$ and $RDF_{SiV}(r)$ in the following discussion.

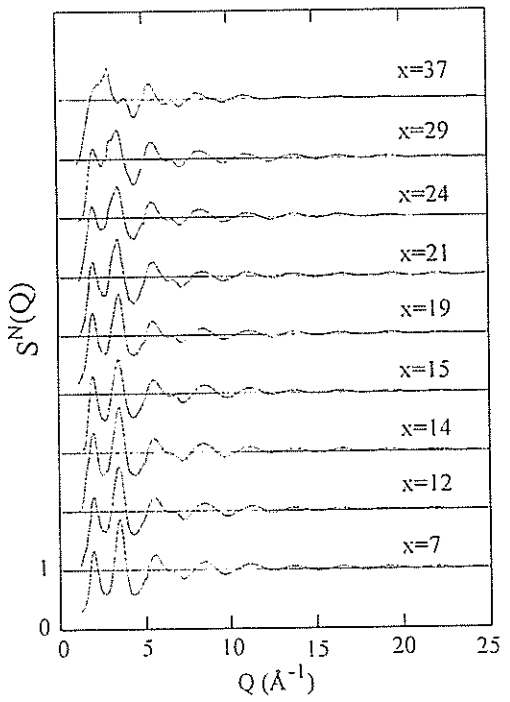

Fig. 1 The structure factors $S^N(Q)$ derived from neutron diffraction studies for a series of amorphous V_xSi_{100-x} alloys.

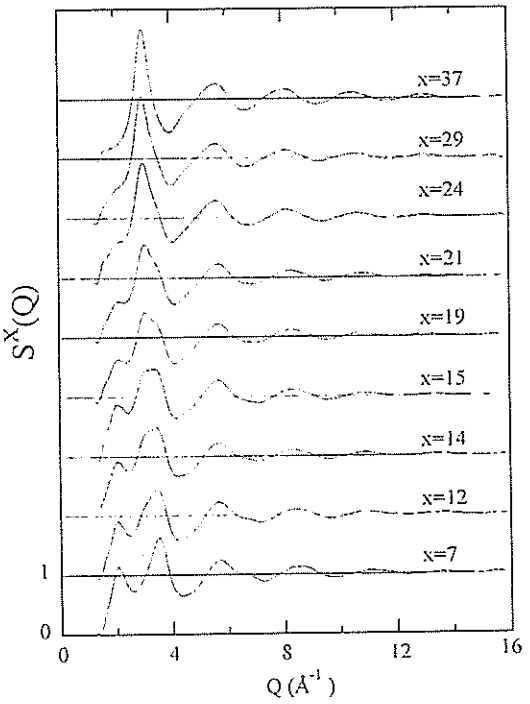

Fig. 2 The structure factors $S^X(Q)$ derived from X-ray diffraction studies with Mo-Kα radiation for a series of amorphous V_xSi_{100-x} alloys.

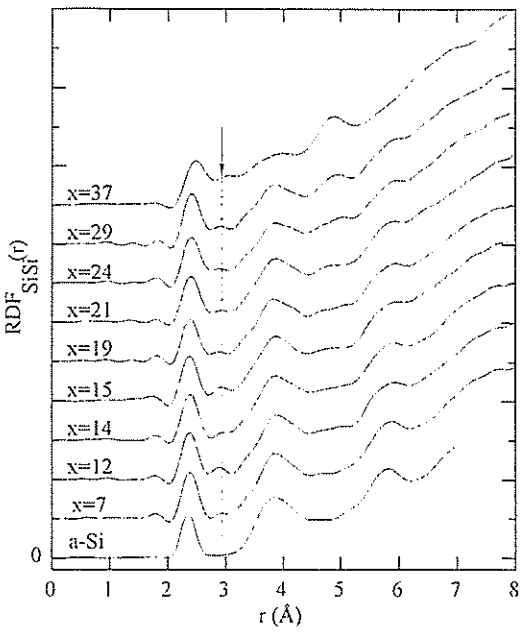

Fig. 3 Radial distribution function (RDF) obtained by the Fourier transform of equation (5) for a series of amorphous V_xSi_{100-x} alloys. A dashed line with an arrow indicates the peak at 2.9 Å.

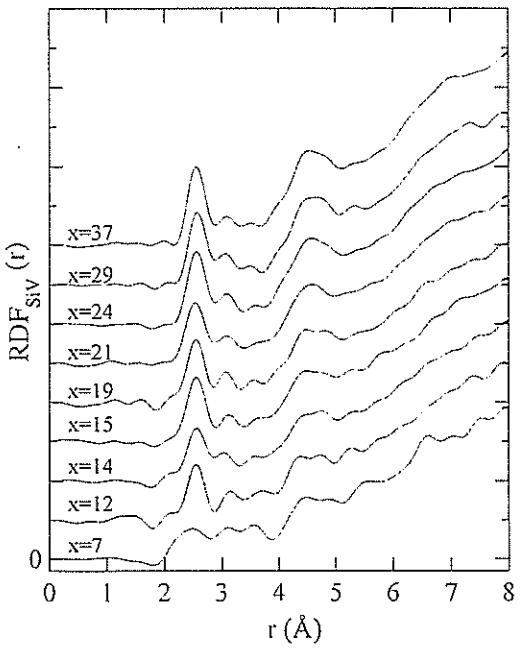

Fig. 4 Radial distribution function (RDF) obtained by the Fourier transform of equation (6) for a series of amorphous V_xSi_{100-x} alloys.

First, we discuss the $RDF_{SiSi}(r)$ spectra shown in Fig.3, into which the data for amorphous Si reported by Fortner and Lannin [7] are incorporated. It can be seen that the first peak at about 2.4 Å remains almost unchanged with increasing V concentration. But a small peak at about 2.9 Å marked by a dashed line with an arrow is found to grow, when V atom is introduced. Its position agrees with the Si-Si distance in the hexagonal VSi_2 compound [8]. This should reflect the distortion of the Si network upon introduction of V atoms.

The radial distribution function (RDF) spectra can be calculated by Fourier-transforming the $S_1(Q)$ and $S_2(Q)$, both of which were truncated at the wavenumber Qmax=15.5 $Å^{-1}$. Note here that both $S_1(Q)$ and $S_2(Q)$ are derived as a linear combination of the X-ray and neutron total structure factors and, hence, the Qmax value is limited by a smaller one; Qmax turned out to be about 15.5 and 23 $Å^{-1}$ for the present X-ray and neutron diffraction measurements, respectively. Since $S_1(Q)$ and $S_2(Q)$ mainly represent the Si-Si and Si-V correlations, the corresponding RDF spectra shown in Figs.3 and 4 may be denoted as $RDF_{SiSi}(r)$ and $RDF_{SiV}(r)$ in the following discussion.

First, we discuss the $RDF_{SiSi}(r)$ spectra shown in Fig.3, into which the data for amorphous Si reported by Fortner and Lannin [21] are incorporated. It can be seen that the first peak at about 2.4 Å remains almost unchanged with increasing V concentration. But a small peak at about 2.9 Å marked by a dashed line with an arrow is found to grow, when V atom is introduced. Its position agrees with the Si-Si distance in the hexagonal VSi_2 compound [8]. This should reflect the distortion of the Si network upon introduction of V atoms.

The $RDF_{SiV}(r)$ spectra show a unique V concentration dependence, as can be seen from Fig.4. Particularly, the spectrum for the x=7 sample is substantially different from the remaining ones. But a new local atomic structure is gradually built up, as x exceeds about 10, and is apparently stabilized above x=20. We have already pointed out that the VSi_2 compound precipitates for the x>20 samples, when heated above the crystallization temperature. This suggests that the local atomic structure for the amorphous alloys with x>20 would be similar to that of the hexagonal VSi_2 compound.

The VSi_2 compound has a layered structure possessing both Si-Si and Si-V pairs at 2.50 and 2.63 Å and V-V pairs at 3.12 Å [8]. The RDF spectra for the samples with x=29 and 37 are compared with the atomic position and coordination number associated with Si-V and V-V pairs in the VSi_2 compound. Remember here that the V-V correlation for the samples with x=29 and 37 is no longer negligible but amounts to about 30 % in $S_2(Q)$. Indeed, as shown in Fig.5, the major peaks observed in the RDF spectra are quite consistent with the local atomic structure of the VSi_2 compound and the peaks associated with Si-V and V-V pairs are fortunately well separated. In the VSi_2 compound, Si atoms are always surrounded by 5 Si atoms and 5 V atoms and V atoms are surrounded by 10 Si atoms. Hence, the coordination number around Si and V atoms is always 10 in sharp contrast to 4 in the amorphous Si. This means that an amorphous alloy possessing the VSi_2-like local atomic structure is typical of a metallic glass and can be differentiated from the amorphous Si-like structure.

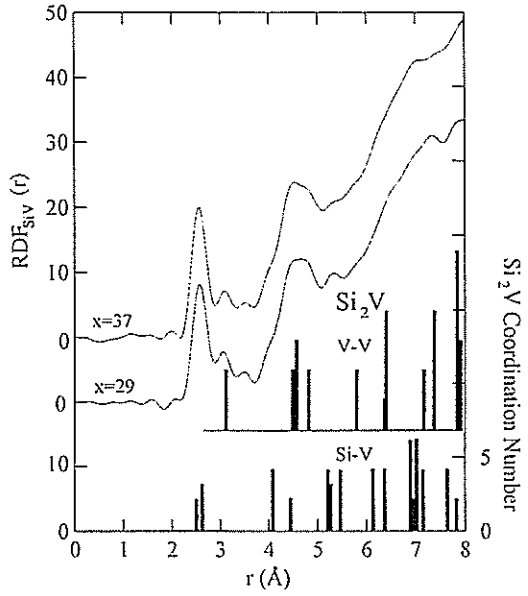

Fig. 5 A comparison of the $RDF_{SiV}(r)$ for the x=29 and 37 samples with the local atomic structure of the VSi_2 intermetallic compound.

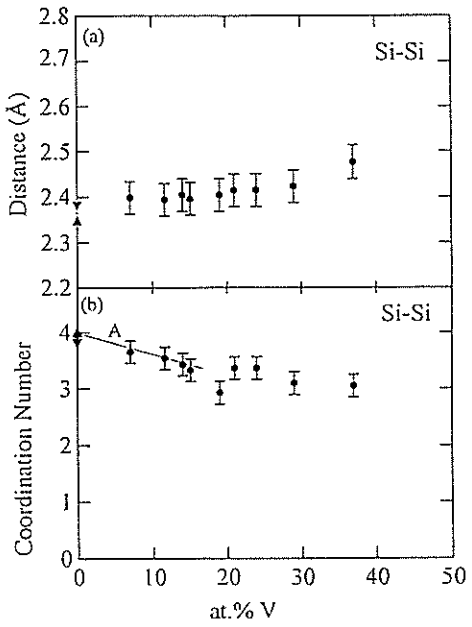

Fig. 6 (a) The Si-Si nearest neighbor atomic distance and (b) the corresponding coordination number as a function of V concentration for the amorphous V_xSi_{100-x} alloys. The line A is drawn in the tetrahedrally-bonded Si network model by passing the coordination 4 and 3 at 0 and 25 at.%V, respectively.

The first peak in $RDF_{SiSi}(r)$ and $RDF_{SiV}(r)$ spectra shown in Figs.3 and 4 is fitted to the Gaussian function to deduce quantitatively the nearest neighbor distance and its coordination number. The results for Si-Si and Si-V correlations are plotted as a function of V concentration in Figs.6 and 7. Let us first discuss the data for the Si-Si correlation. Included are the data for crystalline and amorphous Si from the literature [7]. The Si-Si atomic distance remains unchanged within the accuracy of the measurement up to about x=30, whereas the coordination number decreases more or less linearly up to x=15. A line (A) is drawn through the data points in this composition range. This line intercepts the coordination number 4 at x=0 and passes a coordination number 3 at x=25. This means that one-fourth of Si atoms in the tetrahedrally-bonded network are substituted by V atoms at x=25. Indeed, the data at least up to x=15 fall on this line, suggesting that the semiconducting Si network, over which V atoms are randomly distributed, is a characteristic structural feature in the V-poor amorphous alloys. Here it must be noted that the Si-Si bonding in the tetrahedral network is certainly disrupted and is distorted by the introduction of the V atom, resulting in the formation of the new Si-Si correlation at 2.9 Å as evidenced from the $RDF_{SiSi}(r)$ spectra shown in Fig.4.

The Si-V atomic distance shown in Fig.7 is found to be about 2.56 Å and to be almost independent of V concentration. However, the coordination number shows a unique behavior. The VSi_2 compound possesses the two different Si-V atomic pairs at 2.50 and 2.63 Å and their coordination numbers are 2 and 3, respectively. The observed Si-V atomic distance of 2.56 Å for the x=37 sample, whose V concentration is near the VSi_2 compound, is close to an average of these two sites in the compound. The coordination number for the x=37 sample is 4.2, which is close to 5 in the compound. The line (B) can be drawn through the data points for samples with x>20. This line represents a change in the coordination number of amorphous V_xSi_{100-x} alloys with x>20, the local structure of which is characterized by the VSi_2 compound.

As discussed above, the Si network model was applied to the V-poor amorphous alloys. The line corresponding to (A) in Fig.5 should pass through the origin and 1 at x=25 in the Si-V correlation shown in Fig.7. This is again denoted as (A) and drawn in Fig.7. It is seen that only the data point for the x=7 sample happens to fall on this line but those for x=12, 14 and 15 deviate upwards from this line. The latter deviates not only from the line (A) but also from the line (B). We believe, therefore, that this is the region where both Si network and VSi_2 metallic glass-like structures are competing with each other and the structural frustration occurs. It is this transient region where the metal-insulator transition occurs. Asal et al. [4] studied the local atomic structure in the amorphous Ni-Si alloys by EXAFS technique and pointed out that the tetrahedral network structure changes to a higher coordination metallic structure when Ni content exceeds 20 at.%.

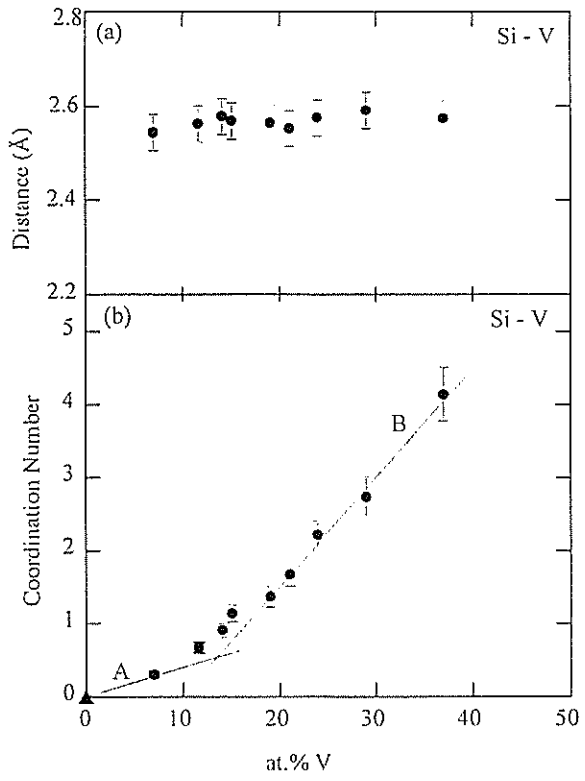

Fig. 7 (a) The Si-V nearest neighbor atomic distance and (b) the corresponding coordination number as a function of V concentration for the amorphous V_xSi_{100-x} alloys. The line A corresponds to the line A in Fig. 6. The line B is drawm through the data points in the range 19<x<37.

In summary, the present structural analysis for the amorphous V_xSi_{100-x} alloys demonstrated that the tetrahedrally-bonded Si network structure, into which V atoms are randomly substituted, persists up to about 10 at.%V and that it changes to a metallic glass structure, which resembles locally that of the VSi_2 intermetallic compound, when x exceeds about 20 at.%. The composition range 10<x<20 corresponds to a region where these two local atomic structures are apparently competing with each other and the metal-insulator transition takes place.

References

1) B.W. Dodson, W.L. McMillan, J.M. Mochel and R.C. Dynes, Phys. Rev. Lett. 46 (1981) 46.
2) N.Nishida, T. Furubayashi, M. Yamaguchi, K. Morinaga and H. Ishimoto, SolidState Electronics, 28 (1985) 81.
3) K.M. Abkemeier, C.J. Adkins, R. Asal and E.A. Davis, Phil. Mag. B65 (1992) 675.
4)R. Asal, S.H. Baker, S.J. Gurman, S.C. Bayliss and E.A. Davis, J. Phys.:Condens. Matter 4 (1992) 7169.
5)M.J. Regan, M. Rice, M.B. Fernandez van Raap and A. Bienenstock, Phys. Rev. Lett. 73 (1994) 1118.
6) D. Mael, S. Yoshizumi and T.H. Geballe, Phys. Rev. B34 (1986) 467.
7) J. Fortner and J.S. Lannin, Phys. Rev. B39 (1989) 5527.
8) P. Villars and L.D. Calvert, "Pearson's Handbook of Crystallographic Data for Intermetallic Phases", vol.1, (American Society of Metals, 1985)

Dynamic Properties of $LiNO_3$-Glycerol Solutions

T. KAMIYAMA, A. MIYAMOTO*, J. KAWAMURA*, Y. NAKAMURA* and Y. KIYANAGI

Department of Nuclear Engineering, Faculty of Engineering, Hokkaido University, Sapporo 060
**Department of Chemistry, Faculty of Science, Hokkaido University, Sapporo 060*

The property of glycerol is interesting because of its high viscosity (about 1400 mPa·s at room temperature) and vitrificability. Glycerol has a complicate network structure binding through its three hydroxides. The highly viscous nature is caused by such twisted three dimensional hydrogen bonds. When an electrolyte is dissolved in the glycerol solvent, the direct hydrogen bond between glycerol molecules is broken off and change the bonds through the cations[1]. So we can vary the network strength by adding the electrolyte in glycerol. In the present system it is considered that $LiNO_3$ is solvated by the hydroxyl groups in glycerol molecule. $LiNO_3$ is soluble by more than 30 mol% and the concentrated solutions become highly viscous liquids and easy to supercool. Figure 1 shows the Angell's plot[2] which indicates the network strength in some glass-forming systems. By Angell's classification, the system which comes on the straight line has the strong networking structure (strong glass) and the system which has a large deviation from the straight line is non-networking structure (fragile glass). The glycerol systems are fragile in such classification and by adding the electrolyte, $LiNO_3$, the fragility increases.

The purpose of this study is to clarify the network variety through the glycerol molecular motion. For this purpose we have to distinguish two motions. One is the translational diffusive motion of the glycerol. We think that this motion is directly correlated to the network strength, e.g. viscosity. The other is the rotational diffusive motion of grycerol molecule which is a indicator of the circumstance around the glycerol molecule. Because of the high viscosity of the system, it is difficult to measure the translational diffusive component in the quasielastic spectrum at low temperature. But in such temperature the rotational component will give us the useful

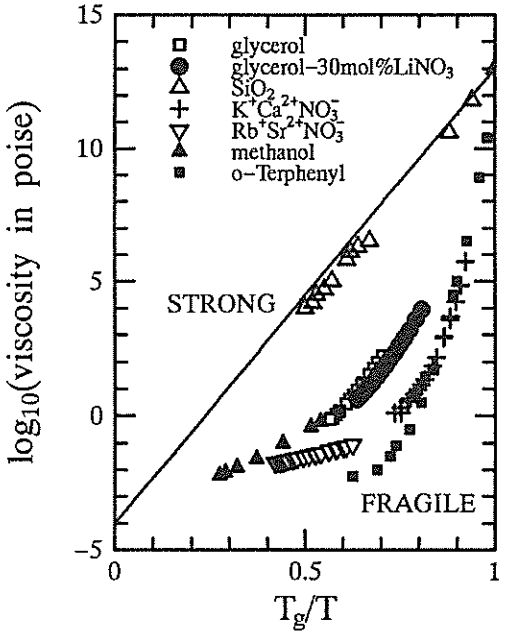

Fig. 1 Arrhenius plot of the viscosity for a variety of glass-forming liquids. The inverse temperature scale has been normalized with respect to the calorimetric glass transition temperature Tg.

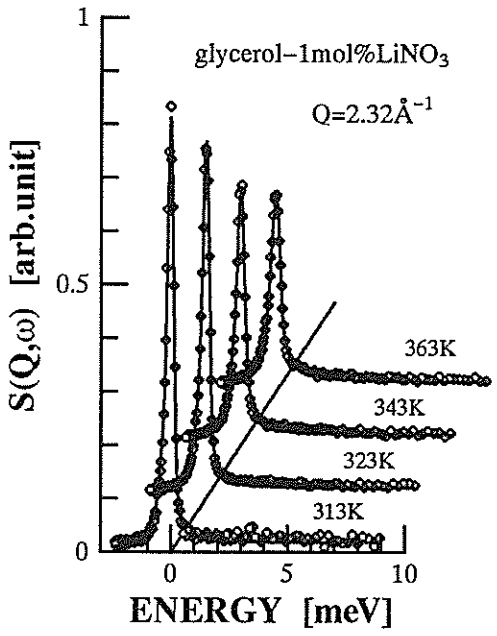

Fig.2 Quasielastic neutron scattering spectrum measured by the LAM-40 spectrometer. Solid lines are fitting results by two Lorentzian model.

information about the network associating with lithium ions.

Until now we have studied viscosity, electric conductivity, density and quasielastic neutron scattering in $LiNO_3$-glycerol solutions. The viscosty and the conductivity data suggest that the lithium ion is captured in the hydrogen bonded network and strengthen the network. From the quasielastic neutron scattering experiment we could get the result only in the dilute region (1 to 5 mol% $LiNO_3$) because of the high viscosity of the solutions. Figure 2 shows the result obtained by the quasielastic neutron scattering spectrometer LAM-40. The resolution of the spectrometer is about 200 μeV at the full width at half maximum (FWHM) of the vanadium elastic peak. By the neutron scattering cross sections the spectrum shows the hydrogen motions in the glycerol molecule. We applied two-Lorentzian model to fit the spectrum and obtained some parameters. It was difficult, however, to get parameters for the slow glycerol translational motion.

Figure 3 shows the Q^2 dependence of the half width at half maximum (HWHM) for the rotational diffusive motion of glycerol molecule. For these data, we try to use the hydrogen jump-diffusion model to get the diffusion coefficients

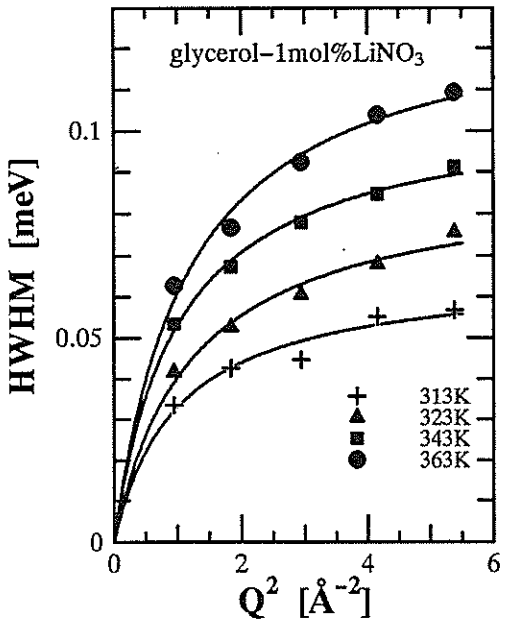

Fig. 3 Q^2 dependence of the half width at half maximum of the broad components in the quasielastic spectrum. Lines are fitting results by jump-diffusion model.

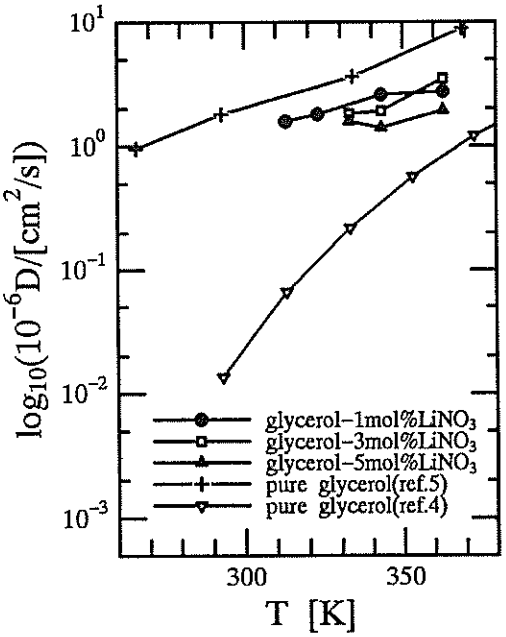

Fig. 4 Temperature dependences of the diffusion constants obtained by several methods.

and residential times.

Figure 4 shows the comparison of the diffusion constants obtained by several methods. For pure glycerol the translational diffusion constant was obtained from the viscosity[3] and NMR[4] measurements. From quasielastic neutron scattering measurement Larsson deduced the glycerol rotational diffusion constants[5]. Taking account of the viscosity results, we suppose our results correspond to the glycerol rotational diffusion coefficients. With increasing the lithium nitrate fraction, the glycerol motions become slower. This fact means the glycerol is incorpolated in the stronger network through cation. In the future we will measure over a wider concentration range of the system to reveal the relation between the microscopic molecular motions and vitryfing nature.

References

1) S. E. Okan, P. S. Salmon, D. C. Champeney and I. Petri, Mol. Phys., 84 (1995) 325
2) C. A. Angell, J. Non-Cryst. Solids, 102 (1988) 205
3) G. M. Glover and A. J. Matheson, Trans. Farad. Soc., 67 (1971) 1960
4) D. J. Tomlinson, Mol. Phys., 25 (1972) 735
5) K. E. Larsson, Phys. Rev., 167 (1968) 171

Neutron diffraction study in liquid S-Se mixtures

F. KAKINUMA, T. FUKUNAGA [a], M. MISAWA [b] and K. SUZUKI [c]

Niigata Institute of Technology, 1719 Fujihashi, Kashiwazaki 945-11
[a]Department of Crystalline Materials Science, Nagoya University, Furo-cho, Chikusa-ku, Nagoya 464
[b]Department of Chemistry, Niigata University, Ikarashi, Niigata 950-21
[c]Institute for Materials Research, Tohoku University, 2-1-1 Katahira, Aoba-ku, Sendai 980

Liquid Sulpher is mainly composed of S_8 rings below 160 °C and becomes a mixture of rings and long chains[1]. Polymerization of very long chains out of rings takes place around 160 °C. On the other hand, liquid Se consists mainly of long chains just above its melting temperature[2]. As temperature is raised, the chain length becomes shorter. In order to study the structure of liquid S-Se mixtures, we have performed neutron diffraction measurements as a function of temperature and composition. The measurements were carried out by using the High Intensity Total scattering spectrometer (HIT II) at KEK. The samples are measured at the temperature of 200 °C and 400 °C for S_xSe_{1-x} with x = 0.2and 0.8 and at 150 °C and 400 °C for $S_{0.5}Se_{0.5}$.

The overall feature of the profile of S(q) for liquid S_xSe_{1-x} mixtures is similar to that for liquid S at higher temperatures and that for liquid Se. The characteristics in features are (i) the height of first peak is smaller than that of second peak, (ii) the oscillation of S(q) still remains at higher q values. Such features suggest that the liquid S_xSe_{1-x} mixtures consist mainly of chain-like network structure.

The distinct change in S(q) has been observed with increasing S concentration. The shoulder grows at low q side of the first peak. On the third peak for $S_{0.8}Se_{0.2}$, the width becomes broad and the peak position shifts to higher q values.

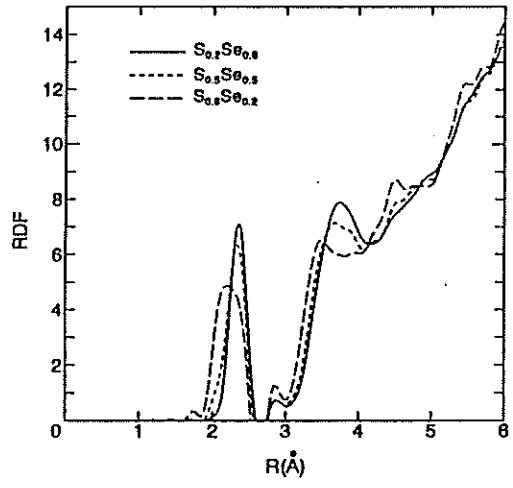

Fig. 1 Radial distribution functions for liquid S_xSe_{1-x} mixtures with x = 0.2, 0.5 and 0.8 at 400 °C.

Figure 1 shows the radial distribution function, RDF, at 400 °C. Systematic change is observed in RDF. The peak position of first peak shifts to lower q side with increasing S concentration. The noticeable variation is observed in the profile of RDF for $S_{0.8}Se_{0.2}$. The peak width becomes very broad and the peak position shows a large shift.

The first peak of RDF for $S_{0.2}Se_{0.8}$ was fitted by a single Gaussian, and those for $S_{0.5}Se_{0.5}$ and $S_{0.8}Se_{0.2}$ were decomposed to two Gaussians. The peak positions and coordination numbers are listed in Table 1. The positions of the first peak for $S_{0.2}Se_{0.8}$ and of second subpeak for $S_{0.5}Se_{0.5}$ are insensitive to the temperature. On the contrary, the positions of first subpeak for $S_{0.5}Se_{0.5}$ and of subpeaks for $S_{0.8}$ $Se_{0.2}$ are temperature dependent.

These results suggest that Se-rich mixtures have a chain-like structure composed of random mixtures with S and Se atoms. The bond length of S-Se is similar to that of Se-Se. For S-rich mixtures, the sulphour-rich region seems to be mixtures of S_8 rings and long chains. The S-S and S-Se bond strength appears to depend on S concentration.

Table 1 Peak positions r_1 and coordination numbers n_1

	$r_1(n_1)$		n_1	
$S_{0.2}Se_{0.8}$	2.35(1.94)		1.94	200 °C
	2.35(1.93)		1.93	400 °C
$S_{0.5}Se_{0.5}$	2.15(0.50)	2.34(1.64)	2.14	150 °C
	2.18(0.53)	2.35(1.45)	1.98	400 °C
$S_{0.8}Se_{0.2}$	2.09(0.94)	2.31(1.22)	2.16	200 °C
	2.12(1.30)	2.35(0.88)	2.18	400 °C

References

1) **R. Bellissent, L. Descots and F. Boué, Phys. Rev. 41, 2135 (1990)**
2) **K. Suzuki, Ber. Bunsenges. Phys. Chem. 80, 689 (1976)**

Boson Peaks in Simple Molecular Glasses

O. YAMAMURO, I. TSUKUSHI*, T. MATSUO, K. TAKEDA[a], T. KANAYA[b], AND K. KAJI[b]

Department of Chemistry, Graduate School of Science, Osaka University, Toyonaka, Osaka 560
[a] Department of Chemistry, Naruto University of Education, Naruto, Tokushima 772
[b] Institute for Chemical Research, Kyoto University, Uji, Kyoto 611

Introduction

Low energy excitation in amorphous materials is one of the current topics in condensed matter physics. It is observed as non-Debye excess heat capacities in the temperature range 10 - 30 K and as a boson peak in the energy range 1 - 5 meV in inelastic neutron and Raman spectra. Various types of amorphous materials have been studied and several models have been proposed to reproduce the experimental results.[1] However, the origin and the microscopic mechanism of the low energy excitation have not been explained with sufficient generality.

We have studied this phenomenon focusing our attention on the glasses formed by simple hydrocarbon molecules. Molecular glasses are suitable for such studies since the intermolecular interaction is simple van der Waals forces (short-range and isotropic) so that the result can be compared with those of theoretical and molecular dynamics studies where similar interactions are assumed. It is also advantageous that the molecular mass and structure can be changed systematically in a homologous series. Inelastic neutron scattering is very useful to study the low-energy excitation since it is the best experimental method to obtain the density of vibrational states $G(\omega)$ in the low energy region. In this report, we summarize our recent studies[2-5] and discuss on the origin of the low energy excitation of molecular glasses.

Experimental

The samples examined so far are propylene (CH_2=$CHCH_3$, M = 42.1, T_g = 55 K), 1-butene (CH_2=$CHCH_2CH_3$, M = 56.1, T_g = 60 K), and 3-methylpentane ($CH_3CH_2CH(CH_3)CH_2CH_3$, M = 86.2, T_g = 70 K). In these samples, incoherent dynamic scattering law $S_{inc}(Q,\omega)$ is obtained easily owing to the large incoherent scattering section of hydrogen atoms. The glassy state of propylene was prepared by vapor deposition using the special cryostat described elsewhere[3] while those of other samples by a usual liquid quenching method.

Inelastic neutron scattering (INS) experiment was performed with the inverted geometry time-of-flight (TOF) spectrometer LAM-40.[6] The data were collected six scattering angles 24°, 40°, 56°, 72°, 88°, and 104°. The energy resolution was 0.2 meV and the energy window extended to 10 meV. The magnitude of the scattering vector Q at the elastic position ranges from 0.2 to 2.4 Å^{-1}. The observed TOF spectrum was converted to a differential scattering cross section after making corrections for empty cell scattering, counter efficiency, the incident neutron spectrum and self-shielding (*ca.* 90 % transmission) and then converted to the incoherent dynamic scattering law as usual.

Results and Discussion

Inelastic Neutron Spectra

Figure 1 shows the symmetrized $S(Q,\omega)$ of the glassy states of the three hydrocarbon molecules propylene,[3] 1-butene[2] and 3-methylpentane[7] at 18 K. The shape of spectra did not depend on the scattering wave vector Q within the experimental precision and so they were added together to produce the Q-independent INS spectrum. The mean Q value was 1.54 Å^{-1}. The data were scaled using total intensity for comparison of the three substances. A clear and large boson peak was observed at 2.5-3 meV for the three samples.

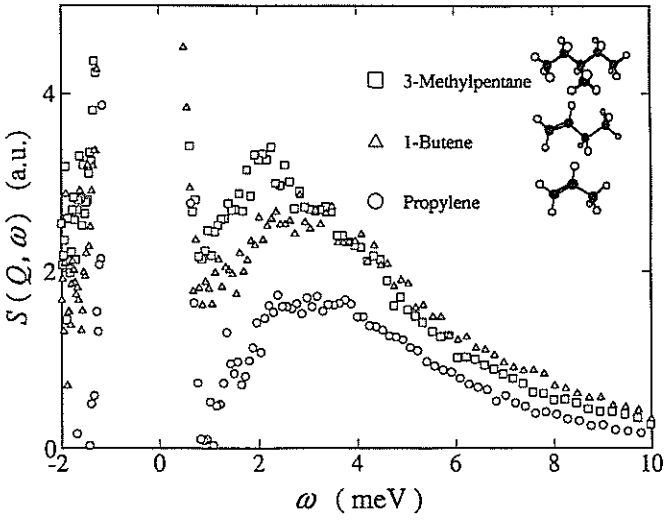

Fig. 1. Incoherent dynamic structure factors of the glassy states of three simple hydrocarbon molecules at 18 K.

Density of Vibrational States

The density of vibrational states $G(\omega)$ was calculated from the incoherent inelastic scattering

functions $S(Q,\omega)$ assuming one phonon scattering process and plotted as $G(\omega)/\omega^2$ in Fig. 2.

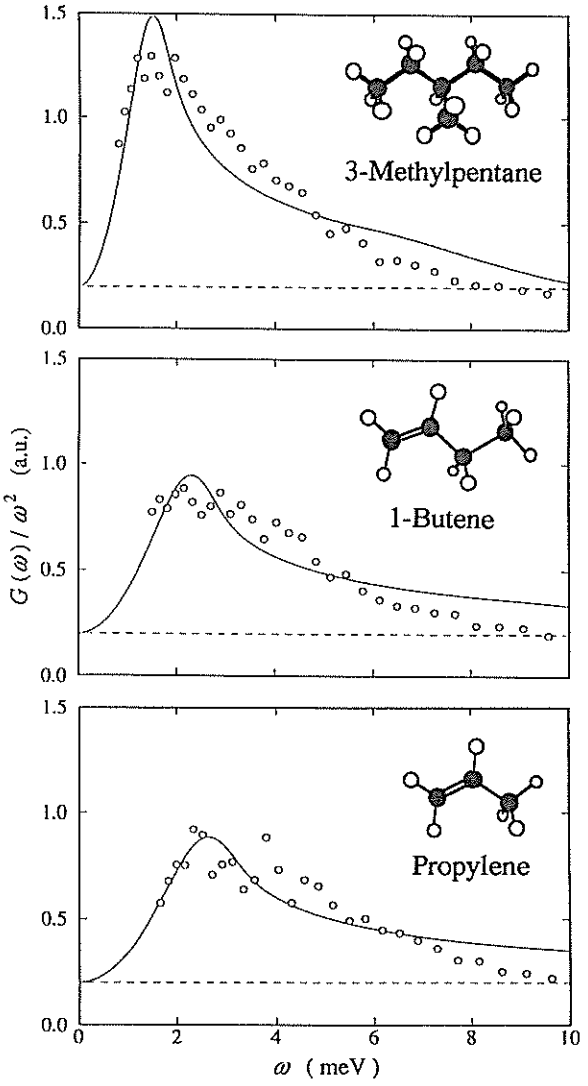

Fig. 2. Density of vibrational states divide by ω^2. The solid curves represent the results of the fitting according to the soft potential model. The dashed lines gives the contribution due to the Debye vibration.

These values were fitted by the combination of the Debye model and the two parameter version of the soft potential model.[8,9] The details of the fitting are described elsewhere.[2] The fitted curves are shown by the solid line in Fig. 2. The dashed lines represent the Debye parts whose frequencies are estimated from the heat capacity data.[5,10] Although it is difficult to discuss on the validity of the model because of the poor data quality, the fitted curve reproduces the general energy dependence of the low energy excitation; *i.e.*, a peak with a long tail on the high energy side.

The molar heat capacity data[5,10] were fitted to a model function repoducing the experimental $G(\omega)$ to obtain the absolute value of $G(\omega)$ ($meV^{-1}\cdot mol^{-1}$). The details of the fitting are described elsewhere.[2] Figure 3 shows the experimental molar heat capacities of glassy (open circles) and crystalline (closed circles) 1-butene.[10] The solid line represent the result of the fitting. The agreement between the experiment and theory is satisfactory up to *ca.* 20 K. The deviation in the high temperature region is due to the contribution from the vibrational modes above 10 meV, which was not included in this calculation. The number of the soft mode per molecule N_{LEE}, which was obtained by integrating absolute $G(\omega)$ subtracted by the Debye part, is given below. 3-methylpentane: 1.8, 1-butene 1.4, propylene: 1.3. These values are much larger than those obtained in the network glasses like SiO2 (< 0.1)[9] and do not depend on the molecules much.

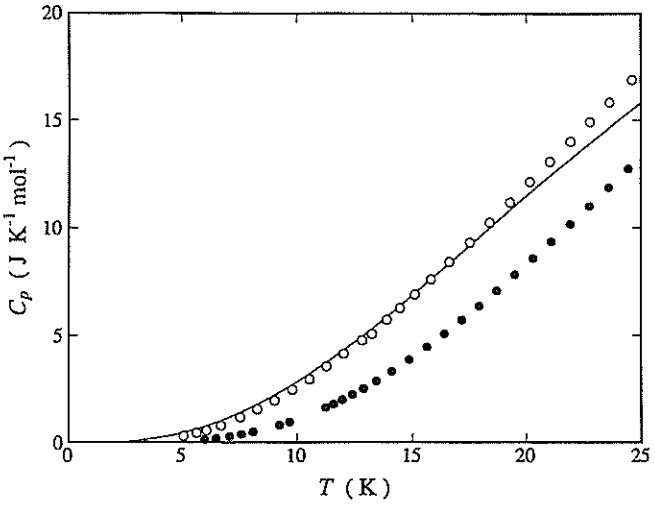

Fig. 3. Low temperature heat capacities of 1-butene. Open circles represent the heat capacities of the glassy state and the closed circles those of the crystalline state. The solid line represents the result of the fitting.

Molecular mass dependence of the boson beak

In Fig. 4, the boson peak energy ω_{bp} of the three molecular glasses measured in this study are plotted as a function of the inverse root of molecular mass ($M^{-1/2}$) along with those of previously studied molecular glasses ethylbenzene,[11] orthoterphenyl[12], glycerol[13], and methanol.[14] It is interesting that all of the data lie on a straight line passing through the origin (0,0). A similar relation will be found if ω_{max} is plotted as a function of the moment of inertia, though there is an ambiguity as to the component (I_X, I_Y, or I_Z) that should be plotted in this case. The plot suggests that the low energy excitation is more closely

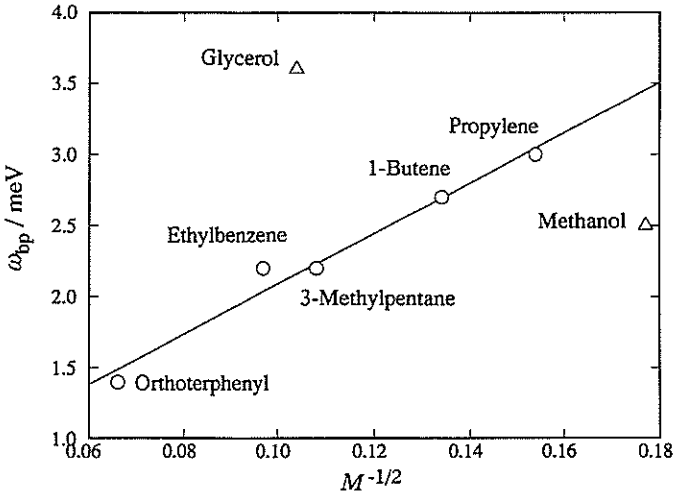

Fig. 4. Molecular mass ($M^{-1/2}$) dependence of the boson peak energy.

related to the overall translational or rotational motion than to the intramolecular vibrations and may be represented as a type of the simple harmonic oscillation. It is noted that molecules with intermolecular hydrogen bonds (methanol and glycerol) exhibit a quite different tendency from the simple hydrocarbon molecules. It is reasonable to find different behavior for substances forming the glassy phase by different types of intermolecular forces (van der Waals and hydrogen-bonding).

The Mechanism of the Low Energy Excitations

From the molecular-mass dependence of ω_{bp}, it is likely that the low-energy excitation of the molecular glasses is associated with the overall motion of the molecules. This motion may be the rotational vibration (libration) since the translational vibration is already considered as the Debye modes with 3 degrees of freedom in the analysis of the density of states. N_{LEE} (< 3) suggests that this motion does not arise from a single molecule but from a group of some molecules (probably 1-4 with distribution). This group of molecules may be called a domain. Its size is not inconsistent with the domain size (3-5) suggested by the entropy analysis in molecular liquids[15,16] and polymer melts.[17] The results of soft potential fits indicate the motion is considerably softened as a result of frozen density fluctuations and local strain fields. This is consistent with the mechanism of the low-energy excitation in other types of amorphous materials studied so far.

As the next stage of the study, we are planning to examine glassy states of simpler molecules (*e.g.*, benzene, ethene, water). It is possible to vitrify these molecules by simple vapor deposition or vapor deposition with some doping gas (rare gases or nitrogen).

References

1) For example; U. Buchenau, in *Dynamics of Disordered Materials*, edited by D. Richter, A. J. Dianoux, W. Petry and J. Teixeira (Springer, Berlin, 1989).
2) O. Yamamuro, T. Matsuo, K. Takeda, T. Kanaya, T. Kawaguchi and K. Kaji, J. Chem. Phys. **105**, 732 (1996).
3) O. Yamamuro, I. Tsukushi, T. Matsuo, K. Takeda, T. Kanaya and K. Kaji, J. Chem. Phys., in press.
4) O. Yamamuro, I. Tsukushi, T. Matsuo, K. Takeda, T. Kanaya and K. Kaji, Prog. Theor. Phys., in press.
5) A. Lindqvist, O. Yamamuro, I. Tsukushi and T. Matsuo, J. Chem. Phys., submitted.
6) K. Inoue, Y. Ishikawa, N. Watanabe, K. Kaji, Y. Kiyanagi, H. Iwasa and M. Kohgi, Nucl. Instrum. Method **A238**, 401 (1984).
7) O. Yamamuro, I. Tsukushi, K. Takeda, T. Matsuo, T. Kanaya and K. Kaji, to be published.
8) L. Gil, M. A. Ramos, A. Bringer and U. Buchenau, Phys. Rev. Lett. **70**, 182 (1993).
9) M. A. Ramos, L. Gil, A. Bringer and U. Buchenau, Phys. Stat. Sol. **A135**, 477 (1993).
10) K. Takeda, O. Yamamuro and H. Suga, J. Phys. Chem. Solids **52**, 607 (1991).
11) B. Frick, J. Williams, S. Trevino and R. Erwin, Physica **B213&214**, 506 (1995).
12) J. Wuttke, M. Kiebel, E. Bartsch, F. Fujara, W. Petry and H. Sillescu, Z. Phys. **B91**, 357 (1993).
13) F. J. Bermejo, A. Criado and J. L. Martinez, Phys. Lett. **A195**, 236 (1994).
14) M. Garcia-Hernandez, R. Burriel, F. J. Bermejo, C. Pique and J. L. Martinez, J. Phys.: Cond. Matter **4**, 9581 (1992).
15) S. Takahara, O. Yamamuro and T. Matsuo, J. Phys. Chem. **99**, 9589 (1995).
16) O. Yamamuro, I. Tsukushi, A. Lindqvist, S. Takahara, M. Ishikawa and T. Matsuo, to be published.
17) S. Matsuoka and X. Quan, J. Non-Cryst. Solids **131-133**, 357 (1991).

* Present address: Institute for Chemical Research, Kyoto University, Uji, Kyoto 611

Origin of Anomalous Heat Capacity of Vitreous Toluene

O. YAMAMURO, I. TSUKUSHI*, T. MATSUO, T. KANAYA[a], AND K. KAJI[a]

Department of Chemistry, Graduate School of Science, Osaka University, Toyonaka, Osaka 560
[a] Institute for Chemical Research, Kyoto University, Uji, Kyoto 611

Introduction

Molecular glasses are the system which is close to the "ideal glass" frequently used in the theoretical and molecular dynamics studies. However, few combined theoretical and experimental works have been done since only glasses of complex molecules have been investigated experimentally because of experimental difficulties; simple molecules tend to crystallizes readily on cooling.

Toluene is a hopeful molecule which can be vitrified by a rapid liquid cooling (> 100 K s^{-1}) though it is a quasi-rigid molecule with only one flexible mode of methyl rotation.[1] Recently, we found that toluene doped with 10 % of benzene can be vitrified by normal liquid cooling (ca. 0.1 K s^{-1}).[2] Figure 1 shows the heat capacity of glassy[2,3] and crystalline[4] toluene; the contribution from the doped benzene has been corrected assuming the additivity of the heat capacities. The glass transition, crystallization and fusion appeared at 117 K, ca. 125 K, and 178 K, respectively. It is the most interesting feature that an anomalous C_p increase appeared in the glassy state starting at about 130 K, which is 48 K lower than T_g. Such a large increase of C_p has never been observed below T_g in any other molecular glasses studied by our group. The aim of the present study is to investigate the origin of this anomaly from the density of states derived by neutron scattering.

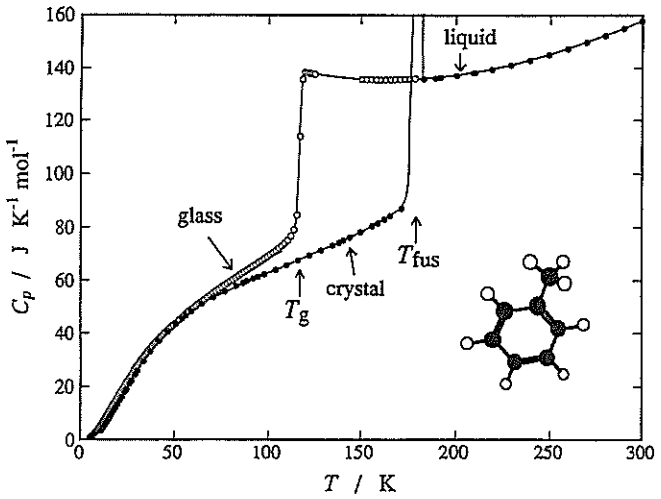

Fig. 1. Molar heat capacities of toluene. Open circles represent the heat capacities of the metastable states (glass and supercooled liquid) and the closed circles those of the stable states (crystal and liquid).

Experimental

The same sample as used in the heat capacity measurement ($toluene_{0.9003}benzene_{0.0997}$) was used in this study. Inelastic neutron scattering (INS) spectrum was collected with the inverted-geometry crystal-analyzer (PG002) type time-of-flight (TOF) spectrometer LAM-D.[5] The data were collected at two scattering angles 35° and 85°, corresponding to the Q vectors of 0.9 and 2.0 Å^{-1} at elastic position. The energy resolution was 0.35 meV and the energy window extended to 200 meV. The observed TOF spectrum was converted to the incoherent dynamic scattering law since the incoherent scattering from the hydrogen atoms is dominant in this sample. The glassy sample prepared by rapid cooling was measured first and then the crystalline state was measured after annealing at 150 K. The temperature and duration of the measurement were 16 K and ca. 24 h, respectively, for both states.

Results and Discussion

Figure 2 shows the $S(Q_{av},\omega)$ of the glassy (open circles) and crystalline (closed circles) sample of

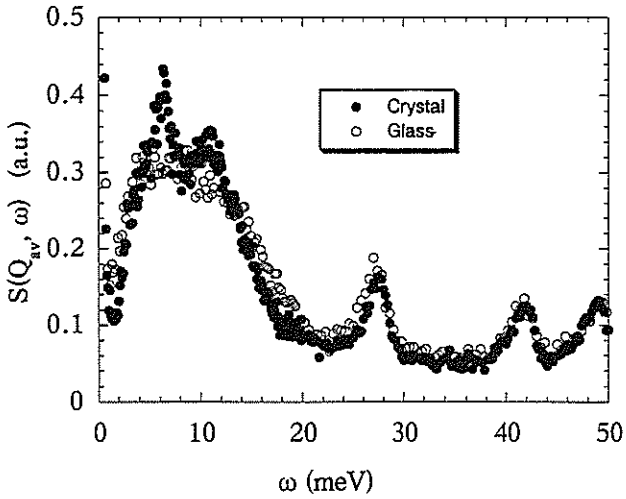

Fig. 2. Incoherent dynamic structure factors of the glassy (open circles) and crystalline (closed circles) toluene at 16 K.

toluene at 16 K (the sum of the data of all counters). From the comparison with the neutron scattering data of crystalline toluene[6-8] and crystalline and glassy ethylbenzene,[9] the peak at 28 meV is assigned to the methyl C_3 rotation and those at 11 and 6 meV to the librations of the molecule. In the glassy states, lower energy peaks tend to be broadened probably due to the local disorder and strain.

The density of vibrational states $G(\omega)$ was calculated from $S(Q_{av},\omega)$ assuming one phonon scattering process and then the heat capacity $C(T)$ was calculated by use of the relation

$$C(T) = \int_0^\infty E(\omega, T) G(\omega) d\omega ,$$

where the $E(\omega,T)$ is the Einstein function. As shown by Fig. 3, anomalous heat capacity in the glassy state was not reproduced from the neutron scattering data. This result indicates that the anomaly is not due to vibrational modes but to some relaxational modes or thermal expansion effect.

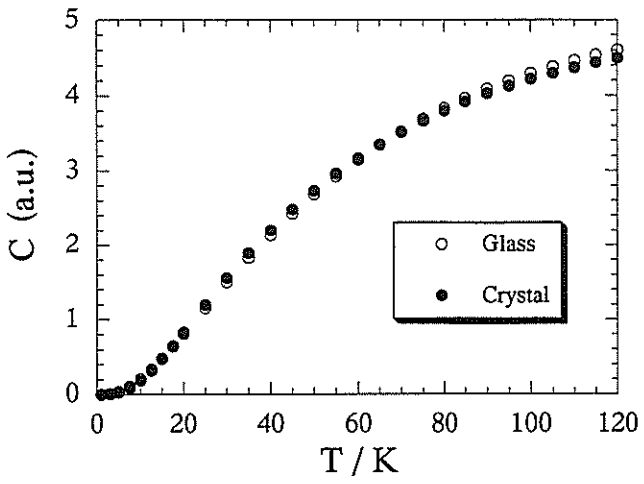

Fig. 3. Heat capacities of the glassy (open circles) and crystalline (closed circles) toluene calculated from the density of states obtained in the present neutron scattering study.

It is noteworthy that the temperature at which the heat capacity anomaly starts to be significant is close to the temperature where the fast relaxation is also significant (ca. 50 K lower than T_g) in neutron scattering experiments (for other systems).[10] It is also predicted by theoretical and MD simulation studies.[10] It is likely that the simplicity (rigidity) of the molecule enhances the relative intensity (or number of the related modes) of the fast relaxation. We are now planning a quasi-elastic neutron scattering experiment to investigate the fast relaxation of the simple molecular glass.

References

1) H. J. de Nordwall and L. A. K. Staveley, Trans. Faraday. Soc. **52**, 1207 (1956).
2) O. Yamamuro, I. Tsukushi, A. Lindqvist, S. Takahara, M. Ishikawa and T. Matsuo, to be published.
3) A. Lindqvist, O. Yamamuro, I. Tsukushi and T. Matsuo, J. Chem. Phys., submitted.
4) D. W. Scott, G. B. Guthrie, J. F. Messerly, S. S. Todd, W. T. Berg, I. A. Hossenlopp and J. P. McCullough, J. Am. Chem. Soc. **66**, 911 (1962).
5) K. Inoue, Y. Ishikawa, N. Watanabe, K. Kaji, Y. Kiyanagi, H. Iwasa and M. Kohgi, Nucl. Instrum. Method **A238**, 401 (1984).
6) D. Cavagnat, J. Lascombe, J. C. Lassegues, A. J. Horsewill, A. Heidemann and J. B. Suck, J. Physique **45**, 97 (1984).
7) B. Frick and J. H. Williams, Europhys. Lett. **20**, 493 (1992).
8) J. Williams and B. Frick, Chem. Phys. **166**, 425 (1992).
9) B. Frick, J. Williams, S. Trevino and R. Erwin, Physica **B213&214**, 506 (1995).
10) For example; U. Buchenau, in "Dynamics of Disordered Materials", edited by D. Richter, A. J. Dianoux, W. Petry and J. Teixeira (Springer, Berlin, 1989). U. Buchenau, in "Phase Transitions and Relaxation in Systems with Competing Energy Scales", edited by T. Riste and D. Sherrington (Kluwer, Dordrecht, 1993). "Non Equilibrium Phenomena in Supercooled Fluids, Glasses and Amorphous Materials", edited by M. Giordana, D. Leporini and M. P. Tosi (World Scientific, Singapore, 1996).

* Present address: Institute for Chemical Research, Kyoto University, Uji, Kyoto 611

Short Range Structure of Superionic Glass System CuI-Cu_2MoO_4

Takao TSURUI, Kaoru SHIBATA and Kenji SUZUKI
Institute for Materials Research, Tohoku University, Sendai 980-77, Japan

The crystalline compounds AgI and CuI are known as a superionic conductor, because they show a very fast conduction of the Ag^+ and Cu^+ ions in the solid state. Minami et al. [1] found that the ionic conductivity of a glass including these compounds, such as AgI-Ag_2MoO_4 and CuI-Cu_2MoO_4, are higher than those of crystalline counterparts. An interesting problem is how these glass structures are correlated to such a high ionic conductivity in the solid state. Concerning this problem, many experimental results have been reported so far. However, some controversial issues still remain to be understood fully the glass structure and anomalous conductivity in these glasses[2,3]. Some of them are the mobile ion's environment and the construction of frame structure of the glass. Neutron diffraction experiment is very useful to analyze the short range structure of oxide glasses quantitatively. In this study the spatial short range structure of CuI-Cu_2MoO_4 glass is characterized to specify the cation's environment and the geometrical framework of the glass by pulsed total neutron scattering.

CuI-Cu_2MoO_4 glass was prepared within a composition range from 40 to 52 mol.%CuI by melt quenching. The neutron total structure factor S(Q) was obtained over a scattering vector range up to 30 $Å^{-1}$ by using the HIT spectrometer installed at the pulsed neutron source in KEK.

Figure 1 shows the total structure factors S(Q) of CuI-Cu_2MoO_4 glasses observed up to 30 $Å^{-1}$ at room temperature. When CuI is included in the glass, small angle scattering obviously appears at $Q<1 Å^{-1}$. This means that the CuI-Cu_2MoO_4 glass is not uniform but rather inhomogeneous in a length scale nearly 10 Å.

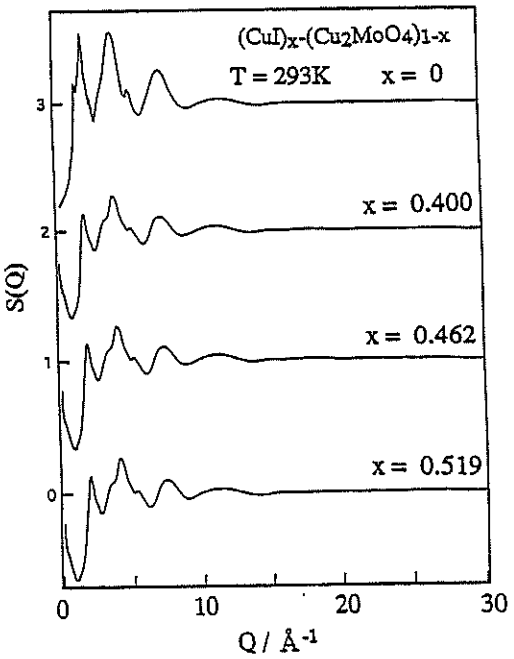

Fig. 1 Neutron total structure factors S(Q) of (CuI)x-(Cu_2MoO_4)1-x glasses

Figure 2 shows the total radial distribution functions $4\pi r^2 \rho g(r)$ of the CuI-Cu_2MoO_4 glasses. The radial distribution functions were evaluated as the Fourier transform of S(Q) truncated at Qmax=30 $Å^{-1}$. Each pair correlation was separated by using the least squared Gaussian functions fitting on the radial distribution functions. The magnitudes of atomic distance and coordination number were gradually decreased with increasing Qmax and saturated beyond Qmax=25 $Å^{-1}$.

The values of atomic distance and coordination number are summarized table 1. Firstly we will describe the pair correlations around Cu atoms and discuss cation's environments. The peaks centered at about 1.8 Å are assigned to Cu-O pair correlation. The

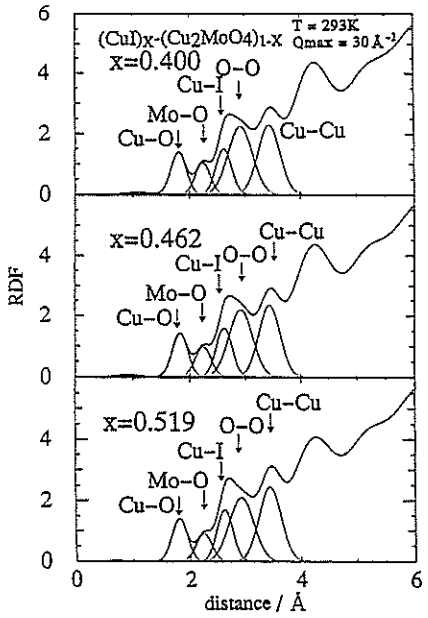

Fig. 2 Neutron total radial distribution functions RDF(r) of $(CuI)_x$-$(Cu_2MoO_4)_{1-x}$ glasses

peaks centered at about 2.6Å and 3.3-3.4Å are assigned to Cu-I and Cu-Cu pair correlation, respectively. These distances accord with the atomic distances in crystalline α-CuI. The coordination number of I atoms around a Cu atom is nearly 4.2-4.4 and that of O atoms around a Cu atom is 1.8-1.9. These results indicate that there are two different kinds of Cu atoms. Cu-I bond in the glass is very similar to that in crystalline α-CuI, and Cu-O bond is very similar to that in Cu_2O insulating crystal.

Secondly we will describe the pair correlations around Mo atoms and discuss the geometrical framework of the glass. The small peak located around 2.1Å corresponds to Mo-O pair correlation. We estimated the coordination number of O atoms around a Mo atom from the area of this small peak. The value is about 5.3-5.6. This result indicates that some Mo atoms are surrounded by 4 O atoms forming $[MoO_4]$-tetrahedron, while the other Mo atoms are situated in the center of $[MoO_6]$-octahedron constructed from 6 O atoms. The peak at about 2.9-3.0 Å separated in the radial distribution function corresponds to the O-O pair correlation in the $[MoO_6]$-octahedron.

In summary, we analyzed the short range structure of superionic glass system CuI-Cu_2MoO_4 by total neutron scattering. There are two different kinds of Cu atoms, which are bound for 2 O atoms or surrounded by 4 I atoms in the glass. CuI and Cu_2MoO_4 are mixed inhomogeneously in the glass. Namely, CuI is expected to be finely dispersed among Cu_2MoO_4 glass matrix connecting with each other. The frame structure of the glass is constructed from a mutual connection of both the $[MoO_4]$-tetrahedron and $[MoO_6]$-octahedron. Further discussion that how $[MoO_6]$-octahedron is connected to $[MoO_4]$-tetrahedron through O-Cu-O bonds in the glass is necessary to understand the ionic conduction mechanism.

References

[1] T.Minani, T. Katsuda and Tanaka : J. Non-Cryst. Solids 29 (1978) 389

[2] N.Machida, M.Chusho and T.Minami : J. Non-Cryst. Solids 101 (1988) 70

[3] M.Saito, K.Sugiyama and Y.Waseda : Mater. Trans. JIM 36 (1996) 1434

Table 1 Atomic distance, d, and coordination number, N, in $(CuI)_x$-$(Cu_2MoO_4)_{1-x}$ glasses

	Cu-O		Mo -O		Cu-I	
X	d(Å)	N	d(Å)	N	d(Å)	N
0.400	1.82±0.02	1.8±0.2	2.15±0.02	5.3±0.3	2.62±0.02	4.2±0.2
0.462	1.82±0.02	1.7±0.2	2.16±0.02	5.5±0.3	2.61±0.02	4.4±0.2
0.519	1.84±0.02	1.8±0.2	2.17±0.02	5.6±0.3	2.61±0.02	4.2±0.2

The Structure of Lithium Tellurite Glasses

N. UMESAKI, M. TATSUMISAGO*, T. MINAMI* and T. FUKUNAGA**

Osaka National Research Institute (ONRI), AIST, 1-8-31, Midoriga-oka, Ikeda, Osaka 563
**Department of Applied Materials Science, Osaka Prefecture University, Sakai-shi, Osaka 591*
***Department of Crystalline Materials Science, Nagoya University, Furo-cho, Chikusa-ku, Nagoya 464*

TeO_2-based glasses, usually called tellurite glasses, have attracted much interest because of the promising optical and electrical properties. For example, these glasses exhibit high refractive index, wide infrared transmitance and high dielectric constant. In addition, tellurite glasses have recently become of interest as one of the best candidates for optical switching materials devices[1] and laser hosts[2] due to these optical and electrical properties. It is believed that these attractive properties arise from the low symmetry of the tellurite structural units, giving rise to considerable interest in the structure of TeO_2-based glasses[3].

It is believed that the structure of tellurite glasses involves partially occupied octahedra in the form of both TeO_4 trigonal bipyramids and TeO_3 trigonal pyramids. Furthermore there is evidence indicating that transformations between these two units can occur relatively easily[4]. Nevertheless the literature contains virtually no direct structural studies using diffraction to investigate the detail of the Te-O coordination polyhedra.

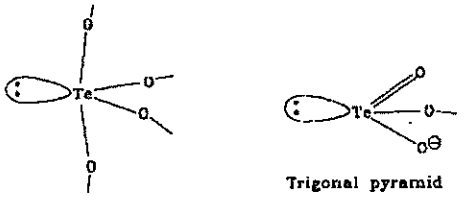

Trigonal bipyramid　　Trigonal pyramid

There has already been quite a few neutron diffraction studies of the structure of alkali tellurite glasses. However, these have all been performed using reactor neutron sources and have suffered from having a very small maximum momentum transfer Q_{max}.

HIT was used to measure the distinct scattering for 20%Li_2O·80%TeO_2 (a) rapidly and (b) press quenched glass samples. Figure 1 shows the structure functions *S(Q)* and Figure 2 shows the radial distribution functions *RDF(R)* of these two glasses.

The general form of the measured *RDF(R)*'s can be understood simply in terms of the following near neighbour distances:

r_{TeO}	r_{OO}	r_{LiO}
1.9~2.2Å	2.85Å	2.0Å

We are in the process of performing a wide-ranging review of the coordination polyhedra which occur in related crystalline compounds and on this basis it may be possible to advance our understanding of the Te-O coordination.

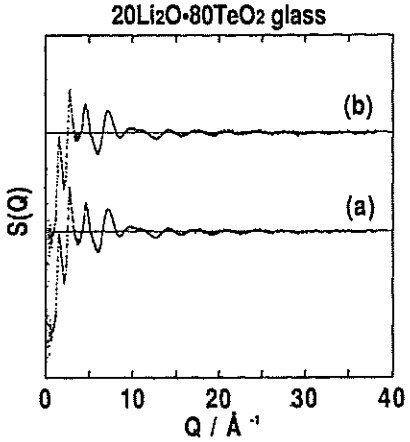

Fig. 1 Neutron structure functions *S(Q)* for the (a) rapidly and (b) press quenched 20Li_2O·80TeO_2 glass.

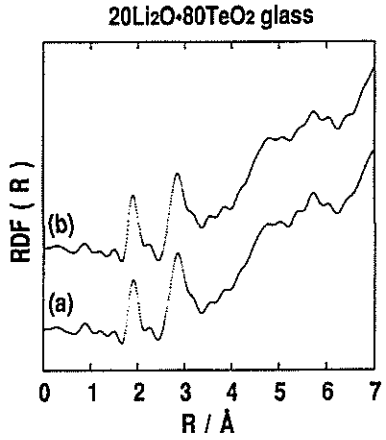

Fig. 2 Radial distribution functions *RDF(R)* of the (a) rapidly and (b) press quenched 20Li_2O·80TeO_2 glass.

References

1) H. Nasu et al., J. Non-Cryst. Solids, 124 (1990) 275.
2) S. Tanabe et al., J. Non-Cryst. Solids, 122 (1990) 275.
3) M. Tatsumisago et al., J. Non-Cryst. Solids, **177** (1994) 154.
4) M. Tatsumisago et al., Phys. Chem. Glasses, **35** (1994) 89.

Intermolecular Correlation of Liquid CS_2 Studied by Reverse Monte Carlo Method

H. EBATA, J. TOKUDA, K. YOSHIDA, T. SATO, K. MARUYAMA, and M. MISAWA

Department of Chemistry, Faculty of Science, Niigata University, Igarashi, Niigata 950-21, Japan

The CS_2 molecule has a linear shape, which is very different from the sphere shape. Therefore in the liquid state, it is expected that there exists orientational correlation between the nearest neighbor molecules. We have investigated the intermolecular correlation in liquid CS_2 by using the reverse Monte Carlo (RMC) method[1,2]. This method can create the three dimensional atomic or molecular configuration which reproduces the diffraction spectrum. The obtained configuration seems to be one of probable configurations.

The neutron diffraction measurement was carried out at ambient temperature using the time-of-flight method with the High Intensity Total Scattering Spectrometer (HIT) equipped with a pulsed spallation neutron source at the National Laboratory for High Energy Physics. The observed intensities were corrected for the TiZr sample cell, background, absorption, multiple and incoherent scattering, and were normalized to obtain the total structure factor $S(Q)$.

By fitting $S(Q)$ over the high Q region ($Q > 10\text{Å}^{-1}$), the C − S bond length was determined as: $r_{C-S} = 1.55 \pm 0.07\text{Å}$. By subtracting the intramolecular structure factor from $S(Q)$, the intermolecular structure factor $S_2(Q)$ was obtained and then by Fourier transforming $S_2(Q)$, the intermolecular pair distribution function $g_2(r)$ was obtained, which represents the correlation between two atoms belonging different molecules and is shown in Fig. 1 by solid line.

The molecular configuration model was created so as to reproduce the experimental $g_2(r)$ by using RMC method. The very short explanation of the procedure[1,2] is as follows: The rigid CS_2 molecules were arranged in a cubic cell with the periodic boundary condition. One randomly selected molecule was moved and rotated randomly. In each step, the intermolecular pair distribution function of the model, $g_2^{calc}(r)$, was calculated. The motion was accepted or rejected as in the usual Monte Carlo simulation with the criterion which was whether the difference between $g_2(r)$ and $g_2^{calc}(r)$ became smaller or not.

After about tens accepted motions per molecule, the $g_2^{calc}(r)$ converged to $g_2(r)$ as shown in Fig. 1 by dashed line. Their agreement is very good. The molecular center distribution function $g_c(r)$ was calculated from the obtained configuration. Figure 2 shows $g_c(r)$'s obtained by RMC method with 1000, 8000, and 27000 molecules. They agree each other very well, which suggests that the obtained molecular configuration is reasonable one. Analyzing the molecular configuration statistically, we can obtain the data on the intermolecular correlation. The following results are based on the simulation with 8000 molecules.

Figure 3 shows the directional distribution of molecules, $p_\theta(r)$, which is the number of molecules lying in the direction from the axis of the central molecule by an angle θ at the distance r. The $p_\theta(r)$ is not normalized by the solid angle. As seen in this figure, the distance to the nearest molecule becomes shorter with increasing θ from 0°to 90°. At the same time, the second peak in $p_\theta(r)$ appears and becomes larger. This means that the distribution of molecules are dependent on the direction.

More detailed analysis using another angle, which is the angle between two axes be-

longing to neighboring molecules shows the following results: The molecule pairs with the distance about 3.8Åalikely form the parallel pairs. A little farther pairs with the distance about 5.0Ålikely form the T-shaped configuration.

In order to obtain clearer information on the intermolecular correlation, the analysis of the diffraction data for l-CS_2 at $-100°C$ is now in progress, which is expected show more distinct intermolecular correlation.

references

1) R. I. McGreevy, M. A. Howe, D. A. Keen, and K. N. Clausen, *IOP Conference Series*, **107** (1990) 165.
2) K. Maruyama, S. Tamaki, S. Takeda, and M. Inui, J. Phys. Soc. Jpn., **62** (1993) 4287.

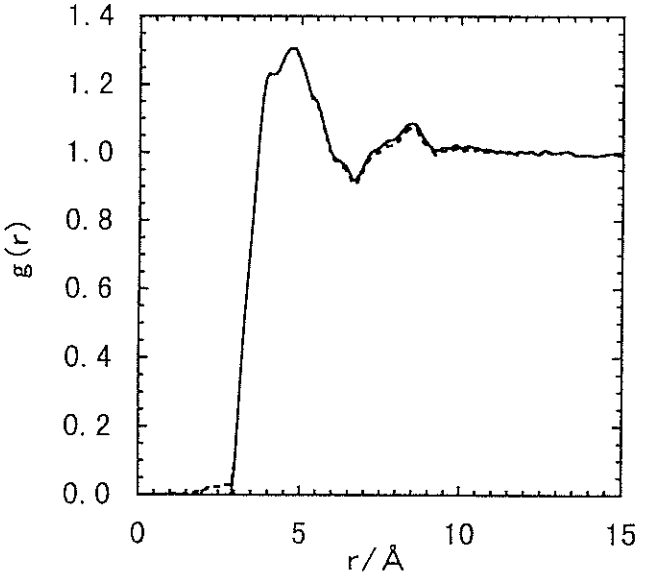

Figure 1. The intermolecular pair distribution functions for l-CS_2 obtained from the diffraction measurement (solid line) and the RMC calculation (dashed line).

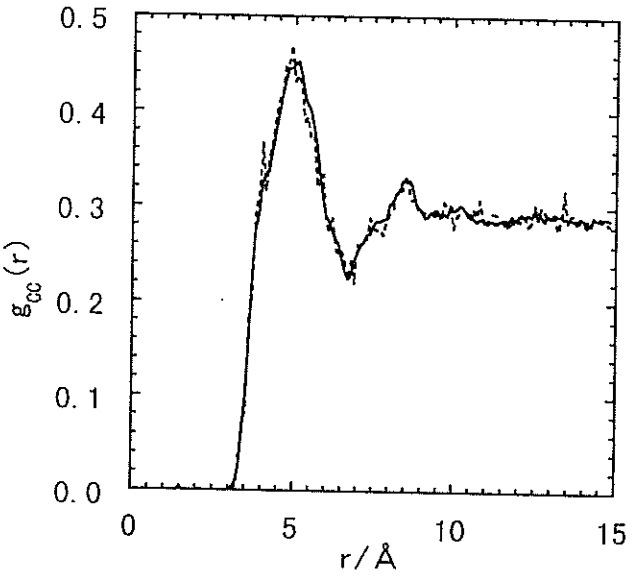

Figure 2. The molecular center distributions derived from the RMC calculations with 1000 (solid line), 8000 (dashed line), and 27000 (dotted line) molecules.

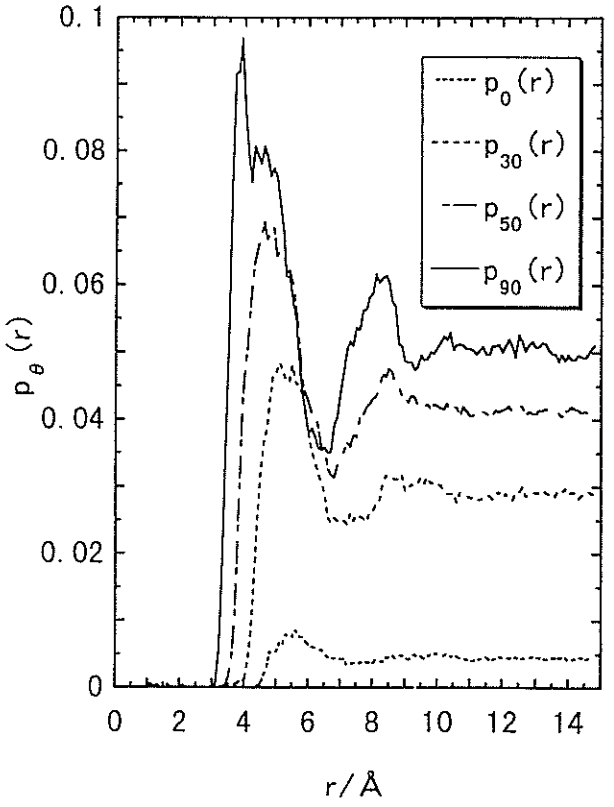

Figure 3. The directional distribution of molecules, $p_\theta(r)$, which is defined in the text.

Annealing Effects on Low-energy Excitation of Amorphous Poly(methyl methacrylate)

T. KANAYA, M. MIYAKAWA, I. TSUKUSHI,T. KAWAGUCHI and K. KAJI

Institute for Chemical Research, Kyoto University, Uji, Kyoto-fu 611, Japan

Extensive inelastic neutron scattering studies have revealed that an anomalous excess excitation peak, so-called *low-energy excitation* peak or Boson peak, appears at around 2~3 meV for most of all amorphous materials at low temperatures far below T_g [1]. This excitation is believed to be an origin of anomalous excess heat capacity observed for most of amorphous materials at 10~20 K. Although much effort has been made by many researchers the origin of the *low-energy excitation* is still unclear . In this work, we have studied annealing effects on the *low-energy excitation* of amorphous poly(methyl methacrylate) below and above the glass transition temperature T_g (=105 °C).

The sample used in the experiment is atactic poly(methyl methacrylate) (PMMA) with molecular weight M_W=200000. A thin file with 0.1 mm thickness was heated at 180 °C for 2 min and then immediately quenched in ice-water. The films thus prepared were annealed at several temperatures Ta below and above the glass transition temperature Tg for 7 days.

Inelastic neutron scattering measurements were carried out with the inverted geometry time-of-flight (TOF) spectrometer LAM-40 installed at the pulsed spallation cold neutron source at KEK, Tsukuba. The energy resolution of LAM-40 is about 0.2 meV. The measurements were performed at 73 K and 300K for all the annealed samples.

The observed dynamic scattering laws $S(Q,\omega)$ at 73 K are shown in Fig. 1(a) for two samples; not annealed and annealed at 90 °C. It is clearly observed that the inelastic scattering intensity below ~3 meV decreases with annealing while no effects are observed above ~ 3 meV. It is considered that the annealing makes molecular packing in the sample closer, especially, at locations with density lower than the average (*open structure*). The decrease of the inelastic scattering intensity below ~3 meV may suggest that the excitation is originated from the *open structure*. It is noted that the decrease of intensity below ~3 meV is observed not only below T_g but also above T_g although the data are not shown here. It suggests that there is a very slow packing process or relaxation process of structural in PMMA [2].

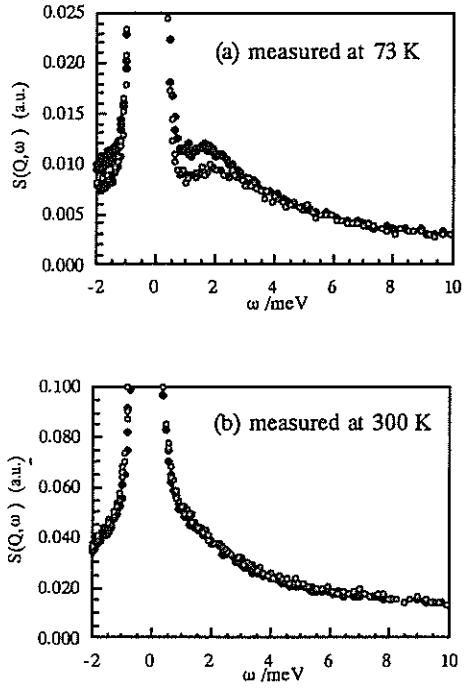

Fig. 1. Dynamic scattering laws S(Q,w) of PMMA measured at 73 K (a) and 300K (b). PMMA not annealed (●) and annealed at 90 °C for 7 days (○).

1) K. Inoue, T. Kanaya, S. Ikeda, K. Kaji, K. Shibata, M. Misawa, and Y. Kiyanagi, *J. Chem. Phys*. **95** (1991) 5332.

2) J. K. Krüger, R. Roberts, H.-G.Unruh, K. -P. Frühauf, J. Helwig and H. E. Müser, *Prog. Coll. Polym. Sci*., **71** (1985) 77.

Onset of the fast process of trans-1,4-poly(chloroprene)

T. KANAYA, T. KAWAGUCHI and K. KAJI

Institute for Chemical Research, Kyoto University, Uji, Kyoto-fu 611, Japan

Glass transition is one of the most important phenomena in polymer science as well as in material science because various properties of polymers such as thermal and mechanical properties change drastically below and above the glass transition temperature T_g. Therefore, lots of investigations have been made on amorphous polymers using various kinds of methods. Most of the investigations have been performed in macroscopic or mesoscopic time and spatial scales using thermal, mechanical and dielectric measurements. Stimulated by the recent mode coupling theory (MCT), lots of microscopic measurements have been made on various kinds of glass-forming materials such as organic and inorganic materials and polymers using quasielastic neutron and light scattering, NMR and dielectric relaxation measurements. From microscopic viewpoints, contributions of quasielastic neutron scattering are outstanding. One interesting contribution from quasielastic neutron scattering experiments is a finding of the *fast process* of picosecond order, which is observed for most glass-forming materials so far studied. The *fast process* is often discussed in terms of the MCT β-process. However, another interpretation has been proposed based on an idea of softening of vibrational modes. The nature of the *fast process* is still unclear.

In the previous paper [1], we found for cis-1,4-polybutadiene that the *fast process* appears at the so-called Vogel-Fulcher temperature T_0. This suggests that the *fast process* is closely related to the glass transition phenomenon. On the other hand, recent neutron scattering studies revealed that similar *fast process* appears far below T_g for amorphous polystyrene (PS) [2] and polycarbonate (PC) [3]. These polymers have large side groups or many internal degrees of freedom. As the *fast process* has been assigned to phenyl ring motions in the case of PS, it is considered that the *fast process* far below T_g is originated from side group motion or internal degree of freedom and that the onset of the *fast process* at the Vogel-Fulcher temperature T_0 is characteristic only to polymers having no large side groups. One of the aims of this study is to confirm this prediction.

The sample used for the scattering experiments was trans-1,4-polychloroprene (PCP) of molecular weight M_W=4 x 10^5. The glass transition temperature T_g was determined by DSC measurements to be 228 K. Inelastic and quasielastic neutron scattering measurements were carried out with the inverted geometry time-of-flight (TOF) spectrometers LAM-40 and LAM-80ET. The energy resolutions of LAM-40 and LAM-80ET are ~0.2 and ~0.02 meV, respectively. The measurements were carried out in a temperature range of 50 to 300 K.

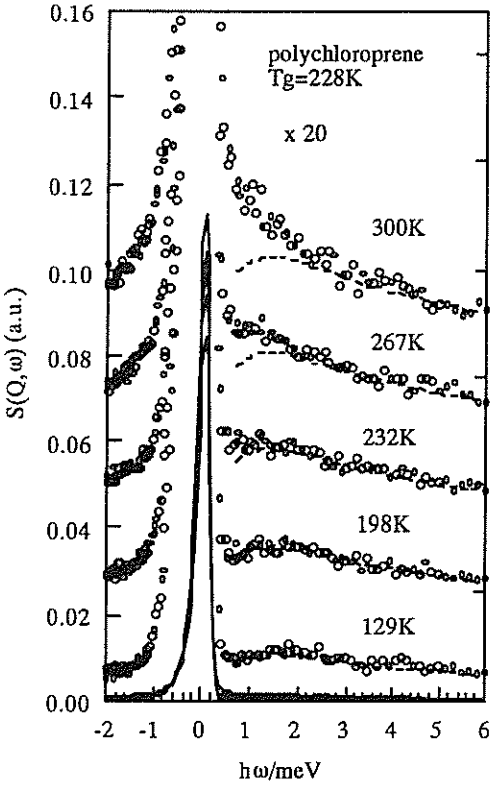

Fig. 1. Dynamic scattering laws $S(Q,\omega)$'s of trans-1,4-polychloroprene measured by LAM-40 as a function of temperature.

Dynamic scattering laws $S(Q,\omega)$'s of PCP observed with LAM-40 are shown in Fig. 1 as a function of temperature covering the glass transition temperature T_g (=228 K). These spectra were obtained by summing up 6 spectra at scattering angles of 8, 24, 40, 72, 88 and 104 degrees because the shape of the spectra are almost independent of the scattering angle.

The sharp peak at around $\hbar\omega = 0$ meV is due to the elastic scattering and the intensity decreases with increasing temperature. The counter part of the elastic scattering, inelastic scattering part, increases with temperature. A very broad inelastic scattering peak, so-called *low energy excitation* peak or Boson peak, is observed at ~1.7 meV at low temperatures below the glass transition temperature T_g. As the temperature further increases, the shape of the spectra changes from inelastic-like to quasielastic-like slightly below the glass transition temperature T_g, suggesting the onset of a new relaxational motion or a damped vibrational motion.

First, we focus our attention on the elastic scattering intensity $I_{el}(Q)$. Temperature dependence of $I_{el}(Q)$ observed at $Q = 1.75$ Å^{-1} is shown in Fig. 2. Logarithm of $I_{el}(Q)$ decreases linearly with increasing temperature below ~170 K; $\log[I_{el}(Q)] \sim T$, indicating that the motion observed at the low temperatures is vibrational, while $I_{el}(Q)$ begins to deviate from the linear relationship and decrease more steeply at around 170K.

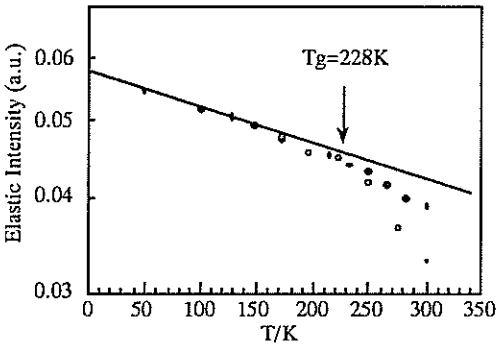

Fig. 2. Temperature dependence of elastic scattering intensities $I_{el}(Q)$ measured by LAM-40 with energy resolution $\delta\varepsilon = 0.2$ meV (●) (Q=1.75 Å^{-1}), and by LAM-80ET with $\delta\varepsilon = 0.02$ meV (○) (Q = 1.64Å^{-1}).

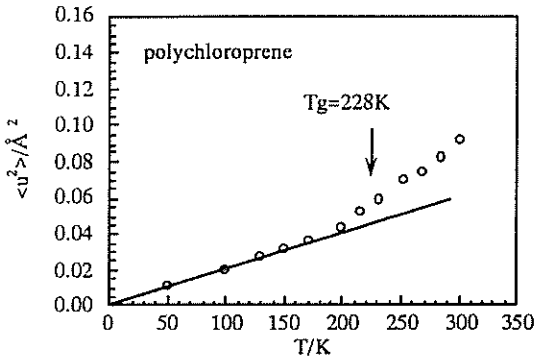

Fig. 3. Temperature dependences of mean square displacement $<u^2>$ evaluated form elastic scattering intensity.

The deviation may suggest the onset of a new relaxational or damped vibrational motion at around 170 K, which is about 60 K below T_g.

Mean square displacement $<u^2>$ was evaluated from Q dependence of incoherent elastic scattering intensity and shown in Fig. 3 as a function of temperature. It is proportional to temperature T in the range below ~170 K. This again suggests that the motion below ~170 K is vibrational. In the temperature range above ~170 K, $<u^2>$ begins to deviate from the linear relationship and to increase more rapidly with temperature. These facts must suggest the onset of a new motion above the temperature.

We now discuss the counter parts of the elastic scattering, inelastic and quasielastic scattering. It is reported for some amorphous materials at low temperatures below T_g that the *low-energy excitation* intensity after correction for the Debye-Waller factor increases with temperature according to the Bose factor. Following the above idea, we calculated inelastic scattering intensities at the higher temperatures by applying the Bose factor to the data at 129K after correction for the Debye-Waller factor. The calculated spectra are indicated by dashed lines in Fig. 1. At 198 K, the expected value agrees with the observed one, confirming that the intensity of the *low-energy excitation* of PCP is also scaled by the Bose factor. On the other hand, at high temperatures above about T_g the observed intensity exceeds the expected one in the energy region below ~2 meV and the shapes of the spectra look like quasielastic. This excess quasielastic scattering must be due to the new relaxational or damped vibrational motion expected from the temperature dependences of

the elastic scattering intensity $I_{el}(Q)$ and of the mean square displacement $<u^2>$. The new motion is just the *fast process* observed for many glass-forming materials.

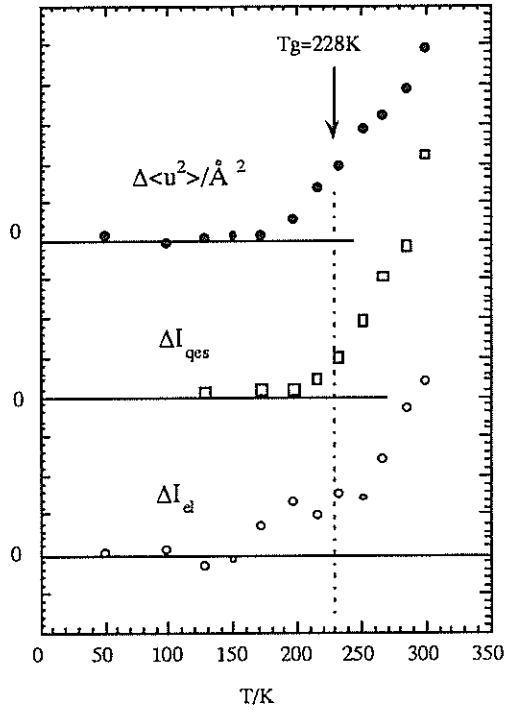

Fig. 4. Excess mean square displacement $\Delta<u^2>$, excess quasielastic scattering intensity $\Delta I_{qes}(Q)$, and excess decrease of elastic scattering intensity $\Delta I_{qes}(Q)$ as a function of temperature.

In order to see the onset temperature of the *fast process*, we evaluated the excess mean square displacement $\Delta<u^2>$, the excess quasielastic scattering $\Delta I_{qes}(Q)$, and the excess decrease of the elastic scattering intensity $\Delta I_{el}(Q)$ at Q=1.75 Å^{-1}. Here $\Delta I_{qes}(Q)$ was obtained by integrating the excess spectra in an energy range of 0.7 to 6 meV. These three excess values are plotted as a function of temperature in Fig. 4. The onset temperatures seem to be between 170 and 190 K, which is 40 to 60 K below T_g. In the previous paper, we reported for cis-1,4-polybutadiene that a similar *fast process* appears at the so-called Vogel-Fulcher temperature T_0, which is 50 K below T_g for most amorphous polymers. In the case of PCP, it is also considered that the fast process appears at the Vogel-Fulcher temperature T_0. The temperature T_0 is sometimes called as the "ideal" glass transition temperature, i.e., an experimentally inaccessible temperature in the limit of infinitely slow cooling. However, the value of T_0 is not affected by the time scale of the experiment, whereas the calorimetric glass transition temperature depends on the time scale. Therefore, T_0 is considered to be a fundamental property of the sample. The temperature T_0 is usually determined by analyzing the temperature dependence of the relaxation time τ of the so-called α-process using the Vogel-Fulcher equation,

$$\log\tau = \log\tau_0 + \frac{B}{T-T_0} \quad (1)$$

where B is constant. Usually, the temperature T_0 is not easily accessible by dynamical measurements. The present measurement as well as the previous one [1] indicates that neutron incoherent experiments can directly detect the temperature T_0 through hydrogen mobility. These results strongly suggested that the *fast process* is a precursor of the glass transition phenomena. However, it should be emphasized that a similar *fast process* of picosecond order is observed deeply below T_g in some amorphous polymers such as polystyrene (PS) [2] and polycarbonate (PC) [3] which have large side groups or large internal degrees of freedom. The *fast process* far below T_g may be originated from side group motion or internal degree of freedom. In the case of PS, it has been assigned to the phenyl ring motion, based on the results of polystyrene with selectively deuterated phenyl rings. At the present stage, it is, therefore, considered that the nature that the *fast process* appears at the Vogel-Fulcher temperature is characteristic to polymers having no side groups like polybutadiene (PB) and polychloroprene (PCP).

1) T. Kanaya, T. Kawaguchi and K. Kaji, *J. Chem. Phys.* **98**, 8262 (1993).
2) T. Kanaya, T. Kawaguchi and K. Kaji, *J. Chem. Phys.* **104**, 3841(1995).
3) U. Buchenau, C. Schönfeld, D. Richter, T. Kanaya, K. Kaji and R. Wehrmann, *Phys. Rev. Lett.* **73**, 2344 (1994).

Modification of Te Chain Structure by the Addition of Alkali Metals

M. YAO, Y. KAWAKITA[a], I. YAMAMOTO* and H. ENDO[b]

Department of Physics, Graduate School of Science, Kyoto Univ., Kyoto 606-01
[a] Department of Physics, Faculty of Science, Kyushu Univ., Ropponmatsu, Fukuoka 810
[b] Faculty of Engineering, Fukui Institute of Technology, 910 Fukui, Japan

Liquid Te shows metallic behaviour above the melting points. It is considered that a strong coupling between short Te chains may be associated with the metallic behaviour. Since alkalis are easily ionized, it is interesting to study how the structure of liquid Te is modified by the addition of alkalis. The electrical conductivity decreases rapidly with alkali concentration and a metal-to-semiconductor transition occurs at about 10 at. % alkali[1].

Neutron diffraction measurements for liquid K-Te and Rb-Te mixtures were carried out by using the time-of-flight (TOF) spectrometer HIT-II. Sample was put into a thin-walled (0.3mm) cylindrical cell made of fused silica with an inner diameter of 8mm. The static structure factor $S(Q)$ was deduced by the standard procedure[2], and then pair distribution functions $g(r)$ derived from the Fourier transform of $S(Q)$

Figure 1 shows $g(r)$ of liquid Te and liquid K-Te mixtures. The position and height of the first peak, which is associated with Te-Te nearest neighbour correlation, do not change much with additional alkalis, suggesting that the chain structure of liquid Te remains in the liquid containing alkalis. It should be noted that the first minimum near 3Å becomes remarkably deep and a new hump rises at 3.6Å for liquid K-Te mixtures. The pair distribution function $g(r)$ for liquid Rb-Te mixtures is shown in Fig.2. A prominent peak is observed at the distance of 3.8Å in $g(r)$ of liquid $Rb_{20}Te_{80}$. The contribution of alkali elements to $g(r)$ appears more clearly in liquid Rb-Te mixtures than in liquid K-Te mixtures, since the neutron scattering length of Rb nucleus is about twice as large as that of K nucleus. It is reasonable to conclude that these peaks (or humps) located at 3.6Å for liquid K-Te and 3.8Å for liquid Rb-Te correspond to the nearest neighbour distance between Te and alkali atoms. In addition, the coordination number of Te around alkali atoms can be estimated to be about four.

In conclusion, the role of the alkali appears to be that of nearly completely charge transfer, stabilizing the short Te chains by the intaraction with four negative-charged Te chain ends. The charge transfer from alkali atom to Te chains weakens interchain coupling in liquid Te and reduces conduction between neighbouring Te chains.

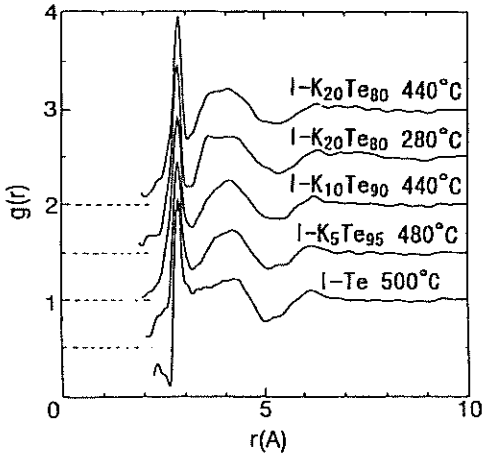

Fig.1 The pair distribution function $g(r)$ for liquid K-Te mixtures.

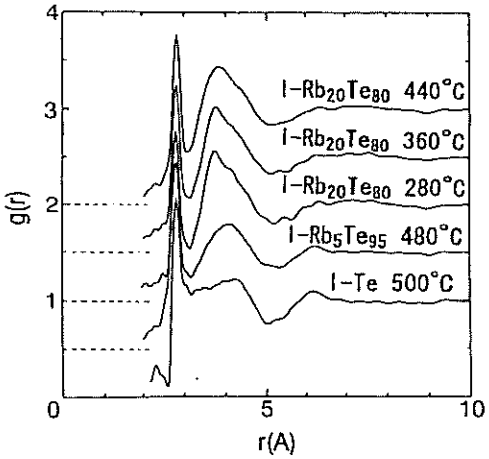

Fig.2 The pair distribution function $g(r)$ for liquid Rb-Te mixtures.

References

1) Y.Kawakita, M. Yao and H. Endo: *to be published in* J. Phys. Soc. Jpn.

2) K. Suzuki, M. Misawa, K. Kai and N. Watanabe: Nucl. Instrum. Methods **147** (1977) 519.

present address
* Faculty of Education, Hirosaki University

Dynamic Structures of Liquid Tellurium Mixtures

M. YAO, Y. KAWAKITA[a], I. YAMAMOTO*, T. SHIGA** and H. ENDO[b]

Department of Physics, Graduate School of Science, Kyoto Univ., Kyoto 606-01
[a] Department of Physics, Faculty of Science, Kyushu Univ., Ropponmatsu, Fukuoka 810
[b] Faculty of Engineering, Fukui Institute of Technology, 910 Fukui, Japan

In 1980 we proposed a phase diagram of liquid Te-Se mixtures[1] (see Fig. 1). Semiconductor-to-Metal (S-M) transition occurs in a relatively narrow temperature range, which is indicated by hatching in Fig.1, being accompanied by anomalies in the thermodynamic properties. The transition region shifts towards higher temperatures as the Se concentration increases. Moreover it is expected that liquid Te, which is metallic above the melting point, can be changed to a semiconductor in a strongly supercooled state.

Inelastic neutron scattering experiments for trigonal (t-) $Te_{70}Se_{30}$ at room temperature and liquid (l-) $Te_{70}Se_{30}$ at 410°C and 580°C were performed using the inverted geometry TOF spectrometer LAM-D[2]. The experimental procedure is the same as previously described[3]. The vibrational density of states $G(E)$ was deduced within the incoherent approximation[4] and shown in Fig. 2. For t-$Te_{70}Se_{30}$ the peaks of $G(E)$ around 6 meV, 12 meV and 22 meV can be assigned to the tortional, bond-bending and -stretching modes, respectively, and a distinct gap appears between 15 and 18 meV in the $G(E)$ curve. A similar gap or a dip in $G(E)$ is also observed in l-$Te_{70}Se_{30}$ at 410°C, which is slightly higher than the melting point. This suggests that the helical chain structure is more or less preserved on melting. Such a gap has been observed near 22 meV for l-Se at 300°C and near 12 meV for supercooled l-Te at 400°C. The stretching modes in l-$Te_{70}Se_{30}$ at 410°C seem to have peaks near 22 meV. When the temperature of l-$Te_{70}Se_{30}$ is raised across the phase boundary indicated in Fig. 1, the $G(E)$ spectrum changes remarkably and the gap around 16 meV becomes buried. This may be associated with the appearance of long (i.e. weak) covalent bonds, which is consistent with our EXAFS data[3].

present address
* Faculty of Education, Hirosaki University
**Toyota Central Research & Development Labs., Inc.

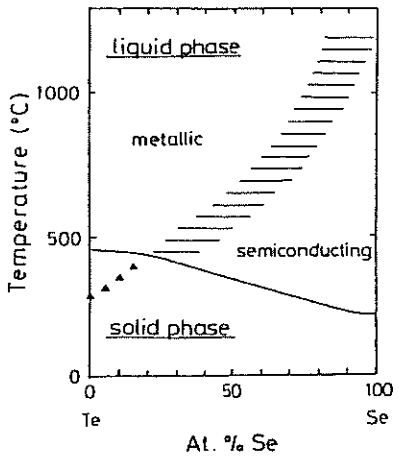

Fig.1 Phase diagram of Te-Se system. The solid line is the liquidus curve and the hatching indicates the S-M transition region. The triangles denote the temperature below which the long Te-Te bonds vanish.

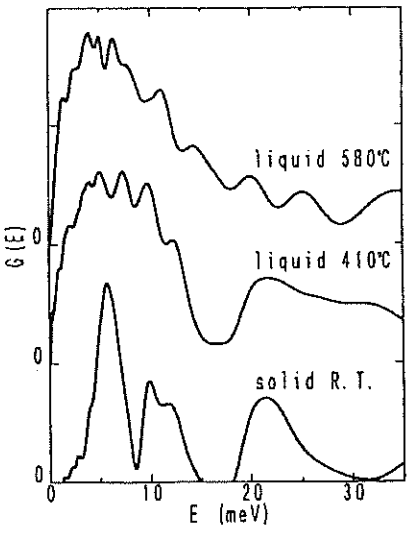

Fig.2 The vibrational density of states $G(E)$ for t-$Te_{70}Se_{30}$ at room temperature, l-$Te_{70}Se_{30}$ at 410°C and 580°C.

References

1) M. Yao, M. Misonou, K. Tamura, K. Ishida, K. Tsuji and H. Endo: J. Phys. Soc. Jpn. **48** (1980) 109.
2) M. Yao and H. Endo: J. Non-Cryst. Solids **205-207** (1996) 85.
3) T. Tsuzuki, M.Yao and H. Endo: J. Phys. Soc. Jpn. 64 (1995) 485.
4) D. L. Price and J. M. Carpenter: J. Non-Cryst. Solids 92 (1987) 153.

Intermediate Range Structure of AgI-CsI-$(CH_3)_4NI$ Glasses

J.Kawamura, T.Itagaki, K.Arakawa, T.Kamiyama and Y.Nakamura
Department of Chemistry, Faculty of Science, Hokkaido University, Sapporo, 060

1. Introduction

Recently, the present authors have developed new types of glassy solid electrolytes containing different size of tetraalkylammonium ions[1,2]. Appearance of a clear transition from superionic conductors to insulators can be explained by percolation models.

In this paper is reported tentative results of the small angle neutron scattering (SANS) and the neutron diffraction in low angle region for these glasses. Intermediate range structure due to the percolation clusters are discussed.

2. Experimental

The glasses composed of AgI-CsI-tetramethylammonium iodide (TMAI) and deuterized tetramethylammoniumiodide (dTMAI) were used.

Small angle neutron scattering experiments were carried out in KENS neutron facility in Tsukuba; the spectrometer **SAN** by pulsed cold neutron source was used, whose Q range was from 0.01 $Å^{-1}$ to 0.2 $Å^{-1}$. SANS experiments were done for the samples of AgI-CsI-dTMAI whose compositions are (7:2:1) which is in the superionic region, and (5:4:1) in the insulator region. The sample of undeuterized AgI-CsI-hTMAI(7:2:1) was also measured for comparison.

Small and medium angle neutron diffractions were also measured by the **WINK** spectrometer installed at KENS, whose Q range is from 0.2 $Å^{-1}$ to 20 $Å^{-1}$. Calibrations were done for vanadium, background and water. The data were smoothed by third order spline functions.

3. Results and Discussion

Small angle scatterings were observed by SAN spectrometer for the samples containing deuterized dTMAI, while only background scattering were seen for the sample containing protons. In figure 1 is shown the log-log plot of scattering intensity of the present data. The fractal dimensions D_f was estimated from the slope; it was 0.39 above q_c and 2.8 below, where q_c is a cross-over wave length: q_c =0.02 for the sample (7:2:1) and 0.05$Å^{-1}$ for (5:4:1). This result strongly supports the existence of percolation clusters (D_f=2.48±0.09) in the glasses as was expected from ionic conductivity measurements.

A significant peak was observed near 1 $Å^{-1}$ by WINK spectrometer. The peak position is close to the so called "pre-peaks" observed at ca. 0.8$Å^{-1}$ in other superionic glasses containing AgI. However, from carefull investigations of the peak we concluded that it is merely due to the existence of large $dTMA^+$ ions whose diameter is estimated to be 5.78 Å corresponding to a correlation at q = 1.1 $Å^{-1}$.

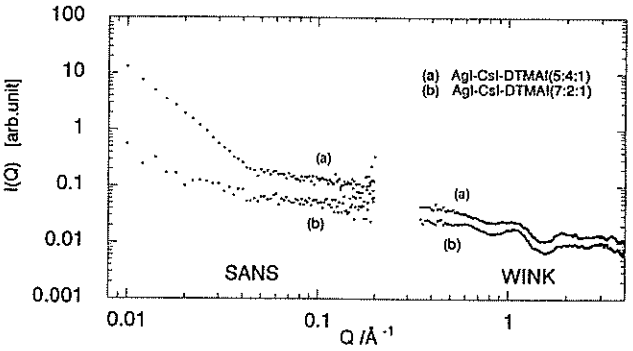

Fig.1 Log-Log plot of the neutron scattering intensity and momentum transfer of (a) AgI-CsI-dTMAI (7:2:1) and (b) AgI-CsI-dTMAI (5:4:1).

Acknowledgement

Authors should express their gratitude to Mr. K.Minemura in Nippon University and Mr. M.Oosawa in Tsukuba University in experiments on SAN and WINK spectrometers.

References

1) J. Kawamura and Hiyama S., Solid State Ionics, **53-6** (1992) 1227.

2) J. Kawamura, K. Arakawa, T. Kamiyama, and Y. Nakamura, Solid State Ionics, **79** (1995) 264.

Incoherent Neutron Scattering from Single Crystal $RbHSO_4$

Y. WADA, S. IKEDA* and K. ITOH

Department of Materials Science, Faculty of Science, Hiroshima Univ., Higashi-Hiroshima 739
*National Laboratoty for High Energy Physics, 1-1 Oho, Tsukuba-shi, Ibaraki 305

It is well known that hydrogen-bonded ferroelectrics such as KH_2PO_4 (KDP) exhibit a large isotope effect on the ferroelectric phase transition T_c, in which the T_c generally goes up by the deuteration. In a striking contrast to those compounds, the T_c of $RbHSO_4$ (RHS) reduces by the deuteration from 265 K to 250 K. [1] To investigate such 'strange' isotope effect of T_c, many experimental studies have been performed with X-ray,[2,3] Raman scattering[4] and neutron scattering[2,5] techniques. By the X-ray measurements in RHS, the accurate crystal structure and the thermal fluctuation were determined.[3] There are two kinds of hydrogen bonds with O-O lengths of 2.526(7) Å and 2.602(6) Å in the paraelectric room temperature phase. It is interesting that these lengths fall into the O-O distance range 2.45 to 2.65 Å, which can exhibit the above mentioned isotope effect of T_c.[6] Both H atoms, H(1) and H(2), are not located in the middle of the respective hydrogen bonds, but close to the one side. The distances between H and O are rather short; i.e. 0.77(8) Å for H(1) and 0.69(6) Å for H(2). It was also suggested that H(1) executes very large thermal vibrations. These structural results have been explained on the basis of the riding model; i.e H(1) fluctuates neary perpendicular to the hydrogen bond in phase with the reoriented motion of the closer SO_4(1) ion.[3] These results about H in RHS are quite different from the well known characteristics of H in KDP, where H is located in the middle of te O-O distance in the average structure with the site symmetry 2 and displaces neary along the hydrogen bond above T_c. Therefore, it is reasonable to expect that H(1) plays an important role on this strange phase transition mechanisn in RHS.

Raman scattering measurements[4] have mainly been performed to observe the excitations of the SO_4 ions. Some small hydrogen-related peaks were observed at about ϵ =98, 102 and 155 meV in the Raman spectra, and were assigned as the out-of-plane bending modes and the in-plane bending modes of H(1) and H(2).

Recently, Kosegawa et al.[5] carried out incoherent neutron scattering measurements of a powder sample of RHS and found some large hydrogen peaks at ϵ =80, 95, 143 and 157 meV. From the local structure around H(1) and H(2), it was expected that, in the ferroelectric phase, the vibration directions of both γ_1 and γ_2 modes are neary parallel to the a^*-axis, those of δ_1 and δ_2 modes are parallel to the c-axis and those of ν_1 and ν_2 modes are parallel to the b-axis. Here, γ, δ and ν are the out-of-plane bending mode, the in-plane bending mode and the stretching mode, respectively. In an inset in Fig. 1, the vibration directins of γ, δ and ν modes are depicted schematically.

In order to observe more clearly those excitation peaks, and to determine the excitation energies and the vibration directions of the hydrogen modes, we have carried out incoherent neutron scattering measurements on the single crystal of RHS, using a crystal analyzer time-of-flight neutron spectrometer (CAT) in the neutron scattering facility (KENS) at the National Laboratory for High Energy Physics in Japan. Single crystals with a total weight of 12 g were used, and set in an alminium container. We made two sets of the experiments at T = 18 K. In one experiment, the single crystals were rotated about the b-axis. We defined the rotation angle as ϕ =

0 for $\boldsymbol{Q} \parallel \boldsymbol{c}$ and $\phi = \pi/2$ for $\boldsymbol{Q} \parallel \boldsymbol{a}^*$, where $\boldsymbol{Q}$ is the momentum transfer. Since $I(\epsilon, \phi) \propto (\boldsymbol{Q} \cdot \boldsymbol{n})^2$, we can observe the largest intensity of the γ_1 and γ_2 modes at $\phi = \pi$ /2. Here, $\boldsymbol{n}$ is the polarization vector of the vibrational mode.

Figure 1 shows a map of the observed scattering intensity $I(\epsilon, \phi)$. It is clear that, as has been expected, the intensity of 95 meV mode assigned as γ_1 in the early study[5] becomes largest at ϕ= π /2 and smallest at ϕ= 0. This is clear evidence that the vibration direction of γ_1 is nearly parallel to the a^*-axis. The ϕ -dependence of the peak at ϵ = 80meV is also similar to that of γ_1. Therefore, we can identify the 80 meV peak as

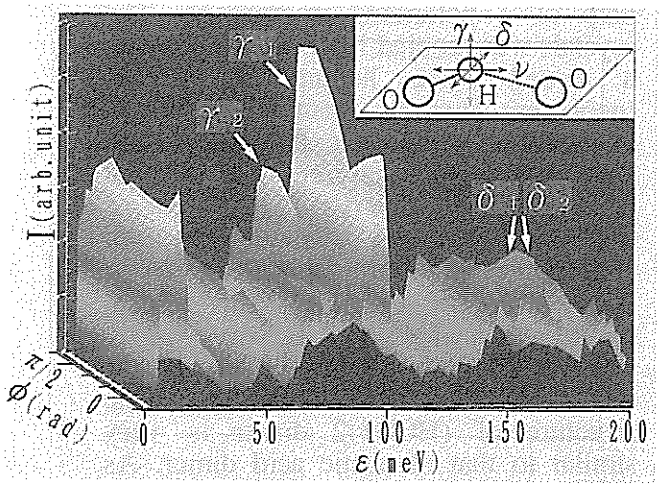

Fig. 1. $I(\epsilon,\phi)$ of single crystals of RHS about b-axis rotation as a function of the rotation angle ϕ (rad) and energy transfer ϵ (meV) at T=18 K. ϕ =0 corresponds to $\boldsymbol{Q} \parallel \boldsymbol{c}$. ϕ is changed from ϕ =0 to π by step scanning with interval $\Delta\phi = \pi/6$. In the inset, the vibration directions of the γ, δ and ν modes are depicted schematiccaly.

the γ_2 mode. This is inconsistent with the previous Raman study in which the γ_2 mode was assigned to the peak at 102 meV. We found no peaks at about 102 meV. Furthermore, it turns out that two peaks at ϵ = 143 and 157 meV become largest at ϕ = 0 and smallest at $\phi = \pi$ /2. This means that these peaks should be assigned to the δ_1 and δ_2 modes.

In another experiment, the single crystals were rotated about the c-axis, and the similar intensity map I (ϵ, θ) was obtained. Here, θ is the rotation angle, and is defined to be θ =0 at $\boldsymbol{Q} \parallel \boldsymbol{b}$ and $\theta = \pi$ /2 at $\boldsymbol{Q} \parallel \boldsymbol{a}^*$. In this map, we certainly find that the peaks of the γ_1 and γ_2 modes at ϵ =95 and 80 meV become largest at $\theta = \pi$ /2 and smallest at θ =0. This gives again clear evidence that those peaks must be assigned to γ_1 and γ_2. Two δ modes are weak for whole range of θ. It is because $\boldsymbol{Q}$ is always perpendicular to $\boldsymbol{c}$. We found two broad peaks around ϵ =300-350 meV. Those make maxima at θ =0. Therefore, we identified those two peaks as the ν_1 and ν_2 modes. This is consistent with the results of the Raman study.

In our present works, we determined the excitation energies and the vibration directions of the hydrogen modes, which have been considered to play an important role on the phase transition mechanism in RHS. Our results obviously show that ϵ of the out-of-plane bending modes of H(1) and H(2) are much smaller than those of other typical hydrogen bonded compounds,[7] though the stretching and in-plane bending modes are similar to these. This means that the hydrogen potential is extremely shallow along the out-of-plane bending direction. The result is consistent with the structure model[3] because two H-attached O atoms have the largest thermal amplitude nearly along the a^*-axis.

References

1) V. S. Ambrazyavichene, A. A. Volkov, G. V. Kozlov, V. S. Krasikov and E. B. Kryukova, Sov. Phys.-Solid State **25**, 925 (1983)
2) J. P. Ashmore and H. E. Petch, Can. J. Phys. **7** 2694 (1974)
3) K. Itoh, H. Ohno and S. Kuragaki, J. Phys. Soc. Jpn. **64**, 379 (1995)
4) N. Toupry, H. Poulet and M. Le. Postollec, J. Raman Spectrosc. **11**, 81 (1981)
5) S. Kosegawa, S. Ikeda and K. Itoh, J. Phys. Soc. Jpn. **64**, 1435 (1995)
6) M. Ichikawa, Chem. Phys. Lett. **79**, 583 (1981)
7) S. Ikeda, Y. Noda, H. Sugimoto and Y. Yamada, J. Phys. Soc. Jpn. **63**, 1001 (1994)

Inelastic Neutron Scattering Study of $KDCO_3$

A. KUWASAWA(1), S. KASHIDA(1), S. IKEDA(2) and Y. YAMADA(3)

1 Faculty of Science, Niigata University Ikarashi 8050, Niigata, 950-21
2 National Laboratory for High Energy Physics, Oho, 1-1, Tsukuba, Ibaraki, 305
3 Advanced Research Center for Science and Engineering, Waseda University, Ohkubo, Shinjyu-ku, Tokyo, 169

Potassium hydrogen carbonate has (HCO3)2 dimers linked by two hydrogen atoms. It is one of the most simple hydrogen bond materials. At room temperature the crystal belongs to the space group P21/a, where the principal axes of the (HCO3)2 dimers are tilted in antiphase at the corner and center of the cell [1,2]. Above 318 K. the crystal transforms to a high temperature phase. In this phase, the dimers at the center and corner sites become equivalent (space group C2/m) [3]. X-ray studies have shown that the structure is represented by a superposition of the two tilted configuration, that is, the local order of the low temperature phase remains, that is, the hydrogen atoms are jumping between the double well potential which is still asymmetric.

The incoherent neutron scattering experiment is a powerful method to study the proton dynamics since it has a large cross section. Fillaux et al.[4] have reported detailed neutron scattering study in powder crystals of KHCO3. Since in KHCO3 the hydrogen bond axes are aligned in a unique direction, using single crystal samples, we can easily extract the stretching and bending motions of hydrogen atoms [5].

In this study, deuterated samples of KDCO3 are used to measure the neutron scattering spectra. The aim of this work is twofold. First, the mass of deuterium is twice that of hydrogen. By comparing the spectra of the two compounds, we can distinguish the local deuteriun modes whose energy may change as $1/\sqrt{2}$, and the collective modes whose energy change little. Second, the incoherent cross section of deuterium is about 1/20 of hydrogen. In the spectra of deuterium sample, we will be able to observe silent modes which are hidden in the spectra of the hydrogen compound.

Powder crystals of KDCO3 were synthesized by bubbling CO2 gas through a concentrated solution of K2CO3 in D2O (99.9%). Large single crystals were grown by seeding a warm solution (45 C) and gradual cooling (about 0.5 C/day) to room temperature. For neutron scattering studies, five crystals with dimensions around 10x15x10 mm were aligned with the help of a polarizing microscope. The crystals were cooled to about 20 K using a closed cycle helium refrigerator. Incoherent inelastic neutron scattering experiments were done on an inverted geometry crystal-analyzer time-of-flight neutron spectrometer (CAT) [6].

The vibrational frequencies of (HCO3)2 dimer are calculated using empirical force constants and normal coordinate analysis [7]. It was used to simulate the infrared and Raman spectra of the formic and acetic acid dimers. The structure of (HCO3)2 dimer is very similar to that of acetic acid dimer. As initial values of the force parameters, we have used the data given for acetic acid dimer, and the parameters are modified so as to fit the experiments. The internal modes appear with energies greater than 50 meV and the external modes with energies below 50 meV. The inelastic neutron scattering spectra are calculated from the obtained atomic displacement vector U and vibrational frequency .

Figure 1 shows the geometry of experimental settings and the related vibrational modes. The observed neutron scattering spectra are shown in Fig. 2. In the first setting (Fig.2a), the incident beam is perpendicular to the hydrogen-bond dimer plane. The most intense peak at 83 meV is assigned to the out-of-plane bending mode, γ OD. In the previous infrared study this mode is observed as a broad band centered at 89 meV. Upon deuteration, the energy of the γ-OH mode shifts as $E(\gamma\text{-OH})/E(\gamma\text{-OD}) \approx 1.4$. The second harmonic of this mode, 2γ-OD, is

observed at 164 meV. The peak at 101 meV is assigned as the out-of-plane γ-CO3 mode. The corresponding infrared peak is reported at 104 meV. In the hydrogen salt, this mode is observed as a shoulder of the intense γ-OH band.

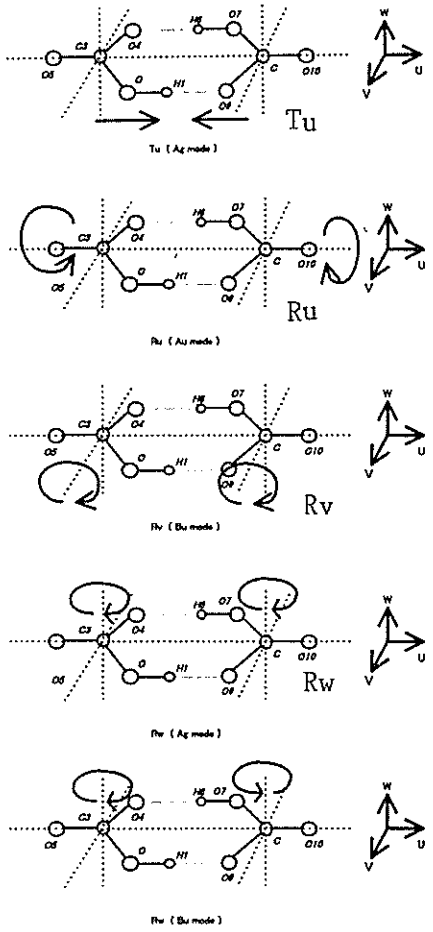

Fig. 1 Schematic representation the vibrational modes discussed in the text.

In the second setting, the incident beam is parallel to the hydrogen-bond axis (Fig. 2b). The broad band centered at 250 meV is assigned to the stretching ν-OD mode (the corresponding infrared value is 258 meV). The energy shift is E(ν--OH)/E(ν-OD) ≈ 1.3. The broad band at 78 meV is assigned, comparing with the infrared data and the calculated values, to the two scissor type modes, δs-CO3 (symmetric) and δa -CO3 (asymmetric). The three weak peaks observed at 132, 167 and 191 meV are assigned to the symmetric stretching νs-CO3 and the two asymmetric stretching νa-CO3 and νa-CO3' modes, respectively.

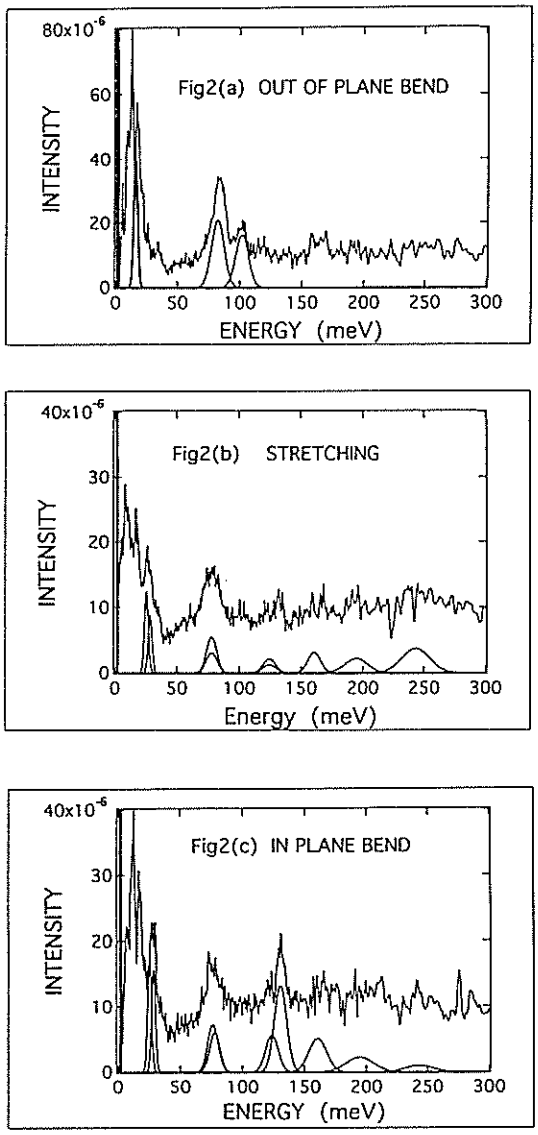

Fig. 2
Inelastic neutron scattering spectra and calculated peak intensity.
(a): incident beam is along the γ-OH(D) out-of-plane bending direction.
(b): incident beam is along the ν-OH(D) stretching direction.
(c): incident beam is along the δ-OH(D) in-plane bending direction.

In the third setting (Fig. 2c), the incident beam is along the b-axis. The peak at 131 meV is assigned to the in-plane bending δ-OD mode, (the corresponding infrared peak is at 135 meV). The energy of the δ-OH mode shifts upon deuteration, E(δ-OH)/E(δ-OD) ≈ 1.3. The width of this δ-OH mode is narrow compared with that of the δ-OH mode. In KHCO3, the pure δ-OH band and the combination band of the δ-OH bending and the O1-C and O2-C stretchings (νa-CO3 modes) have nearly

the same energy around 170 meV (about the definition O1, and O2, see Fig.1), and these two peaks are observed as a single broad band. In KDCO3, these two modes (δ-OD and C-O stretchings) are observed as separate peaks at 131 meV and 170 meV, although the intensity of the latter peak is much weaker. The peak observed in KHCO3 around 200 meV disappears in KDCO3. This may be consistent with our previous assignment that it is a coupled band of the δ-OH bending and C2-O stretching modes. The peak observed at 76 meV is attributed to the two scissor type modes, δs-CO3 and δa-CO3. These in-plane bending modes are also observable in the second setting.

In the low energy region below 50 meV, several peaks are observed. The most prominent one is the band at 26 meV. When the incident beam is parallel to the hydrogen bond axis, this band appears as a single peak at 26 meV, and when the incident beam is parallel to the in plane bending direction, this band appears as two peaks at 27 meV and 29 meV. This band is assigned as due to stretching motions ν-OD..O. There are two such modes, one is the Tu mode which is active in the second setting, and the other is the Rw mode which is active in the third setting. We then assume that the Tu(D) mode is at 27 meV and the Rw(D) mode is at 29 meV. The energy of these modes change little upon deuteration (Tu(H) ≈ 27 meV and Rw(H)≈29 meV). Upon deuteration, the energy and the shape of this band shifts little. Therefore, this band may be attributed not to the local hydrogen mode [4], but to collective motions.

The peaks observed at 17 and 14 meV may be attributed to lattice modes. The energies of the modes change little from those in the hydrogen salt. The present results are summarized in Table I. Further detailed neutron scattering studies and analysis are necessary in order to assign these low energy modes.

Table I

KHCO3		KDCO3	
ν-OH	325	γ-OD	250
νa'-CO3		νa'-CO3	191
νa-CO3		νa-CO3	167
2γ-OH	230	2γ-OD	164
νs-CO		νs-CO	132
δ-OH	170	δ-OD	131
γ-CO3		γ-CO3	101
γ-OH	117	γ-OD	83
δ-CO3	78	δ-CO	76
Rw	30	Rw	30
Tu	27	Tu	27

References

1) I. Nitta, Y. Tomiie and C. H. Koo: Acta Crystallogr. 5 (1952) 292.
2) J. O. Thomas, R. Tellgren and I. Olovsson Acta Crystallogr. B30 (1974) 1155.
3) S. Kashida and K. Yamamoto: J. Solid State Chem. 86 (1990) 180.
4) F. Fillaux, J. Tomkinson and J. Penford: Chem. Phys. 124 (1988) 425.
5) S. Kashida, Y. Nakai and S. Ikeda: J. Phys. Soc Jpn. 63 (1994) 4643.
6) S. Ikeda, N. Watanabe: J. Phys. Soc Jpn. 56 (1987) 565.
7) I Yokoyama. Y. Miwa and K. Machida: J. Am. Chem. Soc., 113 (1991) 6458

Hydrogen Site Occupation in Pd_3Y with $L1_2$ Structure

S. YAMAGUCHI, Z. Q. LI, M. OHHASHI, Y. KAWAZOE
T. KAJ ITANI*, K. AOKI** and S. IKEDA***

Institute for Materials Research, Tohoku Univ., Sendai 980-77
*Department of Applied Physics, Tohoku Univ., Sendai 980-77
**Kitami Institute of Technology, Kitami 090
***National Laboratory for High Energy Physics, Tsukuba 305

A simple model to predict the interstitial sites preferentially occupied by the hydrogen atoms in intermetallic compounds has been suggested by Jacob[1,2] and Griessen[3]. According to this model the occupancy of the interstitial sites is deter-mined by the heat of formation of imaginary hydrides formed between the hydrogen atom and the host metal atoms forming the interstitial site in consideration. Accordingly, a value ΔH which is the sum of these heats of formation is assigned to each site. The relative hydrogen occupancy has been calculated in a quantitative manner using Boatsman's distribution function and the ΔH values. On the other hand, Westlake[4] and Magee[5] have claimed that interstitial hole size and hydrogen-hydrogen interatomic distance are used to predict the hydrogen occupied sites in hydrides of intermetallic compounds. They find that an increase in hole size is accompanied by greater stability.

Neutron diffraction and neutron inelastic scattering experiments on intermetalllic hydrides have provided quantitative in-formation on the distribution of the hydrogen (the relative occupancy) among the various interstitial sites. The purpose of the present reports to examine experimental criteria in the case of YPd_3 com-pounds of $L1_2$ structure.

Neutron diffraction and incoherent inelastic neutron scattering experiments have been carried out on the metallic hydride of $YPd_3H(D)_x$ for x = 0, 0.19 and 0.30 to study the hydrogen (deuterium) sites and their dynamics. The neutron diffraction experiments were made on the Kinken powder diffractometer (KPD)..The neutron wave length was 0.1767 nm and the diffraction patterns were recorded over the angular range $10^\circ < 2\theta < 104^\circ$ in steps of 0.1°. The inelastic incoherent scattering measure-ment were performed using a crystal analyzer time-of-flight (CAT) spectrometer which is installed in KENS.

Analysis of neutron diffraction patterns from the $YPd_3H(D)_x$ for the different H(D) contents have con-firmed that the $L1_2$-type structure of YPd_3 is pre-served on hydrogenation up to x=0.30.

The inelastic incoherent scattering spectrum on the CAT spectrometer for $YPd_3H_{0.30}$ at 6 K is shown in Fig. 1. The inelastic incoherent scattering was employed to determine the relative occupation by hydrogen on the tetrahedral and octahedral sites from the difference of the hydrogen vibrations between the both sites[6]. The large peak observed near 55 meV is identified as the vibrational spectrum of the octahedral site hydrogen. The width of this peak is believed to be result of the dispersion in the optical modes as was observed in the similar system of $PdH_{0.7}$[7]. The peak at 120 meV which is characteristic of the tetrahedral site hydrogen vibration is not recognized in this spectrum. Consequently most H(D) atoms will occupy the octahedral sites.

A quantitative comparison of the diffraction in-tensities was made on the neutron diffraction data from YPd_3, $YPd_3H_{0.30}$ and $YPd_3D_{0.19}$. The observed data are listed in Table 1 in comparison with calculation. It will be seen from Table 1 that the relative intensity of the diffraction lines are considerably different each other; e.g. the 100 diffraction line is stronger

than the 110 diffraction line for $YPd_3H_{0.30}$, while for $YPd_3D_{0.19}$ the 100 diffraction line is weaker than the 110 diffraction line. These characteristic features of the diffraction patterns can be understood quiet well assuming the preferential occupation of the specified octahedral interstitial sites by H(D) atoms.

In the YPd_3 compound of $L1_2$ structure (1Y atom in (0, 0, 0) position and 3Pd atoms in (0, 1/2, 1/2), (1/2, 0, 1/2) and (1/2, 1/2, 0) positions), there are only two different octahedral interstitial sites: a '6Pd site' surrounded by 6 Pd atoms and three '2Y4Pd sites' surrounded by 2 Y and 4 Pd atoms. The co-ordinates of the '6Pd site' and the '2Y4Pd sites' are (1/2, 1/2, 1/2) and (1/2, 0, 0), (0, 1/2, 0) and (0, 0, 1/2). Then, the structure factors for YPd_3H_x are expressed as follows,

$$F(hkl) = b_Y + b_{Pd}(\cos \pi k \cos \pi l + \cos \pi l \cos \pi h + \cos \pi h \cos \pi k) + ub_H \cos \pi h \cos \pi k \cos \pi l + vb_H(\cos \pi h + \cos \pi k + \cos \pi l)$$

where b_Y, b_{Pd} and b_H are the scattering amplitudes of yttrium, palladium and hydrogen respectively and two parameters u and v are occupation probabilities of hydrogen in the '6Pd site' and '2Y4Pd sites' respectively. The parameters u and v are related to the hydrogen fraction per formula unit x; $x = u + 3v$. A good agreement is obtained if we assume the value of the occupation probabilities $u = 0.12$ and $v = 0.06$ for $YPd_3H_{0.30}$ at 300 K, and $u = 0.175$ and $v = 0.005$ for $YPd_3D_{0.19}$ at 70 K. The structure factors calculated using these values are listed in the fourth and sixth columns of Table 1, and the reliability factors are less than 0.03. These results indicate that the H(D) atoms prefer the '6Pd site' to the '2Y4Pd sites'.

According to the semiempirical model by Jacob[1,2] and Driesen[3], the occupancy of the interstitial site is determined by the heat of formation of imaginary ternary metal hydrides formed between the hydrogen atom and the host metal atoms forming the interstitial site in consideration. In YPd_3 structure, there are two kinds of octahedral sites coordinated by 6 nearest neighbor metal atoms and formation of $Y_2Pd_4H_x$ and Pd_6H_x is expected. The heat of

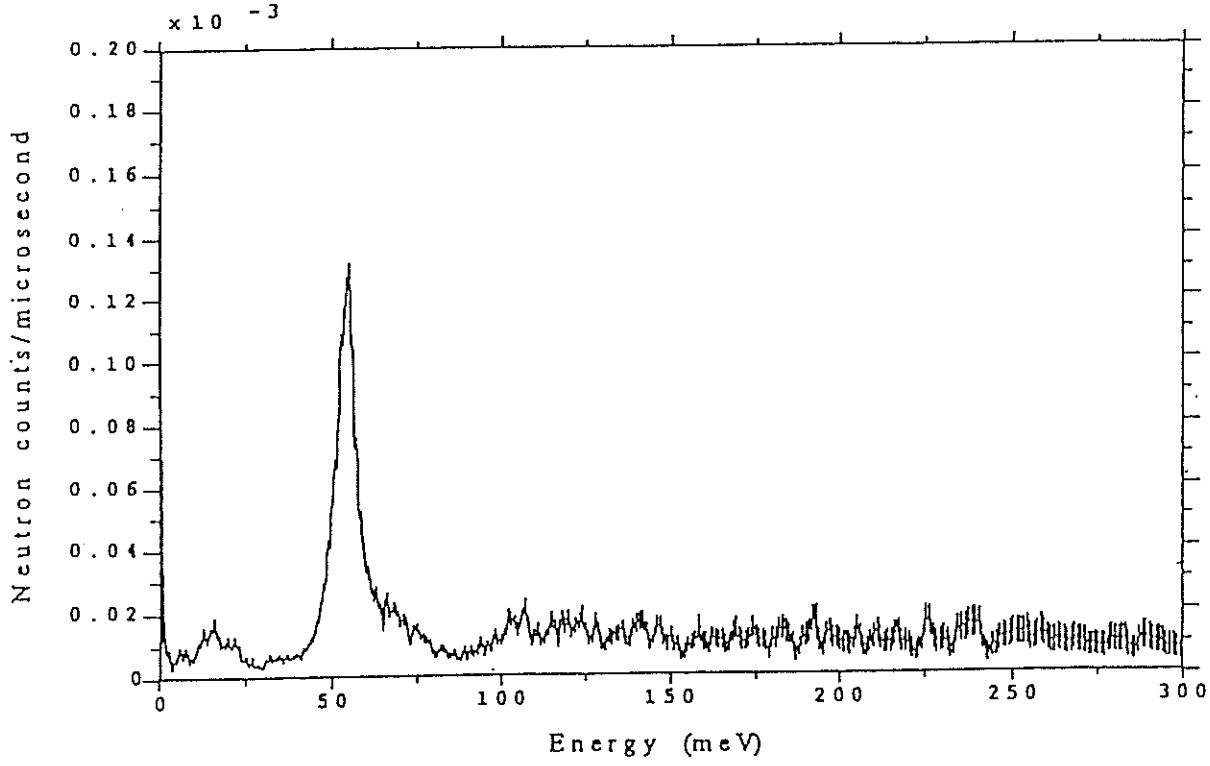

Fig. 1. Incoherent inelastic neutron scattering spectra of $YPd_3H_{0.30}$ measured at 6 K.

Table 1 A comparison of the diffraction intensity with the calculation

h	k	l	YPd_3 (300 K)		$YPd_3H_{0.30}$ (300 K)		$YPd_3D_{0.19}$ (70 K)	
			$F_{Obs.}$	$F_{cal.}$	$F_{Obs.}$	$F_{cal.}$	$F_{Obs.}$	$F_{cal.}$
1	0	0	0.15	0.16	0.18	0.18	–	0.05
1	1	0	0.18	0.16	0.15	0.14	0.28	0.27
1	1	1	2.73	2.68	2.79	2.79	2.56	2.58
2	0	0	2.62	2.68	2.65	2.57	2.86	2.80
2	1	0	0.19	0.16	0.16	0.18	–	0.05
2	1	1	0.15	0.16	0.11	0.14	0.24	0.27
2	2	0	2.76	2.68	2.50	2.57	2.78	2.80

formation of these hydride clusters was calculated by Griesen et al.[8], and the $\Delta H_{2Y\,4Pd}$ site and ΔH_{6Pd} values were evaluated to be -0.38 and -0.20 eV/atom, respectively. As for the size of holes at interstitial sites, the hole radii for the '2Y4Pd sites' and '6Pd site' are evaluated to be 0.42 and 0.76 A, respectively. The present neutron diffraction result which shows the preference of the '6Pd site' occupancy by the H aoms, therefore, is consistent with the hole size criteria, but is in contradiction to the prediction by the imaginary hydride model.

In order to search the preferential site for the H atoms in the YPd_3 compound theoretically, the first-principles calculations concerning the total energy of the hydride cluster with the different hydrogen positions have been carried out. All theoretical results presented in the present calculation are obtained within the local-density-functional theory[9]. The hydride cluster used for the calculation consists of 2x2x2 unit cells, which corresponds to $Y_8Pd_{24}H$ ($YPd_3H_{0.125}$) composition. In order to search the most favorable position of hydrogen, we move the hydrogen atom along the line from the '6Pd site' to the '2Y4Pd site' and calculate the total energy. Fig. 2 shows the result of total energy as a function of distance from the '6Pd site' to the hydrogen. From this figure we find that the '6Pd site' is more energetically favorable than the '2Y4Pd site' and the total energy difference is 0.49 eV. It is conclude, therefore, that the differencein the electronic interaction between hydrogen and host atoms is largely responsible for the hydrogen occupancy of interstitial sites in intermetallic hydrides.

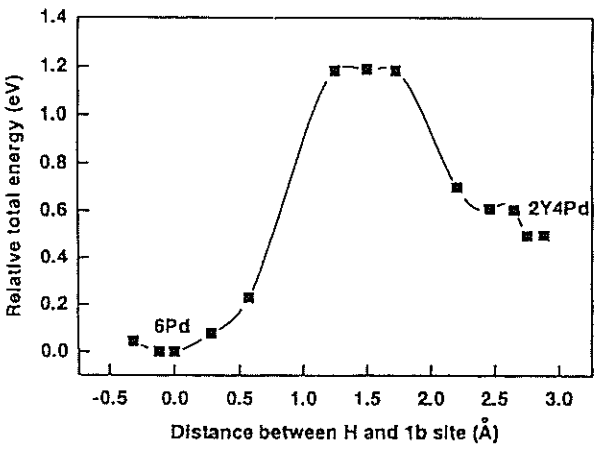

Fig. 2 Total energy as a function of distance from 6Pd site to hydrogen atom.

References

1) I. Jacob et al., Solid State Commun., 35, 155 (1980)
2) I. Jacob and J. M. Bloch, Solid State Commun.,42, 541 (1982)
3) R. Giesssen and A. Driessen,J. Less-common Met., 103, 245 (1984)
4) D. G. Westlake, J. Less-common Met., 75, 177 (1980)
5) C. B. Magee et al., J. Less-Common Met., 78, 119 (1981)
6) J. A. Goldstein et al., Solid State Commun., 49, 475 (1984)
7) Y. Nakai et al., J. Phys. Soc. Jpn., 62, 1834 (1992)
8) R. Griessen et al., J. Less-Common Met., 103, 235 (1984)
9) W. Kohn and L. J. Sham, Phys. Rev., 140, A1133 (1965)

Thermochromism and Dynamics of Organometallic Conjugated Systems

S. TAKEDA,[a] H. FUKUMOTO,[b] K. MASHIMA,[c] G. MARUTA,[d] K. YAMAGUCHI,[d] and A. NAKAMURA[b]

Department of Chemistry[a], Faculty of Engineering, Gunma University, Kiryu, Gunma 376
Department of Macromolecular Science[b] and Chemistry[d], Graduate School of Science, Osaka University, Toyonaka, Osaka 560
Department of Chemistry[c], Graduate School of Engineering Science, Osaka University, Toyonaka, Osaka 560

Conjugation in organic compounds is represented by extended pπ-pπ interactions. A modified conjugation and/or doping category can be seen in organometallic systems, in which extended π-interaction involving metal-carbon bonding is realized. An example is metal π-complexes of organic conjugated systems. Particularly polyene complexes of early transition metals such as zirconium is interesting, since these electron-deficient metal ions are highly reactive and thus polyene system may be largely perturbed by the bonding with zirconium which is both electron-donating (π-type) and -attracting (σ-type) in varying degrees. For the *s-trans* coordinated diene complex, π-conjugation of the diene molecule is maintained and the effect of mixing of the d-electron of the transition metal may be delocalized over the diene molecule. Thus a mixed electronic state of organic pπ-electron and metallic d-electron is expected.

We observed the thermochromism of the deeply colored zirconocene complex of 1,4-diphenyl-1,3-butadiene (DPBD) in the solid state. Semiempirical ZINDO molecular orbital calculation revealed that the deep color of the complex originates in the HOMO-LUMO and HOMO-LUMO+1 transitions. These molecular orbitals are mainly composed of the d-orbitals of Zr and the π-orbitals of DPBD and cyclopentadienyl (Cp) ring and are sensitive to the orientation of the π-orbital of Cp rings, suggesting that the dynamic perturbation is operative for the transition energies.

The dynamic nature of the Cp ring and phenyl group was precisely investigated by the measurements of the spin-lattice relaxation rate of proton NMR and by the incoherent neutron scattering.[1)]

Spin-lattice relaxation rate of proton NMR To investigate the dynamic behavior of the complex in the solid state, the spin-lattice relaxation rate T_1^{-1} of proton NMR was measured between 14 and 300 K at 18.0 and 37.2 MHz. The result of the measurement is shown in Fig. 1. Two maxima were clearly observed near 50 K (10^3×(1/T)=20 (1/K)) and 100 K (10^3× (1/T)=10 (1/K)), indicating that the two motional modes are thermally excited. The high temperature

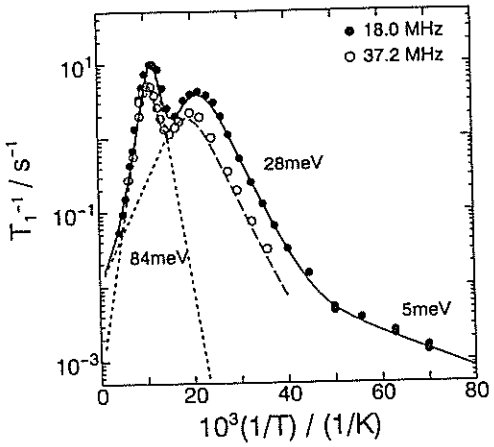

Fig. 1 Temperature dependence of T_1^{-1} of proton NMR of $ZrCp_2$(DPBD).

mode with the activation energy of 84 meV (7.7 kJ/mol) was assigned to the 180°-flip motion of the phenyl ring around the C-C bond and the low temperature mode with the small activation energy of 28 meV (2.6 kJ/mol) was assigned to the rotation of the Cp-ring about the five-fold axis. The break of the slope of T_1^{-1} below 20 K (10^3×(1/T)≥50 (1/K)) was attributed to the excitation energy 5 meV (0.46 kJ/mol) between the librational ground state and the first excited state of the Cp-ring as discussed below.

The T_1^{-1} was calculated by assuming the two motional modes mentioned above. The solid and broken curves are the calculations for the different Larmor frequencies. The temperature dependence of the correlation time of the rotation of the Cp-rings was derived and is shown in Fig. 2. The activation energy for the rotation of the Cp-ring around its five-fold axis is 28 meV and the small activation energy 5 meV in the low temperature region was attributed to the excitation energy between the librational ground and the first excited states. Here the quantum mechanical tunneling of the Cp-ring through the librational first excited state seems to dominate T_1^{-1}. This phenomenon is similar to the tunneling of methyl groups, which has been well investigated experimentally and theoretically.[2,3)] In this case, the Larmor frequency dependence of the spin-lattice relaxation rate is useful to estimate the tunneling frequency and was measured for

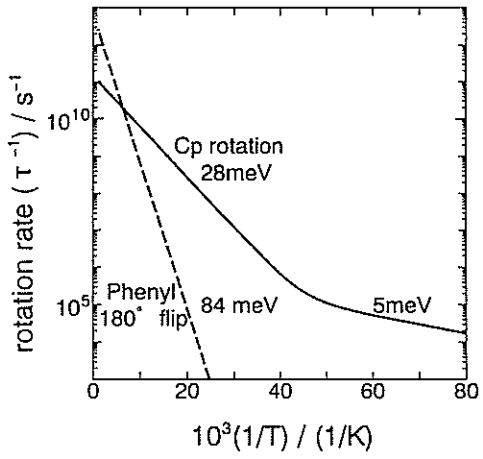

Fig. 2 Temperature dependence of the rate of rotations.

$ZrCp_2(DPBD)$ between 3 and 40 MHz at 17.9 K by use of the field cycling technique. The observed frequency dependence almost obeys the relation $T_1^{-1} \propto \omega_0^{-2}$ at high frequency region and tends to smaller slope below c.a.10 MHz. This trend is not the case of the relaxation due to paramagnetic impurities ($T_1^{-1} \propto \omega_0^{-0.5}$ for wide frequency region) but is very similar to the rotational tunneling of methyl group with the tunneling frequency of the order of Larmor frequency. The librational excitation energy 5 meV was rationalized by the calculation of the energy scheme for the Cp-ring rotation, where the moment of inertia I = 1.9×10^{-45} kg m^2 of the Cp-ring around the five-fold axis was used. Five-fold potential functions with higher order term was assumed. The parameters of the potential were chosen so that the activation energy (28 meV) and the torsional excitation energy (5 meV) determined above agree with the calculation. These criteria do not uniquely fix the parameter values and therefore we adopted the potential function as simple as possible. As a result of trial-and error calculations, we obtained two reasonable potential functions with higher order 10-fold term. One is

$$V / meV = 15.6\{1+cos(5\theta)\} - 3.7\{1+cos(10\theta)\} + 7.3.$$

The librational ground state has 5-fold degeneracy and exhibits small tunneling splittings of the order of a few MHz or less. This is almost consistent with the observed Larmor frequency dependence of T_1^{-1}.

The observed activation energy for the rotation of the Cp-ring in the complex $ZrCp_2(DPBD)$ is very small among the zirconocene complexes investigated hitherto.[4,5] This is an unique character of this complex. Since the activation energy 28 meV corresponds to the thermal energy at 310 K, the thermal population of the Cp-ring near the top of the barrier is large for this complex near room temperature and the fluctuation amplitude of the Cp-ring is extremely large. This fact is in good agreement with the large thermal ellipsoid of the Cp-ring observed by the X-ray diffraction experiment.[6] This motion perturbs the bonding between the Cp-ring and zirconium.

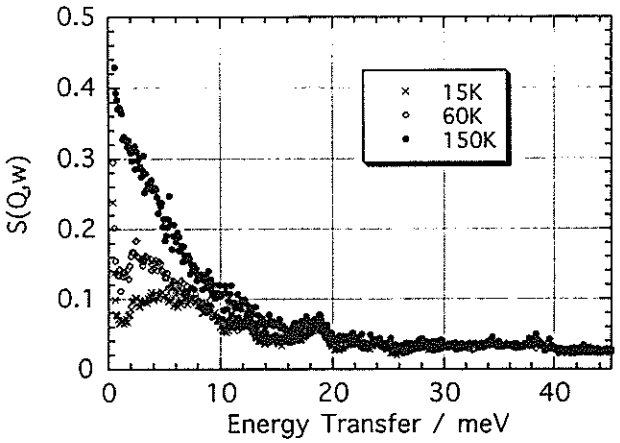

Fig. 3 Temperature variation of INS from $ZrCp_2(DPBD)$.

For the dynamical perturbation on the electronic state of the π-conjugated system of the complex, the motion of the phenyl ring is important. It was revealed that the phenyl rings undergo 180°-flip rotation with the activation energy of 84 meV (7.7 kJ/mol). This motion was observed as a high temperature maximum of T_1^{-1} of proton NMR as shown in Fig. 1. The rate of the 180°-flip motion of the phenyl ring around the C-C bond is expressed by the Arrhenius formula, which is slow in the low temperature region and is the same order near the room temperature compared with the rate of the Cp-ring rotation as shown in Fig. 2. In addition to the large amplitude flip motion (180°flip), more rapid small angle fluctuation of the phenyl ring was suggested by the incoherent neutron scattering measurement as described below.

Incoherent neutron scattering To investigate the rapid fluctuation and the librational modes of the Cp-ring and the phenyl ring, incoherent neutron scattering spectrum was measured in the energy transfer region between -3 and 200 meV with LAM-D spectrometer. In this report the energy transfer region below 20 meV is discussed in which the librational modes of the Cp-ring and of the phenyl ring and quasi-elastic scattering are expected to be observed. Figure 3 shows the neutron scattering spectrum measured at 15, 60, and 150 K. Four spectra with two different momentum transfer values (0.9 and 1.9 $Å^{-1}$) accumulated

simultaneously were added to improve the statistics for each temperature. A characteristic feature of the spectrum observed at 15 K is a broad unresolved peak below 10 meV, in which several excitations overlap. In addition to the librational excitation of Cp-ring around 5 meV and its overtone, the torsional mode of the phenyl ring around the C-C bond and its overtones are expected to appear in this energy transfer region. An estimate of the fundamental excitation of the torsional oscillation of the phenyl ring is ~3meV, where the cyclic two-fold potential function, $V/meV = 42.1(1+\cos(2\theta))$, which is consistent with the observed activation energy of 84 meV for the 180°-flip motion of the phenyl ring, was assumed and the moment of inertia, $I = 1.37\times10^{-45}$ kg m^2, was used. Overlapping of these librational modes of the Cp-ring and the phenyl ring gives the broad unresolved scattering peak.

At elevated temperature, *i.e.* 150 K, it is noted that the scattering intensity around the elastic peak is remarkable as shown in Fig. 3. The result indicates that a rapid motion associated with the fluctuation of protons occurs at 150 K, while this motion is slow and can not be detected by the neutron scattering at 60 K. The quasielastic scattering component at 150 K was tentatively separated from the elastic and inelastic scattering by subtracting the scattering function S(Q, ω) at 60 K from that at 150 K and could be roughly expressed by a single Lorentzian function as shown in Fig. 4. A half-width at half maximum (HWHM) of the observed quasielastic scattering is ~2 meV. HWHM for the five-fold rotation of Cp-ring was calculated with the usual method by taking into account the jumping rate 1.8×10^{10} s^{-1} at 150 K deduced from the proton NMR relaxation measurement. The HWHM is 17 μeV and 24 μeV for the different momentum transfer values, 0.9 and 1.9 Å^{-1}, respectively. The HWHM for the 180°-flip motion of the phenyl ring was also calculated to be 0.12 meV from the jumping rate 1.5×10^{10}s^{-1} determined by the proton NMR. These values are much smaller than the observed one (~2 meV) and the rapid motion detected as the quasielastic scattering is the third motional mode. It is noteworthy that the fluctuation amplitude of the third motional mode is as small as not detected by T_1^{-1} of proton NMR. The dependence of the quasielastic scattering of neutrons on the momentum transfer value is useful to estimate the geometry of the motion. Although the scattering intensity at Q = 1.9 Å^{-1} is larger by about 1.5 times than that at Q = 0.9 Å^{-1} and HWHM is the same for the two momentum transfer values within error, it was difficult to determine unambiguously the geometry of the rapid fluctuation because of the limited momentum transfer values. The rapid fluctuation will give rise to a significant thermal parameter for the structure determination. Such large values of the equivalent isotropic thermal parameters were found for the phenyl carbons except for one linked to the butadiene framework by the X-ray diffraction experiment at room temperature. Assuming that the third motional mode is small angle flipping of the phenyl ring around the C-C bond, the rate of the small angle flipping $\tau^{-1} \sim 3\times10^{11}$ s^{-1} was estimated from the width of the observed quasielastic scattering (Fig. 5) at 150 K by using two sites jump model. This motion is faster than the 180°-flip rotation and induces a rapid fluctuation and change of the electronic state of the π-conjugation of the DPBD molecule in the complex.

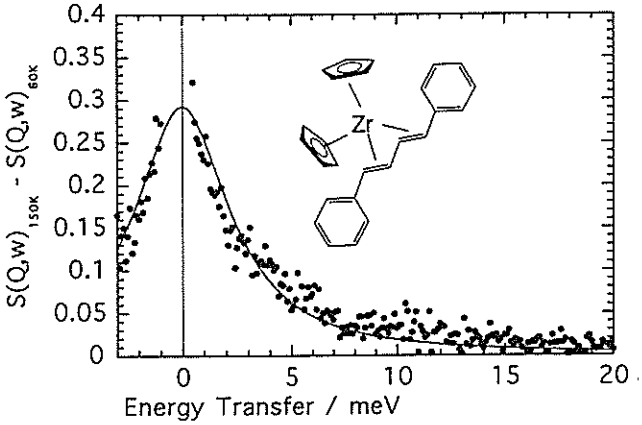

Fig. 4 Quasielastic neutron scattering at 150K.

Acknowledgment The authors are grateful to Dr. K. Shibata of Tohoku University and Prof. S. Ikeda of National Laboratory for High Energy Physics for their help for the INS experiment. This research was supported by grant-in-aid to S. T., K. M., K.Y., and A. N. from the Ministry of Education, Science and Culture of Japan (Specially Promoted Research No. 06101004).

References

1) Takeda, S.; Fukumoto, F.; Mashima, K.; Maruta, G.; Yamaguchi, K.; Nakamura, A. J. Phys. Chem. **1997**, in press.
2) Müller-Warmuth, W.; Schüller, R.; Prager, M.; Kollmar, A. *J. Chem. Phys.* **1978**, 69, 2382.
3) Gilson, D. F. R.; Gomez, G.; Butler, I. S.; Fitzpatrick, P. J. *Can. J. Chem.* **1983**, 61, 737.
4) Braga, D. *Chem. Rev.* **1992**, 92, 633.
5) (a) Kai, Y.; Kanehisa, N.; Miki, K.; Kasai, N.; Mashima, K.; Nagasuna, K.; Yasuda, H.; Nakamura, A. *J. Chem. Soc., Chem. Commun.* **1982**, 191. (b) Kanehisa, N. *Ph. D Thesis*, Osaka University **1992**.

Phonon anomaly of $YBa_2Cu_3O_{6.6}$

T. Nishijima, M. Arai[1], T. Otomo[1], K. Yamaya[2] and A. C. Hannon[3]

Department of Accelerator Science, Grad. Univ. for Advanced Studies, Tsukuba 305, Japan
[1]National Laboratory for High Energy Physics, 1-1 Oho, Tsukuba 305, Japan
[2]Department of Applied Physics, Hokkaido Univ. Sapporo 060, Japan
[3]Rutherford Appleton Laboratory, Chilton, Didcot Oxon, OX11 0QX, UK

One of the most remarkable phenomenon on the high-T_C cuprates is probably a pseudo spin-gap opening in the normal state. This phenomenon was pointed out for the first time in $YBa_2Cu_3O_{6+x}$ by NMR experiments[1]. The nuclear spin-lattice relaxation rate, $1/T_1T$ has a maximum at specific temperature and shows a sudden decrease at lower temperatures. Especially for an under-doped composition the maximum is well above T_C, whereas the optimum doped superconductor has the maximum at T_C. These results are supported by the extended t-J model, whose phase diagram shows the existence of a spin-gap at well above T_C only in the low doping region[2]. Various experimental reports suggest also an anomalous behaviour at well above T_C (T_{SG}~150K) including a lattice instability, i.e. ion channeling[3], resitivity[4] and specific heat measurements[5].

Therefore, in order to clarify the relation between the lattice instability and the pseudo spin-gap opening we have carried out inelastic neutron scattering experiments making use of the INC spetrometer on a typical under-doped superconductor, i.e. $YBa_2Cu_3O_{6.6}$ (Tc~57K).

The long time neutron exposure, 16 hrs, of the sample with mass m=95 grams gave a good statistics. However, due to the relaxed energy resolution of the INC spectrometer cannot recognize a clear structure in G(E). The insufficient background correction and the multiple scattering in the low energy transfer region (< 30meV) give rise to a spurious temperature evolution by the Bose population correction, hence we do not discuss the behaviour in this region in this article. In order to investigate the temperature dependence we have integrated G(E) from 36 meV to 50 meV and from 54 meV to 65 meV. The former energy region includes the B_{1g} mode (~41 meV), which is related to the out-of-plane oscillatory motion of the planar oxygen atoms, and the latter includes the A_{1g} modes (~63 meV), which is the apical oxygen motion parallel to the c-axis. As shown in Fig. 1, both modes have anomalies at Tc (=57 K) and well above Tc (~150 K).

The temperature dependence of phonon intensities measured by infrared absorption spectroscopy on the $YBa_2Cu_3O_7$ have been reported by B. Guttler et al.[6] They discussed that excess intensities of the modes near 300 cm^{-1} and 500 cm^{-1} have a temperature dependence of BCS-like gap energy, i.e. the order parameter. Our results, shown in Fig 1, show a similar behavior below T_C (=57 K), although we cannot assert it clearly because of the small number of data points. We also found that the anomalies occur around T_{SG}, which may suggest a strong lattice-spin coupling. Recently Normand et al. calculated the coupling effect under the extended t-J model[7] and suggested an anomalous behaviour on the B_{1g} phonon mode , which has the d-wave symmetry. Our results are indeed consistent with this theoretical prediction, although we also found an anomaly of the phonon mode with non-d-wave symmetry, which may be explained by a spin interaction between the CuO_2 planes.

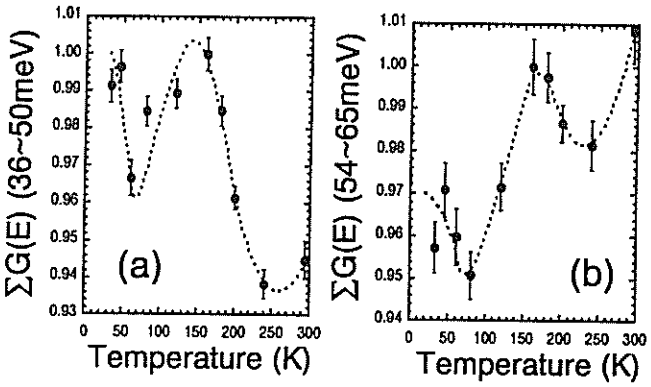

Fig. 1 Temperature dependence of the intensity between 36 and 50 meV (a), and between 54 and 65 meV (b). The dotted lines are a guide to the eye.

References

1) H. Yasuoka et al. in *Strong Correlations and superconductivity*, eds. H. Fukuyama et al., Springer Verlag, 254 (1989)
2) T. Tanamoto et al., *J. Phys. Soc. Jpn.* **61**, 1886 (1992) and *ibid* **62**, 717 (1993)
3) T. Haga et al., *Phys. Rev. B* **41**, 826 (1990)
4) T. Ito et al., *Phys Rev. Lett.* **70**, 3995 (1993)
5) J. W. Loram et al., *Phys. Rev. Lett.* **71**, 1740 (1993)
6) B. Guttler et al., *J. Phys.: Condence Matter* **2**, 8977 (1990)
7) B. Normand et al., *Phys Rev.* **B53**, 856 (1996)

Low Energy Excitations in Yttria-Stabilized Zirconia

T. SHIRAKAMI*, T. TOJO, T. ATAKE and H. YAMAMURA**

*Department of Material Chemistry, Faculty of Science and Technology, Ryukoku University, Otsu, 520-21
Materials and Structures Laboratory, Tokyo Institute of Technology, Yokohama, 226
**Department of Applied Chemistry, Faculty of Engineering, Kanagawa University, Yokohama, 221

Cubic form of zirconia is stabilized by adding yttria, calcia, magnesia, etc., which leads to formation of defects at the oxygen sites in the crystal and results in high oxygen conductivity at high temperatures. Recently, the vacancies in yttria-stabilized zirconia have been studied extensively, and the low energy excitations were found in the phonon density of states by heat capacity measurements at low temperatures.[1-3] In the present study, inelastic neutron scattering experiments have been carried out on the sintered samples of yttria-stabilized zirconia, and the existence of such low energy excitation has been confirmed. The results of the experiments will be presented and the low energy excitation will be discussed.

Fine powders (0.45 μm) of yttria-stabilized zirconia were synthesized by hydrolysis method from solution of $ZrOCl_2 \cdot 8H_2O$ and YCl_3. The sintered samples were prepared from the powder. The powders were uniaxially pressed into a plates under 50 MPa, and then isostatically cold-pressed at 200 MPa. The green compacts were sintered at 1500 ℃ in air for 4 hours. Thus two samples of $(ZrO_2)_{1-x}(Y_2O_3)_x$ (x=0.0776, 0.113) were used for the neutron inelastic scattering experiments. The experiments were carried out with the inverted geometry time-of-flight spectrometer LAM-D installed at the pulsed spallation neutron source in the National Laboratory for High Energy Physics (Tsukuba). The pieces of the sintered specimens (about 20 g) were put in an aluminum cylinder (14 mm in diameter, 80 mm in height, 0.25 in wall-thickness). The measurements were made at 14 K and at room temperature.

The density of states obtained for $(ZrO_2)_{1-x}(Y_2O_3)_x$ (x=0.0776) at 14 K is shown in Fig. 1. Besides the ordinary acoustic and optical modes, a broad hump below about 10 meV and a sharp peak at about 16 meV are clearly seen. The similar results were obtained also for the sample of $(ZrO_2)_{1-x}(Y_2O_3)_x$ (x=0.113).

The details of the low energy region of the density of states can be seen for the two samples of

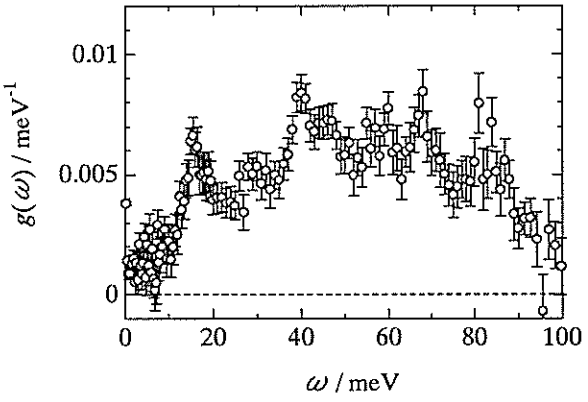

Fig. 1. Density of states in $(ZrO_2)_{1-x}(Y_2O_3)_x$ (x = 0.0776) measured at 14 K.

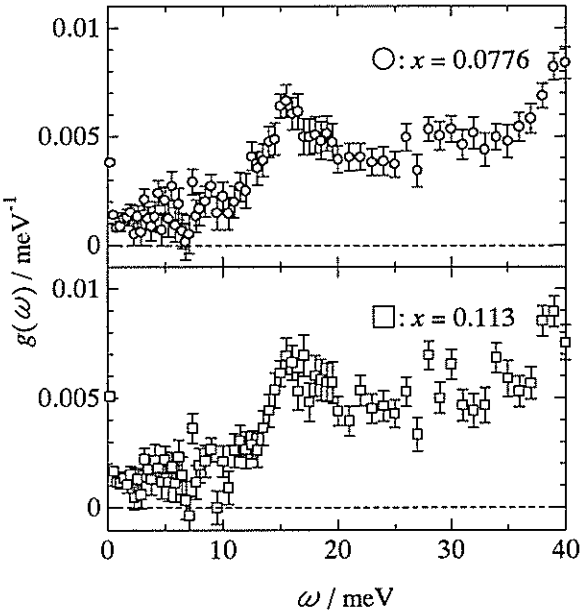

Fig. 2. Density of states in $(ZrO_2)_{1-x}(Y_2O_3)_x$ (x = 0.0776 and 0.113) measured at 14 K.

$(ZrO_2)_{1-x}(Y_2O_3)_x$ (x=0.0776, 0.113) at 14 K in an enlarged scale in Fig. 2. The broad hump below about 10 meV should correspond to the abnormal heat

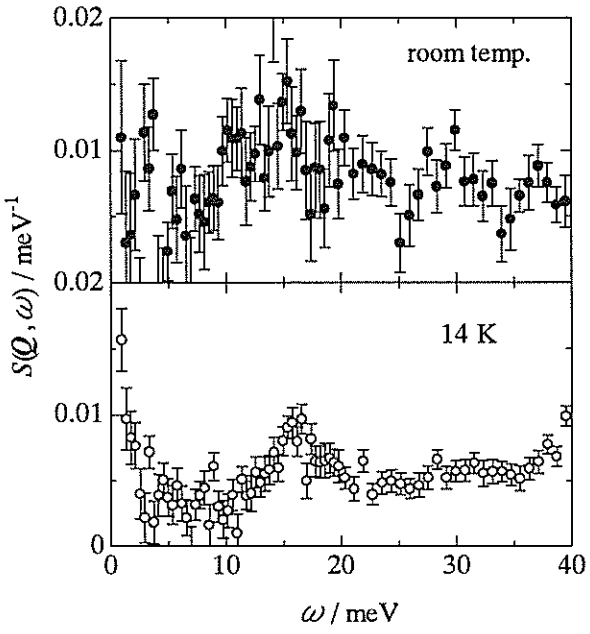

Fig. 3. Dynamic structure factors of $(ZrO_2)_{1-x}(Y_2O_3)_x$ (x = 0.0776) at 14 K (open circles) and room temperature (closed circles).

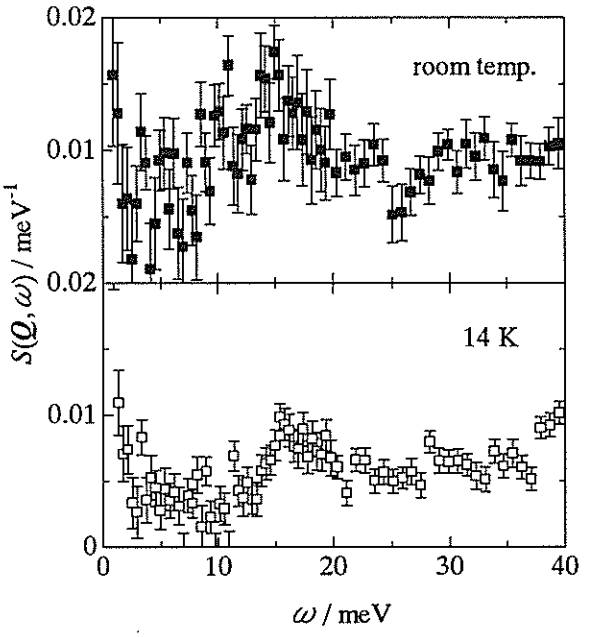

Fig. 4. Dynamic structure factors of $(ZrO_2)_{1-x}(Y_2O_3)_x$ (x = 0.113) at 14 K (open squares) and room temperature (closed squares).

capacity observed in the lowest temperature region down to about 100 mK[4]. On the other hand, the sharp peak at about 16 meV can be attributed to so-called low energy mode which was detected as an excess heat capacity in the low temperature region around 20 K[5]. The difference between the two samples is rather ambiguous. Further detailed studies are strongly required to clarify the mechanism of the oxygen conductivity and the effects of the oxygen defects in yttria-stabilized zirconia.

The dynamic structure factors obtained for $(ZrO_2)_{1-x}(Y_2O_3)_x$ (x=0.0776, 0.113) at 14 K and at room temperature are shown in Figs. 3 and 4. The sharp peak observed at about 16 meV at 14 K shifts to lower energy and the shape becomes broader at room temperature. Such a temperature dependence of the dynamical structure factor is inconsistent with the model proposed for amorphous solids[6,7]; the transition energy from the first excited state to the second excited state is larger than that from the ground state to the first excited state, that is so-called soft potential model. Further detailed studies should also be required on this points, which is in progress in our laboratory.

References

1) T. Shirakami, T. Atake, T. Mori and H. Yamamura, Solid State Ionics, 79, 143 (1995).
2) T. Shirakami, T. Tojo, T. Atake, T. Mori and H. Yamamura, Thermochim. Acta, 267, 415 (1995).
3) T. Tojo, T. Shirakami, T. Atake, T. Mori and H. Yamamura, Solid State Ionics, 86-88, 89 (1996).
4) T. Shirakami, T. Tojo, T. Atake, T. Mori and H. Yamamura, in preparation.
5) T. Tojo, T. Atake, T. Mori and H. Yamamura, in preparation.
6) V.G. Karpov, M.I. Klinger and F.N. Ignat'ev, Zh. Eksp. Teor. Fiz. 84, 760 (1983) [Sov. Phys. JETP 57, 439 (1983)].
7) M.A. Il'in, V.G. Karpov, and D.A. Parshin, Zh. Eksp. Teor. Fiz. 92, 291 (1987) [Sov. Phys. JETP 65, 165 (1987)].

Phase Transition and Orientational Disorder of Tetrakis(methylthio)methane Monolayer Adsorbed on Graphite

A. INABA and S. NAKAMURA

Department of Chemistry, Graduate School of Science, Osaka University, Toyonaka, Osaka 560

A globular molecule $C(SCH_3)_4$ forms a two-dimensional solid phase on the surface of graphite (Papyex). According to our heat capacity measurement,[1] the monolayer shows two phase transitions between the 2-D solid phases; one at 170 K and the other at 181 K. It melts around 260 K. Because of the shape of the molecule, the mechanism of the phase transitions is supposed to be an orientational order-disorder type.

The purpose of the present study was to investigate the dynamics of the $C(SCH_3)_4$ monolayer by neutron scattering. Orientational disordering of the whole molecule and rotational motion of the methyl groups are particularly interesting.

We only investigated the in-plane modes. The experiment on LAM-D showed that the torsional modes of the methyl groups exist around 20 meV (Fig. 1). The band is rather broad probably because of the splitting into several and the frequency is rather high, which shows that the rotational motion of the methyl groups is highly hindered. Since a quasielastic component appeared above roughly 100 K, we investigated the feature in detail on LAM-40 (Fig. 2) and LAM-80ET (Fig. 3) spectrometers.

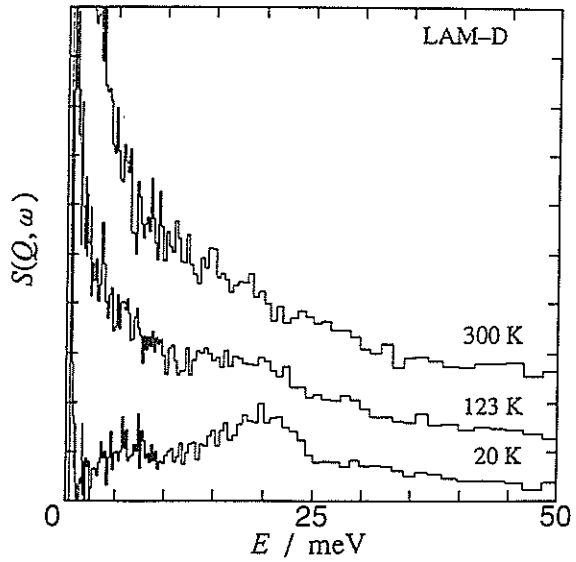

Fig. 1 Inelastic scattering obtained on LAM-D from the $C(SCH_3)_4$ monolayer adsorbed on Papyex.

The spectra favor the orientational disorder of the whole molecule and also the translational diffusion on the surface.

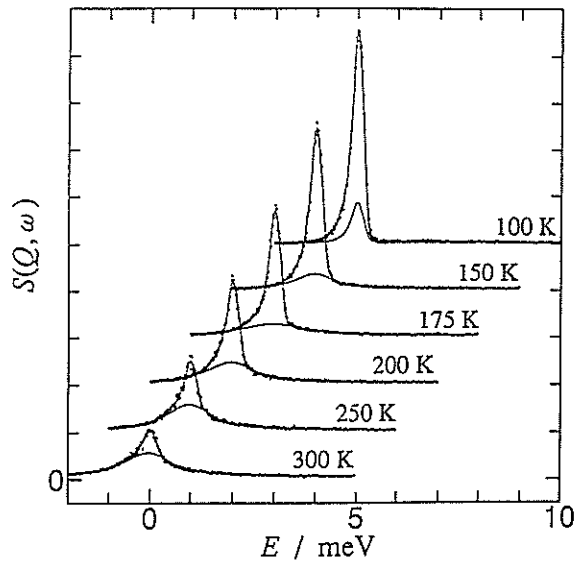

Fig. 2 Quasielastic scattering obtained on LAM-40 from the $C(SCH_3)_4$ monolayer adsorbed on Papyex.

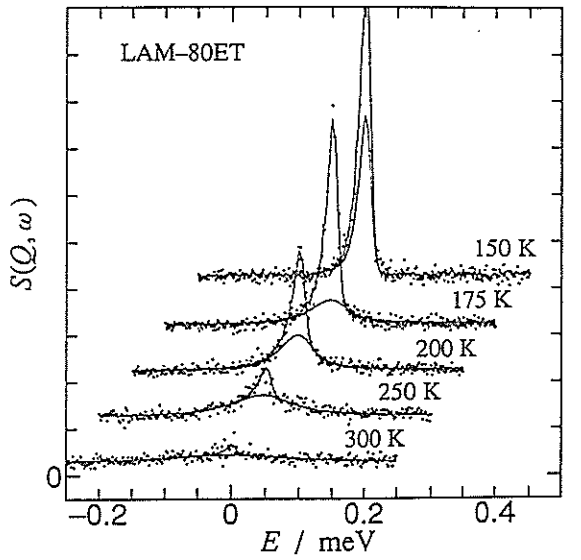

Fig. 3 Quasielastic scattering obtained on LAM-80ET from the $C(SCH_3)_4$ monolayer adsorbed on Papyex.

References

1) A. Inaba and S. Nakamura, unpublished work.

Phase Transition and Orientational Disorder of Neopentane Monolayer Adsorbed on Graphite

A. INABA

Department of Chemistry, Graduate School of Science, Osaka University, Toyonaka, Osaka 560

A globular molecule neopentane (tetramethyl methane) forms a two-dimensional solid at low temperatures on the surface of graphite. According to our heat capacity measurement,[1] the monolayer exhibits a 2-D solid-solid phase transition at 59 K.

The purpose of the present study was to investigate the dynamics of the neopentane monolayer by inelastic neutron scattering.

The spectrometer LAM-D was employed to obtain the spectra in the energy range up to 100 meV at 15 K (Fig. 1). Since the graphite specimen which we used (Papyex) has a preferred orientation, we saw some modes parallel to the surface (Q//). It should be noted that the spectrum in the range 20-60 meV was almost exactly the same as in the bulk solid, which shows that the molecules on the surface are not affected by the surface field at least in those intramolecular modes.

The spectrometers LAM-40 and LAM-80ET were employed to investigate molecular motions in the monolayer, particularly in its high-temperature 2-D solid phase, where the molecules are supposed to be orientationally disordered. In fact, we observed an appearance of a beautiful quasielastic contribution (Figs. 2 and 3) depending upon the temperature. The orientation of the whole molecule is disordered in the high-temperature 2-D phase. It is also interesting to know whether the disorder is anisotropic, appreciating the surface field. However, any discernible effect was not obtained in its polarization, namely that the disorder would be rather isotropic.

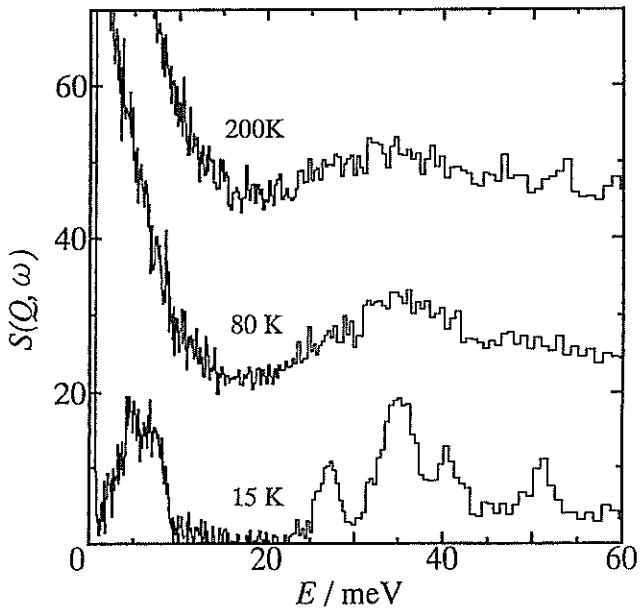

Fig. 1 Inelastic neutron scattering obtained on LAM-D from the neopentane monolayer adsorbed on Papyex.

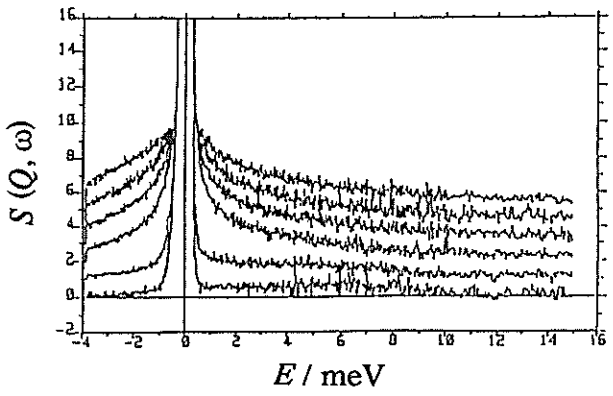

Fig. 2 Quasielastic scattering obtained on LAM-40 from the neopentane monolayer adsorbed on Papyex.

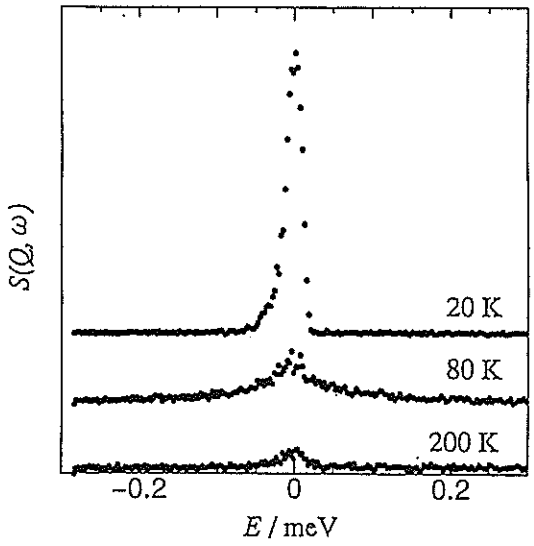

Fig. 3 Quasielastic scattering obtained on LAM-80ET from the neopentane monolayer adsorbed on Papyex.

References

1) A. Inaba, unpublished work.

Phase Transition and Orientational Disorder of Adamantane Monolayer Adsorbed on Graphite

A. INABA and S. NAKAMURA

Department of Chemistry, Graduate School of Science, Osaka University, Toyonaka, Osaka 560

A globular molecule adamantane forms a two-dimensional solid on the surface of graphite (Papyex). According to our calorimetric measurement,[1] the monolayer exhibits a 2-D solid-solid phase transition at 193 K. The structure of both phases has been determined by diffraction experiments[2] as well as by some potential calculation.

The purpose of the present study was to investigate the dynamics of the 2-D adamantane monolayer by neutron scattering.

We only saw the in-plane modes. The experiment on LAM-D showed a large quasielastic contribution appearing above 200 K. To investigate the detailed feature, we employed the spectrometers LAM-40 and LAM-80ET (Figs. 1 and 2). The results are summarized in an activation plot (Fig. 3). Those components can be accounted for by the rotational diffusion and the translational diffusion of the whole molecule on the surface.

In conclusion, neutron inelastic (and quasielastic) scattering experiments must be ideal to study the dynamics of those surface adsorbed monolayers which contain hydrogen atoms, even when the system is so diluted.

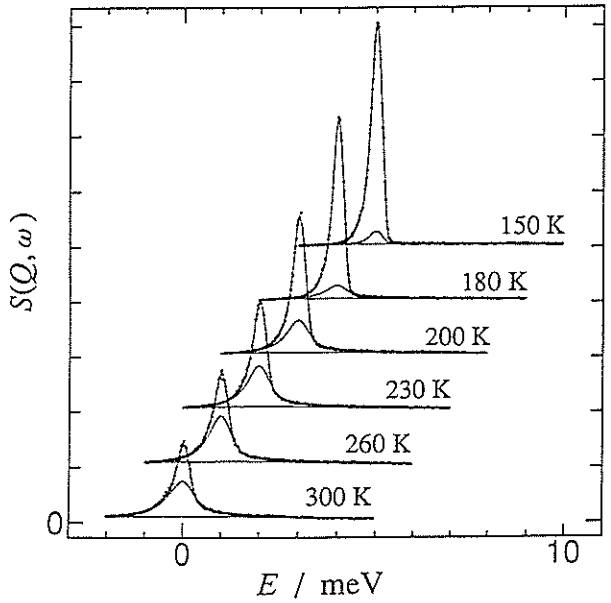

Fig. 1 Quasielastic scattering obtained on LAM-40 from the adamantane monolayer adsorbed on Papyex.

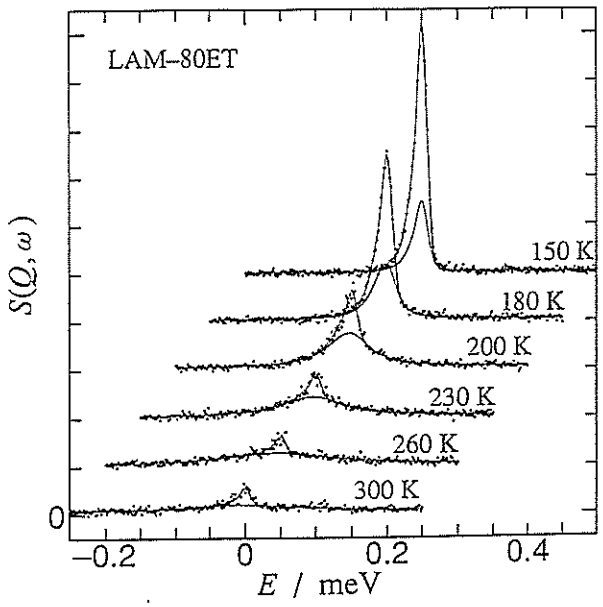

Fig. 2 Quasielastic scattering obtained on LAM-80ET from the adamantane monolayer adsorbed on Papyex.

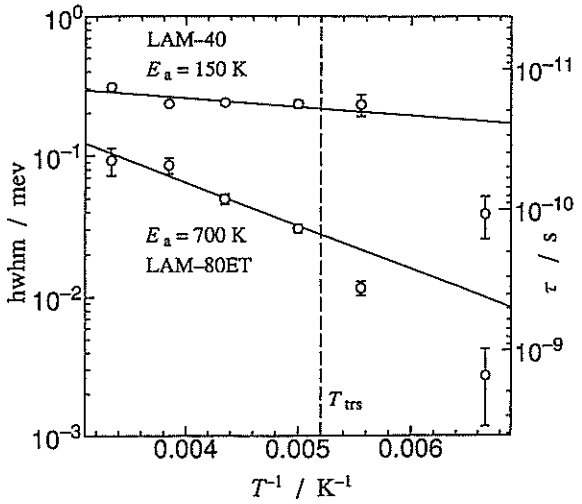

Fig. 3 An activation plot for the quasielastic contributions obtained on LAM-40 and LAM-80ET from the adamantane monolayer adsorbed on Papyex.

References

1) A. Inaba and S. Nakamura, unpublished work.

2) A. Inaba and S. Nakamura, KENS REPORT-XI (1997) in press.

Structure and Phase Transition of Adamantane Monolayer Adsorbed on Graphite

A. INABA and S. NAKAMURA

Department of Chemistry, Graduate School of Science, Osaka University, Toyonaka, Osaka 560

A globular molecule adamantane ($C_{10}H_{16}$) forms a 2-D solid on the surface of graphite. According to our heat capacity measurement,[1] the monolayer exhibits a 2-D solid-solid phase transition at 193 K. Because of the shape of the molecule, the mechanism of the phase transition is supposed to be an orientational order-disorder type.

The purpose of the present study was first to investigate the structure of both phases by neutron diffraction. Since we already did an X-ray diffraction experiment for this particular monolayer, the complementary information may enable us to determine the structure exactly. From it we could have some idea about the mechanism of the phase transition. As a matter of fact, the dynamical aspect is also important to study the mechanism, which we also report in this issue.[2]

We used the fully-deuterated adamantane (d-16) to reduce the incoherent background. The spectrometer VEGA was employed to obtain the diffraction patterns from the low-temperature phase (at 70 K) and from the high-temperature phase (at 300 K) (Fig. 1). The 90 degree detector bank was used to cover the longer d-spacing region, which is normally quite important to determine the lattice parameters of such monolayers. The graphite specimen that we used (Papyex) has a preferred orientation to show a saw-tooth shape profile of the Bragg peaks. This is exactly what we obtained in this 2-D solid. The lattice was found to be hexagonal in both phases. The 2-D space group for the low-temperature phase is $p3$. Since the symmetry is so high and the number of the 2-D Bragg peaks that we observed was so limited, we ought to have some calculation to determine the orientation of the whole molecules. We applied an atom-atom potential calculation. The final structure that we reached (Fig. 2) seems quite reasonable to explain all the diffraction data as well as the intermolecular contact.

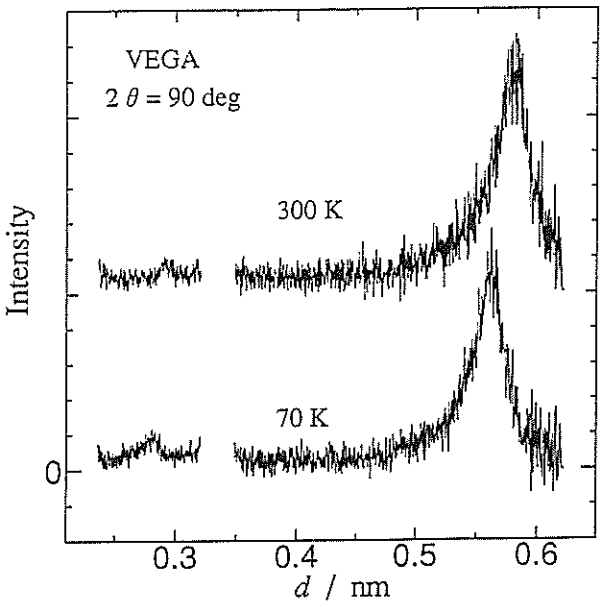

Fig. 1 Neutron diffraction patterns obtained for the adamantane (d-16) monolayer at 70 K (low-temperature phase) and at 300 K (high-temperature phase).

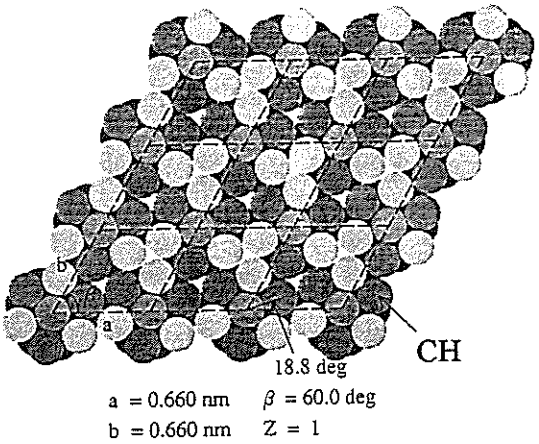

Fig. 2 The structure of the low-temperature phase of the adamantane monolayer.

For the high-temperature phase, we assumed some disorder to explain the transition entropy. We finally obtained the structure which is disordered in the orientation of the whole molecules. The 2-D space group was determined to be $6m$.

References

1) A. Inaba and S. Nakamura, unpublished work.
2) A. Inaba and S. Nakamura, KENS REPORT-XI (1997) in press.

Small Angle Neutron Scattering Study of N- and C-Terminal Fragments of Ovotransferrin

H. YAJIMA, H. YAMAMOTO, M. NAGAOKA, K. NAKAZATO*, T. ISHII, and N. NIIMURA**

Department of Applied Chemistry, Faculty of Science, Science University of Tokyo, 1-3 Kagurazaka, Shinjuku-ku, Tokyo 162
* PRESTO, JST, Photosynthesis Research Laboratory, The Institute of Physical and Chemical Research, Wako Saitama 351-01
**Advanced Science Research Center, Japan Atomic Energy Research Institute, Tokai, Naka-gun, Ibaraki 319-11

1. Introduction

Transferrins (Tfs) are a homologous family of iron-binding proteins, e.g., serum transferrin, lactoferrin, ovotransferrin, widely distributed in the animal kingdom[1]. Most of the members of the Tf family are monomeric glycoproteins with a molecular weight of about 80 kDa, each consisting of two major structural lobes (N- and C-lobe) and a short connecting part[2,3]. Each lobe is made up of a pair of domains containing a single high affinity metal-binding site in the interdomain cleft. In the cleft, the ferric iron is six coordinate (2 Tyr, 1 Asp, 1 His and 2 oxygens from a (bi)carbonate anion)[4], where a network of hydrogen bonds is formed between the anion and the amino acid residues of the Tf. The amino acid sequences of two lobes show considerably homology and the residues in the metal-binding sites are the same[4,5]. The two lobes are also capable of binding various metal ions such as Cu(II), Al(III), Tb(III), etc., besides Fe(III) with different binding affinities[6,7]. X-ray crystallographic and solution X-ray scattering studies have revealed that the Tfs undergo a conformational change upon metal binding due to the interdomain closure without changes in the secondary structure of the Tf[8]. The conformational change is reflected by a higher denaturation temperature[9] and increased resistance against proteases and disulfide-reducing reagents[10]. The closed conformation has been suggested as an important step in the receptor recognition. The physiological functions of the Tfs attract a lot of attention in connection with serious diseases from metal toxicities such as Alzheimer's disease, leukaemia, etc[11,12].

Numerous studies have suggested the physicochemical nonequivalence of the two lobes of the transferrins[1,13,14]. As for ovotransferrin (OTf), the C-lobe has 9 disulfide bridges whereas the N-lobe has 6[15]. In the kinetic study of Yamamura et al.[16], it was presented that on Fe(III), Al(III), and Cu(II) binding, the binding affinity of the metal is greater for the N-site, whereas lanthanide ions bound to the C-site more preferably. Further, the stability of the metal-OTf complex at the C-site was shown to be higher than that at the N-site. DSC studies of Lin et al.[9] for the isolated fragments corresponding to the N- and C-terminal half of OTf (OTf/2N, OTf/2C) have revealed that the denaturation temperature of either apo- or ferric OTf/2C is higher than that of each OTf/2N, and thus the C-lobe has been inferred to be thermodynamically stabler. Moreover, Sasaki et al.[17] have reported in a dynamic light scattering (DLS) study of OTf that the decrease in the diffusion constant with metal binding corresponding to the opened→closed conformational change is predominantly induced by metal binding to the C-site. It should be noted that from the small angle X-ray scattering (SAXS) studies of Grossman et al.[18], both interdomain clefts in the N- and C-lobes were characterized to be open before iron uptake and close when iron is incorporated into the binding site.

In order to rationalize the heterogeneity between the N- and C-lobes of OTf, we have scrutinized the internal structural characteristics of the OTf/2N and OTf/2C fragments with and without iron by means of small angle neutron scattering (SANS) with contrast variation method, using D_2O/H_2O solvents with various D_2O contents.

2. Experimental

Chicken OTf (99%) from Sigma Chemical Co. was used without further purification. The apo-OTf/2N (Ala1-Arg332) and apo-OTf/2C (Leu336-Lys686) fragments were prepared according to the procedures of Williams et al.[19] and Nakazato et al.[20], respectively. The amino acid sequences the OTf/2N and OTf/2C fragments were analyzed using a pulse-liquid sequencer (Applied Biosys-tem 477A). The N-terminal amino acid sequence of OTf/2C fragment was identified as Leu336-Thr-Pro-Ser-Pro-Arg-Glu-[21]. The molecular weights of the OTf/2N and OTf/2C

fragments were estimated to be 35kDa and 39kDa, respectively, by SDS-polyacrylamide gel electrophoresis, where each prepared fragment migrated as a single band. Apo-OTf/2N or apo-OTf/2C (40mg/mL) solutions for SANS measurements were prepared by dissolving the OTf/2N or OTf/2C fragment in 0.01M Tris-HCl buffer at pH8.0 containing 0.03 M $NaHCO_3$, using D_2O/H_2O solvents with different D_2O contents (ϕ_D= 0, 10, 60, 80, 90, 100 %). Then, each iron-saturated fragment solution was prepared by adding 20μL Fe-NTA complex ($7.25x10^{-2}$ M $Fe(NO_3)_2$ in $1.5x10^{-1}$ M nitrilotriacetic acid disodium salt) to 1mL of the apo-solution. For reference, the intact OTf solutions were prepared in the same way.

SANS measurements were made using *Thermal Neutron Small Angle Scattering Instrument* named WIT (in National Laboratory for High Energy Physics (KEK), Tsukuba, Japan) with the time-of-flight spectrometer, in the range of scattering vector $Q(=4\pi\sin(\theta/2)/\lambda)$ of 0.05 - 0.20 $Å^{-1}$ at room temperature. The analyses of the SANS data with contrast variation method were carried out following the same procedure as described in the previous report[22]. Then, the three structural characteristic-parameters, the radius of gyration of the solute at infinite contrast ($\bar{\rho} = \infty$), Rgc ; the radial second moment of the scattering density (SD) distribution, α ; the deviation of center of the SD distribution with the center of geometrical shape, β, were determined by the least-squares fitting of Stuhrmann plot[23].

3. Results and Discussion

Figures 1 and 2 show typical Guinier plots and Stuhrmann plots for the iron-loaded OTf/2N and OTf/2C fragments, respectively, where I(Q) refers to neutron scattering intensity at a Q. The ϕ_D values corresponding to the matching points ($\bar{\rho}$ = 0) for apo-OTf/2N, OTf/2C, and intact OTf were, respectively, 43.8, 42.7, and 42.4%, whereas for the iron-loaded molecules 41.4, 42.6, 42.1%. The determined structural parameters, Rgc, α, and β, are summarized in Table 1, including the diffusion coefficient (D) and hydrodynamic radius (R_h) determined by the DLS measurements, and ρ-parameter ($\rho=R\text{gc}/R_h$) dependent strongly on the structure of a molecule[24]. The Rgc value for each molecule coincided approximately with the Rg value from the SAXS measurements by Grossmann et al. The α value for OTf/2N with or without iron was larger than that for OTf/2C. This implies that the interior SD of OTf/2C is intrinsically greater than OTf/2N. However, the α value for each fragment was not affected by the interdomain closure induced by the iron binding. Furthermore, the β value for OTf/2N with or without iron was larger than that for OTf/2C. The structural distortion for OTf/2C is suggested to be smaller than OTf/2N. On the other hand, the R_h value for OTf/2C with or without iron was larger than that for OTf/2N. The change in the D or R_h value induced by iron binding for OTf/2C was greater than OTf/2N. This result conformed to the findings in the previous DLS studies[17] that the interdomain closure due to the iron-binding to the C-site brings about a significant increase (or decrease) in the D (or R_h) value of the intact OTf, but the iron-binding to the N-site does not appreciably give rise to it. As for molecular architecture, from the ρ value, it is presumed that the OTf/2C molecule with or without iron is harder than the OTf/2N molecule[24].

The foregoing results led us to the conclusion that the heterogeneity between the N- and C-lobes of OTf, in particular, the thermal and metal-binding stabilities of the C-lobe is ascribed to the more hardness and less distortion than those of the N-lobe.

References

1. J. H. Brock, in *Topics in Molecular and Structural Biology* (P. Harrison, ed.), Vol.7, pp.183-262, Verlag Chemie, Weinheim Basel, 1985.
2. B. F. Anderson, H. M. Baker, E. J. Dodson, G. E. Norris, S. V. Rumball, J. M. Waters, and E. N. Baker, *Proc. Natl. Acad. Sci. USA*, **84**, 1769-1772 (1987).
3. H. Kurokawa, B. Mikami, and M. Hirose, *J. Mol. Biol.*, **254**, 196-207 (1995).
4. E. N. Baker, *Perspect. Bioinorg. Chem.*, **2**, 161-205 (1993).
5. G. S. Baldwin, *Comp. Biochem. Physiol.*, **106B**, 203-218 (1993).
6. K. Ichimura, H. Kihara, T. Yamamura, and K. Satake, *J. Biochem.*, **106**, 50-54 (1989).
7. S. Welch, in *Transferrin : The Iron Carrier*, Chaps. 4 & 5, pp.61-127, CRC Press, 1992.
8. J. G. Grossmann, M. Neu, R. W. Evans, P. F. Lindley, H. Appel, and S. S. Hasnain, *J. Mol. Biol.*, **229**, 585-590 (1993).
9. L.-N. Lin, A. B. Mason, R. C. Woodworth, and J. F. Brandts, *Biochemistry*, **33**, 1881-1888 (1994).
10. H. Oe, N. Takahashi, E. Doi, and M. Hirose, *J. Biochem.*, **106**, 858-863 (1989).

11. S. J. McGregor and J. H. Brock, *Clin. Chem.*, **38**, 1883-1885 (1992).
12. S. Welch, in *Transferrin : The Iron Carrier*, Chap. 10, pp.253-275, CRC Press, 1992.
13. P. Aisen, A. Leibman, and J. Zweier, *J. Biol. Chem.*, **253**, 1930-1937 (1978).
14. K. Nakazato, T. Yamamura, and K. Satake, *J. Biochem.*, **103**, 823-828 (1988).
15. M. H. Metz-Boutigue, J. Jollès, J. Mazurier, F. Schoentgen, D. Legrand, G. Spik, J. Montreuil, and P. Jollès, *Eur. J. Biochem.*, **145**, 659-676 (1984).
16. T. Yamamura, K. Ichimura, T. Tsuda, A. Hayashi, T. Taniguchi, R. Toi, Y. Maeda, H. Kihara, and K. Satake, *Nippon Kagaku Kaishi* (in Japanese), 452-458 (1988).
17. N. Sasaki, H. Honda, H. Yajima, H. Momomi, K. Ichimura, K. Satake, and R. Endo, *ibid.*, 185-191 (1990).
18. J. G. Grossmann, M. Neu, E. Pantos, F. J. Schwab, R. W. Evans, E. Townes-Andrews, P. F. Lindley, H. Appel, W.-G. Thies, and S. S. Hasnain, *J. Mol. Biol.*, **225**, 811-819 (1992).
19. J. Williams and K. Moreton, *Biochem. J.*, **251**, 849-855 (1988).
20. K. Nakazato, I. Enami, Y. Tanaka, Y. Uchiyama, A. Tsugita, and K. Satake, *Biosci. Biotech. Biochem.*, **56**, 687-688 (1992).
21. J. Williams, T. C. Elleman, I. B. Kingston, A. G. Wilkins, and K. A. Kuhn, *Eur. J. Biochem.*, **122**, 297-303 (1982).
22. H. Yajima, M. Nagaoka, Y. Tezuka, T. Ishii, and N. Niimura, *KENS Rep.*, **10**, 150-152 (1995).
23. V. Luzzati, A. Tardieu, L. Mateu, and H. B. Stuhrmann, *J. Mol. Biol.*, **101**, 115-127.
24. W. Burchard, *Adv. Polym. Sci.*, **48**, 1-124 (1983).

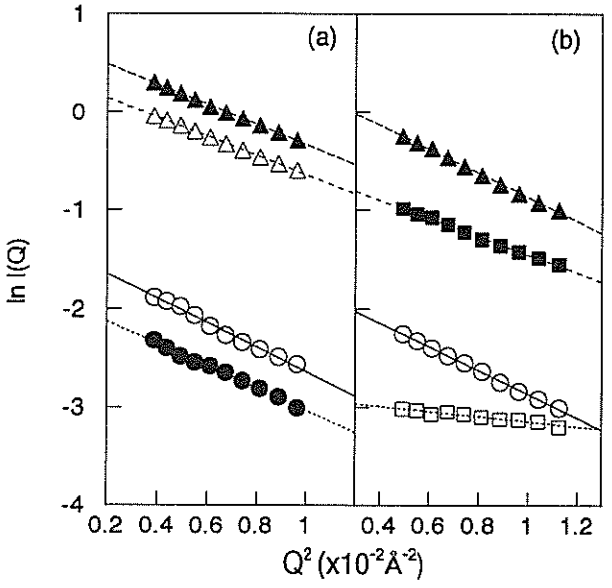

Fig.1 Guinier plots for the iron-loaded OTf/2N (a) and OTf/2C (b) fragments at ϕ_D (volume %) : ○, 0 ; ●, 10 ; □, 60 ; ■, 80 ; △, 90 ; ▲, 100.

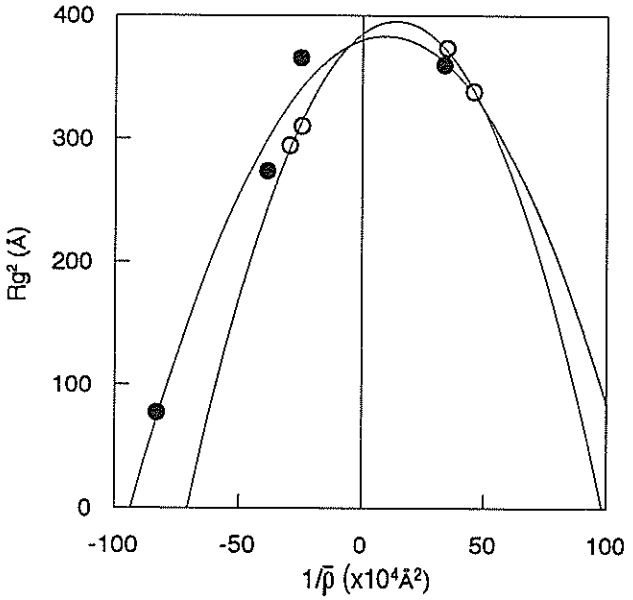

Fig.2 Stuhrmann plots for the iron-loaded OTf/2N (○) and OTf/2C fragments (●).

Table 1. Determined structural parameters, Rgc, α, and β from SANS measurements, D and R_h† from DLS measurements at 25°C, and the ρ (=Rgc / R_h) parameter

Sample	R_{gc} (Å)	ΔR_{gc} (Å)	α x 10^4	β x 10^{10} (Å^{-2})	D x 10^{-6} (cm^{2}s^{-1})	R_h (Å)	ΔR_h (Å)	ρ
apo-OTf/2N	21.4	-1.8	1.6	9.3	0.97	24.8	-1.2	0.86
Fe-OTf/2N	19.6		1.5	5.5	1.02	23.6		0.83
apo-OTf/2C	21.2	-1.5	0.7	6.8	0.83	29.1	-3.7	0.73
Fe-OTf/2C	19.4		0.7	3.4	0.95	25.4		0.76
apo-OTf	30.3	-1.0	1.9	3.1	0.61	40.2	-3.3	0.75
Fe$_2$-OTf	29.3		1.9	3.7	0.67	36.9		0.79

† R_h was calculated from the Stokes-Einstein equation, $R_h = k_B T/6\pi\eta_S D$, where k_B, T, and η_S are Boltzmann constant, the absolute temperature, and the viscosity of the solvent, respectively.

Changes in Protein Dynamics upon Folding

M. KATAOKA, H. KAMIKUBO, F. TOKUNAGA, T. KANAYA* and Y. IZUMI#

Department of Earth and Space Science, Graduate School of Science, Osaka University, Toyonaka, 560
** Institute for Chemical Research, Kyoto University, Uji, Kyoto 611*
 # Macromolecular Research Laboratory, Faculty of Engineering, Yamagata University, Yonezawa, 992

Proteins play crucial roles in substantially all vital phenomena. To understand the molecular basis of life, it is inevitable to understand the principles how proteins function and how proteins fold. A protein synthesized in a cell as a polypeptide with a definite amino acid sequence which is given by the instruction describing in gene, DNA base sequence. The nascent polypeptide takes its unique tertiary structure spontaneously to be a functional protein. The unique tertiary structure is required to express the specific function. Therefore, it is impossible to understand the complete information written in DNA sequences, the essential design principles of proteins, without the knowledge how a primary structure dictates a unique tertiary structure.

The elucidation of the tertiary structures of proteins at atomic resolution should be the first step. In this decade, the number of proteins whose tertiary structures have been solved to an atomic resolution is increasing steeply. By the recent progresses in both X-ray crystallography and NMR solution structure analysis, we can expect that the structures of any protein which we are interested in will be solved in near future. The tertiary structure solved in these studies are essentially static, even though we can guess flexibility of proteins by the temperature factors. The next step, therefore, should be elucidation of dynamics and energetics of proteins based on their tertiary structure. The recent theoretical studies on protein dynamics such as molecular dynamics simulation and normal mode analysis lead to the conclusion that low-energy collective modes are important for functions of proteins. Neutron inelastic scattering would be the most effective way to investigate protein dynamics over wide energy range. Some pioneer works with the use of this method exemplify its effectiveness and suggest the importance of low frequency modes. We raise the question whether there are vibrational modes specific to the folded state. If some low frequency collective modes would be important for the function, such modes would be specific to the folded protein. To answer the question, we have attempted to compare vibrational modes over wide energy range between the folded tertiary structure and the intermediate state (molten globule), using Staphylococcal nuclease (SNase).

The tertiary structures determined by X-ray crystallography or NMR solution structure analysis are the final destination of folding process. On the other hand, we have little structural information on the initial or the intermediate states of folding. To identify the folding intermediates is necessary to determine the folding pathway. Recently, much interest has been focused on the molten globule as a common folding intermediate of globular proteins. Molten globules of some proteins are stabilized under low pH and high salt condition. Since the major contribution to inelastic neutron scattering from proteins comes from hydrogen, the measurements under different solvent conditions such as different pH or different concentration of denaturant will brings some difficulties in analyzing spectrum. We have revealed that the truncated SNase which lacks 13 amino acid residues from its C-terminus is in a compact denatured state under a physiological condition, while the whole SNase is in the folded and functional state under the same solvent condition. Further, the truncated SNase takes the folded conformation identical to the whole protein by addition of an inhibitor, pdTp. Therefore the truncated SNase is the most suitable specimen for the inelastic neutron scattering experiment. We cannot expect to crystallize nor to analyze structure by NMR such non-native states because these states would be ensemble of many conformations. However, from the theoretical view, the truncated SNase would be also a good model to simulate the unfolded state.

The truncated and the whole SNase were overproduced in *Escherichia coli* and purified with an ordinary protein purification method. Horse myoglobin was purchased from Sigma. The proteins were dissolved into D_2O buffer, and then lyophilized. The procedure was repeated at least twice to exchange all of the exchangeable H into D. Protein solutions in D_2O buffer or lyophilized powder were used as specimen. Quasi-elastic and inelastic neutron scattering spectra were recorded with LAM-40 and LAM-D

spectrometer. Using SNase, we observed some interesting results: there are differences in the density of states between the folded and the intermediate states, especially in low energy region; the folded SNase shows little quasi-elastic scattering even at room temperature; the folded SNase shows very small and broad low-energy excitation (boson peak) at 25K. The latter two observations are quite suprising and inconsistent with the expectation from the general concept believed so far. However, there are serious problems in the reproducibility of the data. No quasi-elastic and inelastic neutron scattering data have been reported for SNase.

In order to examine the performance and the quality of the data taken with LAM-40 spectrometer, we tried to compare the spectrum with that taken at ILL. Figure 1 shows quasi elastic and inelastic neutron scattering spectra taken with LAM-40 for myoglobin at some temperatures. The sample amount was 1g of myoglobin powder, and the data collection time was 16 hours. The data are essentially identical with the data taken at IN6, ILL, with 300mg myoglobin and 3-8 hours data collection (1). At 100K, there is a broad peak around 25 cm^{-1}, which is a similar peak known as the "boson peak" for amorphous materials, glasses or polymers. The origin of the peak is still unknown. No significant quasi-elastic scattering was observed, indicating that the dynamical properties of myoglobin at 100K is represented as "vibrational". Upon raising temperature, quasi elastic scattering appears, suggesting that myoglobin obtains some anharmonic motions. At 220K, quasi elastic scattering is already observed. Transition is occurred around 180K, which is known as glass transition of proteins.

The results were quite encouraging for us. If the experiments are carried out very carefully using a considerable amount of protein, the spectrum taken with LAM-40 will be satisfactory for the analysis even for protein samples. So far, we utilized 100mg of SNase powder as a specimen. It is turned out that the sample amount was extremely low to obtain data with a reasonable quality. To obtain a good quality data, we have introduced the high expression system. We are now planning to measure inelastic neutron scattering with 1g of SNase.

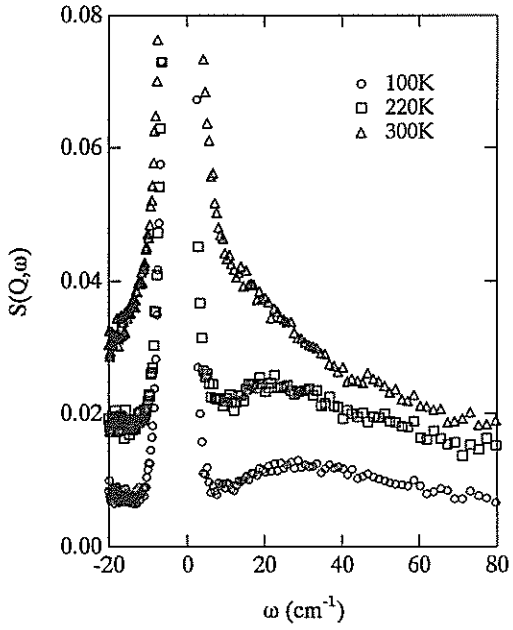

Figure 1. Inelastic neutron spectra for myoglobin powder taken at 100K, 220K and 300K.

REFERENCE

1. Cusack, S. & Doster, W. (1990) *Biophys. J.* **58**, 243-251.

The structure and physical property of water-soluble carboxymethyl alanyl disulfide keratins and its gelation.

Y. Miyauchi, S. Naito, S.Shimizu*, K.Kurita* and M.Furusaka**

Biological Research Laboratory, Kao Co.,2606 Akabane,Ichikai,Haga,Tochigi 321-34
*Collage of Science and Technology,Nihon Univ.,1-8 Surugadai,Kanda,Tokyo 101
**National Laboratory for High Energy Physics, 1-1 Oho, Tsukuba-shi, Ibaraki 305

The aim of this study was to characterize the disordered regions containing many SS linkages in keratin fiber (Fig. 1).

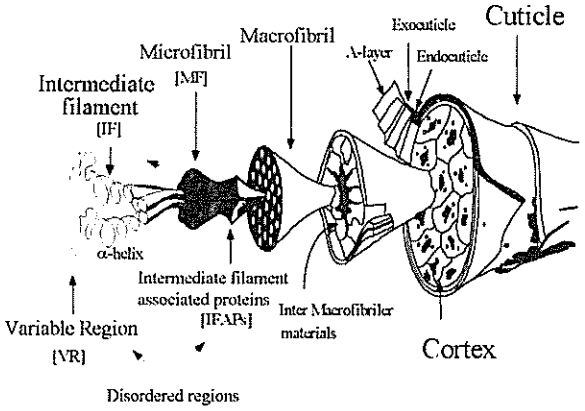

Fig. 1 Schematic Diagram of Hair Structure.
R.D.B. Fraser et al. Inter Report of CSIRO Division Of Protein Chemistry, Parkville, Australia(1981)

The high-order structure formed by non-helical regions of intermediate filaments (IFs) and intermediate filament associated proteins (IFAPs) were closely related to the static modulus of rigidity and the macroscopic shape of fiber. Especially, it has been proved that the configurational changes caused by the cleavage and reconstruction of hydrogen bonds in relative hydrophobic domain influenced on the anisotropy of the disordered structures by measurement with a small-angle x-ray and neutron scattering (SANS and WINK)[1)2)3)4)6)]. In this report, the reconstruction of IFs *in vitro* from the chemically modified and solubilized IF and the configurational changes were described.

Water soluble IF was provided by introducing carboxymethyl alanyl disulfide residue (CMAD,R-S-S-CH_2COOH) into keratin fibers, as shown Fig. 2[5)]. It was found that the gelation of CMAD solution took place upon heating at 100℃ for 1 hour. Small-angle neutron scattering measurements were carried out (WINK) to investigate the structural changes due to the gelation of CMAD solution[7)].

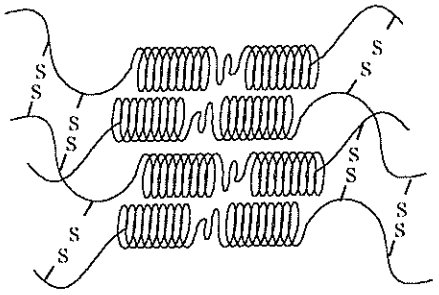

Protofibril(α-helix) and Veriable Region of Hair.

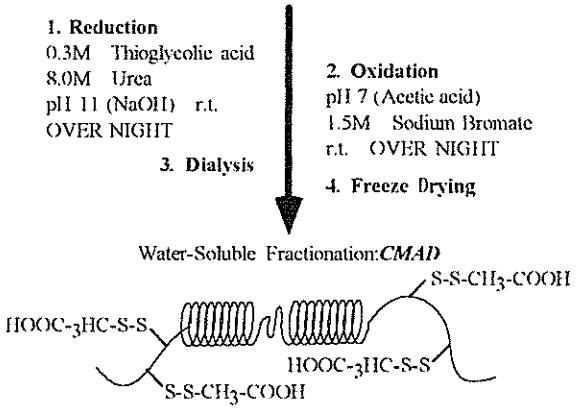

Fig.2:Preperation of *CMAD*

It was observed the dispersion which originated in heterogeneity with domain of q<1[1/nm] in case of CMAD gel and solution (Fig, 3). The dependence of

scattering intensity I(q) was about I(q) ~ q^{-2} with CMAD solution, and the segment density of the correlation function was Ornstein-Zernike block. On the other hand, the extensive decrease of the scattered intensities in the small angle ranges (q>0.03) was observed in CMAD gel. The scattered intensity was inversely proportional to the 4th power of momentum transfer q.

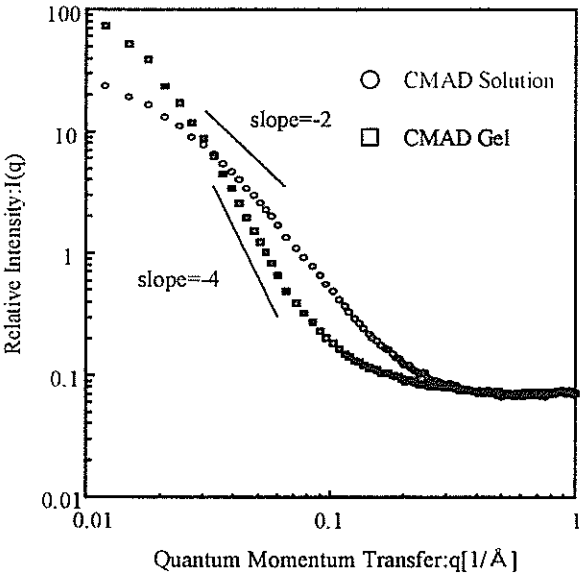

Fig.3 Small Angle Neutron Scattering Analysis of CMAD solution and gel.

This relation was typical Porod's law and suggested that highly segmented density domain-like structures, in which D_2O could not permeate, were produced by the gelation. This relation was also observed by the small angle x-ray scattering from the CMAD gel. Molecular weight of IF is approximately 50000, and IF has crystal and variable regions (70% a-helix, 30% α-amino and β-carboxy terminal, respectively.). There is a lot of hydrophobic amino-acids in the crystal region and 70 % of total cysteine exists in the variable regions. IFs are linked by the intermolecular SS bonds. It has been confirmed previously that the gelation of CMAD solution was caused by the partial reproduction of SS linkages between IFs. Therefore, these results suggest that the gelation of the CMAD solution caused by the formation of hydrophobic domains results when intermolecular SS bonds are produced between the hydrophilic variable regions of CMAD proteins by the heating. It can be considered that the gelation is a good model of IFs formation *in vitro*. As for a physical function of IFAPs in the disordered region, we will study from a point of view as a filler in the fibrous network in future.

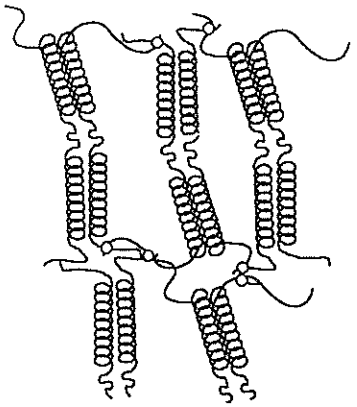

Fig.4: Model of CMAD gel.

References.

1) S. Naito, and K. Arai, *Appl. Polym. Sci.*, **61**, 2113(1996).
2) T. Ichimura, H. Tanamachi, S. Naito and K. Kurita, Polymer Preprints, Japan vol. 42, No. 4, 1460(1993)
3) T. Ichimura, S. Naito and K. Kurita, Polymer Preprints, Japan vol. 43, No. 10, 3663(1994)
4) S. Naito, T. Ichimura, S. Shimizu, K. Kurita and M. Furusaka, Polymer Preprints, Japan vol. 43, No. 10, 3665(1994)
5) M. Yoneyama, T. Kawada, K. Arai, and S. Naito, *Proc. 9th. Inter. Wool Text.. Res. Conf.* II, 450(1995)
6) S. Naito, *Structure of Keratin Fibers and Its Relation to Chemical and Physical Properties*, (1995)
7) Y. Miyauchi, T. Ichimura, S. Naito and K. Kurita, Polymer Preprints, Japan vol. 43, No. 3, 354(1996)

Phase Separation and Ordering in Ni-13at.%Al and Ni-17at.%Ga Alloys

M. OSAWA, M. FURUSAKA, T. HIRANO**, H. ASANO and S. SHIMIZU****

Institute of Materials Science, Univ. of Tsukuba, 1-1-1 Tennoudai, Tsukuba-shi, Ibaraki 305
** National Laboratory for High Energy Physics, 1-1 Oho, Tsukuba-shi, Ibaraki 305*
*** National Research Institute for Metals, 1-2-1 Sengen, Tsukuba-shi, Ibaraki 305*
**** College of Science and Technology, Nihon Univ., 1-8 Kanda Surugadai, Chiyoda-ku, Tokyo 101*

Introduction

Ni-based superalloys are important materials for industrial application, especially for the use under high temperature. A number of studies concentrating upon the mechanisms of phase separation processes with ordering on these alloys have been performed by small-angle scattering of X-rays[1] and neutrons, X-ray diffraction[1], transmission electron microscopy[2], AP-FIM[3], computer simulation[4] etc. However simultaneous quantitative measurements of chemical fluctuation change and ordering have not been performed. For the purpose, we performed high temperature in-situ measurements of small-angle neutron scattering and neutron diffraction for single crystals of Ni-based superalloys.

Experimental

Ni-13at.%Al and Ni-17at.%Ga single crystals were grown by the floating-zone method. The samples were homogenized at 1200℃ in vacuum and quenched into salted iced water. The high temperature in-situ neutron scattering measurements were performed at 500℃ for Ni-13at.%Al and 450℃ for Ni-17at.%Ga under vacuum on the small/medium-angle neutron diffractometer Wink.

Results and Discussion

Small-angle scattering gives us information of phase separation, while 011 superlattice reflection represents information about ordering. We compared the small-angle scattering and the 011 superlattice reflection for Ni-13at.%Al in Fig. 1. In this figure, for 011 superlattice reflection, q represents the difference of momentum transfer from bragg position. At the same time, to compare

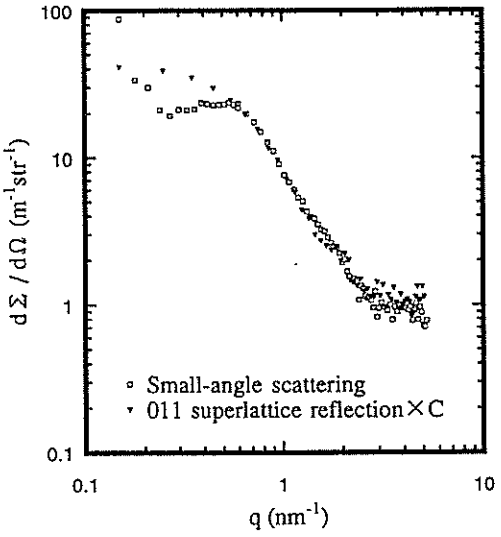

Fig.1 Small-angle scattering and 011 superlattice reflection from Ni-13at.%Al sample aged for 19h15min

these two diffractions the 011 superlattice reflection intensity was multiplied by some constant. These two diffractions show good

agreement in the range $q > 0.7\ nm^{-1}$, which tells us that the precipitates are ordered. On the other hand, these two diffractions did not agree each other in the range $q < 0.7\ nm^{-1}$. This difference is originated in the interference term of the two kinds of diffractions. Intensity of the small-angle scattering is given as

$$I(q) = n_p F_p(q)(1 + \frac{1}{n_p} \sum_i \sum_j e^{iq(R_j - R_i)}), \qquad (1)$$

while intensity of the superlattice reflection is given as

$$I(q) = n_o F_O(q)(1 + \frac{1}{n_o} \sum_{L=1}^{4} (-1)^{L+1} P(L) \sum_{\delta ij = L} e^{iq(R_j - R_i)}), \qquad (2)$$

here n_p represents number density of precipitates, n_o number density of ordered regions, $F_p(q)$ mean form factor of precipitates, $F_o(q)$ mean form factor of ordered regions and P(L) probability that an ordered region belongs to the L-th kind of ordered region[5]. There are four kinds of sublattices in the $L1_2$ structure; the first sum of the second notation should be taken over all kinds of sublattices, and the second and third sums should be taken over all precipitates which belongs to L-th sublattice. In the case of 011 superlattice reflection, if ordered regions have random phase relation the interference term in eq.(2) becomes 1 independent of q. On the other hand, in eq.(1), the interference term becomes apparent in small q range. Now the disagreement in the range $q < 0.7\ nm^{-1}$ is originated in the random phase relation between each ordered regions.

To extract information of chemical fluctuation and ordering, mean radius of the precipitate was obtained from the Guinie-plot. The Al concentrations in precipitate and in matrix were calculated from mean radius of precipitate and absolute intensity of small-angle scattering. Together with absolute 011 superlattice reflection intensity, we could also obtained order parameter η defined by the following equation

$$\eta = \frac{\text{(number of atoms in right position)}}{\text{(total number of atoms)}} - \frac{\text{(number of atoms in wrong position)}}{\text{(total number of atoms)}}.$$

In completely ordered state of stoichiometric Ni_3Al and Ni_3Ga, the order parameter becomes 1.

The result shows that in the precipitate the Al concentration becomes 25at.% and η becomes 1. Time evolution of these calculated results shows that the observed phenomenon was coarsening stage of precipitate with the equilibrium chemical concentration and equilibrium order parameter, and total volume fraction of the precipitates was preserved.

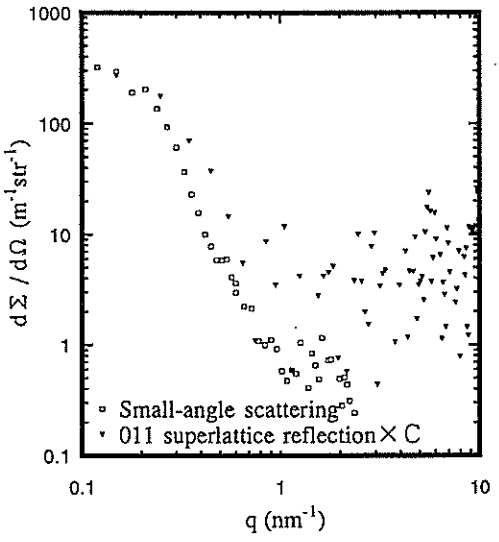

Fig.2 Small-angle scattering and 011 superlattice reflection from Ni-17at.%Ga sample aged for 7h15min

The same plot for Ni-17at.%Ga is given in Fig. 2. In contrast with the case in Ni-13at.%Al, these two diffractions don't agree in all q range, which means that the average size and shape of

the precipitates differs from that of ordered regions. Mean radius of the precipitates obtained from the Guinie-plot shows that the mean precipitate size of Ga-rich regions was larger than that of ordered regions. Calculated chemical concentrations in precipitate and matrix reached the equilibrium value as well.

Time evolution of the results for Ni-17at.%Ga represents that the observed phenomenon was coarsening stage of precipitate which has equilibrium chemical concentration, and the total volume fraction of the precipitates was preserved. In contrast with the case in Ni-13at.%Al, however, order parameter of the precipitate in this sample can't be determined without some assumption. Therefore we examined two models A and B defined as follows, and calculated order parameters for these cases. They are, i) a precipitate contains a few ordered regions which have different phases (model A), and ii) a precipitate contains an ordered region which is smaller than the precipitate (model B).

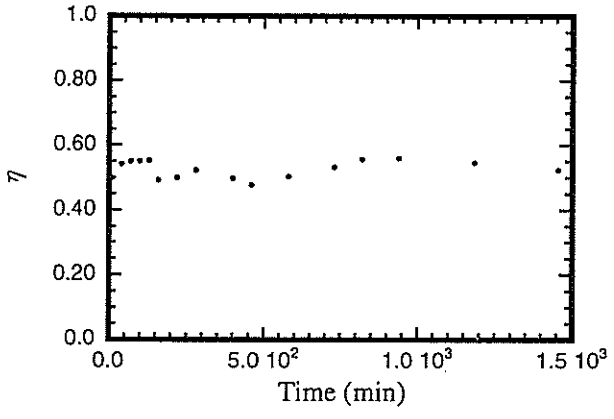

Fig.3 Time dependence of η on Ni-17at.%Ga (model A)

In the case of model A the calculated η stayed around 0.6 as shown in Fig. 3. While in the case of model B the calculated order parameter gradually goes up to 1 as shown in Fig. 4.

The Ni-Ga system has a wider concentration region of the $L1_2$ structure in phase diagram than the Ni-Al system. This fact suggests that Ni_3Ga has lower ordering energy than Ni_3Al. Furthermore lattice constant of ordered Ni_3Ga is longer than that of disordered Ni_3Ga[6]. In contrast, the ordered Ni_3Al has shorter lattice constant than the disordered one[6]. Therefore in the Ni_3Ga case, elastic misfit between matrix and precipitate seems to be moderated by lowering the order parameter. These consideration seems to be consistent with the model B.

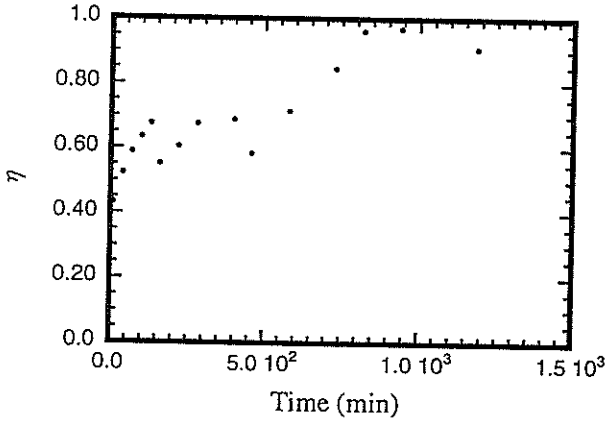

Fig.4 Time dependence of η on Ni-17at.%Ga (model B)

Conclusion

We carried out high temperature in-situ neutron-scattering study of single-crystals Ni-13at.%Al and Ni-17at.%Ga, and obtained both macroscopic scattering cross-section for small-angle scattering and 011 superlattice reflection in absolute scale. The absolute measurements enable us to calculate size, chemical concentration and order parameter of precipitate.

In the Ni-13at.%Al case, the precipitate and the matrix rapidly reached to the equilibrium chemical concentration and to the equilibrium

ordering state, i.e. $L1_2$ structure. The process observed here can be regarded as coarsening stage of these precipitates.

In the Ni-17at.%Ga case, the precipitate and the matrix reached to the equilibrium chemical concentration rapidly. Concerning the ordering phenomenon, we assumed two models represented above. We suppose that the model B, namely there is only one ordered region smaller than the precipitate, is more plausible, but no definite conclusions can be obtained at present. We are planning to determine which model is valid by using some other methods such as electron microscopy.

References

1) M. Yu and H. Chen: "The Second Workshop on Phase Separation with Ordering" (1992) 13.
2) H. Yoshida, M. Arita, A. Cerri and G. Kostorz: Acta Metall. **34** (1986) 1401.
3) H. Wendt and P. Haasen: Acta Metall. **31** (1983) 1649.
4) C.G. Windsor, R.M. Barron and J.R. Russell: "Dynamics of Ordering Processes in Condensed Matter" ed. S. Komura and H. Furukawa, Plenum, (1988) 127.
5) H. Okuda: private communication.
6) M. Ellner: J. Less-Common Metals **60** (1978) P15.

Change of Modulated Structure during Spinodal Decomposition in Fe-Cr Alloys

T.UJIHARA, H.OKUDA and K.OSAMURA

Department of Materials Science and Engineering, Kyoto University, Sakyo-ku, Kyoto, 606-01

It is generally believed that the phase decomposition from supersaturated solid solution may be initiated by the alternative mechanisms of nucleation-growth and spinodal decomposition. Fe-Cr alloys have been reported that the spinodal decomposition takes place during annealing within miscibility gap after quenching. The spinodal theory has been developed by many researchers[1-6]. Most of models are based on the Cahn's diffusion equation[7],

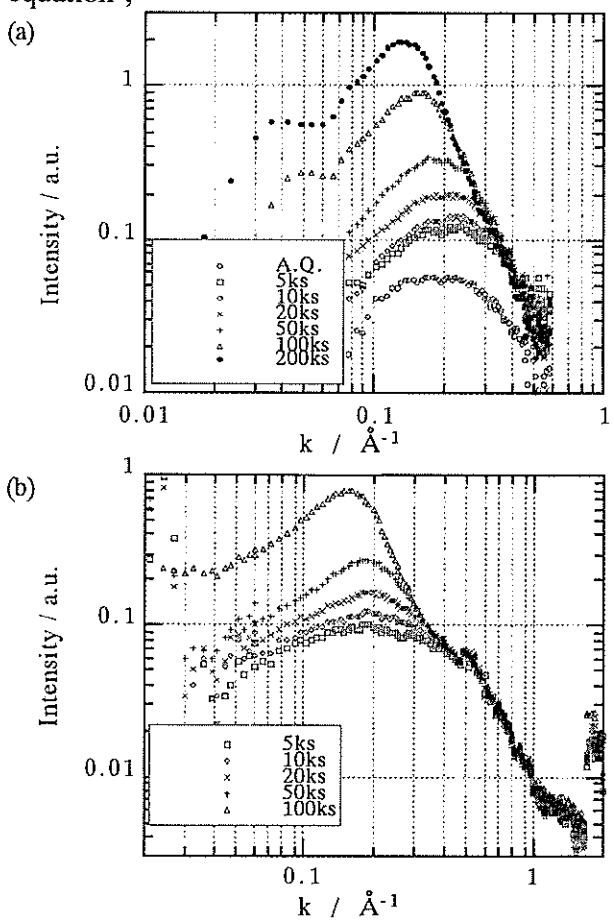

Fig. 1: Change of SANS intensities as a function of scattering vector for Fe-30at%Cr alloys aged at 773K measured by (a) SAN and (b) WINK.

$$\frac{\partial c(\mathbf{r},t)}{\partial t} = -\mathrm{div}\left(-M\,\mathrm{grad}\frac{\delta F}{\delta c}\right) \qquad (1)$$

where c is the composition at the position r, M is the mobility, F is Helmholtz's free energy

$$F = \int_V \left[f_0 + \kappa(\nabla c)^2 \right] dV \qquad (2)$$

where f_0 is the free energy density of homogeneous material of average composition and κ is the gradient coefficient. Further, the models are modified in consideration of non-linear term and called "non-linear continuum model". As distinct from the models, Binder expressed the spinodal decomposition in terms of cluster reactions explained by transition probability of clusters, that is, the master equation,

$$\frac{\partial n_l(t)}{\partial t} = \sum_{l'=1}^{\infty} S_{l+l',l'} n_{l+l'}(t) - \frac{1}{2}\sum_{l'=1}^{l-1} S_{l,l'} n_l(t) + \frac{1}{2}\sum_{l'=1}^{l-1} c_{l-l',l'} n_l(t) n_{l-l'}(t) - \sum_{l'=1}^{\infty} c_{l,l'} n_l(t) n_{l'}(t) \qquad (3)$$

where S and c are transition probabilities. (ref.[8] in detail). This model is called "cluster model".

In this study, mechanism of structure modulation during spinodal decomposition was evaluated via the analysis of small angle neutron scattering intensities.

Alloys with composition Fe-30at%Cr were used for present study. Small angle neutron scattering (SANS) experiments were carried out using SAN and WINK, which are installed in the KENS. In laboratory the specimens were solution treated at 1273K for 12 hours, quenched into water and then aged at 773 K for various times from 5ks to 200ks. After this treatments, we carried out the static SANS measurements.

Fig.1 shows the changes of SANS intensities measured by SAN and WINK. In the previous

paper we reported a part of the results, as follows. The mechanism of structural change was divided into two stages and explained by Cahn's linear theory in the first stage and by Binder's theory (BS theory) in the second stage. We suggested that the transition of the mechanism occurred after forming the interfaces.

In the present report, we calculated correlation functions from experimental scattering intensities to investigate the mechanism of decomposition further in the case of Fe-30%Cr. Fig.2 shows the changes of correlation functions $G(r)$ divided by $G(0)$ during isothermal aging at 773K. Because of the error of experimental scattering intensity in the high scattering vector range, the values $G(r)$ in the range of r<15Å are not quantitative. Two arrows in the Fig.2 show two maxima. Fig.3(a) shows time dependence of peak positions and reciprocal number of wave number k_m at maximum intensities from Fig.1(a). Peak positions are corresponding to the wave length of composition fluctuation. First peak position r_1 slightly changes for the early stage. Behavior of second peak is same as that of first peak. At the aging time 50ks, the first peak position shifts to higher r and the value of $G(r)$ decreases radically. At the aging time 100ks, the first peak moves to r~50Å and overlaps the second peak. At 200ks, the value of $G(r)$ increases. Fig.3(b) shows the changes of peak positions scaled by Guinier radius R_G. The first peak is roughly constant for the whole time range.

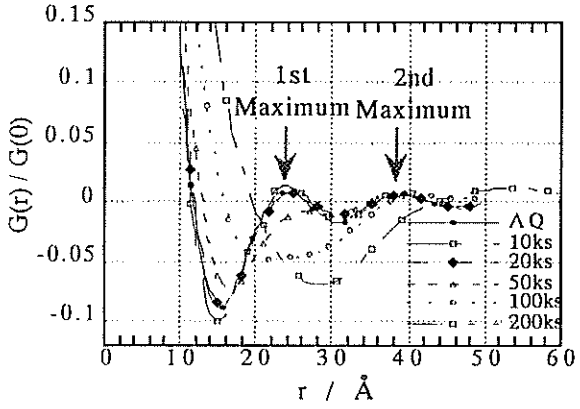

Fig.2: Change of correlation functions $G(r)$ divided by $G(0)$ from SANS intensities for Fe-30at%Cr alloys aged at 773K.

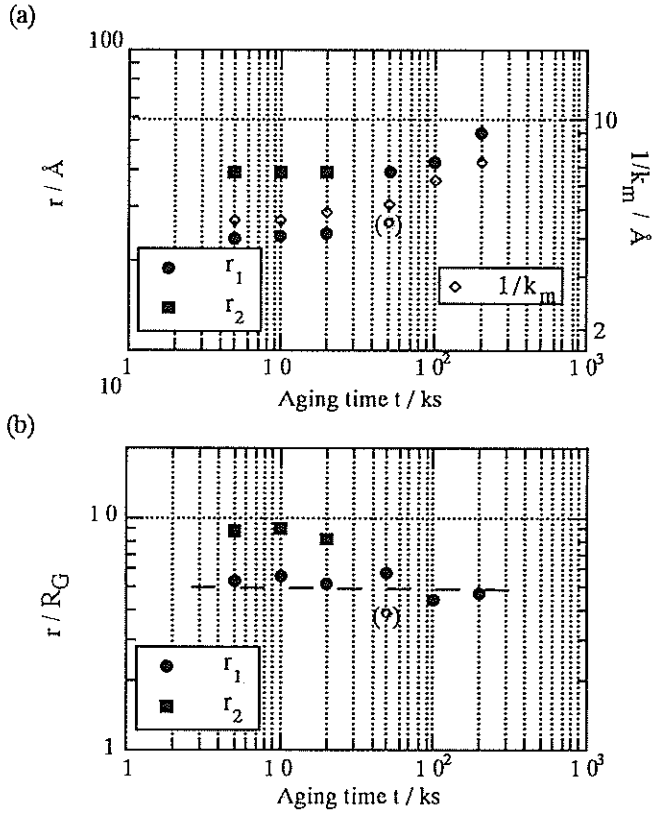

Fig.3: Change of (a) peak positions (r_1: the first peak, r_2 :the second peak), reciprocal number of wave number k_m at maximum scattering intensity and (b) the peaks divided by Guinier Radius R_G as a function of aging time.

In the Cahn's theory, the wave length of composition fluctuation does not change, but the amplitude increases during spinodal decomposition. The change of maxima of correlation function for early stage is explained by Cahn's theory. On the other hand, for the late stage, the radical movement of the first peak suggests that amplitude of fluctuation of which wave length are smaller decreases. And first peak position scaled by R_G is constant, and the rate of change of the peak position is similar to of reciprocal number of k_m. Therefore, concentration fluctuation changes keeping dynamically scaling.

References
[1]J. W. Cahn, Acta Metall. **9**, 795 (1961)
[2]M. Hillert, Acta Metall. **9**, 525 (1961)
[3]H. Cook, D. de Fontaine, and J. E. Hilliard, Acta Metall. **17**, 765 (1969)
[4]J. S. Langer, M. Bar-on, and H. Miller, Phys. Rev. **A 11**, 1417 (1975)
[5]K. Binder, C. Billotet, and P. Mirold, Z. Phys. **B 30**, 183 (1978)
[6]T. Tsakalalos, Ph.D.thesis, Northwestern University, 1977
[7]J. W. Cahn and J. E. Hilliard, J. Chem. Phys., **28**, 258 (1958)
[8]K. Binder and D. Stauffer, Phys. Rev. Lett., **33**, 1006 (1974)

Small-Angle Neutron Scattering Study of Bis(quaternary ammonium bromide) Surfactant Micelles in Water. Effect of the Spacer Chain Length on Micellar Structure.

HIROHITO HIRATA, NORIKATSU HATTORI, MAKOTO ISHIDA, HIROFUMI OKABAYASHI,
MICHIHIRO FURUSAKA* and RAOUL ZANA**

Department of Applied Chemistry, Nagoya Institute of Technology, Gokiso-cho,
Showa-ku, Nagoya 466, Japan
*BSF, National Laboratory for High Energy Physics, 1-1 Oho, Tsukuba-shi, Ibaraki 305, Japan
**Institut Charles Sadron (CRM-EAHP), CNRS-ULP, and GDR " Nouveaux Matériaux Tensioactifs ",
CNRS, 6, rue Boussingault, 67083 Strasbourg Cedex, France

Considerable attention has been given to the solution behavior of bis (quaternary ammonium bromide) surfactants [1, 2] of general formula

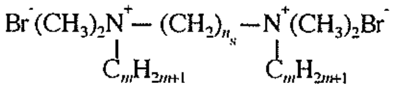

$$\mathrm{Br^-(CH_3)_2}\underset{\substack{|\\ \mathrm{C}_m\mathrm{H}_{2m+1}}}{\mathrm{N^+}}-(\mathrm{CH_2})_{n_s}-\underset{\substack{|\\ \mathrm{C}_m\mathrm{H}_{2m+1}}}{\mathrm{N^+}}\mathrm{(CH_3)_2Br^-}$$

$n_S = 2, 3, 4$ and 6

in which two alkyldimethylammonium bromide moieties are connected by a polymethylene chain, referred to as a spacer. These dimeric surfactants continue to attract interest, because of their potent bactericidal activity and peculiar solution behavior.[3]

In the present study, for the dimeric surfactants with $m = 10$ and $n_s = 2$, 3, 4 and 6, the effect of the spacer chain length on the aggregation number and micellar shape in water is discussed in detail, using small angle neutron scattering (SANS) spectra.

The microstructure of n-alkyltrimethylammonium bromide micelles (so-called C_nTAB) has already been investigated in detail by Berr et al.,[5, 6] using SANS spectra. As the bis (quaternary ammonium bromide) surfactants can be considered as " dimers " of the C_nTAB molecules, elucidation of the microstructures of C_nTAB micelles by SANS will provide useful data for analysis of the SANS spectra of dimeric surfactant micelles.

Synthesis of bis(quaternary ammoniumbromide) surfactants (DS, $m = 10$, $n_s = 2$, 3, 4, and 6) was shown in elsewhere.[1, 2] The small angle neutron scattering (SANS) measurements were carried out using the samall / medium-angle neutron diffractometer (WINK) installed at the pulsed neutron source KENS at the National Laboratory for High Energy Physics, Tsukuba, Japan. The sample solutions were placed in a quartz cell of 1 or 2 mm path length at 23 ℃.

In the present study, both prolate and oblate spheroid models for the DS micelles have been calculated by assuming mono-dispersity. It has been found that the prolate model provides consistently better fits to the observed SANS intensity data than does the oblate model. A structural model of the DS micelle, used in the calculation of the single particle form factor $P(Q)$, is based on the assumption of the result of the SANS analysis for n-alkyltrimethylammonium bromide micelles, made by Berr et al.[4, 5]

$S(Q)$ is calculated by use of the model proposed by Hayter and Penford.[6, 7] In this model, the micelle is assumed to be a rigid charged sphere of diameter σ,[8,9] interacting through a dimensionless screened Coulombic potential. The dimensionless screened Coulombic potential is calculated by using the inverse screening length of the Debye-Hückel theory, defined by the ionic strength of the solution.

The scattering intensity spectra observed for the DS micellar solutions ($m = 10$, $n_s = 2$) and the theoretically calculated results are shown in Fig. 1. The closeness of fit between the observed and calculated data is excellent. The observed intensity data were analyzed with the aggregation number ($\boldsymbol{n}$), degree of ionization (α) and the number of hydrated methylene groups (n_{wet}) as fitting parameters, and the $\boldsymbol{a}$, $\boldsymbol{b}$ and $\boldsymbol{t}$ values are calculated using n_{wet} and $\boldsymbol{n}$. The extracted parameter values are listed in Table 1.

From the result of caluculation, the aggregation number for the DS micellar solutions is found to depend upon the length of the spacer methylene chain (n_s). In fact, as the n_s value increases, the value of $\boldsymbol{n}$ tends to decrease. In particular, it should be noted that there exists a marked

difference in aggregation number between the two different spacers $(CH_2)_2$ and $(CH_2)_3$.

For a series of the DS micellar solutions, the n values increases with an increase in $(X - X_{CMC})^{1/2}$, where $(X - X_{CMC})^{1/2}$ is the square root of the mole fraction of the monomer concentration, and all the n values fall on a straight line, indicating that a ladder model of micellar growth can be applied to the micellar formation of DS cations.[10]

Extrapolation of the linear $(X - X_{CMC})^{1/2}$ vs. n plots provides the minimum aggregation number of a micelle at the CMC. When we compare the minimum aggregation numbers (n_0) for DS molecules (m =10 and n_s =2, 3, 4 and 6) with each other, the difference among the n_0 values seems to be very small, revealing that the aggregation number of a minimum micelle formed by the DS molecules with m = 10 at the CMC is not so dependent on the length of a spacer methylene chain. This may imply that the main hydrocarbon chain (n-decyl group) of the DS surfactants plays an important role in formation of a minimum micelle.

Moreover, it can be seen in Table 1 that the $(a+t)/(b+t)$ ratio of the prolate spherical micelles decreases as the concentration approaches the CMC. This result indicates that the shape of a DS micelle varies with an increase in micellar concentration. For a new-born micelle having a minimum aggregation number of $n_0 = 22 \sim 25$, the $(a+t)/(b+t)$ ratio is very close to 1.0, indicating that the minimum micelle may be spherical. Thus, we may assume that both i) micellar growth and ii) sphere to prolate shape variation occur with an increase in micellar concentration.

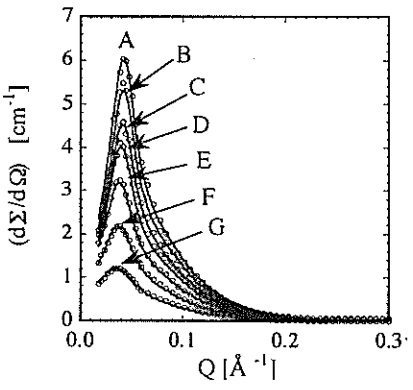

Fig. 1 Observed scattering intensity spectra (open circle) for the DS (m =10, n_s = 2)-D_2O system at 23 °C: (A) 4.0 wt%; (B) 3.5 wt%; (C) 3.0 wt%; (D) 2.5 wt%; (E) 2.0 wt%; (F) 1.5 wt%; (G) 1.0 wt%; (solid lines) fitting scattering intensity profiles. The average percentage deviation per data point was within ±4% for all spectra.

TABLE 1: Scattering Intensiity Spectra Obserbed for DS (m = 10, n_s = 2) Micellar Solutions (23°C) and Theoritically Calculated Results[a]

wt%	n	α	n_{cw}	a [Å]	b [Å]	t [Å]	$\frac{(a+t)}{(b+t)}$	N_S	κ [Å]	σ [Å]
1.0	85	0.24	3.3	59.5	11.5	9.7	3.26	24.8	20.5	70.8
1.5	105	0.22	3.5	74.8	11.2	9.9	4.01	24.3	19.7	78.9
2.0	123	0.19	3.5	87.6	11.2	9.9	4.62	23.3	19.2	85.4
2.5	135	0.16	3.7	97.9	11.0	10.1	5.12	23.7	19.0	90.5
3.0	140	0.12	4.2	107.6	10.3	10.5	5.70	25.8	19.2	94.7
3.5	156	0.12	4.2	118.2	10.3	10.5	6.19	25.3	18.7	100.4
4.0	170	0.11	4.5	132.4	9.9	11.2	6.81	26.3	18.6	100.6

[a] n : The average aggergation number of a micelle. α : The degree of ionization of a micelle.
In the present SANS analysis, it was assumed that the micellar solution is a one-component macrofuid and the finite size of the counter ion is ignored. Therefore, the α values listed in Table 1 is an apparent charge.[27] n_{cw} : The number of hydrated methylene groups in the Stern layer. a : The major axis of prolate micelle given by $a = (3\,n\,V_{tal}) / (4\pi b^2)$. b : The minor axis of a prolate micelle. t : The thickness of the Stern layer. ,N_S : The number of water molecules associated with a *DS* molecule. κ : The inverse Debye-Hückel screening length. σ: The macroion diameter.

We may conclude as follows. The aggregation number of the micelles strongly depends on the length of the spacer methylene chain. Moreover, the aggregation number of a minimum micelle has been found to be almost independent of the spacer chain length.

This report is a summary of The J. Phys. Chem., 99, 17778(1995).

References

1) Zana, R.; Benrraou, M.; Rueff, R. Langmuir 7, 1072(1991)
2) Alami, E.; Levy, H.; Zana, R.; Skoulios, A. Langmuir, 9, 940(1993)
4) Alami, E.; Beinert, G.; Marie, P.; Zana, R. Langmuir, 9, 1465(1993)
5) Berr, S. S.; Coleman, M. J.; Jones, R. R. M.; Johnson, J. S., Jr. J. Phys. Chem., 90, 6492(1986)
6) Berr, S. S. J. Phys. Chem., 91, 4760(1987)
7) Hayter, J. B.; Penfold, J. Mol Phys., 42, 109(1981)
8) Hansen, J.; Hayter, J. B. Mol Phys., 46, 651(1982)
9) Kotlarchyk, M.; Chen, S. H. J. Phys. Chem. 79, 2461(1983)
10) Chen, S. H.; Lin. T. L. Method of Experimental Physics, Vol 23 Part B; Academic: London; Chapt. 16(1987)
11) Missel, P. J.; Mazer, N.A.; Benedek, G. B.; Young, C. Y.; Carey, M. C. J. Phys. Chem., 84, 1044(1980)

SANS from semidilute solutions of Poly(N-isopropylacrylamide) in methanol-water mixture

K. OKANO*, S. SHIMIZU**, K. KURITA** and M. FURUSAKA***

*The University of Tokyo, Hongo, Bunkyo-ku, Tokyo 113
**College of Science and Technology, Nihon Univ., 1-8 Surugadai, Kanda, Tokyo 101
***Booster Synchrotron Utilization Facility, National Laboratory for High Energy Physics, Tsukuba 305

The aqueous solution of poly(N-isopropylacrylamide)(PNIPAM) has a lower critical temperature(LCST) at about 31°C. PNIPAM is also soluble such organic solvents as methyl alcohol, ethyl alcohol, tetrahydrofuran and dioxane which are capable of hydrogen bonding. In these solvents, however, PNIPAM does not show LCST up to their boiling point; they are regarded as good solvents from the results of viscometry. On the other hand, the addition of such an organic solvent to an aqueous solution of PNIPAM gives rise to a lowering of LCST. Thus, the addition of a good solvent results in a narrowing of the solubility range: a phenomenon referred to as cononsolvency[1]. In spite of many efforts[1] the mechanism of the cononsolvency is not yet clarified.

Towards the understanding of this phenomenon we have measured the small-angle neutron scattering(SANS) from semidilute solutions of PNIPAM in water and methanol-water mixture. From the concentration dependence of the correlation length obtained by the scattering experiment we evaluated the interaction parameters(binary and ternary cluster integrals of polymer segments). We then calculate the contributions of the segment-segment interaction to the entropy S_{int} and enthalpy H_{int} from the temperature dependence of the interaction parameters.

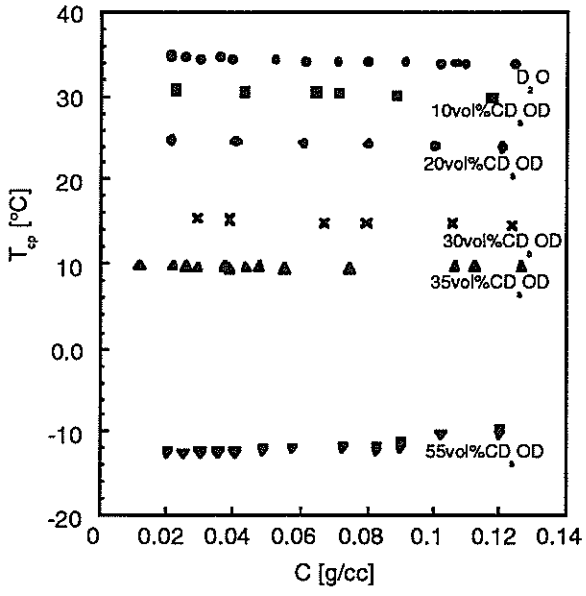

Fig. 1 Phase diagrams for the PNIPAM solutions

The PNIPAM is supplied by Kohjin Co., Ltd. The number average molecular weight was determined from the intrinsic viscosity of aqueous solution at 20°C[2](M_n=5×10^5). Polymer concentration was in the range from 0.03 to 0.12 g/cm^3, which corresponds to semidilute range. The measured systems were PNIPAM in D_2O and in several concentrations of deuterated methanol(CD_3OD) and D_2O mixture. The volume concentrations of CD_3OD in mixed solvents were 35, 55%. Fig.1 shows the phase diagrams for the PNIPAM solution. SANS measurement were performed with KENS-SAN spectrometer. A two dimensioanl position sensitive detector placed at 3m from the sample position was used. The sample cell was made of quartz 1mm thick and thickness of the sample was 2mm. The temperature of the sample was controlled within ±0.05°C.

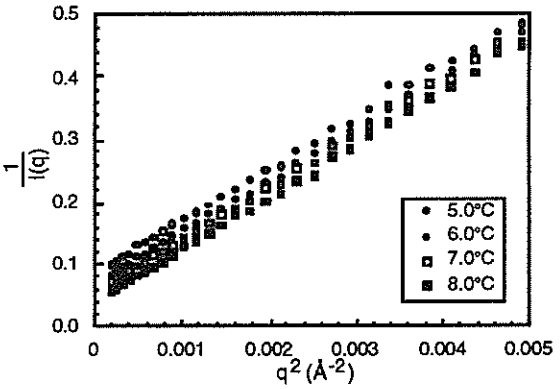

Fig.2 Inverse of the small-angle scattering Intensity, $I(q)^{-1}$, against q^2 for PNIPAM-35vol%CD_3OD(C=0.1266 g/cm^3) systems at several temperatures.

A typical example of inverse scattering intensity $I(q)^{-1}$ against q^2 is shown in Fig.2. From the figure it is evident that I(q) is linear against q^2 in the region below 5×10^{-3} Å^{-1}. Therefore, the Ornstein-Zernike formula is valid in this region. For all other systems measured this is true. Then we obtained the correlation length ξ from the slope and intercept of this figure. The concentration dependence of ξ corresponds to C$^{-0.5\sim-1}$. This means the systems are in the condition of

marginal and theta regime, i.e., the so-called poor solvent regime. Therefore we confirmed the systems used were in the semidilute poor regime.

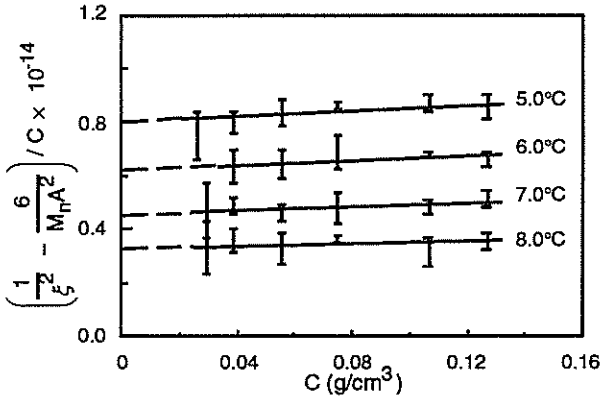

Fig.3 Concentration dependence of ξ at several temperatures near the Θ temperature for PNIPAM in 35vol%CD_3OD(C=0.1266g/cm^3) system.

As shown in Fig.3, the plots of the concentration dependence of ξ for each temperature fit linear relations express by Eq.(1)[5].

$$\xi^{-2} = \frac{6}{M_n A^2} + 12N_A \frac{B_1}{A^2} C + 36N_A^2 \frac{B_2}{A^2} C^2 \qquad (1)$$

where M_n is the number average molecular weight of the polymer, A the short range interaction parameter, N_A Avogadro's number and C the weight concentration of the polymer. Then we can determined separately the temperature dependence of binary and ternary cluster integrals, B_1 and B_2, using the short range interaction factor A=0.8Å evaluated from literature[3,4].

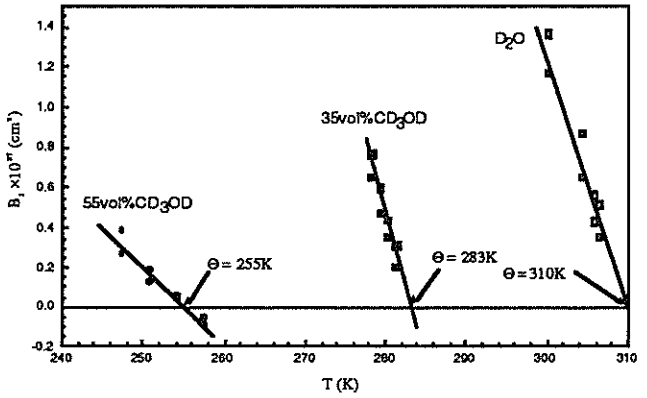

Fig.4 Temperature dependence of binary cluster integral(B_1) of polymer segments.

Fig.4 shows the temperature dependence of B_1.

Here we define the Θ point as the temperature at which B_1 vanishes. The obtained Θ temperatures decreased with increasing CD_3OD content which corresponds to the result of cloud point measurements(Fig.1). B_2 for our systems decrease with increasing temperature in the same way as poly(vinyl methyl ether) in aqueous solutions[5]. Since B_1 is proportional to the reduced temperature $\tau(\equiv 1-\Theta/T)$ in the temperature range near Θ temperature, B_1 can be expressed by the following linear equation with initial slope B_{10}

$$B_1 = B_{10}\tau \ . \qquad (2)$$

From the temperature dependence of B_1 and B_2, we can evaluate the contributions of the segment-segment interaction to the entropy S_{int} and enthalpy H_{int}[5]. Using following equations, we obtain the S_{int} and H_{int} respectively as

$$S_{int} = -\frac{1}{2}N_A R\left[\frac{\partial}{\partial T}(TB_1)C^2 + N_A \frac{\partial}{\partial T}(TB_2)C^3\right] \qquad (3)$$

and

$$H_{int} = -\frac{1}{2}N_A RT^2\left(\frac{\partial B_1}{\partial T}C^2 + N_A \frac{\partial TB_2}{\partial T}C^3\right) \qquad (4)$$

where R is the gas constant, T the temperature. We define S_1 and S_2 as the first and the second terms on the right hand side of Eq.(3), respectively. Then with the use of Eq.(2) we have

$$S_1 = -\frac{1}{2}N_A RB_{10}C^2 \qquad (5)$$

and

$$S_2 = -\frac{1}{2}N_A^2 R\left[\frac{\partial (TB_2)}{\partial T}\right]C^3 \qquad (6)$$

Similarly, we define H_1 and H_2 for Eq.(4), which turn out to be

$$H_1 = -\frac{1}{2}N_A RB_{10}\Theta C^2 \qquad (7)$$

and

$$H_2 = -\frac{1}{2}N_A^2 RT^2\left[\frac{\partial B_2}{\partial T}\right]C^3 \qquad (8)$$

The values of S_1, S_2, H_1 and H_2 at Θ temperature and C=0.1gcm^{-3} thus calculated are listed in Table 1. For all systems both S_{int} and H_{int} were positive in the measured temperature range.

Table 1. Θ temperatures and B_{10} together with the entropy and enthalpy parameters.

Solvent	Θ (K)	$B_{10}\times10^{26}$ (cm^3)	S_{int} $S_1\times10^3$ ($JK^{-1}cm^{-3}$)	$S_2\times10^3$ ($JK^{-1}cm^{-3}$)	H_{int} H_1 (Jcm^{-3})	$H_2\times10^2$ (Jcm^{-3})
D_2O	310	- 4.4	1.1	0.24	0.34	6.0
35%CD_3OD	283	- 4.2	1.1	0.03	0.30	0.85
55%CD_3OD	255	- 0.9	0.23	0.06	0.057	0.17

From Table 1 we see that an increase of CD3OD content results in the lowering of Θ-temperature in conformity with LCST. At the same time we notice that the reduction of H_{int} is more steep than that of S_{int}, which might be responsible for the phenomenon of cononsolvency.

References

1) H. G. Schild, Prog. Polym. Sci., **17**, 163(1992).
2) S. Fujishige, Polymer J., **19**, 297(1987).
3) O. Chiantore, L. Trossarelli and M. Guatia, Makromol, Chem., **183**, 2257(1982).
4) K. Kubota, S. Fujishige and I. Ando, Polymer J., **22**, 15(1990).
5) K. Okano, M. Takada, K. Kurita and M. Furusaka, Polymer, **35**, 2284(1994).

Self-Organization in an Amphiphilic System AOT/Water/n-Decane

S. KOMURA and H. SETO

Faculty of Integrated Arts and Sciences, Hiroshima University, Higashihiroshima 739

1. Introduction

Amphiphiles are intriguing materials that self-assemble in various forms when mixed with oil and water. In disordered phases they take a structure of spherical droplets of water-in-oil (or oil-in-water) or a bicontinuous structure, in which both water and oil are separated from each other by intertwined interfacial films. In ordered phases they take a rather regular structure of hexagonal arrays of cylindrical tubules made of oil (or water) in surrounding water (or oil) or parallel arrays of alternative oil and water sheets. In these mixtures amphiphile molecules are mostly located at the interface of oil and water with their polar heads directed into water media and with apolar acyl tails into oil media, thus forming interfacial monolayers. The phase diagram of these structures depends strongly on temperature, pressure, kinds and concentrations of the three constituents and addition of fourth or fifth elements such as salts or cosurfactants.

In order to probe the microscopic structures in such systems an experiment using small angle neutron scattering (SANS) is a powerful tool. It is possible to obtain structure functions $S(q)$ of the system, which can be compared with those calculated from various proposed models. From the comparisons we can determine not only structural parameters that characterize the system but also interaction parameters among different molecules inherent in the system.

The present paper describes our recent studies by means of SANS on the structures in an ionic amphiphilic AOT/water/n-decane system in bicontinuous microemulsion phase and illustrates the powerfulness of such methods to elucidate the structure and interaction parameters in amphiphilic systems. We have found a scaling relation of the scattering profiles similar to that found in the decomposition process in binary systems

2. Theoretical models

Teubner and Strey[1] have proposed the following equation for X-ray or neutron scattering intensities from surfactant/oil/water ternary system on the basis of phenomenological Ginzburg-Landau free energy expansion

$$I^{\mathrm{TS}}(q) = \frac{1}{A + Bq^2 + Cq^4}, \tag{1}$$

where $A>0$, $B<0$, $C>0$ for bicontinuous system with almost equal oil and water volume fractions resulting in a peak in the scattering profile.

On the other hand Gompper and Schick[2] have proposed the following equation for scattering on the basis of spin lattice model of ternary systems

$$I^{\mathrm{GS}}(q) = \frac{1}{a + b\cos(qd) + c\cos(2qd)}, \tag{2}$$

where d is the lattice size and the constants a, b, c are related to A, B, C by the following equations for small q

$$\begin{aligned} a &= A + \frac{15}{6d^2}B + \frac{6}{d^4}C \\ b &= -\frac{8}{3d^2}B - \frac{8}{d^4}C \\ c &= \frac{1}{6d^2}B + \frac{2}{d^4}C \end{aligned} \tag{3}$$

Once the fitting parameters A, B, C are determined from the scattering profiles, one can determine the structural parameters such as the repeat distance D between oil and water, the structural correlation length ξ and the area a_H per head of the surfactant molecule in the interface by the following equations[1, 3]

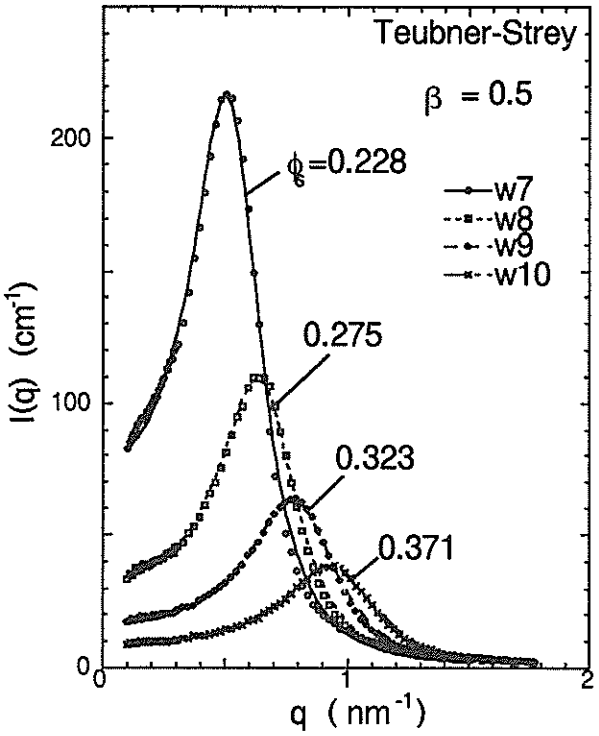

Fig.1 Neutron scattering cross section $I(q)$ from AOT/D_2O/n-decane bicontinuous microemulsion systems with equal volume fraction of D_2O and decane at different AOT volume fractions ϕ_S at room temperature obtained from SANS-U in JRR-3M, Tokai. Curves are fittings to Eq (1).

$$D = 2\pi\left[\frac{1}{2}\left(\sqrt{\frac{A}{C}} - \frac{B}{2C}\right)\right]^{-\frac{1}{2}} \tag{4a}$$

$$\xi = \left[\frac{1}{2}\left(\sqrt{\frac{A}{C}} + \frac{B}{2C}\right)\right]^{-\frac{1}{2}} \tag{4b}$$

$$a_H = 4\beta(1-\beta)\frac{v_S}{\xi\,\phi_S} \tag{4c}$$

From a, b, c one can also determine the interaction parameters such as repulsive energy J between oil and water and the amphiphilicity L of surfactant molecule toward oil and water molecule as a ratio to the thermal energy T and the critical surfactant volume fractions $\phi_S{}^c$ below which an emulsification failure occurs by the following equations[2]

$$\frac{J}{T} = -\frac{b}{6a(1-\phi_S)} \tag{5a}$$

$$\frac{|L|}{T} = \frac{c}{6\,\phi_S\,a\,(1-\phi_S)} \tag{5b}$$

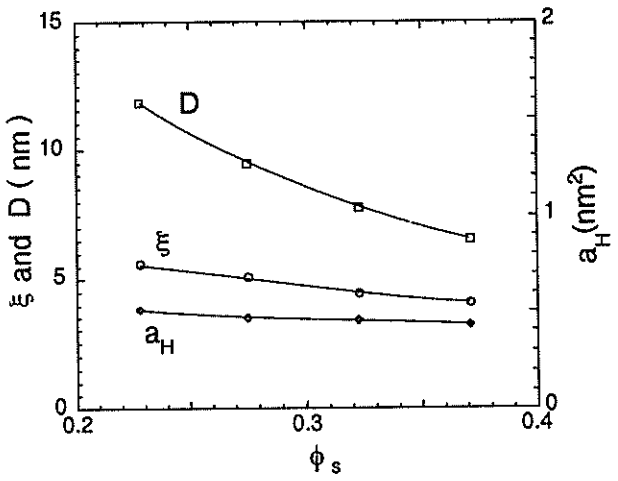

Fig.2 Structure parameters obtained from the data in Fig.1, by Eq.(4), such as repeat distance D, structure correlation length ξ and area per head a_H of surfactant molecules.

$$\phi_s^c = -\frac{b\phi_s}{4c} \tag{5c}$$

where ϕ_S is the volume fraction of the surfactants.

3. Results and discussions

We have studied [3] the structural changes associated with a change of the concentrations of oil against water or the concentrations of amphiphiles against the rest in an ionic amphiphilic AOT/water/n-decane system in bicontinuous microemulsion phase by means of SANS at room temperature. The results of neutron scattering intensity $I(q)$ for different surfactant volume fraction ϕ_S at equal volume fraction of oil and water $\beta=\phi_O/(\phi_O+\phi_W)$ = 0.5 are shown in Fig. 1. The fitting to the Teubner and Strey's Eq. (1) are also shown in the same figure. From the fitting we could obtain the repeat distance D between oil and water, the correlation length ξ and the interfacial area a_H per amphiphile molecule by Eq. (4). They have a general trend to become small as ϕ_S increases as shown in Fig. 2. The same data are further analyzed by Eq.(3) and Eq.(5) in order to obtain the strength of segregation J, the amphiphilicity L of the amphiphile and the critical

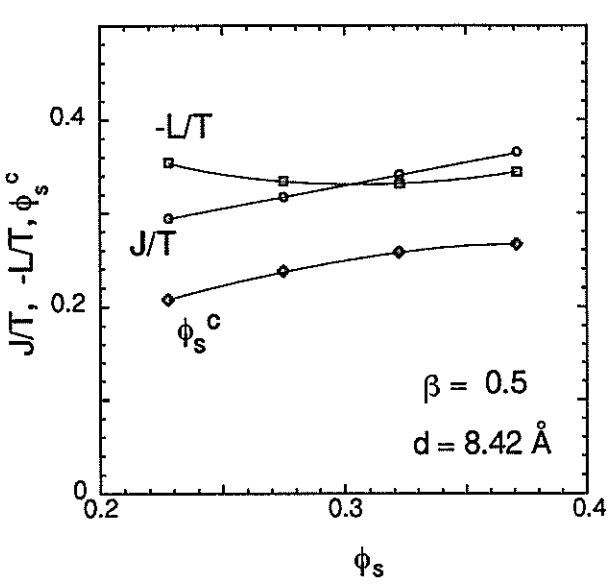

Fig.3 Interaction parameters obtained from the data in Fig.1 by Eq.(5), such as the strength J of segregation between water and decane, the amphiphilicity L<0 of surfactant molecules and the critical concentrations ϕ_S^c of surfactant.

volume fraction ϕ_S^c. The results are shown in Fig. 3. They maintain almost constant values as ϕ_S is changed. The structural and interaction parameters are all in reasonable order of magnitude.

We could obtain similar results for different oil volume fractions against water from β = 0.1 to 0.4 at constant ϕ_S = 0.181. From these results we can probe the relation between the structure and the interaction constants.

One of our interesting findings is that there is a scaling relation of the scattering profiles such that

$$I(q, \phi_S) = [q_m(\phi_S)]^{-3} \tilde{I}(q / q_m(\phi_S), k\xi) \qquad (6)$$

where $q_m(\phi_S)$ is the value of q that gives the maximum of the profile for a system with ϕ_S and $k = 2\pi/D$. Fig. 4 demonstrates that $[q_m(\phi_S)]^3 I(q, \phi_S)$ plotted against $x = q/q_m$ collapses into a single curve $\tilde{I}(x, k\xi)$ for a fixed value of $k\xi$ supporting the scaling relation (6). This phenomenon is very similar to that found in the decomposition process in binary systems

4. Conclusion

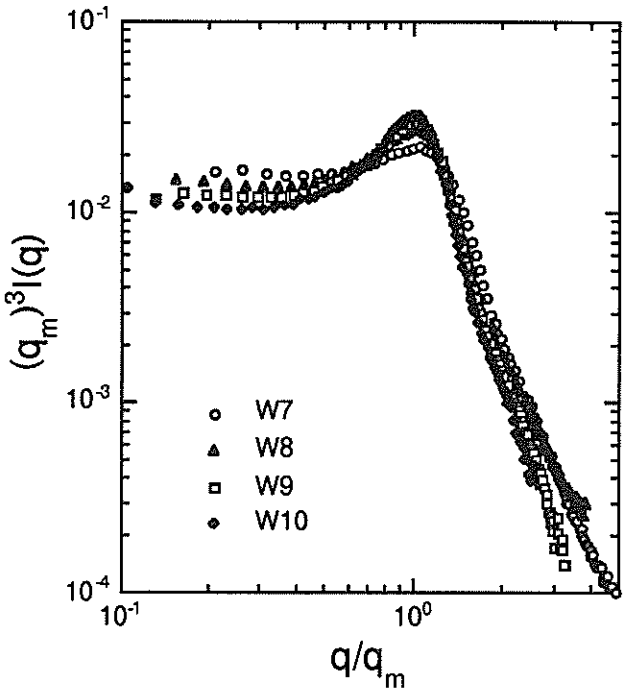

Fig.4 Plotting $[q_m(\phi_S)]^3 I(q, \phi_S)$ as a function of $x = q/q_m(\phi_S)$, which collapses into a single function $\tilde{I}(x, k\xi)$ in accordance with a scaling relation Eq.(6). These data are obtained from SAN at KENS, Tsukuba in close agreement with those obtained from SANS-U in JRR-3M, Tokai.

In terms of interaction parameters J and L within the spin lattice model, Gompper and Schick have calculated the structure function of bicontinuous microemulsion systems. Comparing the structure functions obtainable from SANS with those calculated ones by Gompper and Schick, we could determine the interaction parameters in right order of magnitude. We have found a scaling relation of the scattering profiles similar to that found in the decomposition process in binary systems.

References

1.M. Teubner, R. Strey, J. Chem. Phys. 87, 3195-3200 (1987)

2.G. Gompper, M. Schick, Phys. Rev. B41, 9148-9162 (1990)

3.S. Komura, H. Seto, T. Takeda, M. Nagao, Y. Itoh, M. Imai, J. Chem. Phys. 105, 3264-3277 (1996)

SAN Analysis of Silica Aerogels with Different Density

K.TAJIRI, K.IGARASHI, T.FUKUNAGA* and R.NANBU*

National Industrial Research Institute of Nagoya, Hirate-cho Kita-ku, Nagoya 462
*Department of Crystalline Materials Science, Nagoya Univ., Furo-cho Chikusa-ku, Nagoya 464

Monolithic silica aerogel has properties such as high porosity, high transparency in visible light, and very low thermal conductivity. Such properties arise from a microstructure of the aerogels, which includes three dimensional network of silica particles. The microstructure can be controlled by preparation conditions such as pH in gelation, aging, and supercritical drying medium, and by heat treatment of the aerogels. Small angle neutron and X-ray scattering are powerful tool to characterize the microstructure[1-2]. The structural difference produces a variation of the macroscopic properties like density, transmittance, and elasticity. However, preparation of aerogels is skilled work, so the structure and macroscopic properties might be different if the preparation conditions described in papers is simular. The result of IEA round robin test on thermal conductivity of silica aerogels gives a example of those differences[3]. Therefore, to investigate the relations between preparation, structure and properties of aerogels precisely, it is needed to use the samples by identical preparation for the structural analysis and for the measurements of properties.

In this paper, we report the effects of density and heat treatment on the structure of silica aerogels obtained by SAN measurements.

Aerogel samples were prepared by the method described previously[4]. Firstly, silica alcogels with different silica concentration were prepared by the hydrolysis of tetramethylorthosilicate (TMOS) diluted with methanol. The molar ratios of TMOS, water and methanol used were 1:6:5, 1:6:10 and 1:6:20. An anmonium aqueous solution of 0.1N as a catalyst was used in the reaction. The gels obtained were soaked into anhydrous methanol for 2 days to remove water and catalyst remainning in the gels. After those processes, the gels were placed in an autoclave and were then dried under supercritical condition (250°C, 9MPa) of methanol to remove solvent. The bulk densities of aerogels were 0.16, 0.14 and 0.08g/cm^3.

By heating in atmosphere, methyl groups bonded chemically with silica network are decomposed rapidly at 259°C. Sintering of the network also proceeds with the increase of the temperature. To study the effect of the heat treatment on the silica network, one sample of the aerogels with the density of 0.16g/cm^3 was heated at 500°C for 2.5hrs in dry air.

SAN measurements were carried out at room temperature. Samples were directly mounted in the beam. A distance of sample-2 dimension detector used was 3m, and Q-range of 0.008-0.2Å^{-1} were covered in the measurements. Water spectra from 1mm H_2O in a quartz cell served to eliminate differences in the detector efficiency. Background and sample transmissions were also normalized.

SAN spectra for aerogels with different densities are shown in Figure 1. Comparison between SAN spectra for the heat treated sample and for untreated one is shown in Figure 2. Those spectra show two power law regions separated at about 0.8 of Q-value.

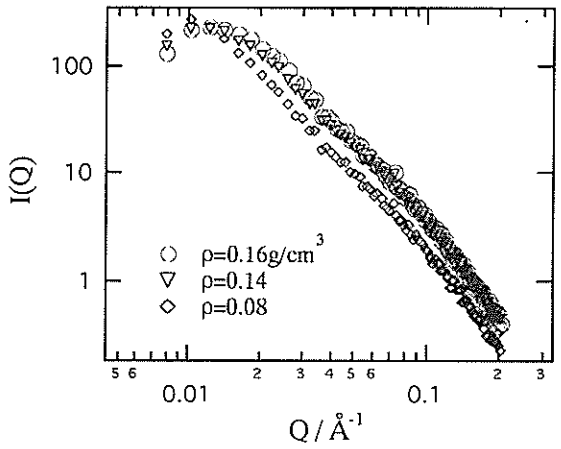

Fig. 1 SAN spectra of silica aerogels with different densities.

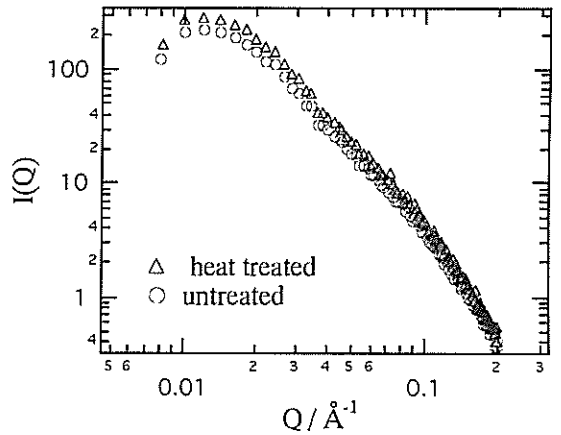

Fig. 2 SAN spectra of heat treated and untreated silica aerogels. (ρ=0.16g/cm^3)

For porous materials like aerogels, the characteristics of the small angle scattering spectum can be related to the different structural features on the respective length scale[5]. At the smallest Q-values, the intensity is constant because of a uniform long-range structure. The crossover between this constant intensity region and smaller power law region gives correration range, ξ, which correspond to the size of network unit in first approximation. The power law region of smaller Q-value is represented as $I \propto Q^{-D}$. The exponent D is a mass fractal dimension. It reflects the self-simularity of the network structure. The power law region of larger Q-value is represented as $I \propto Q^{Ds-6}$. Ds is a surface fractal dimension, and reflects the surface morphology. Ds=2 means a smooth surface, and Ds increases up to 3 with the increase of surface roughness. The crossover between those two power low regions gives the size of silica particles, b, constracting the network.

Table 1. Charastaric values obtained from SAN spectra. (0.16H is heat treated sample)

ρ(g/cm^3)	D	Ds	ξ(Å)	b(Å)
0.16	2.28	2.88	70	~12
0.14	2.28	2.89	80	~12
0.08	2.29	2.95	100	~12
0.16H	2.31	2.73	70	~12

Obtained D, Ds, ξ and b values for each spectrum is shown in Table 1. With the decrease of the density, Ds and ξ increased but D and b were constant. From those data, following results can be obtained: a) Fractal structure of the silica network structure does not change within the this density range, but the unit size of the network increases with the decrease of the density. b) The surface roughness is slightly increase with the decrease of the density. The size of silica particles is simular in this density range. c) By the heat treatment, the surface becomes slightly smooth because of sintering. The other characteristics do not change.

Those results agree with the previous report for base-catalized silica aerogels[6] qualitatively. However, the values are different, especially for Ds (Ds≅2). These differences is supposed to be related to the aging time in the alcogel preparation. So it is suggested that detailed preparation conditions are needed to discuss the structure of aerogels precisely. The decrease of the transmittance of visible light with the decrease of the density of the aerogel[4] might be related to the variation of ξ values. But measurements of wider Q range is needed to discuss deeply.

References

1) D.W.Schaefer and K.D.Keefer, Phys. Rev. Lett., 56, 2199 (1986).
2) R.Vacher, T.Woignier, J.Pelous and E.Courtens, Phys. Rev. B37, 6500 (1988).
3) S.Svendsen, IEA Solar Heating and Cooling, Task18 report (1995).
4) K.Tajiri, K.Igarashi and T.Nishio, J. Non-Cryst. Solids, 186, 83 (1995).
5) A.Emmerling and J.Fricke, J. Non-Cryst. Solids, 145, 113 (1992).
6) D.Posselt, J.S.Pedersen and K.Mortensen, J. Non-Cryst. Solids, 145, 128 (1992).

A study of magnetic excitations in a Kondo semiconductor, CeRhSb

K. OHOYAMA, M. KOHGI [A], H. TANAKA [B], T. YOSHINO [B] and T. TAKABATAKE [B]

Institute for Materials Research, Tohoku University, Sendai 980-77, Japan
[A] *Faculty of Sciences, Tokyo Metropolitan University, Tokyo 192-03, Japan*
[B] *Faculty of Sciences, Hiroshima University, Hiroshima 724, Japan*

CeRhSb, which has a orthorhombic ε-TiNiSi type structure, is thought to be a "Kondo semiconductor" which belongs to the same group of materials as CeNiSn. From transport property measurements, the gap energy in CeRhSb is estimated to be several kelvins, which is nearly the same order as that in CeNiSn, but much smaller than that in other Kondo semiconductors[1,2]. Moreover, the magnetic susceptibility in CeRhSb is weakly dependent on temperature, and exhibits a broad hump at 120 K[1,2]. This is quit similar behaviour to that in typical valence fluctuation systems. We believe that the hybridisation between the conduction band and the 4f state plays an important role in the characteristic features in CeRhSb.

In order to obtain information about magnetic response of the 4f state in CeRhSb, we have performed neutron scattering experiments at KENS in KEK. In this paper, we report results of neutron inelastic scattering experiments. We measured inelastic scattering spectra of a polycrystal sample of CeRhSb using the crystal analyser type spectrometer, CAT. In the experiments, CAT used a fixed final neutron energy E_f of about 3.5 meV.

Figure 1 shows energy spectra of CeRhSb at 3.2 K, 24 K and 100 K. The data were corrected for the absorption effect of the sample and for the wave length variation of the incident neutron flux of KENS. However, no correction was done for phonon contribution.

In fig. 1, we observed two clear peaks at 18 meV and 35 meV. This spectra in CeRhSb is quit different from that in CeNiSn. CeNiSn shows a broad quasi-elastic type spectrum at low temperatures[3], which is a common feature of spectra in typical valence fluctuation systems. As shown in fig. 1, however, the scattering intensity of the peaks are almost independent of temperature. This behaviour can not be explained by the temperature dependence of the magnetic scattering which is caused by crystal field excitations. Since it is almost impossible to measure Q dependence of spectra using CAT, we could not determine the origin of the peaks from the Q-dependence. On the other hand, spectra of the same sample of CeRhSb at a different Q position observed by INC show extremely broad magnetic scattering at around 30~40 mev[4], but show no obvious peak structure. Since we have checked the sample quality by neutron powder diffraction, we can say the effect of impurities in the sample is not serious. Up to this time, unfortunately, we have no clear explanation of the origin of the two peaks in fig. 1. In order to make clear the magnetic response in CeRhSb at low temperatures, further neutron inelastic scattering experiments of CeRhSb and a phonon reference material, LaRhSb, on CAT and other instruments are under way.

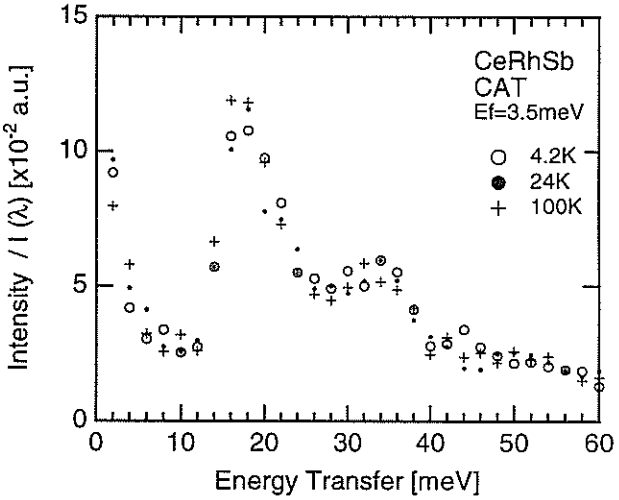

Fig. 1 Energy spectra of CeRhSb using CAT at 3.2 K(Open circles),24 K(Closed circles) and 100 K(crosses).

References

[1] S.K. Malik, D.T. Adroja, Phys. Rev. B 43(1991)6277
[2] T. Takabatake, G. Nakamoto, H. Tanaka, Y. Bando, H. Fujii, S. Nishigori, H. Goshima, T. Suzuki, T. Fujita, I. Oguro, T. Hiraoka and S.K. Malik, Phys. Rev. B199-200(1994)457
[3] M. Kohgi, K. Ohoyama, T. Osakabe, M. Kasaya, T. Takabatake and H. Fujii, Phisica B186-188(1993)409
[4] K. Ohoyama, M. Kohgi, H. Tanaka and T. Takabatake, KENS Report -X

Spin Dynamics in $CsCrCl_3$

Shinichi ITOH, Hidekazu TANAKA* and Toshiya OTOMO

Booster Synchrotron Utilization Facility, National Laboratory for High Energy Physics, 1-1 Oho, Tsukuba 305
**Department of Physics, Faculty of Science, Tokyo Institute of Technology, 2-12-1 Ookayama, Meguro-ku, Tokyo 152*

The dynamical property of a one-dimensional (1D) Heisenberg antiferromagnet has been a long-standing problem in physics. For lower spin (S=1/2 and 1) systems, quantum theories have been intensively developed, and the predicted features have been experimentally confirmed.[1] In an S=3/2 system, observed linewidths of magnetic excitations cannot be described by classical theory.[2] On the other hand, it is well established that an S=5/2 system behaves classically.[3] Observing the spin dynamics in an S=2 system is one of the remaining problems. $CsCrCl_3$ is a compound recognized to be one of the good realizations of an S=2 Heisenberg antiferromagnetic chain above the three-dimentional (3D) ordering temperature (T_N=16K).[4] We report here on an inelastic neutron-scattering experiment of $CsCrCl_3$ at temperatures above T_N.

An inelastic neutron-scattering experiment was performed on INC. The INC spectrometer is a direct-geometry chopper spectrometer coupled to a pulsed-neutron source. Scattered neutrons are detected at a detector system covering a wide range of scattering angles from 5° to 130°. The low scattering-angles from 5° to 12° are densely covered by six hexagonally-configured detector-banks, two of which are placed horizontally (horizontal banks) and the other four are out of the horizontal plane (out-of-plane banks). The six low-angle banks accommodate 30 detectors. Our sample comprises four single crystals, of which the c^*-axes (the chain direction) were aligned in the same direction, and the entire weight of the sample was 40g. The mosaic spread of the sample crystal, including the misalignment among the single crystals, was measured to be 3° at the full width at half maximum (FWHM). The four crystals were configured so that the self-shielding effect cannot be changed by turning the sample, and therefore, a background correction was able to be realized experimentally. The c^*-axis of the sample was mounted in the horizontal plane and measurements were performed with an incident neutron energy of E_i=46.3 meV. In the present experimental set-up, the energy resolution of 1.5 meV (FWHM) was observed at around the zero energy transfer.

In the scan geometry with the scattering angle (ϕ) and the crystal angle (ψ) between the incident wave vector (k_i) and the c^*-axis (the direction of these angles are defined against k_i), the 1D momentum transfer (q) is given by

$$q = k_i \cos\psi - k_f \cos(\phi + \psi), \qquad (1)$$

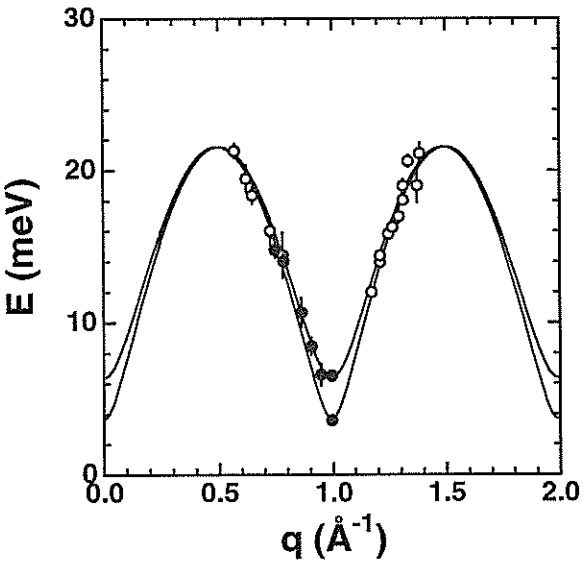

Fig. 1 Dispersion relation of the magnetic excitation measured at 20K. The solid lines are the fitted dispersion curve with two branches. The open and closed circles are the data taken in scans with ψ=90° and ψ=78°, respectively.

where k_f is the final wave vector. In a scan with ψ=90° (i.e., $k_i \perp c^*$) , the overall profile of the magnetic excitations can be observed.[2] Since there is a missing scattering-angle zone at between 12° to 17° on INC, the excitations near to the magnetic zone center cannot be observed in a scan with ψ=90°. By combining the two scans with ψ=90° and ψ=78°, the overall dispersion curve was determined. Figure 1 shows the observed positions of the magnetic excitations at 20K. The peak positions were well fitted to the classical spin-wave dispersion relation of an antiferromagnet. At present, the two excitation peaks were observed only at the zone center. Assuming two branches, the scattering intensity of the lower branch was simulated to be much smaller than that of the upper branch. This is consistent with the present result that the two peaks

were observed only at the zone center. Further experiments are required to determine the dispersion relation near the zone center. We then tried to fit the observed peak positions to a single branch,

$$E(q) = [\, A^2 \sin^2 aq + E_0^2]^{1/2}, \qquad (2)$$

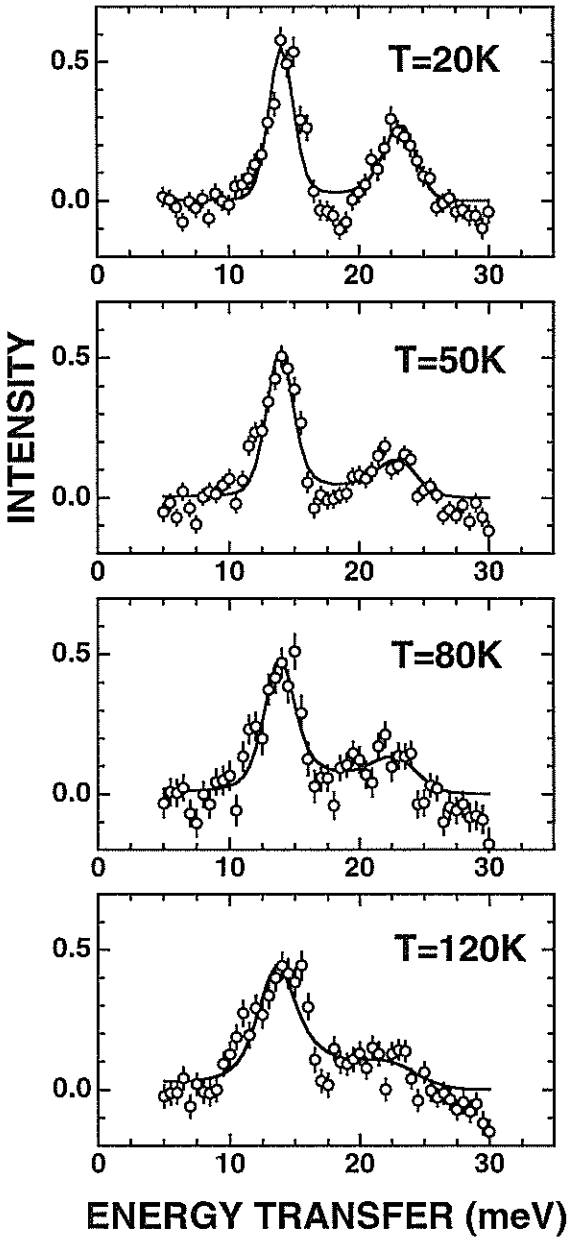

Fig. 2 Temperature dependence of the magnetic excitation spectra at a scan geometry with ψ=0° (k_i//c*) and E_i=46.3 meV. The scan locus is indicated in the insert. The background was subtracted and the kinematical factor (k_f/k_i) was corrected. The solid lines are the fitted Lorentzian scattering function with the q-independent Γ.

and the parameters were obtained to be A=20.6±1.2meV and E_0=6.5±0.3meV, where a is the lattice constant. In the following analysis of the scattering function, we obtained the same result within the statistical error based on the assumption of a single branch and on that of two branches. Therefore we discuss the scattering function based on the assumption of a single branch, as described by eq. (2).

In order to analyze the scattering function, scans with ψ=0° (k_i//c*) were performed. This scan geometry enables the integration of all scattering intensities detected at lower scattering-angles, since q is almost unchanged at low scattering-angles (5°~12°) as shown in eq. (1).[2] Since thirty of detectors were installed at low scattering-angles, a large intensity gain can be realized. The measurements were performed at T=20, 50, 80 and 120K in order to investigate a 1D property of this system, where the detected signals at all the six low-angle detector-banks were used for the data analysis. Background measurements were also performed at T=20, 50, 80 and 120K at the out-of-plane detector banks by turning the sample to the ψ=90° position. Figure 2 shows the background-subtracted spectra on the scan locus displayed in the insert. The observed spectra were well fitted to a Lorentzian magnetic scattering function convoluted with the instrumental resolution. The linewidth of the excitations (Γ) is assumed to be independent of q, as predicted in classical theory.[5]

A classical 1D Heisenberg antiferromagnetic system is in the ordered state (the Néel state) at T=0K, and dynamical scaling can apply to the phase transition. The scattering function is predicted to be described by a Lorentzian function, where Γ is independent of q and proportional to the inverse correlation length, κ. The q-independent Γ was experimentally observed in an S=3/2 system ($CsVCl_3$)[2] and in an S=5/2 system (TMMC).[3] Since the present system is an S=2 system (3/2<2<5/2), we assumed the q-independent Γ. Because the observed spectrum was well fitted to the scattering function, we also confirmed the q-independent Γ in an S=2 system. The classical theory[5] has predicted that the T-dependence of Γ and the zone boundary energy (ε_{ZB}) results from that of the inverse correlation length, as $\Gamma(T)=2JS\kappa(T)a$ and $\varepsilon_{ZB}(T)=4JS(1-\kappa(T)a/2)$. Based on a thermodynamical consideration,[6] κ is proportional to T at lower temperatures, and consequentially, $\Gamma(T)=k_BT/S$ and $\varepsilon_{Z\,B}(T)=4JS-k_BT/S$. This zone boundary energy is given to the Heisenberg antiferromagnet without anisotropy. In the present system, since an apparent energy gap due to anisotopy is observed at the zone center, the T-dependence of

parameter A in the dispersion relation in eq. (2) can be interpreted as $A(T)=4JS-k_BT/S$. As shown in Fig. 3, $\Gamma(T)$ was well described by classical theory without any parameter; $A(T)$ was also well described by classical theory and the exchange constant was determined to be J=32.5±1.5K. In classical theory, $\Gamma(T)$ and $A(T)$ depend on T through $\kappa(T)$, and therefore, the present result suggests the validity of the linear relation between $\Gamma(T)$ and $\kappa(T)$.

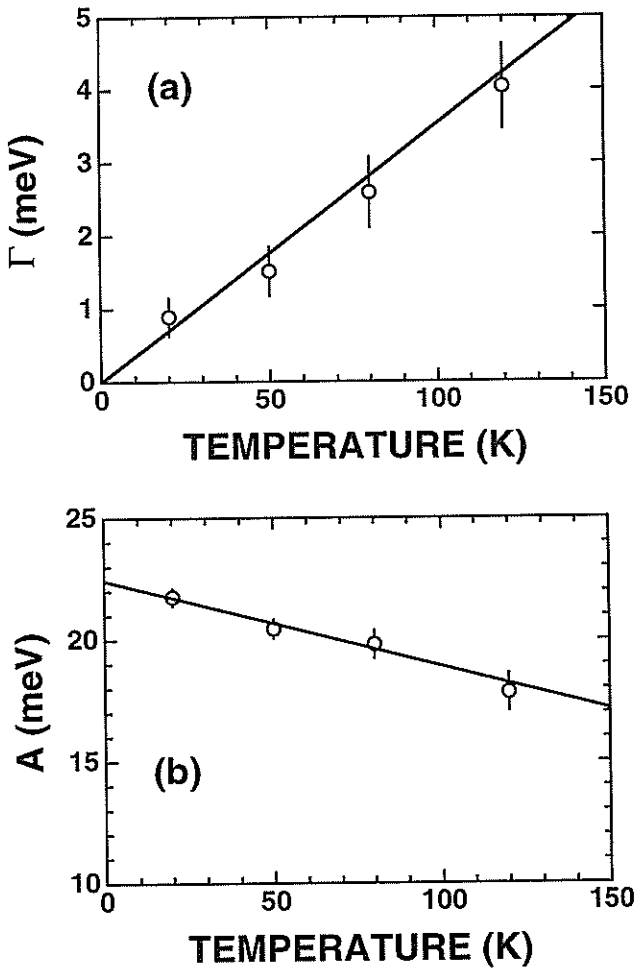

Fig. 3 Temperature dependence of the linewidth Γ (a) and the excitation energy A (b). The solid lines are the classical prediction, $\Gamma=k_BT/S$ and $A=4SJ-k_BT/S$. The exchange constant was determined to be J=32.5±1.5K.

The ratio of the exchange constant from the excitation energy to that from the susceptibility[4] was obtained to be 1.17±0.05. Since the accuracy of the ratio mainly comes from the statistical error in J from the excitation energy, it can be concluded that an appreciable enhancement in the excitation energy was detected. The correction in the excitation energy has been theoretically estimated. From the classical point of view, a spin-wave theory has been developed in the terms of the $1/S$ expansion. For a smaller spin system, higher orders of the expansion should be included; the enhancement of 1.09 in the excitation energy has been estimated for S=2.[7] Recently, using a quantum Monte Carlo method, the excitation spectrum in a system with any spin could be calculated; an enhancement of about 1.1 has been estimated for S=2.[8] For S=2, there is no appreciable difference between the $1/S$ expansion and the quantum Monte Carlo calculation in the correction. This suggests that an S=2 system is almost classical, and that the present result is consistent with these estimations.

In conclusion, we found that the spin dynamics in an S=2 system, $CsCrCl_3$, above T_N was well described by classical theory. In an S=2 system, such quantum effects as the Haldane gap can be expected.[9,10] Since such quantum effects are expected to be detectable at temperatures well below the temperature in the present study, the spin dynamics observed in the present system at the temperatures of the present study does not contradict the predicted quantum behaviors.

References

1) for example, H. A. Bethe: Z. Phys. **71** (1931) 205; F. D. M. Haldane: Phys. Lett. A **93** (1983) 464; Phys. Rev. Lett. **50** (1083) 1153.
2) S. Itoh et al.: Phys. Rev. Lett. **74** (1995) 2375.
3) M. T. Hutchings et al.: Phys. Rev. B **5** (1972) 1999; M. T. Hutchings and C. G. Windsor, J. Phys. C **10** (1977) 313.
4) Y. Tazuke et al.: J. Phys. Soc. Jpn. **53** (1984) 3191.
5) G. Reiter and A. Sjölander: Phys. Rev. Lett. **39** (1977) 1047; J. Phys. C **13** (1980) 3027.
6) M. E. Fisher: Am. J. Phys. **32** (1964) 343.
7) T. Oguchi: Phys. Rev. **117** (1960) 117.
8) S. Yamamoto: Phys. Rev. Lett., **75** (1995) 3348.
9) S. Yamamoto: Phys. Rev. B **53** (1996) 3364.
10) N. Hatano and M. Suzuki: J. Phys. Soc. Jpn. **62** (1993) 1346.

Magnetic Excitations of the Spin Density Wave in Chromium

T. FUKUDA, Y. ENDOH, K. YAMADA, M. TAKEDA, S. ITOH*, M. ARAI* AND T. OTOMO*

Department of Physics, Faculty of Science, Tohoku University, Sendai 980-77
* Booster Synchrotron Utilization Facility, National Laboratory for High Energy Physics, Oho, Tsukuba 305

Cr is an itinerant electron antiferromagnet with $T_N \approx 311$K, below which the spin density wave (SDW) state is realized with the incommensurate wave vectors $|\boldsymbol{Q}_\pm| = 2\pi(1\pm\delta)/a$. Here δ is the incommensurability and a is the lattice constant. And spin flip transition occurs at T_{sf} ($\approx$121K): The spin direction $\boldsymbol{S}\perp\boldsymbol{Q}$ at the temperature between T_N and T_{sf} (transversely polarized SDW; TSDW), but $\boldsymbol{S}//\boldsymbol{Q}$ below T_{sf} (longitudinally polarized SDW; LSDW).[1)]

Theoretically, the static properties of the ordered state of Cr are successfully interpreted by the two band model, where the SDW state is stabilized by the nesting of 'electron' and 'hole' Fermi surfaces centered at Γ and H points in the reciprocal space with opposite electron spin, respectively.[2)] However recent observations such as unique magnetic excitations (Fincher-Burke mode,[3-6)] critical scattering,[7)] longitudinal spin fluctuation mode of spin wave,[8)] etc.) of Cr observed by the neutron scattering experiments, are not fully understood yet.

At the same time, using the triple axis neutron spectrometer (TOPAN) at JAERI, we measured magnetically excited states at wide temperature ($20\le T\le 300$K) as well as energy ($0<\omega\le 40$meV) range.[9,10)] Then we observed that even in the LSDW state, where only spin wave excitations were expected to observe, the inelastic scattering spectrum in $\boldsymbol{q}$ has triple peaks around the antiferromagnetic superlattice position; two incommensurate magnetic scattering (ICMS) peaks and a commensurate magnetic scattering (CMS) peak. The integrated intensity of the ICMS in $\boldsymbol{q}$ increases from 0 at $\omega\approx$0meV, has maximum around $\omega\approx$20meV, then decreases as ω increases. On the other hand the integrated intensity of CMS in $\boldsymbol{q}$ increases linearly from 0 as ω increases from 0meV up to 40meV. There are some experiments measuring magnetic excitations at the energy of about 150 and 500meV,[11,12)] but the investigation at intermediate energy region is not yet done thoroughly. Thus it is necessary to measure at ω>40meV, but it is very difficult to perform by using triple axis spectrometer. Therefore we tried to study the magnetically excited states of Cr at higher energy region with chopper spectrometer.

The experiments were performed on the INC spectrometer at KENS. Three high quality single crystals of pure Cr, all of which have almost the same shape of a cylindrical shape (10mmϕ×50mm), were assembled to be a virtual large single crystal with the volume of about 12cm^3. The assembled sample was sealed in an aluminum can filled with helium exchange gas, which was set on the goniometer so that two principle axes ([100] and [010]) can be included in the scattering plane. Neutron intensity is expected to be weak to measure the magnetic excitations at $\boldsymbol{q}$=(210) or (120) due to the magnetic form factor. Consequently we measured the excitations around $\boldsymbol{q}$=(100) and (010). Moreover, by setting $\boldsymbol{k}_i$ along [110] direction, neutron counts of the detectors at the symmetrical positions are summed up. However, all the crystals were field cooled to be Single-$\boldsymbol{Q}$//[100] state, therefore, strictly speaking, the $\boldsymbol{q}$=(100) and (010) positions are not equivalent. But the asymmetry caused by the $\boldsymbol{Q}$ direction is not serious with coarse $\boldsymbol{q}$ resolution. In fact we confirmed that the intensities of the magnetic signals are almost equal both at $\boldsymbol{q}$=(100) and (010).

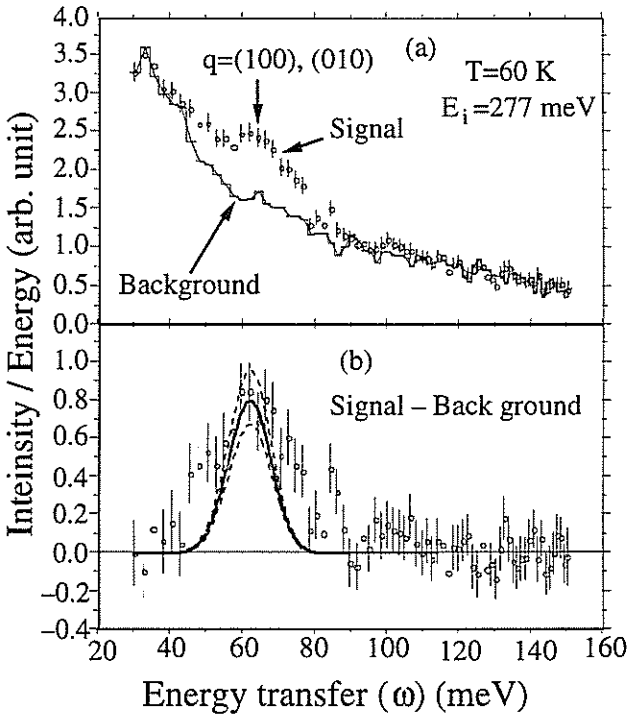

Fig.1 The scattering spectra of TOF as a function of energy with E_i=277meV at 60K.

Figure 1 shows the scattering spectrum as a function of energy with E_i=277meV at 60K. Under these experimental conditions, the magnetic excitations around q=(100) or (010) correspond to the position at ω≈60meV. Although signal from the magnetic excitations is weaker than the back ground scattering as shown in (a) it is clearly determined to be magnetic signals. Here the back ground was determined by the average intensities detected at a few degrees apart from the signal peak positions, and it is subtracted in (b). The solid curve is the simulation, assuming the magnetic response function to be $\chi''(q,w) = C\delta(q-Q_0)$ and taking the instrumental resolution function into account. Moreover the dashed curves are determined by changing C, so that almost the whole curve is included in the error bars of the experimental data. The fact that observed spectrum is a little wider than the simulated curve is mainly affected by the sample mosaicness.

The integrated intensity in q around antiferromagnetic superlattice position, $\int dq\chi''(q,\omega)$, is plotted in Fig.2, where the data points taken on triple axis spectrometer (open circles) and on chopper spectrometer (closed circles) are adjusted to be equal at ω≈25meV. For the coarse q resolution, the ICMS peaks cannot be observed separately from the CMS peak with the chopper neutron spectrometer. Hence the sum of the CMS and the ICMS peak intensities are plotted as triple axis data in this figure, and the dashed line represents the CMS peak component. The top and the bottom of error bars of the TOF data are determined from a factor C of dashed curves in Fig.1 (b). $\int dq\chi''(q,\omega)$ seems to increase from 0 at ω≈0meV linearly, making two maximums at around 20 and 60meV, though the latter one is not definite. Since the maximum around 20meV corresponds to the ICMS peak components, the second maximum can be conjectured to be the CMS peak one. Subtracting the estimated ICMS peak components, we can also get the CMS peak at around 60meV.

As a matter of fact, it is not clear that the CMS peak has maximum or only saturates around ω=60meV for lack of data points. In order to elucidate this point, it is very important to perform more experiments to fill the gap. Furthermore, recent theoretical study explains the CMS peak as a phason mode by using the three band model with random phase approximation. It was predicted that the maximum position of the CMS peak changes with the temperature and electron concentration.[13,14] Therefore, the measurements at different temperatures or from dilute Cr alloys are highly required.

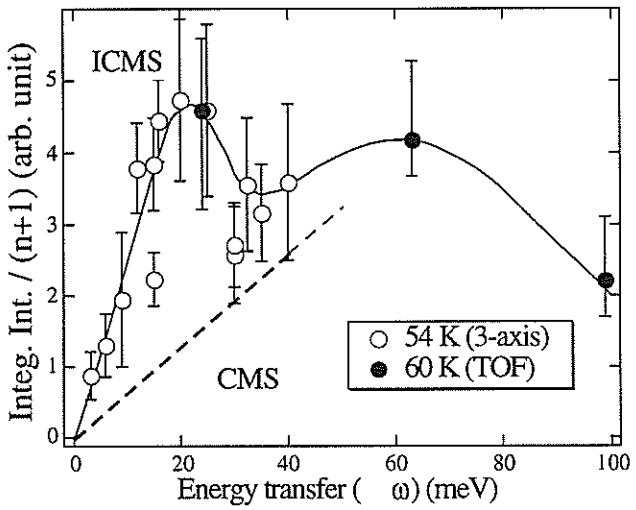

Fig.2 Energy dependence of the integrated intensity at the temperature of 54K with triple axis (open circles) and 60K with TOF (closed circles) spectrometer.

References

1) E. Fawcett, Rev. Mod. Phys. 60 (1988) 209.
2) W. M. Lomer, Proc. Phys. Soc. London 80 (1962) 489.
3) C. R. Fincher, G. Shirane and S. A. Werner Phys. Rev. Lett. 43 (1979) 1441.
4) C. R. Fincher, G. Shirane and S. A. Werner, Phys. Rev. B24 (1981) 1312.
5) S. K. Burke, W. G. Stirling, K. R. A. Ziebeck and J. G. Booth, Phys. Rev. Lett. 51 (1983) 494.
6) B. J. Sternlieb, G. Shirane, S. A. Werner and E. Fawcett, Phys. Rev. B48 (1993) 10217.
7) B. J. Sternlieb, J. P. Hill, T. Inami, G. Shirane, W. T. Lee, S. A. Werner and E. Fawcett, Phys. unpublished.
8) J. E. Lorenzo, B. Sternlieb, G. Shirane and S. A. Werner, Phys. Rev. Lett. 72 (1994) 1762.
9) Y. Endoh, T. Fukuda, K. Yamada, M. Takeda, J. Phys. Soc. Jpn. 63 (1994) 3572.
9) T. Fukuda, Y. Endoh, K. Yamada, M. Takeda, S. Itoh, M. Arai, T. Otomo: J. Phys. Soc. Jpn. 65, (1996) 1418.
11) R. T. Heap, P. W. Mitchel, A. D. Taylor and R. Osborn, Physica B174 (1991) 22.
12) J. R. Lowden, P. W. Mitchell, S. Itoh, Y. Endoh, T. G. Perring, J. Magn. Magn. Mater. 140-144 (1995) 1971.
13) R. S. Fishman and S. H. Liu, unpublished.
14) R. S. Fishman and S. H. Liu, Phys. Rev. Lett. 76 (1996) 2398.

Phase Transitions in $Mn_{1-x}Fe_xP$

Y. TODATE, Y. OKAMOTO, K. NAKAMURA and A. OKAMURA

Department of Physics, Faculty of Science, Ochanomizu Univ. Tokyo 112

MnP and FeP exhibit an unique double-spiral spin structure at low temperatures[1,2]. In MnP ferromagnetic phase appears at a certain temperature range higher than the screw phase. This unusual ferromagnetic to screw transition was interpreted as a result of temperature variation of the second nearest neighbor exchange parameter[3]. The nature of the transition, however, has not been revealed completely. It has been reported that the ferromagnetic phase remains at the region with lower Fe concentrations. Fig.1 shows the magnetic phase diagram of solid solution system $Mn_{1-x}Fe_xP$[4]. It should be noted that the pitch angle of the screw is not the same for MnP and FeP. In FeP the spins are more rapidly twisted than in MnP. It may be probable that Fe substitution for small amount of Mn seems to modify the competing situation of the exchange interactions in MnP. Therefore investigation of $Mn_{1-x}Fe_xP$ system will be helpful in understanding the magnetic properties of these monophosphide by means of neutron and Mössbauer spectroscopy. Single crystals of $Mn_{1-x}Fe_xP$ with several Fe concentrations have been prepared. Magnetic scattering were surveyed along (h00) direction, which is the direction of the screw propagation, using a diffraction detector of MAX.

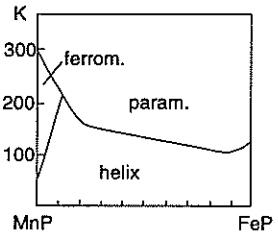

Fig. 1 Phase diagram reported on $Mn_{1-x}Fe_xP$ [4].

The results are rather complicated exhibiting anomalously broadened satellites $(200)^+$ and $(200)^-$ at low temperatures. Figure 2 shows the peak profiles observed in $Mn_{0.95}Fe_{0.05}P$. Note the sufficientry sharp (200) nuclear Bragg peak which indicates the good quality of this single crystal. Higher Fe concentration results in wider satellite broadenings. Temperature dependence of the intensity is also unusual. There is little increase in intensity at the ferromagnetic (200) position in zero external field at the temperature where the system is reported to be ferromagnetic, while the Mössbauer spectrum measured at this temperature region actually shows ferromagnetic character with finite internal field[5]. The satellite intensity in mixed system with Fe concentraton of about a few % seems to vary continuously, while the ferromagnetic-screw transition in pure MnP is of first-order.

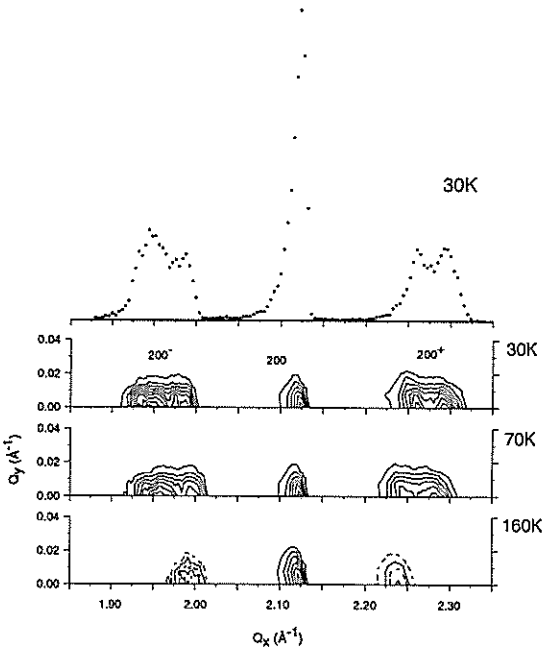

Fig. 2 Peak profiles of the nuclear (200) and its magnetic satellites measured on single crystal of $Mn_{0.95}Fe_{0.05}P$.

These results indicate that the propagation of the screw is not uniform at low temperature but substantially disturbed in $Mn_{1-x}Fe_xP$. Furthermore the state in which the system is considered to be ferromagnetic is not actually a simple ferromagnetic one. A clear microscopic descreption has not been obtained but the results suggest the occurrence of energetically nearly degenerated configurations or microscopic domains which can be seen in systems with the frustration such as spin-glasses. Elastic and inelastic scattering measurements under external magnetic fields using MAX spectrometer are planned.

We acknowledge help of Prof. M. Tanaka.

References

1) J. B. FORSYTH et al., Proc. Phys. Soc., **88** (1966) 333.
2) G. P. FELCHER et al., Phys. Rev. **B3** (1971) 3046.
3) K. TAJIMA et l., J. Magn. & Magn. Mater. **15-18** (1980) 373.
4) J. P. SÉNATEUR et al., Acad. Sci. Ser. **C269** (1969) 1385.
5) A. OKAMURA et al., unpublished.

Neutron Depolarization Measurement of $LiNiO_2$

S. ITOH, M. TAKEDA*, K. KAKURAI**, R. KANNO*** and A. HIRANO***
Booster Synchrotron Utilization Facility, National Laboratory for High Energy Physics, Tsukuba 305
**Department of Physics, Faculty of Science, Tohoku University, Sendai 980-77*
***Neutron Scattering Facility, Institute for Solid State Physics, University of Tokyo, Tokai 319-11*
****Department of Chemistry, Faculty of Science, Kobe University, Kobe 657*

$LiNiO_2$ is a possible candidate of quantum two-dimensional triangular antiferromagnet[1] and its magnetic properties have been extensively investigated.[2-6] More recent studies indicate that the magnetic properties strongly depends on the stoichiometry of the compound.[4,5] For nearly stoichiometric sample, the temperature dependence magnetic susceptibility shows a maximum or cusp at around 10K like a spin glass.[4,5] Neutron depolarization can be expected at temperatures below the cusp temperature in a case of a spin glass, and this technique gives us a magnetic structure in a semi-macroscopic length scale. Therefore, we tried to perform a neutron depolarization measurement of a nearly stoichiometric sample of $LiNiO_2$, in order to investigate magnetic properties at around the cusp temperature.

The $LiNiO_2$ sample used in the present study was a sintered powder synthesized at 650°C, and therefore, the composition, x, in $Li_{1-x}Ni_{1+x}O_2$ can be estimated to be 0~0.01, i.e. almost stoichiometric.[4] A neutron depolarization measurement of $LiNiO_2$ was performed on the TOP spectrometer at KENS. The polarized polychromatic neutrons with a wavelength band were transmitted through the sample under a guide magnetic field of 5 Oe, the polarization of the transmitted neutron beam was analyzed with a spin analyzer, and then the intensities were detected. The sample had a disk shape with the diameter of 8 mm and thickness of 2 mm, and the neutron beam direction was normal to the disk surface. After cooling the sample without an external magnetic field, the temperature (T) dependence of the polarization was measured under the guide magnetic field at T=13~250K. The lowest temperature in the present experiment was 13K.

Figure 1 shows the polarization of the transmitted beam though the sample as a function of neutron wavelength. The wavelength-dependent polarization was converted from the time-of-flight spectra of the detected intensities as follows:

$$P(\lambda) = \frac{I^+ - I^-}{I^+ + I^-} \Big/ \frac{I_0^+ - I_0^-}{I_0^+ + I_0^-}$$

where I^+ (I^-) is the detected intensity with the incident beam polarization parallel (antiparallel) to the sample magnetization along the guide magnetic field and I_0^+ (I_0^-) is that without the sample. The depolarization observed at 13K and no depolarization was observed at T≥15K. Although the lowest temperature in the present experiment was unfortunately 13K, we detected neutron depolarization just above the cusp temperature (~10K), which was also reported for a different sample of $LiNiO_2$ where the depolarization was observed below 50K.[6] $P(\lambda)$ at 13K was well fitted to a functional form of $\exp(-\alpha\lambda)$. The exponential wavelength dependence suggests an existence of a semi-macroscopic size of a ferromagnetically correlated region in a magnetic domain.[7] In order to elucidate the magnetic property at around the cusp temperature, further measurements at temperatures lower than those in the present experiment were required.

Reference

1) K.Hirakawa et al., J.Phys.Soc.Jpn.54 (1985) 3526.
2) K. Hirakawa and H. Kadowaki, Physica B 136 (1986) 335.
3) K. Hirota et al., J. Phys.: Condens. Matter 3 (1991) 4721.
4) A. Hirano et al. Solid State Ion. Diffus. React. 78 (1995) 123.
5) J. N. Reimers et al., J. Solid State Chem. 102 (1993) 542.
6) S. Itoh et al., Physica B 213&214 (1995) 220.
7) S. Mitsuda and Y. Endoh, J. Phys. Soc. Jpn. 54 (1985) 1570.

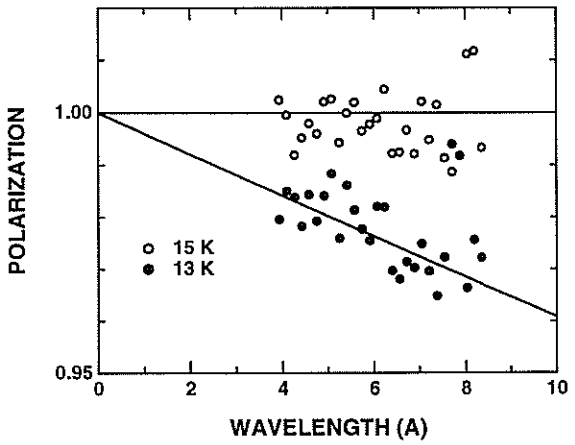

Fig.1 $P(\lambda)$, polarization of the neutron beam transmitted through the $LiNiO_2$ sample. For the 13K data, the solid line is a fitted curve of $e^{-\alpha\lambda}$ with α=0.004Å^{-1}.

Magnetization process in helical - spin glass reentrant $Cr_{0.81}Mn_{0.19}Ge$

T. Sato[1], T. Taniyama[2], T. Oku[2], S. Ito[3] and M. Takeda[4]

[1]Department of Applied Physics and Physico-Informatics, Faculty of Science and Technology, Keio University, 3-14-1, Hiyoshi, Kohoku-ku, Yokohama, Kanagawa 223
[2]Department of Materials Science, Faculty of Science and Technology, Keio University, 3-14-1, Hiyoshi, Kohoku-ku, Yokohama, Kanagawa 223
[3]National Laboratory for High Energy Physics, 1-1 Oho, Tsukuba-shi, Ibaraki 305
[4]Department of Physics, Tohoku University, Aramaki Aoba, Sendai, 980

1. Introduction

Our recent small-angle neutron-scattering (SANS) measurements presented some evidence supporting a double transition in $Cr_{1-x}Mn_xGe$ with $x = 0.17$ and 0.19, i.e., a paramagnetic to a helical magnetic phase and to a mixed state of helical and spin glass-like ordering[1,2]. The helical spin modulation having a long period can be interpreted in terms of an itinerant-electron picture, which is also consistent with our previous magnetic data[3]. Conventional magnetic measurements provide only limited information of such complex field-dependent spin structure since they reflect properties averaged on macroscopic scale. SANS experiment is also insufficient to obtain information on magnetism in semi-macroscopic scale, e.g., magnetic domain configuration. On the other hand, the resolution of neutron depolarization analysis is adequate to investigate the magnetic structure of such a scale[4]. We analyze the wavelength-dependent neutron-depolarization in $Cr_{0.81}Mn_{0.19}Ge$ sample to discuss the field dependent spin structure and spin glass transition in comparison with our previous data.

2. Experimental procedure

A plate sample of $Cr_{0.81}Mn_{0.19}Ge$ of 1 mm thick was used for the neutron depolarization analysis. The neutron-depolarization measurements were performed using the TOP spectrometer at the cold neutron guide hall of the Booster Synchrotron Utilization Facility at KEK. All the incident neutron spins are polarized along the z-direction. The polarization $P(\lambda)$ along the z-direction was measured as a function of the wavelength λ (3 - 9Å) using the polarization analyzer just after the neutron passed through the sample along the x-direction, where the sample plate was set parallel to the y-z plane. An external field was applied up to 2 kOe along the z-direction.

3. Experimental results and discussion

The general equation for neutron depolarization in the conventional ferromagnetic materials was deduced as follows:

$$P(\lambda) = \left| \left\langle \frac{B_{//}^2}{B^2} \right\rangle_B + \left\langle \frac{B_{\perp}^2}{B^2} \right\rangle_B \langle \cos(c\,B\,\delta\,\lambda) \rangle_\delta \right|^N , \quad (1)$$

where brackets $< >_B$ and $< >_\delta$ represent the ensemble average over the local induction B in each domain and the domain size, respectively. The symbols // and $\perp$ show the components of local induction parallel and perpendicular to the incident neutron polarization. N is the average number of the domains which neutrons pass over, and c is a constant. For the non-random domain and mono-domain configurations, we can use the following approximate forms, respectively,

$$P(\lambda) = \exp\{-c_1 |1 - \cos(c_2 \lambda) \exp(-c_3 \lambda^2)|\} \quad (2)$$

and

$$P(\lambda) = (1 - c_1) + c_1 \cos(c_2 \lambda) , \quad (3)$$

where

$$c_1 = N \left\langle \frac{B_{\perp}^2}{B^2} \right\rangle_B \quad (4)$$

and

$$c_2 = c\,B\,\delta , \quad (5)$$

where c_3 is related to the width of distribution in the domain size. In Eq.(3), corresponding to the mono-domain state, the average domain size δ should be regarded as the sample thickness d.

We show the typical wavelength dependent polarization in $Cr_{0.81}Mn_{0.19}Ge$ measured at 5.1 K in Fig.1. Although only small depolarization is observed at low magnetic field, the higher field data show characteristic wavelength dependence which is definitely different from that expected for ferromagnetic multi-domain configuration (Fig.1(b)). The higher field data can be fitted by both equations (2) and (3). However, we claim that the Eq.(3) is valid for the present data, judging from the unreasonable facts that the domain size deduced from Eq.(2) monotonically

decreases with increasing magnetic field.

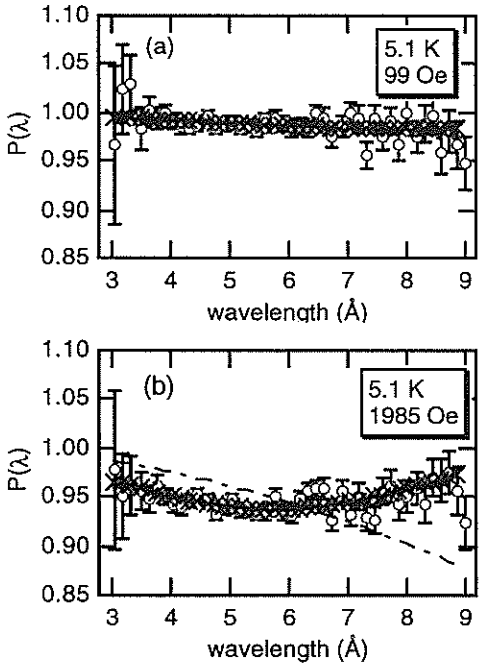

Fig.1 Wavelength dependence of polarization P(λ). Dashed line corresponds to randomly oriented spin configuration. Solid line and symbol x show Eqs. (2) and (3), respectively.

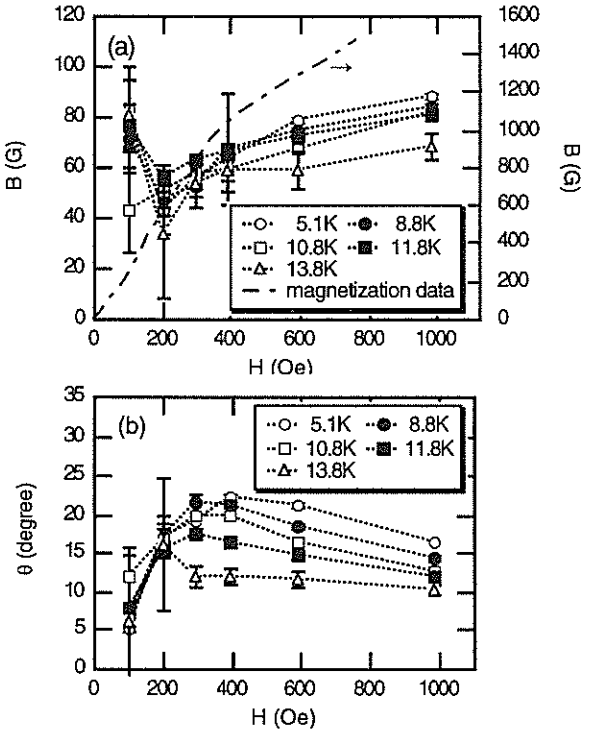

Fig.2 Field dependent value of B and the angle θ between **B** and **H** deduced from Eq.(3).

Figure 2 shows the field dependent values of the magnetic induction B and θ obtained from Eq .(3), where θ is the angle between **B** and **H**. First, we should pay attention to the magnitude of B which is much smaller than that deduced from the magnetization data (Fig.2(a)).The value of B should be identical to the spontaneous magnetization in conventional ferromagnetic materials. In helical magnetic materials, on the other hand, the physical meaning of B deduced from Eq.(3) can not be defined. Based on the present reduction of B, we understand that this neutron depolarization procedure does not directly detect the magnitude of longitudinal ferromagnetic spin component induced with changing to a conical spin modulation from the helical type in finite magnetic field. We can propose a plausible explanation to interpret the discrepancy based on the following idea: the modulated transverse spin components would act on neutrons passing through the present magnetic media as an effective rotational field, since $Cr_{0.81}Mn_{0.19}Ge$ has the helical spin modulation with large period so that the neutron can detect the periodic structure. Such an idea has been introduced to explain the neutron depolarization data in connection with the vortex-like spin structure in the reentrant spin glass $Ni_{77}Mn_{23}$[5]. When the rotational field brings about neutron spin rotation opposite to the Larmor precession, thus, we may observe the decrease in parameter c_2, i.e., the effective value of B smaller than the intrinsic magnetic induction obtained from magnetic data.

On the other hand, the value of c_1, irrelevant to such modification, should directly reflect the angle between the directions of field induced ferromagnetic spin component and magnetic field. The field dependent angle θ in Fig.2(b) shows a maximum at a field H_{max} which tends to decrease with increasing temperature. This field dependence suggests that the long range ferromagnetic ordering of the longitudinal component of conical spins tends to be disturbed with firming of the local ferromagnetic component in comparatively weak magnetic field. In other words, the interaction between local magnetic moments must be non-ferromagnetic. This is consistent with the spin-glass characteristics in the system.

References

1) T.Sato et al., Phys. Rev. B 49, 11864 (1994)
2) T.Sato et al., J.Magn.Magn.Mater. 140-144, 1785 (1995)
3) T.Sato et al., J.Phys.Soc.Jpn. 57, 639 (1988)
4) S.Mitsuda and Y.Endoh, J.Phys.Soc.Jpn.54, 1570 (1985)
5) T.Sato et al., Phys.Rev.B 48, 6074 (1993)

Intraparticle Structure in Ultra-fine $ZnFe_2O_4$ Particles

M. Yokoyama[A], T. Oku[A], T. Taniyama[A], T. Sato[B], E. Ohta[B], T. Sato[C], K. Haneda[D], S. Itoh[E], and M. Takeda[F]

[A]Dept. of Mater. Sci., Fac. of Sci. & Tech., Keio Univ., Yokohama, Kanagawa 223
[B]Dept. of Appl. Phys. & Physico-Inform., Fac. of Sci. & Tech., Keio Univ., Yokohama, Kanagawa 223
[C]Dept. of Elec. Eng., Fac. of Eng., Tokyo Engineering Univ., Hachioji, Tokyo 192
[D]Dept. of Elec. Mater., Sch. of Sci. & Tech., Ishinomaki Senshu Univ., Ishinomaki, Miyagi 986
[E]National Laboratory for High Energy Physics, Tsukuba, Ibaraki 305
[F]Dept. of Phys., Fac. of Sci., Tohoku Univ., Sendai, Miyagi 980

It is well known that zinc ferrite ($ZnFe_2O_4$) has an almost normal spinel structure with a tetrahedral A-site occupied by Zn^{2+} ions and an octahedral B-site by Fe^{3+} ions. It exhibits anomalous antiferromagnetic behavior with the Néel temperature of about 9 K[1]. Lotgering[2] has suggested that a small number of Fe^{3+} ions occupy the tetrahedral A-site in $ZnFe_2O_4$, and around such a Fe^{3+} ion the neighboring Fe^{3+} ions at the octahedral B-site form a magnetic cluster through a coupling by the A-B interaction.

In our previous papers[3-5], we reported that ultra-fine $ZnFe_2O_4$ particle, prepared by the coprecipitation method, shows the extraordinarily large magnetization compared with that of bulk materials. The size dependence of magnetization has been explained by assuming an intraparticle structure consisting of magnetically inactive surface layer and ferromagnetic core. However, our recent small angle polarized neutron scattering measurements suggest that there is no magnetically inactive surface layer[6]. We suspect that this result may be attributed to insufficient evaluation of neutron scattering intensity from the sample holder. In this work, we carefully evaluate the small angle polarized neutron scattering intensity only from the ultra-fine $ZnFe_2O_4$ particles to discuss whether or not the magnetically inactive surface layer exists.

The small angle scattering intensities were measured using the TOP spectrometer at 30 K in a field of 9.4 kOe. The intraparticle structure of $ZnFe_2O_4$ particles, prepared by the coprecipitation method, was analyzed based on the differential neutron scattering intensity as follows[7]:

$$I^+(Q) - I^-(Q) = \alpha \langle F_N(Q) F_M(Q) \rangle, \qquad (1)$$

where $F_N(Q)$ and $F_M(Q)$ are the nuclear and magnetic form factors, respectively. The signs of $I^+(Q)$ and $I^-(Q)$ represent the incident neutron polarization parallel and antiparallel to H, respectively. α is dependent on the magnetic moment of the sample. $F_N(Q)$ and $F_M(Q)$ for a spherical particle are expressed as follows:

$$F_N(Q) = \frac{4}{3}\pi b a^3 g(Qa), \qquad (2)$$

$$F_M(Q) = \frac{4}{3}\pi p a_m^3 g(Qa_m) \qquad (3)$$

with

$$g(x) = \frac{3(\sin x - x\cos x)}{x^3}, \qquad (4)$$

where a and a_m the mean radii of a particle and the magnetic core, and b and p are nuclear and magnetic scattering length densities. We used $b=6.59\times10^{10}$ cm^{-2} and $p=6.89\times10^{9}$ cm^{-2}, where the latter was estimated from the magnetization curve of the $ZnFe_2O_4$ particles sample.

Figure 1 shows $I^+(Q)$ - $I^-(Q)$ at 30 K in H = 9.4 kOe. The differential intensity shows

monotonic decrease with increasing Q. To evaluate the intraparticle structure of the $ZnFe_2O_4$ particle, the $I^+(Q) - I^-(Q)$ was fitted using Eq. (1). Here, we note that our previous TEM observation of $ZnFe_2O_4$ particles[8] showed the spherical shape of particle and the log-normal distribution of radius with a median of 2.1 nm and a standard deviation of 0.28. The fitting procedure was performed by parameterizing the thickness of magnetically inactive layer given by $a - a_m$ and using the distribution of radius obtained from the TEM observation. We obtained the best fitted curve at $a - a_m = 0$. This result is consistent with our previous work performed under various experimental conditions of temperature and magnetic field which are different from the present one. In conclusion, we confirmed no magnetically inactive surface layer in the ultra-fine $ZnFe_2O_4$ particles using the small angle polarized neutron scattering experiment.

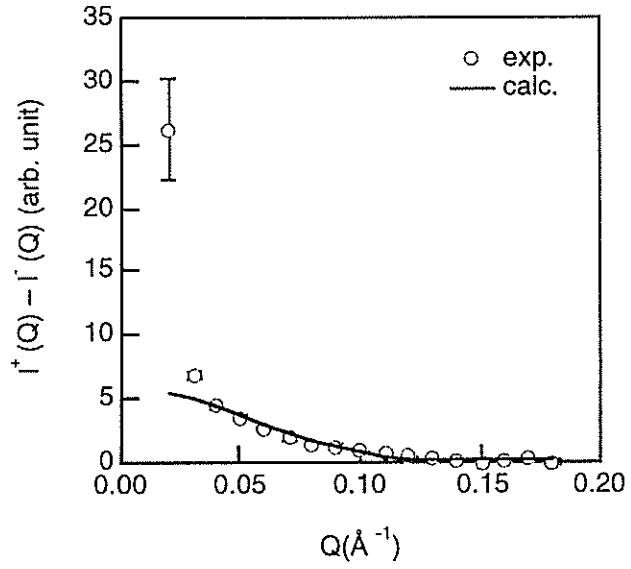

Fig. 1. The differential neutron scattering intensities $I^+(Q) - I^-(Q)$ at 30 K in H = 9.4 kOe, which are fitted with Eq. (1) using the best fit parameter a-a_m =0.

References

1) J.M. Hastings and L.M. Corliss, Phys. Rev. 102 (1956) 1460.
2) F.K. Lotgering, J. Phys. Chem. Solids 27 (1966) 139.
3) T. Sato, K. Haneda, M. Seki and T. Iijima, Proc. Intern. Symp. Phys. of Magnetic Materials (World Scientific, Singapore 1987) 210.
4) T. Sato, K. Haneda, M. Seki and T. Iijima, Appl. Phys. A 50 (1990) 13.
5) T. Sato, K. Haneda, T. Iijima and M. Seki, Sixth Intern. Conf. Ferrites (1992) 984.
6) M.Yokoyama, T. Oku, T.Taniyama, T.Sato, E.Ohta, T. Sato, K. Haneda, S.Itoh, K. Kurahashi and M. Takeda, Physica B 213&214 (1995) 251.
7) S. Itoh, Y. Endoh, S. Taketomi and S. Chikazumi, J. Magn. Magn. Mat. 103 (1992) 126.
8) M. Seki, T. Sato and S. Usui, J. Appl. Phys. 63 (1988) 1424.

Small Angle Polarized Neutron Scattering Study on PdFe Fine Particles

T. TANIYAMA[†,*], E. OHTA[†], T. SATO[††], and M. TAKEDA[†††]

[†]Department of Materials Science, Faculty of Science and Technology, Keio University, Yokohama 223
[*]National Research Insititute for Metals, Tsukuba 305
[††]Department of Instrumentation Engineering, Faculty of Science and Technology, Keio University, Yokohama 223
[†††]Department of Physics, Tohoku University, Sendai 980

Magnetic properties of Pd are very sensitive to the mixing of 3d transition metal impurities, e.g., Fe atom induces strong polarization of the Pd matrix in PdFe alloy which results in the giant magnetic moment of ~ 10 μ_B per Fe atom. Bulk $Pd_{1-x}Fe_x$ with the concentration between x = 0.022 at. % Fe and x = 0.1 at. % Fe exhibits a spin glass properties owing to the RKKY interaction between the local giant magnetic moments via conduction electrons, and the ferromagnetism appears above this percolation threshold (x = 0.1 at. % Fe)[1]. So far, however, there has not been sufficient information about the magnetic behavior in the fine particle of such Pd based dilute alloys. We can suppose two possible magnetic changes in PdFe fine particles. First, we expect the more magnetically enhanced surface region of PdFe particle to accompany the strongly magnetic Pd host in the confined geometry[2]. Alternatively, the doping of Fe atoms may break down the ferromagnetic ordering at the surface as opposed to the situation of the pure Pd particle[2] because of the decrease in the mean free path of conduction 4d electrons; this plays an important role in the ferromagnetic ordering in this material. In this report, we intend to clarify the Fe doping effect in Pd particle by paying attention to the magnetic behavior of its surface [3].

PdFe fine particles were prepared by conventional gas evaporation method under Ar gas (purity 99.9995 %) atmosphere. The arc melted $Pd_{95}Fe_5$ ingot was annealed for 50 hours at 900 °C and then quenched in cold ice water. This homogenized $Pd_{95}Fe_5$ ingot were used for the gas evaporation. PdFe fine particles evaporated on the inner wall of the chamber were collected in vacuum by Teflon brushes into the quartz tube attached to the bottom of the chamber. To seal the quartz tube in vacuum prevents adsorbing of active gases on the surface of particles. The size of particles can be controlled by changing the pressure of Ar gas in the chamber from 2 to 12 Torr. The compositions of evaporated PdFe particles, determined by means of electron probe microanalysis (EPMA), were 2.9 at. % Fe in all the samples.

Small angle polarized neutron scattering (SAPNS) experiments were performed using the TOP spectrometer. The neutron scattering intensities $I_\perp^+(Q)$ and $I_\perp^-(Q)$ were counted separately for incident neutrons whose spins are parallel and anti-parallel to the magnetic field at 8.0 K. The magnetic field of 9 kOe was applied perpendicular to the momentum transfer vector Q. Neutron scattering intensities $I_\perp^+(Q)$ and $I_\perp^-(Q)$ in a large saturating magnetic field are expressed as follows[4]:

$$I_\perp^\pm(Q) = \left\langle \left(F_n(Q) \pm F_m(Q)\right)^2 \right\rangle S_\perp(Q) + I_{incoh},$$

where $F_N(Q)$ and $F_M(Q)$ are the nuclear and magnetic scattering form factors of particles, respectively, $S_\perp(Q)$ is the interparticle correlation, I_{incoh} is the incoherent scattering intensity, and <...> denotes the average over the particle's size distribution. Since the incoherent scattering intensity is not negligible in the present SAPNS experiments, we thus analyzed the Q-dependent subtracted intensity:

$$I_\perp^+(Q) - I_\perp^-(Q) = 4\left\langle F_n(Q)F_m(Q)\right\rangle S_\perp(Q).$$

In such manner the incoherent scattering intensity is automatically cancelled using the polarized neutrons.

Fig.1 shows the subtracted intensity recorded in the Q-range of 0.02 - 0.1 Å^{-1} under a magnetic field of 9 kOe at 8.0 K. This can be analyzed by assuming the intraparticle magnetic structure and interparticle correlation.

Preliminarily, we measured the magnetization of PdFe fine particles and it was found that decreasing a particle size results in the reduction of saturation magnetization at 5 K. This indicates the non-magnetic surface shell in PdFe fine particles. Thus, we suppose that the particle consists of the magnetic core and non-

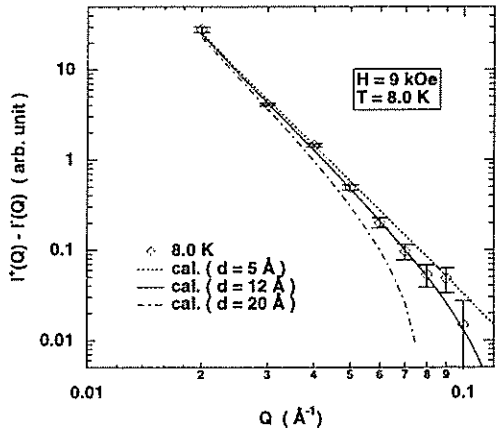

Fig.1 Q-dependent $I_\perp^+(Q) - I_\perp^-(Q)$ counted at 8.0 K ; the lines are calculated curves based on the core-shell model.

magnetic surface shell. (Fig.2). Assuming the shape of particle is spherical, the magnetic and nuclear form factors are expressed as follows:

$$F_n(Q) = \frac{4}{3}\pi r^3 b \frac{3j_1(Qr)}{Qr},$$

$$F_m(Q) = \frac{4}{3}\pi r_0^3 p \frac{3j_1(Qr_0)}{Qr_0},$$

$$j_1(x) = (\sin x - x\cos x)/x^2,$$

where b and p are the nuclear and magnetic scattering length density, r and r_0 are the radii of particle and magnetic core, and $j_1(x)$ is the first-order spherical Bessel function.

The present PdFe sample has the size distribution which follows the log-normal distribution function with median radius r_m=162 Å and σ = 0.4, and the magnetic scattering density of 0.37×10^{10} cm^{-2} as determined from TEM micrograph and the saturation magnetization, respectively. Only the non-magnetic surface shell thickness is unknown to analyze the neutron data. Based on the subtracted intensity calculated by parameterizing non-magnetic shell thickness, we obtain the best fitted shell thickness of 12 Å (Fig. 2). In addition, we should mention that the neutron data cannot be explained on the basis of the intraparticle structure with magnetically enhanced surface, as predicted for the Pd particle. In this analysis we intentionally neglected the interparticles correlation $S_\perp(Q)$ because it is almost unity in the experimental Q-range of $Q>0.04$ $Å^{-1}$ in the case of present particle size r_m = 162 Å.

We discuss the origin of non-magnetic surface shell validated by both the magnetization and neutron scattering data. We pay close attention to the possible localization of the conduction electrons at the surface owing to the surface effects. Such electron localization leads to the depletion of conduction electrons via which local magnetic Fe moments ferromagnetically interact in PdFe. This brings about the break down of the ferromagnetic coupling between Fe atoms so that the Fe moment at the surface should behave as paramagnetic. Thus, the non-magnetic surface region of the PdFe particle can be formed by the mechanism specific to the magnetic origin that the conduction electrons play an important role in the ferromagnetic ordering. This situation is very different from the case of the ferrite particles in which the superexchange interaction is the main origin of magnetic ordering. Alternatively, the magnetic moments of Fe atoms may dissolve into the 4d electrons sea of host Pd. In other words, the well localized Fe moments may become partly itinerant owing to the change in the Fermi level of 4d electrons sea of host Pd at the surface. This may be supported by the itinerant nature of the Fe rich PdFe system, e.g., $PdFe_3$[5].

The oxidation can be also responsible for the non-magnetic shell of particles, e.g., Ni particles[6], Co particles[7] and ferrite particles[8] exposed to the samples in air. However, we exclude the oxidation as a candidate for the origin for the non-magnetic shell because we kept the particles in evacuated quartz tubes after evaporation in this study with the purpose of not exposing them to air. Further, provided that the oxidation occurs during evaporation process, the uniform magnetic structure should be recognized in the PdFe particle even if the magnetism is weakened. The neutron scattering data, however, denies such uniformly oxidized particles. Thus, we believe that the non-magnetic surface is not a result of the oxidation process.

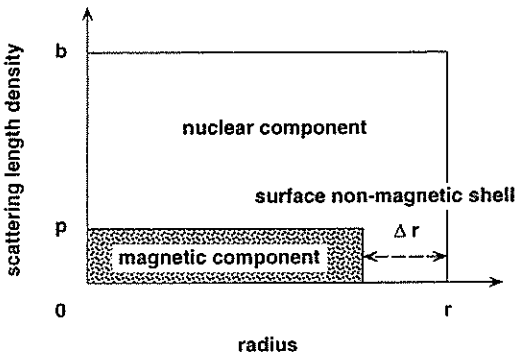

Fig.2 Schematic drawing of the intraparticle magnetic structure of the PdFe fine particle.

References

1) G. J. Nieuwenhusy, Adv. Phys. **24**, 515 (1975); J. A. Mydosh and G. J. Nieuwenhusy, in Ferromagnetic Materials, edited by E. P. Wohlfahrth (North-Holland, Amsterdam, 1980).
2) T. Taniyama, E. Ohta, and T. Sato, Europhys. Lett. (submitted).
3) T. Taniyama, E. Ohta, T. Sato, and M Takeda, Phys. Rev. B **55** (1997).
4) T. Taniyama, T. Sato, E. Ohta, and M. Takeda, Physica B **213&214**, 254 (1995).
5) P. Mohn, E. Supanetz, and K. Schwarz, Aust. J. Phys. **46**, 651 (1993); C. A. Kuhnen and E. Z. da-Silva, Phys. Rev. B **46**, 8915 (1992).
6) A. H. Morrish and K. Haneda, J. Magn. Magn. Mater. **35**, 105 (1983); M. Sato and K. Hirakawa, J. Phys. Soc. Jpn. **39**, 1467 (1975).
7) S. Itoh, Y. Endoh, and S. W. Charles, J. Magn. Magn. Mater. **111**, 56 (1992).
8) Z. X. Tang, C. M. Sorensen, K. J. Klabunde, and G. C. Hadjipanayis, Phys. Rev. Lett. **67**, 3602 (1991).

Non-uniform Magnetization Process of Fe/Au GMR Multilayers Investigated by Polarized Neutron Diffraction

N.HOSOITO, T.EMOTO and T.SHINJO

Institute for Chemical Research, Kyoto University, Uji, Kyoto-fu 611

In Fe/Au trilayer[1] and multilayer[2] systems, the existence of the magnetic indirect exchange coupling and the antiparallel alignment of adjacent Fe layers intervened by an Au layer was reported. This implies the occurrence of the giant magnetoresistance(GMR) effect. However the observed magnetoresistance change is very small[2] compared with typical GMR systems like Fe/Cr[3] and Co/Cu[4]. In order to judge whether the small GMR ratio $\Delta\rho/\rho$ is due to the inherent nature of the Fe/Au system or due to the imperfect antiparallel alignment of adjacent Fe magnetizations, it is important to determine the detailed magnetization process of the Fe/Au system. As the relevant property is the difference in the magnetization vectors of two Fe layers $M_{Fe1}-M_{Fe2}$, a conventional magnetization curve measurement cannot afford us substantial information because it is related to the sum of the magnetizations $M_{Fe1}+M_{Fe2}$. Neutron diffraction is a unique method in this context because both the sum $M_{Fe1}+M_{Fe2}$ and the difference $M_{Fe1}-M_{Fe2}$ are obtained from it.

We have carried out polarized neutron diffraction measurements of a multilayer sample of [Fe(9 A)/Au(34.5 A)]×60 grown on a GaAs substrate with using the TOP spectrometer. The thickness of the Au layer corresponds to the 2nd maximum of the magnetoresistance change as a function of the Au layer.[2] The intensities of the half and first order Bragg peaks, which come from the artificial periodicity, were obtained at room temperature with changing the applied field. From these data and conventional *M-H* curve data obtained by VSM, we have elucidated a non-uniform nature of the magnetization process of the Fe/Au multilayer.

In this report, we will deal with the applied field dependence of the sample polarization of the first order peaks defined as $P_1\equiv(I_+-I_-)/(I_++I_-)$, where $I_+(I_-)$ is a peak intensity when the incident neutron polarization is parallel (antiparallel) to the applied field. We considered three different magnetization processes and compared the calculated polarization P_1 with observed one. The first model is that two magnetization vectors, M_{Fe1} and M_{Fe2}, rotate uniformly with one vector clockwise and the other anticlockwise (Fig.1 model a). The second is that two magnetization vectors take either parallel or antiparallel alignment and the relative areas of two magnetic domains change during the magnetization process (model b). The third is a mixture of model a and b (model c). We attempt to fit the applied field dependence of 1) the half order diffraction intensity $I_{1/2}(H)$, 2) the first order diffraction intensity $I_+(H) + I_-(H)$, 3) the first order polarization $P_1(H)$ and 4) magnetization curve $M(H)$ based on the models a, b and c. In the case of model a, fitting parameters are the saturation magnetization M_s and the angle between the magnetization vector and the applied field θ. In the case of model b, the parameters are M_s and the relative ratio of parallel-alignment domain $x_{//}$. In the case of model c, besides the parameters used in the models a and b, the relative ratio of the magnetic domain corresponding to the model a x_a is a new parameter. After several trial and error processes, we have determined θ and $x_{//}$ from M/M_s. As for x_a, we simply assume $x_a=0.5$.

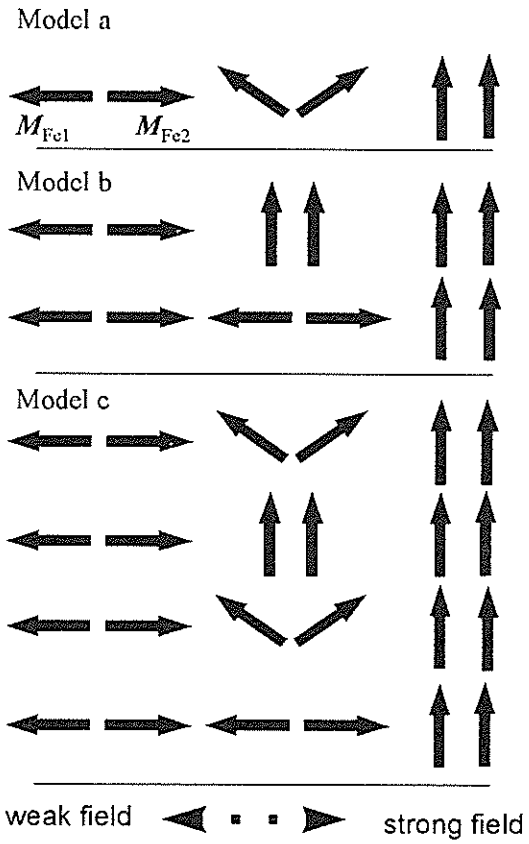

Fig.1 Three different models for the magnetization process

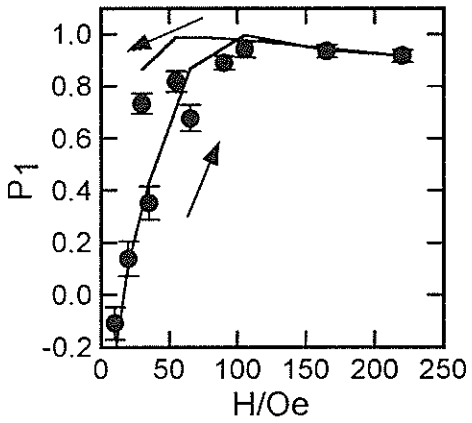

Fig.2 Observed (circle) and calculated (line) polarization of the first Bragg peaks in model a.

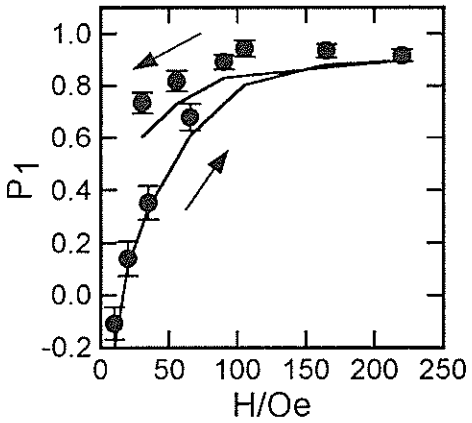

Fig.3 Observed (circle) and calculated (line) polarization of the first Bragg peaks in model b.

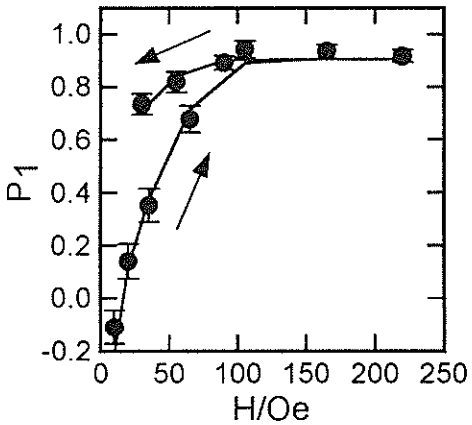

Fig.4 Observed (circle) and calculated (line) polarization of the first Bragg peaks in model c.

The applied field dependence of the calculated P_1 based on the model a and the observed P_1 is plotted in Fig.2. The uniform rotation model of the magnetization vectors is often used in the analysis of the *M-H* curves consisting of the exchange coupled trilayer and/or multilayer systems. Actually the magnetization process of the Fe/Cr multilayer is well reproduced with this model.[5] However in the present Fe/Au multilayer, the calculated P_1's are larger than the observed ones in most field range, and especially in the range of 30-90 Oe, the difference is much larger than the experimental error. This indicates that the magnetization process of the Fe/Au multilayer is by no means a simple rotation of the magnetization vectors. Figure 3 shows a comparison of the observed P_1 and the calculated P_1 based on the model b. Obviously this model cannot reproduce the observed date. The calculated P_1's are always smaller that the observed ones.

Failure in the fitting of the applied filed dependence of the polarization P_1 with the models a and b suggests that the magnetization process of the Fe/Au multilayer goes through a magnetic multidomain structure with large dispersion of the direction of the magnetization vectors. Therefore we attempt to sum up two magnetization processes, models a and b. The result is shown in Fig.4. A reasonable fitting is obtained in all applied field region. Of course there are so many possibilities of the magnetic domain structures if the magnetization process develops via magnetic multidomain structures, and a unique solution cannot be deduced from the obtained neutron diffraction and magnetization data. However, these analyses indicate that the magnetization reorientation from antiparallel to parallel is a non-uniform process in the Fe/Au multilayer.

References

1) A.Fuß, S.Demokritov, P.Grünberg and W.Zinn, J. Magn. Magn. Mater. 103, L221(1992)
2) K.Shintaku, Y.Daitoh and T.Shinjo, Phys. Rev. B47, 14584(1993)
3) M.N.Baibich, J.M.Broto, A.Fert, F.N.Van Dau, F.Petroff, P.Etienne, G.Creuzet, A.Friederich and J.Chazelas, Phys. Rev. Let. 61, 2472(1988)
4) D.H.Mosca, F.Petroff, A.Fert, P.A. Schroeder, W.P.Pratt Jr. and R.Laloee, J. Magn. Magn. Mater. 94, L1(1991)
5) N.Hosoito, K.Mibu, S.Araki, T.Shinjo, S.Itoh and Y.Endoh, J. Phys. Soc. Jpn. 61, 300(1992)

Polarized Neutron Reflectivity Measurements of Co/Cu Multilayers

M. Takeda, K. Saitoh, Y. Endoh, M. Suzuki* and Y. Taga*

Physics Department, Graduate School of Science, Tohoku University, Sendai 980-77, Japan
**TOYOTA Central Research and Development Laboratories, Inc., Nagakute, Aichi 480-11, Japan*

A Co/Cu multilayer is a typical example which shows a giant magnetoresistance (GMR) effect [1]. The GMR effect is the phenomenon which appears in metallic multilayers with a structure alternate magnetic and nonmagnetic layers. In these multilayers such as Fe/Cr [2], NiFeCo/Cu [3] and NiFe/Cu [4], ferromagnetic moments in the magnetic layers are coupled antiferromagnetically through adjacent nonmagnetic layers. The antiferromagnetic alignment is changed to ferromagnetic one by an external magnetic field. An anomalously large change of resistivity is accompanied by the transition. As well as this change of magnetic structure, it is believed that interfacial scattering of conduction electrons is essential to the GMR effect. Therefore the interfacial roughness between magnetic and nonmagnetic layers is closely related to the GMR effect. Up to now there are a lot of works to reveal the relation between the interfacial roughness and the GMR effect. Neutron reflection measurement is a powerful technique for the investigation of such interfacial roughness. X - ray reflection measurement is also available, however, neutron has the advantage of X - ray because the neutron is sensitive to magnetic moments in the multilayers.

Recently Co/Cu multilayers with different interfacial roughness were synthesized by codeposition of Co and Cu at the interface of these two layers and have been investigated by X-ray diffraction and NMR [5]. We have done the polarized neutron reflectivity measurements of such Co/Cu multilayers to study the interfacial roughness and magnetic disorder at the interfaces induced by the existence of mixed layers.

The Co/Cu multilayers are prepared on Si substrates with the SiO_2 surface by a magnetron sputtering. The samples are described as follows : substrate / Fe(50) / Cu(22 - t_{mix} / 2) / CoCu(t_{mix}) / [Co(10 - t_{mix}) / CoCu(t_{mix}) / Cu(22 - t_{mix} / 2) / CoCu(t_{mix})]$_{15}$ / Co(10 - t_{mix}) / Cu(22 - t_{mix} / 2), where the values in the parentheses are the thickness of layers in units of Å and the subscript of the square bracket is the number of Co/Cu bilayer. The t_{mix} expresses the thickness of the Co/Cu mixed layers. The thicknesses of t_{mix} used in this experiment are 0, 1.0, 1.5 and 2.5 (Å) . Hereafter these samples are denoted by sample A, B, C and D, respectively.

The polarized neutron reflectivity measurements have been performed on the TOP spectrometer at KENS. Unpolarized neutrons with a wavelength band of 3 - 9 Å were polarized by a polarizing neutron device which consists of Fe/Si polarizing supermirrors and then introduced to the sample. Collimation of the incident neutrons was defined by two pairs of slit with distance of 1,800 mm and is 0.8 (mrad). The reflected neutrons were detected by one of positional channel of a 1D position sensitive detectors where the reflected neutrons hit. The measurements covered the Q range of 0.01 - 0.15 Å^{-1} by changing the scattering angles. In this report the data in the low Q region are discussed. External magnetic fields were applied in the sample plane.

Figure 1 shows the polarized neutron reflectivities of the sample A in the field of 40 Oe which is a guide field to maintain the polarization of neutrons. The field is not large enough to destroy the antiferromagnetic alignment of the ferromagnetic moments in the Co layers. Reflectivities when the polarization of incident neutrons is parallel to the guide fields are plotted by open circles and that of antiparallel by solid circles. The differences between open and solid circles are observed although antiferromagnetic structures should make no difference between them. This is due to the ferromagnetic moments in the seed layer of Fe on the substrate.

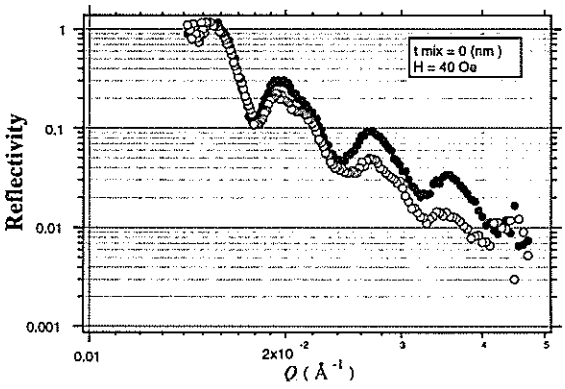

Fig. 1 Polarized neutron reflectivities of Co/Cu multilayer with no mixed layer, sample A (t_{mix} = 0 Å). Open circles are reflectivities under the condition that polarization of incident neutrons is parallel to the guide field of 40 Oe, and solid circles antiparallel.

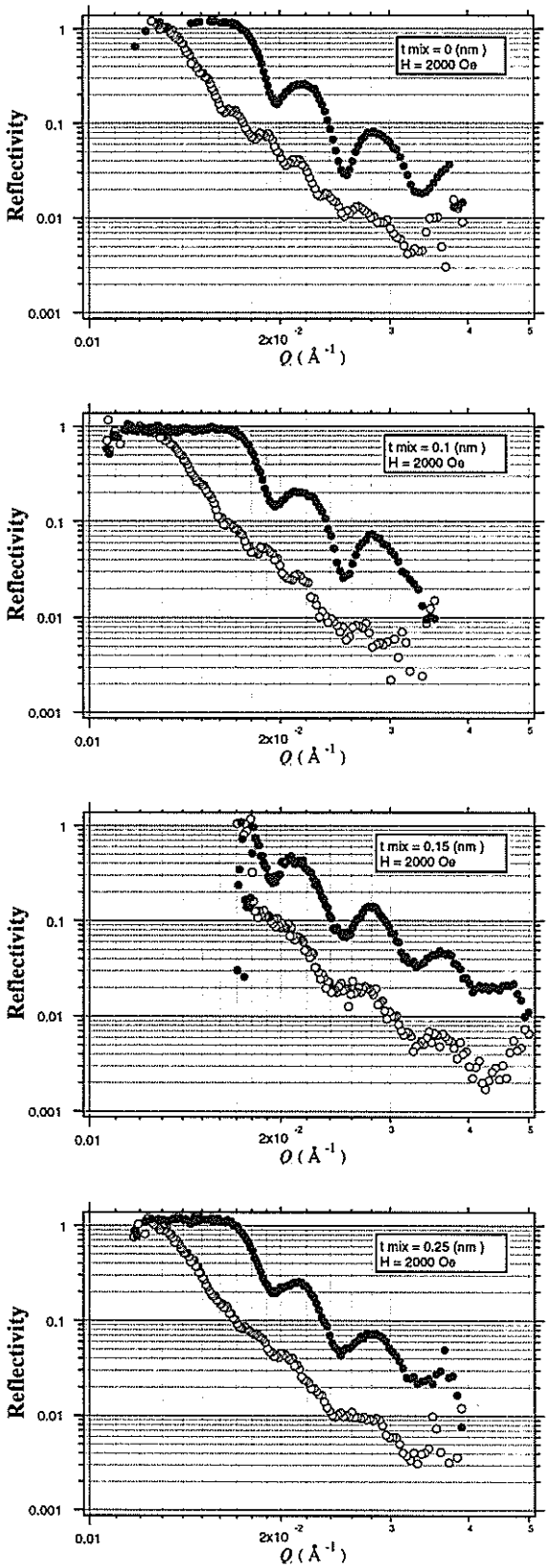

Fig. 2 Polarized neutron reflectivities of Co/Cu multilayers with different interfacial roughness, sample A, B, C and D, respectively, in the ferromagnetic alignment of the Co layers under magnetic fields of 2000 Oe.

Under the weak external field there are domain structures in the ferromagnetic Co layers. Such domain structures which depend on hysteresis has an influence on reflectivities. To exclude the influence of the domain structures the reflectivities were measured in the ferromagnetic alignment induced by strong magnetic fields. The magnetic field dependence of reflectivity curves of sample A, B, C and D in the ferromagnetic alignment induced by external fields of 2000 Oe are plotted in Fig. 2. Open and solid circles are the same as in Fig. 1.

Figure 2 shows that the difference of thickness of the mixed layer, t_{mix}, clearly appeared in the profile of reflectivity curves. Preliminary simulation of the t_{mix} dependence of the reflectivity curves has been performed by using the standard matrix method [6]. In the calculation the mixed layer was regarded as a homogeneous layer which had the average density of scattering length of Co and Cu atoms. In other words, interfacial structure of atomic configuration of Co and Cu atoms was ignored. In this approximation the reflectivity in the low Q region was insensitive to the t_{mix} while the peak height and half width of half maxima of Bragg peak, which appears at around Q = 0.098 Å^{-1} (= 2π / 32 (Å)), from Co/Cu bilayer was affected by the mixed layers. Although the approximation is too simple to explain the observed reflectivity curves shown in Fig. 2, it is conclude that the polarized neutron reflectivity is very sensitive to the interfacial roughness. The analysis including the detailed structure of interface is now in progress.

This work was supported by a Grant-in-Aid for Scientific Research (A) (No. 05402011) and (C) (No. 06640463) from the Ministry of Education, Science, Sports and Culture .

References

1) S.S.P. Parkin, Z. G. Li and D. J. Smith, Appl. Phys. Lett. **58** (1991) 2710.
2) M. N. Baibich, J. M. Broto, A. Fert, F. Nguyen, Van Dau, F. Petroff, P. Etienne, G. Creuset, A. Friedrich and J. Chazelas, Phys. Rev. Lett. **62** (1988) 2472.
3) H. Sakakima and M. Satomi, J. Magn. Magn. Mater. **121** (1993) 374.
4) T. Shinjo and H. Yamamoto, J. Phys. Soc. Jpn. **59** (1990) 3061.
5) M. Suzuki, Y. Taga, A. Goto and H. Yasuoka, Phys. Rev. **B24** (1994) 18580.
6) M. Born and E. Wolf: *Principles of optics*, (Pergamon Press, Oxford, 1970).

Small Angle Neutron Scattering Study of the Magnetic Correlation in Magnetic Particles Dispersed in Polymer.

T. OKU, T. SATO and M. FURUSAKA[1]

Department of Materials Science, Keio University, 3-14-1, Hiyosi Kohoku-ku, Yokohama 223
[1]National Laboratory for High Energy Physics, 1-1 Oho, Tsukuba-shi, Ibaraki 305

Systems consisting of single-domain magnetic particles show spin-glass-like behavior such as relaxation of remanence, susceptibility peaks and irreversibility [1-6]. Such a magnetic behavior is generally determined by the intraparticle anisotropy and the interparticle dipole interaction. When the intraparticle anisotropy is dominant, the spin-glass-like behavior should be interpreted based on the modified superparamagnetic (blocking) model [4,5]. On the other hand, when the energy of the interparticle interaction is comparable with that of the intraparticle anisotropy, the system exhibits magnetically complex behavior based on the magnetic ordering via the interparticle interaction[6]. To understand such magnetically complex properties of a strongly interacting system in detail, we need information on the magnetic structure, i.e., the interparticle magnetic correlation. Neutron scattering experiment is particularly appropriate for studying magnetic structure, since it provides us direct information on the magnetic correlations. However, there has been no detailed neutron scattering study on the interparticle magnetic correlation in single-domain particle systems. In this study, we performed small-angle neutron scattering (SANS) measurements on MnZn-ferrite particles randomly dispersed in polystyrene matrix in which a strong interparticle interaction is realized [7].

In the present neutron scattering experiment, we used unpolarized cold neutrons with energy E ~ 1 meV. The measuring time of this neutron scattering measurement is $\sim 10^{-12}$ s which is much shorter than the attempt frequency ν_0 of the present particle moments ($\sim 10^{-9}$ s). Therefore, the neutron scattering measurements observe the static particle moment at even sufficiently high temperatures. In the case of unpolarized cold neutrons, it is possible to deduce only the magnetic scattering attributed to the interparticle magnetic correlation by subtracting the background scattering from the total neutron scattering obtained at low temperatures, because the interference term between nuclear and magnetic structure factors is automatically cancelled out.

The SANS intensity was measured at 78 and 320 K by using the time of flight (TOF) type small-angle neutron scattering instrument (SAN) installed at the guide hall of the pulsed neutron facility (KENS) at the National Laboratory for High Energy Physics (KEK). In the neutron scattering experiment using the SAN spectrometer, we used pulsed beams of incident neutron wavelength in the range of 3 - 8 Å, which makes it possible to measure the scattering intensity over a q-range of $0.008 \leq q \leq 0.2$ Å^{-1}. In this apparatus, a two-dimensional position sensitive detector (2D-PSD) system composed of 43 one-dimensional detectors was positioned at 3 m from the sample.

The SANS spectrum of the polymer matrix without particles was obtained as background data. The scattering intensity from the magnetic particles was extracted by subtracting the polymer data from the total scattering intensity. Fig. 1 shows the q-dependence of the scattering intensity I_P from the magnetic particle obtained at 77 and 320 K. The inset in Fig. 1 shows the difference between the SANS intensities at 77 and 320K, I_{77K}-I_{320K}. The scattering line shape is dependent on temperature at q-values less than 0.03 Å^{-1} above which it is independent of temperature. Therefore, the scattering intensity for

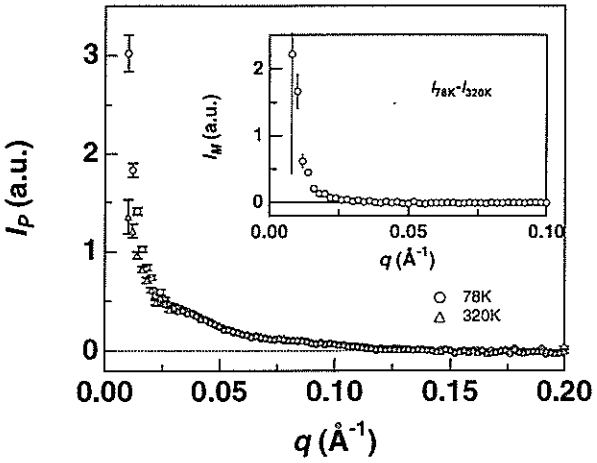

Fig. 1 The small-angle neutron scattering intensity from particles I_p as a function of temperature.

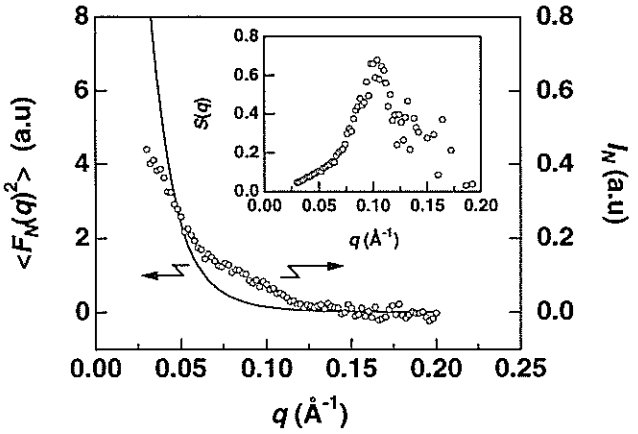

Fig.2 The calculated $<F_N(q)^2>$ and the neutron nuclear scattering intensity I_N are plotted as a function of q. (Inset : $S(q)$ vs q)

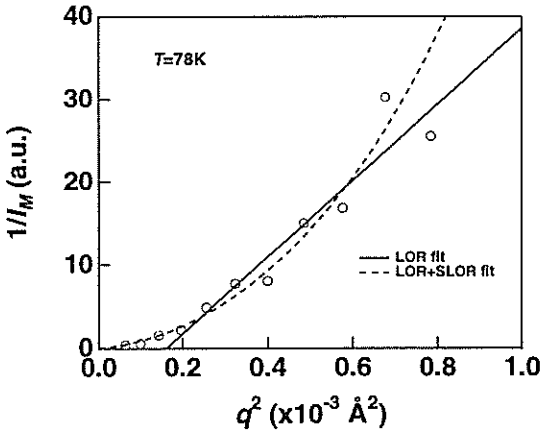

Fig.3 Inverse intensity $1/I_M$ vs q^2 plot.

q>0.03 Å^{-1} is mainly attributed to the nuclear scattering from particles. The nuclear scattering intensity I_N from the particles are described by

$$I_N(q) = \alpha <F_N(q)^2> S(q) + I_{\text{incoh}}, \quad (1)$$

where α is a constant related to the number density of particles and the instrumental coefficient, $F_N(q)$ the nuclear scattering amplitude, $S(q)$ the structure factor and I_{incoh} the incoherent scattering intensity. The bracket <...> represents the average over the distribution of the particle size. Since I_{incoh} is negligibly small under the present condition, we can estimate $S(q)$ by calculating $<F_N(q)^2>$. To calculate $<F_N(q)^2>$, we took account of the particle size distribution obtained by the transmission electron microscopy (TEM) observation. The nuclear scattering amplitude $F_N(q)$ is given for spherical particles as follows:

$$F_N(q) = \frac{4}{3}\pi (b - b_S) a^3 g(qa) + \frac{4}{3}\pi b_S a_S^3 g(qa_S) \quad (2)$$

$$g(x) = 3(\sin x - x\cos x)/x^3, \quad (3)$$

where a and a_S are the physical radius of particles and whole radius of a particle including the surfactant layer, b and b_S are the nuclear scattering length densities of the particles and the surfactant material, respectively. Fig.2 shows the calculated value of $<F_N(q)^2>$ and the obtained nuclear scattering intensity I_N as a function of q. The inset of Fig.2 shows $S(q)$ estimated based on Eq. (1). A peak in $S(q)$ is shown around q=0.104 which corresponds to the average interparticle distance $<d_i>$ =60.4 Å. This interparticle distance suggests that the surfactant layer of a particle is in contact with those of the neighboring particles. Thus, the strong interparticle interaction is expected in this sample.

The inverse magnetic scattering intensity I_M^{-1} is plotted against q^2 in Fig.3. The solid straight line in Fig.3 denotes a conventional Lorentzian obtained by the least-squares fitting performed over a q-range from 0.015 to 0.03 Å^{-1}. However, I_M^{-1} is insufficiently represented by the Lorentzian at low q. The dotted line in Fig.3 denotes the function of Lorentzian (LOR) plus squared Lorentzian (SLOR) with the same inverse correlation length κ for both terms:

$$I(q) = \frac{A}{(q^2 + \kappa^2)} + \frac{B}{(q^2 + \kappa^2)^2} \quad (4)$$

where A and B are the LOR and SLOR coefficients. It is found that the magnetic scattering line shape at 78 K is well described with the function of LOR plus SLOR appropriate for a system in which random fields destroy the long-range order. It is well known that the LOR term represents the long-range spin fluctuation while the SLOR is used to describe the short-range spin fluctuation [8,9] relevant to the destruction of ferromagnetic ordering by the random field [10] or the random-size cluster formation [11]. This suggests that in the present sample local ferromagnetic cluster configuration is attained through the interparticle dipole interaction at 77 K, where the long-range order does not exist probably due to the random field. The origin of the random field is expected to be the intraparticle anisotropy, since the anisotropy axes of particles are randomly oriented in the present sample. In the present system, however, the intraparticle anisotropy energy E_A is about ten times smaller than the interparticle interaction energy E_I. We must check the feasibility of such

weak intraparticle anisotropy for the random field which prevents the occurrence of the long-range order via the interparticle interaction in the present system. A magnetic property of a ferromagnet with such weak random anisotropy was theoretically studied by Chudnovsky et al [12]. According to their study, for such weak anisotropy case, a long-range order is destroyed by the random anisotropy and divided into domains. Moreover, Fe-rare earth metal amorphous alloys with such weak anisotropy is experimentally studied by means of small angle neutron scattering, and a reduction of correlation length due to the random field effect was observed [13]. Their results are consistent with our picture which explains the result of the present neutron scattering experiment. Therefore, we believe that intraparticle anisotropy behaves as an effective random field.

In conclusion, the neutron magnetic scattering line shape of the MnZn-ferrite particles randomly dispersed in polymer is well represented by the function of Lorentzian plus squared Lorentzian which is appropriate for a random anisotropy field system. The local ferromagnetic clusters form via the interparticle interaction at 78 K in the present system. The intraparticle anisotropy could have a random field effect which prevents the occurrence of the long-range order via the interparticle interaction.

References

[1] J. L. Dormann, L. Bessais and D. Fiorani, J. Phys. C: Solid State Phys. **21** (1988) 2015.
[2] M. Holmes, K. O'Grady and J. Popplewell, J. Magn. Magn. Mater. **85** (1990) 47.
[3] R. W. Chantrell, M. El-Hilo and K. O'Grady, IEEE Trans. Magn. **27** (1991) 3570.
[4] M. El-Hilo, K. O'Grady and R.W. Chantrell, J. Magn. Magn. Mater. **144** (1992) 295.
[5] M. El-Hilo, K. O'Grady and R.W. Chantrell, J. Magn. Magn. Mater. **144** (1992) 307.
[6] S. Mørup, F. Bødker, P. V. Hendriksen and S. Linderoth, Phys. Rev. B **52** (1995) 287.
[7] T. Oku, T. Sato and E. Ohta, J. Magn. Magn. Mater. **148** (1995) 116.
[8] K. Motoya, S. M. Shapiro and Y. Muraoka, Phys. Rev. B **28** (1983) 6183.
[9] G. Aeppli, S. M. Shapiro, R. J. Birgeneau and H. S. Chen, Phys. Rev. B **28** (1981) 5160.
[10] A. Aharony, Y. Imry and S. Ma, Phys. Rev. Lett. **37** (1976) 1364.
[11] H. R. Child, J. Appl. Phys. **52** (1981) 1732.
[12] E. M. Chudnovsky, W. M. Saslow and R. A. Serota, Phys. Rev. B **33** (1986) 251.
[13] J. J. Rhyne, IEEE Trans. Magn. MAG-**21** (1985) 1990.

Inelastic Neutron Scattering of a Spin-Peierls system.

M.FUJITA[a], M.ARAI[b], M.MOTOKAWA[c], O.FUJITA[d], J.AKIMITSU[d] and S.M.BENNINGTON[e]

[a] Department of Physics, Kobe University, 1-1 Rokkodai, Nada, Kobe 657
[b] National Laboratory for High Energy Physics, 1-1 Oho, Tsukuba 305
[c] Institute of Material Research, Tohoku University, Katahira, Sendai 980
[d] Department of Physics, Aoyama-Gakuin University, Chitosedai, Setagaya, Tokyo 157,
[e] ISIS facility, Rutherford Appleton Laboratory, Chilton, Didcot, Oxford shire, OX11 0QX

In the low-dimensional antiferromagnetic (AF) system, quantum effects are extremely important for the spin dynamics at low temperature. The strong quantum spin fluctuation brakes the classical Néel state. However, detailed physical pictures are not entirely understood. In addition, their intrinsic physics links with high temperature superconductivity. Therefore study on the ground state of the quantum spin system is one of the most attractive and important problem in the modern solid state physics.

Recent discovery of the first inorganic spin-Peierls(SP) compound $CuGeO_3$[1] (T_{sp}=14K) have an important meaning.

SP transition is a structural phase transition which is combined to the spin system, and occurs in a strong fluctuated spin system. Hence $CuGeO_3$ is one of the ideal compounds to study quantum magnetism as well as SP transition itself. Therefore, we have performed inelastic neutron scattering measurements in order to investigate the spin dynamics of $CuGeO_3$ and to clarify some possible difference from that of the uniform AF system. Experiments have been done on the INC spectrometer installed at the KENS pulsed neutron facility of National Laboratory for High Energy Physics in Japan. We prepared five single crystals grown by the floating-zone method. The volume of each crystal was about $5\times10\times25mm^3$ and the total weight was 12.8g. The sample was mounted, as the one-dimensional chain direction (c*-axis) is vertical and perpendicular to the incident neutron beam, so that the magnetic excitation spectrum in the wide range of the q-ω space can be observed simultaneously. The experiment was performed at 10K, with incident energy Ei=35meV and 90meV.

The magnetic excitation of one dimensional AF system is characterized by a spin excitation continuum which results from spin fluctuation It is surrounded between lower excited state, i.e., des Cloizeaux-Pearson (dCP) mode[2,3]. and the upper state with twice the energy and periodicity of dCP. They are illustrated in Fig.1 with scan loci of time of flight (TOF) scans made by detectors of INC when the c*-axis was aligned vertical to the incident neutron vector $\boldsymbol{k}_i$ with Ei=90meV

Figure 2 indicates the observed S(q,ω) along each solid line in Fig.1 with the calculated S(q,ω) in which the experimental resolution was taken into account.[5] Their

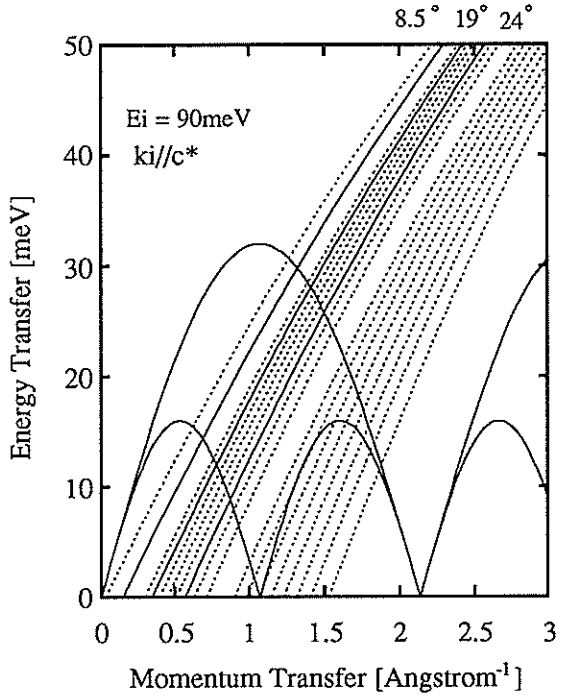

Fig.1 Magnetic excitation spectrum and TOF scan loci for INC.

scattering angle are 8.5 ° ,19 ° and 24° ,respectively. The continuum region can be seen along each scan locus. The intensity along the high angle detector agrees well with theoretical result. However, the intensity along the low angle detector cannot be reproduced by using the same parameters. The observed intensity is strong at the zone boundary(ZB) where scan locus crosses dCP mode. This behavior is consistent with each results for different geometrical configurations of the measurement and incident energies.

Though the one dimensionality of the magnetic correlation of $CuGeO_3$ is considerably relaxed, the spin excitation continuum can be seen clearly in our experiment. Hence, we should consider in more detail what is the origin of spin fluctuations. Recently, it was reported that a competing exchange interaction between nearest neighbor(NN) and next nearest neighbor(NNN) has an important role for the magnetic properties of $CuGeO_3$[6,7]. This is one the possibility.

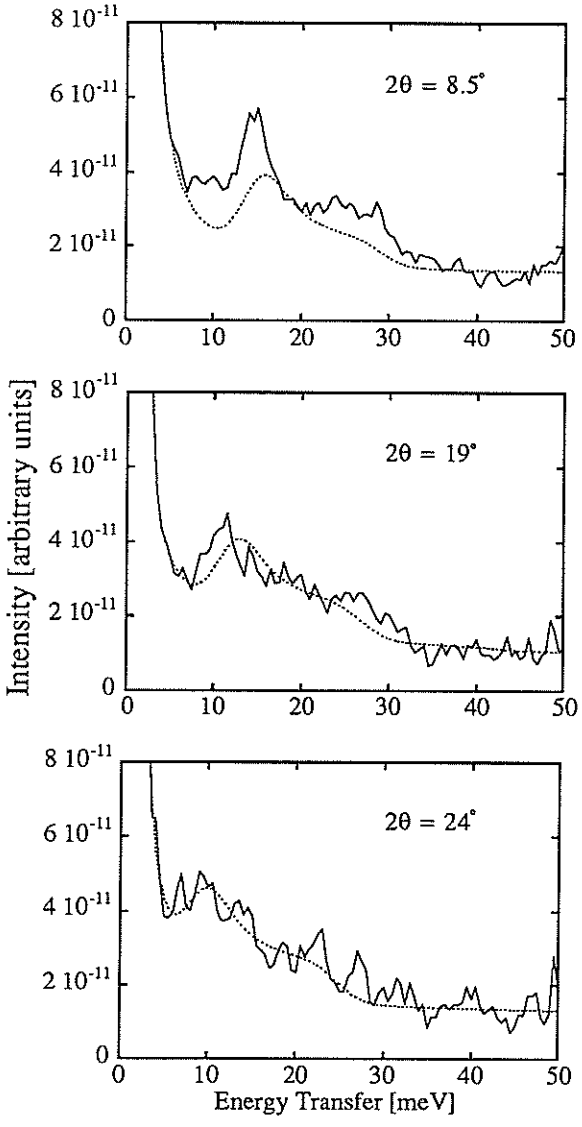

Fig.2 The comparision of the observed S(q,w) with the calculated results along each scan locus.

The observed intensive peak at the ZB is consistent with previous result under independent condition.[8] Therefore, we consider that the intensive peak at the ZB is characteristic of $CuGeO_3$. However, the behavior can not be seen in the experimental result of uniform AF system which was obtained by Endoh et al., Nagler et al., and Dender et al., respectively.[9,10,11]
The difference also could be explained by the competition between NN and NNN interaction. We should compare our results with theoretical results for SP system which is taken a competing of interaction and dimensionality into account.

[1] M.Hase et al., Phys. Rev. Lett. **70**, 3651 (1993)
[2] T.Yamada, Prog. Theor. Phys. Jpn. **41**, 880 (1969)
[3] J.des Cloizeaux and J.J.Pearson, Phys. Rev. **128**, 2131 (1963)
[4] S.E.Nagler et al., Phys. Rev. B **44** 12361 (1991)
[5] G.Müller et al., Phys. Rev. B **24**, 1429 (1981)
[6] G.Castilla et al., Phys. Rev. Lett. **75**, 1823 (1995):
[7] S.Haas et al., Pyhs. Rev. B **52**, R14396 (1995)
[8] M. Arai et al., Phys. Rev. Lett. **77** 3649 (1996)
[9] Y.Endoh et al., Phys. Rev. Lett. **32** 170 (1974)
[10] S.E.Nagler et al., Phys. Rev. B **44** 12361 (1991)
[11] D.C.Dender et al., Prys. Rev. B **53** 2583 (1996)

Neutron Depolarization Measurements of $YBa_2Cu_3O_{7-\delta}$

K. KURAHASHI, M. TAKEDA, Y. ENDOH and S. ITOH*

Physics Department, Graduate School of Science, Tohoku University, Sendai 980-77
**National Laboratory for High Energy Physics, 1-1 Oho, Tsukuba-shi, Ibaraki 305*

The mixed state in high-T_c superconductors has been intensively investigated in order to determine the symmetry of Cooper pairs (s - wave or d -wave). Neutron depolarization is one of the useful techniques to study the symmetry [1]. We have done depolarization measurements of a single crystal of $YBa_2Cu_3O_{7-\delta}$ (YBCO) which was grown by TSSG (Top Seeded Solution Growth) method.

Neutron depolarization measurements have been performed on the TOP spectrometer at KENS. The wavelength dependencies of depolarization are shown in Fig. 1. The sample was cooled down under a magnetic field of 120 Oe which was removed before starting the measurements. During the measurements a weak external field (7 Oe) was applied to the sample in order to maintain the polarization of incident neutrons and to make its direction to be perpendicular to the trapped flux. In Fig. 1, the oscillation of depolarization spectra appeared with decreasing temperature. This indicates that magnetic flux was excluded from the pinning centers due to thermal fluctuations near T_c (~ 65 K).

Figure 2 shows the lower critical field, H_{c1} , parallel to the c -axis which was determined by fitting the depolarization spectra obtained in the following procedure with the Bean model [2]. After zero field cooling, a weak magnetic field was applied parallel to the c - axis for one minute and removed before the measurements. When the magnetic fields were higher than H_{c1}, the magnetic flux penetrated into the sample and the deporalization spectra oscillated against wavelength. If no oscillation appeared at one measurement, the magnetic fields were slightly increased at the next measurement. The procedure was continued until the oscillation was observed. H_{c1} was defined as the lowest field in which the oscillation occurs. As a preliminary result, the temperature dependence of H_{c1} indicates the s - wave symmetry of Cooper pair.

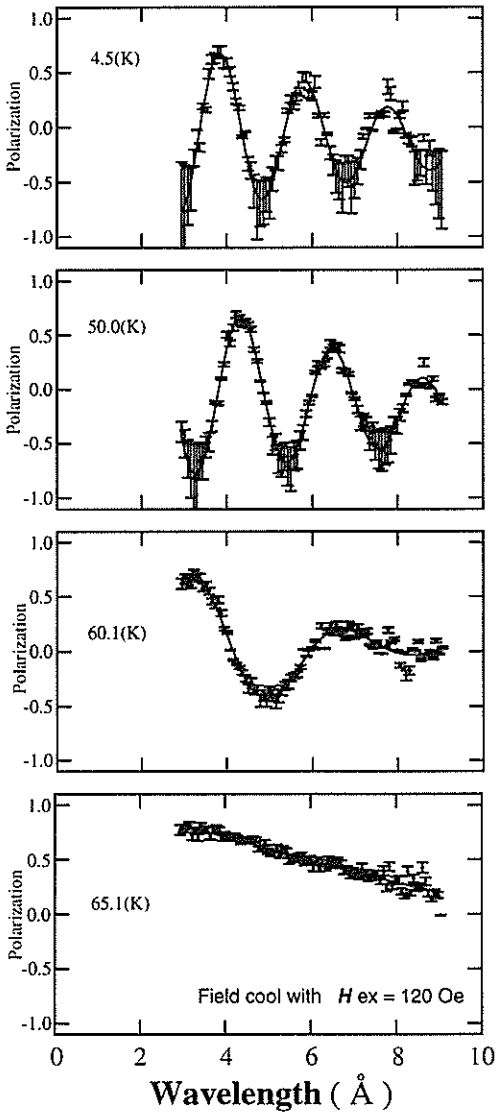

Fig. 1 Depolarization Spectra of YBCO

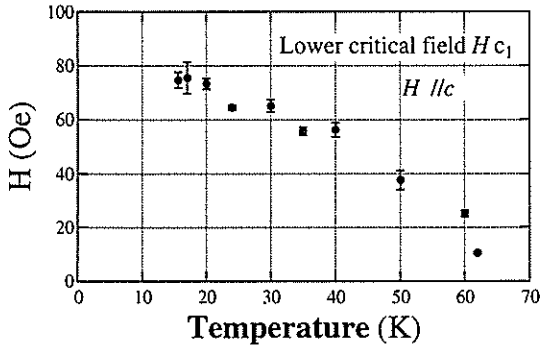

Fig. 2 Temperature dependence of H_{c1}

References

1) T. Watanabe, Y. Endoh, S. Itoh, H. Kojima, I. Tanaka and N. Toyoda: KENS REPORT-VIII (1989/90) 132.
2) C.P.Bean: Rev. Mod. Phys. 36(1964) 31.

Space time symmetry violation

Y. Masuda

National Laboratory for High Energy Physics, 1-1 Oho, Tsukuba-shi, 305 Japan

In this report, we discuss the experimental studies on *P*- and *T*-violation in neutron nucleus interaction which have been carried out in the PEN collaboration. The members of the collaboration are T. Adachi (KEK), K. Asahi (TIT), S. Ishimoto (KEK), A. Masaike (Kyoto), Y. Matsuda (Kyoto), K. Morimoto (KEK), S. Muto (KEK), K. Sakai (TIT), H. Sato (TIT), H.M. Shimizu (Riken), A. Yoshimi (TIT) and some other students. We have been carrying out the *P*-violation experiments and developing experimental methods in order to carry out the *T*-violation experiment. Here, the summary of these studies.

I Introduction

Since the discovery of the parity (*P*) violation in nuclear β decay, symmetry violations under space and time reversals have been a matter of great concern in fundamental physics. Many experiments have been carried out on *P*-, *T*- and *CP*-violating processes. Experiments in the baryon-baryon interaction give us unique knowledge of the weak interaction, the quark-quark neutral current.[1] In the low energy nuclear processes, the weak interaction is discussed in terms of meson exchange, since heavy weak boson exchange is suppressed in nucleon-nucleon (NN) interaction by the nuclear repulsive core. W or Z exchange is hidden in the nucleon-nucleon-meson (NNM) vertex. In the NN weak interaction, no contribution is from π^o exchange according to the Barton's theorem. $\pi^{\pm}$ exchange by the charged weak current is suppressed by a factor of $\sin^2\theta_c$, while $\pi^{\pm}$ exchange by the neutral current has no suppression of the Cabibbo mixing. θ_c is the Cabibbo angle. The next light meson is ρ meson. Since ρ meson is a vector meson, the Cabibbo-allowed amplitude in ρ exchange is not suppressed by the Barton's theorem. The contribution of ρ exchange is relatively enhanced.

The effect of the weak NN interaction is found in a helicity dependent term. The helicity dependent term induces a small spin rotation around the momentum and a helicity dependent cross section. In neutron propagation through a Bi target, the spin-rotation angle is $\theta_w = 6 \times 10^{-9}$ rad/cm.[2] The value was estimated by using the sum of *P*-violating NN interactions in the nucleus.

In nuclei, the small *P*-violating effect is occasionally enhanced. The spin rotation for cold neutron propagation through a ^{117}Sn target was found to be $\theta_w = (3.7\pm0.3) \times 10^{-5}$ rad/cm .[3] Large *P*-violating effect was also found in p-wave neutron-nucleus-resonance cross sections.[4,5,6,7] The enhancement has been explained in various ways.[8, 9,10] One of them is an s- and p-wave parity mixing in the compound nucleus resonance. The s-p

mixing theory predicts large enhancement also in T-violating effect.

P- and T- violating NNM couplings induce T-violating neutron propagation through a nuclear target as well as the neutron electric dipole moment (EDM). The neutron EDM gives us a limit for the P- and T- violating NNM coupling constant.[11,12] If we take the ratio of a T-violating to P-violating term in the polarized neutron propagation, nuclear uncertainty is greatly reduced. As a result, comparison with the neutron EDM becomes possible.

Here, we discuss P- and T-violating experiments on the neutron propagation through a nuclear target.

II P- and T- violating neutron propagation

The effect of the neutron-nucleus interaction upon propagation through a target is found in a phase shift of a neutron wave. After propagation through matter, the neutron wave is represented in terms of a incident neutron wave Ψ_0 and a interaction Hamiltonian H_I.

$$\Psi = \exp(-\mathrm{i}\, H_I\, t/\hbar)\ \Psi_0\,. \tag{1}$$

The exponential term is a dynamical phase shift. The dynamical phase shift upon propagation through a nuclear target is represented in terms of forward scattering amplitude $f(0)$,

$$\Delta = -H_I\, t/\hbar = \lambda\, l\, \rho\, f(0). \tag{2}$$

Here, λ is the neutron wave length, l a neutron propagation length and ρ a nuclear number density. The general form of the scattering amplitude for the polarized nucleus can be described as[13,14]

$$\begin{aligned} f(0) &= F_0 + F_1\,\sigma_x + F_2\,\sigma_y + F_3\,\sigma_z \\ &= F_0 + F_1\,\sigma\cdot\hat{\boldsymbol{I}} + F_2\,\sigma\cdot(\hat{\boldsymbol{k}}\times\hat{\boldsymbol{I}}) + F_3\,\sigma\cdot\hat{\boldsymbol{k}}. \end{aligned} \tag{3}$$

Here, σ is the Pauli spin operator, $\boldsymbol{I}$ the nuclear spin and $\boldsymbol{k}$ the neutron momentum. F_i ($i = 0, 1, 2, 3$) are spin dependent scattering amplitudes. The phase shift Δ is represented in the same form as Eq. (3) by replacing F_i with ϕ_i.

$$\phi_i = \lambda l \rho F_i. \tag{4}$$

The first and second terms of Eq. (3) are the coherent scattering amplitude and spin incoherent amplitude, respectively, which are due to the strong interaction. The fourth term is a P-violating weak interaction term. In the low energy neutron-nucleus resonance, the P-violating effect is greatly enhanced because of very narrow level spacing between resonance states. Further enhancement is expected in the p-wave resonance because of a difference in a centrifugal barrier between s- and p-wave states. According to the s-p mixing theory, the P-violating scattering amplitude is represented as[11]

$$\begin{aligned} F_3 \propto \lambda\, &\{\sqrt{\Gamma_s^n}/(E - E_s + \mathrm{i}\Gamma_s/2)\} \\ &\langle s\,|\,H_w\,|\,p\,\rangle\{\sqrt{\Gamma_p^n}/(E - E_p + \mathrm{i}\Gamma_p/2)\}. \end{aligned} \tag{5}$$

The real part of F_3 induces a neutron-spin rotation around its momentum by $2\mathrm{Re}(\phi_3)$ rad. In the p-wave resonance, the rotation angle has a dispersion like shape as a function of neutron energy. The imaginary part induces a helicity

dependent cross section. The helicity dependent cross section has a form of Breit-Wigner shape.

The third F_2 term in Eq. (3) is a T-odd and P-odd triple correlation term. The measurement of the F_2 term has three advantages as a T-violation experiment. Firstly, a large enhancement is expected as in the P-violating term. Secondly, the effect is free from final state interactions, since the initial and final states are the same plane wave. Thirdly, the ratio of the T-violating to P-violating term is insensitive to the nuclear wave-function. As a result, the measurement can be compared with other elementary-particle experiments, for example neutron EDM measurements. Therefore, many experimental methods have been proposed to measure the triple correlation term.[14,15,16,17]

III. Measure of T-violation

We discuss a new method, where the neutron spin rotates by 180° around the nuclear spin from the forward to backward direction during propagation through a polarized nuclear target. The T-violation effect is found in a change in a neutron-spin-flip probability upon the reversal of the incident neutron spin, nuclear spin or neutron-spin rotation.

The density matrices of the incident neutron-spin state is

$$\rho = 1/2 \cdot (1 + \boldsymbol{P}_o \cdot \sigma). \quad (6)$$

$\boldsymbol{P}_o$ is an incident neutron polarization. After propagation, the density matrix is modified in the presence of the phase shift as

$$\rho_f = F\,\rho\,F\dagger, \quad (7)$$

where, F is

$$F = \exp(i\Delta). \quad (8)$$

The flipped neutron spin state is singled out after the propagation. The selection of the spin state is represented in terms of the projection operator for the parallel or anti-parallel spin state to the z axis,

$$P = 1/2 \cdot (1 + \boldsymbol{P}_a \cdot \sigma). \quad (9)$$

$\boldsymbol{P}_a$ is an analyzer nuclear polarization. In the ideal experiment, the incident neutron spin and analyzer polarization are along the neutron-momentum axis (z axis) and the nuclear spin along the x axis. In a real experiment, we can not exclude small misalignment in the neutron spin and nuclear spin.[18,19] The effect of the misalignment is explained in terms of mixing angles ε's, ξ's and δ's for incident neutron polarization, analyzer polarization, nuclear target polarization ($\boldsymbol{P}_I$), respectively. The poalrizations and spin dependent phase shift are represented as

$$\boldsymbol{P}_o = (\varepsilon_x P_o, \varepsilon_y P_o, P_o), \quad (10)$$
$$\boldsymbol{P}_a = (\xi_x P_a, \xi_y P_a, P_a), \quad (11)$$
$$\boldsymbol{P}_I = (P_I, \delta_y P_I, \delta_z P_I). \quad (12)$$
$$(\phi_1', \phi_2', \phi_3') = (\phi_1 P_I, \delta_y \phi_1 P_I + \phi_2 P_I, \delta_z \phi_1 P_I + \phi_3). \quad (13)$$

Here, we neglect higher order terms of ϕ_2. The change in the spin-flip probability upon reversal of the incident neutron spin is

$$R_{+-} - R_{-+} = \mathrm{Tr}(F\rho(P_o)\,F\dagger\,P(-P_a))$$

$$- \mathrm{Tr}(F\rho(-P_o)\, F\dagger\, P(P_a))$$
$$= \exp(-2\mathrm{Im}(\phi_0))\ \{-[2\varepsilon_x P_o - 2\xi_x P_a + 2\varepsilon_y P_o \delta_y - 2\xi_y P_a \delta_y + 2(P_o - P_a)\delta_z]\ \cos b\ \sin b/b\ P_I\ \mathrm{Im}(\phi_1)$$
$$+[2\varepsilon_x P_o \delta_y + 2\xi_x P_a \delta_y - 2\varepsilon_y P_o - 2\xi_y P_a]$$
$$(\sin b/b)^2\ P_I\ \mathrm{Im}(\phi_1\, \phi_3^*)$$
$$- 2(P_o - P_a)\ \cos b\ \sin b/b\ \mathrm{Im}(\phi_3)$$
$$+ 2(P_o + P_a)\ (\sin b/b)^2\ P_I^2\ \mathrm{Im}(\phi_1\, \phi_2^*)\}. \quad (14)$$

$\mathrm{Re}(\phi_1) \cdot \mathrm{Im}(\phi_3)$ and $\mathrm{Re}(\phi_1) \cdot \mathrm{Im}(\phi_2)$ terms are dominant in the second and fourth therm in Eq. (16), respectively, since

$$\mathrm{Im}(\phi_3) \gg \mathrm{Re}(\phi_3) \quad (15)$$
$$\mathrm{Re}(\phi_1) \gg \mathrm{Im}(\phi_1) \quad (16)$$

in the p-wave resonance of ^{139}La at $E_n = 0.734$ eV. Here,

$$b = \sqrt{|\phi_1|^2 + |\phi_2|^2 + |\phi_3|^2}$$

$$= \mathrm{Re}(\phi_1) + \delta_\phi/2 \quad (17)$$

IV *P*-violation experiment

The experimental arrangement for the *P*-violation experiment is shown in Fig. 1.[20] Neutrons from a spallation-neutron source at KEK are polarized upon transmission through a polarized proton filter. After the neutron polarizer, the neutron spin is held by a longitudinal magnetic field in a neutron beamline up to a flipper section, where a horizontal transverse (*y* axis) dipole magnet is placed. The direction of the magnetic field is gradually rotated from the longitudinal to transverse direction so that the neutron spin follows the magnetic field change. The magnetic field at the flipper is reversed at a

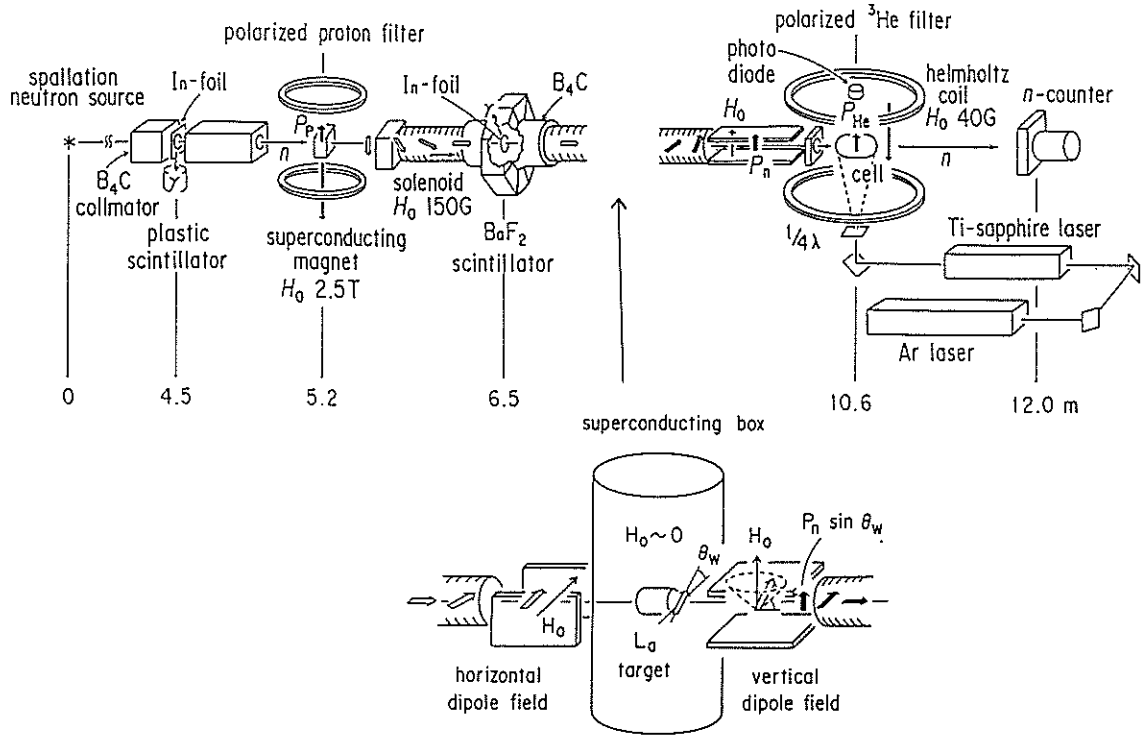

Fig. 1 Experimental arangement for *P*-violating neutron-spin rotation.

suitable period. The neutron spin is also reversed upon the reversal of the field. After the flipper, neutrons enter into a niobium superconducting box,[21, 22] in which a 5-cm length and 3-cm diameter lanthanum target is placed. The neutron spin enters into the box without any change in its direction, because the rate of the magnetic field change is very fast compared with the Larmor frequency. In the box, magnetic field is less than 1 mG so that the Larmor precession is negligible. The neutron spin rotates by $\theta_W = 2\mathrm{Re}(\phi_3)$ rad upon transmission through the target, then enters into a downstream dipole magnet. The direction of the downstream dipole field is vertical (x axis). The vertical component of the neutron polarization, $P_0 \sin \theta_W$ is held by the downstream field and is guided to a polarized ^{3}He neutron polarimeter.[23] A flipping ratio R for neutron counting upon the reversal of the incident neutron spin is

$$R = (T_+ - T_-)/(T_+ + T_-)$$
$$= A(^3\mathrm{He}) \cdot P_0 \sin \theta_W \qquad (18)$$
$$A(^3\mathrm{He}) = \tanh(\rho\, l\, \sigma_0\, P_{\mathrm{He}}). \qquad (19)$$

Here, $T_\pm$ are neutron counts for non-flipped and flipped spin states, respectively. $A(^3\mathrm{He})$ is an analyzing power of the polarized ^{3}He. σ_0 is the neutron cross section of the ^{3}He nucleus and P_{He} is the ^{3}He nuclear polarization. The analyzing power is 31% for a 6.4 x 10^{20} atoms/cm^2 thick and 50% polarized ^{3}He filter at E_n = 0.7 eV. A preliminary result is shown in Fig. 2.[24] The solid curve is a predicted rotation angle by the s-p mixing theory. The present result is consistent with the s-p mixing theory. The measurement is continued to get higher counting statistics.

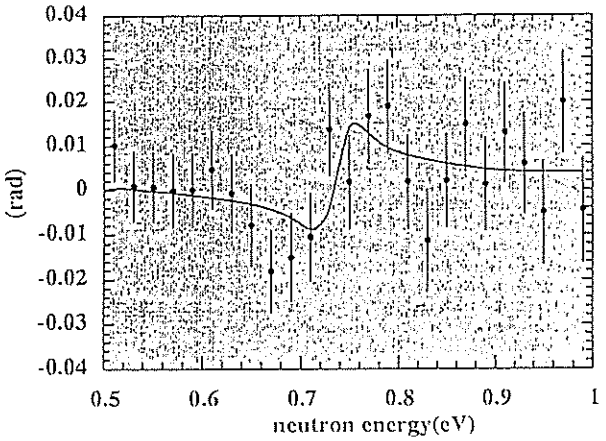

Fig. 2 P-violating spin rotation in the p-wave resonance of ^{139}La at E_n = 0.734 eV.

V *T*-violation experiment

The experimental scheme of the *T*-violation experiment is shown in Fig. 3.[25] The apparatus of Fig. 3 will be placed at the position where the superconducting box for the *P*-violation experiment is placed. The neutron spin is manipulated as follows. After transmission through the polarizer, the neutron spin is held by the static magnetic field in the neutron beamline up to the flipper section. The magnetic field of the flipper is along the y axis. After the flipper, neutrons enter into a 90° coil through a superconducting sheet. In the 90° coil, the magnetic field direction is along the x axis. The neutron spin rotates from the y to -z direction before entering into a polarized nuclear target. In the target section, a magnetic field (H_0) is applied in order to hold the nuclear polarization. In addition to the magnetic field, neutrons see a field called "pseudomagnetic field (H^*)" due to the F_1 term during transmission through the target. Therefore, the neutron spin rotates around the

sum of these fields, ($H_0 + H^*$). The magnetic field is adjusted so that the rotation angle is either 180° and -180° during the transmission. After the transmission, the neutron-spin rotates from the z to y direction in another 90° coil and is then analyzed by the ^{3}He neutron polarimeter. If we use the same neutron-spin manipulation which was used in the P-violation experiment, a rotation-angle accuracy of $\delta\theta < 1.7 \times 10^{-3}$ rad is possible.

Lanthanum nuclear polarization is developed at KEK for a LaF_3 or $LaAlO_3$ single crystal.[26, 27] Paramagnetic centers are doped into the lanthanum compound single crystals for the electron-spin resonance (ESR). The paramagnetic electron polarization which is almost 100% at a temperature of 0.5 K and a magnetic field of 2.3 T, is transferred to a nuclear spin system upon the ESR. The

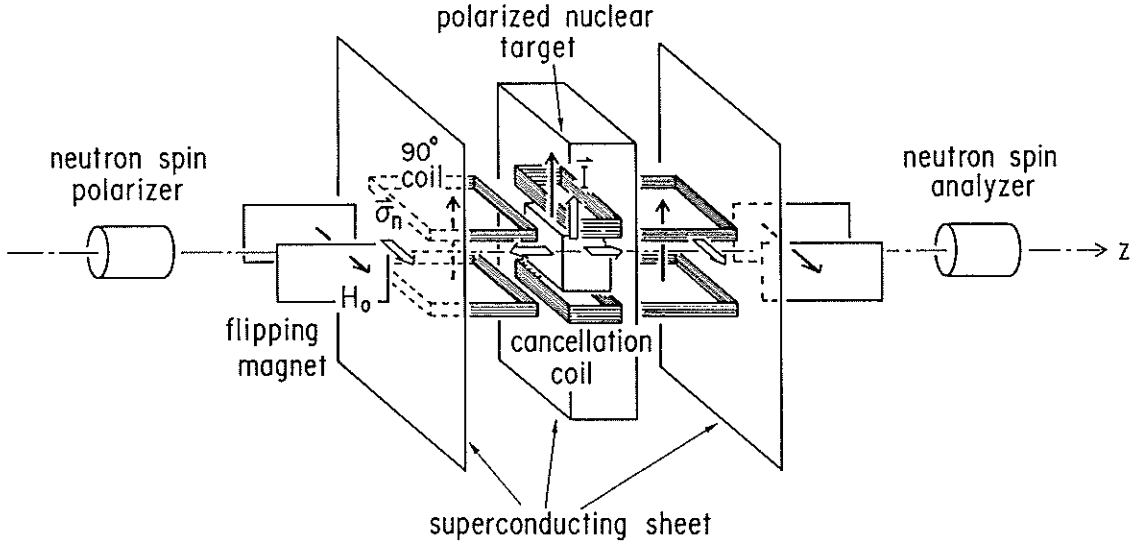

Fig. 3 Experimental scheme for T-violating neutron-spin rotation.

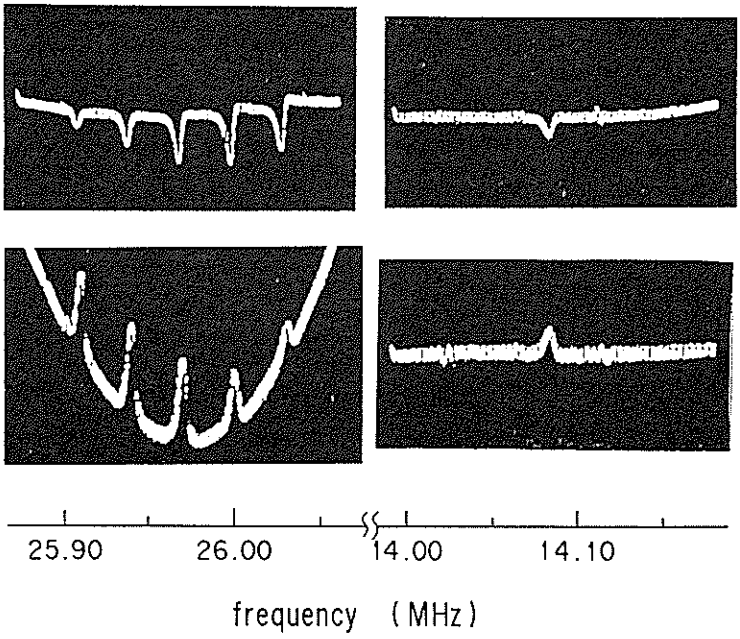

Fig. 4 NMR signals of ^{27}Al and ^{139}La nuclei in a $LaAlO_3$ crystal.

microwave frequency for the ESR is 70 GHz. The nuclear polarization was observed by nuclear magnetic resonance (NMR) and neutron transmission.[28] A typical example of the NMR is shown in Fig. 4. The left-side pictures are the NMR spectra for ^{27}Al (I = 5/2) nuclei in a $LaAlO_3$ single crystal. The single NMR line for $\delta m = \pm 1$ transitions between Zeeman levels splits into 5 lines as it is shown in Fig. 4 because of a quadrupole field in the crystal. If we assume thermal equilibrium for the nuclear polarization, magnetic substate population, a_m is

$$a_m \propto \exp(-E_m/kT). \qquad (20)$$

The difference in the NMR signal amplitude in Fig. 4 is explained by Eq. (20). The nuclear polarization is reversed, if we shift the microwave frequency for the ESR, for example by
150 MHz. The result is shown in the lower side of Fig. 4. For the ^{139}La (I = 7/2) NMR, the result is shown in the right-side pictures. Other 6 NMR lines are out of the frequency modulation range, since the quadrupole coupling for the lanthanum nucleus is large.

The nuclear polarization was also measured by using the F_1 term in Eq. (3). The ^{139}La nucleus has a s-wave resonance (I = 3) at E_n = 72 eV. The neutron transmission T for polarized nuclei becomes

$$T = T_0 \cosh(P_I \sigma_0 \rho l). \qquad (21)$$

T_0 is neutron transmission for unpolarized nuclei. In Fig. 5, a neutron transmission spectrum T_0 and a ratio T/T_0 are shown. The effect in the ratio shown in Fig. 5 corresponds

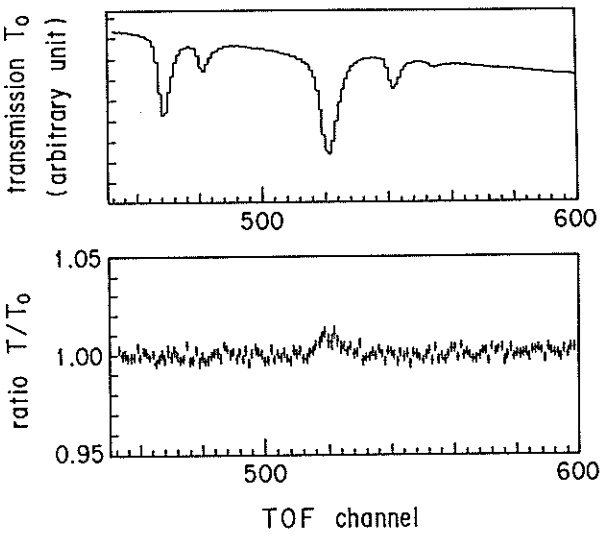

Fig. 5 Neutron transmission of a $LaAlO_3$ crystal. The polarization effect is found at the transmission dip at ~520 ch which is due to 72-eV resonance of ^{139}La.

to the lanthanum nuclear polarization of about 10%.

The systematic errors in the T-violation experiment are discussed in the followings. The first and third terms in Eq. (14) are canceled by the rotation reversal, the sign reversal of $\mathrm{Re}(\phi_1)$. In the second term of Eq. (14), the first and second terms are small. Therefore, the essential point to reduce the systematic error is to control the mixing angles ε_y and ξ_y. The second term in Eq. (14) is canceled by reversing the nuclear polarization $\boldsymbol{P}_I$. However, the magnetic field is also changed upon the reversal. It may induce a change in the angles, ε_y and ξ_y. In this case, we can not cancel the effect of ε_y and ξ_y.[19] In the target arrangement in Fig. 3, the distance between the superconducting sheet and the target, where we can not control the neutron-spin rotation, should be very small. An 1-μm distance corresponds to a mixing angle

uncertainty of 1.5 x 10^{-3} rad at 1 kG. For comparison with the neutron EDM, a ratio of the F_2 to F_3 term, η is used. The mixing angle uncertainty corresponds to an error of the ratio,

$$\delta\eta < 1.5 \times 10^{-3} \quad \text{for a 1 } \mu\text{m distance} \quad (30)$$

$$\delta\eta < 1.5 \times 10^{-4} \quad \text{for a 0.1 } \mu\text{m distance.} \quad (31)$$

The neuron EDM experiments give a constraint for the value of η as

$$\eta < 4 \times 10^{-3} \quad (\text{n EDM of} < 1 \times 10^{-25} \text{ cm}).[11,12] \quad (32)$$

[1] E.G. Adelberger and W.C. Haxton, Ann. Rev. Nucl. Part. Sci. 35(1985)501.
[2] F.C. Michel, Phys. Rev. 133(1964)B329.
[3] M. Forte et al., Phys. Rev. Lett. 45(1980)2088.
[4] V.P. Alfimenkov et al., Nucl. Phys. A398(1983)93.
[5] Y. Masuda et al., Hyp. Int. 34(1987) 143; Nucl. Phys. A478(1988)737c; Nucl. Phys. A504(1989)269.
[6] S.A. Biryukov et al., Sov. J. Nucl. Phys. 45(1987)937.
[7] C.D. Bowman et al., Phys. Rev. C39(1989)1721.
[8] O.P. Sushkov and V.V. Flambaum, Sov. Phys. Usp. 25(1982)1.
[9] V.E. Bunakov and V.P. Gudkov, Nucl. Phys. A401(1983)93.
[10] Y. Yamaguchi, J. Phys. Soc. Jpn. 57(1988)1518L; ibid. 1522L; 1525L.
[11] V.P. Gudkov, Phys. Rep. 212(1992)77.
[12] P. Herczeg, Hyp. Int. 75(1992)127.
[13] I.I. Grevich and L.V. Tarasov, "Low-Energy Neutron Physics", North Holland (1968).
[14] L. Stodolsky, Physics Lett. B172(1986)5.
[15] V.E. Bunakov and V.P. Gudkov, Z. Phys. A308(1982)363.
[16] P.K. Kabir, Phys. Rev. Lett. 60(1988)686.
[17] Y. Masuda et al., Hyp. Int. 74(1992)149.
[18] A.P. Serebrov, JETP Lett. 58(1993)14.
[19] S.K. Lamoreaux and R. Golub, Phys. Rev. D50(1994)5632.
[20] Y. Masuda, Neutron Research 1(1993)53.
[21] M. Ishida et al., KEK Progress Report 84-2(1984)207.
[22] Similar apparatus is independently developed at Grenoble. F. Tasset, Physica B156&157(1989)627.
[23] H. Sato et al., Hyp. Int. 84(1994)205.
[24] K. Sakai et al., Hyp. Int. 84(1994)199; to be published.
[25] Y. Masuda, Proc. XXXth Recontress de Moriond, Villars-sur Ollon, Suisse, Jan.21_28, 1995.
[26] Y. Masuda et al., KEK report 90-25 (1991) 1002.
[27] Y. Takahashi et al., Nucl. Inst. Meth. A336(1993)583.
[28] to be published.

Design for a new high resolution powder diffractometer, *Sirius*

T. KAMIYAMA, M. FURUSAKA* and S. ITOH*

Institute of Materials Science, University of Tsukuba, Tsukuba-shi 305
*National Laboratory for High Energy Physics, Tsukuba-shi 305

Since superconductivity "fever" spread around the world, neutron powder diffraction has become much popular and been widely used by crystallographers, physicists, chemists, mineralogists, and materials scientists. The resolution, $\Delta d/d$, of $2\text{-}5\times10^{-3}$ is usually adopted for high resolution neutron powder diffractometers because usual unit-cell volumes of many materials of interest are less than 1000 Å^3. Figure 1 shows the distribution of unit-cell volumes measured on HRPD and POLARIS diffractometers reported in a RAL report.[1]

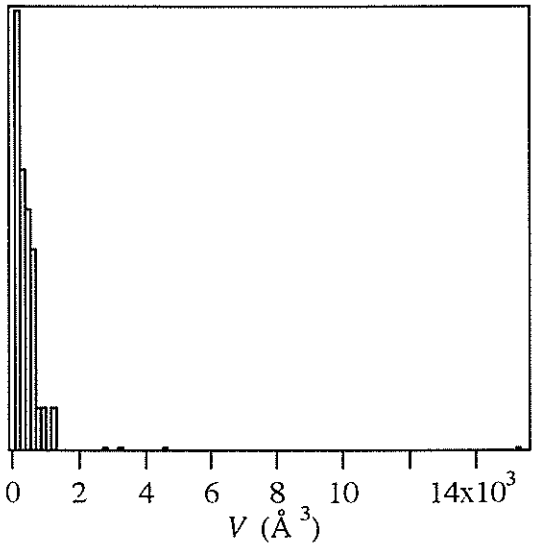

Fig. 1 The distribution of unit-cell volumes indicates most of materials measured had unit-cell volumes less than 1000 Å (see text).

In the cubic cell of dimension, a for example, the separation, δd, between adjacent Bragg peaks in the POLARIS diffractometer ($\Delta d/d = 5\times10^{-3}$) is larger than the peak width Δd for $d > 1$ Å and POLARIS could give 90 resolved peaks for $a = 10$ Å and $d > 1$ Å. This number is a measure that number of atomic parameters should be much less than this one. Of course, the Rietveld method is powerful in extracting structural information from overlapping reflection to some extent, but still $\delta d/d$ could be used as a measure of complexity that can be solved by powder diffraction. For C_{60} with $a = 14$ Å, Vega[2] ($2\text{-}3\times10^{-3}$) gives resolved Bragg peaks at $d = 0.9$ Å. Separation of peaks at smaller d is important to determine the local atomic displacement.

In the system with lower symmetry, reflection multiplicity, m, decreases by 1/24 at most and total number of reflections, N, increases; for triclinic crystal system, m is at least 2 because of the Friedel's law. Generally, $\delta d/d$ is $d^3m/2\pi V$ and N with $d > d_0$ is given by $N = 2\pi V/3md_0^3$, where V is the unit-cell volume. This formula indicates that doubling the unit cell volume doubles N and requires 2-times better resolution.

In the discussion given above, only the average density of Bragg peaks is considered. This is not satisfactory for most cases. In order to observe subtle symmetry changes, required resolution is much higher. Figure 2 shows part of diffraction pattern of a distorted spinel (V = 560 Å^3) measured by Vega.[3] Careful analysis enables us to convince that the crystal system is no longer cubic. However the result of the analysis would depend on the model one chooses.

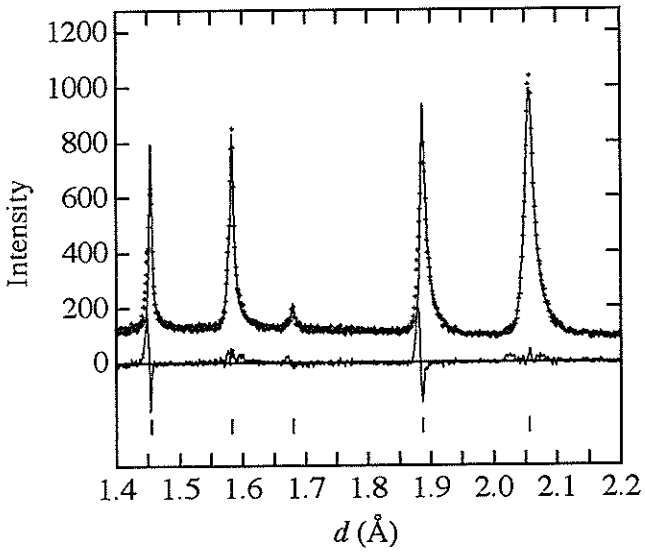

Fig. 2 Part of diffraction pattern of a distorted spinel (V = 560 Å^3) measured by Vega. Calculation model is based on the cubic crystal system.

$YbInCu_4$ (cubic, V = 370 Å^3) exhibits a first-order valence phase transition at 40 K from an Yb^{3+} state to a valence fluctuating state without any symmetry change. Change in a is less than $2x10^{-3}$. With usual resolution data, the result of the Rietveld analysis depends on the profile model in the region where two phases coexists, because diffraction patterns of both phases have resemblance.[4] Similar situations occur quite often in the first order phase transition. Then, higher resolution is necessary even if the density of Bragg peaks is small.

High resolution would open up other new possibilities: *ab initio* structure determination using direct methods, structure refinement of more hydrogenous samples, accurate lattice parameter determination and studies on line broadening effects from small crystallite size, strain, stacking fault, anti-phase domain boundaries and composition variations.

There are increasing demands for higher resolution neutron powder diffraction experiments at KENS. Higher resolution will permit to explore the larger unit-cell volume where the average Bragg intensity will decrease with increasing V. Since neutron beam intensity at KENS is 40 times weaker than ISIS, resolution must not be obtained at the expense of intensity. This makes it difficult to simply copy the existing diffractometer. Motivated by these requirements, we have designed a new high resolution time-of-flight (TOF) powder diffractometer, *Sirius* (it was called HRP-II in the COE budget proposal) which has a resolution of $\Delta d/d = 1\times10^{-3}$ at the best.

Since no choice of changing the 20 K CH_4 moderator to poisoned one, long flight path is essential to achieve high resolution. Flight path of more than 40 m is required to satisfy $\Delta d/d = 1\times10^{-3}$. Longer the flight path, shorter the d range at one experiment. The d range should be larger than 2.5 Å in the Rietveld refinement that corresponds to 40m in the 20 Hz pulsed source.

Long flight path demands the use of a neutron guide tube to avoid loss of intensity.[5] If natural nickel is used for the coating materials of the guide, the intensity is very small at shorter wavelength than 4 Å while resolution can be selected easily. These are important for powder diffractometer because number of Bragg peaks is large in this region. In the case of NiC/Ti-supermirror with critical angle 3 times larger than that of natural nickel, the intensity around 1 Å is large but inhomogeneity might cause loss of intensity at long wavelength at the end of long flight path. Considering future use in JHP, we decided to use supermirrors with the beam cross section of 4 cm x 5 cm manufactured by Osmic Inc. Since inhomogeneity was expected, the guide tube started at 5.5 m from the moderator, 0.5 m from biological shield. The total length of guide tube, 28.5 m was chosen to meet the geometrical limitation. Curved guide is preferable to avoid fast neutron contamination, but 40 m is short to have both curved section and straight section.

An overall flight path of 39.5 m introduces frame overlap that may be eliminated by a tail cutter. The tail cutter is designed to rotate at 20 Hz and enable wavelength window of 5 Å that corresponds to the d range of 2.5 Å and beam window of 45 degree. Between the end of biological shield and guide tube entrance, a beam shutter and the tail cutter are situated.

Because the COE project of *Sirius* should be completed within one year including design work, we had no time to develop a new detector system. We decided to adopt PSD system similar to that of Vega.[2),6)] The PSD-VME data-acquisition system adopted in Vega involves a VME single-board computer with a 68040 processor for data handling. In *Sirius*, CPU is removed from VME and the position-encoding, data-transfer and histograming are carried out by Macintosh.

Fig. 3 illustrates a layout of *Sirius* with large backward band and 90 degree banks comprising one-dimensional PSD's. Each PSD has a diameter of 1.27 cm and an effective length of 60 cm, containing 10 atm of ^{3}He with appropriate stopping gases. The secondary flight path of 2 m is adopted to reduce $\cot\theta\Delta\theta$ contribution to the resolution. Contrary to Vega, backward bank cannot be evacuated because detector area is as large as 3 x 3 m. The supporting frame against a vacuum window produces large dead area of idetectors, which restricts detector solid angle in Vega. Then, backward bank is separated from the sample chamber and filled with He gas. The neutron beam is transported by evacuated collimator tube which runs through the backward bank to the place near the sample position.

A detailed account of the resolution and profile function of *Sirius* will be given elsewhere.[7)] The results of resolution calculation are shown in Fig. 4. It is noted that, using long wavelength, long d diffraction can be carried out with excellent resolution.

As for the resolution and intensity, two types of diffractometers are required in practice at KENS: a high resolution instrument with data-collection time of several tens of hours, and a high intensity one with data-collection time of several tens of minutes. *Sirius* has these two features. The resolution and intensity can be selected by changing slit between the end of guide tube and the entrance of collimator tube. The

calculated ratio of intensity of *Sirius* to that of Vega is at most 15 times larger which will not be far from the real value[5]; The preliminary measurement of intensity ratio at monitor positions indicated 15.1±0.2. Then, high intensity mode is one of promising applications of *Sirius*. It enables us measure intensity data for small amounts of samples, e.g., those containing expensive elements (isotopes) or those prepared under special conditions.

This research was supported by the COE project of the Ministry of Education, Science, Sports and Culture.

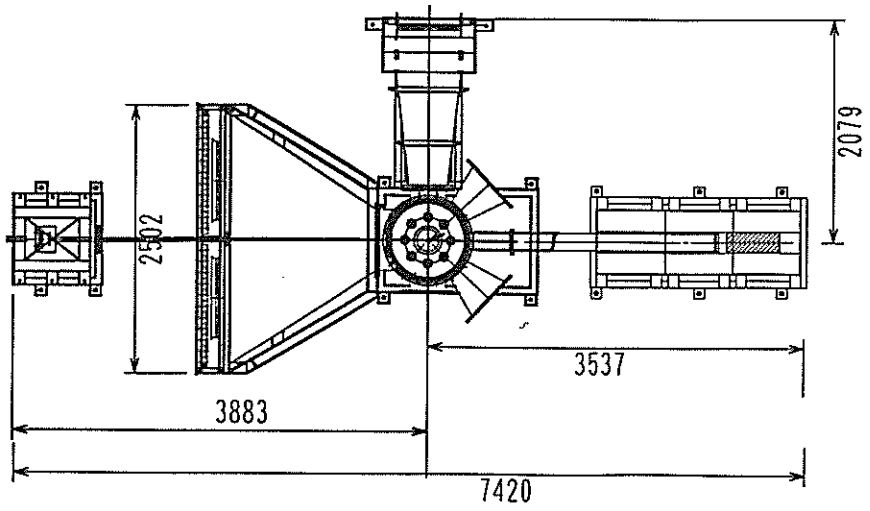

Fig. 3 High resolution TOF powder diffractometer *Sirius*.

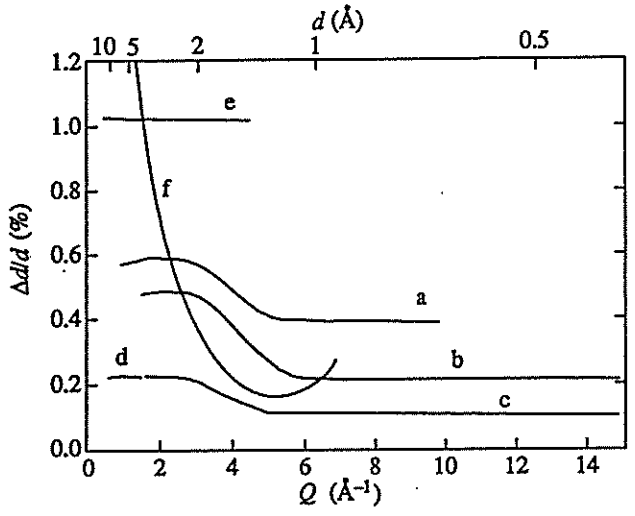

Fig. 4 Resolution and *Q* range. (a) 90° bank of Vega, (b) backscattering bank of Vega, (c) backscattering bank of *Sirius*, (d) backscattering bank of *Sirius* (long-wavelength mode), (e) 30° bank of Vega, (f) angle-dispersive type with $\alpha 1 = \alpha 3 = 8'$, $\alpha 2 = \beta = 20'$, $2\theta_M = 90°$, $\lambda = 1.82$ Å.

References

1) Annual report 1994-95, RAL-TR-95-050 (1995)
2) T. Kamiyama et al., Physica B 213&214 (1995) 875.
3) K. Oikawa et al., to be submitted.
4) K. Kojima et al., to be submitted.
5) S. Itoh et al., KENS Report-XI (1997).
6) S. Satoh et al., submitted to Proc. DAENF97.
M. Furusaka et al., submitted to Proc. DAENF97.
7) F. Izumi et al., in preparation.

Supermirror Guide Tube on HRP-II

S. Itoh, T. Kamiyama*, M. Furusaka and S. Ikeda
Booster Synchrotron Utilization Facility, National Laboratory for High Energy Physics, Tsukuba 305
**Institute of Materials Science, University of Tsukuba, Tsukuba 305*

A guide tube is a device transporting neutrons to an instrument installed far from the neutron source, ideally without intensity loss, via total reflection from the smooth surface of the neutron guide coating. Among common materials, natural nickel has been the best choice for the coating with the critical wavenumber, $Q_c^{Ni}=0.0217Å^{-1}$. The critical angle (θ_c) of the total reflection from nickel surface for a neutron wavelength, λ(Å), is $\theta_c=(Q_c^{Ni}/4\pi)\lambda=1.73\lambda$mrad. The critical wavelength of a guide tube (λ_c) is mainly determined by a geometrical configuration between the moderator and the guide tube. The transported neutron intensity at the exit of the guide tube is proportional to the solid angle of the moderator at the entrance of the guide tube at $\lambda>\lambda_c$, and, at $\lambda<\lambda_c$, the transported intensity decreases as λ decreases, where the beam divergence is limited to the λ-dependent θ_c. Therefore, λ_c can be obtained to be a wavelength with $\theta_m=\theta_c$, where θ_m is the glancing angle of the moderator at the guide tube entrance.

On the high resolution powder diffractometer, HRP-II,[1] installed at the C3 beam line at KENS, a guide tube with the length of 28.5m and with the beam cross section of 4 cm x 5 cm (width x height) is installed between the moderator and the diffractometer. The distance between the moderator and the guide tube entrance is 5.5 m and the moderator surface area of 8 cm x 10 cm can be seen at the entrance. If natural nickel is used for the neutron guide coating in this system, λ_c becomes about 4Å and the transported neutron intensity drastically decreases at shorter wavelengths required on HRP-II. In order to gain more transported intensity at shorter wavelengths on HRP-II, we decided to use a guide tube, comprising supermirrors with the critical wavenumber of $3Q_c^{Ni}$, manufactured by Osmic Inc.

The principle of a supermirror is to use multilayers with slowly varying d-spacings which give a superpositioning of Bragg reflections over a range of wavelengths from λ_{min} to λ_{max}. If the wavenumber corresponding to λ_{max}, i.e., maximum d-spacing, is chosen to be the critical wavenumber determined by the average scattering length density of all over the multilayer coating, neutrons with $\lambda>\lambda_{min}$ are reflected. The minimum wavelength λ_{min} is determined by the minimum d-spacing. The performance of a supermirror is characterized by the critical wavenumber, Q_c, corresponding to the minimum d-spacing ($Q_c=2\pi/d_{min}$), and normally Q_c is represented in the unit of Q_c^{Ni}.

Recently supermirrors with $Q_c\sim3Q_c^{Ni}$ have become commercially available.[2] We employed NiC/Ti-supermirror[3] with $Q_c\sim3Q_c^{Ni}$ for the guide tube coating. The multilayer of Ni and Ti is a typical combination of materials of a supermirror for unpolarized neutrons. Carbon in Ni layers was introduced to minimize distortions in the layers, and the composition of a NiC layer is about $Ni_{72}C_{28}$.[3] In the guide tube on HRP-II, the supermirror structure is coated on a boron glass. The wavenumber (Q) dependence of the reflectivity of the supermirror, R(Q), can be calculated[4] from the thickness distribution of NiC and Ti layers presented by the manufacturer.[5] In the critical region, the wavenumber where the reflectivity drops to R=0.95 was calculated to be $Q=0.062Å^{-1}$ and R(Q)=1 at the smaller wavenumbers. Therefore the thickness distribution is well designed. The wavenumber of $0.062Å^{-1}$ is almost $3Q_c^{Ni}$, or Q_c is calculated to be $0.063Å^{-1}$ if Q_c is defined as $R(Q_c)=1/2$. The manufacturer presented the specification of R(Q) as shown in Table 1.[2] The decrease in R(Q) with increasing Q in Table 1 is caused by the interlayer roughness. In the calculation mentioned above, the interlayer roughness was not introduced. Figure 1 shows a measured reflectivity of a sample supermirror with the same supermirror structure as those used in the present guide tube.[6] The observed reflectivity is well satisfied with the specification in Table 1. A supermirror is characterized by Q_c and R(Q) at $Q<Q_c$; the former determines the wavelength range of transported neutrons through a guide tube and the latter limits the transported intensity.

Table 1. The specification of R(Q) of the supermirror presented by the manufacturer.

Wavenumber	Reflectivity
$Q \le 0.020$ Å^{-1}	$R \ge 0.99$
$Q \le 0.040$ Å^{-1}	$R \ge 0.95$
$Q \le 0.056$ Å^{-1}	$R \ge 0.90$
$Q \le 0.060$ Å^{-1}	$R \ge 0.85$

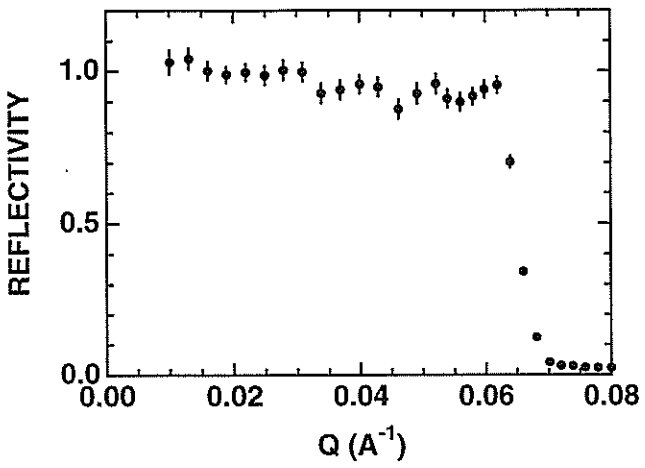

Fig. 1 Measured reflectivity of a sample of the $3Q_c^{Ni}$-NiC/Ti-supermirror used in the present guide tube.

Now we evaluate the λ-dependent transported neutron intensity through the supermirror guide tube. The intensity at the sample position of HRP-II was estimated in comparison with that of Vega,[7] the already-existing powder diffractometer on the C4 beam line. Figure 2 shows typical geometrical-configurations of the two diffractometers. On HRP-II, the beam cross section in the collimator entrance is variable in order to control the resolution, in the following discussion, the most coarse collimation with the entrance of 4 cm x 4 cm is assumed. We preliminarily measured the neutron intensities detected at the monitors of the two diffractometers. At λ=4Å, the ratio of the intensity at the monitors on HRP-II (cross section: 4 cm x 4 cm) to that on Vega (2.2 cm x 4 cm) was observed to be 15.1±0.2, after correcting the efficiencies of the monitors and the measuring time. The intensities on the two diffractometers in the geometries in Fig.2 can be calculated by a Monte Carlo code,[8] and the ratio was calculated to be 15.8. The observed intensity ratio was well agreed with the calculation. The measuring point of λ=4Å is greater than λ_c. In order to evaluate the critical region of the supermirror and the intensity at around λ_c, the observation of the λ-dependent intensity at shorter λ is required. Since we experimentally confirmed that the transported neutron intensity was well reproduced by the calculation as mentioned above (at one wavelength point), we can estimate the λ-dependent intensity at the sample position by using the Monte Carlo code. Figure 3 shows the calculated ratio of the intensity at the sample position of HRP-II (cross section: 2 cm x 2 cm) to that of Vega (2 cm x 4 cm). The calculations were performed for both materials of the supermirror and natural nickel for the guide tube coating. For the supermirror used in the present guide tube, an empirical form of R(Q) reproducing the specification in Table 1 and Fig.1 was established, and used in the calculation, and the Q-dependent reflectivity from a bulk nickel was also used. We also calculated the intensity for an ideal $3Q_c^{Ni}$-supermirror having R(Q)=1 at $Q<Q_c$. By using the supermirror instead of nickel, the intensity at the shorter wavelength region required on HRP-II is well improved. The intensity drop at the critical region for the actual supermirror, in comparison with the ideal supermirror, is caused by the finite reflectivity at around Q_c. Furthermore, the factor more than 10 in the intensity gain at the sample position, in comparison with Vega, can be expected.

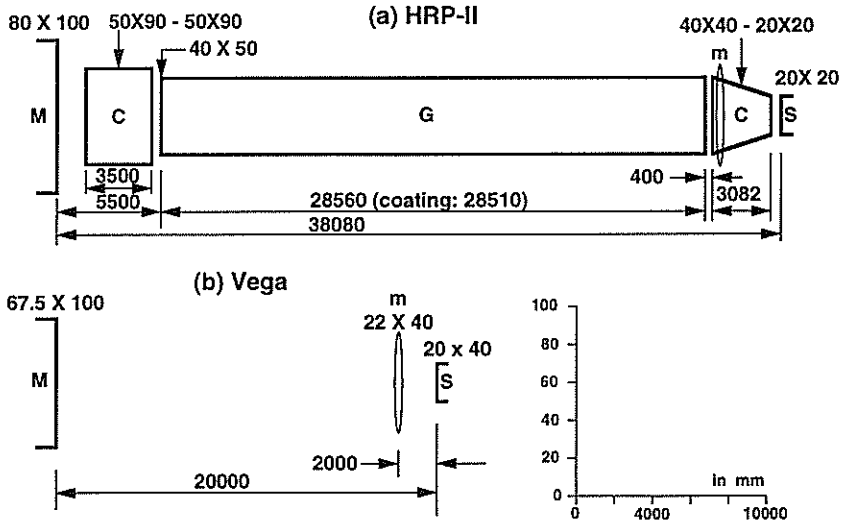

Fig.2 Geometrical configurations of HRP-II (a) and Vega(b). M, G, m, C and S indicate moderator, guide tube, monitor, collimator section and sample, respectively. The entrance cross section of the collimator section on HRP-II is variable, the monitor is located just after the collimator entrance, and therefore, the cross section of the monitor on HRP-II is the same as that of the collimator entrance. There is no guide tube on Vega.

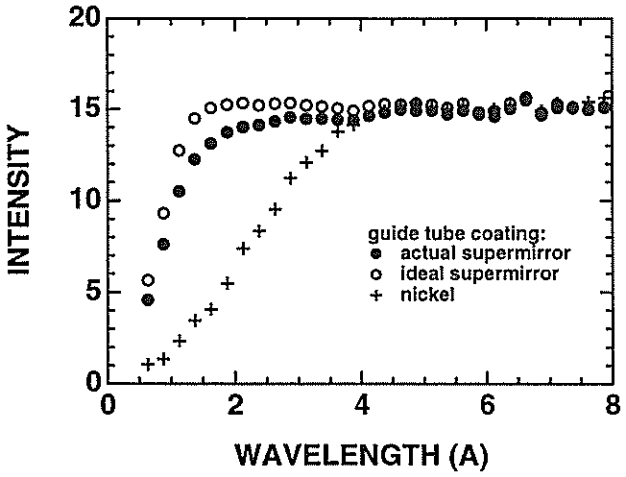

Fig.3 Wavelength dependence of the transported neutron intensity through the guide tube on HRP-II. The calculated intensities are presented as a ratio of the transported intensity at the sample position on HRP-II to that on Vega.

Reference

1) T. Kamiyama et al., KENS Report-XI (1997).
2) J. L. Wood, private communication (July 1995).
3) J. L. Wood, SPIE Proc. 1738 (1992) 22.
4) for example, S. Yamada, T. Ebisawa, N. Achiwa, T. Akiyoshi and S. Okamoto, Annu. Rep. Res. Reactor Inst. Kyoto Univ. 11 (1978) 8.
5) J. L. Wood, private communication (September 1995).
6) This reflectivity data was shown here through the good kindness of the manufacturer, Osmic Inc. The data was taken at a reflectometer at BNL by a team including Osmic Inc.
7) T.Kamiyama, K.Oikawa, N.Tsuchiya, H.Asano, N.Watanabe, M.Furusaka, S.Satoh, I.Fujikawa, T.Ishigaki and F.Izumi, KENS Report-X (1995) 200.
8) H. M. Shimizu, "*GUIDE*", a simulation code (1995).

Polarizing Neutron Guide for Pulsed Neutron Sources

M. Takeda, K. Kurahashi, Y. Endoh, and S. Itoh*

Physics Department, Graduate School of Science, Tohoku University, Sendai 980-77, Japan
**Booster Synchrotron Utilization Facility, National Laboratory for High Energy Physics, Tsukuba 305*

TOP is a pulsed-cold-polarized-neutron spectrometer for the investigation of mesoscopic magnetism at KENS [1]. A polarizer is the most important component for every polarized neutron spectrometer. To date a variety of polarizers for neutrons have been proposed [2]. TOP has used a polarizing Soller guide which consisted of curved Co/Ti supermirrors. The polarizer was satisfactory for actual experiments, however, it left room for improvement. The reflectivity was very low, and the polarizing efficiency gradually dropped with increasing wavelength. Needless to say the reflectivity and polarizing efficiency, a critical momentum transfer (Q_c), under which total reflection of neutrons occurs, is an important factor to get better supermirror polarizers especially for the pulsed neutron sources.

A magnetized supermirror has different Q_c value for each spin state of incident neutrons: Q_c^+ for neutrons of the up-spin state and Qc^- for that of down-spin one where up-spin state expresses that neutron spin is parallel to the magnetization of the supermirror and down one opposite. The difference makes it possible to filter one spin state in the Q range between Q_c^+ and Q_c^- as schematically shown in Fig. 1. The larger Q_c^+ value is, the wider wavelength band of polarized neutrons are available in the case of polarizers using supermirrors.

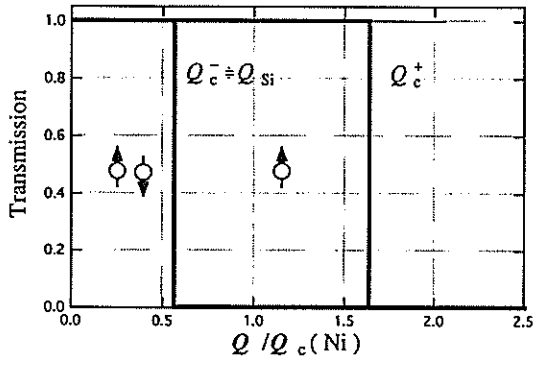

Fig. 1 Transmission of a magnetized supermirror for neutrons of different spin states.

Recently an Fe/Si polarizing neutron supermirror has been developed and achieved to have both a very high polarizing efficiency and a large Q_c^+ value [3]. The mirror is a possible candidate of new polarizer for the TOP spectrometer in order to increase intensity and to get better polarization of neutrons at sample position. We made a new polarizer, a polarizing neutron device (PNG), for TOP using the Fe/Si supermirrors. This is a test report of PNG.

PNG was assembled by CILAS, It consists of a straight natural Ni guide tube with a beam cross section of 20 mm × 50 mm, and 28 pieces of the Fe/Si supermirrors on Si substrate hold in the guide tube. The mirrors make a V-shape in the tube as shown in Fig.2 in order to reduce the length of the device to a half compared with straight configuration.

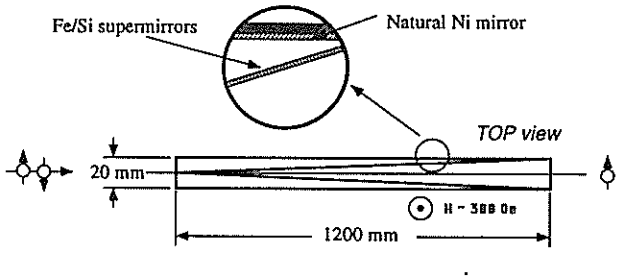

Fig. 2 Schematic representation of the polarizing neutron guide (PNG).

In an Fe/Si supermirror evaporated on Si substrate, Q_c^- is the same as Q_c of Si. Therefore the higher limit of available wavelength is defined by this value in using transmitted polarized neutrons. On the other hand, Q_c^+ can be controlled by evaporation sequence and was set to be $1.6 \times Q_c$(Ni) where the Q_c(Ni) is the critical momentum transfer of natural Ni. The Q_c^+ value was required from the beam width of 20 mm and total length of PNG of 1,200 mm which is very convenient in mounting PNG on TOP by replacing the end section of an ordinary natural Ni guide tube with PNG. These dimensions fix the glancing angle of incident neutrons to mirrors to be 0.5 degree. Polarized neutrons with the wavelength band of 3 - 10 Å are theoretically available using the glancing angle.

The polarizing Soller guide of Co/Ti supermirrors and a Drabkin spin flipper were employed to measure polarizing efficiencies of PNG. Unpolarized neutron with natural collimation were introduced to PNG. Outgoing polarized neutrons were collimated by two pairs of slit before the analyzer. The intensity of neutrons at the sample po-

sition was estimated by measuring of incoherent scattering from light water by a 1D position sensitive detector (PSD). Before starting the measurement, PNG was carefully set to its optimum position. However, it was difficult to settle the position because the angle divergence of incoming neutrons to PNG was not symmetric.

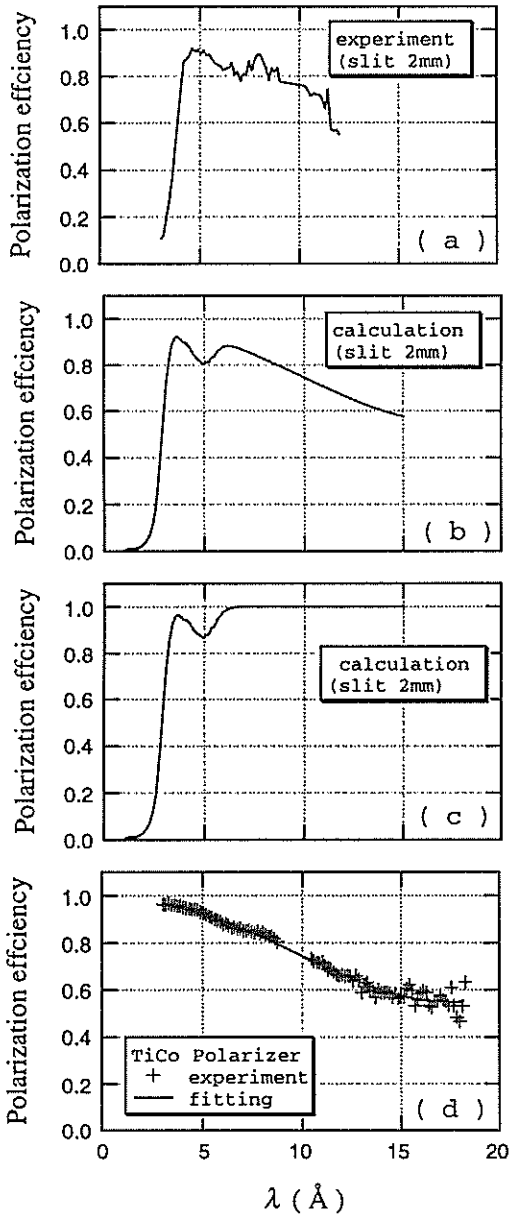

Fig. 2 Observed wavelength dependence of polarizing efficiencies of PNG (a) and the simulation (b). (c) and (d) are the polarizing efficiencies of PNG and of the Co/Ti analyzer, respectively.

Figure 2 (a) and (b) show the observed and calculated wavelength dependence of polarizing efficiency in the case of beam collimation, 0.06 deg., defined by 2 mm wide slits. The observed curves is the product of polarizing efficiencies of PNG and that of the analyzer. Figure 2 (c) is the calculated polarizing efficiency of PNG itself by the standard matrix method [4]. In this calculation the experimental resolution was taken into account, but absorption effect was ignored. The polarizing efficiencies of the Co/Ti analyzer in Fig. 2 (d) were estimated by other experiments. The curve in Fig. 2 (b) is the product of the values in Fig. 2 (c) and (d) at each wavelength. The simulated curve not completely but almost reproduces the observed one. It indicates that the polarizing efficiency of PNG keep higher than 90 % for the wavelength band of 3-9 Å. The difference between observation and the simulation is thought to originate from misalignment of PNG.

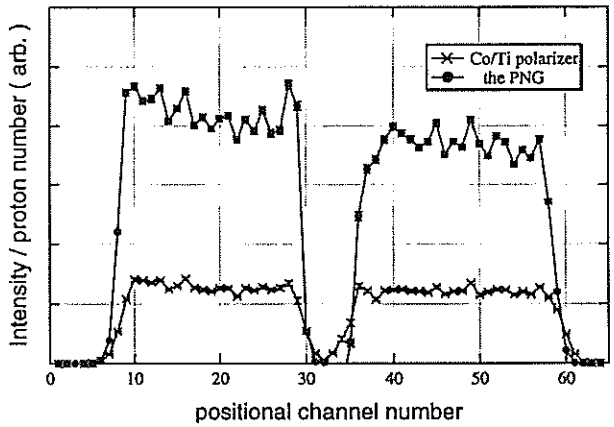

Fig. 3 Intensities of incoherent scattering of light water at the sample position detected by 1D PSD .

Figure 3 shows comparison of beam intensities at the sample position between PNG and previous Co/Ti polarizer. The abscissa is the positional channel number of PSD, and the ordinate is the integrated intensities of incoherent scattering detected at each positional channel over the whole wavelength. The dip appearing at around center position is a shadow of a direct beam stopper. This figure clearly shows that PNG provides more than twice as many neutrons at the sample position than the Co/Ti polarizer.

This work was supported by a Grant-in-Aid for Scientific Research (A) (No. 05402011) and (C) (No. 06640463) from the Ministry of Education, Science, Sports and Culture .

References

1) S. Itoh, T. Watanabe and Y. Endoh: Proceedings of ICANS-XI, Tsukuba (1991) 797.
2) W. G. Williams: *Polarized Neutrons*, (Oxford University Press, Oxford, 1988).
3) C.F. Majkrzak, V. Nunez, J. R. D. Copley, J. F. Ankner and G. C. Greene: SPIE **1738** (1992) 90.
4) M. Born and E. Wolf:*Principles of optics*, (Pergamon Press, Oxford, 1970).

Polarizing Beam-Splitter Device at a Pulsed Neutron Source

Shinichi ITOH and Masayasu TAKEDA*

Booster Synchrotron Utilization Facility, National Laboratory for High Energy Physics, Tsukuba 305

**Department of Physics, Tohoku University, Sendai 980-77*

It is necessary to install as many spectrometers as possible at a neutron scattering facility having a limited number of beam holes. At a steady neutron source, since most spectrometers use a monochromatic beam, many neutron beam lines can easily be made to branch from one beam line by using the Bragg reflection from a crystal. At a pulsed neutron source, however, the Bragg reflection from a crystal is not suitable for a beam branch, because each spectrometer requires a wide wavelength band, and, therefore, a device using a supermirror is a possible candidate to satisfy such a requirement. The beam separation with twice the angle of the grazing angle of the supermirror is obtained in such a device as the transmitted beam as well as reflected beam from the supermirror is used.[1,2] We designed a polarizing beam-splitter device in order to obtain two polarized neutron beam lines with a practical beam size suitable for studies of condensed matter. The polarizing beam-splitter device (manufactured by Osmic Inc.) has a trapezoidal shape from the top view; supermirrors were mounted on the line between the apex and the middle point of the opposite side. The outlet area is twice that of the inlet area (1.8 cm x 5 cm (width x height)). Half of the outlet area is for the transmitted beam through the supermirrors; the other half is for the reflected beam. Since Q_c of the supermirrors used in the present device was ~$3Q_c^{Ni}$ (Q_c^{Ni}, critical wavenumber of total reflection from natural nickel), the supermirrors were mounted by keeping a grazing angle of θ_0=0.9° for the incoming neutrons to the supermirrors in the present device in order to obtain a polarized neutron beam at λ>3Å; eventually, the length of the device became 118 cm including flanges. The supermirrors were assembled in a boron-glass tube and the inside walls of the tube were coated with natural nickel. A boron-glass tube was mounted in a magnetic housing to apply a magnetic field of 300 Oe to the supermirrors. The present device was mounted after a guide tube (natural nickel coating) on the TOP spectrometer at KENS.

We chose Fe/Si supermirrors evaporated onto a silicon substrate because less neutron absorption from the substrate is suitable for the transmitted beam.[3] The thickness of substrate was 0.6 mm. The same coating as that of the supermirror structure was performed on both sides of the silicon substrate in order to improve the flatness of the supermirror.[4] When the supermirror structure was coated on a single side, the flatness (deviation of the surface) was 0.4°; on the other hand, the flatness of the original substrate (less than 0.02°) was almost maintained by coating both sides. Since a flatness of 0.4° was not negligible for the present device, where the grazing angle was 0.9°, coating both sides was chosen in the present manufacturing. First, in order to characterize the supermirror used in the present device, the reflectivity measurement was performed in a magnetic field of 9.6 kOe. The neutron beam was collimated with a slit system, which determined the beam collimation to be $\Delta\theta$=0.057°. The observed polarization and reflectivities of the sample supermirror are shown in Fig.1.

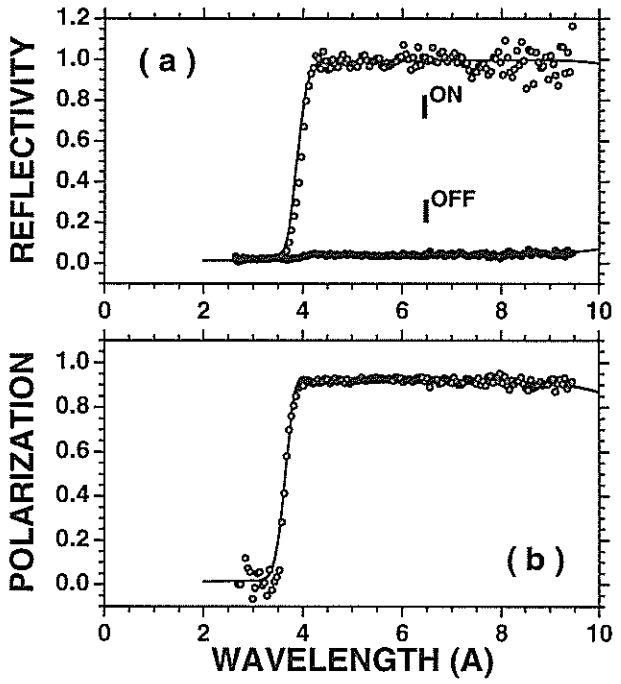

Fig.1 Observed spin-dependent reflectivity (a) and polarization (b) of the sample Fe/Si supermirror. The solid lines are calculations based on the thickness distribution of the supermirror.

The Q-dependence of the reflectivities of the supermirror ($R^+(Q)$ and $R^-(Q)$) for up-spin and down-spin, respectively, can be calculated from the thickness distribution of the supermirror.[4] In the critical region, the wavenumber where the reflectivity drops to 0.95 was calculated to be 0.064Å^{-1} and 0.0117Å^{-1} for $R^+(Q)$ and $R^-(Q)$, respectively. The wavenumber of 0.064Å^{-1} is almost $3Q_c^{Ni}$. The critical wavelengths of

the present device ($\lambda_c^{\pm}$) are converted from the critical wavenumbers for up-spin and down-spin by using the grazing angle. The λ-dependent reflectivities ($I^{\pm}(\theta,\lambda)$) are calculated at a fixed grazing angle (θ) with the actual beam collimation, from $R^{\pm}(Q)$, and the following polarizations were defined;

$$P_0(\lambda)=\frac{(1-I^-(\theta_0,\lambda))-(1-I^+(\theta_0,\lambda))}{(1-I^-(\theta_0,\lambda))+(1-I^+(\theta_0,\lambda))} \quad (1)$$

$$P_1(\lambda)=\frac{I^+(\theta_1,\lambda)-I^-(\theta_1,\lambda)}{I^+(\theta_1,\lambda)+I^-(\theta_1,\lambda)} \quad (2)$$

where θ_0 and θ_1 are the grazing angles of the supermirror in the present device and that of the sample supermirror, respectively. $P_0(\lambda)$ is the polarization of the beam transmitted through the supermirror in the present device, $P_1(\lambda)$ is that of the reflected beam from the sample supermirror and the observed polarization is compared with $P(\lambda)=P_0(\lambda)P_1(\lambda)$. The reflectivities corresponding to the experimental condition are calculated as follows:

$$I^{ON}(\lambda)=P_0^+(\lambda)I^+(\theta_1,\lambda)+P_0^-(\lambda)I^-(\theta_1,\lambda) \quad (3)$$

$$I^{OFF}(\lambda)=P_0^-(\lambda)I^+(\theta_1,\lambda)+P_0^+(\lambda)I^-(\theta_1,\lambda) \quad (4)$$

where $P_0^{\pm}(\lambda)=(1\pm P_0(\lambda))/2$, and, "ON" and "OFF" indicate the states of the spin flipper. The observed quantities were well described by a calculation with θ_0=1.07° and θ_1=1.16°, as shown in Fig.1. In other words, the observed behavior is consistent with a calculation using only the thickness distribution without any interdiffusions between layers. The polarization at $\lambda>\lambda_c^+$ was 0.92, where $P_0(\lambda)$ and $P_1(\lambda)$ were calculated to be 1.00 and 0.92, respectively. $P_1(\lambda)$ is determined by the layer structure with the contrast; on the other hand, $P_0(\lambda)$=1 if $R^+(Q)$=1, as shown in eq.(1).

We now discuss the performance of the polarizing beam-splitter. The quantities describing the performance are listed with the calculation formulae as follows:

$$P_T(\lambda)=\frac{(1-I^-(\theta_0,\lambda))-(1-I^+(\theta_0,\lambda))}{(1-I^-(\theta_0,\lambda))+(1-I^+(\theta_0,\lambda))} \quad (5)$$

$$P_R(\lambda)=\frac{I^+(\theta_0,\lambda)-I^-(\theta_0,\lambda)}{I^+(\theta_0,\lambda)+I^-(\theta_0,\lambda)} \quad (6)$$

$$I_T(\lambda)=e^{-n\sigma t/\sin\theta_0}(2-I^-(\theta_0,\lambda)-I^+(\theta_0,\lambda)) \quad (7)$$

$$I_R(\lambda)=I^+(\theta_0,\lambda)+I^-(\theta_0,\lambda) \quad (8)$$

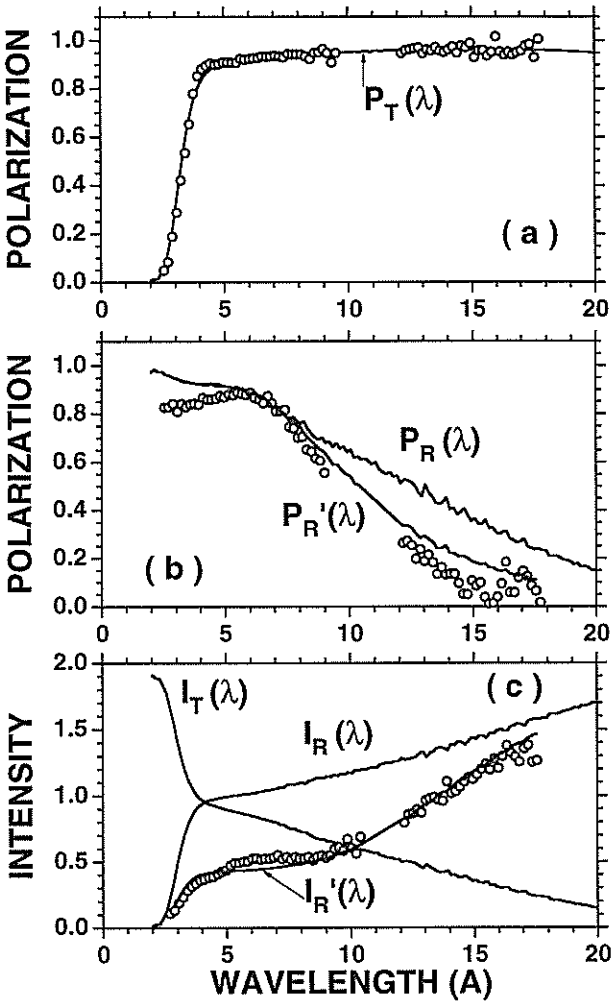

Fig.2 Performance of the polarizing beam-splitter device. The marks are the observed data of the polarization of the transmitted beam (a), the polarization of the reflected beam (b) and the intensity of the reflected beam (c); the solid lines are the calculations. $P_T(\lambda)$, $P_R(\lambda)$, $I_T(\lambda)$ and $I_R(\lambda)$ were calculated based on the reflectivity of the supermirror; $P_R'(\lambda)$ and $I_R'(\lambda)$ include the attenuation of the intensity and the contamination of the unpolarized neutrons for the reflected beam.

where "P" and "I" denote the polarization and intensity (sum of the intensities of both spin states); the subscripts "T" and "R" denote the transmitted and reflected beams, respectively. The exponential factor in eq.(7) is the intensity loss due to absorption through the substrate. The λ-dependent reflectivities ($I^{\pm}(\theta_0,\lambda)$) in the actual beam collimation were calculated from the supermirror reflectivities (described below). Figure 2 shows these calculated quantities along with the experimental results. Since up-spin neutrons are

reflected at $\lambda>\lambda_c^+$, the main component of the transmitted beam is the down-spin neutrons and that of the reflected beam the up-spin neutrons. The polarization of the transmitted beam ($P_T(\lambda)$) increases with λ and $P_T(\lambda)=1$ at $\lambda>\lambda_c^+$ if $I^+(\theta_0,\lambda)=1$. At $\lambda<\lambda_c^+$, $I_T(\lambda)$ is greater than 1 due to the transmission of down-spin neutrons, where the intensity of the incident unpolarized beam is defined to be 2. At $\lambda=\lambda_c$, $I_R(\lambda)$ increases due to the reflection of up-spin neutrons and becomes greater than 1 at larger λ due to the reflection of the down-spin neutrons. At $\lambda>\lambda_c^-$, $I_R(\lambda)$ should be 2 because of the total reflection of neutrons in both spin states; however, the critical region of the down-spin reflectivity is smeared out due to the large beam divergence, and eventually the intensity gradually increases. The experimental data shown in Fig.2 were obtained by correcting the polarizing efficiency of the spin analyzer and the flipping efficiency of the spin flipper for the observed polarizations.

The polarization of the transmitted beam can be calculated using eq.(5) with the actual beam collimation. First, by using the above-mentioned $R^{\pm}(Q)$ calculated from only the thickness distribution, $P_T(\lambda)$ was calculated to be 1 at $\lambda>\lambda_c^+$, contrary to the observed polarization less than 1. As mentioned above, $P_T(\lambda)=1$ results from $R^+(Q)=1$. Therefore, we introduced the factor, $\alpha(Q)$, to reproduce the actual reflectivity, and calculated the polarization in eq.(6) using $\alpha(Q)R^{\pm}(Q)$ instead of $R^{\pm}(Q)$, where a monotonous empirical formula for $\alpha(Q)$ was established on the assumption that $\alpha(Q)$=1, 0.99, 0.95 and 0.93 at Q=0, 0.02, 0.04 and 0.06Å^{-1}, respectively. This Q-dependent factor is consistent with a nominal specification of the reflectivity of a $3Q_c^{Ni}$ supermirror.[4] As shown in Fig.2(a), the observed polarization was well described by the calculation.

On the other hand, as shown in Figs.2(b) and (c), the observed polarization and intensity of the reflected beam was much less than the calculation. The observed spectrum was comparable to the quantity in eq. (7) or (8) multiplied by the incident-beam spectrum ($I_i(\lambda)$). Since the polarization of the transmitted beam was well described by the calculation, assuming the observed spectrum of the transmitted beam to be $I_i(\lambda)I_T(\lambda)$, the incident-beam spectrum can be deduced by using the calculated value of $I_T(\lambda)$. The observed intensity of the reflected beam shown in Fig.2(c) was obtained by using $I_i(\lambda)$ deduced from the transmitted beam spectrum. The less intensity and less polarization result from the more divergent beam of the reflected neutrons and the existence of unpolarized neutrons coming to the spin analyzer without reflecting on the supermirror in the present device, respectively. In fact, the following intensity greatly improved the calculation describing the observed intensity:

$$I'_R(\lambda) = AI_R(\lambda) + \frac{B}{\Delta\theta_i(\lambda)}\exp\left(-\frac{(4\ln 2)\theta^2}{\Delta\theta_i(\lambda)^2}\right) \quad (9)$$

where the first term is the attenuation of the intensity and the second term is the contamination of unpolarized neutrons. In the first term, the geometrically-obtained attenuation factor, $A=(w_1/L_1)/(w_0/L_0)$, was used, where w_0=1.8 cm and L_0=59 cm are the outlet area and the half length of the present device, respectively, w_1=2.0 cm is the aperture of the spin analyzer, and L_1=203 cm is the distance between the center of the present device and the inlet of the spin analyzer. The second term is the beam spread of the incident neutrons through the guide tube, detected at the spin-analyzer direction of θ=1.2°. The factor, B, is an adjustable parameter and $\Delta\theta_i(\lambda)$ is the λ-dependent incident beam divergence ($\Delta\theta_i=\lambda Q_c^{Ni}/4\pi$, as a result of the total reflection on the nickel surface of the guide tube). The calculated polarization, $P'_R(\lambda)$, corresponding to eq.(9) well improved the calculation describing the observed polarization shown in Fig.2(b).

We demonstrated an investigation of the performance of the polarizing beam-splitter device installed at a pulsed cold-neutron source. The present device is more optimized for the transmitted beam and the transmitted beam is suitable for polarization-required or collimation-controlled experiments. Although the reflected beam is more divergent and less polarized, it is more intense than the transmitted beam, therefore, the reflected beam is suitable for intensity-required experiments.

References

1) F. Mezei: SPIE Proc. 983 (1989) 10; Th. Krist et al.: Physica B 213&214 (1995) 939.
2) S.Itoh et al.: KENS Report X (1995) 208.
3) C. F. Majkrzak et al.: SPIE Proc. 1738 (1992) 90: J. L. Wood: SPIE Proc. 1738 (1992) 22.
4) J. L. Wood (Osmic Inc.): private communication (1995).

Resolution Corrections Using Monte Carlo Method and Application to the Analysis of Phonon and Magnon Spectra

S.Taniguchi, Y.Todate* and K.Tajima

Department of Physics, Keio University, Hiyoshi, Yokohama 223
*Department of Physics, Ochanomizu University, Tokyo 115

Resolution corrections for inelastic neutron scattering data taken by MAX spectrometer[1] were made using a formalism which is modified from a conventional method developed by Cooper and Nathans[2] for the triple axis spectrometer in the steady reactor. Symmetrical Gaussian shape is always assumed for the distribution of neutrons, which makes easy to formulate the resolution function in a simple form. In the pulse neutron source, however, the approximation with the symmetrical Gaussian is not appropriate for the time distribution of the incident pulse neutrons from the moderator, which makes it difficult sometimes the fitting analysis of experimental results. Another disadvantage for the conventional calculations of the resolution function of this method are time consuming and inefficient because the calculations for a large number of time channel and multi detectors are required.

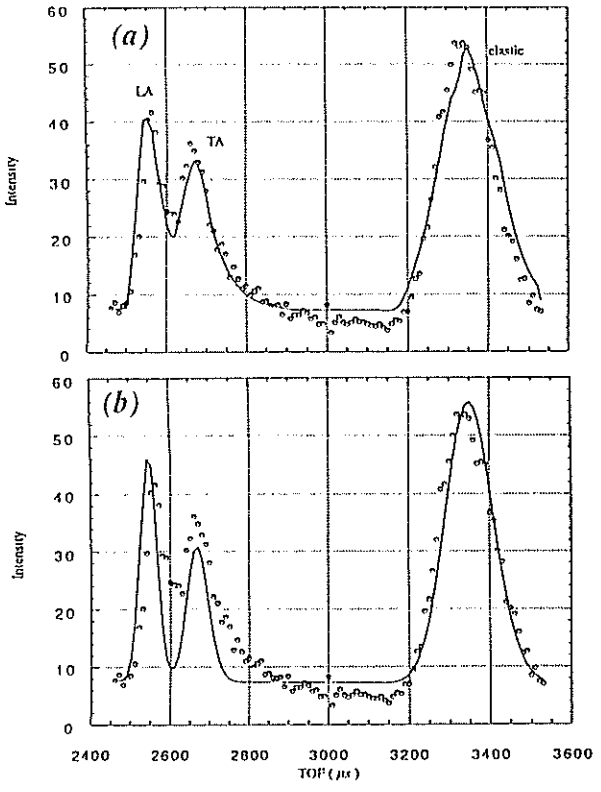

Fig.1. TOF phonon spectrum of Cu. The solid line in (a) is the calculated result with Monte Carlo method and (b) is the result with conventional method.

In order to improve the resolution correction of inelastic scattering measurements in MAX, Monte Carlo method was examined[3] for the one-dimensional spin wave and a reasonable result could be obtained. In this report, the correction has been extended for the three dimensional system and the time of flight spectra of phonons in Cu and spin waves in Fe_3Pt observed by MAX have been analysed by Monte Carlo method. Time of flight spectra of phonons in Cu at room temperature are shown in Fig.1, and results of fitting with Monte Carlo and conventional methods are compared in Fig.1-(a) and (b) respectively. The life time of phonons is assumed as infinity in both calculations. The shape of calculated result with conventional method exhibits symmetrical and can not well reproduce tails of the phonon profiles. With Monte Carlo method, on the other hand, good agreement between the calculation and observation is obtained even at asymmetrical tails which is caused by the time asymmetry distribution of incident neutrons. An asymmetrical shape of the spectrum for magnons in Fe_3Pt can be also well reproduced as shown in Fig.2. Thus, Monte Carlo method is quite useful to perform the resolution correction for time of flight inelastic scattering measurements.

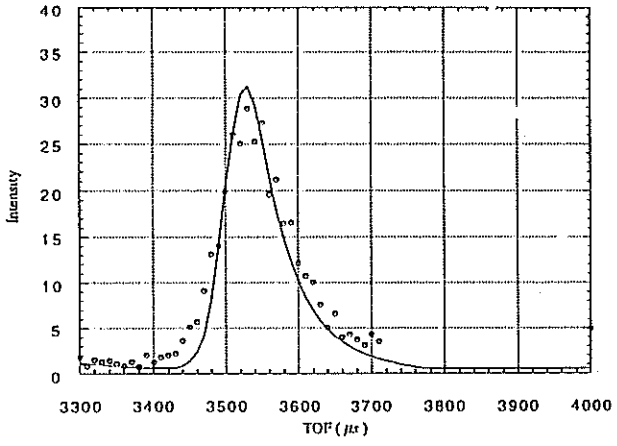

Fig.2. TOF spectrum of magnon in Fe_3Pt and calculated result with Monte Carlo method.

References

1)Y.Todate et al., Jpn. J.Appl. Phys. **29** (1990) 1220.
2) M.Cooper and R.Nathans, Acta Cryst. **23** (1967)357
3)Y.Todate et al., KENS-Report X(1995) 207.

Development of 25 T repeating pulsed magnetic fields system for neutron diffraction experiments

H. NOJIRI, K. TAKAHASHI, T. FUKUDA, M. MOTOKAWA, N. ARAI[A] and M. ARAI[B]

Institute for Materials Research, Tohoku University, Sendai 980-77, Japan
[A]Department of physics, Kobe University, Rokkodai, Kobe 657, Japan
[B]National Laboratory for High Energy Physics, 1-1 Oho, Tsukuba-shi, Ibaraki 305, Japan

1. Introduction

Magnetic fields are one of important parameters to study phase transitions in condensed matters, especially in magnetic substances. The determination of the magnetic structures is the important base to study such new phases induced by strong magnetic fields and the neutron diffraction is the most powerful probe to determine the magnetic structures. However, the magnetic fields available by superconducting magnets for neutron diffraction experiments have been limited to below 10 T. Since 1991, a new type of system called "repeating pulsed magnetic fields(RPMF)" has been employed in KEK[1]. As the first stage of this project, the magnetic fields as high as 16 T were generated and they are applied for several experimental studies[2-4]. One of the important concepts of RPMF is the combination of the pulsed magnetic fields and the pulsed neutron sources. The Joule's heating of the magnet is much decreased by the use of instantaneous pulsed fields. To accumulate the data quickly, the field generation is repeated by using a water cooled Bitter magnet. In these senses, RPMF is the crossbreed of the steady and the pulsed magnetic field generators.

The new stage of the project to generate magnetic fields above 20 T was started in 1995[5]. The important keywords for the design of the new type magnets are the use of Cu-Ag alloy and the multi-layered structure. Recently, we succeeded in generating 25 T fields by this new type magnet and the installation of this magnet for the real experiment is now under operation.

2. Design and test of the magnet

As is well know, both the good mechanical strength and the electrical conductivity are required for the conductors for high field magnets. As the new material for the magnet, we used the Cu-Ag alloys. The mechanical and the electrical specifications are listed in Table 1. The mechanical strength of the Cu-Ag alloys corresponds to the Maxwell stress in 35 T magnetic fields. It has also good electrical conductivity compared with other conductors such as Cu-Be alloy.

Another important point for the design of the Bitter plates is to disperse the very strong electromagnetic forces acting against the magnets. Fig. 1 shows the shapes of the Bitter plates of the old(a) and the new type (b). In the Bitter plate (a), the electromagnetic force concentrates to the corner of the connective part of the Bitter plate where the thickness is processed to the half. This design is good to keep the electrical contact between Bitter plates, but is not favorable from the mechanical strength consideration. In the new design, we employed the double layered structure with the Bitter plate (b). The thickness of the Bitter plate is 0.5 mm. These are stacked forming the two helixes. The places connecting two successive Bitter plates are changed about 180 degree between two helixes. For this design, the concentration of the electromagnetic stress can be avoided. Two glass fiber reinforced epoxy resin

Table 1. Specifications of magnet conductors.

Material	Yield strength (Kgw/mm^2)	Resistivity at R. T. ($\mu\Omega$ cm)
Cu	30	1.7
CuAg(50 %) 1	54	2.0
CuAg(50 %) 2	57	2.1
CuBe(0.5% Be)	80	3.1

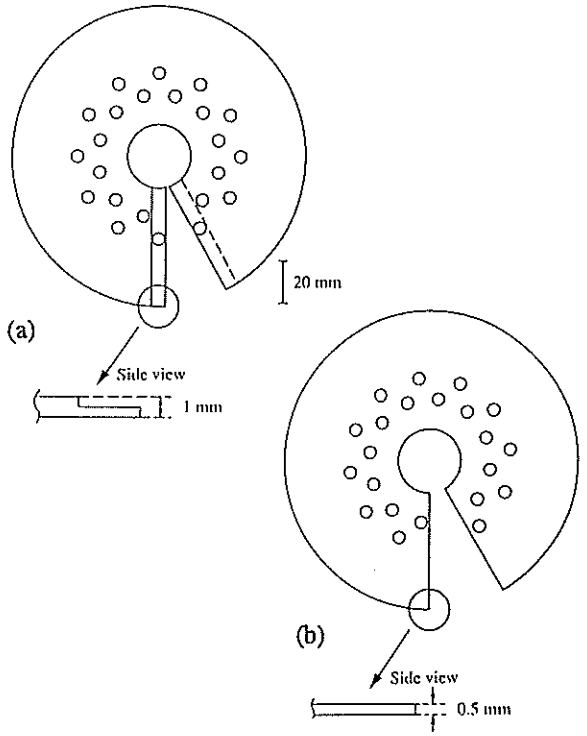

Fig. 1 The Bitter plate for old (a) and new(b) magnets.

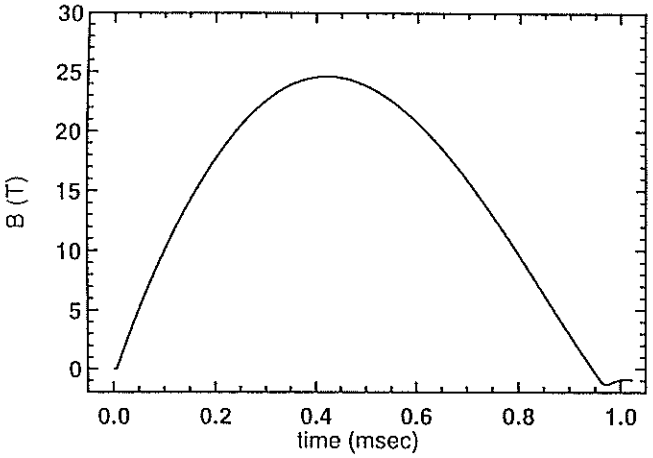

Fig. 2 The waveform of the generated magnetic fields of the new type magnet.

sheets of 0.2 mm thickness is inserted for the electrical insulation between conductor layers.

The solenoid magnet made of Cu-Ag Bitter plates with 31 mm bore is assembled and tested. The magnet with Cu plates is also tested for the comparison. The field generation is repeated more than 5000 times in high magnetic fields above 20 T up to the maximum field of 25 T for Cu-Ag magnet. The Cu magnet is tested up to 20 T. The trace of the generated field is in Fig. 2. The magnets are disassembled after the test for the inspection and the no-damage of the Bitter and the insulating plates are found in Cu-Ag magnet. The present results indicate that we can generate 25 T by the new designed magnet. The life time of about 0.1 millions of shots of the old type magnet will be much improved for this design. The test and the installation of the split-type magnet for MRP spectrometer at KENS are now under operation. The more detailed information of the development of the new magnet will be appeared in the different article.

3. Summary and future plan

We have succeeded in generating 25 T with RPMF magnet developed for neutron diffraction experiments. The key factors of the present improvement is the double layered structure and the use of the Cu-Ag alloy.

To generate much higher magnetic fields of 30 T, the optimization of the cooling hole arrangement of the Bitter plate and the extension of the storing energy of the capacitor bank power source is needed. These are now under consideration. Such development will lead to fruitful results by the application of our system to not only elastic but also inelastic neutron scattering experiments with the intense pulsed neutron source constructed in JHP project.

References

(1) H. Nojiri *et al.*, Physica B 180&181, 31-33 (1992)
(2) H. Nojiri *et al.*, J. Phys. Soc. Jpn. 60, 2380-2387(1991)
(3) M. Mino *et al.*, Physica B 201, 213-216(1994)
(4) M . Motokawa *et al.*, J. Mag. Mag. Mater. 140-144, 1107 (1995)
(5) M. Motokawa *et al.*, IEEE Trans. on Magnetics 32, 2534-2537(1996)

A Cryostat for Vapor-Deposited Amorphous Solids Designed for LAM Spectrometer

O. YAMAMURO, I. TSUKUSHI*, T. MATSUO, K. TAKEDA[a], T. KANAYA[b] AND K. KAJI[b]

Department of Chemistry, Graduate School of Science, Osaka University, Toyonaka, Osaka 560
[a] Department of Chemistry, Naruto University of Education, Naruto, Tokushima 772
[b] Institute for Chemical Research, Kyoto University, Uji, Kyoto 611

Recently, great attention has been paid for various properties of amorphous solids (structural relaxation, low energy excitation etc.). Simple molecular systems are suitable for such studies since the intermolecular interaction is simple van der Waals forces (short-range and isotropic) so that the result can be compared with those of theoretical and molecular dynamics studies where similar interactions are assumed. However, there exists a serious problem that the simpler the molecular structure is, the more difficult it is to prepare the substance in a glassy state. This is because the simple molecules tend to crystallize readily on cooling. In the present study, therefore, we developed a new type of a cryostat, with which one can form glassy states of simple molecular substances by depositing their vapor on a cold substrate inside the sample cell and examine it in situ by neutron scattering. This type of cryostat has never been constructed before.

Figure 1 shows a schematic drawing of the cryostat. It is mounted into the vacuum chamber of the neutron spectrometer at the O-ring flange N. For the temperature control of the sample, a cylindrical copper block F (40 mmϕ, 30 mmH) and a cylindrical aluminum sample can J (52 mmf, 130 mmH, 0.5 mmT (at beam position)) are screwed to the second stage E (ca. 6 K) of the refrigerator A (Iwatani CryoMini M310). The manganin heater wire G1 and $(Au_{99.93}Fe_{0.07})$-Chromel thermocouple H1 are attached on the surface of F. The temperature of F is controlled within the fluctuation of 0.1 K by using a PID circuit. The cylindrical substrate K (16 mmϕ, 90 mmH, 0.5 mmT) on which the vapor is deposited is positioned inside J. The aluminum effusion pipe L is located at the center of J and connected to the sample-gas supplying system located outside the cryostat through a sample transfer tube Q (1 mmϕ, 0.15 mmT) made of stainless steel. The effusion pipe L is densely perforated, the diameter of the pin holes being 0.2 mm. Manganin heater wires G2 and G3 are wound on the surfaces of L and Q. $(Au_{99.93}Fe_{0.07})$-Chromel thermocouples H2 and H3 are fixed to L and Q for measurement and control of their temperatures. Temperature control of these parts was necessary to prevent condensation of the sample vapor inside L and Q during vapor-deposition. The space in J is

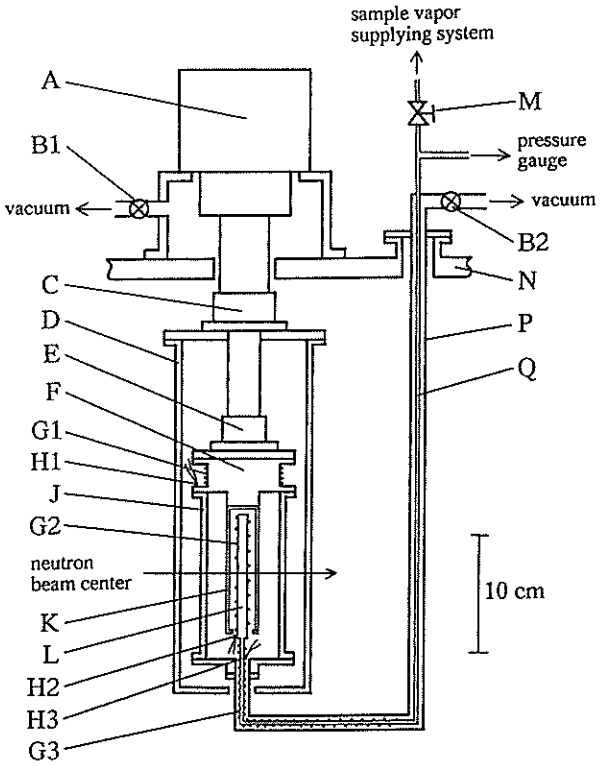

Fig. 1. Schematic drawing of the cryostat for neutron inelastic scattering experiment of vapor-deposited glasses. A: refrigerator, B: vacuum valves, C: first stage of the refrigerator, D: radiation shield, E: second stage of the refrigerator, F: Cu block for temperature control, G: heater wires, H: thermocouples, J: sample can, K: substrate, L: sample effusion pipe, M: precision needle valve, N: flange, P: flexible bellows tube, Q: sample transfer tube.

connected to evacuation and He-gas supplying systems outside the cryostat through a flexible bellows tube P (8.5 mmϕ) made of stainless steel. PTFE wire, which is not shown in the drawing, is sparsely wound around Q as a spacer between Q and P. The cylindrical aluminum radiation shield D, which is cooled down to about 70 K by the first stage C of the refrigerator, shuts the ambient radiation away from F and J. A larger cylindrical aluminum vacuum can (not shown in the drawing) connected at the flange N encloses the entire system. Aluminum is used because

of its high thermal conductivity and high transparency to a neutron beam, while stainless steel is used for its low thermal conductivity.

The sample vapor was deposited as follows. (1) All the spaces inside the cryostat were evacuated down to a vacuum of 10^{-6} torr by a turbo vacuum pump through the valves B1, B2, and M. (2) The cryostat was cooled down to the lowest temperature (ca. 10 K). (3) The temperature of the effusion pipe L and the sample transfer tube Q were controlled at a temperature higher than the condensation temperature of the sample vapor. This is a function of the vapor pressure. (4) After closing the valve B2 and M, the sample gas was introduced into the effusion pipe L by opening the precision needle valve M slowly; the sample gas was sprayed through the pin holes in the effusion pipe and deposited on the substrate K. (5) During the vapor-deposition, the pressure inside the transfer tube (Q) was monitored by the high precision pressure gauge. The pressure was controlled by adjusting M. (6) After the deposition, the valve M was closed and small amount of helium gas was introduced into J through P by opening B2. This established a uniform temperature inside J.

Propylene, which cannot be vitrified by normal liquid quenching, was vapor-deposited onto the substrate at 20 K.[1] The vapor pressure during the deposition was controlled at about 2 torr and it took about 5 h to complete the deposition. The mass of the deposited sample was estimated to be 0.308 g from the pressure measurement of the sample. This sample mass corresponds to an area of 36.8 cm^2 and thickness of 0.13 mm assuming a uniform thickness.

Inelastic neutron scattering (INS) experiment was performed with the inverted geometry time-of-flight (TOF) spectrometer LAM-40.[2] The data were collected at six scattering angles 24°, 40°, 56°, 72°, 88°, and 104°. The duration of the experimental time was about 24 hours for a given temperature. The observed TOF spectrum was converted to a differential scattering cross section after making corrections for empty cryostat scattering, counter efficiency, the incident neutron spectrum and self-shielding (90 % transmission) and then converted to the incoherent dynamic scattering law as usual.

Figure 2 shows the incoherent inelastic scattering functions $S(2\theta,\omega)$ of the as-deposited (open circles) and annealed (closed circles) samples of glassy propylene at 18 K. The annealing was done at around T_g (55 K) for 7 h. Both data were the sum of the spectra at the seven scattering angles (Q_{av} = 1.54 $Å^{-1}$) and symmetrized using the Bose factor of 18 K. The as-deposited sample exhibited a broad but clear peak at around 3 meV. This peak was attributed to the low energy excitation. The annealing reduced the intensity

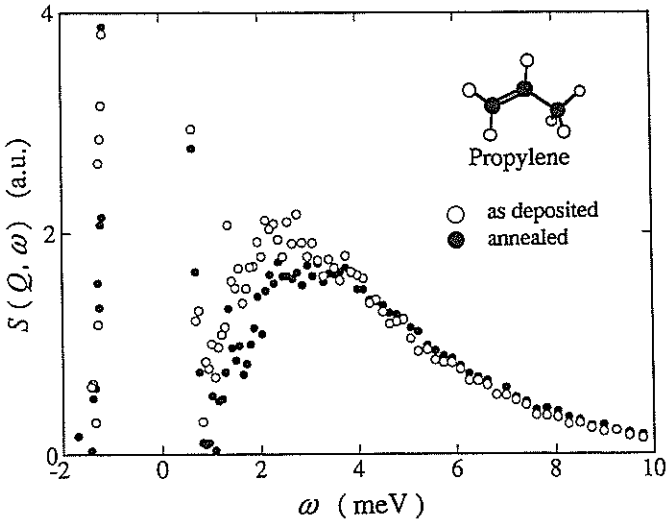

Fig. 2. Incoherent dynamic structure factor $S(2\theta,\omega)$ of vapor-deposited glassy propylene observed by the LAM-40 neutron spectrometer. The open and closed circles denote the data of the as-deposited and annealed samples, respectively.

of the low-energy excitation peak in the lower energy region.

We are now planning to do experiments on simpler molecular glasses such as ethene, methane, hydrogen and rare gases if they do form glass. For such experiments, it is necessary to deposit sample vapor very slowly onto a very cold substrate to form very thin sample layer. The amorphous argon doped with 3 % of hydrogen has been successfully formed by very slow vapor-deposition at 10 K.[3] Our apparatus can be applied to this system with a little improvement.

We thank Professor Susumu Ikeda (KEK) and Dr. Kaoru Shibata (Tohoku University) for their help in the construction of this cryostat.

References

1) O. Yamamuro, I. Tsukushi, T. Matsuo, K. Takeda, T. Kanaya and K. Kaji, J. Chem. Phys., in press.
2) K. Inoue, Y. Ishikawa, N. Watanabe, K. Kaji, Y. Kiyanagi, H. Iwasa and M. Kohgi, Nucl. Instrum. Method **A238**, 401 (1984).
3) A. Kouchi, Jpn. J. Appl. Phys. Pt. 2, **29**, L807 (1990).

* Present address: Institute for Chemical Research, Kyoto University, Uji, Kyoto 611

Development of Data Acquisition Electronics System for Neutron Scattering Experiment

S. SATOH and M. FURUSAKA

National Laboratory for High Energy Physics, 1-1, Tsukuba-shi, Ibaraki 305

We have developed two data acquisition electronics (DAE) systems for neutron scattering experiment based on VME system. One is a position-sensitive neutron-detector (PSD) system, and the other is time-analyzer (TA) system. We employed a modular system approach, therefore they are flexible and extensible. For example, we have been using the system with a few hundred PSD's with reasonable position resolution and time channel numbers as described in this paper. Furthermore, the systems are relatively low cost and easy to set up, therefore they are also suitable for very small experiments which only need a few detectors.

Position-sensitive neutron-detector system

In recent years, the requirement for a large-area detector system with a relatively good positional resolution has become more crucial for neutron-scattering instruments such as high-resolution powder diffractometers, and small-angle scattering instruments.

We have developed a versatile system based on Reuter Stokes made linear position-sensitive He-3 gas detectors of 1/2 inch diameter and 607mm effective length. The system consists of detector-amplifier units, encoding modules and computers. Each unit holds 8 PSD's, and arbitrary number of units can be lined up so as to cover a large area with very thin gaps. The encoding modules (PSDXC) encode the position and time, and histograms are made by personal computers.

We have been using a system with 250 PSD's on the high-resolution powder diffractometer, Vega, at KENS; also, other 500 PSD's are being installed to our new high-resolution powder diffractometer, Sirius. The system has been improved from that for Vega. It is easier to setup and the cost is lower. A general view in Fig. 1 shows overall PSD-XC system structure.

The following are the specifications of the system:

1. The PSD unit is very compact (width 104 mm length 680 mm depth 60 mm), and each unit supports 8 PSD's. The signals from both ends of a PSD are fed to charge-sensitive-preamplifiers and shaping-amplifiers located inside of the unit behind the PSD's. The output signals from the units are transmitted to PSDXC modules by a twisted-pair flat cable.

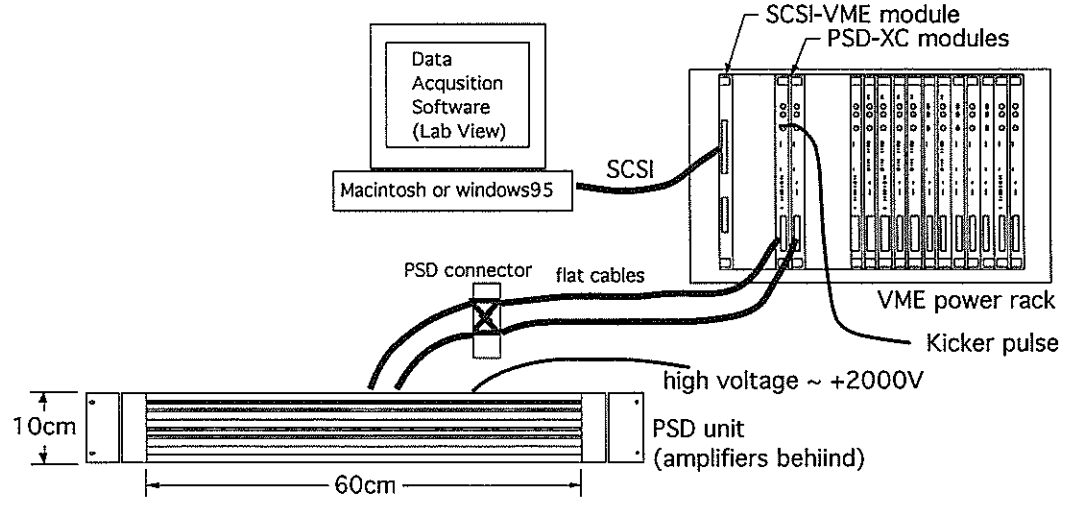

Figure 1 A general view of PSD system

2. The position and time associated with a neutron detection event are then encoded by a PSDXC VME double-height 1-span module (width 20 mm height 233 mm depth 160 mm). Since the module can analyze signals from four PSD's, two modules are necessary to serve for a PSD unit. Position is encoded with a resolution of 256, time with 65536 in 1 μS step. The encoded events are then stored into a FIFO buffer-memory which can hold 32 kwords as 32-bit events. The overall position resolution is approximately 7 mm FWHM. We put cadmium masks around a PSD tube like shown in Fig. 2, and the response function is shown in Fig. 3.

3. We also developed an interface module (SCSI-VME) that can read/write data from/to VME modules through a standard SCSI connection. By employing the SCSI standard we can, in principle, use any personal computers or workstations. Although we are currently using Apple Macintosh computers, the system was tested on a PC running Windows 95 operating system. We are able to eliminate an expensive VME CPU module that is usually necessary to use with a VME system. The transmission time was 1.2μs/byte, when we read the events from the PSD-XC modules.

4. Histogramming is performed on a computer with a program written in a package software, LabVIEW, of NATIONAL INSTRUMENTS. We have developed a SCSI driver software module for it. Since the histogramming system is very versatile, we can easily change the position and time resolution, and can have multiple histograms with different setups simultaneously. The system also supports on-the-fly time-focusing.

The computers are connected on a network with TCP/IP, and we can control remote computers across the network.

Eight-input amplifier and time-analyzer system

To serve for the demands to install a considerable number of detectors (over a few hundreds) for time-of-flight neutron-scattering instruments, we have developed a low-cost, compact and versatile system. The system consists of amplifier units, time-analyzer(TA) modules and front-end computers.

The overall system structure is schematically shown in Fig. 4. It has the following characteristics:

1. The amplifier unit is compact (width 106 mm length 268 mm depth 39 mm for eight inputs) and has LEMO-type connectors for the detector input. Signals from neutron He-3 gas detectors are collected by charge-sensitive-

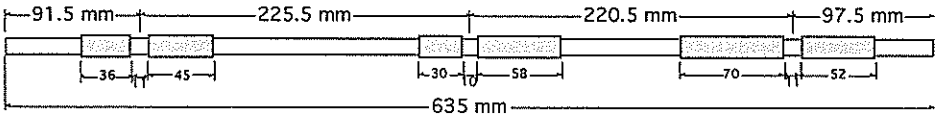

Figure 2 cadmium masks around the PSD

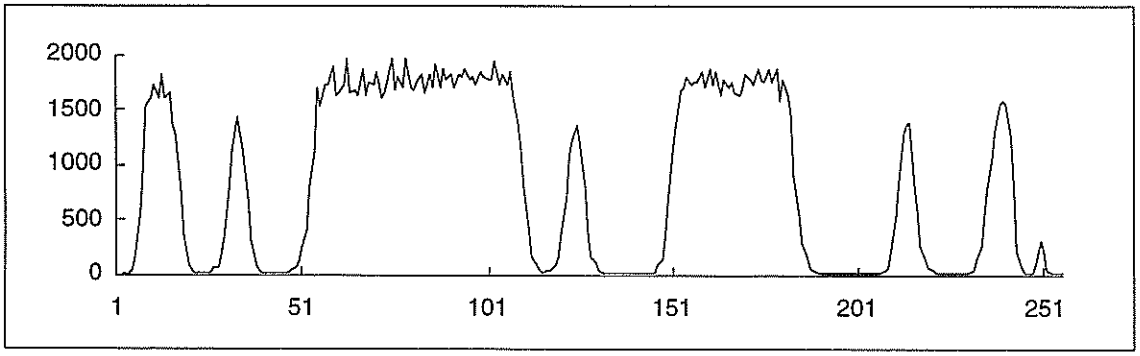

Figure 3 PSD data of position

amplifiers and are conditioned by shaping-amplifiers. The output is then transmitted by a twisted-pair flat cable. We use the same type of amplifier boards as the PSD system.

2. TA is housed in a VME double-height 1-span module (width 20 mm height 233 mm depth 160 mm). It accepts signals from up to eight detectors through a flat cable from the amplifier unit. LEMO-type connectors are also provided for individual detector inputs. TA modules have discriminator circuits that are adjusted from the front panel of the module. The digitized signals are then time analyzed and histogrammed into built-in memory. The memory can hold 4095 words (2^{12}-1) with 24 bits/word for each input.

3. We have two types of TA's. One is called TA17XC, which is for general purposes; the other is TA19XC, which is for time-focusing experiment.

TA17XC modules have a 4095-word time channel width memory that is common to all eight channels. It can have a flexible time channel width; each time channel bin can have a minimum of 1 μs up to about 4 ms with an integer multiple of 62.5 ns.

Although the TA19XC module can only have constant time channel bins for individual inputs, it can have different bin widths for different inputs. The time channel width can be ranged from 1 μs up to 15.9375 μs with an integer multiple of 62.5 ns.

4. We also developed an interface module (SCSI-VME) that can read/write data from/to VME modules through a standard SCSI connection. Although we are currently using Apple Macintosh computers, the system was tested on a PC running the Windows 95 operating system. We use the same type of module as the PSD system.

5. Instrument-control software is written in a package software, LabVIEW, of NATIONAL INSTRUMENTS. We have developed a SCSI driver software module for it similar to the PSD system. The computers are connected on a network with TCP/IP, and we can control remote computers across the network.

References

1) S. Satoh, T. Adachi, and M. Furusaka Development of Data Acquisition Electronics System for Neutron Scattering Experiment, KEK Internal 96-14 (in Japanese)
2) S. Satoh, M. Furusaka and K. Oikawa, Development of PSD system for Neutron Scattering Experiment, KEK Internal 93-10 (in Japanese)

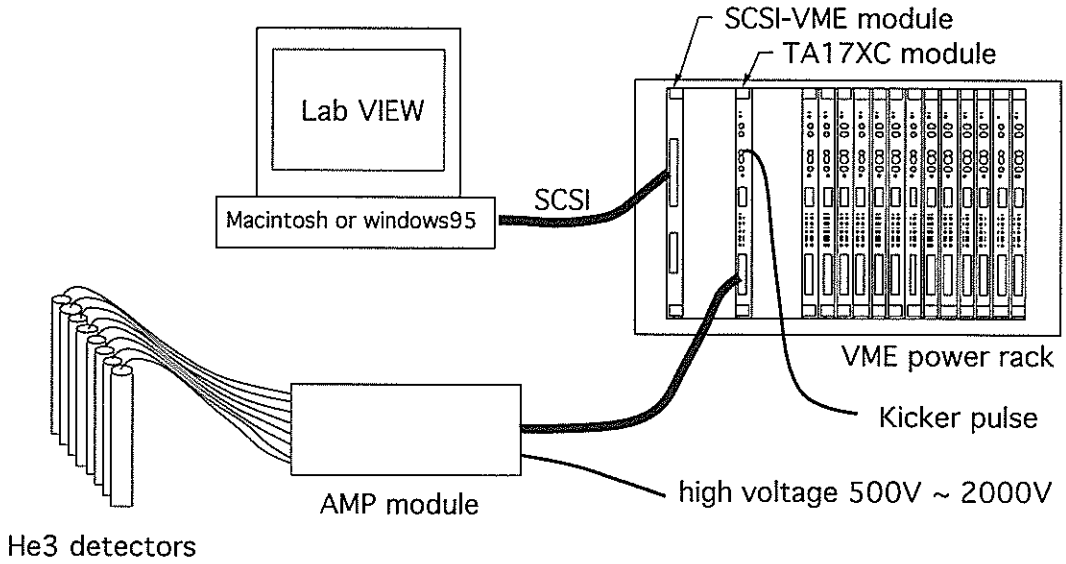

Fig. 4 A general view of Amplifier and TA system.

Polarized Proton Filter at Liquid Nitrogen Temperature

H.M.SHIMIZU, Y.TAKAHASHI*, M.IINUMA*, I.SHAKE*, M.ODA*, A.MASAIKE*, T.YABUZAKI*, M.FURUSAKA**, T.OKU*** and Y.OGAWA****
The Institute of Physical and Chemical Research (RIKEN), 2-1 Hirosawa, Wako 351
*Department of Physics, Faculty of Science, Kyoto University, Kyoto 606-01
**National Laboratory for High Energy Physics (KEK), 1-1 Oho, Tsukuba 305
***Faculty of Science and Technology, Keio University, Houhoku-ku, Yokohama 223
****Faculty of Engineering, Hokkaido University, Kita-ku, Sapporo 060

Polarized proton filter can be used as a wide band neutron spin polarizer and analyzer according to the large spin dependent interaction between neutrons and protons. Dynamical nuclear polarization (DNP) is a well established method to obtain a large nuclear polarization under thermal non-equilibrium condition. In the DNP method, a sufficiently large electron polarization of paramagnetic centers at a thermal equilibrium, which is obtained at the temperatures less than 1K and under a magnetic field of a few tesla, is transferred to nuclear polarization according to spin double flip processes enhanced by a microwave irradiation. Low temperature is required also for the suppression of spin-lattice relaxation of proton and for the narrow ESR line width. The application of the polarized proton is sometimes limited by the low temperature and the strong magnetic field.

We report the experimental results of 20% proton polarizations obtained at liquid nitrogen temperature under the magnetic field of 3kG based on a new method[1,2,3,4].

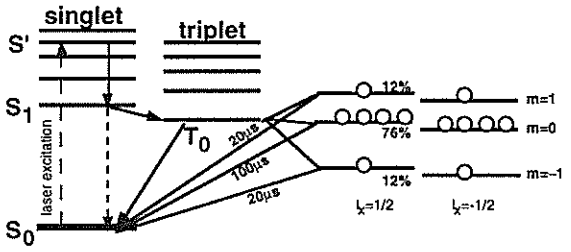

Fig. 1 Energy levels of the pentacene molecule. The electron spin in the lowest triplet state is spontaneously aligned. The solid arrows represents non-radiative transitions, the dotted arrow a radiative transition and the dashed arrow the laser excitation.

In the new method, the electron polarization is obtained in an excited state of pentacene molecule. Pentacene is introduced into single crystals of naphthalene and p-terphenyl as a dopant so that pentacene molecules are aligned to be magnetically equivalent. The energy diagram of pentacene molecule is schematically shown in Fig.1. The ground state is a singlet state S_0, and can be excited up to higher singlet states S'. S' is relaxed to the lowest excited singlet state S_1 with the time scale of psec through non-radiative processes. S_1 is branched to the S_0 and the lowest triplet state T_0[5,6]. Population distribution of magnetic substates of T_0 is given by a selection rule independent of temperature and external magnetic field strength, as shown in Fig.1 when the magnetic field is applied along x-axis of pentacene molecule[7]. The population unbalance between m=1↔m=0 and m=0↔m=-1 corresponds to 73% electron polarization far from thermal equilibrium.

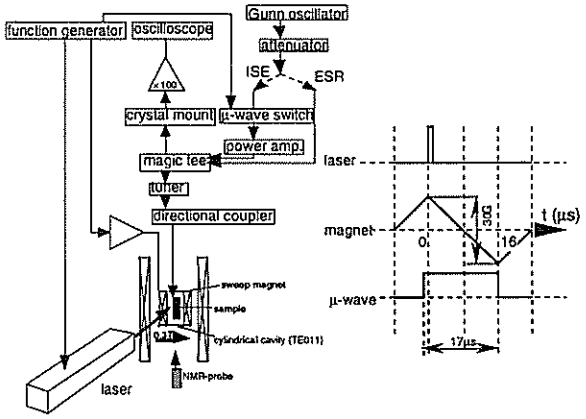

Fig. 2 Experimental setup and timing chart of laser irradiation, magnet sweep and μ-wave irradiation. A cw microwave power of 22mW was input for ESR detection. During a pulsed microwave (width~17μs, input power~1W) was applied after a laser excitation, the magnetic field was swept for 30G in about 16μs.

The electron polarization was transferred to nuclear polarization within the lifetime of the T_0 state (~20μs) by means of an improved DNP based on integrated solid effect (ISE)[8,9] as shown in Fig.2. The ESR linewidth should be narrow enough to selectively activate one of the forbidden transitions since each forbidden transition enhances nuclear polarization in the opposite direction. In our case, however, ESR line width is broader than the spacing of the nuclear Zeeman splitting. ISE was introduced to enhance nuclear polarization under such condition. The broad ESR line is an envelope of individual ESR lines of

which center frequencies are varied due to the variation of local magnetic fields.

Just after the laser irradiation by a pulse dye laser (average power: 500mW, dye: Rhodamine-6G) whose wavelength matches pentacene absorption peak, double spin flip process was induced one by one by sweeping magnetic field strength by ~30G around 3kG in 16μs. The electron polarization is flipped according to a fast adiabatic passage on passing the allowed transition frequency and additional spin transfer is induced at the other forbidden transition. In the second transition, the nuclear spin is pumped up to the same direction as the first transition since electron polarization is reversed on the fast adiabatic passage.

A single crystal of naphthalene doped with pentacene (0.01mol%, 8mm×5mm×3mm) was placed in a cylindrical cavity and 3kG magnetic field was applied. Microwave of 9.3GHz was applied and the input power was 1W which satisfied the Hartmann-Hahn condition in the sample cavity for the maximum spin transfer efficiency. The orientation of the crystal was adjusted so that the x-axis of pentacene was parallel to the magnetic field by maximizing the amplitude of ESR signal.

The proton polarization was measured by observing transmittance enhancement of cold neutron beam at KEK-BSF SAN beam line in the energy range of 1-3meV after stopping laser and microwave irradiation. Relaxation of proton polarization was measured as shown in Fig.3. The maximum proton polarization was 20.0±3.6%. The holding field was reduced to 7G for a faster relaxation, and we still obtained t_1=165min even with such a low field.

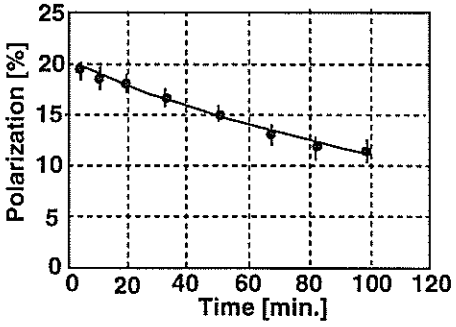

Fig. 3 Relaxation of the polarized proton in the naphthalene single crystal doped with pentacene at liquid nitrogen temperature under the magnetic field of 7G. The polarization was determined from the measurement of cold neutron transmittance enhancement. A pulse dye laser of average power of 500mW with the dye of Rhodamine-6G was used for laser excitation. The maximum value of the polarization was 20.0±3.6% and the relaxation time was 165min.

The proton polarization was measured also with p-terphenyl doped with pentacene of 0.1mol% at liquid nitrogen temperature. P-terphenyl is considered to be more suitable for DNP at room temperature. The advantages of p-terphenyl over naphthalene are (1) a pentancene concentration of up to 0.1mol% is possible giving a larger buildup rate, (2) t_1 of protons in pentacene increases with increasing temperature beyond 193K, giving a stable buildup rate which can be expected to be suitable against local heating, although t_1 itself is shorter than naphthalene.

We obtained proton polarization of 18.9±1.2% in the neutron transmission experiment as shown in Fig.4. The relaxation time was 30 minutes under the holding field of 3kG.

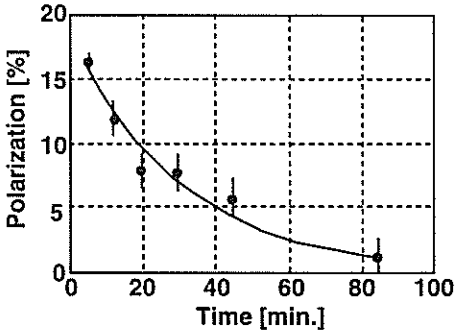

Fig. 4 Relaxation of proton polarization, determined by measuring neutron transmittance, in p-terphenyl single crystal doped with 0.1mol% pentacene at liquid nitrogen temeprature under the magnetic field of 3kG with the pulse dye laser.

20% proton polarization was obtained at liquid nitrogen temperature under the magnetic field of 3kG using single crystals of naphthalene and p-terphenyl doped with pentacene. P-terphenyl has a potential to be polarized even at room temperature. Polarized proton at such high temperatures enables us to apply polarization under various experimental conditions.

References

1) M.Iinuma et al, Phys Lett. **A208** (1995) 251.
2) H.M.Shimizu et al., Proc. 8th Intl. Workshop on Polarized Target Materials and Techniques, May27-29, 1996, Vancouver, Canada.
3) M.Daigo et al., AIP conf. proc. **343** (1995) 567.
4) M.Daigo et al., Proc. 6th Workshop on High Energy Spin Physics, Sep.18-23, 1995, Protovino, Russia.
5) H. de Vries and D.A.Wiersma, J. Chem. Phys. **70** (1979) 5807.
6) Wm.R.Lambert and A.H.Zewail, Chem Phys. Lett. **69** (1980) 270.
7) D.J.Sloop et al., J. Chem. Phys. **75** (1981) 3746.
8) A.Henstra et al., Chem Phys. Lett. **165** (1990) 6.
9) A.Henstra el al., Phys. Lett. **A134** (1988) 134.

A Solid-state UCN Detector

H.M.SHIMIZU, T.KAWAI*, T.EBISAWA* and S.TASAKI*

The Institute of Physical and Chemical Research, 2-1 Hirosawa, Wako 351
*Research Reactor Institute, Kyoto University, Kumatori-cho, Osaka 590-04

A solid-state ultracold-neutron (UCN) detector was developed[1] with a multilayer of ^{6}Li and Ti evaporated on a surface barrier type semiconductor, which can be operated at liquid helium temperature and enables us to study the performance of UCN sources based on the superthermal method[2] directly in liquid helium.

Multilayer of ^{6}Li and Ti was used as a neutron converter to cancel the effective potential almost perfectly. The structure of the detector is shown in Fig.1 and Table 1. Incident neutrons are absorbed by ^{6}Li and the reaction products are observed by the semiconductor of the sensitive area of 150mm^2.

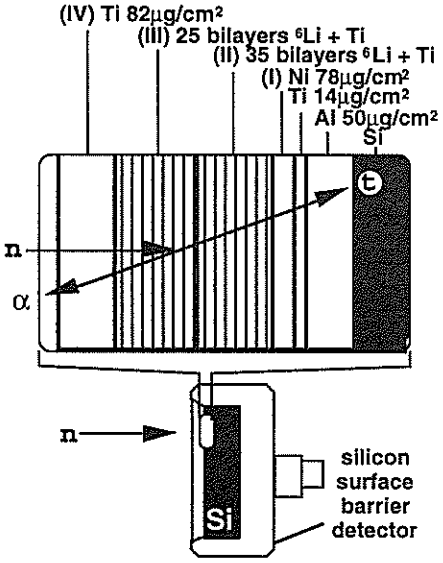

Fig. 1 Detector configuration.

Table 1. Effective potential and thickness of layers formed on the surface of the detector.

Region	U [neV]	thickness [μg/cm^2]
(I) Ni	240	78
(II) ^{6}Li+Ti	-2.2-2.0 i	35×(0.23+1.4)
(III) ^{6}Li+Ti	-7.4-1.8 i	25×(0.23+1.8)
(IV) Ti	-50	82

The surface of the detector reported in Ref.1) was investigated by measuring the neutron reflectivity of multilayers deposited on silicon substrates in the same evaporation processes using the cold neutron reflectometer at JRR-3M of JAERI. The reflectivity rose up at the wavelength of 800Å and approached 0.9[3], which implied UCNs of wavelength longer than 800Å cannot reach the multilayer neutron converter.

The wavelength dependence of the neutron reflectivity was well explained as a result of oxidation of titanium layers. The evaporation process was improved so that the layers are formed in the vacuum of 5×10^{-7}Torr, which is better than the vacuum in the previous processing by one order of magnitude.

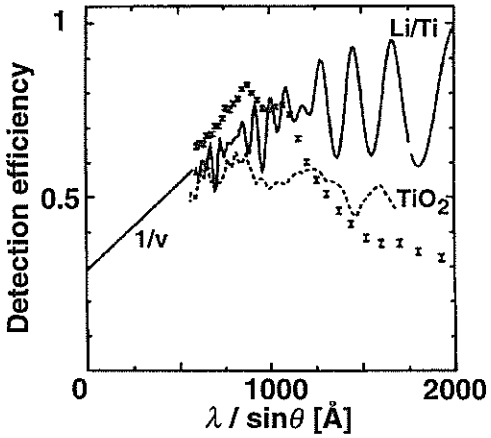

Fig. 2 Detection efficiency of the UCN detector deduced from the neutron reflectivity measurement. The curve with error bars represents the measured value, solid and dotted lines calculations with entirely pure titanium layers and with the outmost titanium layer oxidized by 300Å deep.

Neutron reflectivity of the newly evaporated multilayer was measured by performing θ/2θ scan using the cold neutron reflectometer[4]. Fig.2 shows the neutron detection efficiency as a function of λ/sinθ deduced from the result of the reflectivity measurement. In the figure, the curve with error bars represents the measured values, solid and dotted lines represent calculations with non-oxidized titanium layers and with the outmost titanium layer oxidized by 300Å deep in the form of TiO_2, respectively.

UCN detection efficiency was improved in the wavelength range of 560-1200Å sufficiently large for practical applications in UCN experiments. Further improvements at longer wavelengths are expected with better vacuum quality in evaporation processes.

References

1) H.M.Shimizu et al., Nucl. Instr. and Meth. **A350** (1994) 296.
2) R.Golub,J.M.Pendlebury,Phys.Lett.**62A** (1977) 337.
3) T.Kawai et al., Physica **B213-214** (1995) 969.
4) T.Kawai et al.,Nucl.Instr.andMeth.**A378**(1996)561.

A Multilayer Cold Neutron Polarizing Mirror Working under a Low Magnetic Field

T.KAWAI,T.EBISAWA,S.TASAKI,M.HINO,D.YAMAZAKI,T.AKIYOSHI,
Y.MATSUMOTO*,N.ACHIWA*, Y.OTAKE**,H.FUNAHASHI***

Research Reactor Inst., Kyoto Univ., Kumatori-cho, Osaka 590-04
**Dept. of Physics, Kyushu Univ., Hakozaki, Fukuoka 812*
***Spring 8, Inst. Physical and Chemical Research, Kamigori, Hyogo 678-12*
****Dept. of Physics, Kyoto Univ., Sakyo-ku, Kyoto 606-12*

A multilayer neutron mirror is an artificial lattice with a large interplanar spacing and gives the simple one dimensional neutron optical potential including the magnetic one for cold neutrons. The width and height of the potential are controlled arbitrarily. The potential width is determined by the distribution of layer thicknesses during vacuum evaporation and the height by selecting layer materials [1, 2].

We have developed a Permalloy/Ge multilayer(PGM) cold neutron polarizing mirror working under a magnetic field of 10 Gauss and used it in various neutron interference experiments [3, 4, 5, 6]. The motivation of this work was to develop a device for generating polarized cold neutron pulses without a mechanical chopper, and it had its origin in UCN experiments made at KEK. Since this type of magnetic mirror works under a very low magnetic field, it has the following useful characteristics: 1)the magnetic effects to the nearby devices is small since the stray field is very low, 2) a high-precision control of the neutron spin state is easy, because it is easy to control the low magnetic field. These features lead to the feasibility for developing the compact and energy-saving instruments in the field of cold neutron optics.

A multilayer polarizing cold neutron mirror placed in the pulsed magnetic field, we call it a multilayer cold neutron pulser or in abbreviation a cold neutron pulser, is going to be developed as a switching device of a delayed choice experiment related to the observation problem in quantum mechanics. For this purpose, it should produce a rectangular neutron pulse having no ripplings and a rising time of a neutron pulse should be in the order of magnitude of 100 μ s.

PGM have been evaporated on Si wafer in the magnetic field of about 130 Gauss parallel to the surface of the wafer. A cold neutron pulse was obtained from the PGM cold neutron pulser under a magnetic field of 15 Gauss. A neutron pulse rise time was 300 μ s with rather longer lag compared to 100 μ s of a current pulse supplied to the magnetic coil. The cold neutron pulser was applied to a delayed choice experiment using the Jamine type neutron interferometer [7]. The results suggested the feasibility of this device as a switching device for the delayed choice experiment [8, 9].

References

1)S.Yamada et al., Ann.Rep.Res.Reactor Inst.,Kyoto Univ.11(1978)8.
2)T.Ebisawa et al., J.Nucl.Sci.Technol., 16(1979)647.
3)T.Ebisawa et al., Nucl.Instrum.Methods A344(1994)597.
4)T.Ebisawa et al., J.Neutron Res., 4(1996)157.
5)M.Hino et al., J.Phys.Soc.Japan Suppl. A65(1996)277.
6)N.Achiwa et al., J.Phys.Soc.Japan Suppl. A65(1996)181.
7)H.Funahashi et al., Phys.Rev. A54(1996)649.
8)T.Kawai et al., J. Neutron Res., (in press).
9)T.Kawai et al., J.Phys.Soc.Japan Suppl. A65(1996)227.

Spallation Source and Superthermal UCN Production*

H.Yoshiki

Department of Engineering, Ibaraki University, Hitachi, 316. Japan
KEK, National Laboratory for High Enregy Physics, Tsukuba, Ibarki, 305, Japan

It was not until 1992 that the production of ultra cold neutrons (UCN) by means of superthermal method predicted by Golub and Pendlebury[1] was verified quantitatively by changing incident cold neutron wavelengths to observe the maximum of UCN production at a certain wavelength[2]. At this wavelength the dispersion curve of the superfluid liquid helium and the energy-momentum curve of a free neutron cross and the energy and momentun of incident neutron can be converted entirely to those of a produced phonon, leaving the neutron with an infinitesimal energy, a UCN. The value obtained was 8.78±0.06A, in contrast to the value hitherto often quoted number of 8.9 for 1.1K liquid, and it fits exactly to our particular liquid temperature of 0.45K. What we have learned here is that the calculation by Cohen and Feynman is correct and we can now calculate the rate of UCN production per unit time. The resultant UCN intensity is overwhelming, compared to the Turbine or Boltzmann methods. It must be emphasized that 1) this method allows cold neutrons to come from whole 4π-directions to produce UCNs, unlike the Turbine, where rather fine beam collimation of cold neutrons is necessary; 2) the produced UCNs are automatically trapped in the superfluid helium vessel, whereas the parent cold neutrons can penetrate freely through the wall, resulting in the build-up of UCN density in time in the vessel. In other methods the UCN transfer to an experimental volume, like a Ramsey Chamber, is necessary and the balancing between inflow and out flow of UCNs to and from it occurs quickly. Golub predicted that required temperatures would be below 0.8K, where production of UCN creating phonons (down-scattering) would not be surpassed by phonons reabsorbed by UCN(up-scattering). This statement is experimentally demonstrated by the experiment[2]. The attenuation coefficient at 0.45K is mainly attributed to a vertical duct open downward on the storage vessel (so-called gravity acceleration tube) which was adopted to detect UCN with good efficiency.

In 1987, we calculated the heat that would be produced in the liquid helium, if it was exposed to a cold neutron field of 3 x 10^{12}/cm^2/s. If such situation is realized it would produce 5000 UCN/cm^3/s (defined UCN energy upper limit=2 x 10^{-7}eV), a strongest UCN source up till now. However the final estimate of the heat to be removed from the liquid amounts to

* Based on the talks given in the international workshops at Los Alamos(7.Dec,.1995) and Oakridge(29.May,1996)

3000 mW under a certain number of assumptions. The answer to the problem is to combine a new set of circulation pumps for He^3 and a new heat exchanger which has four times as many number of fins as before. The proposed set of circulation pumps for He^3, which were purchased in 1994, is five times larger in displacement than before. We can extrapolate that this combination is enough to stand 3 x 10^{12}cold neutrons/cm^2/s, which is to produce **2 x 10^7 UCN/s** in the aforementioned part of the liquid. Such irradiation will be accomplished most conveniently and most realistically by use of a spallation source, and *not* by a reactor.

The two main objectives for getting a strong UCN source are the more precise determination of the neutron lifetime and the search for the electric dipole moment of neutron, a manifestation of the time irreversibility. As for neutron lifetime, there is a proposal with superthermal source and magnetic confinement, and we are planning a similar device incorporated in Cooling Tower of the cryostat under construction, Mark 3001. The search for the electric dipole moment of free neutron has been carried out by two groups, whose latest upper limit for this quantity is ~1.2 x 10^{-25}e.cm.[4,5] In order to go a step further it would be necessary 1) to have UCN more in number and 2) to control systematic errors more in precision, such as magnetic field in its stability an uniformity, or problem of dark current when a strong electric field is applied. Since we are to produce UCN by the low-temperature engineering, the logical solution for 2) would be to take advantage of this orientation.

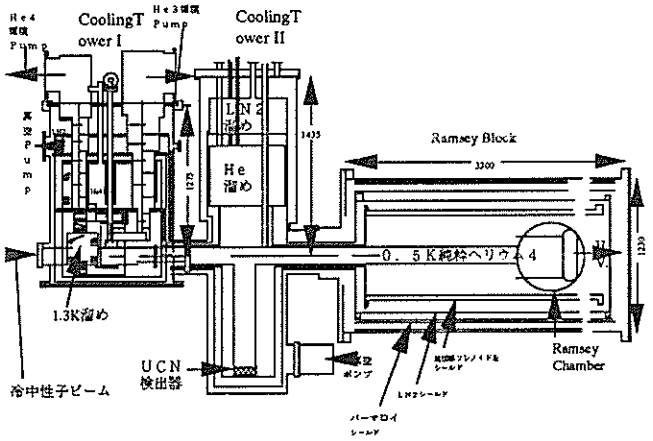

In the Fig., we show the edm measurement machine integrated with refrigeration parts, Mark3001. Cooling Tower I does the He^3 refrigeration, Cooling Tower II supplies liquid helium to superocnducting shield and

solenoid and furnishes a space for gravity acceleration and UCN detection. The part where the edm is measured is conventional in layout except that the shields have to be coaxial by technical reasons and the chamber is filled with 0.5K purified liquid helium in place of vacuum. The Ramsey Block, a cylindrical object 3m long and 0.8 m in diameter is a vacuum chamber. It contains three layers of high-permeability magnetic shield at room temperature. Coaxially toward the center, a superconducting magnetic shield and superconducting solenoid exist, which are enclosed in a double layered cylinder containing liquid helium to keep them at 4.2K. Those are all made out of aluminum except for the superconducting material. We are aiming at a magnetic field whose instability in space and time will be in the oder of 10 ngauss.

	type	chamb. volume	UCN CM^{-3}	stored UCN	values	system. error	statistical e.	upper limits
DONE								
ILL (PREVIOUS,89)	R.T. BEAM	5 *l*	40	$2\ 10^5$	-3.3	± 3.9	± 1.9 10^{-26}e.cm	$<1.2\ 10^{-25}$
GATCHINA (91)	R.T.	20 *l*	10	$2\ 10^5$	$+2.6$	± 1.6	± 2	$<1.2\ 10^{-25}$
KEK/JAERI (91)	Hell BEAM	15 *l*	5	$8\ 10^4$	NO ATTEMPT MADE FOR EDM			
FORECAST								
ILL (PRESENT)	R.T. BEAM	20 *l*	50	$1\ 10^6$	X	2.0	1.0	$<5\ 10^{-26}$
ILL/KEK	Hell BEAM	20 *l*	350	$7\ 10^6$	X	1.0	0.2	$<2\ 10^{-26}$
spallation s./KEK	Hell BATH	20 *l*	5000	$1\ 10^8$	X	X'	<0.1	$<X''\ 10^{-27}$

In the Table we present the achievement in past[3-5] and the prospect in future of the electric dipole measurement of neutron. The intensity of UCN depends on the intensity of parent cold neutrons and it can change orders of magnitude whether one use a cold neutron beam, or a field of cold neutrons (neutron bath created by spallation source). This is because of the difference in solid angle. The cold neutron intensities in various laboratories at present and in future are compared in the Fig. at right. 5000 UCN/cm^3, the number in the Table, corresponds to this case and is still a conservative number even taking into account the diffusion of UCN into the whole vessel out of the region they are created (we envisage a vessel, 50 cm long, 10 cm wide), resulting in dilution in density. We therefore believe that we will not face the paucity of UCN in future but rather the problem of the systematic errors in measuring the edm. As for the N-$\overline{N}$ Oscillation experiment, this vast quantity of UCN could even open a way to look at the $\overline{N}$ amplitude in the random walk fashion, not only in the coherence mode as reported by Golub (the Bootstrap Method)[6].

The issues on neutron spallation sources with particle accelerators have been discussed by many laboratories (JHP, LANL, ORNL, Savannah River, Jülich, Wien etc). The main advantage of spallation source is that it is pulsed and has a high peak intensity, suited for neutron spectroscopy very well. We should not however overlook another big advantage in spallation source. It is the **dedicatability** of a source (or sources) to a particular experiment (or experiments). By dedicatability we mean that each experimenter is able to easily adjust his beam specifications at his own. This is impossible in case of a reactor. If a cold neutron source or a superthermal source are to be installed near the core of a reactor, it would need a very precise evaluation of flux distributions in planning, Once the reactor is on, it is virtually impossible to move these equipments and the relations among different experiments are fixed. On the other hand, a proton beam can be tailored to orders by experimenters. It can be controlled in current, space and time. The primary beam can be even fanned out. By owning one's own spallation target, the experimenter can design his own neutron source(s) or beam(s), taking no attentions to other groups. The serious contradictions among different types of experiments, whether a high time resolution or a high intensity, will be solved by designing a target station in each case. For instance the Superthermal UCN production need no time resolution but a little proton current (~10μA) **adjustable** in intesity or able to be even **shut off** if it is not wished. The experimenters will benifit much from the mobility and the dedicatability of the spallation source in this way and this is one of the essential advantages in working with spallation sources.

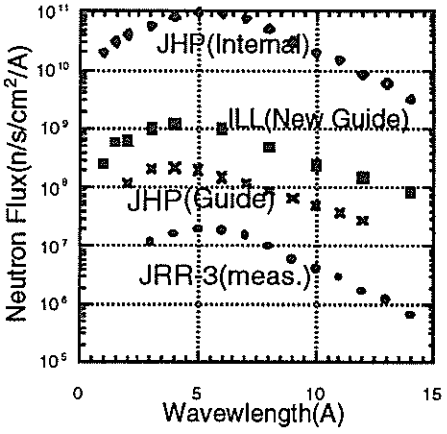

References

1)R.Golub and Pendlebury,Phys.Ltrs.**62A**(1977)337
2)H.Yoshiki *et al*, Phys.Rev.Ltrs.**68**(1992)1323
3)K.F.Smith *et al*, Phys. Ltrs.**234**(1990)191
4)I.S.Altarev *et al*, Phys. Ltrs.**B276**(1992)242
5)J.M.Pendlebury *et al*, Phys. Ltrs.**136B**(1984)327
6)R.Golub et al, Nucl.Inst.&Meth.inP.R.**A284**(1989)

Construction of a Stable and Homogeneous Magnetic Field at 10 milligauss for Neutron Electric Dipole Measurements*

E.B.Gravador[a], F.-Z.Huang[a], E.Gutsmiedl[d] and H.Yoshiki[b,c]

[a]*Graduate School of Ibaraki University, Hitachi, 316*
[b]*Faculty of Engineering, Ibaraki University, Hitachi, 316*
[c]*KEK, National Laboratory for High Energy Physics, 1-1 Oho, Tsukuba-shi, Ibaraki 305*
[d]*Technical University of Munich, Munich, Germany*

More than three decades have passed since the *CP* violation was discovered. Its implication is the violation of symmetry laws in time if CPT=1 is true. The search for electric dipole moment in an isolated, non-degenerate state like a bare neutron directs to the immediate demonstration of the time irreversability. The ultracold neutrons (UCN), very slow neutrons with velocities less than 7 m/s, are especially suited for such studies. Several review articles on this subject are available[1-4]. In order to advance a step further (a) the magnetic field stability and homogeneity, (b) the longer neutron storage time, and (c) the higher UCN stored density must be pursued. Items (b) and (c) can be achieved by using superthermal UCN source (where UCN are produced by downscattering of neutrons in superfluid liquid helium). Golub *et al*[5] and Yoshiki *et al*[6] observed production of UCN in superfluid helium. In a new type of superthermal source (Mark3001) at KEK, a high-permeability magnetic shield, a superconducting magnetic shield and a superconducting solenoid are incorporated for the construction of a stable and homogeneous magnetic field. This is expected to bring an improvement of neutron edm upper limit almost by an order of magnitude.

The magnetic shield of Mark3001 consists of a 3-layer high-permeability ferromagnetic (μ metal) shield at room temperature and a superconducting shield at liquid helium temperature. The relative positions of the shields and solenoid are shown in Fig.1. The coaxial ferromagnetic cylinders have the same length (3200 mm) and thickness (1.6mm), and relative permeability (10^5, manufactured by Tokin, Sendai, Japan). They are heated to 1050°C~1150°C for 3 hours and cooled down to 600°C~300°C at 80°C~150°C/hour. The coercive force is 2 amp/meter. The cylinders are spaced equally at 40 mm.

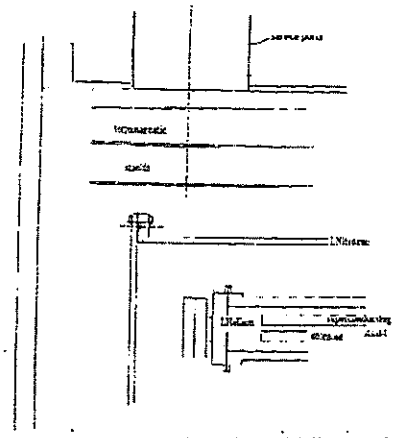

Fig1. Cross Sectional View of Mark3001

The superconducting shield (2830 mm in length and 724 mm in diameter) is constructed by winding lead foil on an aluminum cylinder which is fabricated with an accuracy of one hundredth of a millimeter near the center. The lead foil are fastened by Kapton tapes.

The superconducting solenoid (2830 mm in length and 684 mm in diameter) is constructed using NbTi/Cu composite wire (ϕ0.48 mm after insulation) wound on a aluminum cylinder, double-layer, with 4129 turns/meter. The persistent current necessary to generate 10 milligauss of magnetic field at the center of the solenoid is no more than 2 milliamperes.

The superconducting shield and solenoid are contained in a double-layer cylinder containing liquid helium.

Shielding effectiveness can be expressed by shielding factors which are the ratios of the external magnetic field to the attenuated field inside the shield.

*Reported by the first author at the 51 JPS meeting (Kanazawa, 996,3a-WF-8)

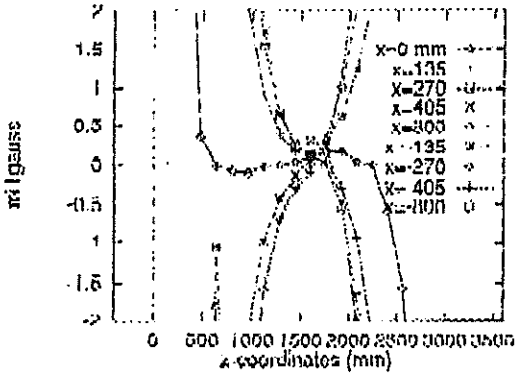

Fig.2 Attenuated ambient magnetic field distributions parallel to the axis at different radii, x.

μ-shield -We measured the ambient magnetic field and the attenuate field inside the high-permeability ferromagnetic shield using Bartington™ flux-gate meter. Fig.2 describes the shielding of external magnetic field. At the center of the shield we observe a shielding factor of 10^4. Analytic solution says that the fall-off should be $Ae^{(-kz/R)}$ where k is the first zero of 0th Bessel function, which is 2.405. From the figure our found value was 2.44, satisfying the analytical predition well. Formula for calculation shielding effects with an end open have been given by Wadey[7], Marger[8] , Freak and Thorp[9], Sumner, Pendlebury and Smith[10]. For equally spaced layers, the trnasverse shielding factor inside the shield of infinite length is given by

$$S_T^{perm} = S_{T_1} S_{T_2} S_{T_3} \left[1-\left(\frac{R_1}{R_2}\right)^2\right]\left[1-\left(\frac{R_2}{R_3}\right)^2\right] \qquad (1)$$

where

$$S_{T_i} \equiv \frac{\mu t_i}{D}, \qquad (2)$$

S_T^{perm} denotes transverse shielding factor of high-permeability shield. S_{T_i} denotes sheilding factor of the i th cylinder of thickness t_i , outer radius R_i, and mean diameter D_i. $i=1$ refers to the innermost cylinder. Using our designed values given and relative permeability of 10^5 given by the manufacturer we find that $S_T^{perm}=2 \times 10^4$. This is satisfactorily in agreement with the measurements as shown. For three layers of equal length[10],

$$S_A^{perm} = 1 + S_{A_1} + S_{A_2} + S_{A_3}. \qquad (3)$$

Our measurement turned out $S_A^{perm}=6 \times 10^4$ at the center of the high-permeability shield, while the expected value by calculation for Eq(3) is about 7×10^4.

Superconducting shield-Hildebrandt[13] has treated the shielding by a semi-finite superconducting hollow cylinder of radius R. The component fields attenuate as

$$B_T \propto \exp(-k_T z/R) \quad , \quad \text{transverse} \quad (4)$$

$$B_A \propto \exp(-k_A z/R) \quad , \quad \text{axial} \quad (5)$$

where $k_A=3.83$ and $k_T=1.84$ correspond to the first zeros of Bessel functions J_0' and J_1' respectively. z is measured from the open end along the axis of the shield. In order to assess a shielding factor of a superconducting shield it is necessary to know the parameter k_A and k_T for the shield in question. To pursue this end we constructed a model sheild made form the same lead foil used in the actual shield and investigated its shielding factor, which is governed by Eq(5). The lead foil was wound on a Teflon tube of 200 mm in length and 92 mm in diameter. For the measurement of the magnetic field a dc SQUID with a 3-turn, ϕ25mm pick up coil made of niobium wire having an inductance of 0.8 microhenry was used. The external magnetic field was provided by a solenoid wound on the body of the cryostat. Fig, is a typical plot of the inverse of the shielding factor against depth when the excitation current is 10 milliamperes. The mean value of k_A thus obatined is 3.73 ± 0.11 compared with the theoretical value, 3.83.

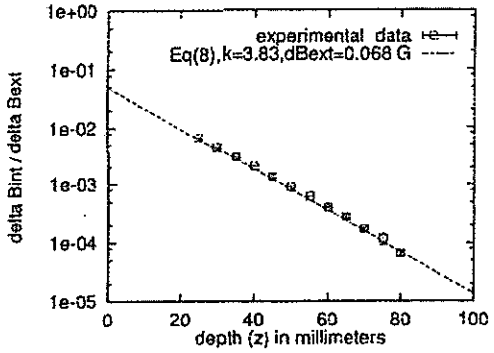

REFERENCES

1)R.GolubandS.K.Lamoreaux,Phys.Rep.237 (1994)1.
2) J.M.Pendlebury, Annu. Rev. Nucl. Part. Sci. 43(1993)687.
3) K.F. Smith et al Phys.Lett. B 234(1990)191.
4) I.S.Altarev et al. Phys. Lett. B276(1992)242.
5) R.Golub et al. Z.Phys. B51(1983)187
6) H.Yoshiki et al. Phys.Rev.Lett.68(1992)1323
7) W.G.Wadey, Rev.Sci. Instrum. 27(1956)910
8) A.J.Mager,IEEETrans.Magn.MAG6(1970)67
9) S.M.Freak and T.L.Thorp, Rev, Sci. Instr. 42 (1971)141
10) T.J.Sumner, J.M.Pendlebury andK.F.Smith, J.Phys.D 20(1987)1095
11) D.U.Gubser et al.Rev.Sci.Instr.50(1979)751
12) B.Cabrera, Ph.D. Thesis,StanfordUniversity (Stanford, California, USA),1975
13)A.F.Hildebrandt, Rev.Phys.App.5(1970)49

Three metre long horizontal cryostat producing ultracold neutrons using superfluid liquid helium at 0.5K

H.Yoshiki[a,b], K.Sakai[b], T.Kawai[c] and S.Goto'o[d]

[a]Faculty of Engineering, University of Ibaraki, Hitachi, 316, Japan
[b]KEK, National Laboratory for High Energy Physics, Oho, Tsukuba, 305, Japan
[c]Research Reactor Institute, Kyoto University, Osaka 590-04, Japan
[d]To'orisha, Aoki 3-5-1, Kawaguchi, 332, Japan

After the discovery of violation of CP invariance in K decays, the expectation is that there is also a violation of time symmetry based on the CPT principle. In order to examine this possibility experimentally, the search for electric dipole moment (edm) in any quantum mechanical non-degenerate system with spin is suited. In particular, the search for the edm in neutrons is supposed to be the most sensitive and crucial examination of T-violation in this field.

Ultracold neutrons (UCN) are very slow neutrons, with speeds in the range of <7 m/s, or with wavelengths of more than several hundred angstroms, and kinetic energies corresponding to $<3 \times 10^{-7}$eV or a few millikelvin. They exhibit very interesting phnomena such as total refelections at all angles in many materials. In 1977 Ramsey argured that even with the cold neutrons which he used for the edm detection, the systematic error originating from the relativity and a slight misalignment in B and E is large enough to mask the true edm signal. If the UCN were used in place of the cold neutron beam, this is not the case. Therefore the measurement of edm by means of UCN has been a common practice

The production of UCN in superfulid liquid helium was successfully demonstrated , as had been pointed out by Golub and Pendlebury in 1977[1]. In 1980 Yoshiki started to work on a cryostat which could later be irradiated by cold neutrons from a cold source installed at KENS. A few years later this prototype cryostat was replaced with a model called Mark 280, which had a UCN production vessel 80mm in diameter and 280 mm in length. The same work was continued and extended in collaboration with S.Ishimoto, to build Mark 3000, which has a horizontal extended part 3000 mm in length. In this context we published a paper on future plans[2], where we discussed what would happen to the nuclear heating and the temperature of the superfluid if this cryostat were inserted in the field of a strong flux of cold neutrons, say 10^{12}/cm^2/s. Such nuclear heat will be removed by the heat exchanger developed by us.

The cross-section of Mark3000 is shown in Fig.1, whose main part is the vessel containg the superfluid liquid helium of 15 liters. The detailed description of Mark3000 and its performance were published in Cryogenics. Its main contribution was identifying the superthermal UCN production at a cold neutron energy. This was done by changing the cold neutron energy by means of a pair of choppers 8 m apart. The UCN were observed in fact at the wavelength of 8.78±.06Å, in contrast to the often quoted number of 8.9Å for 1.1K liquid helium temperature, fitting exactly to our particular liquid of 0.45K, which Mark3000 attained. These results were reported in Ref 3. The success of Mark3000 led us to a design of Mark3001, which will remove nuclear heat of 3 watts combining a new extended heat exchanger and a set of He^3 circulation pumps. He^3 is the refrigerant of our systems. Mark3001 is currently being assembled, and if it is submerged in the aforementioned cold neutron field, it is expected to produce 5000 UCN/cm^3.

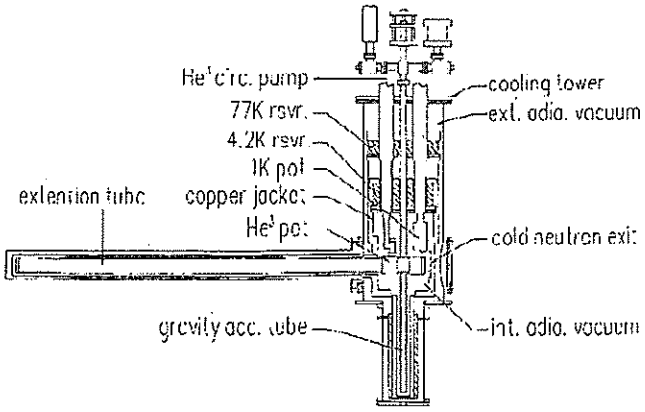

Fig 1. The cross-section of Mark3000

References

1) R.Golub and J.M.Pendlebury, Phys. Ltrs. 62A (1977)337.
2) H.Yoshiki, S. Ishimoto and M.Utsuro, Z.Phys. B 67(1987)161
3) H.Yoshiki, K.Sakai, T.Kawai and S.Goto'o, Cryogenics **34** (1994)277
4) H.Yoshiki,K.Sakai,M.Ogura,T.Kawai,Y.Masuda, T.Nakajima,T.Takayama, S.Tanaka and A. Yamaguchi, Phys. Rev. Ltrs. 68 (1992) 132.

Transmission of slow neutrons (9-15 Å) through superfluid liquid helium

F.-Z. Huang#, H.Yoshiki, K.Sakai* and E.Gutsmiedl**

#Faculty of Engineering, Ibaraki University, Hitachi, Ibaraki, 316, Japan
National Laboratory for High Energy Physics, 1-1 Oho, Tsukuba-shi, Ibaraki 305
*Faculty of Science, Tokyo Institute of Technology, Tokyo, 152,Japan
**Technische Hochschule, Garching, Muenchen, Germany

For the production of ultracold neutrons (UCN), the dispersion property of superfluid liquid He^4 is used. At a liquid temperature of 0.45K, the energy and momentum of a phonon of $0.72Å^{-1}$(12K) equal to those of a free neutron. The cross point of the two kinematical curves in energy-momentum plane, the neutron can exchange its energy and momentum entirely with those of a produced phonon, resulting in a neutron with infinitesimal energy, a UCN. Such a mechanism was discussed by Feynman and Cohen[1], by Golub and Pendlebury[2], and later the location of the cross point of two kinematical curves was measured by producing UCN by energy-controlled cold neutrons for liquid helium at 0.45K[3]. This was a clear demonstration that the single phonon process does take place at the right energy. The interaction of superfluid helium with neutron , whose wavelengths longer than 9Å, and the liquid helium temperatures below 1K however was a relatively unexplored area. Sommers, Dash and Goldstein[4] measured the total cross sections of cold neutron on the liquid He^4 in the temperature region between 1.25 and 4.6K. We carried out this transmission experiment with the liquid temperature down to 0.45K. To measure the transmission of the cold neutrons through such a low temperature liquid He^4, a horizontal cryostat with which the production of UCN was observed in 1992[3] was used in this experiment.

In regard to our experimental setup, remarks are not more than in the report made earlier[3] except two points. One is the characteristics of the velocity selector. It is a pair of disks, 380mm in diameter with a 30mm wide window, 8.13 meters apart, rotating at a speed of 20 rps by a pair of step-motors whose speed and phase are precisely controlled by an electronic pulse generator. It is the relative phase of these disks that determines the speed of neutrons. Each phase signal is measured by a clock which ticks at a rate of 10 μs and locks each other at a predetermined value after changing one of the discs' rotation speed by 0.04%. It turned out that the time jitter of the relative phase is less than 0.2% at 9Å. The λ determined by the relative phase was systematically corrected for the l-5 dependence of the flux. The correction was not more than one percent in contrast with the 25% of S. D. G[4], who used a short single rotor with a synchronous motor. The other remark is the quantity of He^3 remaining after the heat-flush separation through a superleak. Commercial helium contains 0.16 ppm of He^3 in He^4. By mass spectrograph we have established that this was reduced to less than $1.3x10^{-8}$ (1s c.l.) by our superleak. This upper limit was improved to 3×10^{-9} by observing storage time of UCN[3]. McClintock discusses that this can be as low as 10^{-12} by a single heat flush. Ref(3) did not give us any new information because we had an escape duct (the gravity acceleration tube) for UCN which was open always, becoming the main source of limited life time of UCN in the setup. The UCN confinement measurement in fact would be the best and the only way to determine how effective the heat-flush separation is. The absorption cross section of He^3 for 9Å neutron is 25000 barns and corresponding effective contribution to the total cross section will be 0.3 mb, taking the measured upper limit of Ref(3), or less, which is negligible compared to numbers we are interested in now.

we introduce a parameter, Y , which is defined as

$$Y=1-(S/M)_T/(S/M)_{0.45K}, \qquad (1)$$

where S is the signal counts behind helium sample (in the horizontal cylindrical container which measures ϕ80mm and 3000mm long) and M is the monitor counts in front of helium sample. The lowest attainable temperature of the liquid in this cryostat is 0.45K and it is quite stable and precisely reproducible. In the measurement, once a wavelength is set by the velocity selector, temperatures of the liquid were set by a heater submerged in the liquid. The machine stability is excellent up to 1.5K for a heater setting. In place of interposing sample and vacuum as mentioned before, at a proper interval, we returned from a higher temperature to 0.45K, the lowest attainable temperature of the cryostat, to confirm $(S/M)_{0.45K}$ in eq(1). They are not precisely same each time and Ys scatter around zero, giving idea of the errors in Y. The value $(S/M)_{0.45K}$ in eq(1) is the average of multiple values of those, in order to calculate the final Y' s. It takes about thirty minutes to cool down from 1.5K to 0.45K. Temperatures above 1.5 to 2.4K, the machine

becomes unstable and it also takes some time to bring down the temperature back to below 1.5K.

According to the single phonon theory, the temperature dependence is hardly observable in one-phonon production, while it is in phonon absorption that the effect of temperature becomes apparent. The Y can be expressed in the following way according to its definition

$$Y=1-\exp(-N(\sigma(T)-\sigma(0.45K))L), \qquad (2)$$

where $\sigma(T)=\sigma_{prod}(T)+\sigma_{anni}(T)$, is the sum of the cross sections for one-phonon production and annihilation processes. Because the cross sections of the one-phonon production processes depend little on the liquid temperature, the difference of the cross sections in (2) is nearly $\sigma_{anni}(T)-\sigma_{anni}(0.45K)$.The number of the excited phonons is few at T=0.45K and $\sigma_{anni}(0.45K)$ is almost 0. Therefore $Y\sim NL\sigma_{anni}(T)$.

In Fig. 1 to Fig.3, we show our measured results comparing with calculated Y from the sum of the calculated single phonon production and annihilation cross sections. Our measured wave lengths are 9, 11, 13 and 15Å. The data of the static structure factor $S(Q)$ used in eq(1) were taken from R. B. Hallock[5] at T=0.38K and E. C. Svensson et al.[6] in the temperature range from 1 to 3K. The temperature dependence of $S(Q)$ was calculated by interpolating the two set of data mentioned above.

From the Fig.1 to 3, we can see that the Y does not change its values in the temperature range from 0.45 to 0.7K for all the wavelengths measured. The agreements between the calculated and the measured data are fairly good. What are indicated in these agreements would be that the single phonon process can account for the measured data in the low temperature region(T<1.3K) and low momentum transfer region($Q<0.25$Å^{-1}), where $S(Q,\omega)$ include single sharp peak only. For the higher T and Q regions, $S(Q,\omega)$ may include a broad peak in higher w, which is not single phonon excitation process, in addition to the sharp peak. In this case, it should not be declared that the single phonon process can describe the measured data even with good agreements between calculations and measurements.

References

[1] M.Cohen and R.P.Feynman, Phys.Rev. 107(1957)13.

[2] R.Golub and J.M.Pendlebury, Phys. Ltrs. 62A (1977)337.

[3] H.Yoshiki,K.Sakai,M.Ogura,T.Kawai,Y.Masuda, T.Nakajima,T.Takayama, S.Tanaka and A. Yamaguchi, Phys. Rev. Ltrs. 68 (1992) 132.

[4] H.S.Sommers, J.G.Dash and L.Goldstein, Phys. Rev. 97 (1955) 855.

[5] R.B.Hallock, Phys. Rev. A5(1972)320; H. N. Robkoff and R.B.Hallock, Phys.Rev B24 (1981) 159.

[6] E.C.Svensson, V.F.Sears, A.D.B.Woods and P.Martel, Phy. Rev. B21(1980)3638.

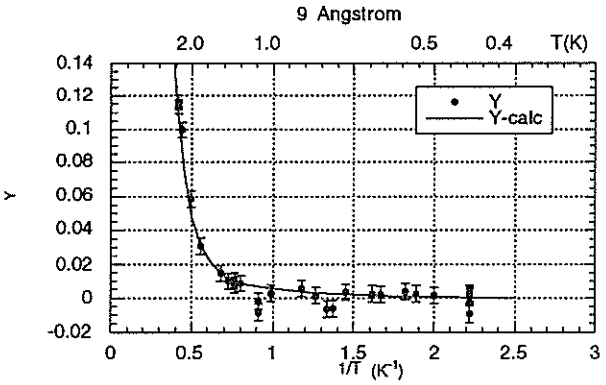

Fig. 1 Comparisons between calculated and measured data of Y at λ_n=9Å.

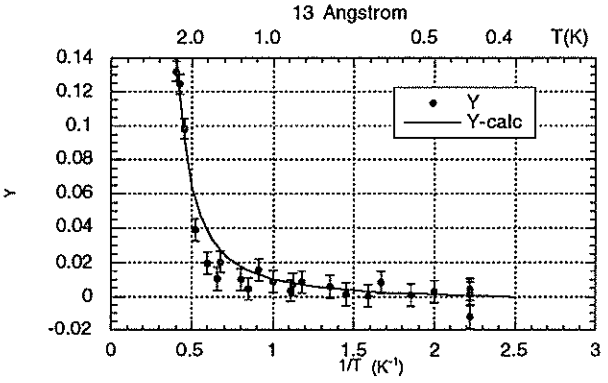

Fig. 2 Comparisons between calculated and measured data of Y at λ_n=13Å.

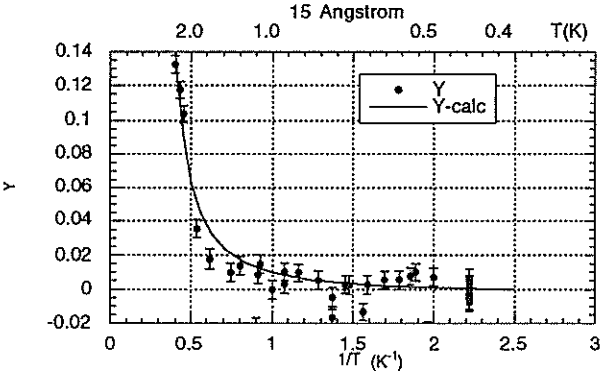

Fig. 3 Comparisons between calculated and measured data of Y at λ_n=15Å.

LIST OF PROPOSALS ACCEPTED

(1995 - 1996)

Snapshot of the International Workshop on Science in Neutron-Arena of JHP held at KEK on March 26 - 27, 1996.

Proposals accepted (April 1995 - March 1996).

95-A2-1		Yoshiki H	Ibaraki Univ.
	Development of edm Measuring Equipment		
95-A2-2	LAM-80C	Ikeda H	KEK
	Application of LAM-80C to Experiments under Extreme Conditions		
95-A2-3		Shimizu H	RIKEN
	Very Cold Neutron Bending in a Magnetic Field and Position-sensitive Solid-state Neutron Detector		
95-B1-1	FOX	Ohshima K	Univ.of Tsukuba
	Study on Structural Fluctuation and Phase Transition from Single Crystals of Alloys and Compounds		
95-B1-2	MAX	Todate Y	Ochanomizu Univ.
	Study of Elementary Excitations Using Multi-Crystal Analyser Spectrometer		
95-B1-3	LAM	Kanaya T	Kyoto Univ.
	Neutron Scattering Studies on Relaxational and Excitational Modes in Condensed Matters		
95-B1-4	HIT	Fukunaga T	Nagoya Univ.
	Structure Study of Liquids and Amorphous Solids		
95-B1-5	VEGA	Kamiyama T	Univ.of Tsukuba
	Structural Studies Using VEGA		
95-B1-6	SAN	Furusaka M	KEK
	Materials Science by Small-Angle Neutron Scattering Instrument (SAN)		
95-B1-7	WINK	Furusaka M	KEK
	Materials Science by Small/Medium-Angle Diffractometer(WINK)		
95-B1-8	PEN	Masuda Y	KEK
	Polarized Neutron Experiment by Using PEN		
95-B1-9	RAT/CAT	Ikeda S	KEK
	Condensed Matter Research Using eV Neutrons		
95-B1-10	INC	Arai M	KEK
	Study on Condensed Matter by Means of a Chopper Spectrometer		
95-B1-11	TOP	Takeda M	Tohoku Univ.
	Study of Magnetism by TOP		
95-B1-12	MRP	Motokawa M	Tohoku Univ.
	Study on Crystal Structure and Magnetic Structure in High Magnetic Field by MRP		

95-B2-1 LAM Nakamura Y Hokkaido Univ.
Dynamical Structure of Molten Carbonate Mixtures

95-B2-2 LAM Nakamura Y Hokkaido Univ.
Dynamical Properties of Electrolyte Systems Diluted by Heterobond Materials

95-B2-3 LAM/HIT Kawamura J Hokkaido Univ.
Ionic Diffusion and Structural Relaxation in Organic-Inorganic Mixed Superionic Glasses

95-B2-4 SAN Ichikawa K Hokkaido Univ.
Nonmetal-Metal Transition under the Concentration Fluctuation :Growth of Polybismuth Ions to Cluster

95-B2-5 MRP Kohgi M Tokyo Met. Univ.
Magnetic Structure of the Low Carrier System CeX (X=P,As) under High Magnetic Field

95-B2-6 INC Yamada K Tohoku Univ.
Study on High Energy Excitation of High-Tc Superconductors

95-B2-7 LAM Kajitani T Tohoku Univ.
Hydrogen Vibration Modes in Organic Conductors

95-B2-8 INC/LAM Motokawa M Tohoku Univ.
Inelastic Neutron Scattering of a Spin-Peierls System

95-B2-9 CAT Yamaguchi S Tohoku Univ.
Inelasic Neutron Scattering of Hydrogen in Ordered Alloys

95-B2-11 INC Yamaguchi Y Tohoku Univ.
A Study of Spin Wave in Itinerannt Electron Antiferromagnetic System $Mn_{3-x}T_xSi$(T=Fe,Cr)

95-B2-12 WINK Sumiyama K Tohoku Univ.
A Small Angle Neutron Scattering Study on Topological and Magnetic MediumRange Structure in Fe/Cu Granular Films

95-B2-14 HIT Uemura O Yamagata Univ.
Short-Range Order of Amorphous and Liquid Ge-Te Alloys

95-B2-15 HIT Kameda Y Yamagata Univ.
Inter-Ionic Structure in Highly Concentrated Lithium Carboxylate Solutions

95-B2-17 VEGA Takita K Univ. of Tsukuba
Structural Modulation Depending on the Pr Content and Oxygen Deficiency in the Solid Solution of YBCO-PBCO.

95-B2-18 LAM Ikeda H KEK
Dynamic Critical Scattering from a Two-Dimensional Percolating Antiferromagnet

95-B2-19 WINK Hirai M Gunma Univ.
Structural Properties of Ganglioside-Protein Complexes in Aqueous Solvents

95-B2-21 HIT Yasui I Univ. of Tokyo
Structure Analysis of Mixed Alkali Glasses

95-B2-22 LAM Imai M Univ. of Tokyo
Dynamical Structure of Crystalline Polymer near Glass Transition Temperature

95-B2-23 VEGA Takahashi H Univ. of Tokyo
Studies of Crystal Structure under High Pressure

95-B2-24 VEGA Kawazoe H Tokyo Inst. Tech.
Neutron Diffraction Study of Mixed Valence Tl Oxide

95-B2-25 RAC Enoki T Tokyo Inst. Tech.
Lattice Dynamical Properties of Hydrogen in Alkari Metal-Hydride

95-B2-26 LAM Shirakami T Tokyo Inst. Tech.
Low-Energy Excitations in Yttria-Stabilized Zirconia

95-B2-28 MAX Kashida S Niigata Univ.
Inelastic Neutron Scattering Study of the Structural Phase Transition in $KDCO_3$

95-B2-29 LAM Misawa M Niigata Univ.
Dynamics of Water Molecules near the Upper- and the Lower-Critical Points

95-B2-30 LAM Misawa M Niigata Univ.
Quasielastic Scattering of the Liquid Carbon Tetrachloride

95-B2-31 SAN Okano K Shinshu Univ.
SANS from Semidilite Solutions of Poly(N-isopropylacrylamide) in Methanol-Water Mixture

95-B2-32 WINK Imae T Nagoya Univ.
Investigation for Fibrous Supermolecular Structure by Small-Angle Neutron Scattering

95-B2-33 HIT Mizutani U Nagoya Univ.
Structure of $Mg_{90-X}Ga_XCa_{10}$ Ternary Amorphous Alloys

95-B2-34 WINK Fukunaga T Nagoya Univ.
Density Fluctuation and Structural Relaxation for Amorphous Se Prepared by Mechanical Milling

95-B2-36 INC Fukunaga T Nagoya Univ.
Dynamic Structure of Amorphous Se Formed only by Chain Molecules or Ring Ones

95-B2-37 WINK Okabayashi H Nagoya Inst. Tech.
Aggregate Structures of Surfactants Having Asymmetric Structure

95-B2-38 SAN/WINK Okabayashi H Nagoya Inst. Tech
Super Secondary Structure of Oligopeptide Aggregates in Solvent

95-B2-39	LAM	Yao M	Kyoto Univ.
	Dynamical Structure of Liquid Tellurium Mixtures		
95-B2-40	SAN	Osamura K	Kyoto Univ.
	Structure Change during Decomposition in Fe-Cr Based Alloy		
95-B2-41	LAM/WINK	Kaji K	Kyoto Univ.
	Low-Energy Excitation of Polymer Liquid Crystals		
95-B2-42	TOP	Shinjo T	Kyoto Univ.
	Giant Magnetoresistance and Magnetic Structure of Metallic Multilayer Films		
95-B2-43	HIT	Yoko T	Kyoto Univ.
	Precise Structure Analysis of PbO-TeO_2Binary Glasses and Melts		
95-B2-45	VEGA	Matsuo T	Osaka Univ.
	Deuterium-Induced Phase Transitions in $(ND_4)_2MX_6$Crystals (M=Se,Pt,X=Cl,Br)		
95-B2-46	VEGA	Matsuo T	Osaka Univ.
	Rotational Correlation between $ND_4^+$and $PbCl_6^{2-}$ Ions and Structural Phase Transition in $(ND_4)_2PbCl_6$ Crystal		
95-B2-47	LAM	Matsuo T	Osaka Univ.
	Low-Energy Exitations and Low-Temperature Heat Capacities in Molecular Ground Amorphous Solids		
95-B2-48	LAM	Kataoka M	Osaka Univ.
	Low-Energy Dynamics of Proteins and its Change upon Folding		
95-B2-49	LAM	Inaba A	Osaka Univ.
	Phase Transition and Orientational Disorder in Adamantane Monolayeres		
95-B2-50	LAM	Inaba A	Osaka Univ.
	Phase Transition and Orientational Disorder in Tetrakis(methylthio)methane Monolayers		
95-B2-51	VEGA	Inaba A	Osaka Univ.
	Structure and Phase Transition in Adamantane Monolayers		
95-B2-52	LAM	Takeda S	Gunma Univ.
	Thermochromism and Dynamics in Organometallic Compound, ZrCp2-diphenylbutadiene		
95-B2-53	LAM	Yamamuro O	Osaka Univ.
	Low-Energy Exitations and Low-Temperature Heat Capacities in Simple Molecular Glasses		
95-B2-54	SAN/VEGA	Arai M	KEK
	Diffraction Measurement of Single-Crystal High-Tc Superconductors		

95-B2-57 VEGA Kanno R Kobe Univ.
Study on Ionic Conduction Mechanism of Layered Rock-Salt Type Oxides

95-B2-58 VEGA Hashimoto M Kobe Univ.
Crystal Structures of Trihaloace Tamides as Studied by Neutron Powder Diffraction

95-B2-59 VEGA Eda K Kobe Univ.
Crystal Structure of $(Na \cdot 2D_2O)_{0.25}D_xMoO_3$, x=0.5

95-B2-61 LAM Seto H Hiroshima Univ.
The Structural Transformation and its Dynamics in Microemulsion

95-B2-62 SAN Gohtani S Kagawa Univ.
Structural Investigation for Adsorbed Film of Saponin on Droplet Surface of Saponin Emulsion

95-B2-63 HIT Kamimori T Ehime Univ.
Study of the Structure of Amorphous Cu_2Mn (Al • Y) by Nneutron Diffraction

95-B2-66 WINK/SAN Kurita K Nihon Univ.
Small-Angle Neutron Scattering of Human Hair

95-B2-67 MRP Mitsuda S Science Univ. of Tokyo
Magnetic Structure of Triangular Lattice Antiferromagnet $CuFe_{1-x}Al_xO_2$ in High Magnetic Field

95-B2-68 WINK Konakahara T Science Univ. of Tokyo
Determination of Structure of DNA-Ethidium Bromide Complex in Aqueous Solution by Contrast Variation Method

95-B2-69 WINK Fukai F Science Univ. of Tokyo
Analysis of Conformation Change in Fibronectin Fragment during the Heparin-Induced Activation of Cell Adhesion-Inhibiting Activity

95-B2-70 CAT Horiuchi N Waseda Univ.
Nonlinear Optical Effect and Hydrogen Bonds of the Organic Crystal 2A5NPDP

95-B2-71 VEGA Sato T Tokyo Engineering Univ.
Crystal and Magnetic Structure of Zn Ferrite Ultra-Fine Particles Having Anomalous Magnetization

95-B2-72 TOP Sato T Keio Univ.
Stability of the Localized Magnetic Moments in PdFe Fine Particles

95-B2-74 TOP Sato T Keio Univ.
Intraparticle Structure in Ultra-Fine $ZnFe_2O_4$ Particles

95-B2-75 SAN Sato T Keio Univ.
Study on the Magnetic Property of Magnetic Particles Dispersed in Polymer and LB Film of Magnetic Particles

95-B2-78 HIT Kakinuma F Niigata College of Parmacy
Neutron Diffraction Study of Local Structural Change on Liquid S-Te Mixtures

95-B2-79 VEGA Shigematsu T Konan Univ.
Powder Neutron Diffraction Study on the Crystal Structure of ZrO_2-$CeO_{2-\delta}$

95-B2-80 LAM Kittaka S Okayama Univ. of Science
Dynamic Properties of Monolayer Water Molecules on the Ionic Crystalline Solid Surface

95-B2-81 HIT Yamaguchi T Fukuoka Univ.
Neutron Diffraction of Aqueous NaCl Solution around the Critical Temperature of Water

95-B2-84 SAN Yamaguchi T Fukuoka Univ.
Small-Angle Neutron Scattering from Aqueous Solutions of Bile Salts

95-B2-86 VEGA Akiba E NIMC
Structure Refinement of Metal Hydrides

95-B2-87 CAT Ueda T NIMC
Dynamical Behavior of Hydrogen Atom in NbH_xDy and VH_xDy

95-B2-88 CAT Ueda T NIMC
Local Structure and Hydrogen Dynamics in $Mg_2NiH_{4-x}D_x$

95-B2-89 WINK Watanabe Y NFRI
Small-Angle Neutron Scattering Studies of Plant Virus Coat Proteins in Complex with Sodium Dodecyl Sulfate

95-B2-90 HIT Igarashi K GIRI, Nagoya
Neutron Diffraction Analysis of Silica Aerogels Treated under Different Temperatures

95-B2-91 SAN Tajiri K GIRI, Nagoya
Neutron Small Angle Analysis of Silica Aerogels with Different Densities

95-B2-92 HIT Umesaki N GIRI, Osaka
Structure of Short-Medium Range Order of Tellurite Melts

95-B2-93 LAM Kitamura N GIRI, Osaka
Inelastic Neutron Scattering of CaO-P_2O_5 Glasses

95-B2-94 INC/LAM Suzuya K JAERI
Dynamic Response of Structural Transitions in Alkali Phosphate Glasses

95-B2-95 MRP M. Steiner HMI
Determination of the Phase Diagram of $MnTiO_3$ in High Magnetic Fields

95-B2-96 INC ULF DAHLBORG SNRL
Dynamic Scattering Function of High Density Amorphous Ice

95-B2-97 HIT Kita Y Osaka Univ.
Pulsed Neutron Scattering Measurements on Li_2O-B_2O_3 Melts

95-B2-99	CAT	Ohoyama K	Tohoku Univ.

A Study of Magnetic Excitation in a Kondo Semiconductor CeRhSb

95-Urg.-1	SAN	Shimizu H	KEK

Measurement of Transmittance of a Polarized Proton Target at Liquid Nitrogen Temperature

95-Urg.-2	MRP	H.Nakotte	ANL

Magnetic Structures of the Frustrated Antiferromagnet UNi_4B in High Magnetic Fields

Proposals accepted (April 1996 - March 1997).

96-A1-1		Kiyanagi Y	Hokkaido Univ.
	Design and Construction of Neutron Reflectometer		
96-A1-2	HRP-II	Kamiyama T	Univ. of Tsukuba
	HRP-II, the Super High Resolution Neutron Powder Diffractometer		
96-A2-1		Yoshiki H	Ibaraki Univ.
	Development of edm Measuring Equipment		
96-A2-2	LAM	Ikeda H	KEK
	Application of LAM-80C to Experiments under Extreme Conditions		
96-A2-3		Shimizu H	RIKEN
	Research and Development of New Devices for Cold Neutron Scattering Experiment		
96-B1-1	FOX	Ohshima K	Univ. of Tsukuba
	Study on Structural Fluctuation and Phase Transition from Single Crystals of Allays and Compounds		
96-B1-2	MAX	Todate Y	Ochanomizu Univ.
	Study of Elementary Excitations Using Multi-Crystal Analyser Spectrometer		
96-B1-3	LAM	Shibata K	Tohoku Univ.
	Neutron Scattering Studies on Relaxational and Excitational Modes in Condensed Matters		
96-B1-4	HIT	Fukunaga T	Nagoya Univ.
	Structure Study of Liquids and Amorphous Solids		
96-B1-5	VEGA	Kamiyama T	Univ. of Tsukuba
	Structural Study by the VEGA Diffractometer		
96-B1-6	SAN	Furusaka M	KEK
	Materials Science by Small-Angle Neutron Scattering Instrument (SAN)		
96-B1-7	WINK	Otomo T	KEK
	Materials Science by Small/Medium-Angle Diffractometer (WINK)		
96-B1-8	PEN	Masuda Y	KEK
	Polarized Neutron Experiments by PEN		
96-B1-9	RAC	Ikeda S	KEK
	Condensed Matter Research using eV Neutrons		
96-B1-10	INC	Itoh S	KEK
	Study on Condensed Matter by Means of a Chopper Spectrometer		
96-B1-11	TOP	Takeda M	Tohoku Univ.
	Study of Magnetism by TOP		

96-B1-12	MRP	Arai M	KEK
	Study on Crystal Structure and Magnetic Structure in High Magnetic Field by MRP		
96-B2-1	HIT	Yoko T	Kyoto Univ.
	Precise Structure Analysis of $PbO\text{-}TeO_2$ Binary Glasses and Melts		
96-B2-2	HIT	Kakinuma F	Niigata College of Pharmacy.
	Neutron Diffraction Study of Local Structural Change on Liquid S-Te Mixtures		
96-B2-3	HIT	Yamaguchi T	Fukuoka Univ.
	Neutron Diffraction of Aqueous NaCl Solution around the Critical Temperature of Water		
96-B2-4	HIT	Mizutani U	Nagoya Univ.
	Structure of $Mg_{90-X}Ga_XCa_{10}$ Ternary Amorphous Alloys		
96-B2-5	HIT	Kita Y	Osaka Univ.
	Pulsed Neutron Scattering Measurements on $Li_2O\text{-}B_2O_3$ Melts		
96-B2-6	LAM	Imai M	Univ.of Tokyo
	Dynamical Structure of Crystalline Polymer near Glass Transition Temperature		
96-B2-7	LAM	Kaji K	Kyoto Univ.
	Low-Energy Excitation of Polymer Liquid Crystals		
96-B2-8	LAM	Kittaka S	Okayama Univ. of Science
	Dynamic Properties of Monolayer Water Molecules on the Ionic Crystalline Solid Surface		
96-B2-9	LAM	Kajitani T	Tohoku Univ.
	Hydrogen Vibration Modes in Organic Conductors		
96-B2-10	LAM	Misawa M	Niigata Univ.
	Quasielastic Scattering of the Liquid Carbon Tetrachloride		
96-B2-11	LAM	Yamamuro O	Osaka Univ.
	Low-Energy Excitations and Low-Temperature Heat Capacities in Simple Molecular Glasses		
96-B2-12	INC/LAM	Suzuya K	JAERI
	Dynamic Response of Structural Transitions in Alkali Phosphite Glasses		
96-B2-13	VEGA	Takahashi H	Univ. of Tokyo
	Studies of Crystal Structure under High Pressure		
96-B2-14	SAN/VEGA	Arai M	Kobe Univ.
	Diffraction Measurement of Single-Crystal High-Tc Superconductors		
96-B2-15	VEGA	Hashimoto M	Kobe Univ.
	Crystal Structures of Trihaloacetamides as Studied by Neutron Powder Diffraction		
96-B2-16	VEGA	Eda K	Kobe Univ.
	Crystal Structure of $(Na \cdot 2D_2O)_{0.25}\ D_x\ MoO_3$, x=0.5		

96-B2-17 VEGA Shigematsu T Konan Univ.
Powder Neutron Diffraction Study on the Crystal Structure of ZrO_2-$CeO_{2-\delta}$

96-B2-18 MAX Kashida S Niigata Univ.
Inelastic Neutron Scattering Study of the Structural Phase Transition in $KDCO_3$

96-B2-19 SAN Ichikawa K Hokkaido Univ.
Nonmetal-Metal Transition under the Concentration Fluctuation: Growth of Polybismuth Ions to Cluster

96-B2-20 WINK/SAN Kurita K Nihon Univ.
Small-Angle Neutron Scattering of Human Hair

96-B2-21 SAN Yamaguchi T Fukuoka Univ.
Small-Angle Neutron Scattering from Aqueous Solutions of Bile Salts

96-B2-22 WINK Sumiyama K Tohoku Univ.
A Small Angle Neutron Scattering Study on Topological and Magnetic Medium-Range Structure in Fe/Cu Granular Films

96-B2-23 WINK Hirai M Gunma Univ.
Structural Properties of Ganglioside-Protein Complexes in Aqueous Solvents

96-B2-24 WINK Fukunaga T Nagoya Univ.
Density Fluctuation and Structural Relaxation for Amorphous Se Prepared by Mechanical Milling

96-B2-25 WINK Okabayashi H Nagoya Inst. Tech.
Aggregate Structures of Surfactants Having Asymmetric Structure

96-B2-26 WINK Okabayashi H Nagoya Inst. Tech.
Super Secondary Structure of Oligopeptide Aggregates in Solvent

96-B2-27 INC Yamaguchi Y Tohoku Univ.
A Study of Spin Wave in Itinerannt Electron Antiferromagnetic System $Mn_{3-x}T_xSi$(T=Fe,Cr)

96-B2-28 INC Fukunaga T Nagoya Univ.
Dynamic Structure of Amorphous Se Formed only by Chain Molecules or Ring Ones

96-B2-30 MRP Kohgi M Tokyo Met. Univ.
Magnetic Structure of the Low Carrier System CeX(X=P,As) under High Magnetic Field

96-B2-31 MRP Mitsuda S Science Univ. of Tokyo
Magnetic Structure of Triangular Lattice Antiferromagnet $CuFe_{1-x}Al_xO_2$ in High Magnetic Field

96-B2-33 CAT Ueda T NIMC
Local Structure and Hydrogen Dynamics in $Mg_2NiH_{4-x}D_x$

96-B2-40 HIT Iwadate Y Chiba Univ.
Network Structure and Oxygen Coordination around Rubidium in B_2O_3-Rb_2O Glasses

96-B2-41 HIT Imai M Univ.of Tokyo
Orientation Ordering of Polymers during Induction Period of Crystallization

96-B2-43 HIT Kamimori T Ehime Univ.
Study of the Structure of Amorphous Cu_2MnAl_{1-x} $(Zr \cdot Y)_x$ by Neutron Diffraction

96-B2-44 HIT Takeda S Kyushu Univ.
Middle Range Order in the Structure of Molten Oxcide

96-B2-45 HIT Yamaguchi H ETL
Structure Analysis of Non-Crystalline $CuGeO_3$

96-B2-46 HIT Umesaki N GIRI, Osaka
Structural Analysis of Li_2S-SiS_2 Superionic Conducting Glasses by Pulsed-Neutron Diffraction

96-B2-47 HIT Kitamura N GIRI, Osaka
A Study of Structure for Densified Lithium-Silicate Glass

96-B2-48 LAM/WINK Kaji K Kyoto Univ.
Low-Energy Excitations of Oriented Amorphous Polymers

96-B2-50 LAM Kataoka M Osaka Univ.
Changes in Low-Energy Dynamics of Proteins upon Folding

96-B2-51 LAM Inaba A Osaka Univ.
Dynamics in Halogeno-mesitylene Monolayers Adsorbed on Graphite

96-B2-52 LAM Inaba A Osaka Univ.
Dynamics in Neopentane Monolayer Adsorbed on MgO

96-B2-53 LAM Takeda S Gunma Univ.
Proton Dynamics in $Rb_3H(SO_4)_2$

96-B2-55 LAM Seto H Hiroshima Univ.
Dynamics in a Structural Phase Transition and a Phase Separation in a Microemulsion

96-B2-56 LAM Aoki Y Tokyo Met. Univ.
Coexistence of Superconductivity and Magnetism in Heusler Compound $RePd_2Sn$

96-B2-57 LAM Nakamura Y Hokkaido Univ.
Chemical Effects for Dynamical Structures of Glass-Forming Nitrate Melts

96-B2-58 LAM Misawa M Niigata Univ.
Dynamics of Water Molecules in the Closed-Loop Phase Separating System

96-B2-59 LAM Tamaki S Niigata Univ.
Dynamics of Glycerol-methoxyphenol at the Upper and Lower Points of Loop in Phase Diagram

96-B2-60	LAM/CAT/HIT/WINK	Arai M	KEK
	Study on the Structure and the Dynamics of Permanenly Densified SiO_2 Glass		
96-B2-61	LAM	Itoh S	KEK
	Quantum Effect on Spin Dynamics in $CsNiCl_3$		
96-B2-62	INC	Kitamura N	GIRI, Osaka
	Inelastic Neutron Scattering of $Ca(PO_3)_2$ Glass and Crystal		
96-B2-63	LAM	Shirakami T	Tokyo Inst. Tech.
	Temperature Dependence of the Dynamical Structure Factor of Yttria-Stabilized Zirconia		
96-B2-64	LAM	Fukunaga T	Nagoya Univ.
	Dynamics of C-Li Intercalation Compounds Prepared by Mechanical Milling		
96-B2-65	LAM	Takeda K	Narto Univ. of Education
	Low-Energy Excitations of Molecular Glasses with Structure Controled by Hydrogen Bonds		
96-B2-66	TOP	Hosoito N	Kyoto Univ.
	Giant Magnetoresistance and Magnetic Polarization of Nonmagnetic Layers in Metallic Multilayers		
96-B2-67	TOP	Sato T	Keio Univ.
	Vortex-Like Spin Structure in Ni(Pt)Mn		
96-B2-69	VEGA	Yamamuro N	Univ. of Tsukuba
	Structures and Phase Transitions of Ionic Plastic Crystals Including NO_2-Ions		
96-B2-71	VEGA	Yashima M	Tokyo Inst. Tech.
	Structural Phase Transition of Hydroxyapatite		
96-B2-73	VEGA	Matsuo T	Osaka Univ.
	Effect of Deuterium Substitution on Phase Transitions of Anti-Fluorite Type Ammonium Salts		
96-B2-74	VEGA	Inaba A	Osaka Univ.
	Structural Study of Adsorbed Monolayers on Graphite		
96-B2-75	VEGA	Kanno R	Kobe Univ.
	Structure and Charge Disproportionation of the Iron Containing Perovskite Oxides		
96-B2-76	VEGA	Uesu Y	Waseda Univ.
	Mechanism of Diffuse Phase Transition in Relaxor Ferroelectrics		
96-B2-77	VEGA	Akiba E	NIMC
	Structure Refinement of Metal Hydrides		
96-B2-78	VEGA	Akiba E	NIMC
	Structure Refinement of Li Containing Oxides		

96-B2-79 VEGA Mochiku T NRIM
Crystallographic Study of the $Sr_2LnCu_2MO_8$-Type Compounds and the Related High-T_c Superconductors

96-B2-80 MAX Kashida S Niigata Univ.
Inelastic Neutron Scattering Study of the Structural Phase Transition in $KHCO_3$

96-B2-82 WINK Osamura K Kyoto Univ.
Meso-Scale Pattern Forming during Phase Decomposition in Alloys

96-B2-83 SAN Gohtani S Kagawa Univ.
Structural Investigation for Adsorbed Film of Saponin on Droplet Surface of Emulsion

96-B2-84 TOP Sato T Keio Univ.
Study on the Magnetic Property of Magnetic Particles Dispersed in Polymer and LB Film of Magnetic Particles

96-B2-86 HIT/WINK/LAM Kawamura J Hokkaido Univ.
Short and Intermediate Range Order of Organic-Inorganic Mixed Superionic Glasses

96-B2-89 WINK Hirai M Gunma Univ.
Denaturation Process of Globular Proteins Studied by Using Medium-High Angle Scattering

96-B2-90 WINK Imae T Nagoya Univ.
Investigation for Fibrous Supermolecular Structure by Small-Angle Neutron Scattering

96-B2-91 WINK Aoi K Nagoya Univ.
Investigation for a New Micelle Structure of a Chitin Derivative

96-B2-92 WINK Okabayashi H Nagoya Univ.
Studies of Aggregate Structure of Surfactants Having Special Molecular Structures in Aqueous Solutions

96-B2-93 WINK Kanaya T Kyoto Univ.
Annealing Effects on Low-Energy Excitations and Changes in Structures of Amorphous Polymers

96-B2-94 WINK Yamamuro O Osaka Univ.
Short-and Medium-Range Structures and Their Annealing Effects of Vapor-Deposited Molecular Glasses

96-B2-95 WINK Yoshida H Tokyo Met. Univ.
Cluster Structure of Water in Hyaluronic Acid Hydrogel

96-B2-96 WINK Yamaguchi T Fukuoka Univ.
Small-Angle Neutron Scattering from Aqueous Solutions of MEGA-8

96-B2-97 WINK Watanabe Y NFRI
Neutron Scattering Studies of Sodium Dodecyl Sulfate-octylglucoside Mixed Micellar System

96-B2-98 INC/CAT Yamaguchi Y Tohoku Univ.
A study of Ce 4f States in a Heavy Fermion Compound System Ce_2X(X=Sb, Bi)

96-B2-99 INC Kadowaki H Univ. of Tokyo
Magnetic Excitation of Valence Fluctuation Compound $CeRu_2$

96-B2-100 FOX Arai M Kobe Univ.
Study on the Dynamics and the Structural Instability of High-Tc Superconductors

96-B2-102 INC Igarashi K GIRI, Nagoya
Dynamics in Silica Aerogels Treated under Different Temperatures

96-B2-103 INC Metoki N JAERI
Giant Crystal Field Excitation of Kondo Ferromagnet $CeRh_3B_2$

96-B2-104 INC Metoki N JAERI
Inelastic Neutron Scattering Study of Crystal Field Level in $PrCu_2$

96-B2-105 CAT Ohoyama K Tohoku Univ.
Neutron Spectroscopy Study of a "Kondo semiconductor" CeRhSb under Pressure

96-B2-106 CAT Yamaguchi S Tohoku Univ.
Inelastic Neutron Scattering of Hydrogen in Ordered Alloys

96-B2-107 RAC Iwasa K Tokyo Met. Univ.
Charge Order and Local Atomic Vibrations of Yb Ions in the Low-Carrier System Yb_4As_3

96-B2-108 RAT Kamiyama T Hokkaido Univ.
Neutron Resonance Scattering for Glasses Containing Nanosize Ag Metal Particles

96-B2-109 RAT Misawa M Niigata Univ.
Atomic Vibration in Micro-Clusters by Neutron Resonance Absorption Method

96-Urg.-2 HIT Fujii H Hiroshima Univ.
Structural Characterization of Amorphized Mg-Ni-D System

96-Urg.-4 VEGA Ikeda S KEK
Study on Impurity Motions with Neutron Resonance Method

APPENDICES

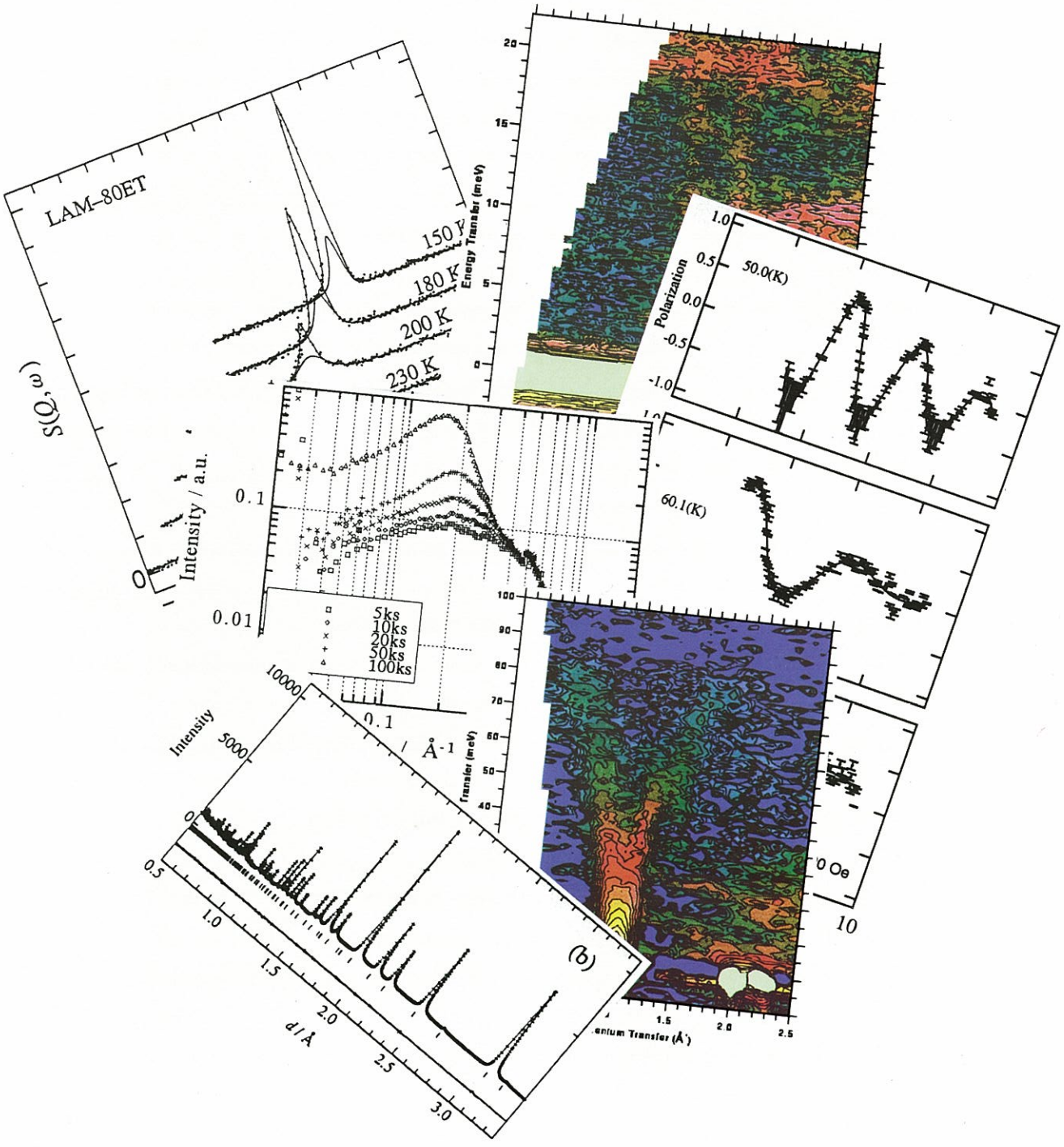
LAM-80ET
150 K
180 K
200 K
230 K
S(Q,ω)
Intensity / a.u.
Energy Transfer (meV)
Polarization
50.0(K)
60.1(K)
5ks
10ks
20ks
50ks
100ks
Intensity
Å-1
d/Å
(b)
0 Oe
10

Publications

1. General

Status of KENS-I' and KENS-II

Watanabe N.

Proc. 11th Meeting of the Int. Collaboration on Advanced Neutron Sources (KEK, Tsukuba, Oct. 22-26, 1990)61

The Research of Condensed Matter Physics Research by Using Intense Proton Accelerator

Endoh Y.

Proc. of the 2nd International Symposium on Advanced Nuclear Energy Research -Evolution by Accelerators - (Mito, Jan. 24-26, 1990)141

KENS Neutron Scattering Facility (Correspondents' Reports)

Furusaka M.

Neutron News 3(1992)8

Status of the KENS Facility

Watanabe N and Ikeda H.

Proc. 12th Meeting of Int. Collaboration on Advanced Neutron Sources (Abingdon Oxfordshire, UK)

2. Accelerator and Beam Line

Particle Tracking in the BSF Beam Line

Adachi T.

Proc. 11th Meeting of the Int. Collaboration on Advanced Neutron Sources (KEK, Tsukuba, Oct. 22-26, 1990)270

Non-Destructive Profile Monitor in a Beam Transport Line

Adachi T and Kawakubo T.

Proc. Int. Workshop on Advanced Beam Instrumentation (Apr. 22-24, 1991, KEK)160

Progress during the Decade of the BSF Beam-Line

Irie Y, Adachi T, Yano Y, Fujimori H, Kaneko N, Kobayashi Y and Tahara T.

KEK Report 91-6, July 1991

Precise Measurement of Pulsed-Beam Intensity

Irie Y and Yano Y.

Nucl. Inst. Methods A320(1992)27

Beam-Halo Measurement

Tahara T, Irie Y, Adachi T and Muto S.

Proc. 9th Symp. Accelerator Science and Technology (25-27, Aug., 1993, KEK J,apan)357

Cathode-Follower RF for High-Intensity Proton Synchrotron

Irie Y, Kaneko N, Kobayashi Y and Yano Y.

Nucl. Inst. Methods A346(1994)17

Beam-Steering Dipole Magnet in both the Horizontal and Vertical Directions

Fujimori H, Irie Y and Muto S.

KEK Report 94-8(1995)1

3. Neutron Source

Reflector Optimization for Coupled Liquid Hydrogen Moderator

Kiyanagi Y, Watanabe N, Furusaka M and Iwasa H.

Proc. 11th Meeting Int. Collaboration on Advanced Neutron Sources (KEK, Oct. 22-26 1990)401

A Design Concept for KENS-II Cold Neutron Souce

Watanabe N, Furusaka M and Kiyanagi Y.

Proc. Int. Workshop on Cold Neutron Source (Los Alamos, March 5-8, 1990)491

Optimization Studies on Coupled Liquid Hydrogen Moderator

Kiyanagi Y, Watanabe N, Furusaka M, Iwasa H and Fujikawa I.

Proc. 11th Meeting Int. Collaboration on Advanced Neutron Sources (KEK, Oct. 22-26 1990)388

A Design Concept of Target-Moderator-Reflector Assemblies for KENS-II

Watanabe N.

Proc. 11th Meeting Int. Collaboration on Advanced Neutron Sources (KEK, Oct. 22-26 1990)471

Intense Neutron Source for Material Research

Watanabe N.

Proc. of the 2nd International Syymposium on Advanced Nuclear Energy Research -Evolution by Accelerators - (Mito, Jan. 24-26, 1990)

Some Neutronic Studies on Flux-Trap Type Moderator

Kiyanagi Y and Watanabe N.

Proc. 11th Meeting Int. Collaboration on Advanced Neutron Sources (KEK, Oct. 22-26 1990)408

Experimental Studies on Neutronic Performance of Coupled Liquid-Hydrogen Moderator for Pulsed Spallation Neutron Souces

Kiyanagi Y, Watanabe N and Iwasa H.

Nucl. Inst. Methods A312(1992)561

Towards a High-Efficiency Pulsed Spallation Neutron Source

Watanabe N and Kiyanagi Y.

Physica B 180&181(1992)893

Some Optimization Studies on Flux-Trap Moderators for Increasing the Slow Neutron Beam Intensity

Kiyanagi Y, Watanabe N and Nakajima M.

Proc. 12th Meeting of Int. Collaboration on Advanced Neutron Sources (Abingdon Oxfordshire, UK)T-172

Premoderator Studies for a Coupled Liquid-Hydrogen Moderator

Kiyanagi Y, Watanabe N, Iwasa H and Nakajima M.

Proc. 12th Meeting of Int. Collaboration on Advanced Neutron Sources (Abingdon Oxfordshire, UK)T-196

Studies of Decoupled Composite Moderators of Liquid-Hydrogen and Zirconium Hydride

Kiyanagi Y, Carpenter J. M, Watanabe N, Iwasa H and Nakajima M.

Proc. 12th Meeting of Int. Collaboration on Advanced Neutron Sources (Abingdon Oxfordshire, UK)T-206

Tailoring Intensities and Pulsed Shapes in Coupled Moderator Reflector Systems

Carpenter J. M, Kiyanagi Y, Watanabe N, Iwasa H and Nakajima M.

Proc. 12th Meeting of Int. Collaboration on Advanced Neutron Sources (Abingdon Oxfordshire, UK)T-164

An Intense Pulsed Spallation Neutron Source Using a High-Power Proton Linac for Nuclear Transmutation

Watanabe N.

Proc. 12th Meeting of Int. Collaboration on Advanced Neutron Sources (Abingdon Oxfordshire, UK)P-24

Comparison of the Slow Neutron Intensity-0.8GeV vs 3 GeV Protons

Kiyanagi Y, Watanabe N and Arai M.

Proc. 12th Meeting of Int. Collaboration on Advanced Neutron Sources (Abingdon Oxfordshire, UK)T-90

Comparison of Slow-Neutron Intensities in Pulsed Neutron Sources with Various Proton Energies 0.8-3 GeV

Kiyanagi Y, Watanabe N and Arai M.

Jpn. J. Appl. Phys. 33(1994)2774

Premoderator Studies for a Coupled Liquid-Hydrogen Moderator in Pulsed Spallation Neutron Sources

Kiyanagi Y, Watanabe N and Iwasa H.

Nucl. Inst. Methods A343(1994)558

Neutronic Studies on Flux-Trap Moderators in Spallation Neutron Sources

Kiyanagi Y, Watanabe N and Nakajima M.

Nucl. Inst. Methods A343(1994)550

Neutronics of Coupled Solid Methare Moderator with Premoderator

Kiyanagi Y, Watanabe N, Hiraga F, Iwasa H and Satoh S.

Proc. Int. Seminar on Advanced Pulsed Neutron Sources (Dubna, June 14-16, 1994)

Development of High-Efficiency Moderators for Pulsed Neutron Soruces

Watanabe N and Kiyanagi Y.

Proc. Int. Seminar on Advanced Pulsed Neutron Sources (Dubna, June 14-16, 1994)

4. Instrumentations

Applications on Pulsed Cold Neutron Small Angle Scattering Instruments

Furusaka M.

Proc. of the 2nd International Syymposium on Advanced Nuclear Energy Research -Evolution by Accelerators - (Mito, Jan. 24-26, 1990)632

First Results from the UK-Japanese Spectrometer MARI

Taylor A. D, Arai M, Bennington S. M, Bowden Z. A, Osborn R, Andersen K, Stirling W. G, Nakane T, Yamada K and Welz D.
Proc. 11th Meeting Int. Collaboration on Advanced Neutron Sources (KEK, Oct. 22-26 1990) (1990)705

Recent Progress in TOP Spectrometer

Itoh S, Watanabe T and Endoh Y.
Proc. 11th Meeting Int. Collaboration on Advanced Neutron Sources (KEK, Oct. 22-26 1990) (1990)792

Crosscorrelation Method Using a Pulsed White Polarized Neutron Beam

Kohgi M, Fujimoto H, Ohoyama K, Yamada K and Motoya M.
Proc. 11th Meeting Int. Collaboration on Advanced Neutron Sources (KEK, Oct. 22-26 1990)733

Crystal Analyzer Type Spectrometer LAM-D at KENS Spallation Thermal Neutron Source

Inoue K, Kanaya T, Kiyanagi Y, Shibata K, Kaji K, Ikeda S, Iwasa H and Izumi Y.
Proc. 11th Meeting of the Int. Collaboration on Advanced Neutron Sources (KEK, Tsukuba, Oct. 22-26, 1990)1082

Several Experiences of Using Li-Glass Scintillators

Niimura N, Hirai H, Aizawa K, Yamada K and Okamura F.
Proc. 11th Meeting Int. Collaboration on Advanced Neutron Sources (KEK, Oct. 22-26 1990)967

Performance of Chopper Spectrometers

Arai M, Taylor A. D, Bennington S. M, Bowden Z. A, Osborn R, Kohgi M, Ohoyama K and Nakane T.
Proc. 11th Meeting Int. Collaboration on Advanced Neutron Sources (KEK, Oct. 22-26 1990) (1990)644

Why Total Performance

Watanabe N.
Proc. 11th Meeting Int. Collaboration on Advanced Neutron Sources (KEK, Oct. 22-26 1990) (1990)637

Recent Progress on MAX

Todate Y, Ikeda H, Tajima K and Tomiyoshi S.
Proc. 11th Meeting Int. Collaboration on Advanced Neutron Sources (KEK, Oct. 22-26 1990) (1990)739

Resolution Function and Recent Developments of the Multi Analyzer Crystal Spectrometer MAX

Todate Y, Tajima K, Ikeda H and Tomiyoshi S.
Jpn. J. Appl. Phys. 29(1990)1220

Thermal Neutron Small-Angle Scattering Spectrometer (WIT)

Niimura N, Aizawa K, Hirai M, Sangawa U and Yamada K
Proc. 11th Meeting Int. Collaboration on Advanced Neutron Sources (KEK, Oct. 22-26 1990)1091

Total Performance of LAM-80ET

Inoue K, Kanaya T, Kiyanagi Y, Shibata K, Kaji K, Iwasa H and Izumi Y.
Proc. 11th Meeting Int. Collaboration on Advanced Neutron Sources (KEK, Tsukuba, Oct. 22-26, 1990)684

Total Performance of Small-Angle Machines at Pulsed Source

Furusaka M, Watanabe N, Suzuya K, Fujikawa I and Satoh S.
Proc. 11th Meeting Int. Collaboration on Advanced Neutron Sources (KEK, Oct. 22-26 1990)677

A Semicircle One-Dimensional Position Sensitive Detectors for the Neutron Time-of-Flight Single Crystal Diffractometer

Niimura N, Kawada I, Isove M, Okamura F and Yamada K.
J. Appl. Cryst. (1990)

MARI-A New Spectrometer for Liquid and Amorphous Materials

Arai M, Taylor A. D, Bennington S.M and Bowden Z. A.
Recent Developments in the Physics of Fluids, Int. Symp. Oxford UK 1991 Section 5F321

Small Angle Thermal Neutron Scattering Spectrometer (WIT)

Niimura N, Aizawa K, Hirai M and Sangawa U.
Proc. Int. Conf. Neutron Scattering (Oxford, 27-30 Aug. 1991), P3-B-155, Physica B

A TOF Neutron Diffraction System for High Pressure and Low Temperature

Kamigaki K, Ishikawa Y, Suzuki T and Tomiyoshi S.
High Pressure Research 8(1991)501

Sealing Performance of Gaskets & Flanges Against Superfluid Helium

Ishimaru H and Yoshiki H.
Cryogenic 31(1991)456

A High-Resolution Neutron Spectrometer Using Mica Analyzers and the Pulsed Cold Neutron Source

Inoue K, Kanaya T, Kiyanagi Y, Ikeda S, Shibata K, Iwasa H, Kamiyama T, Watanabe N and Izumi Y.
Nucl. Instrum. Methods. A309(1991)294

A Crystal Analyzer Type Inelastic Spectrometer Using the Pulsed Thermal Neutron Source

Inoue K, Kanaya T, Kiyanagi Y, Shibata K, Kaji K, Ikeda S, Iwasa H and Izumi Y.
Nucl. Instrum. Methods. A327(1992)433

Engineering of Ultra-Low Energy Neutrons / New Possibilities

Utsuro M, Kawabata Y, Yamaguchi A and Yoshiki H.
J. Atomic Energy Soc. Jpn. 35(1993)493

Three Metru Long Horizontal Cryostat Producing Ultracold Neutrons Using Superfluid Liquid Helium at 0.5K

Yoshiki. H, Sakai K, Kawai T and S. Goto'o
Cryogenics 34(1994)277

A Flat-Type ^{3}He Proportional Counter for Ultracold Neutron (UCN) Detector

Yamaguchi H, Ishimoto S and Yoshiki H.
Nucl. Inst. Method A343(1994)573

Development of A Solid-State Detector with a ^{6}Li/Ti Multilayer Converter for Ultracold Neutrons

Shimizu H. M, Kawai T, Ebisawa T, Eguchi Y and Sakai K.
Nucl. Instrum. Methods. A350(1994)296

A new TOF neutron powder diffractometer with arrays of one-dimensional PSD's

Kamiyama T, Oikawa K, Tsuchiya N, Osawa M, Asano H, Watanabe N, Furusaka M,
PHYSICA B CONDENSED MATTER (1995)875

5. Crystal Structures

Neutron and X-Ray Diffraction Study of a Valence Fluctuating Compound $YbInCu_4$

Kojima K, Nakai Y, Suzuki T, Asano H, Izumi F, Fujita T and Hihara T.
J. Phys. Soc. Jpn. 59(1990)792

Neutron Diffraction Studies of High-Tc Superconductors at KENS

Asano H.
Proc. of the 2nd International Syymposium on Advanced Nuclear Energy Research -Evolution by Accelerators - (Mito, Jan. 24-26, 1990)633

Crystal Structure of the Ferromagnetic Copper Oxide $La_{4-x}Ba_{2+x}Cu_2O_{10}$

Mochiku T, Asano H, Mizuno F, Masuda H, Hirabayashi I, Tanaka S and Izumi F.
Proc. 3rd Int. Symp. Superconductivity (Sendai, 1990)347

Effect of Annealing under High Oxygen Pressure on the Structure and Superconductivity of $(Ba_{0.85}Nd_{0.15})_2NdCu_3O_{6+z}$

Mochiku T, Asano H, Akinaga H, Ohshima T, Takika K, Izumi F, Takeda Y, Takano M and Mizoguchi K.
Physica C 167(1990)560

Effect of Deformation on Pd_2MnSn Heusler Alloy Studied with Transmission Electron Microscopy, Profile Analysis of Neutron Powder Diffraction Pattern

Kamiyama T, Shinohata T, Tomiyoshi S, Minonishi Y, Asano H and Watanabe N.
J. Appl. Phys. 68(1990)4741

Neutron Diffraction Study of the Cu Ferromagnet $La_4Ba_2Cu_2O_{10}$

Ogawa N, Mizuno F, Masuda H, Hirabayashi I, Tanaka S, Mochiku T, Asano H and Izumi F.
Physica B 165&166(1990)1687

Structural Analysis of Orthorhombic ZrO_2 by High Resolution Neutron Powder Diffraction

Ohotaka O, Yamanaka T, Kume S, Hara N, Asano H and Izumi F.
Proc. Jpn. Academy 66(1990)193

Rietveld Analysis of the Modulated Structure in the Superconducting Oxide $Bi_2(Sr, Ca)_3Cu_2O_{8+x}$

Yamamoto A, Onoda M, Takayama-Muromachi E, Izumi F, Ishigaki T and Asano H.
Phys. Rev. B 42(1990)4228

Neutron-Diffraction Study of $Tl_2Ba_2CuO_{6+\delta}$ with Various T_c's from 0 to 73 K

Shimakawa Y, Kobo Y, Manako T, Igarashi H, Izumi F and Asano H.
Phys. Rev. B 42(1990)10165

Anomalous Paramagnetic Property of $NdNbO_4$ Single Crystals

Yamauchi H, Tsunekawa S, Tomiyoshi S, Fukuda T, Kamiyama T and Asano H.
J. Phys. Soc. Jpn. 59(1990)2602

Sr-Induced Oxygen Defects in $La_{2-x}Sr_xCuO_{4-\delta}$: A Neutron Powder Diffraction Study

Kamiyama T, Izumi F, Asano H, Takagi H, Uchida S, Tokura Y, Takayama-Muromachi E, Matsuda M, Yamada K, Endoh Yand Hidaka Y.
Physica C 172(1990)120

Nonstoichiometry and Mixed Pr Valency in $(Pr_{1-x}Sr_x)(Pr_{1-y}Ce_y)CuO_{4-z}$

Kito H, Sawa H, Akimitsu J, Izumi F, Ishigaki T and Asano H.

Jpn. J. Appl. Phys. 29(1990)L1803

Crystal Structure Analysis of the Dense Kondo System $CeSi_x$

Kohgi M, Ito M, Satoh T, Asano H, Ishigaki T and Izumi F.

J. Magn. Magn. Mater. 90&91(1990)433

Three-Dimensional Antiferromagnetic Order and Anisotropic Magnetic Properties in Bi_2CuO_4

Yamada K, Takada K, Hosoya S, Watanabe Y, Endoh Y, Tomonaga N, Suzuki T, Ishigaki T, Kamiyama T, Asano H and Izumi F.

J. Phys. Soc. Jpn. 60(1991)2406

Relationship between Crystal Structure and Long-Time Response to DC Electric Field in Niobium-Doped $BaTiO_3$ Ceramics

Ikeda M, Yoshida M, Satoh A, Nishikawa K, Izumi F and Asano H.

Jpn. J. Appl. Phys. 30(1991)2295

Neutron Diffraction Study of Superconducting $La_{1.82}Ca_{1.18}Cu_2O_6$

Kinoshita K, Izumi F, Yamada T and Asano H.

Physica C 185-189(1991)537

Neutron Diffraction Study of the Ferromagnetic Copper Oxide $La_{1.8}Ba_{1.2}CuO_5$

Mochiku T, Asano H, Izumi F, Mizuno F, Masuda H, Hirabayashi I and Tanaka S.

J. Phys. Soc. Jpn. 60(1991)1959

Structural Study of Oxide Superconductors by Neutron Diffraction

Asano H.

Solid State Ionics 49(1991)17

Oxygen and Cation Nonstoichiometry in Tl-Based Superconductors

Shimakawa Y, Kubo Y, Manako T, Igarashi H, Izumi F and Asano H.

Solis State Ionics 49(1991)53

Oxygen Contents, Crystal Structures and Physical Properties of $Tl_2Ba_2CuO_{6+z}$

Kubo Y, Shimakawa Y, Manako T, Igarashi H, Izumi F and Asano H.

Supercond. Sci. Technol. 4(1991)S82

Neutron Powder Diffraction Study of the Pb-Based Copper Oxide Containing Thick Fluorite Blocks: $(Pb,Cu)Sr_2(Ho,Ce)_3Cu_2O_{11+z}$

Wada T, Ichinose A, Izumi F, Nara A, Yamauchi H, Asano H and Tanaka S.

Physica C 179(1991)455

Hole-Doping Effects on the Magnetic Properties of the $La_4Ba_2Cu_2O_{10}$ Ferromagnet

Mizuno F, Masuda H, Hirabayashi I, Tanaka S, Mochiku T, Asano H and Izumi F.

Proc. 2nd ISSP Int. Symp. (Tokyo, 1991)389

Low-Temperature Specific Heat and Ferromagnetism in $La_4Ba_2Cu_2O_{10}$ and Related Compounds

Mizuno F, Masuda H, Hirabayashi I, Tanaka S, Hasegawa M, Mizutani U, Mochiku T, Asano H and Izumi F.

Supercond. Sci. Technol. 4(1991)S301

High-Resolution Neutron Powder Diffraction of Superconducting $La_2CuO_{4+\delta}$

Kamiyama T, Asano H, Shibutani K, Ogawa R, Endoh Y, Izumi F, David W.I.F, Ibberson R and Yamaguchi Y.

Proc. 3rd Int. Symp. Superconductivity (Sendai, 1990)343

Crystal Structure and Superconducting Properties of Layered Copper Oxides Containing "123" Block and Single-MO_2-Unit Fluorite Block

Ichinose A, Wada T, Yaegashi Y, Nara A, Izumi F, Yamauchi H, Asano H and Tanaka S.

Physica C 185-189(1991)609

Structural Changes Accompanying Oxygen Incorporation in $(Pb_{0.65}Cu_{0.35})Sr_2(Y_{0.7}Ca_{0.3})Cu_2O_{7+\delta}$

Maeda T, Sakuyama K, Izumi F, Yamauchi H, Asano H and Tanaka S.

Physica C 175(1991)393

Synthesis and Structure Refinement of $SrT_xV_{6-x}O_{11}$ (T=Ti, Cr and Fe)

Kanke Y, Izumi F, Takayama-Muromachi E, Kato K, Kamiyama T and Asano H.

J. Solid State Chem. 92(1991)261

Oxygen Nonstoichiometry and Metal Substitution in $TlSr_2CaCu_2O_{7-x}$

Izumi F, Kondo T, Shimakawa Y, Manako T, Kubo Y, Ishigaki H and Asano H.

Physica C 185-189(1991)615

Superconductivity in Pb-Based "1222" Copper Oxides

Sakai N, Maeda T, Izumi F, Asano H and Yamauchi H.

Proc. 4th Int. Symp. Superconductivity (Tokyo, 1991)217

Temperature Dependence of the Structure of $Tl_2Ba_2CuO_{6+\delta}$: A Neutron Powder Diffraction Study

Kamiyama T, Izumi F, Asano H, Shimakawa Y, Kubo Y, Manako T and Igarashi H.

Physica C 185-189(1991)881

Phase Transformation of Baddekeyite(ZrO_2) to an Orthorhombic Phase: Structural Analysis of Ortho-ZrO_2 by Neutron Diffraction

Ohtaka O, Yamanaka T, Kume S, Hara N, Asano H and Izumi F.

High-Pressure Research463

The Crystal Structure of the Superconducting Copper Oxide Carbonate $(Ba_{1-x}Sr_x)_2Cu_{1+y}O_{2+2y+z}(CO_3)_{1-y}$.

Izumi F, Kinoshita K, Matsui Y, Yanagisawa K, Ishigaki T, Kamiyama T, Yamada T and Asano H.

Physica C 196(1992)227

Structure Refinements of Superconducting and Nonsuperconducting $La_{1.82}Ca_{1.18}Cu_2O_{67\delta}$

Kinoshita K, Izumi F, Yamada T and Asano H.

Phys. Rev. B 45(1992)5558

Cation Distribution in $ZnFe_2O_4$ Fine Particles Studied by Neutron Powder Diffraction

Kamiyama T, Haneda K, Sato T, Ikeda S and Asano H.

Solid State Comm. 81(1992)563

Rietveld Analysis of the Composite Crystal in Superconducting $Bi_{2+x}Sr_{2-x}CuO_{6+y}$

Yamamoto A, Takayama-Muromachi E, Izumi F, Ishigaki T and Asano H.

Physica C 201(1992)137

Neutron Diffraction Studies of Oxide Superconductors

Asano H and Kamiyama T.

JJAP Series 7 Mechanisms of Superconductivity (1992)55

Structural Changes and Redistribution of Holes by Sr-Doping in $YBa_2Cu_4O_8$

Ishigaki T, Izumi F, Wada T, Suzuki N, Yaegashi Y, Asano H, Yamauchi H and Takada S.

Physica C 191(1992)441

Structural Properties of the Nonsuperconductor $(Ho,Ce)_2(Sr,Ba,La)_2\ Cu_3O_{8+z}$

Ichinose A, Wada T, Yaegashi Y, Izumi F, Yamauchi H, Asano H and Tanaka S.

Physica C 191(1992)205

Crystal Structures of the Two Dimensional Antiferromagnets RFe_2O_4 (R=Y, Er) and Their Magnetic Properties under Pressure

Matsumoto T, Mori N, Iida J, Tanaka M, Siratori K, Izumi F and Asano H.

Physics B 180&181(1992)603

Structural Properties of (Pb,Cu) $(Sr,Nd)_2(Ho,Ce)_2Cu_2O_{9-\delta}$

Maeda T, Sakai N, Izumi F, Wada T, Yamauchi H, Asano H and Tanaka S.

Physica C 193(1992)73

Neutron Diffraction Study of High Ionic Conductor $Rb_4Cu_{16}I_{7+x}Cl_{13-x}$ at 50-300 K: Correlation with Ionic Conductuvuty

Kanno R, Ohno K, Kawamoto Y, Takeda Y, Yamamoto O, Kamiyama T, Asano H, Izumi F and Kondo S.

J. Solid State Chem. 102(1993)79

Precise Structure Analysis by Neutron Diffraction for RNb and Distortion of NbO_4 Tetrahedra

Tsunekawa S. Kamiyama T, Sasaki K, Asano H and Fukuda T.

Acta Crystallogr. Sect. A49(1993)595

Structure Analysis of $K_3H(SO_4)_2$ by Neutron Powder Diffraction

Murakami S, kuroiwa Y, Noda Y, Nakai Y, Kamiyama T and Asano H.

Japan Atomic Energy Research Institute, Mito, Ibaraki, Japan, 1993 (1993)915

Phase Transitions and Structures of Methylammonium Compounds

Yamamuro O, Onoda-Yamamuro N, matuo T, Suga H, Kamiyama T, Asano H, Ibbersib R. M and David W.I. F.

Prc. 5th Int. Symp. Advanced Nuclear Energy Research -Neutron as Microscopic Probes-604

Oxygen Deficiency and Structural Phase Transition in $(La_{1-x}Ba_x)_2CuO_4$

Takayama-Muromachi E, Izumi F and Kamiyama T.

Physica C 215(1993)329

Refinement of the Crystal Structures of Cu_6O_8InCl and $Cu_6O_8Cu_2Cl$ by Neutron Powder Diffraction

Hayakawa H, Akiba E, Ono S, Ihara H, Izumi F and Asano H.

J. Chem. Soc. Jpn. 101(1993)726

Phase Relationship and Lithium Deintercalation in Lithium Nickel Oxides

Kanno R, Kubo H, Kawamoto Y, Kamiyama T, Izumi F, Takeda Y and Takano M.

J. Solid State Chem. 110(1994)216

Neutron Powder Diffraction Study of Phase Separation in $La_2CuO_{4+\delta}$ Oxidezed in $KMnO_4$ Solutions

Izumi F, Kim Y.-I, Takayama-Muromachi E and Kamiyama T.

Physica C 235-240(1994)841

Neutron Diffraction and Calorimetric Studies of Methylammonium Chloride

Yamamuro O, Onoda-Yamamuro N, Suga H, Kamiyama T, Ishigaki T and Asano H.

J. Phys. Chem. Solids 55(1994)383

Structure Refinements of Orthorhombic $(La_{1-x}Ca_x)_2CuO_4(x=0.05)$

Kito H, Akimitsu J, Izumi F, Kamiyama T and Asano H.

J. Phys. Soc. Jpn. 63(1994)695

Neutron Diffraction Study of the High-Fluoride-Ion Conductor, PbSnF4, Prepared under an HF Atmosphere

Kanno R, Ohno K, Izumi H, Kawamoto Y, Kamiyama T, Asano H and Izumi F.

Solid State Ionics 70/71(1994)253

Structural Changes of $PbBaSr(Y_{0.8}Ca_{0.2})Cu_3O_{7+z}$ on Oxygen Introduction into Block Layers

Ishigaki T, Tokiwa-Yamamuro A, Izumi F, Kamiyama T, Asano H and Syono Y.

Physica C 231(1994)357

X-Ray and Neutron Diffraction Studies of Methylammonium Tetrafluoroborate: Highly Disordered Orientations of $CH_3NH_3^+$ and BF_4^- Ions

Yamamuro O, Onoda-Yamamuro N, Matsuo T, Suga H, Kamiyama T, Ishigaki T and Asano H

J. Phys. Chem. Solids 56(1995)183

Neutron diffraction study of oxygen monolayers

Murakami Y, I.N.Makundi, Shibata T, Suematsu H, Arai .M, Yoshizawa H, Ikeda H, and Watanabe N

PHYSICA B CONDENSED MATTER (1995)233

XRAY AND NEUTRON DIFFRACTIONS STUDIES OF METHYLAMMONIUM TETRAFLUOROBORATE: HIGHLY DISORDERED ORIENTATIONS OF $CH_3NH_3^+$

Yamamuro O, Onoda-Ymamamuro N, Matsuo T, Suga H, Kamiyama T, Ishigaki T, and Asano H

Phys Chem. Solids 56(1995)183

Neutron Diffraction Study on Orientationnal Disorder of ND_4^+ Ions in $(ND_4)_2$ $SeCl_6$ Crystal

Yamamuro O, Muraoka H, Ohta T, Matsuo T, Kume Y, Onoda-Yamamuro, Oikawa K and Kamiyama T

J Phys Soc JAPAN 64(1995)2722

Hydrogen-Bonded Structure in Aqueous Sulfuric Acid Solutions

Kameda Y. Hosoya K. Sakamoto S. Suzuki H. Usuki T and Uemura O

MOLECULAR LIQUIDS 65/66(1995)305

Relationship between Covalence and Displscive Phase Transition Temperature in RAO_4 and $LIAO_3$ (R=Rare-Earth Element and A= Nb and Ta)

Tsunekawa S, Kamiyama T, Asano H, and Fukuda T

Solid State CHEMISTRY 116(1995)28

Neutron-Diffraction Study of CD3ND3SnBr3:Semiconductor-Insulator Transition with Orientational Ordering

Onoda N-Yamamuro, Yamamuro O, Matsuo T, SUga H, Oikawa K, Tsuchiya N, Kamiyama T, Asano H

Physica B 213&214(1995)411

Structure of Concentrated Aqueous Sodium Formate Solutions

Kameda Y, Mori T, Nishiyama T, Usuki T and Uemura O

Bull. Chem. Soc. Jpn. 69(1996)1495

6. Structure of Liquids and Glasses

Molecular Dynamics Studies on Molten Alkali Hydroxides. II. Rotational and Translational Motions of Ions in Molten LiOH

Okazaki S, Ohtori N and Okada I.

J. Chem. Phys. 93(1990)5954

Orientational Correlation in Liquid Phosphorous Tribramide Studied by Pulsed Neutron Total Scattering

Misawa M, Fukunaga T and Suzuki K.

J. Chem. Phys. 92(1990)5486

Pulsed Neutron Diffraction Study on a Molten NaOD Structure using a Nickel Metal Cell

Ohtori N, Okazaki S, Odawara O, Okada I, Misawa M and Fukunaga T.

J. Phys.: Condense. Matter 2(1990)5825

Diffraction and X-ray Absorption Studies of Electrolyte Solutions

Yamaguchi T.

Pure & Appl. Chem. 59(1990)2251

Effective Diameter of Molecules and Liquid-Gas Critical Point

Misawa M.

J. Chem. Phys. 93(1990)8401

Molecular Dynamics Studies on Molten Alkali Hydroxides. I. Static Properties of Molten LiOH

Okazaki S, Ohtori N and Okada I.

J. Chem. Phys. 92(1990)7505

Structure of Vitreous and Molten B_2O_3 Measured by Pulsed Neutron Total Scattering

Misawa M.

J. Non-Cryst. Solids 122(1990)33

Structure of Liquid Benzene and Naphthalene Studied by Pulsed Neutron Total Scattering

Misawa M and Fukunaga T.

J. Chem. Phys. 92(1990)3495

Structural Study on Molten MOD (M=^{7}Ki, Na and K) by Pulsed Neutron Diffraction

Ohtori N, Okazaki S, Odawara O, Okada I, Misawa M and Fukunaga T.

J. Phys.: Condense. Matter 2(1990)8439

Amorphization of Immiscible Cu-Ta System by Mechanical Alloying and its Structure Observation

Fukunaga T, Nakamura K, Suzuki K and Mizutani U.

J. Non-Cryst. Solids 117/118(1990)700

The Ni-Ni Partial Structure in Ni-V Alloy System Observed by Neutron Scattering during Mechanical Alloying Amorphization Process

Fukunaga T, Homma Y, Misawa M and Suzuki K.

J. Non-Cryst. Solids. 117/118(1990)721

Structure Factor of X_4 Tetrahedral molecular Liquid : Competition between Intramolecular and Intermolecular Atomic Spacing

Misawa M.

J. Chem. Phys. 93(1990)6774

Structure of Borate Glasses Containing Heavy Metal Ions

Yasui I, Hasegawa H, Saito Y and Akasaka Y.

J. Non-Cryst. Solids 123(1990)71

Molecular Dynamics Studies on Molten Alkali Hydroxides. III. One-Particle Dynamics of Ions in Molten LiOH

Okazaki S and Okada I.

Mol. Simul. 6(1991)265

Local Structure of Polyethylene Melt Studied by Pulsed Neutron Total Scattering

Misawa M, Kanaya T and Fukunaga T.

J. Chem. Phys. 94(1991)8413

Intra-and Intermolecular Correlations in Liquid Selenium-Halogen Systems

Murayama K, Kawakita Y, Yao M, Endoh H and Misawa M.

J. Phys. Soc. Japan 60(1991)3032

Pulsed Neutron Diffraction Studies on Lanthanide (III) Hydrogen in Aqueous Perchlorate Solutions

Yamaguchi T, Tanaka S, Wakita H, Misawa M, Okada I, Soper A. K. and Howells S. W.

Z. Naturforsch. 46a(1991)84

Amorphization in Immiscible Cu-V System by Mechanical Alloying and its Structure Observation by Neutron Diffraction

Fukunaga T, Mori M, Inou K and Mizutani U.

Mat. Sci. Eng. A 134(1991)863

Neutron-Diffraction Investigation of the Intramolecular Structure of a Water Molecule in the Liquid Phase at High Temperatures

Ichikawa K, Kameda Y, Yamaguchi T, Wakita H and Misawa M.

Molec. Phys. 73(1991)79

Structural Characterization of Ni-V Amorphous Alloys Prepared by Mechanical Alloying

Fukunaga T, Homma Y, Misawa M and Suzuki K.

Mat. Sci. Eng. A134(1991)987

The Structure around the Nitrite Ion in Concentrated Aqueous Solutions

Kameda Y, Arakawa H, Hangai K and Uemura O.

Bull. Chem. Soc. Jpn. 65(1992)2154

Direct Correlation between Lithium Cation and Carboxyl Anion in Highly Concentrated Aqueous Solution

Ichikawa K, Kotani S, Izumi M and Yamanaka T.

Molec. Phys. 77(1992)677

Orientational Correlation in Molecular Liquids Estimated from Experimental S(Q)'s

Misawa M.

J. Non-Cryst. Solids 150(1992)58

Chemical Short-Range Order Structure of Ni-Ti Neutron Zero Scattering Amorphous Powders Synthesized by MA

Fukunaga T, Misawa M, Suzuki K and Mizutani U.

Material Science Forum (Trans Tech. Pub.) 88-90(1992)325

Nitrogen-Induced Amorphization due to Mechanical Alloying

Fukunaga T, Ishikawa E, Kuroda N, Lee C. H and Mizutani U.

Proc. 4th Japan-Russia Sympo. on Mechnochemistry (Nagoya 23-26 March 1992)69

Diffraction Study of the Sol-Gel-Derived SiO_2 Gels

Kamiya K, Wada M, Matsuoka J, Nasu H, Fukunaga T and Misawa M.

Bol. Soc. Esp. Ceram. Vid. 31-C(1992)33

Structure and Dynamics of Undercooled and Glassy Aqueous Ionic Solution by NMR, X-Ray and Neutron Diffraction

Yamaguchi T, Yamagami M, Takamura T, Hirano T and Wakita H.

AIP Conf. Proc. 256(1992)89

Crystal-to-Amorphous Transition of NiV and NiZr Intermetallic Compound by Mechanical Milling

Homma Y, Fukunaga T, Misawa M and Suzuki K.

Material Science Forum (Trans Tech Pub.) 88-90(1992)339

The Intramolecular Structure of Oxonium Ion in Concentrated Aqueous Deuterochloric Acid Solutions

Kameda Y and Uemura O.

Bull. Chem. Soc. Jpn. 65(1992)2021

Structural Analysis of Sol-Gel Derived SiO_2 Gels by Neutron Diffraction

Wada M, Kamiya K, Nasu H, Matsuoka J, Yoko T, Fukunaga T and Misawa M.

J. Non-Cryst. Solids 149(1992)203

Structural Analysis of AlF_3-CaF_2-YF_3 Glass by Diffraction Methods

Akasaka Y, Nanba T, Inoue H, Osuka T and Yasui I.

J. Non-Cryst. Solids. 140(1992)249

Structural Evidence for the Amorphization of Mechanically Alloyed Cu-Ta Powders Studied by Neutron Diffraction

Lee C.H, Mori M, Fukunaga T, Sakurai K and Mizutani U.

Material Science Forum (Trans Tech. Pub.) 88-90(1992)399

Short Range Structure of $(C_{40}Ti_{60})_x(Ni_{40}Ti_{60})_{1-x}$ ($0<x<1$) Ternary Metallic Glasses Studied by Neutron Diffraction

Fukunaga T, Suzuki K and Mizutani U.

J. Non-Crys. Solids. 150(1992)10

Structural Study of Liquid Sb-Se Alloys

Kakinuma F, Fukunaga T, Misawa M and Suzuki K.

J. Non-Cryst. Solids 150(1992)53

Structural Observation of Metastable Phases Prepared by MA in V-M (M=Fe, Cu) Systems

Fukunaga T, Mori M, Misawa M and Mizutani U.

Material Science Forum (Trans Tech. Pub.) 88-90(1992)663

Inter-Molecular Structure around Lithium Monovalent Cations and Nitrogen Atoms in Molten $LiNO_3$

Kameda Y, Kotani S and Ichikawa K.

J. Molec. Phys. 75(1992)1

Atomic Structure of $Al_{55}(Cr_{1-x}Mn_x)_{15}Si_{30}$ Metallic Glasses

Fukunaga T, Suzuki K and Mizutani U.

J. Non-Cryst. Solids 150(1992)15

Network Structure of AlF_3-BaF_2-CaF_2 Glass

Nanba T, Osaka A, Takada J, Miura Y, Inoue H, Akasaka Y, Hagihara H and Yasui I.

J. Non-Cryst. Solids. 140(1992)269

Structural Studies of Multilayered Films Composed of Immiscible Pair Cu and Ta

Koyano T, Lee C.H, Fukunaga T, Mizutani U, Ikeda S, Higuchi Y, Nishikawa M, Kita e and Tasaki A.

J. Magn. Magn. Mater. 126(1993)161

Temperature Dependence Studies of the Liquid Structure of GaSb by Neutron Diffraction

Mizuki J, Kakimoto K, Misawa M, Fukunaga T and Watanabe N.

J. Phys. Condens. Matter 5(1993)3391

Pulsed Neutron Diffraction Study on the Structures of Glassy ^{7}LiX-KX-CsX-BaX_2 (X=Cl, Br, and I)

Kinugawa K, Ohtori N, Kadono K, Tanaka H, Okazaki S, Misawa M and Fukunaga T.

J. Chem. Phys. 99(1993)5345

Structural Analysis of Na_2O-B_2-O_3 Melts by Pulsed Neutron Tatal Scattering Method and Molecular Dynamics Simulation

Kita Y, Misawa M, Umesaki N, Kirihara T, Fukunaga T and Iida T.

ISIJ International 33(1993)188

Medium-Range Structure Variations in the Solid State Amorphizing Transformation of Metallic Alloys by Mechanical Milling

Suzuki K and Fukunaga T.

J. All. Comp. 194(1993)303

Neutron Diffraction Study of Liquid Bi-Se Alloys

Kakinuma F, Fukunaga T, Misawa M and Suzuki K.

J. Non-Cryst. Solids 156-158(1993)76

The Hydration Structure of NO_3^- in Concentrated Aqueous Sodium Nitrate Solutions

Kameda Y, Saitoh H and Uemura O.

Bull. Chem. Soc. Jpn. 66(1993)1919

Short-Range Structure of As-S-I System

Kameda Y, Sugawara Y and Uemura O.

J. Non-Cryst. Solids 156-158(1993)725

Is There Any Correlation between the Intermolecular Structures around Main-Group Metal Ion in Liquid and Crystalline States?

Ichikawa K, Kameda Y and Kotani S.

Prc. 5th Int. Symp. Advanced Nuclear Energy Research -Neutron as Microscopic Probes- (1993)641

Neutron Diffraction Study on the Structure of Na-Si-O-N Oxynitride Glasses

Jin J, Yoko T, Miyaji F, Sakka S, Fukunaga T and Misawa M.

J. Am. Ceram. Soc. 76(1993)630

Static Structure of Amorphous Solids and Liquids by Pulsed Neutron Diffraction

Misawa M and Fukunaga T.

Current Topics in Amorphous Materials: Physics and Technology (1993)4

Nitrogen Induced Amorphization Observed by X-ray and Neutron Diffractions in the Immiscible V-Cu System

Fukunaga T, Kuroda N, Lee C. H, Koyano T and Mizutani U.

J. Non-Cryst. Solids 176(1994)98

Microscopic Structure in Concentrated Aqueous Solutions -New Aquo Complex Observed by Neutron Probe-

Ichikawa K.

Kagaku to Kyoiku 42(1994)821

Chemical Atomic Arrangement of Amorphous Alloys

Fukunaga T.

J. Advanced Sci. 6(1994)101

Neutron Diffraction Study of the Li-Cl Distance in Molten Mixture Systems (Li, K)Cl and (Li, Cs)Cl

Miyamoto Y, Okazaki S, Odawara O, Okada I, Misawa M and Fukunaga T.

Molecular Phys. 82(1994)887

Neutron and X-ray Diffraction Studies on PbO-Ga_2O_3 and Bi_2O_3-Ga_2O_3 Glasses

Miyaji F, Yoko T, Jin J, Sakka S, Fukunaga T and Misawa M.

J. Non-Cryst. Solids 175(1994)211

Hydration Strucutre of SCN^- in Concentrated Aqueous Sodium Thiocyanate Solutions

Kameda Y, Takahashi R, Usuki T and Uemura O.

Bull. Chem. Soc. Jpn. 67(1994)956

A Molecular Dynamics and Neutron Diffraction Study of the Structure of Na_2O-B_2O_3 Melts

Umesaki N, Kita Y, Kirihara T, Iida T, Fukunag T and Misawa M.

J. Non-Cryst. Solids 177(1994)200

Nuetron Diffraction and Solid MAS-NMR Studies on the Structure of Y-AlSi-O-N Oxyritride Glasses

Jin J, Yoko T, Miyaji F, Sakka S, Fukunaga T and Misawa M.

Phil. Mag. 70(1994)191

Dynamics structure of supercooled-liquid in Ni_{15} $Pt_{60}P_{25}$amorphous ally-An in-situ observation by neutron diffraction

Otomo T, A.P.Tasai, Shibata K, Furusaka M, Inoue A, Masumoto T, Suzuki K

PHYSICA B CONDENSED MATTER 213&214(1995)541

An observation of the structural relaxation of a $Ni_{40}Pd_{40}P_{20}$ amorphous alloy by neutron inelastic scattering

Otomo T, Arai M, Shibata K, Mizuseki H, Suzuki K

PHYSICA B CONDENSED MATTER 213&214(1995)544

The coordination structure of Li^{+}in highly concentrated methanolic LiBr and LiI solutions

Kameda Y, Ebata H, Usuki T, Uemura O

PHYSICA B CONDENSED MATTER 213&214(1995)477

NO^{-}_{3}ion dynamics in liquid $0.38Ca(NO_3)_2 \cdot 0.62KNO_3$

Kamiyama T. Shibata K. Suzuki K and Nakamura Y

Journal of Non-Crystalline Solids 192&193(1995)272

structural study of supercritical carbon dioxide by neutron diffraction

Ishii R, Okazaki S, Odawara O, Okada I, Misawa M, and Fukunaga T

FLUID PHASE EQUILIBRIA 104(1995)291

Mechanical Alloying Cu-V and Cu-Ta Systems Characterized by Positive Heat of Mixing(Overview)

Mizutani T and Lee C.H

MATERIALS TRANSACTIONS, JIM 36(1995)210

A neuton scattering study of the structure of supercritical carbon dioxide

Ishii R . Okazaki S . Okada I . Furusaka M . Watanabe N . Misawa M . Fukunaga T .

CHEMICAL PHYSICS LETTERS 240(1995)84

Dynamical structures of simple and glass-forming nitrate melts

Kamiyama T. Shibata K. Suzuki K. Nakamura Y

Physica B 213&214(1995)483

The local structure around hydrogen atoms in a hydrogenated amorphous $LaNi_{5.0}$ film studied by neutron diffraction

Sakaguchi H, Suenobu T, Moriuchi K, Yamagami M, Yamaguchi T, and Adachi G

ALLOYS AND COMPOUNDS 221(1995)212

Structure Analysis of ZnO-TeO2 Glasses by Means of Neutron Diffraction and Molecular Dynamics

Matsumoto H, Mabuchi T, Shigesato Y and Itaru Y

Jpn. J, Appl. Phys 35(1996)694

Density dependence of structure of supercritical carbon dioxide along an isotherm

Ihii R, Okazaki S, Okada I, Fususaka M, Watanabe N, Misawa M and Fukunaga T

J. Chem. Phys 105(1996)7011

Chemical Short-Range Order in $(Ti_{76}Ni_{24})_x(Ti_{70}Cu_{30})_{1-x}$ Neutron Zero Scattering Amorphous Alloy

Fukunaga T, Okasaka K and Mizutani U.

J. Non-Cryst. Solids 156-158(1993)120

7. Magnetic Structures and Excitations

Neutron Depolarization in a Reentrant Spin-Glass System: Amorphous Fe-Mn

Mirebeau I, Itoh S, Mitsuda S, Watanabe T, Endoh Y, Hennion M and Papoular R.

Phys. Rev. B 41(1990)11405

Measurements of Two-Dimensional Antimagnetic Spin Wave by Using Chopper Spectrometer Installeed in Pulsed Neutron Source

Yamada K, Arai M, Taylor A. D, Hosoya S, Sano A, Nakajima K, Ohoyama K, Kohgi M, Nakane T, Perring T and Endoh Y.

Proc. 11th Meeting Int. Collaboration on Advanced Neutron Sources (KEK, Tsukuba, Oct. 22-26, 1990)1078

Neutron Depolarization from Re-Entrant Spin Glass

Endoh Y.

Prog. Theor. Phys. Suppl. 101(1990)567

Crystal Field Excitations in $CeSi_x$

Kohgi M, Satoh T, Ohoyama K, Arai M and Osborn R.

Physica B 163(1990)137

Magnetic Excitations in Mn_3Pt at High Energies by the TOF Method

Tomiyoshi S, Yasui H, Kaneko T, Yamaguchi Y, Ikeda H, Todate Y and Tajima K.

J. Magn. Magn. Mat. 90&91(1990)203

Evidence for Antiferromagnetic Coupling between Fe Layers through Cr from Neutron Diffraction

Hosoito N, Araki S and Mibu K.

J. Phys. Soc. Jpn. 59(1990)1925

Neutron Depolarization in Reentrant Spin Glasses $Ni_{1-x}Mn_x$

Mirebeau I, Itoh S, Mitsuda S, Watanabe T, Endoh Y, Hennion M and Calmettes R.

J. Appl. Phys. 67(1990)5253

Crystal Field Excitations in Yb Monopnictides

Kohgi M, Ohoyama K, Oyamada A, Suzuki T and Arai M.

Physica B 163(1990)625

Magnetic Phase Transition in $CsVF_4$

Ikeda H, Hidaka M and Wanklyn B. M.

Physica B 160(1990)287

Neutron Scattering at Ultra-Low Temperatures

Kakurai K.

Proc. 11th Meeting Int. Collaboration on Advanced Neutron Sources (KEK, Oct. 22-26 1990)1010

Anomalous Region in the Magnetic Phase Diagram of (Fe, Co) Si

Ishimoto K, Yamauchi H, Yamaguchi Y, Suzuki J, Arai M, Furusaka M and Endoh Y.

J. Magn. Mang. Mater. 90&91(1990)163

Small Angle Neutron Scattering Studies on $Fe_{0.715}Al_{0.285}$ Reentrant Spin Glass

Suzuki J, Endoh Y, Arai M, Furusaka M and Yoshizawa H.

J. Phys. Soc. Jpn. 59(1990)718

Ordering Kinetics in a Two-Dimensional Percolation Magnet

Ikeda H, Endoh Y and Itoh S.

Physical Review Letters 64(1990)1266

Neutron Diffraction Study in Pulsed High Magnetic Field

Motokawa M, Nojiri H, Uchi M, Watamura S, Kawai H and Endoh Y.

Proc. 11th Meeting Int. Collaboration on Advanced Neutron Sources (KEK, Oct. 22-26 1990) (1990)979

Magnetic Excitation in Highly Diluted Magnets

Ikeda H and Ohoyama K.

Proc. Int. Conf. Neutron Scattering (Oxford, 27-30 Aug. 1991), P1-A-72, Physica B

Kinetics of Ordering in the Percolation Magnet

Ikeda H.

Presented at Int. Symp. Slow Dynamics in Conclensed Matter (Fukuoka, Nov. 4-8, 1991)

Two Dimensional Antiferromagnetism and Spin Dynamics in "2-1-4" Oxides

Yamada K, Arai M, Birgeneau R.J, Endoh Y, Hosoya S, Kakurai K, Kastner M.A, Matsuda M, Nakajima K, Shirane G, Taylor A.D, and Thurston

Proc. Int. Conf. Neutron Scattering (Oxford, 27-30 Aug. 1991), S4-C-2, Physica B

Neutron Diffraction Study of $PrCo_2Si_2$ in Pulsed High Magnetic Field

Nojiri H, Uchi M, Watamura S, Motokawa M, Kawai H, Endoh Y and Shigeoka T.

J. Phys. Soc. Jpn. 60(1991)2380

Neutron Depolarization Study of Flux Distribution in Superconducting State

Endoh Y, Watanabe T, Yamada K, Itoh S, Tanaka I and Kojima H.

Physica C 185-189(1991)1839

Evidence of Magnetic Domains in Reentrant Spin Glasses $Ni_{1-x}Mn_x$ by Neutron Depolarization

Mirebeau I, Itoh S, Mitsuda S, Watanabe T, Endoh Y, Hennion M and Calmettes P.

Phys. Rev. B 44(1991)5120

Neutron Depolarization Studies on Reentrant Spin Glass AuFe Alloy

Mitsuda S, Yoshizawa H, Watanabe T, Itoh S, Endoh Y and Mirebeau I.

J. Phys. Soc. Jpn. 60(1991)1721

High Energy Spin-Waves in the Chain Antiferromagnet $KFeS_2$

Welz D, Arai M, Nishi M, Kohgi M and Endoh Y.

Proc. Int. Conf. Neutron Scattering (Oxford, 27-30 Aug. 1991), S1-C-3, Physica B

Magnetic Excitations in Isolated Clusters of a Diluted Heisenberg Magnet $RbMn_{0.15}Mg_{0.85}F_3$

Takahashi M, Ikeda S and Ikeda H.

J. Phys. Soc. Jpn. 60(1991)387

Magnetic Excitations in Mn_3Pt

Tomiyoshi S, Kaneko T, Steigenberger U, Chappell A.J, Hagen M and Todate Y.

Proc. Int. Conf. Neutron Scattering (Oxford, 27-30 Aug. 1991), P1-A-66, Physica B

Dynamics of Percolation Magnets with Fractal Geometry

Ikeda H, Itoh S and Takahashi M.

Proc. Int. Conf. Neutron Scattering (Oxford, 27-30 Aug. 1991), S2-A-4, Physica B

Competition between the Kondo Effect and RKKY Interactions in $CeSi_x$

Kohgi M, Satoh T, Ohoyama K and Arai M.

Physica B 169(1991)501

Dynamical process of Disordering in a Percolation Magnet under Random Fields

Itoh S, Ikeda H, Suzuki T and Endoh Y.

J. Phys. Soc. Jpn. 60(1991)3238

Complete Two-Dimensional Antiferromagnetic Spin-Wave Disperison Relation of La_2NiO_4 Determined by Chopper Spectrometer Installed at the Pulse Nuetron

Yamada K, Arai M, Endoh Y, Hosoya S, Nakajima K, Perring T and Taylor A.D.

J. Phys. Soc. Jpn. 60(1991)1197

Crystal Field Excitations in $Ce(Zn_{1-x}Cu_x)_2$

Kohgi M, Osakabe T, Ohoyama K and Kitai T.

J. Magn. Magn. Mater. (1991)

Crossover from Magnetic to Non-Magnetic Ground State in the Aooly System $Ce(Ni_{1-x}Pd_x)Sn$

Kasaya M, Tani T, Suzuki H, Ohoyama K and Kohgi M.

J. Phys. Soc. Jpn. 60(1991)2542

Neutron Diffraction on Metamagnetic $PrCo_2Si_2$ in Pulsed High Magnetic Fields

Motokawa M, Nojiri H and Endoh Y.

Physica B 177(1992)279

Coexistence of Ising Cluster Excitations and Intra-Culuster Exciations in Highly Diluted Ising Magnets

Ikeda H and Ohoyama K.

Phys. Rev. B 45(1992)7484

Coexistence of Ising cluster excitations and intracluster excitations in diluted Ising magnets

Ikeda H, and Ohoyama K

PHYSICAL REVIEW B 45(1992)7484

Magnetic Properties of the Dense Kondo Compounds CePdSn and YbNiSn

Kasaya M, Tani T, Ohoyama K, Kohgi M and Ishikawa Y.

J. Magn. Magn. Mater. 104-106(1992)665

Reentrant Spin Glass Properties of $Ni_{77}Mn_{23}$Studied by Neutron Depolarization Analysis

Sato T, Ando T, Watanabe T, Ito S and Endoh Y.

J. Magn. Magn. Mat. 104-107(1992)1625

Neutron Diffraction Experiment in Pulsed High Magnetic Fields

Nojiri H, Motokawa M, Nishida N and Endoh Y.

Physica B 180&181(1992)31

Pressure Dependence of the Crystal Field State of a Low Carrier System CeP

Kohgi M, Osakabe T, Mori N, Takahashi H, Okayama Y, Yoshizawa H, Ohora Y, Ikeda S, Suzuki T and Haga Y.

Physica B (1992)

Spin Reorientation in Fe/Nd Multilayered Films from Neutron Diffraction Experiments

Hosoito N, mibu K, Shinjo T and Endoh Y.

J. Phys. Soc. Jpn. 61(1992)2477

Polarized Neutron Studies of Ferrofluids

Itoh S, Endoh Y and Charles S. W.

J. Magn. Magn. Mat. 111(1992)56

Neutron Depolarization Studies on Mesoscopic Magnetism

Endoh Y, Itoh S, Watanabe T and Mitusda S.

Physica B 180&181(1992)34

Small Angle Scattering on Reentrant Spin Glass $Fe_{1-x}Al_x$

Suzuki J, Endoh Y and Arai M.

J. Magn. Magn. Mat. 104(1992)1657

Neutron Scattering in Yb Monopunictides

Ohoyama K, Kohgi M, Nakane T, Arai M, Taylor A.D and Oyamada A.

Physica B 180&181(1992)250

Anomalous Crystal Field Splitting in YbN

Ohoyama K, Kohgi M, Osakabe T, Arai M, Taylor A.D, Oyamada A and Suzuki T.

Physica B 180&181(1992)250

Neutron Scattering Studies of CeTSn (T=Ni, Pb)

Kohgi M, Ohoyama K, Osakabe T and Kasaya M.

J. Magn. Magn. Mat. 108(1992)187

Polarized Neutron Diffraction Studies of Fe/Cr Multilayered Films with Giant Magnetoresistance Effect

Hosoito N, Mibu K, Araki S, Shinjo T, Itoh S and Endoh Y.

J. Phys. Soc. Jpn. 61(1992)300

Neutron-Depolarization Studies on Re-Entrant Spin Glass

Mitsuda S, Yoshizawa H and Endoh Y.

Phys. Rev. B 45(1992)9788

Electron Paramagnetic Resonance of Co: Rb_2MgF_4 and Anomalous g-Value of Paired Spin

Motokawa M, Ohta H, Makita N and Ikeda H.

J. Phys. Soc. Jpn. 61(1992)322

Detrmination of Intraparticle Structure of Magnetite Particles in a Solvent by Contrast Variation Method Using Polarized Neutrons

Itoh S, Endoh Y, Taketomi S and Chikazumi S.

J. Magn. Magn. Mat. 103(1992)126

Crystal Field levels in YbBiPt

Robinson R. A, Kohgi M, Osakabe T, Canfield P. C, Kamiyama T, Nakane T, Fisk Z and Thompson J. D.

Physica B (1992)

EPR of Co^{2+} in Rb_2MgF_4 and Anomalos g-Values of Pair and Trimer Spin Systems

Motokawa M, Ohta H, Yoshida K and Ikeda H.

J. Magn. Magn. Mater 104&107(1992)947

Neutron Scattering Study of CeNiSn

Kohgi M, Ohoyama K, Osakabe T, Kasata M, Takabatake T and Fujii H.

Physica B 186&188(1993)409

Neutron Scattering Studies of Ce $(Zn_{1-x}Cu_x)_2$

Osakabe T, Kohgi M, Ohoyama K and Kitai T.

Physica B 186&188(1993)574

Neutron-Depolarization Analysis and Small-Angle Neutron-Scattering Studies of the Reentrant Spin Glass $Ni_{77}Mn_{23}$

Sato T, Ando T, Watanabe T, Itoh S, Endoh Y and Furusaka M.

Phys. Rev. B 48(1993)6074

Neutron-Depolarization Analysis and Small-Angle Neutron-Scattering Studies of the Reentrant Spin Glass $Ni_{77}Mn_{23}$

Sato T, Ando T, Watanabe T, Itoh S, Endoh Y and Furusaka M.

Phys. Rev. B 48(1993)6074

Development and Use of Pulsed High Magnetic Fields for Neutron Diffraction Experiments

Motokawa M, Arai M, Mino M, Ubukata K, Bokui T and Fujita M.

Proc. 12th Meeting of Int. Collaboration on Advanced Neutron Sources (Abingdon Oxfordshire, UK)I-260

Local Structure of Mn Atoms and Spins in Ag-Mn Spin-Glass Alloys

Koga K, Ohshima K and Nlimura N.

J. Appl. Phys. 73(1993)5457

Determination Paramagnetic $x(\theta,\omega)$ for a Metallic Antiferromagnet Mn_3Pt by TOF Method

Todate Y, Tajima K, Yazaki A Tomiyoshi S and Ikeda H.

Proc. 5th International Symposium on Adv. Nucl. Energy Research, Mito, vol 2366

Crossover from Propagating Spin Waves to Localized Ising-Cluster Excitations in Diluted Heisenberg Antiferromagnets

Takahashi M and Ikeda H.

Phys. Rev. B 47(1993)9132

Self-Similarity of Magnetic order in Two-Dimensional Percolating Antiferromagnets

Ikeda H, Iwasa K and Andersen K.H.

J. Phys. Soc. Jpn. 62(1993)3832

Electron Paramagnetic Resonance of $CsCo_xMg_{1-x}Cl_3$ and the Determination of Exchange Interactions

Ohota H, Imagawa S, Motokawa M and Ikeda H.

J. Phys. Soc. Jpn. 62(1993)2481

Magnetic Phase Transition of $CsCuCl_3$ in Pulsed Magnetic Field

Mino M, Ubukata K, Bokui T, Arai M, Tanaka H and Motokawa M.

Proc. 5th International Symposium on Adv. Nucl. Energy Research, Mito410

Spin Dynamics of YbX (X=N, P, As)

Ohoyama K, Kohgi M, Otomo T, Osakabe T, Oyamada A and Suzuki T.

Physica B 186&188(1993)451

Atomic and Magnetic Short-Range Order in Ag-Mn Spin-Glass Alloys

Koga K and Ohshima K.

Phys. Rev. B 47(1993)5783

Magnetic Structures of Ginant Magnetoresistance Systems, Fe/Cr and NiFe/Cu/Co/Cu, Studied by Neutron Diffraction

Hosoito N, Mibu K, Ono T, Shinjo T and Endoh Y.

J. Magn. Magn. Mat. 126(1993)255

A Simple Method to Examine Individual Magnetizations in Fe/Rare Earth Multilayer Films by Polarized Neutron Diffraction

Hosoito N, Mibu K, Shinjo T.

Bull. Inst. Chem. Res. Kyoto Univ. 70(1993)443

High-Resolution Inelastic Neutron Scattering from $RbMncMg_{1-c}F_3$ (c=0.10 and 0.15) under Magnetic Fields

Iwasa K, Andersen K.H, Takahashi M and Ikeda H.

J. Phys. Soc. Jpn. 63(1994)2826

The Valence of Pr in $PrBa_2Cu_3O_{7-\delta}$ and the Related Compounds as Determined by Neutron Powder Diffraction

Ohshima T, Kuroda S, Baba H, Asano H and Takita K.

Physica B 194-196(1994)2245

Neutron Scattering Studies on Spin-Peierls Material $CuGeO_3$

Arai M, Fujita M, Ubukata K, Bokui T, Tabata K, Ohta H, Motokawa M, Otomo T, Ohoyama K, Mino M, Akimitsu J and Fujita O.

J. Phys. Soc. Jpn. 63(1994)1661

Fracton Excitations in a Diluted Heisenberg Antiferromagnet near the Percolation Threshold: $RbMn_{0.39}Mg_{0.61}F_3$

Ikeda H, Fernandez-Baca J.A, Nicklow R.M, Takahashi M and Iwasa K.

J. Phys. Cond. Matter 6(1994)10543

Spin dynamics in the two-dimensional percolating Ising antiferromagnet

Ikeda H

PHYSICA A (1994)328

Itinerant-Electron-Type Helical - Spin-Glass Reentrant Transition in $Cr_{0.81}Mn_{0.19}Ge$

Sato T, Ando T, Oku T and Furusaka M.

Phys. Rev. B 49(1994)11864

Neutron Diffraction of $CsCuCl_3$ in High Field

Mino M, Ubukata K, Bokui T, Arai M, Motokawa M and Tanaka H.

Physica B 201(1994)213

Crystallography and Magnetism of the Hevy-fermion Compound YbBiPt

Robinson R.A, Purwanto A, Lynn J.W, Erwin R, Peterson E and Movshovich R.

Phys. Rev. B 50(1994)9595

Magnetic Structure of DyAg in High Field

Bokui T, Mino M, Arai M, Motokawa M and Morin P.

Physica B 201(1994)163

Neutron Paramagnetic Scattering from Antiferromagnetic $RbMnF_3$ and Mn_3 Pt Using time of Flight Technique

Yazaki A, Tajima K, Todate Y, Tomiyoshi S and Ikeda H.

J. Phys. Soc. Jpn. 63(1994)748

Small-angle neutron diffraction from the helical magnet $Fe_{0.8}Co_{0.2}Si$

Ishimoto K, Yamaguchi Y, Suzuki J, Arai M, Furusaka M, Endoh Y

PHISICA B CONDENSED MATTER (1995)381

Spin Dynamics in an Ising-Like Quantum Spin Chain with Nonmagnetic Impurities

Itoh S, Ikeda H, Sugimoto D, Iwasa K, amd Eccleston S Roger

Physical Society of Japan 64(1995)927

Spin correlations in percolating networks with fractal geometry

Ikeda I, Iwasa K, J.A Fernandez-Baca, and R.M.Nicklow

PHYSICA B CONDENSED MATTER (1995)146

Polarized Neutron Transmission Studies of $LiNiO_2$

Itoh S, Kakurai K, Takeda M and Hirota K

Physica B 213&214(1995)200

Polarized neutron transmission studies of $LINIO_2$

Itoh S, Kakurai K, Takeda M and Hirota K

PHISICA B CONDENSED MATER 213&214(1995)200

Intraparticle structure of Pd fine particles

Taniyama T, Sato T, Ohta E, and Takeda M

PHYSICA B CONDENSED MATER 213&214→ł(1995)254

Helical-Spin-Glass Reentrant Transition in Itinerant Electron Type Magnet $Cr_{1-x}Mn_xGe$

Sato T, Ando T, Oku T and Furusaka M.

J. Magn. Magn. Mater. 140-144(1995)1785

Intraparticle structure in ultra-fine $ZnFe_2O_4$ particles

Yokoyama M, Oku T, Taniyama T, Sato T, Ohta E, Sato T, Haneda K, Itoh S, Kurahashi K, and Takeda M

PHISICA B CONDENSED MATER 213&214(1995)251

Intraparticle structure of Pd fine particles

Taniyama T, Sato T, Ohta E and Takeda M

Physica B 213&214(1995)254

Intraparticle structure in ultra-fine $ZnFe_2O_4$ particles

Yokoyama M, Oku T, Taniyama T, Sato T, Ohta E, Sato T, Haneda K, Itoh S, Kurahashi K and Takeda M

Physica B 213&214(1995)251

Localized magnons in a two-dimensional mixed antiferromagnet

Iwasa K, and Ikeda H

PHYSICA B CONDENSED MATTER (1995)197

Rotational tunneling of methyl groups of $Sc(CH_3COO)_3$ and $Sc(CD_3COO)_3$

Takeda S. Kataoka H. Ikeda S and Yamaguchi K

Phisica B 226(1996)174

Magnetization Process in Helical-spin Glass Reentrant $Cr_{0.81}Mn_{0.19}Ge$ Studied By Neutron Depolarization ANalysis

Sato T, Taniyama T, Oku T, Ito Sand Takeda M

Cryst. Res. Technol. 31(1996)589

フラクタル磁性体のダイナミクス

Ikeda.H

日本物理学会誌 51(1996)115

8. Dynamics in Solids and Liquids

Low-Energy Excitation in Copper Ion Conductors

Sakuma T, Shibata K and Hoshino S.

Solid State Ionics 40/41(1990)337

Hydrogen Wave Functions in the Metal Hydrides ZrHz and $NbH_{0.3}$

Ikeda S, Furusaka M, Fukunaga T and Taylor A.D.

J. Phys. Condens. Matter 2(1990)4675

Dynamic Structure of Molten $0.80RbNO_3$-$0.20Sr(NO_3)_2$ Mixture by Neutron Quasielastic Scattering

Shibata K, Kamiyama T, Suzuki K and Inoue K.

J. Non-Cryst. Solids 117/118(1990)120

Phonon Density of States of $La_{1.85}Sr_{0.15}Cu_{1-x}Zn_xO_4$ (x=0, 0.02)

Arai M, Yamada K, Taylor A.D, Endoh Y and Hidaka Y.

Physica C 181(1991)45

High Resolution Neutron Spectrometer LAM-80ET and Rotational Tunneling in 4-Methylpyridine N-Oxide

Ikeda S, Watanabe N, Inoue K, Kiyanagi Y, Inaba A, Takeda S, kanaya T, Shibata K, Kamiyama T, Izumi Y, Ozaki Y and Carlile C.J.

J. Phys. Soc. Jpn. 60(1991)3340

Rotational Tunneling and LAM-80ET

Ikeda S, Watanabe N, Inoue K, Kiyanagi Y, Inaba A, Takeda S, Kanaya T, Shibata K, Kamiyama T, Izumi Y, Ozaki Y and Carlile C. J.

Proc. Int. Conf. Neutron Scattering (Oxford, 27-30 Aug. 1991), P3-B-113, Physica B

Isotope Effects in Hydrogen-Bonded Crystal KH_2PO_4

Sugimoto H and Ikeda S.

Phys. Rev. Lett. 67(1991)1306

Local Dynamics of cis-1.4-Polybutadiene near the glass Transition Temperature T_g

Kanaya T, Kawaguchi T and Kaji K.

Physica B 182(1992)403

A Coherent Quasielastic Neutron Scattering Study of NO_3^- Ion Motion in Molten $RbNO_3$

Kamiyama T, Shibata K and Suzuki K.

J. Non-Cryst. Solids 150(1992)292

High Resolution S(Q,w) Measurement on g-SiO_2

Arai M, Hannon A.C, Wright A.C, Sinclair R.N, Misawa M, Price D.L and Taylor A.D.

Physica B 180&181(1992)834

Incoherent Inelastic Neutron Scattering from Hydrogen-Bonded Compound KH_2PO_4

Shibata K and Ikeda S.

J. Phys. Soc. Jpn. 61(1992)411

The Polycarbosilane-to-Si_xC_{1-x} Conversion Studied by Inelastic Neutron Scattering and Infrared Absorption

Suzuya K, Shibata K, Okamura K and Suzuki K.

J. Non-Cryst. Solids 150(1992)255

Low-Energy Excitation in CuI

Sakuma T, Shibata K and Hoshino S.

Solid State Ionics 53-56(1992)1278

Dynamical Properties of Solutions of $LiNO_3$ in (1, 3)-Diaminopropane in the Liquid and Glassy States

Hayashi H, Kamiyama T, Nakamura Y and Izumi Y.

J. Non-Cryst. Solids 150(1992)297

Low-Energy Excitation and Fast Motion near T_g in Amorphous cis-1, 4-Polybutadiene

Kanaya T, Kawaguchi T and Kaji K.

J. Chem. Phys. 98(1993)8262

Molecular Dynamics Study of the Lauryl Alchol-Laurate Model Bilayer

Fukuda T, Ozaki S and Okada I.

Biophys. J. 64(1993)1344

A Neutron Scattring Study of the Dynamics in a $K(D_xH_{1-x})_2PO_4$ System

Todate Y, Ikeda S, Nakai Y, Agui A and Tominaga Y.

J. Phys. Condens. Matter 5(1993)7761

A Simulation Approach to Vibrational Dynamic of the OH^- ion in Molten LiOH

Ozaki S and Okada I.

J. Chem. Phys. 1(1993)607

Hydrogen and PO_4 Modes of RbH_2PO_4

Agui A, Nakai Y, Mizoguchi K, Ikeda S and Tominaga Y.

J. Phys. Soc. Jpn. 62(1993)959

Dynamical Properties of Protons in KH_2PO_4 Studied by Icoherent Neutron Scattering

Ikeda S, Noda Y, Sugimoto H and Yamada Y.

J. Phys. Soc. Jpn. 63(1994)1001

Incoherent Neutron Scattering from KDP

Ikeda S, Noda Y, Sugimoto H and Yamada Y.

Ferroelectrics 156(1994)291

Inelastic Neutron Scattering Study of $KHCO_3$

Kashida S, Ikeda S and Yamada Y.

J. Phys. Soc. Jpn. 63(1994)4643

Low Energy Excitation and Fast Motion near T_g in Amorphous Polymers

Kanaya T, Kawaguchi T and Kaji K.

J. Non-Cryst. Solids 172-174(1994)327

Quantum Precession of HCl Molecule in Hydroquinone Clathrate

Takeda S, Kataoka H, Shibata K, Ikeda S, Matsuo T and Carlile C.J.

Physica B 202(1994)315

Quasielastic and Inelastic Neutron Scattering of Liquid Tellurium

Endo H, Tsuzuki T, Yao M, Kawakita Y, Shibata K, Kamiyama T, Misawa M and Suzuki K.

J. Phys. Soc. Jpn. 63(1994)3200

Incoherent Neutron Scattering from Ferroelectric $RbHSO_4$

Kosegawa S, Ikeda S, Wada Y and Itoh K

J. Phys. Soc. Jpn. 64(1995)1435

Inelastic Neutron Scattering Study of Low Energy Exicitations in Glassy 1-Butene

Yamamura O, Matsuo T, Takeda K, Kanaya T, Kawaguchi T and Kaji K

J. Chem. Phys 105(1996)732

9. Materials Science

Light Scattering and Small-Angle Neutron Scattering Investigation for the L_1 Phase in a Ternary System

Imae T, Okamura H and Furusaka M.

J. Colloid and Interface Science 168(1994)217

Mesoscopic structure of Sic fibers by neutron and x-ray scattering

Suzuya K, Furusaka M, Watanabe N, Osawa M, Okamura K, Shibat K, Kamiyama T and Suzuki K

Journal of Materials Research 11(1996)1169

中性子小角散乱による第2種超伝導体中の磁束構造の観察

Osamura M, Miyata S, Furusaka M, Suzuki J

応用物理 第65巻 4(1996)367

10. Polymers

Thermoreversible Gelation of the System of Atactic Polystyrene-Carbon Disulfide. VIII

Izumi Y, Katano S, Funahashi S, Furusaka M and Arai M.

Repts. Prog. Polym. Phys. Jpn. 33(1990)15

Low-Energy Excitations in Amorphous Polymers

Inoue K, Kanaya T, Ikeda S, Kaji K, Shibata K, Misawa M and Kiyanagi Y.

J. Chem. Phys. 95(1991)5332

Structural Study on the Sol-Gel Transition of Atactic Polystyrene in Carbon Disulphide

Izumi Y, Katano S, Funahashi S, Furusaka M and Arai M.

Proc. Int. Conf. Neutron Scattering (Oxford, 27-30 Aug. 1991), P1-B-112, Physica B

Local Motions of cis-1.4-Polybutadiene in the Melts. A Quasielastic Neutron-Scattering Study

Kanaya T, Kaji K and Inoue K.

Macromolecules 24(1991)1826

Small Angle Neutron Scattering from Poly (vinyl alcohol) Gels

Kanaya T, Ohkura M, Kaji K, Furusaka M, Misawa M, Yamaoka H and Wignall G. D.

Physica B 180&181(1992)549

Dynamics of Polyethylene Studied by High Resolution Nuetron Spectrometer LAM-80ET

Kanaya T, Kaji K, Inoue K, Ikeda S, Shibata K, Izumi Y, Kamiyama T and Furusaka M.

J. Phys. Soc. Jpn, 61(1992)1984

Quasielastic Neutron Scattering on the Sol-Gel-Glass Transition of Atactic Polystyrene in Carbon Disulphide

Izumi Y, Kanaya T, Shibata K and Inoue K.

Physica B 180&181(1992)542

Conformation of Atactic Polystyrene in Carbon Disulphide Observed at a Low Temperature

Izumi Y, Katano S, Funahashi S, Furusaka M and Arai M.

Physica B 180&181(1992)539

Low Energy Excitations in Amorphous Polystyrene

Kanaya T, Kaji Kand Inoue K.

Physica B 180&181(1992)814

Dynamics of Polymers in the Bulk State by Neutron Scattering

Kanaya T, Kaji K, Kawaguchi T and Inoue K.

Bull. Inst. Chem. Res. Kyoto Univ. 70(1992)236

Structure of Poly(vinyl alcohol) Gels Studied by Wide- and Small-Angle Neutron Scattering

Kanaya T, Ohkura M, Kaji K, Furusaka M and Misawa M.

Macromolecules 27(1994)5609

Theories and Computer Simulations of Self-Assembling Surfactant Solutions

Kawakatsu T, Kawasaki K, FUrusaka M, Okabayashi H and Kanaya T.

J. Phys. Condens. Matter 6(1994)6385

Small-Angle Neutron Scattering Study of Poly(vinyl alcohol)-Iodine Complex with Contrast Variation Method

Yajima H.

J. Cryst. Soc. Jpn. 36(1994)142

Dynamics of Amorphous Polymers near Glass Transition

Kanaya T and Kaji K.

Kotaibutsuri 29(1994)303

Interaction parameters of Poly(vinyl methylether) in Aqueous Solution as Determined by Small-Angle Neutron Scattering

Okano K, Takada M, Kurita K and Furusaka M.

Polymer 35(1994)2284

Gelation Process of Poly(viny alcohol) As STUDIED by Small-Angle Neutron and Light Scattering

Kanaya T, Ohkura M, Takeshita H, Kaji K, Furusaka M, YamaokaH, Wignall G.D

Macromolecules 28(1995)3168

Small-angle Neutron-scattering Study of Bis (quaternary ammonium bromide) Surfactant Micelles in Water. Effect of the Spacer Chain

Hirata H, Hattori N, Ishida M, Okabayashi H, Furusaka M and Raoul Zana

J Phys Chem 99(1995)17778

Small-Angle Neutron-Scattering Study of Bis(quaternary ammonium bromide) Surfactant Micelles in Water. Effect of the Spacer Chain

Hirata H, Hattori N, Ishida M, Okabayashi H, Furusaka M, and Raoul Zana

J. Phys. Chem 99(1995)17778

Phase Separation Dynamics in the Presence of Surfactant Molecules with an Asymmetric Shape

Kawakatsu T, Kawasaki K, Furusaka M, Okabayashi H and Kanaya T.

J. Chem. Phys. 102(1995)2247

Investigation of Mixed of Dodecyldimethylamine Oxide and Sodium Dodecyl Sulfate by SANS: Shape, Size, Charge, and Interaction

Kakitani M, Imae T and Furusaka M

J .Phys. Chem 99(1995)16018

Polymer branching by physical gelation as revealed by small-angle neutron scattering

Izumi Y, Kobayashi M, and Furusaka M

PHYSICA B CONDENSED MATTER (1995)727

A Small angle neutron scattering study of the sodium di-pentyl phosphate micelles in water

Hirata H, Okabayashi H, Furusaka M, Kawakatsu T

Colloid & Polimer Science 273(1995)1193

A Small-angle Neutron Scattering Study of the Ethyl (n-octyl) Phosphate Micelles in Water

Hirata H, Katayama S, Okabayashi H, Furusaka M and Kawakatsu T

Colloid Polym Sci 274(1996)245

11. Biology

Small Angle Thermal Neutron Scattering of Hen Egg-White Lysozyme in Aqueous Solution

Nimura N and Sungawa U.

Proc. Int. Conf. Neutron Scattering (Oxford, 27-30 Aug. 1991), P3-B-130, Physica B

Structure Study of Phosphatidylinositol Diphosphate and Bovine Scrum Albumin Complex

Niimura N, Mikami K and Hayashi K.

Proc. Int. Conf. Neutron Scattering (Oxford, 27-30 Aug. 1991), P3-B-129, Physica B

Hydration Structure of Glycine Molecules in Concentrated Aqueous Solutions

Kameda Y, Ebata H, Usuki T, Uemura O and Misawa M.

Bull. Chem. Soc. Jpn. 67(1994)3159

Structural Study of Ganglioside in Solution using Complimentary and Solvent Contrast Variation Methods

Hirai M, Takizawa T, Yabuki S, Hayashi K, Nakata Y, Mitomo H, Kobayashi K, Furusaka M and Hirai T.

Repts. Prog. Polym. Phys. Jpn. 37(1994)651

Characteristic Structure of Phosphatidylinositol Diphosphate (PIP_2) Complex with Bovine Serum Albimin and Water in PIP_2 Bilayers

Niimura N, Mikami K, Hayashi K, Yabuki S and Takizawa T.

Synchrotron Radiation in the Biosciences, et. al. B. Chance, CALARENDON PRESS (1994)238

Complexes of gangliosides with proteins in solution

Hirai M. Takizawa T. Yabuki S. Nakata Y. Mitomo H. Hirai T. Shimizu s. Furusaka M. Kobayashi K. Hayashi K

Physica B 213&214(1995)751

Complexes of gangliosides with proteins in solution

Hirai M, Takizawa T, Yabuki S, Nakata Y, Mitomo H, Hirai T, Shimizu S, Furusaka M, Kobayashi K and Hayashi K

PHYSICA B CONDENSED MATER 213&214(1995)751

Ganglioside structure in solution

Hirai M. Yabuki S. Takizawa T. Nakata Y. Mitomo H. Hirai T. Shimizu S. Kobayashi K. Furusaka M. Hayashi K

Physica B 213&214(1995)748

thermochimica acta

Takizawa T. Hirai M. Yabuki S. Nakata Y. Takahashi A. Hayashi K

Thermochimica Acta 267(1995)355

12. Non-Equilibrium Systems

Computer Simulations of Domain Growth under Shear Flow

Ohta T, Nozaki H and Doi M.

Phys. Lett. A 145(1990)304

Phase Separation of Al-Li Alloys Studied by Small Angle Neutron Scattering

Fujikawa S, Furusaka M.

Proc. Int. Conf. on Recent Advances in Science and Engineering of Light Metals (1991, Sendai)965

Late Stage Dynamics of Phase Separation Processes of Binary Mixtures Containing Surfactants

Kawakatsu T, Kawasaki K, Furusaka M, Okabayashi H and Kanaya T.

J. Chem. Phys. 99(1993)8200

Phase Separation and Ordering Process in Al-Li Alloys Studied by Small-Angle Neutron Scattering and Neutron Diffraction

Furusaka M, Fujikawa S.-I and Tranquada J.M.

Proc. 5th Int. Symp. Advanced Nuclear Energy Research -Neutrons as Microscopic Probes- (March 10-12, 1993, Mito, Ibaraki, Japan)

Small-Angle Neutron Scattering Study of Phase Decomposition in Fe-Cu Binary Alloy

Osamura K, Okuda H, Takashima M, Asano K and Furusaka M.

Materials Transactions 34(1993)305

SANS Study of Phase Decomposition in Fe-Cu Alloy Added by Ni and Mn

Osamura K, Okuda H, Asano K, Furusaka M, Kishida K and Kurosawa F.

J. Physique IV 3(1993)317

Phase Separation in Fe-Cr-Mo Alloy

Osamura K, Ujihara T, Okuda H and Furusaka M.

Solid-Solid Phase Transformations Ed. Johnson W.C, Howe J.M, Laughlin D.E and Soffa W.A. The Minerals, Metals & Materials Society (1994)377

Spinodal Decomposition in Alloys

Furusaka M and Fujikawa S.

J. Cryst. Soc. Jpn. 36(1994)113

Precipitation Hardening in Fe-Cu Binary and Quaternary Alloys

Osamura K, Okuda H, Ochiai S, Takashima M ,Asano K, Furusaka M, Kishida K and Kurosawa F.

ISIJ International 34(1994)359

13. Nuclear Physics

Present Status of P Violation and Future T Violation Experiments on Neutron-Nucleus Interaction at KEK

Masuda Y, Adachi t, Ishimoto S, Masaike A, Morimoto K and Shimizu H.M.

Proc. The 18th INS Int. Symp. on Physics with High-Intensity Hadron Accelerators (Tokyo, Mar. 14-16, 1990)

P-Violation and T-Violation Experiments on Neutron-Nucleus Interaction at KEK

Masuda Y.

Proc. the VI Int. School on Neutron Physics (Alushta, USSR, Oct. 8-18, 1990)

Scintillation Detector System in Neutron-Nucleus Experiments

Shimizu H. M, Adachi T and Masuda Y.

Proc. 11th Meeting Int. Collaboration on Advanced Neutron Sources (KEK, Oct. 22-26 1990)937

Lanthanum Nuclear Polarization for T-violation Experiment

Masuda Y, Adachi T, Ishimoto S, Masaike A, Morimoto K and Shimizu H.M.

Proc. 11th Meeting Int. Collaboration on Advanced Neutron Sources (KEK, Oct. 22-26 1990)1002

T Violation in Neutron-Nucleus Interaction

Masuda Y.

Proc. Int. Workshop on Polarized Ion Sources and Polarized Gas Jets KEK Report 90-15 (Feb. 12-17, 1990, KEK)249

Parity-Non-Conservation in Neutron Radiative Capyure Reaction

Adachi T, Masaike A, Masuda Y, Morimoto K and Shimizu H.M.

Proc. 4th Conf. the Intersections between Particle and Nuclear Physic, (Tucson, Arizona, May 24-29, 1991)

A Resonance Spectrometer without Doppler Broadening

Masuda Y, Adachi T and Shimizu H.M.

Proc. Int. Conf. Neutron Scattering (Oxford, 27-30 Aug. 1991), P3-B-167, Physica B

Neutron Spin as a Probe Concerning P- and T-Violation

Masuda Y, Adachi T, Asahi K, Doi M, Ishimoto S, Masaike A, Matsuda Y, Morimoto K, Mori Y, Sakai K, Sato H, Shimizu H.M and Jian Z.Z.

Proc. III Int. Symp. "Weak and Electromagnetic Interactions in Nuclei", (JINR, Dubna, Russia, 16-22 June, 1992)

T-Violation Neutron Experiment and Polarized ^{3}He

Masuda Y, Asahi K, Kura J, Mori Y, Sato H and Shimizu H.M.

Hyperfine Interactions 74(1992)149

Ultra-Cold-Anti-Neutron (UCN): (II). Production Probability under Magnetic & Gravitational Fields

Golub R and Yoshiki H.

Nucl. Physics A536(1992)648

Neutron Spin Rotation and P-Violation

Sakai K, Masuda Y, Sato H, Doi M, Asahi K, Jian Z.Z, Matsuda Y, Shimizu H.M, Iinuma M and Masaike A.

Hyperfine Interactions 84(1992)199

Parity Nonconservation in Neutron Radiative Capture Reactions

Shimizu H. M.

Memories of the Faculty of Science, Kyoto Univ. Series A of Physics, Astrophysics, Geophysics and Chemistry XXXVIII(1992)203

Neutron Polarization for P- and T-Violation Experiments

Masuda Y, Adachi T, Asahi K, Doi M, Iimura M, Ishimoto S, Masaike A, Matsuda Y, Moritomo K, Mori Y, Sakai K, Sato H, Simizu H.M and Jian
Riken Int. Symp. "Unstable Nuclei and Particles as Probes in Physics and Chemistry", (Wako, Saitama, Aug. 31-Sept. 2, 1992)

Longitudinal Asymmetry and g-ray Angular Distribution in Neutron Radiative Capture Reactions

Shimizu H.M, Adachi T, Ishimoto S, Masaike A, Masuda Y and Morimoto K.

Nucl. Phys. A. (1992)

Observation of Ultracold-Neutron Production by 9-□ Cold Neutrons in Superfluid Helium

Sakai K, Ogira M, Kawai T, Masuda Y, Nakajima T, Takayama T, Tanaka S, Yamaguchi A and Yoshiki H.

Phys. Rev. Lett. 2(1992)1323

Longitudunal Asymmetry and γ-ray Angular Distribution in Neutron-Radiative-Capture Reactions

Shimizu H. M, Adachi T, Ishimoto S, Masaike A, Masuda Y and Morimoto K.

Nuclear Physics A552(1993)293

^{3}He Nuclear Polarization and Neutron Spin rotation Experiment

Masuda Y.

KEK Preprint 92-182

Production & Storate of Ultracold Neutrons in Superfluie He

Golub R, Lamoureaux S. K and Yoshiki H.

Phys. Rev. Lett. 25(1993)517

Three Meter Long Horizontal Cryostat Producing Ultracold Neutrons Using Superfluid Liquid Helium at 0.5K (Mark 3000)

Sakai K, Kawai T, Goto S and Yoshiki H.

Cryogenic 34(1994)277

Polarized ^{3}He System for T- and P-Violation Neutron Experiments

Sato H, Masuda Y, Sakai K, Doi M, Asahi K, Jian Z.Z, Mori Y, Delheij P.P.J, Matsuda Y, Iinuma M, Shimizu H.M and Masaike A.

Hyperfine Interactions 84(1994)205

14. Theories (Condensed Matter)

Computer Simulation of Domain Growth under Shear Flow

Ohota T and Nozaki H.

Phys. Lett. A 145(1990)304

Hybrid Models for the Dynamics of an Immiscible Binary Mixture with Surfactant Molecules

Kawakatsu T and Kawasaki K.

Physica A 167(1990)690

Dynamics of Ordering Processes in Immiscible Binary Mixtures with a Surfactant. II. Analytical Treatments

Kawakatsu T and Kawasaki K.

J. Colloid and Interface Science 145(1991)420

Dynamics of Ordering Processes in Immiscible Binary Mixtures with a Surfactant. I. Computer Experiments

Kawakatsu T and Kawasaki K.

J. Colloid and Interface Science 145(1991)413

Ostwald Ripening in Open Systems

Nakahara A, Kawakatsu T and Kawasaki K.

J. Chem. Phys. 95(1991)4407

Phase Separation kinetics of Binary Systems: Effects of hydrodynamic Interaction and Surfactants

Kawasaki K, koga T and Kawakatsu K.

Proc. of the MRS Fall Meeting 1991

Computer Experiments of Systems Containing Surfactants

Kawakatsu T and Kawasaki K.

Molecular Dynamics Simulations; Proc. Taniguchi Int. Symp. (1991)

A Monte Carlo Study of Phase Separation Processes in Immiscible Binary Mixtures with a Surfactant

Kawakatsu T and Kawasaki K.

J. Colloid and Interface Science 148(1992)23

Phase Transitions in Binary Systems in the Presence of Amphiphilic Molecules

Kawakatsu T and Kawasaki K.

"From Phase Separations to Chaos" (World Scientific)

Molecular Dynamics Simulations of Phase Separation Processes of Binary Soft Sphere Fluid Mixtures Containing Amphiphilic Block

Kawakatsu T and Kawasaki K.

J. Chem. Phys.

Equilibrium Shape of Two-component Unilamellar Membranes and Vesicles

Andelman D, Kawakatsu T and Kawasaki K.

Europhys. Lett.

15. Theories (Nuclear Physics)

On the Value of V_{ud} from the Kobayashi-Masukawa Matrix

Gudkov V. P.

KEK Preprint 90-171 (1990)

About the Resonance Approximation in Nuclear Induced Reactions

Gudkov V.P.

Z. Phys. A-Hadronsand Nuclei 340(1991)1

Parity Violation in Neutron Induced Reactions

Gudkov V. P.

KEK Report 91-2

The In-medium Behavior of the QCD θ-Term and the Value of CP Violation in Nuclei

Gudkov V. P.

Phys. Rev. C (1992)

The Weinberg Gluonic Operator and The CP-Odd Nucleon Coupling Constant

Gudkov V. P.

J. Phys. A (1992)

On CP-Violation in Nuclear Reactions

Gudkov V. P.

Phys. Rep. 212(1992)77

Recoil Effects and CP-Violation in Neutron Scattering

Gudkov V. P.

Phys. Rev. C 46(1992)357

Sign Correlations and the Mechanism for Parity Violation

Gudkov V. P.

Phys. Rev. C (1992)

16. Publications in Japanese

Amorphization in Immiscible Cu-V System by Mechanical Alloying and its Atomic Structure

Mori M, Inou K, Fukunaga T and Mizutani U.

J. S. P. M. 37(1990)648

Influences of Composition and Pressure on the Structures of Superconductors

Izumi F.

J. Jpn. Inst. Met. 29(1990)684

Compulsory Mixing Down to an Atomic level Immiscible Systems by Ball Milling

Fukunaga T.

J. Adv. Sci. 2(1990)241

Refinement of Crystal Structures by the Rietveld Method

Izumi F.

Oyo-Butsuri 59(1990)1

Atomic Structure of Ni-V Amorphous Alloy Prepared by Mechanical Alloying

Fukunaga T, Homma Y and Suzuki K.

J. S. P. M. 37(1990)644

Atomic Structure for Amorphous Materials

Fukunaga T and Misawa M.

Butsuri 46(1991)1042

Formation of Unequilibrium Phase and Structural Changes in V-M (M=Cu, Fe) System Subjected to Mechanical Alloying

Fukunaga T, Mori H and Mizutani U.

Rep. Toyota Phys. Chemi. Res. Inst. 44(1991)104

Dynamics in Noncrystalline States of Polymers

Kanaya T.

Butsuri 46(1991)1035

Crystallochemical Approach to High-Tc Superconductors

Izumi F.

Chemistry Today, May (1991)12

Chemical Structure of Ni-Ti Neutron Zero Scattering Amorphous Powders Prepared by MA

Fukunaga T, Misawa M, Suzuki K and Mizutani U.

J. S. P. M. 38(1991)67

Crystal and Magnetic Structures of High-Tc Copper Oxide Superconductor (Structure Fluctuations and Superconductivity)

Yamada Y.

J. Cryst. Soc. Jpn. 33(1991)55

Crystal Structure of High-Tc Superconductors

Asano H.

Butsuri 46(1991)1023

Neutron Scattering from Fractal Objects

Ikeda H.

Butsuri 46(1991)1021

Neutron Scattering Experiments in High Magnetic Field

Motokawa M.

Butsuri 46(1991)1028

Structural Changes in V-M(Fe, Cu) Systems Induced by Mechanical Alloying

Mori M, Fukunaga T, Mizutani U and Misawa M.

J.S.P.M. 38(1991)71

Instruments at a Pulse Source KENS

Furusaka M.

Butsuri 46(1991)1010

Structural Observations during Amorphoization Process of the $(Cr_{0.7}Fe_{0.3})$-N System by MA

Fukunaga T, Ishikawa E and Mizutani U.

J. S. P. M. 38(1991)102

Hydrophilicity of the Hydrophobic Regions in Biomembranes

Yabuki S.

Butsuri 46(1991)1037

Future prospect-Pulsed Neutron Source

Watanabe N.

Butsuri 46(1991)1016

Invitation to the Neutron Scattering Research

Yamada Y and Watanabe N.

Butsuri 46(1991)998

P and T Violations

Masuda Y.

Butsuri 46(1991)1047

Neutron Magne Magnetic Scattering Studies from Strongly Correlated Electron Systems

Endoh Y.

Butsuri 46(1991)1019

Amorphization of Immiscible Cu-Ta Powders Subjected to Mechanical Alloying

Lee C.H, Sakurai K, Fukunaga T and Mizutani U.

J.S.P.M. 38(1991)83

A Grobal View for Japanese Neutrons

Endoh Y.

Butsuri 46(1991)1013

Production of Ultracold Neutrons -Is Time Reversible?-

Yoshiki H.

J. J. S. M. E. 10(1992)36

Structural Change into Amorphous Phase Subjected to Mechanical Alloying

Fukunaga T.

Engineering Materials 40(1992)38

Neutron Scattering with an Intense Spallation Neutron Source

Watanabe N.

Japan Scientific Monthly 45(1992)1001

TOF Neutron Powder Diffraction

Asano H and Kamiyama T.

J. Cryst. Soc. Jpn. 34(1992)2-22

Variegated Fields of Research Observed by Neutrons

Watanabe N.

Techno News Tsukuba (1992)11

Chemical Short Range Structure of Amorphous Alloy Prepared by MA

Fukunaga T.

Rep. Toyota Phys. Chem. Res. Inst. 45(1992)1

Giant magnetoresistance in Cu-Co Nanogranular Alloys

Kataoka N, Kim I. J, Takeda H, Fukamichi K, Shimada Y, Okuda H, Osamura K and Furusaka M.

Dengakuron A 114(1993)797

Thermal Property and Chemical Short Range Structure for $(Ti_{76}Ni_{24})_x(Ti_{70}Cu_{30})_{1-x}$ Amorphous Alloy Synthesized by MA

Fukunaga T, Okasaka K and Mizutani U.

J.S.P.M. 40(1993)96

Structural Change of Cr-N Powders during Mechanical Alloying Process

Ishikawa E, Koyano T, Fukunaga T and Mizutani U.

J.S.P.M. 40(1993)283

Amorphization of Immiscible Cu-V System by Ma under the N_2 Gas Atmosphere

Kuroda N, Fukunaga T and Mizutani U.

J.S.P.M. 40(1993)92

Structure of Amorphous Alloys Prepared by Mechanical Alloying -Comparison with Amorphous Alloys by Liquid Quenching-

Fukunaga T.

Zairyogijutsu 11(1993)40

Interaction Parameters of Poly(vinyl methyl ether) in 2-Propanol-Water Mixture as Determined by Small-Angle Neutron Scattering

Takada M, Okano K, Kurita K and Furusaka M.

Kobunshi Ronbunshu 51(1994)689

Structurae and Dynamics of Polymer Gels by Small-Angle Scattering

Izumi Y.

Koubunshi 43(1994)878

複雑な構造を有する溶融塩の動的構造

Kamiyama T. Shibata K. Suzuki K

Materia Japan 34(1995)36

Dynamical Structure of Molten Salts with Complex Structures

Kamiyama T, Shibata K and Suzuki K.

Materia Japan 34(1995)36

低温工学協会に於ける冷凍部会の役割

Yosjiki H

低温工学 30(1995)199

17. KEK Internal

Guideline for Designing Accelerator Interlocks and Related Softy Equipments in KEK

Ishii K, Irie Y, Kobayashi K, Kobayashi H, Kondoh K, Sakai S, Takasaki M, Takeda S, Miyajima M, Ban S and Hirayama H.

KEK Internal 90-1 (Apr. 1990)

CAMAC Crate Controller for Macintosh Computer

Satoh S.

KEK Internal 90-25

Development of 8-Input Amplifier (K-AMP2) and Multi-Channel Time-Analyzer Modules (TA15 and TA16) for Nuetron Scattering Experiment

Satoh S and Furusaka M.

KEK Internal 92-4

18. Proceedings of Workshops

Proc. of the Workshop on Polymer Science Studied by Neutron Scattering (KEK, Tuskuba, Mar. 15, 1989)

Ed. Kaji K., Kurita K, Izumi Y and Furusaka M.

KEK Internal 90-3

Proc. of the Workshop on Materials Science Studied by Neutron Scattering (KEK, Tuskuba, Apr. 14-15, 1989)

Ed. Furusaka M.

KEK Internal 90-4

Proc. of the Workshop on Structure Study of Biology by X-Ray and Neutron Scattering (KEK, Tsukuba, Mar. 6-7, 1989)

Ed. Niimura N and Furusaka M.

KEK Internal 90-5

Proc. of the Workshop on Small Angle Neutron Scattering (KEK, Tuskuba, Feb. 23, 1989)

Ed. Furusaka M.

KEK Internal 90-6

TUNNEL 901 (KEK, Tuskuba, March 8, 1990)

Ed. Ikeda S.

KEK Internal 90-7

TUNNEL 902, Japan-UK collaboration on Neutron Scattering Research (KEK, Tuskuba, April 24, 1990)

Ed. Ikeda S.

KEK Internal 90-17

Proc. of The Workshop on Statistical Physics on Magnetic Materials and Neutron Scattering (KEK, Tuskuba, February 23, 19

Ed. Yoshizawa H, Arai M and Endoh Y.

KEK Internal 90-18

Proc. of the Workshop on Polymer Science Studied by Neutron Scattering (KEK, Tsukuba, Mar. 20, 1990)

Ed. Kanaya T and Furusaka M.

KEK Internal 90-26

Current Status and Future Prospects of Powder Diffraction

Ed. Kamiyama T, Asano H and Furusaka M.

Proc. of the Japan-UK Joint Meeting on Neutron Powder Diffraction (KEK, Tuskuba, April 23, 1990), KEK Internal 90-30

Proc. of the Workshop on Neutrons in Biology at KENS (1990) (KEK, Tsukuba, Sept. 29, 1990)

Ed. Niimura N and Furusaka M.

KEK Proceedings 91-11

KDP 902 (KEK, Sept. 18, 1990)

Ed. Ikeda S.

KEK Proceedings 91-3

Proc. of the Workshop on Pulsed Neutron Scattering from Magnetic Materials (KEK, Tsukuba, Mar. 28, 1991)

Ed. Ikeda H.

KEK Proceedings 91-4

Proc. of the Workshop on Scattering Experiments under Extreme Conditions (KEK, Tsukuba, Oct. 12-13, 19

Ed. Sakai N, Ikeda H and Ando M.

KEK Proceedings 91-9

Current Status and Future Prospects of Diffraction JAPAN-USA Joint Meeting -Proc. of the Japan-USA Joint Meeting on Diffraction-

Ed. Kamiyama T, Asano H and Furusaka M.

KEK Proceedings 92-1

Proc. of the Workshop on Formation of Supermolecular structures in Composite Fluid: Phase Rule and Dynamics

Ed. Tanaka F, Ohota T and Ikeda H.

KEK Proceedings 92-10

Current Status and future Prospect of Space and Time Reversal Symmetry Violation on Low Energy Neutron Reactions

Ed. Masuda Y.

KEK Proceedings 92-18

KDP 903 (KEK, Jan. 21-22, 1992)

Ed. Ikeda S.

KEK Proceedings 92-3

19. KENS Report

KENS Report-VIII (1989/90)

Ed. Ikeda H, Furusaka M and Watanabe N.

KEK Internal 90-2 M

KENS Report-IX(1991/92)

Ed. Misawa M, Masuda Y and Ikeda S.

KEK Progress Report 92-2 M

Kens Report-X(1994/95)

Itoh S, Otomo T and Ikeda H

KEK Progress Report 94-3 M (1995)

20. Proc. of Int. Conf.

Proc. of the 11th Meeting of Int. Collaboration on Advanced Neutron Sources (ICANS-XI)

Ed. Misawa M, Furusaka M, Ikeda H and Watanabe N.

(KEK Tuskuba, Oct. 22-26, 1990), Vol. 1 & 2

Members of Committees

*Chairman
**Project Manager

Committee for Booster Synchrotron Utilization Facility

NOMURA, Toru	(Univ. of Tokyo)
AKINE, Yasuyuki	(Univ. of Tsukuba)
ENDOH, Yasuo	(Tohoku Univ.)
KOBAYASHI, Shun-ichi	(Univ. of Tokyo)
NAGAMINE, Kanetada	(Univ. of Tokyo)
IKEDA, Hironobu	(KEK)
TAKADA, Koji	(KEK)
KOBAYASHI, Makoto	(KEK)
IKEDA, Susumu	(KEK)
KONDOH, Kenjiro	(KEK)
YAMANE, Isao	(KEK)

Neutron Scattering Program Advisory Committee

ENDOH, Yasuo	(Tohoku Univ.)
GO, Nobuhiro	(Kyoto Univ.)
FUJII, Yasuhiko	(Univ. of Tokyo)
MATSUO, Takasuke	(Osaka Univ.)
YAMAOKA, Hitoshi	(Kyoto Univ.)
YAMADA, Yasusada	(Waseda Univ.)
IKEDA, Hironobu	(KEK)
IKEDA, Susumu	(KEK)

Japan-UK Steering and Program Advisory Committee

ENDOH, Yasuo	(Tohoku Univ.)
GO, Nobuhiro	(Kyoto Univ.)
FUJII, Yasuhiko	(Univ. of Tokyo)
MATSUO, Takasuke	(Osaka Univ.)
YAMAOKA, Hitoshi	(Kyoto Univ.)
YAMADA, Yasusada	(Waseda Univ.)
KIMURA, Yoshitaka	(KEK)
IKEDA, Hironobu	(KEK)
IKEDA, Susumu	(KEK)
ARAI, Masatoshi	(KEK)
KIHARA, Motohiro	(KEK)